



**HAL**  
open science

# Oxygen evolution reaction at cobalt oxides/water interfaces : heterogeneous electrocatalysis by DFT-MD simulations & metadynamics

Fabrizio Creazzo

► **To cite this version:**

Fabrizio Creazzo. Oxygen evolution reaction at cobalt oxides/water interfaces : heterogeneous electrocatalysis by DFT-MD simulations & metadynamics. Other. Université Paris-Saclay, 2020. English. NNT : 2020UPASE012 . tel-02996678

**HAL Id: tel-02996678**

**<https://theses.hal.science/tel-02996678>**

Submitted on 9 Nov 2020

**HAL** is a multi-disciplinary open access archive for the deposit and dissemination of scientific research documents, whether they are published or not. The documents may come from teaching and research institutions in France or abroad, or from public or private research centers.

L'archive ouverte pluridisciplinaire **HAL**, est destinée au dépôt et à la diffusion de documents scientifiques de niveau recherche, publiés ou non, émanant des établissements d'enseignement et de recherche français ou étrangers, des laboratoires publics ou privés.

**OXYGEN EVOLUTION REACTION AT  
COBALT OXIDES/WATER INTERFACES:**  
heterogeneous electrocatalysis by DFT-MD  
simulations & metadynamics

**Thèse de doctorat de l'université Paris-Saclay**

École doctorale n° 571 Sciences Chimiques : Molécules, Matériaux,  
Instrumentation et Biosystèmes (2MIB)  
Spécialité de doctorat: Chimie  
Unité de recherche : Université Paris-Saclay, Univ Evry, CNRS, LAMBE, 91025, Evry-  
Courcouronnes, France  
Référent : Université d'Evry Val d'Essonne

**Thèse présentée et soutenue à Evry, le 03/07/2020, par**

**Fabrizio Creazzo**

**Composition du Jury**

<b>Rodolphe VUILLEUMIER</b> Professeur, École Normale Supérieure, Paris	Président
<b>Magali BENOIT</b> Directrice de Recherche, Université Toulouse 3	Rapporteuse
<b>Ali HASSANALI</b> Professeur, Institut Abdus Salam International Center – Italy	Rapporteur
<b>Nicolas ALONSO-VANTE</b> Professeur, Université de Poitiers	Examineur
<b>Christophe COLBEAU-JUSTIN</b> Professeur, Université Paris-Saclay	Examineur
<b>Fouad MAROUN</b> Directeur de Recherche, Institut Polytechnique de Paris	Examineur
<b>Marie-Pierre GAIGEOT,</b> Professeure, Université d'Evry Val d'Essonne, Université Paris-Saclay	Directrice de thèse



# Acknowledgements

First and foremost, I would like to express my most sincere gratitude to my supervisor Prof. Marie-Pierre Gaigeot, not only for her invaluable academic and research-oriented guidance, but also for giving unwavering support in all other aspects during my PhD period. She was the first, 4 years ago, to strongly believe in me and in the possibility of winning the *LabEx Charm<sub>3</sub>at* PhD founding. All started from that victory!!! I am truly grateful for that strong conviction she had. She also strongly believe not only in me but also in my scientific ideas, probably more than me.

For all this, I am very grateful! I hope that each PhD student can have a supervisor who believes in it and in his ideas, as she has done with me during all these years. She has believed in my abilities as student and researcher, and fostered my independence and creativity. I have learned so much more than just science. I will be grateful to her forever.

I am truly grateful to Magali Benoit and Ali Hassanali for accepting to be reviewers of my thesis. I am also grateful to Rodolphe Vuilleumier, Nicolas Alonso Vante, Fouad Maroun and Christophe Colbeau-Justin for accepting to be part of the jury of this thesis.

I am extremely grateful to my great friend and colleague Dr. Giuseppe Casone. He was the first, years ago, who introduce me in the scientific research world with patience, professionalism and precision. Thanks to him, I have acquired most of the research abilities and tools I have today. Without his constant and valuable support, most of the novel and fancy results presented in this thesis would never have been possible. I will be grateful to him forever.

A special thanks to my friends and colleagues Daria Galimberti and Simone Pezzotti, who were the first to welcome me into the Gaigeot group and who have always helped and supported me with the countless work problems I encountered.

I would also like to give my thanks to Dr. Franz Saija for the useful scientific discussions and for his support during my researches. Many fancy research ideas came from discussions with him.

Moreover, I want to thank all the members of the *LAMBE*-research groups by starting from the director Jean-Yves Salpin and all the people that I en-

countered during these years: Veronica, Daria, Alessandra, Inès, Anastasiia, Mélanie, Delphine, Wanlin, Flavio, Simone, Louis, Sacha, Jérôme, Mohamed, Burak, Alvaro, Yannick, Riccardo, and also all the "stagiaires" I met, *i.e.* Lise, Charles (Carlo), Vladimir, Dorian, Gurinder. With them, I shared not only a good amount of reciprocal work problems that a student/PhD has to tackle, but also a good amount of fun. Each of them, in different ways, contributed to the person I am today.

I will never forgive my friends Anaïs, Mirta, Nino and Giorgio, with whom I shared a lot of fun in Paris.

I also thank my family for their love and support, for making me the person I am today, and also for giving me all the opportunities I needed to succeed. My parents never faltered in fostering my curiosity and encouraging me unconditionally in my endeavors. I am grateful for their active presence and constant help they have given me, and that they will continue to give now that new challenges of life await me.

Funding for this PhD is gratefully acknowledged. Financial support was received from the *Laboratoire d'Excellence Charm<sub>3</sub>at*. Also some more financial support for the end of my PhD was given by the *LAMBE* laboratory, as well as from the UEVE University during the period of Covid-19 confinement in 2020.

# Abstract

In this thesis, DFT-MD simulations, coupled with state-of-the-art metadynamics techniques, are applied to gain a global understanding of  $\text{Co}_3\text{O}_4$  and  $\text{CoO}(\text{OH})$  cobalt oxide aqueous interfaces in catalyzing the oxygen evolution reaction (OER), and hence possibly help in the design of novel catalysts based on non-precious materials, a current key field of research in science and technology, especially of importance for the hydrogen economy, for green technology in a period of time with an ever more growing demand in green-energy. In this thesis, we step-by-step reveal the OER mechanisms on spinel  $\text{Co}_3\text{O}_4$  and  $\text{CoO}(\text{OH})$  cobalt aqueous electrocatalysts carefully and rationally via novel metadynamics techniques.

Up to now, the literature has never taken into account the atomistic modifications on the electrode structure as well as on the interfacial water into their modeling of OER processes. Such lack of knowledge clearly represents a significant hurdle toward the development of improved catalysts, which could be overcome by employing methods able to track the catalytic features of the OER at the atomistic scale. For the first time, we show how important it is to take into consideration the presence of the liquid water environment in the structural characterization of catalyst surfaces, i.e. for (110)- $\text{Co}_3\text{O}_4$  and (0001)- $\text{CoO}(\text{OH})$  in this work. A detailed characterization of chemical and physical properties of the aqueous interfaces is provided (*i.e.* structure, dynamics, spectroscopy, electric field), for the (110)- $\text{Co}_3\text{O}_4$  and (0001)- $\text{CoO}(\text{OH})$  aqueous surfaces.

A study of the OER is presented not only by looking at the catalysts, but also by addressing the role of the water environment in the catalytic process, not done before in literature. Accordingly, both gas-phase and liquid-phase OER are here investigated at the (110)- $\text{Co}_3\text{O}_4$  and (0001)- $\text{CoO}(\text{OH})$  adopting a novel enhanced sampling metadynamics approach able to address a wide range of chemical reaction mechanisms and to fully include the role of the solvent degrees of freedom, allowing to unveil reaction networks of remarkable complexity. The energetics, kinetics and thermodynamics behind the OER are therefore found at these cobalt oxide surfaces.

To the best of our knowledge, we identify for the first time that water act as OER co-reactant and co-catalyst, and hence show that this coupled water behaviour is crucial in lowering the OER free-energy barrier. The present study

not only provides an innovative state-of-the-art theoretical/computational strategy for the investigation of the OER, but it proves that the synergistic effect between surface catalyst and water environment can be the basis for a rational design of novel catalysts based on non-precious materials for the electrochemically-driven OER.

Furthermore, in this thesis, the water dissociation and proton transfer phenomena are investigated by applying external electric fields in different H-bonded systems such as air-water interface and electrolyte solutions.

This PhD thesis, funded by the *Laboratoire d'Excellence Charm<sub>3</sub>at*, is part of a partnership in between simulations (Evry University-UEVE) and electrochemical characterization experiments performed in Ph. Allongue and F. Maroun group at the *Institut Polytechnique de Paris*.

# Abstract (french version)

Dans cette thèse, des simulations DFT-MD couplées à des techniques innovantes de métadynamique, sont appliquées pour acquérir une compréhension globale des interfaces aqueuses d'oxyde de cobalt  $\text{Co}_3\text{O}_4$  et  $\text{CoO}(\text{OH})$  dans la catalyse de la réaction d'évolution de l'oxygène (OER), et ainsi éventuellement aider à la conception de nouveaux catalyseurs basés sur des matériaux non précieux, un domaine clé de la recherche scientifique et technologique, particulièrement important pour l'économie de l'hydrogène, pour les technologies vertes dans une période de temps avec une demande toujours plus croissante en énergie verte. Dans cette thèse, nous révélons étape par étape les mécanismes de l'OER sur les électrocatalyseurs aqueux d'oxyde de cobalt  $\text{Co}_3\text{O}_4$  et  $\text{CoO}(\text{OH})$  via de nouvelles techniques de métadynamique.

Jusqu'à présent, la littérature n'a jamais pris en compte les modifications au niveau atomique de la structure des électrodes ainsi que de l'eau interfaciale dans leur modélisation des processus OER. Ce manque de connaissances représente clairement un obstacle important au développement de catalyseurs améliorés, qui pourrait être surmonté en utilisant des méthodes capables de suivre les caractéristiques catalytiques de l'OER à l'échelle atomique. Pour la première fois, nous montrons combien il est important de prendre en considération la présence de l'environnement aqueux dans la caractérisation structurale des surfaces du catalyseur, c'est-à-dire (110)- $\text{Co}_3\text{O}_4$  et (0001)- $\text{CoO}(\text{OH})$  dans ce travail. Une caractérisation détaillée des propriétés chimiques et physiques des interfaces aqueuses est fournie (la structure, la dynamique, la spectroscopie, le champ électrique), pour les surfaces (110)- $\text{Co}_3\text{O}_4$  et (0001)- $\text{CoO}(\text{OH})$  en contact avec l'eau liquide.

Une étude détaillée de l'OER est présentée non seulement du point de vue des catalyseurs, mais aussi en abordant le rôle de l'environnement de l'eau dans le processus catalytique, ce qui n'a pas été fait auparavant dans la littérature. En conséquence, l'OER en phase gazeuse et en phase liquide sont étudiés ici aux interfaces aqueuses (110)- $\text{Co}_3\text{O}_4$  et (0001)- $\text{CoO}(\text{OH})$  en adoptant une nouvelle approche de métadynamique d'échantillonnage amélioré, capable d'identifier et caractériser les mécanismes de réaction chimique et d'intégrer pleinement le rôle des degrés de liberté du solvant, permettant ainsi de dévoiler des réactivités chimiques d'une complexité remarquable. L'énergétique, la cinétique et la thermodynamique derrière l'OER sont donc trouvées à ces surfaces d'oxyde de cobalt à l'interface avec l'eau.

Au meilleur de nos connaissances, nous identifions pour la première fois que l'eau agit comme co-réactif et co-catalyseur pour l'OER, et montrons que ce comportement couplé de l'eau est crucial pour abaisser la barrière d'énergie libre requise pour l'OER. Cette étude fournit non seulement un état des lieux innovant des stratégies théoriques/computationnelles pour caractériser l'OER, mais cela prouve que l'effet synergique entre le catalyseur de surface et l'environnement de l'eau peut être la base d'une conception rationnelle de nouveaux catalyseurs basés sur des matériaux non précieux pour l'électrochimie de l'OER.

En outre, dans cette thèse, la dissociation de l'eau et les phénomènes de transfert de protons ont été étudiés en appliquant des champs électriques externes dans différents systèmes "H-bonded", comme l'interface air-eau et en solutions d'électrolytes.

Cette thèse de doctorat, financée par le *Laboratoire d'Excellence Charm<sub>3</sub>at*, fait partie d'un partenariat entre simulations (Evry University-UEVE) et expériences de caractérisation en conditions électrochimiques réalisées dans le groupe de Ph. Allongue et F. Maroun à l'*Institut Polytechnique de Paris*.

# Contents

<b>Full List of Publications</b>	<b>1</b>
<b>1 Introduction to the need of a hydrogen economy</b>	<b>3</b>
1.1 General Context . . . . .	3
1.2 Hydrogen Economy . . . . .	8
1.3 Aim of our research and objectives . . . . .	12
<b>2 Fundamentals of Density Functional Theory (DFT) and First Principles/Ab-Initio Molecular Dynamics Simulations (FPMD/ AIMD/DFT-MD)</b>	<b>17</b>
2.1 Physics of many-body systems . . . . .	18
2.2 Adiabatic Born-Oppenheimer approximation . . . . .	19
2.3 Towards the DFT ( <i>Density Functional Theory</i> ) approach . . . . .	20
2.4 The role of density: the Hohenberg-Kohn theorem . . . . .	21
2.5 The exchange and correlation functional: the Kohn-Sham scheme	22
2.6 Ladder of Functionals . . . . .	23
2.7 Born-Oppenheimer Molecular Dynamics (BOMD) . . . . .	25
2.7.1 NVE ensemble . . . . .	27
2.7.2 NVT ensemble . . . . .	27
2.7.3 Periodic boundary conditions . . . . .	28
2.7.4 PBE+U functional . . . . .	29
2.7.5 BLYP functional . . . . .	31
2.7.6 Dispersion corrections . . . . .	32
2.8 Dual GPW representation in CP2K/Quickstep . . . . .	33
2.8.1 Gaussian basis set . . . . .	33
2.8.2 Pseudopotentials . . . . .	34
2.8.3 Plane Wave basis set . . . . .	34
2.9 Metadynamics and Collective variables . . . . .	35
2.9.1 Generalities on metadynamics technique . . . . .	35
2.9.2 Path collective variables with a new definition of distance metric . . . . .	38
2.10 Umbrella sampling . . . . .	45
2.11 Static electric fields in ab initio simulations . . . . .	45
<b>3 Oxygen Evolution Reaction (OER): principles of thermodynamics</b>	<b>49</b>
3.1 Thermodynamics of the Water Splitting Reaction . . . . .	50

3.2	Principles in Water Electrolysis . . . . .	52
3.3	History of Photocatalysis and Electrolysis . . . . .	55
3.4	Water electrolysis by Proton-Exchange Membranes (PEM) . . . . .	56
3.5	Volcano Plot . . . . .	59
<b>4</b>	<b>Literature Review for the OER</b>	<b>63</b>
4.1	Manganese oxides-Experiments . . . . .	64
4.2	Perovskite oxides-Experiments . . . . .	65
4.3	Nickel and Iron based oxides-Experiments . . . . .	67
4.4	Nanocarbon composite OER catalysts -Experiments . . . . .	69
4.5	Amorphous metal catalysts-Experiments . . . . .	70
4.6	Cobalt-Oxide films as OER catalysts-where it all began . . . . .	72
4.7	Graphene and Carbon Nanotube as Supports for Co-Oxides- Experiments . . . . .	74
4.8	(110)- $Co_3O_4$ as OER catalysts-Experiments . . . . .	76
4.9	Oxidation of $Co_3O_4$ in OER operando conditions-Experiments . . . . .	77
4.10	Surface Reversible Structural Transformation of $Co_3O_4/CoO_x(OH)_y$ - Experiments . . . . .	77
4.11	$Co_3O_4$ -(111)/ $CoO(OH)$ -(001) transition -Experiments . . . . .	79
4.12	$CoO(OH)$ and $Co_3O_4$ catalytic OER performances-Experiments . . . . .	81
4.13	General Insights about $Co_3O_4$ bulk structure-Theory . . . . .	84
4.14	Hubbard Term in DFT-calculations for $Co_3O_4$ -Theory . . . . .	85
4.15	$Co_3O_4$ Bulk Electronic Structure-Theory . . . . .	87
4.16	(110)- $Co_3O_4$ Cut of $Co_3O_4$ oxide-Theory . . . . .	89
4.17	Water adsorption on the (110)- $Co_3O_4$ surface-Theory . . . . .	91
4.18	Oxygen Evolution Reaction at the (110)- $Co_3O_4$ surface-Theory . . . . .	93
4.19	General insights about Cobalt Oxyhydroxide $CoO(OH)$ bulk structure-Theory . . . . .	94
4.20	Theoretical investigation of the OER activity of cobalt oxides $CoO(OH)$ . . . . .	96
4.21	What simulations do we propose? . . . . .	101
<b>5</b>	<b>DFT-MD of (110)-<math>Co_3O_4</math>/water interface: how the water is organized at this interface in non operando conditions</b>	<b>105</b>
5.1	Computational methods . . . . .	107
5.2	$Co_3O_4$ cobalt oxide bulk properties . . . . .	110
5.3	Cutting along the (110) direction: A- and B-terminations in contact with liquid water . . . . .	113
5.4	$Co_3O_4$ cobalt surface at the interface with liquid water . . . . .	118
5.5	Water structure at the $Co_3O_4$ cobalt oxide/liquid water inter- faces: A- vs B-termination . . . . .	121
5.6	Physical observables: electric field, surface work function & SFG vibrational spectroscopy at the interface . . . . .	127
5.7	Discussion and perspectives . . . . .	131

<b>6</b>	<b>OER at the aqueous (110)-<math>\text{Co}_3\text{O}_4</math> oxide by metadynamics DFT-MD</b>	<b>135</b>
6.1	Computational methods and application to the OER at the $\text{Co}_3\text{O}_4$ /liquid water interface . . . . .	136
6.2	Selection of OER active sites at the A- and B- (110)- $\text{Co}_3\text{O}_4$ surfaces for the MetD DFT-MD . . . . .	141
6.3	OER mechanisms, kinetics and thermodynamics from metadynamics DFT-MD . . . . .	146
6.3.1	OER at the B-(110)- $\text{Co}_3\text{O}_4$ /vacuum interface . . . . .	147
6.3.2	OER at the B-(110)- $\text{Co}_3\text{O}_4$ aqueous interface . . . . .	152
6.4	Discussion and perspectives . . . . .	156
<b>7</b>	<b>OER at the aqueous (0001)-<math>\text{CoO(OH)}</math> oxide by metadynamics DFT-MD</b>	<b>159</b>
7.1	Computational details . . . . .	159
7.2	$\text{CoO(OH)}$ cobalt oxide bulk properties . . . . .	161
7.3	(0001)- $\text{CoO(OH)}$ Cut of $\text{CoO(OH)}$ oxide . . . . .	164
7.4	Water structure at the (0001)- $\text{CoO(OH)}$ /liquid water interface . . . . .	167
7.5	OER mechanisms, kinetics and thermodynamics at the (0001)- $\text{CoO(OH)}$ surface . . . . .	170
7.6	Conclusions and Comparison between the (110)- $\text{Co}_3\text{O}_4$ and (0001)- $\text{CoO(OH)}$ oxides . . . . .	177
<b>8</b>	<b>Electrified H-bonded systems</b>	<b>181</b>
8.1	Electric field applied on the air/water interface - Introduction . . . . .	182
8.2	Computational methods . . . . .	183
8.3	Enhanced conductivity of water at the electrified air-water interface . . . . .	186
8.4	The 2-dimensional network (2DN) at the electrified air-water interface . . . . .	188
8.5	The role of the electrified BIL-water in the proton hopping water wires . . . . .	190
8.6	Conclusions . . . . .	193
8.7	Other works performed during this PhD/ Electric field applied on monovalent and divalent electrolyte water solutions . . . . .	195
<b>9</b>	<b>Summary, conclusions, perspectives</b>	<b>227</b>
	<b>Appendix</b>	<b>236</b>
	<b>Bibliography</b>	<b>276</b>



# Full List of Publications

1. DFT-MD of the (110)-Co<sub>3</sub>O<sub>4</sub> cobalt oxide semiconductor in contact with liquid water, preliminary chemical and physical insights into the electrochemical environment.  
F. Creazzo, D. Galimberti, S. Pezzotti, M. P. Gaigeot.  
*J. Chem. Phys.*, 150, 041721, **2019**;
2. Enhanced conductivity of water at the electrified air-water interface: a DFT-MD characterization.  
F. Creazzo, S. Pezzotti, S. Bougueroua, A. Serva, J. Sponer, F. Saija, G. Cassone, and M. P. Gaigeot.  
*Phys. Chem. Chem. Phys.*, 22, 10438, **2020**;
3. Ions Tune Interfacial Water Structure and Modulate Hydrophobic Interactions at Silica Surfaces.  
A. Tuladhara, S. Dewana, S. Pezzotti, F. S. Brigiano, F. Creazzo, M.-P. Gaigeot and Eric Borguet.  
*J. Am. Chem. Soc.*, 142, 15, 6991-7000, **2020**;
4. A novel water-assisted electrochemical route toward the Oxygen Evolution Reaction at the (110)-Co<sub>3</sub>O<sub>4</sub> cobalt oxide surface: a DFT-MD and metadynamics investigation.  
F. Creazzo, G. Cassone, D. Galimberti, S. Pezzotti, J. Sponer, M. P. Gaigeot.  
*In Preparation, to be submitted.*

We report hereafter the 4 published works performed during my PhD period, as a result of a personal scientific collaboration with Prof. A. M. Saitta at Sorbonne University-Paris and Dr. F. Saija at CNR-IPCF in Messina-Italy. I have continued these collaborations during my PhD period at UEVE.

5. Ab-initio molecular dynamics study of NaCl water solutions under an external electric field.  
G. Cassone, F. Creazzo, P. V. Giaquinta, F. Saija, A. M. Saitta.

*Phys. Chem. Chem. Phys.*, 18, 23164-23173, **2016**;

6. Ionic diffusion and proton transfer in aqueous solutions of alkali metal salts.

G. Cassone, F. Creazzo, P. V. Giaquinta, J. Sponer, F. Saija.

*Phys. Chem. Chem. Phys.*, 19, 20420-20429, **2017**;

7. Ionic Diffusion and Proton Transfer in Aqueous Solutions under an Electric Field: State-of-The-Art.

F. Creazzo.

*Editorial in J. Mol. Sci.* Vol. 1, No. 1:2, **2017**;

8. Ionic diffusion and proton transfer of  $MgCl_2$  and  $CaCl_2$  aqueous solutions: an ab initio study under electric field.

G. Cassone, F. Creazzo, F. Saija.

*Mol. Simul.*, Special Issue 1-8, Vol. 40, **2018**.

# Chapter 1

## Introduction to the need of a hydrogen economy

### 1.1 General Context

The biggest (or one of the biggest) issue that the world human population faces in this and in the next century is the urgent need for clean and renewable technologies. Nowadays, the main energy source of our modern societies is given by fossil fuels which support industries and economic growth.

According to the energy consumption distribution statistics reported by the U.S. energy information administration in Fig. 1.1, fossil fuels such as coal, natural gas and crude oil account for about 80% in primary energy usage in the world, making up the majority of the total energy consumption. The statistics scream out that 10,000 million tons of petroleum were consumed in the 2000s (up to now) which is presumably to be doubled by 2030 as predictions show [1].

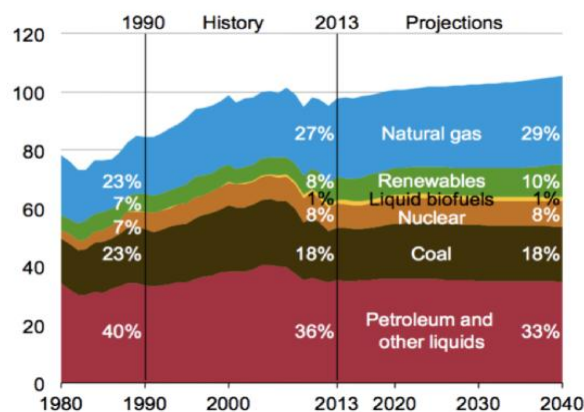


Figure 1.1: *Projected world energy consumption distribution. From U. S. E. I. Administration, Annual Energy Outlook, 2015 [1].*

Moreover, despite the fast speed of extraction, the formation and accumulation of fossil fuels require millions of years. Therefore, most of the fuels we

are mining and burning today were formed millions of years ago. Accordingly, fossil fuels are limited resources and unevenly distributed around the world, and therefore they are not enough to fix the increasing and huge energy world demand in the long term.

Fossil fuels are estimated to be the driving energy source for the following several decades only, thus boosting the current price of fossil fuels, especially the oil price, affecting the global economy and politic in a non beneficial way.

Based on all these data, the estimations indicate that fossil fuels are currently at their peak of supplies. Furthermore, a huge amount of polluting gases and micro-particles are generated/released during coal-firing, petroleum burning and industrial processes. The main pollutant from the petroleum treatment and industries is  $CO_2$ . Some researchers estimate that approximately one billion tons of  $CO_2$  would be produced and emitted into the atmosphere by the year 2053 if the situation is left without any human intervention [2, 3]. See Fig. 1.2 for projected greenhouse gas concentrations.

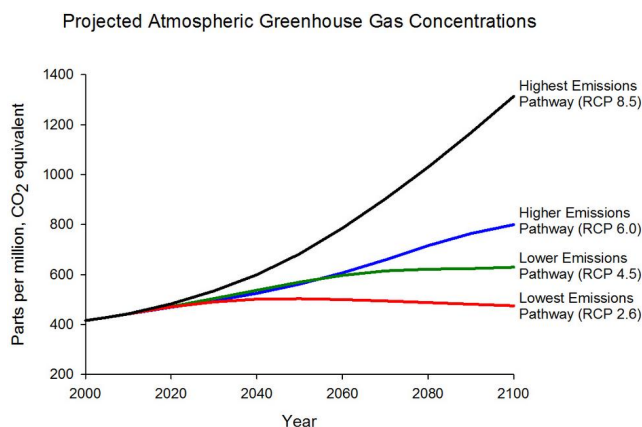


Figure 1.2: *Projected greenhouse gas concentrations for four emission pathways. The top pathway assumes that greenhouse gas emissions will continue to rise throughout the current century. The bottom pathway assumes that emissions reach a peak between 2010 and 2020, declining thereafter. Source: graph created from data in the Representative Concentration Pathways Database (Version 2.0.5) <http://www.iiasa.ac.at/web-apps/tnt/RcpDb>.*

Our societies face terrible environmental issues. It turns out that the increase in the average worldwide temperature, known as global warming, is related to the growth of  $CO_2$  concentration in the atmosphere over the years. Carbon-dioxide  $CO_2$  and methane  $CH_4$  are nowadays major greenhouse gases produced as a result of fossil fuels consumption. As greenhouse gases,  $CO_2$  and  $CH_4$  are very difficult to be reduced from the atmosphere, and thus the rise up in the global temperature and the increase in the global warming problem as shown in Fig. 1.3.

Statistics estimations predict an additional increase by 0.3 - 1.7 °C in the best case and 2.6 - 4.8 °C for the worst scenario in 2100's, which implies non-negligible effects on physical, ecological, and social systems, like extreme weather with high temperatures and larger precipitation [5, 6, 7]. Models

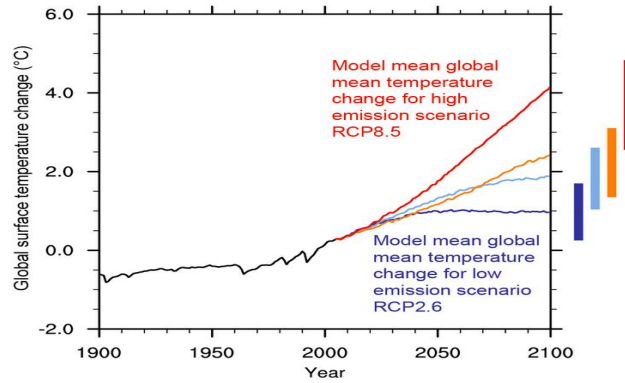


Figure 1.3: *Observed and projected changes in global average temperature under four emission pathways. The vertical bars at the right side show likely ranges in temperature by the end of the century, while the lines show projections averaged across a range of climate models. Changes are relative to the 1986-2005 average. Source:[4]*

predict a sea level increase by 1 - 4 m so that coastal regions (containing much of the world's major cities) and island nations (such as e.g. Maldives) will be completely flooded [5]. Moreover, dangerous effects on marine and sea life up to mammals will arise, which consequently implies distortions on social systems based on food security and water resources in areas negatively affected by the increasing global warming.

The global warming is thus primarily caused by anthropogenic activities that include emission of greenhouse gases and aerosols as well as mass man-made ecological changes such as deforestation [5, 8]. **The environmental concerns will not be eliminated from the root unless a revolutionary energy solution is developed.**

Our modern societies and industries thus need to progressively leave out the polluting industrial processes related to the petroleum treatment and consumption and start to find alternative energy sources, possibly based on green-energy and renewable sources, in order to face the increasing environmental issues.

Taking into account the huge progress in hydraulic fracturing technology, the exploration and production of shale gas has experienced rapid growth over the last decade. The natural gas started to be considered a new abundant supply of less polluting energy than traditional fossil fuels, however, regardless of the large amount of technically recoverable sources and the expected trend of continuous growth in production, shale gas is still a limited, unevenly distributed source. Shale gas, as additional energy supply to traditional fossil fuels, is thus not the ultimate solution to power the world in the long run.

Thus the full alternative is in the development of green-energy, renewable fuels, currently indeed undergoing intensive research. Biomass, hydropower, wind power, solar energy, and other renewable energy sources have been estimated to contribute to almost 20% of the global final energy consumption

in 2016, see Fig. 1.4. The 2018 European law imposes a 28% reduction in  $CO_2$  and methane  $CH_4$  emissions by 2050, and accordingly renewable energy sources have to contribute to almost 60-70% of the global final energy consumption. Therefore, developing renewable energies nowadays becomes a key field in science and technology, see Fig. 1.5.

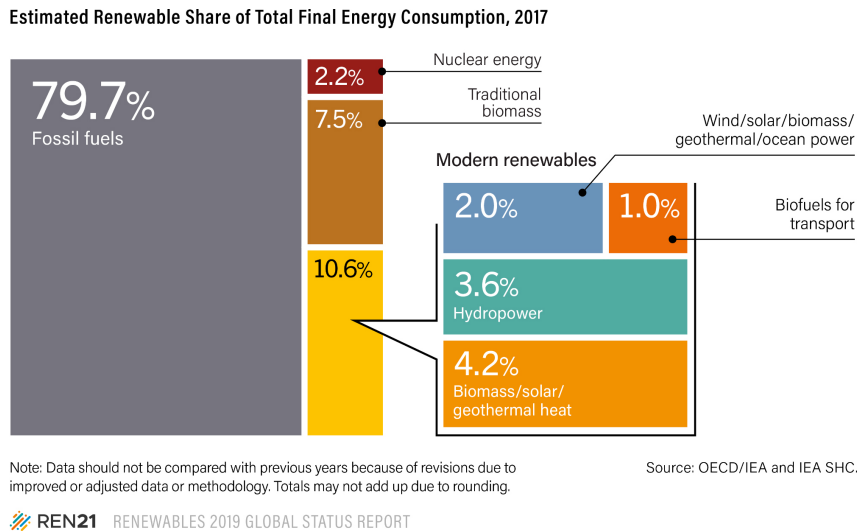


Figure 1.4: Data on global usage of fossil fuels and renewable energy.

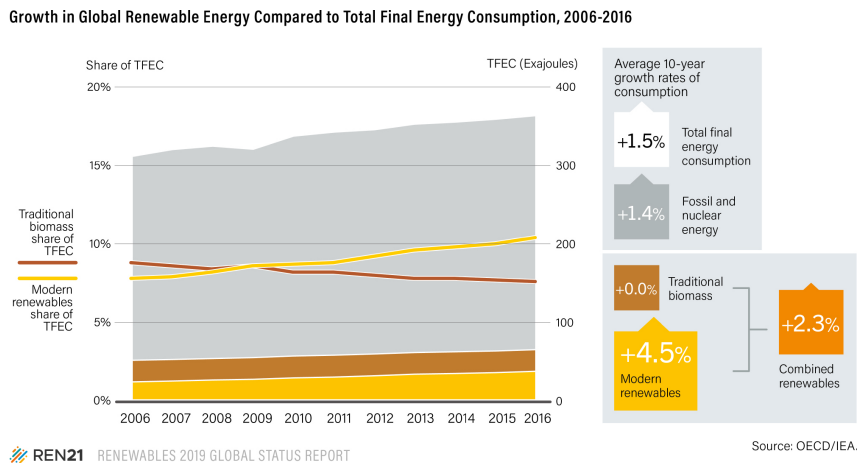


Figure 1.5: Data in the growth in global renewable energy usage compared to total final energy consumption.

In this context, the demand and confidence in renewable-green-energy development are reflected in the fast increase of money investment, in particular starting from 2013 for which the largest increase could be seen, as shown in Fig. 1.6.

The most attractive renewable energy source would be solar, considering sunlight irradiates almost everywhere, it is abundant, widely-distributed, and

Global New Investment in Renewable Energy by Technology, Developed and Developing Countries, 2014

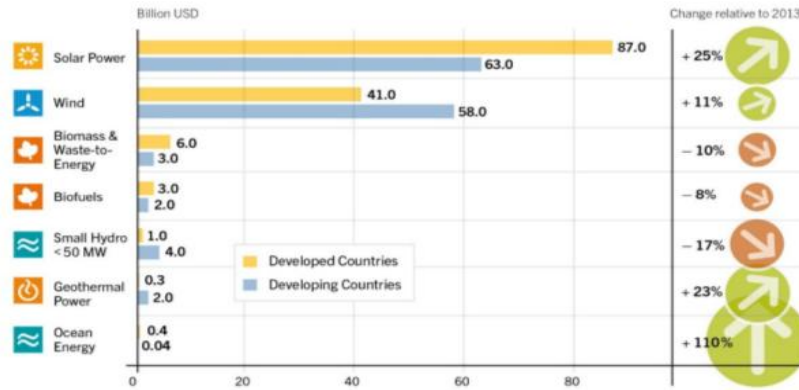
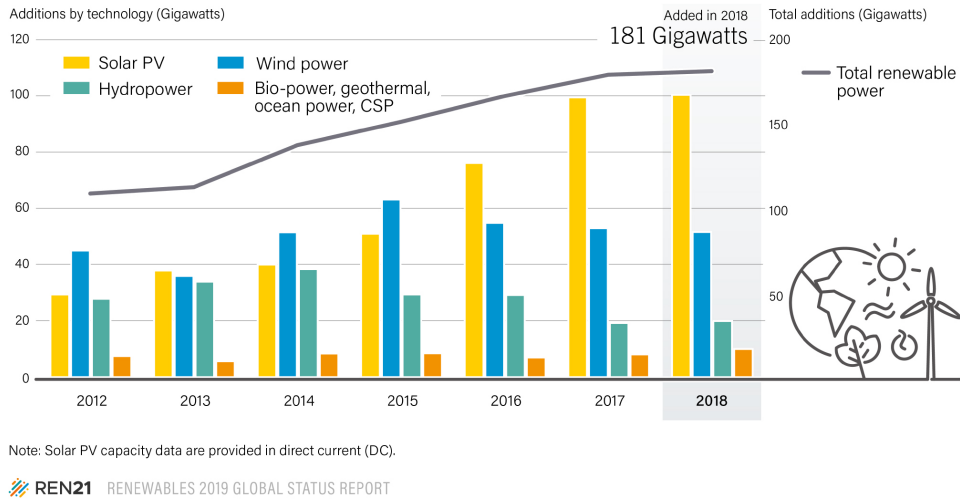


Figure 1.6: Data on global new investment in renewable energies by technology in developed and developing countries. Adapted from Renewable Energy Policy Network for the 21<sup>st</sup> century (<http://www.ren21.net/status-of-renewables/global-status-report/>).

basically free [9, 10]. Approximately about 128,000 ZJ ( $10^{21}$  J) of solar radiation arrives on the Earth every year (source: <http://gcep.stanford.edu/research/exergy/resourcechart.html>), which is converted to around 100 GigaWatts of annual power as shown in Fig. 1.7.

Annual Additions of Renewable Power Capacity, by Technology and Total, 2012-2018



Note: Solar PV capacity data are provided in direct current (DC).

REN21 RENEWABLES 2019 GLOBAL STATUS REPORT

Figure 1.7: Annual additions of renewable capacity.

The sun radiation is expected to be converted into electrical power directly by using photovoltaics, however the big issue of the intermittent solar flux requires the development of technological devices able to store solar electricity. Big efforts have been (and are still) devoted to the development of electrical energy storage technologies such as batteries and super conductors [11]. While batteries are widely used for energy storage in portable electronics and elec-

trical vehicles, they may not be suitable for large-scale applications due to the poor cost effectiveness and technical barriers in scaling up.

Alternatively, the electrical power generated from solar cells can be utilized to produce hydrogen through water electrolysis and store the energy in a chemical form [12, 13]. The obtained hydrogen can then be used to power fuel cells and produce electricity for further use.

Considering hydrogen as the main carrier of global energy, the technology combination of solar cells, electrolyzers and fuel cells represent the only renewable energy scheme based on electrochemical energy conversion and storage which could be able to replace our addiction on fossil fuels and mitigate carbon dioxide emissions [14, 15, 16].

As a result of these new technologies, major changes in the current technology infrastructures are required. Accordingly, in the last decades a great increase of interest and financial investments have been directed towards the so-called 'hydrogen economy'.

## 1.2 Hydrogen Economy

The term hydrogen economy was coined by John Bockris during a talk he gave in 1970 at General Motors (GM) Technical Center [17].

A hydrogen economy was proposed by the University of Michigan to solve some of the negative effects of using hydrocarbon fuels where the carbon is released into the atmosphere (as carbon dioxide, carbon monoxide, unburnt hydrocarbons, etc.). Modern interest in the hydrogen economy can generally be traced to a 1970 technical report by Lawrence W. Jones of the University of Michigan [18]. **The hydrogen based-economy is the use of hydrogen as carbon fuel, particularly for heating, hydrogen vehicles [19], seasonal energy storage and long distance transport of energy [20] in order to phase out fossil fuels and limit global warming.**

**Hydrogen is not found in pure form on Earth, however, it can be produced from other compounds such as natural gas, biomass, alcohols or water. In all cases it takes energy to convert these into pure hydrogen.**

Currently, hydrogen is most commonly produced from natural gas. In this situation, a typical fuel cell car generates 70-80 g of  $CO_2$  for each kilometer driven, similar to the  $CO_2$  generated by a modern gasoline hybrid or to a battery electric vehicle charged with today's UK grid electricity. These emissions can be reduced towards zero if the hydrogen is produced using low-carbon electricity sources such as renewables, nuclear or carbon capture and storage (CCS) technology to electrolyse water.

In June 2018, the France Minister for Ecological and Inclusive Transition Nicolas Hulot vowed to make France a world leader in hydrogen as he unveiled a 100 million euros investment plan for the hydrogen technology. Meanwhile, Hydrogene de France (HDF) promotes a 90 million euros investment in a hydrogen project in French Guiana. Paris has emerged as one of the place of

the hydrogen economy, next to Japan, Germany, California, along with Korea and China. September 2019 saw the French country deploying its first hydrogen-powered passenger bus, see Fig. 1.8, and in October 2019 the Auvergne Rhône-Alpes region committed 200 million euros toward 1000 hydrogen vehicles and 15 electrolyzers, to cite just two recent examples of progress into the hydrogen technology and economy.



Figure 1.8: *The hydrogen bus operates in the French city of Pau in the south of France since September 2019.*

The French industrial giant *Air Liquide* (Fig. 1.9) announced plans to make renewably produced liquid hydrogen at an upcoming plant near Las Vegas-USA. The company said its facility will have a production capacity of 30 tons of liquid hydrogen a day. Most of this would be destined to California, where there are plans for 200 hydrogen filling stations by 2025.



Figure 1.9: *The Air Liquide company adds two hydrogen stations in Ile-de-France in 2018.*

”Germany saw hydrogen potentially being used in various applications, including transport, and to decarbonize industries”– Martin Hablutzet said, head

of strategy at Siemens in Australia. The German country, already a front-runner in hydrogen technology development, is aiming to up its game with plans for 20 research labs, with a total budget of 100 million euros, being unveiled over the summer 2020. "Hydrogen is one of the hottest topics in the energy transition in the country at the moment"— Inga Posch said in August 2019, managing director at FNB Gas, the federation of Germany's gas network operators.

In september 2019, the U.K. government unveiled a 12 billion euros plan to use 4 gigawatts of offshore wind for renewable hydrogen production in the early 2030s. Meanwhile, U.K. hydrogen interests have been attracting international attention in 2019, with the chemicals giant Linde paying 38 million euros for a 20% stake in listed technology developer ITM Power.

While the U.S. as a whole barely merits a mention in terms of green hydrogen development, one state, California, is racing to become a world-leading market. California's interest in hydrogen is driven partly by aggressive decarbonization targets, including phasing out all diesel or natural-gas-powered buses by 2040, and partly by the presence of some of the industry's most high-profile technology developers. Foremost among these is Silicon Valley-based fuel-cell maker Bloom Energy.

In 2017, the San Francisco meeting was the first U.S. gathering of the Hydrogen Council, established as a CEO-led coalition of leading companies in the energy, transport and industrial sectors. The coalition had a chance to welcome 14 new members, alongside its founding members which include Air Liquide, Airbus, Air Products, Cummins, EDF, Johnson Matthey, KOGAS, SINOPEC, Thyssenkrupp, AFC Energy, Mitsubishi Heavy Industries Ltd., Re-Fire Technology, Sumitomo Mitsui Banking Corporation, Sumitomo Corporation, and Southern California Gas. The coalition has quadrupled in memberships over the past year.

The Hydrogen Council sees the potential for hydrogen to power at least 10 million cars and 500,000 trucks by 2030, as well as tap into emerging uses in feedstocks, heating and power for buildings, power generation and storage and mostly helping decarbonizing the key industries and other heavy transportation sectors. Annual demand for hydrogen could increase tenfold by 2050 to meet 18% of the total final energy demand in order to meet the 2-degree cap of the Paris Agreement on Climate Change

Some scientists, including late cosmologist and theoretical physicist Stephen Hawking, have said threats such as nuclear war and climate change are so serious humans may have to eventually leave the Earth in order to survive as a species. Briton Stanley Whittingham, awarded the 2019 Nobel Prize for Chemistry along with American John Goodenough and Akira Yoshino of Japan for inventing the lithium-ion battery, said a pragmatic approach was needed to the climate crisis.

Again, nobel laureate and former Energy Secretary, Professor Steven Chu, arrived in "grand style" as the keynote speaker to the 232nd ECS meeting via the world's first commercially available fuel cell electric vehicle – the very first at any ECS conference! –. His entrance, in Fig. 1.10, was particularly fitting as electrochemistry was at the heart of enabling this technology, and the celebration of National Hydrogen and Fuel Cell Day was on October 8th 2017 (aptly chosen for the atomic weight of hydrogen (1.008)).



Figure 1.10: *Professor Steven Chu's entry to the ECS meeting via fuel cell electric vehicle on October 8th 2017.*

At his keynote speech, Professor Chu spoke of exciting advances in the carbon-free production of hydrogen and CO from electrochemical reduction of  $CO_2$  to  $H_2$ , and CO being the first step to the production of liquid fuels.

The hydrogen economy, despite it is nowadays still not a reality in our daily life, is the future economy we must accept in our life by the european laws in the coming decades. Accordingly, in the european law of 2018, Europe must sell its last internal combustion engine car in the early 2030s (within 10 years from today), with the goal to decarbonise its transportation by 2050, and achieve the environmental target of the *Paris agreement* signed in 2018. The EU can most easily achieve a zero-emission fleet by switching to battery-electric and hydrogen cars as the analysis by green transport group Transport and Environment (TandE) shows.

But even an ambitious package of demand reduction measures will only deliver, at most, a 28% reduction in emissions by 2050. The heavy lifting in terms of emission reductions requires a shift to zero-emission vehicles by 2035 at the very latest. Any remaining combustion engine cars still on the road in 2050 will need to be banned.

Nowadays, there are three fuel cell car models commercially available in limited regions with a driving range of up to 360 miles, with a few minutes to refuel.

*PlugPower* is making commercially viable hydrogen fuel cells a reality, today. The company has deployed more than 16,000 fuel cells in electric and

hydrogen industrial vehicles, accumulating more than 150 million hours of runtime with customers like Amazon, Walmart and BMW. Customers have performed more than 8.5 million hydrogen fuelings, that's 12,000 fuelings every day, from more than 50 hydrogen stations and 200 fueling dispensers across the United States.

**Hydrogen has thus the potential to decarbonise electricity generation, transport and heat. That's because when produced by electrolysis - using electricity to split water ( $H_2O$ ) into hydrogen and oxygen -, hydrogen does not produce any pollutants.** However, currently only 4% of global hydrogen is produced by electrolysis, whereas 96% is produced by reforming methane ( $CH_4$ ), a process which ultimately produces carbon dioxide  $CO_2$  (9 kg of  $CO_2$  for 1 kg of hydrogen produced). Electrolysis (4%) produces no carbon emissions, but due to inadequate and less efficient electrolyzers and capture and storage devices (CCS), the cost of such a hydrogen production is still too high.

**Hydrogen clearly has several potential uses, but more research, particularly in production, transport and safety, is needed before we can use it at much larger scale.**

### 1.3 Aim of our research and objectives

Water electrolysis has been proposed as a promising technology for the production of  $H_2$  that can be directly used as the clean fuel. A promising technology toward the large-scale production of renewable fuel is the electrochemical water splitting [21, 22] involving both the Oxygen Evolution Reaction (OER) capable to efficiently catalyze water oxidation into  $O_2$  and the Hydrogen Evolution Reaction (HER) to produce  $H_2$ .

However, the efficiency of the electrolyser is mainly determined by the potential cost needed at the anode side, where the oxygen evolution reaction (OER) is a thermodynamic up-hill reaction, which usually requires a high potential to drive the reaction. Extensive research on this subject has shown that the potential needed to split water at rates provided, for example, by the solar flux (*e.g.*, 10 mA/cm<sup>2</sup>) [23] is limited primarily by the OER [24, 25]. Currently, most of the OER catalysts are based on noble metal oxides such as iridium oxide  $IrO_2$ , ruthenium oxide  $RuO_2$  and platinum oxide  $PtO_2$  [26, 27, 28]. The disadvantage of using these materials and their large-scale deployment is hindered by their rareness and high cost. Thus, efficient and earth-abundant electrocatalysts for high-performance OER are essential for the development of sustainable energy conversion technologies.

The aim of this thesis is to help in the modelling of highly efficient and low cost OER catalyst materials based on non-precious metals as possible substitutes for the currently employed expensive noble metal based catalysts, which would ultimately enable the large-scale implementation of electrolytic water splitting devices. In particular, transition metal oxides and hydroxides based on cobalt (Co), have shown promising electrocatalytic activity towards the

oxygen evolution reaction (OER) and the hydrogen evolution reaction (HER).

Spinel cobalt oxide  $Co_3O_4$  and its hydroxide  $CoO(OH)$  (heterogenite) are earth-abundant elements which have been already studied as effective OER electrolysers due to their competitive activity compared to the expensive noble catalysts. These cobalt catalysts will be here modelled following the designing guidelines established by investigating the influence of surface area, morphology, and substrates of materials that provide a decent OER efficiency and importantly long-term stability.

Quantum mechanical simulations based on Density Functional Theory (DFT) have become an extremely powerful tool to understand, predict and design the properties of these complex materials or devices. Simulation of the catalytic and electrochemical processes can provide significant data to help develop new materials for energy storage or for energy conversion. A rational catalyst design starts from understanding the processes that occur at the atomic level following the important aspects related to catalysis: how active, selective and stable a catalyst is. DFT allows these insights and can be used to test directly a large range of catalysts, fast and efficiently, with the possibility to develop different models that can be summarized in a series of descriptors [29].

In our studies, DFT-based molecular dynamics simulations are used to reveal step-by-step the OER mechanisms on spinel cobalt oxide  $Co_3O_4$ -(110) and its hydroxide  $CoO(OH)$ -(0001), carefully and rationally. Our tools are DFT molecular dynamics, and thermodynamic models to calculate the surface structures, reaction intermediates on different surfaces, assess the catalytic surface sites, and extract overpotentials. The novel element in the work developed in this thesis compared to previous studies present in the literature, is that most of the existing first-principles calculations published on the water splitting on cobalt anode catalysts (and on other anode materials) stand in the context of 'surface science calculations', consisting in static DFT calculations without considering an explicit presence of the aqueous environment in contact with the oxide material, at finite temperature.

Calculations of the OER cycle are exclusively done in literature by DFT static calculations, where the water is ignored or at the best modeled as implicit solvent or through only one layer of explicit water [29, 30, 31, 32]. Here, in the present investigations, not only the gas phase OER will be investigated, but a more realistic OER view will be given by including an entire liquid water slab in direct contact with the catalyst.

Moreover, with the aim of determining the possible OER chemical pathways (*i.e.*, the reaction network both in the gas and liquid phases), the energetics and kinetics, we couple the DFT-MD simulations with a state-of-the-art metadynamics approach capable to probe the configurational space and, simultaneously, to reconstruct the free-energy landscape of the chemical process [33, 34, 35]. With this developed model we manage to successfully predict the electrocatalyst activities and to calculate the theoretical OER overpotentials.

This project aims to provide new methodologies to help design novel structured OER catalysts for efficient water oxidation through the following objectives:

1. elucidate the structure of the bulk material of the spinel cobalt oxide  $Co_3O_4$  and its hydroxide  $CoO(OH)$ ;
2. characterize in details the surface of the (110) facet of the spinel  $Co_3O_4$  and (0001) facet of the  $CoO(OH)$  hydroxide;
3. conduct DFT+U-MD simulations to characterize the interaction of liquid water with the spinel cobalt oxide  $Co_3O_4$ -(110) and its hydroxide  $CoO(OH)$ -(0001);
4. identify the surface OER catalyst sites of both modeled cobalt oxides in gas and liquid phase water environments;
5. characterize in detail the energetics of the OER reaction pathways and the catalytic mechanisms on the  $Co_3O_4$ -(110) and (0001)- $CoO(OH)$  hydroxide surfaces;
6. calculate the OER energy barriers and overpotentials, including the chemical oxidation states of the main chemical species involved in the OER;
7. make systematic comparisons between our DFT+U-MD results with the available experimental data from the literature.

This thesis is organized as follows:

- Chapter 1 introduces the reader to the general context and highlights the main targets of the thesis;
- Chapter 2 introduces all the theoretical background behind the DFT formalism, the *ab-initio* MD simulations and the free energy sampling in the metadynamics framework.
- Chapter 3 highlights all the thermodynamic principles on which the OER is based.
- Chapter 4 provides a state-of-the-art of the main experimental and theoretical results about  $Co_3O_4$  and its hydroxide  $CoO(OH)$ , and about the OER on these cobalt oxides.
- Chapter 5 shows our DFT-MD results on the  $Co_3O_4$  bulk structure and its (110) facet, focusing on  $Co_3O_4$ -(110) interactions with liquid water.
- Chapter 6 provides our metadynamics data on the OER pathways and catalytic mechanisms at the  $Co_3O_4$ -(110)/liquid water interfaces.
- Chapter 7 proposes the same perspectives as chapters 5 and 6 for  $Co_3O_4$ , now applied on (0001)- $CoO(OH)$ /water interface.
- Chapter 8 is focused on the main results obtained by the application of an electric field on the water/air interface and electrolytic solutions.
- Chapter 9: conclusions and perspectives are discussed.

This PhD thesis has been funded by the *Laboratoire d'Excellence Charm<sub>3</sub>* at the Paris-Saclay University. It is part of a partnership in between simulations (Evry University-UEVE) and electro-chemical experiments performed by Philippe Allongue and Fouad Maroun at the *Institut Polytechnique de Paris*

(ex Ecole Polytechnique).



## Chapter 2

# Fundamentals of Density Functional Theory (DFT) and First Principles/Ab-Initio Molecular Dynamics Simulations (FPMD/ AIMD/DFT-MD)

In the last decades, computer simulations gained a key role in obtaining detailed physical and chemical information concerning the microscopic properties of matter. In particular, a great effort has been done in developing more and more accurate numerical approaches. A widely employed approach is represented by *ab-initio* molecular dynamics simulations. Within this framework, first principles molecular dynamics allow simulate molecular systems sizes up to hundreds/thousands atoms with a quantum-mechanical accuracy (of course depending on the electronic level of representation) together with an exploration of the phase space of a few 100' ps time-scale.

In this chapter, starting from the problem of many-body systems towards the DFT electronic representation, we will highlight some of the theoretical backgrounds for first principles simulations. We will treat the fundamentals of Born-Oppenheimer molecular dynamics (BOMD), the DFT formalism, and how BOMD/DFT-MD is addressed in the CP2K package used throughout this work. Moreover, we will provide a general introduction to the basis of the metadynamics (biased MD) technique, including a novel MetD approach based on the so-called 'contact-matrix' adopted in the present calculations, to finally conclude with a brief description of the theoretical background behind the implementation of electric fields (also of interest in this work).

## 2.1 Physics of many-body systems

To study the properties of molecules (individual or assembled in liquids for instance) or any material in the condensed phase using quantum mechanics means solving the well-known time-dependent Schrödinger equation that governs the behavior of all particles that make up the system, *i.e.* electrons and nuclei:

$$(\hat{T}_{el} + \hat{T}_{ion} + \hat{V}_{el-el} + \hat{V}_{ion-ion} + \hat{V}_{ion-el})|\psi\rangle = i\hbar \frac{\partial}{\partial t}|\psi\rangle \quad (2.1)$$

where:

$$\hat{T}_{el} = - \sum_{i=1}^n \frac{\hbar^2}{2m_e} \nabla_i^2$$

is the operator associated with the kinetic energy of the electrons, each electron of mass  $m_e$ ,  $\hbar$  is the Planck constant,

$$\hat{T}_{ion} = - \sum_{I=1}^N \frac{\hbar^2}{2M_I} \nabla_I^2$$

is the operator associated with the kinetic energy of the nuclei, each nucleus of mass  $M_I$ ,

$$\hat{V}_{el-el} = \frac{1}{4\pi\epsilon_0} \frac{1}{2} \sum_i^n \sum_{j \neq i}^n \frac{e^2}{|\mathbf{r}_i - \mathbf{r}_j|}$$

is the potential energy due to the repulsion interaction between the electrons; this is a pair-wise Coulomb interaction in between 2 electrons located respectively at  $\mathbf{r}_i$  and  $\mathbf{r}_j$  positions in space,

$$\hat{V}_{ion-ion} = \frac{1}{4\pi\epsilon_0} \frac{1}{2} \sum_I^N \sum_{J \neq I}^N \frac{Z_I Z_J e^2}{|\mathbf{R}_I - \mathbf{R}_J|}$$

is the potential energy due to the repulsion interaction between nuclei; this is a pair-wise Coulomb interaction in between 2 nuclei located respectively at  $\mathbf{R}_i$  and  $\mathbf{R}_J$  positions in space,  $Z_I$  is the charge of nucleus I located at  $\mathbf{R}_I$ ,

$$\hat{V}_{ion-el} = - \frac{1}{4\pi\epsilon_0} \sum_{i=1}^n \sum_{I=1}^N \frac{Z_I e^2}{|\mathbf{R}_I - \mathbf{r}_i|}$$

is the potential energy due to the attraction interaction between electrons and nuclei,

and  $|\psi\rangle$  is the ket-representation of the wave function and  $\langle \mathbf{r}, \mathbf{R} | \psi \rangle = \psi = \psi(\mathbf{r}_1, \dots, \mathbf{r}_n, \mathbf{R}_1, \dots, \mathbf{R}_N, t)$  is its position projected representation, with a time-dependence. It is the many-body wave function based on the electrons positions  $\mathbf{r}_i$  and nuclei positions  $\mathbf{R}_I$ , at time t (spin variables are neglected for simplicity of writing).

Thus defined, equation 2.1 is a problem that "cannot be solved exactly": it is a partial differential equation which must describe the behavior of a number of interacting particles of the order of Avogadro's number ( $\mathcal{N}_a = 10^{23}$  particles), therefore out-of-range numerically. For this type of equation the exact and analytical solution in 3 dimensions 'is only known for one electron' in a potential and for the hydrogen atom [36].

Moreover, even with the support of computers and numerical approaches, the possibility to obtain the many-body wave function remains limited to systems which have a reduced number of particles. When trying to explore more complex systems, we face the so-called "*Exponential Wall*" [37], which effectively limits the possibility of direct resolution of the equation for systems holding about ten electrons. To employ quantum mechanics, it is thus neces-

sary to transform the equation 2.1 into a solvable problem and so introduce approximations.

## 2.2 Adiabatic Born-Oppenheimer approximation

Introduced by *Max Born* and *Robert Oppenheimer* in 1927 [38], the adiabatic approximation is the starting point in the study of many-body systems: it consists in formally decoupling the motions of the electrons and the motions of the nuclei in any system, starting from the assumption that the difference of 3 orders of magnitude between the masses of one electron and any nucleus implies a great difference in the respective speed and time scale which characterize the dynamics of both particles. The Born -Oppenheimer (BO) approximation thus considers the motions of the electrons to be so fast in comparison with the nuclei motions, that the nuclei can be considered as "fixed in the space" while the electrons move.

From a mathematical point of view, this means that we can ideally separate the Schrödinger equation into two parts: the first one for the electrons in which the positions of the nuclei are considered as fixed and therefore as "parameters", and the second one for the atoms which we can solve once the electronic wave function has been calculated/found.

We consider now a system of  $N$  nuclei of mass  $M_I$  and charge  $Z_I$  with  $I = 1, \dots, N$  and  $n$  electrons of mass  $m_e$  and charge  $-e$ . We denote by  $\mathbf{R}_I$  the position vector of the  $I$ -th nucleus and by  $\mathbf{r}_i$  the position vector of the  $i$ -th electron. Within the adiabatic BO approximation, the Schrödinger equation is now re-expressed into 2 time independent equations, and the only one of interest for us will be the electronic Schrödinger equation (we make the assumption that nuclei are treated as classical particles in all our systems):

$$\hat{H}_e|\Psi_e\rangle = E_e|\Psi_e\rangle = E|\Psi\rangle \quad (2.2)$$

where  $E_e$  is the electronic energy,  $|\Psi_e\rangle$  is the electronic wave-function, and  $\hat{H}_e$  is now the electronic Hamiltonian operator:

$$\begin{aligned} \hat{H}_e &= \hat{T}_{el} + \hat{V}_{el-el} + \hat{V}_{ion-el} = \\ &= - \sum_{i=1}^n \frac{\hbar^2}{2m_e} \nabla_i^2 + \frac{1}{4\pi\epsilon_0} \frac{1}{2} \sum_i^n \sum_{j \neq i}^n \frac{e^2}{|\mathbf{r}_i - \mathbf{r}_j|} - \frac{1}{4\pi\epsilon_0} \sum_{i=1}^n \sum_{I=1}^N \frac{Z_I e^2}{|\mathbf{R}_I - \mathbf{r}_i|} \end{aligned} \quad (2.3)$$

The term  $\hat{H}_e$  is the Hamiltonian operator of a system composed by electrons subjected to the electrostatic field from the nuclei at fixed positions. This field can be seen as an external field and an interaction with the same field is described by the single-body operator external potential  $\hat{V}_{ext}$  whereas the two-body operator  $\hat{V}_{el-el}$  represents the potential energy due to the repulsion interaction between electrons.

The state of the electrons is described by a wave-function  $\Psi_e(\mathbf{r}_1, \mathbf{r}_2, \dots, \mathbf{r}_n; \{\mathbf{R}_I\})$  of the  $3n$  variables  $\mathbf{r}_i$  (in addition to spin variables  $\sigma_i$  that are omitted for simplicity of writing), that depends parametrically on

the  $3N$  coordinates  $\mathbf{R}_I$  of the nuclei. The stationary states of such a system are described by the electronic eigenstates of  $\hat{H}_e$  and thus by the stationary solutions of the electronic Schrödinger equation:

$$\hat{H}_e \Psi_e(\mathbf{r}_1, \mathbf{r}_2, \dots, \mathbf{r}_N; \{\mathbf{R}_I\}) = E_e \Psi_e(\mathbf{r}_1, \mathbf{r}_2, \dots, \mathbf{r}_N; \{\mathbf{R}_I\}) \quad (2.4)$$

$\Psi_e$  does not describe the dynamics of the nuclei but only the electronic wave-function when the nuclei are in a given set of positions. The dynamics of the nuclei come in a second step as described in section 2.7. Note that in the following, we will use short notations as follow

$$\psi_e(\mathbf{r}_1, \dots, \mathbf{r}_n, \mathbf{R}_I) = \psi(\mathbf{r}) \quad (2.5)$$

## 2.3 Towards the DFT (*Density Functional Theory*) approach

The *Hartree* and *Hartree – Fock* (*HF*) methods are the first approaches to the resolution of the many-body system.

The Hartree method [39] (1928) maintains the simple features from the independent electron model and builds the total wave function  $\Psi(\mathbf{r})$  of the  $n$  electrons as a simple product of single electronic wave-functions  $\psi_i(\mathbf{r}_i)$ :

$$\Psi(\mathbf{r}) = \prod_{i=1}^n \psi_i(\mathbf{r}_i) \quad (2.6)$$

thus neglecting the correlation between the electrons, *i.e.* neglecting the interactions between electrons. The *Hartree – Fock* (*HF*) approximation puts back both the correlation between electrons and the fact that the N-body wave-function has to be anti-symmetric within the exchange of 2 fermionic electrons. This latter is the Slater determinant for writing  $\Psi_{HF}(\mathbf{r}_1, \dots, \mathbf{r}_n)$  as shown in the equation:

$$\Psi_{HF} = \frac{1}{n!} \begin{vmatrix} \psi_1(\mathbf{r}_1) & \psi_2(\mathbf{r}_1) & \cdots & \psi_N(\mathbf{r}_1) \\ \psi_1(\mathbf{r}_2) & \psi_2(\mathbf{r}_2) & \cdots & \psi_N(\mathbf{r}_2) \\ \vdots & \vdots & \ddots & \vdots \\ \psi_1(\mathbf{r}_n) & \psi_2(\mathbf{r}_n) & \cdots & \psi_n(\mathbf{r}_n) \end{vmatrix} \quad (2.6.1)$$

where  $\psi_i(\mathbf{r}_j)$  refers to the  $i$ -th single-electron spin-orbital, and  $\mathbf{r}_j$  indicates the spatial and spin coordinates of the  $j$ -th electron, that we could condense into a single variable  $\mathbf{x}_j = (\mathbf{r}_j, \sigma_j)$  (*spin-orbital*). Furthermore the correlation/interaction between the electrons is now taken into account through a mean-field approach in which the electron is subjected to the mean-electrostatic potential arising from the  $(n-1)$  other electrons, instead of calculating all the pair  $e^- - e^-$  interactions. The Hartree-Fock method then consists in finding the combination of spin-orbitals  $\psi_i(\mathbf{r}_j)$  so that the Slater determinant gives the minimum energy according with the variational theorem. The spin

orbitals are expressed on a basis set which can be either based on plane-waves or gaussian functions (see section 2.8).

Writing the electronic wave function as a single Slater determinant is an approximation, more accurate theories require a linear combination of Slater determinants. Beyond this issue, the issue of the mean-field interaction for each electron is a strong assumption preventing the correct treatment of the electronic correlation. Going beyond this issue, while still having a reasonable computational cost for solving the Schrödinger equation, is typically given by the density functional theory (DFT).

*Thomas* [40] and *Fermi* [41], where the first to introduce the electronic density  $\rho(\vec{r})$  as the key to solve the many-body electronic problem, hence creating the background for the so-called Density Functional Theory (DFT).

## 2.4 The role of density: the Hohenberg-Kohn theorem

The modern Density Functional Theory (DFT) was introduced in Hohenberg and Kohn's work published in 1964 [42], with the original aim to rewrite the time-independent electronic Hamiltonian in terms of the electronic density  $\rho(\mathbf{r}) = n \int \dots \int |\psi_e(\mathbf{r}_1, \mathbf{r}_2, \dots, \mathbf{r}_n)|^2 d\mathbf{r}_2 \dots d\mathbf{r}_n$  instead of the  $n$ -electron wavefunction. By doing this, the  $3n$  complex wavefunction  $\psi_e(\mathbf{r}_1, \mathbf{r}_2, \dots, \mathbf{r}_n)$  is reduced to a density function composed of only the coordinates  $\mathbf{r}$  of one electron in space, *i.e.* 3 coordinates in the cartesian space.

The starting point of the DFT theory is the *Hohenberg-Kohn theorem*, which states that given a many-body electronic system (*i.e.* the electrons/nuclei interactions), there is a one-to-one relationship between the external potential  $V_{ext}$  applied to the system (which is in particular arising from the nuclei attraction to the electrons) and the ground state density of the system  $\rho_0(\mathbf{r})$  as:

$$V_{ext} \Leftrightarrow (\psi_0(\mathbf{r}_1, \mathbf{r}_2, \dots, \mathbf{r}_n)) \Leftrightarrow \rho_0(\mathbf{r}) \quad (2.7)$$

and such that the fundamental following theorem holds:

$$\langle \Psi_e | \hat{V}_{ext} | \Psi_e \rangle = \int \rho_0(\mathbf{r}) V_{ext}(\mathbf{r}_1, \mathbf{r}_2, \dots, \mathbf{r}_n) d\mathbf{r} \quad (2.8)$$

where basically one goes from an integral over  $3n$  coordinates (left side) to an integral over only 3 coordinates (right side).

At this stage, all properties become a functional of the density  $\rho_0(\mathbf{r})$ , hence any physical observable can be obtained as a functional of the density  $\rho_0$  ( $\rho_0 = \rho = \rho(\mathbf{r})$  for simplicity of writing):

$$O[\rho] = \langle \Psi[\rho] | \hat{O} | \Psi[\rho] \rangle, \quad (2.9)$$

The ground state energy of the  $n$ -electron system is then also a functional of the density  $\rho_0(\mathbf{r})$ :

$$E[\rho] = \langle \Psi[\rho] | \hat{H} | \Psi[\rho] \rangle = \langle \Psi[\rho] | \hat{T}_{el} + \hat{V}_{el-el} + \hat{V}_{ext} | \Psi[\rho] \rangle = F[\rho] + \int V_{ext}(\mathbf{r}) \rho(\mathbf{r}) d\mathbf{r} \quad (2.10)$$

where

$$F[n] = \langle \Psi[n] | \hat{T}_{el} + \hat{V}_{ext} | \Psi[n] \rangle \quad (2.11)$$

is a universal functional. Universal, however without an analytical expression (thus unknown).

Despite in principle the two theorems from Hohenberg and Kohn provide all the means to calculate the electronic energy solely from the electron density, eq. 2.10 cannot be solved as it is. This is due to  $\hat{T}_{el}[\rho]$  and  $\hat{V}_{el-el}[\rho]$  terms: while  $\hat{V}_{ext}$  is known for each given spatial arrangement of the nuclei, the exact expressions of  $\hat{T}_{el}[\rho]$  and  $\hat{V}_{el-el}[\rho]$  are unknown for interacting electrons. These two terms are however exactly known for non-interacting electrons ( $\hat{T}_{el}[\rho]$ ) and for classical particles ( $\hat{V}_{el-el}[\rho]$ ), and this knowledge represents the starting point for the Kohn-Sham approach and its approximations, which is nowadays used to solve the electronic Schrödinger equation within the DFT formalism. The underlying approximations are detailed hereafter.

## 2.5 The exchange and correlation functional: the Kohn-Sham scheme

Kohn and Sham [43] demonstrated that there is always a non-interacting electronic system with the same density as the interacting electronic system. With this in hand, the main idea of Kohn and Sham is therefore to use a fictitious system of non-interacting electrons (KS) for which the electronic density is simply expressed as  $\rho(\mathbf{r}) = \sum_i^n |\psi_i(\mathbf{r}_i)|^2$  where  $\psi_i(\mathbf{r}_i)$  are the mono-electronic wave-functions (of the non-interacting electronic system) used in the Slater determinant in eq. 2.6.1. With this in hand, one can easily rewrite the electronic kinetic energy term  $\hat{T}_{el}[\rho]$  of the universal functional in equation 2.11. The total kinetic energy of the non-interacting electronic system  $T_{KS}[\rho]$  thus becomes:

$$T_{KS}[\rho] = - \sum_{i=1}^n \frac{\hbar^2}{2m_e} \langle \psi_i(\mathbf{r}_i) | \nabla^2 | \psi_i(\mathbf{r}_i) \rangle$$

$T_{KS}[\rho]$  is only a part of the total electronic kinetic energy  $\hat{T}_{el}[\rho]$  of the electronic interacting system, which by construction should also include the correlation part of the electrons (it has to be reintroduced later).

From the knowledge of  $\rho(\mathbf{r})$ , it is also possible to calculate the classical electron-electron interaction energy, which is known as the Hartree energy  $E_H[\rho]$  (*i.e.* as if the electrons were classical particles and not quantum ones):

$$E_H[\rho] = \frac{1}{4\pi\epsilon_0} \frac{1}{2} \int \int \frac{\rho(\mathbf{r})\rho(\mathbf{r}')}{|\mathbf{r} - \mathbf{r}'|} d\mathbf{r} d\mathbf{r}' \quad (2.13)$$

$E_H[\rho]$  is however only a part of the total electron-electron interaction energy  $\hat{V}_{el-el}[\rho]$  of the electronic interacting system which also includes the non-classical contribution from the quantum nature of the electrons, *i.e.* the exchange of the electron spins (it has to be reintroduced later).

Using the Kohn-Sham methodology, we then can rewrite equation (2.10) using a "trick", *i.e.* adding and subtracting the two terms in the equations above 2.12 and 2.13:  $E_H[\rho]$ , the classical Coulomb Hartree term and  $T_{KS}[\rho]$ , the kinetic energy of the non-interacting electronic system. It is now possible to rewrite the total energy  $E[\rho]$  of the interacting electronic system in the following way:

$$E[\rho] = T_{el}[\rho] + V_{el-el}[\rho] + V_{ext}[\rho]$$

$$E[\rho] = (T_{el}[\rho] - T_{KS}[\rho] + T_{KS}[\rho]) + (V_{el-el}[\rho] - E_H[\rho] + E_H[\rho]) + V_{ext}[\rho]$$

$$E[\rho] = T_{KS}[\rho] + E_H[\rho] + V_{ext}[\rho] + (T_{el}[\rho] - T_{KS}[\rho]) + (V_{el-el}[\rho] - E_H[\rho])$$

$$E[\rho] = T_{KS}[\rho] + E_H[\rho] + V_{ext}[\rho] + E_{XC}[\rho]$$

(2.14)

In equation 2.14,  $T_{KS}[\rho]$ ,  $E_H[\rho]$ ,  $V_{ext}[\rho]$  are known and they are all based on the density  $\rho$  of the (free) non-interacting electrons.  $E_{XC}[\rho]$  is called the exchange-correlation energy functional, which includes all unknown of the quantum nature of the electrons. Equation (2.14) has the following expression:

$$E[\rho] = T_{KS}[\rho] + \frac{1}{2} \int \int \frac{\rho(\mathbf{r})\rho(\mathbf{r}')}{|\mathbf{r} - \mathbf{r}'|} d\mathbf{r}d\mathbf{r}' + \int \rho(\mathbf{r})V_{ext}(\mathbf{r})d\mathbf{r} + E_{XC}[\rho] \quad (2.15)$$

The last term  $E_{XC}[\rho]$  is defined as the energy difference between the electronic interacting system and the non-interacting electronic system. In particular, it consists in the sum of the difference between the kinetic energy of the two underlying system and the difference between the total electron-electron interaction  $V_{el-el}$  term and the classical Hartree energy  $E_H[\rho]$  term, as follows:

$$E_{XC}[\rho] = (T_{el}[\rho] - T_{KS}[\rho]) + (V_{el-el}[\rho] - E_H[\rho]) \quad (2.16)$$

$E_{XC}[\rho]$  is usually also written as:

$$E_{XC}[\rho] = E_X[\rho] + E_C[\rho] \quad (2.17)$$

This functional is crucial as it contains all the subtle correlation and exchange interactions between the electrons. The redefinition of the functional, as in 2.17, puts in  $E_{XC}[\rho]$  all the difficulties of electronic correlation calculations. In practice  $E_{XC}[\rho]$  must be approximated, giving rise to the ladder of functionals described below.

## 2.6 Ladder of Functionals

A lot of expressions exist in the literature to express  $E_{XC}[\rho]$ , that give rise to various DFT functionals (also known as the "zoo of functionals"). Research

in DFT consists in particular in the development of new forms and parameters to obtain the best exchange correlation functional in terms of accuracy and computational price. I will now briefly describe the three main categories of functionals existing for this exchange and correlation functional term. All the expressions hereafter are based on the general expression:

$$E_{XC}[\rho] = \int d\mathbf{r} \mathcal{F}(\rho(\mathbf{r}), \nabla\rho(\mathbf{r}), \nabla^2\rho(\mathbf{r}), \dots) \quad (2.18)$$

*i.e.* on a Taylor expansion of a function of the density  $\rho(\mathbf{r})$ , its gradient  $\nabla\rho(\mathbf{r})$ , and successive derivatives  $\nabla^2\rho(\mathbf{r}), \dots$ .

Depending where this expression is stopped, it gives rise to a different functional, therefore the ladder: local functional ( $\rho(\mathbf{r})$ ), gradient-corrected functional ( $\rho(\mathbf{r})$  and  $\nabla\rho(\mathbf{r})$ ), meta-functionals ( $\rho(\mathbf{r})$  and ( $\nabla\rho(\mathbf{r})$  and  $\nabla^2\rho(\mathbf{r})$ ), etc.

1) The Local-(spin)-Density Approximation (L(S)DA) was the first, and simplest approximation made for the exchange and correlation functional. This functional is based on the assumption that the electronic density is uniformly distributed over the space, and accordingly express  $E_{XC}[\rho]$  as a simple functional of the density  $\rho(\mathbf{r})$ . The *LSDA* is obtained by:

$$E_{XC}^{LSD}[\rho_{\uparrow}, \rho_{\downarrow}] = \int \rho(\mathbf{r}) e_{XC}(\rho_{\uparrow}(\mathbf{r}), \rho_{\downarrow}(\mathbf{r})) d^3\mathbf{r} \quad (2.19)$$

where  $e_{XC}(\rho_{\uparrow}(\mathbf{r}), \rho_{\downarrow}(\mathbf{r}))$  is the exchange-correlation energy of a homogeneous electron gas with uniform spin density  $\rho_{\uparrow}$  (spin up) and  $\rho_{\downarrow}$  (spin down). LDA functionals provide satisfying energy estimations for metals but not for molecular systems where covalent bonds between atoms drive away from the approximations. They are thus non appropriate in order to describe water at interfaces, one goal of the investigations performed in this thesis work.

2) To overcome some weaknesses of the crude LDA approximation, gradient expansion of the electron density can be taken into account in eq. 2.18. This means that density inhomogeneities, in other words density spatial variations, can be included. *GGA* (Generalized Gradient Approximations) thus add a term which includes the gradient of the electronic density functionals onto the general expression, partially taking into account the non-homogeneous distribution of electron density and hence the non-local spatial effects:

$$E_{XC}^{GGA}[\rho_{\uparrow}, \rho_{\downarrow}] = \int f(\rho_{\uparrow}, \rho_{\downarrow}, \nabla\rho_{\uparrow}, \nabla\rho_{\downarrow}) d\mathbf{r} \quad (2.20)$$

In terms of performance, GGA functionals indeed improve energies, structural and dynamical properties, but still include self-interaction terms (between the electrons) and do not provide systematic improved results for metals or semiconductors. However, from the point of view of molecular dynamics simulations on large systems, they represent the best compromise between speed and accuracy. GGA functionals have been consequently chosen to perform all the DFT-MD simulations presented in this manuscript.

3) Since several failures of the GGA functionals originate from an incomplete treatment of the exchange interaction, some improvements have to be made in this direction. Hybrid functionals are a class of approximations to the exchange-correlation functionals that incorporate a fraction of exact exchange from the Hartree-Fock theory, and keeping other elements of the exchange-correlation from other sources, for instance LDA or GGA. Despite the improved accuracy reached on average with this third generation of functionals, the higher computational cost of such hybrid functionals makes them often too computationally expensive for DFT-MD simulations. For instance, it is the case for the simulations done in this work, which could not be performed with sufficiently large box-dimensions and simulations time-lengths using hybrid functionals (roughly 40 times more computationally expensive than GGA).

## 2.7 Born-Oppenheimer Molecular Dynamics (BOMD)

To advance in space and time the nuclei, one has to solve the Newton's equations of motions of classical mechanics. We remind the reader here that nuclei will systematically be treated as classical particles in our work, and not as quantum, therefore we do not solve the nuclei Schrödinger equation. The set of coupled Newton's equations of motions for the classical nuclear degrees of freedom is formally (within the wave-function representation):

$$\forall I : \quad \mathbf{F}_I = M_I \frac{d^2 \mathbf{R}_I(t)}{dt^2} = - \frac{\partial}{\partial \mathbf{R}_I} \langle \Psi(\mathbf{r}) | \hat{H}_e | \Psi(\mathbf{r}) \rangle - \frac{\partial V_{ion-ion}(\mathbf{R})}{\partial \mathbf{R}_I}, \quad (2.21)$$

where the right-hand side represents the force vector acting on the nucleus I-th and

$$\hat{H}_e = - \frac{\hbar^2}{2m_e} \sum_{i=1}^n \nabla_i^2 + \frac{1}{4\pi\epsilon_0} \frac{1}{2} \sum_i^n \sum_{j \neq i}^n \frac{e^2}{|\mathbf{r}_i - \mathbf{r}_j|} + \frac{1}{4\pi\epsilon_0} \sum_{I=1}^N \sum_{i=1}^n V_{ext}(\mathbf{r}_i - \mathbf{R}_I) \quad (2.22)$$

Within the DFT formalism, the force arising from the electrons onto the nucleus I-th is reduced to:

$$\begin{aligned} \mathbf{F}_I &= - \frac{\partial E_{KS}[\rho]}{\partial \mathbf{R}_I} - \frac{\partial V_{ion-ion}(\mathbf{R})}{\partial \mathbf{R}_I} = \\ &= - \int \rho(\mathbf{r}) \frac{\partial V_{ext}(\mathbf{r} - \mathbf{R}_I)}{\partial \mathbf{R}_I} d\mathbf{r} - \frac{\partial V_{ion-ion}(\mathbf{R})}{\partial \mathbf{R}_I} = M_I \frac{d^2 \mathbf{R}_I(t)}{dt^2} \end{aligned} \quad (2.23)$$

To solve this second order differential equation (2.23) requires the discretization of time in small time-intervals. This is how the time-step  $\delta t$  of an MD simulation is defined. Many propagation algorithms have been developed, generally based on a Taylor expansion of the particle positions around the positions at a certain instant  $t$  (i.e. at each MD-step). All most commonly used

propagation methods derive from the seminal Verlet algorithms. It is based on two Taylor expansions, one for positive times and the other for negative times:

$$\forall I = 1, \dots, N : \mathbf{R}_I(t + \delta t) = \mathbf{R}_I(t) + \mathbf{V}_I(t)\delta t + \frac{\mathbf{F}_I(t)}{2M_I}\delta t^2 + O(\delta t^3) \quad (2.24)$$

$$\forall I : \mathbf{R}_I(t - \delta t) = \mathbf{R}_I(t) - \mathbf{V}_I(t)\delta t + \frac{\mathbf{F}_I(t)}{2M_I}\delta t^2 - O(\delta t^3) \quad (2.25)$$

and summing these two equations, one obtains:

$$\forall I : \mathbf{R}_I(t + \delta t) = 2\mathbf{R}_I(t) - \mathbf{R}_I(t - \delta t) + \frac{\mathbf{F}_I(t)}{M_I}\delta t^2 + O(\delta t^3) \quad (2.26)$$

The estimate of the new position at time  $t + \delta t$  contains an error of the order of  $\delta t^3$ , where  $\delta t$  is the time step. Note that this algorithm does not use the velocity to compute the new position. However, we can derive the velocity at time  $t$  from the knowledge of the positions at times  $t - \delta t$  and  $t + \delta t$  :

$$\forall I : \mathbf{V}_I(t) = \frac{\mathbf{R}_I(t + \delta t) - \mathbf{R}_I(t - \delta t)}{2\delta t} \quad (2.27)$$

It is possible to cast the Verlet algorithm into a form that uses positions and velocities computed at equal times, and this is the so-called velocity Verlet algorithm, used in our work:

$$\forall I : \mathbf{R}_I(t + \delta t) = \mathbf{R}_I(t) + \mathbf{V}_I(t)\delta t + \frac{\mathbf{F}_I(t)}{2M_I}\delta t^2 \quad (2.28)$$

$$\forall I : \mathbf{V}_I(t + \delta t) = \mathbf{V}_I(t) + \frac{\delta t}{2M_I}(\mathbf{F}_I(t) + \mathbf{F}_I(t + \delta t)) \quad (2.29)$$

Another algorithm equivalent to the Verlet method is the so-called Leap-Frog algorithm [44], that evaluates the velocities at half-integer time steps and uses these velocities to compute new positions.

Note that all common algorithms derived from Verlet are symplectic, thus capable to conserve the total energy of the system in their basic form (if  $\delta t$  is sufficiently small). An MD simulation performed with these symplectic algorithms will always provide the time evolution of the simulated system in the NVE (microcanonical) ensemble. However, other ensembles can be simulated (NVT, NPT), if required.

As a summary, within the BOMD, the time-independent Schrödinger equation is solved at each time step of the dynamics, *i.e.* for each fixed nuclear configuration, together with advancing the nuclei positions and velocities. This gives rise to the coupled equations:

$$\begin{cases} E_0|\Psi(\mathbf{r}; \mathbf{R})\rangle = H_e|\Psi(\mathbf{r}; \mathbf{R})\rangle \\ \forall I : M_I\ddot{\mathbf{R}}_I(t) = -\nabla_{\mathbf{R}_I}E_0 \end{cases} \quad (2.30)$$

where  $\mathbf{R}_I$  represents the (cartesian) coordinates of nucleus  $I$ ,  $\mathbf{r}$  represents all electronic (cartesian) coordinates,  $\mathbf{R}$  represents all nuclei coordinates and  $E_0$  is the ground state electronic energy for the ensemble of fixed nuclei positions  $\mathbf{R}$ .  $\Psi$  is the associated ground-state electronic wave-function. As there is no intrinsic dynamics for the electrons, these equations can be integrated with a time-step corresponding to the characteristic time of the nuclear motion (0.4-0.5 fs in our BOMD dynamics).

### 2.7.1 NVE ensemble

Let us take  $N$  classical point charges representing the atomic nuclei in a fixed volume. The trajectory obtained via the resolution of the classical Newton's equations of motion (EOM) naturally generate the microcanonical ensemble (NVE), keeping the total energy  $E$  as a constant of motion (if  $\delta t$  is well chosen for the numerical integrations).

Our first principles molecular dynamics simulations are done in the NVE microcanonical ensemble (after few picoseconds of thermalization), where the number of electrons and nuclei is constant, the volume  $V$  and the total energy  $E$  (kinetic+potential  $E_{KS}$ ) of the system, all remain constant over time.

A fundamental criterion to judge the quality of a MD numerical simulation is the conservation of the constants of motion. As the EOM have to be discretized in time, numerical errors might arise. The numerical stability, probed by negligible drifts in the total energy, is reached only for small time steps  $\delta t$ , but this time-step should not be too small for efficiency (minimal number of force evaluations for computational cost). We thus mean that a proper choice of  $\delta t$  is crucial. In practice, when electronic structure calculations are required to compute the forces acting on the nuclei (what we will call *ab initio* MD), typical time-steps consist of a few tens of femtoseconds, generally 0.1-0.5 fs in Born-Oppenheimer Molecular Dynamics.

### 2.7.2 NVT ensemble

Even though the microcanonical ensemble NVE is the most natural for molecular dynamics simulations, it does not strictly represent experimental conditions where the temperature can be fixed instead of the total energy. In the NVE ensemble, the temperature is extracted from the average kinetic energy of the nuclei and from the energy equipartition theorem [45] by

$$\left\langle \sum_I \frac{1}{2} m_I \mathbf{v}_I^2 \right\rangle_{NVE} = \frac{3}{2} N k_B T \quad (2.31)$$

Temperature can however be controlled in MD simulations by the use of thermostats in the canonical ensemble NVT. The average temperature is thus targeted, with specific algorithms, usually based on baths.

The most popular method was developed by Nosé [46] and Hoover [47] and further corrected by Martyna *et al.* [48]. Let us consider only one heat bath treated as a new degree of freedom  $s$  with  $p_s$  momentum. The coupling of this bath with the studied molecular system is achieved via a fictitious "mass"  $Q$ , to be chosen with care. The new Hamiltonian includes an additional kinetic energy term for the heat bath,  $p_s^2/(2Q)$ , and a "temperature" term involving the number of dynamical degrees of freedom concerned by the thermostat ( $g$ ),  $gk_B T \ln s$ . Moreover, the momenta of the system coupled to the bath have to be scaled by  $s$ , *i.e.* they are virtual:  $\mathbf{p}_{real} = \mathbf{p}_{virtual}/s$ . The full Hamiltonian for the NVT ensemble is thus presented below:

$$H = \sum_I \frac{\mathbf{p}_{real,I}^2}{2M_I s^2} + V(\mathbf{R}) + \frac{p_s^2}{2Q} + gk_B T \ln s \quad (2.32)$$

In practice, chains of thermostats are chosen since they were shown to ensure ergodicity, contrary to the original Nosé-Hoover scheme [48]. Note that the total energy as expressed by the new Hamiltonian in Equation 2.32 is the conserved quantity in NVT molecular dynamics simulations [45].

In CP2K, other strategies can be used for temperature control: velocity rescaling (fast but not canonical) or Canonical Sampling through Velocity Rescaling (CSVr) where a random factor is used to rescale velocities [49], however ensuring ergodicity.

### 2.7.3 Periodic boundary conditions

As most of MD codes, the CP2K package uses periodic boundary conditions [50] in the three directions of space. This allows mimic a continuous medium composed of an infinite number of the unit cell. One of the cells is the "true" simulation box, and the other cells are the replica.

An illustration of a simulation box containing the unit cell of the  $Co_3O_4$  cobalt oxide and its replica (here displayed along  $-x$  and  $y$  directions only) is presented in Fig. 2.1. The main box is bordered with the blue lines.

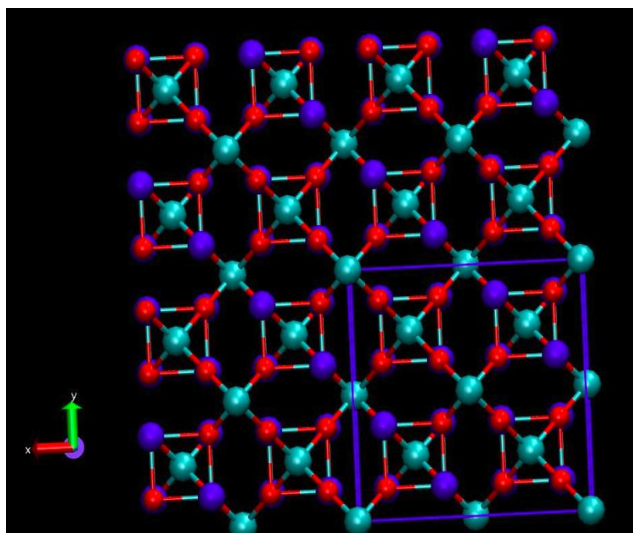


Figure 2.1: *Illustration of PBC. Unit cell of  $Co_3O_4$  cobalt oxide and its replica. Replica are along the three directions of space, in the picture only along  $-x$  and  $y$  are visible. The blue square is the limit of the central simulation box, all other boxes are its replica.*

Now, if an atom leaves the central box through for instance the right wall, its image will enter the box through the left wall from the neighbouring box. The resulting model becomes quasi-periodic, with a periodicity equal to the dimension of the box. One consequence is that each box interacts with its replica. Note that the imposed artificial periodicity may cause errors when considering properties which are influenced by long-range interactions, such as for dipolar and charged systems.

The size of the simulation box is thus crucial. A too big simulation box would

be of course the best in order to reduce as much as possible interactions between the replica, but it will be computationally expensive. One has to choose a box reasonable in size for reasonable computational costs and no artefact of interactions. In order to choose the best compromise in box size, in practice we change gradually the box dimensions, we do geometry optimisations for the different dimensions of the simulation box and the final size chosen for the simulations corresponds to the size for which the electronic energy reaches a plateau (convergence criterion).

## 2.7.4 PBE+U functional

As will become clear in chapters 5, 6 and 7, the  $E_{XC}[\rho]$  DFT functional used in all our works is the GGA-PBE. The analytical expression of the correlation part of the PBE [51] functional is:

$$E_{PBE}^C[\rho] = \int \rho \cdot (\epsilon_{HEG}^C(\rho) + H^C[\rho, t]) d\mathbf{r}, \quad t = \frac{|\nabla\rho|}{2k_s\rho} \quad (2.33)$$

where  $\epsilon_{HEG}^C[\rho]$  is the correlation part of the energy density of a uniform electron gas [52],  $t$  is a dimensionless density gradient,  $1/k_s$  is the Thomas-Fermi screening wave-length, and

$$H^C(\rho, t) = \frac{a_2 m}{\hbar^2} \ln \left[ 1 + \frac{a_1}{a_2} t^2 \left( \frac{1 + At^2}{1 + At^2 + A^2 t^4} \right) \right], \quad (2.34)$$

where

$$A = \frac{a_1}{a_2} \frac{1}{\exp(-\epsilon_{HEG}^C/(a_2 m/\hbar^2)) - 1} \quad (2.35)$$

with  $a_1 = 0.066725$  and  $a_2 = (1 - \ln 2)/\pi^2$ .

The exchange part is:

$$E_{PBE}^X[\rho] = \int \rho(\mathbf{r}) \epsilon_{HEG}^X[\rho] F^X(s) d\mathbf{r}, \quad s = 2(3\pi^2/2)^{1/3} \sqrt{r_s} t, \quad (2.36)$$

where  $\epsilon_{HEG}^X[\rho]$  is the exchange part of the energy density of a uniform electron gas [52],  $s$  is a dimensionless gradient and

$$F^X(s) = 1 + b_1 - \frac{b_1}{1 + \frac{b_2 s^2}{b_1}} \quad (2.37)$$

with  $b_1 = 0.804$  and  $b_2 = a_2 \pi^2/3$ .

The exchange-correlation energy per particle of a homogeneous electron gas (HEG)  $\epsilon_{HEG}^{XC}[\rho_\uparrow, \rho_\downarrow]$  is well established [52]. Semi-empirical GGA can be remarkably successful for small molecules but fail for delocalized electrons (*i.e.* away from the uniform electron gas) and thus in simple metals and semi-conductors such as the cobalt oxides systems investigated in this thesis. It is often claimed that this method is even useless for strongly correlated materials,

*i.e.* materials with incomplete filled  $d$ - or  $f$ -electron shells atoms with narrow energy bands such as in many transition metal oxides and semi-conductors. For instance, the seemingly simple material NiO has a partially filled 3d-band (the Ni atom has 8 3d-electrons over a total of 10 electrons) and therefore would be expected to be a good conductor. However, strong Coulomb repulsion (a correlation effect) between d-electrons makes NiO instead a wide-band gap insulator. Thus, strongly correlated materials have electronic structures that are neither simply free-electron-like nor completely ionic, but a mixture of both.

In this context, it is generally accepted that strongly correlated systems are quite well described by the multiband Hubbard or Anderson-lattice type of models [53, 54, 55]. The essential assumption of these models is that the strongly correlated  $d$  or  $f$  electrons are subject to on-site quasiatomic interactions. The most important of these interactions is expressed with the Hubbard parameter  $U$  [56], defined as

$$U = E(d^{n+1}) + E(d^{n-1}) - 2E(d^n) \quad (2.38)$$

*i.e.*, the Coulomb-energy cost to place two electrons at the same site. If we consider the simple case of a system, characterized by a single band of correlated  $d$  electrons, subjected to a Hubbard-type interaction:

$$H = \sum_i U n_{di\uparrow} n_{di\downarrow} \quad (2.39)$$

where  $n_{di\sigma}$  is the number operator of the  $d$  electron at site  $i$  with spin  $\sigma$ . In the mean-field (MF) theory, the fluctuations around the average occupancies  $\langle n_{di\sigma} \rangle$  are neglected and Eq. 2.39 is approximated as

$$H^{MF} = \frac{1}{2} \sum_i U [n_i(n_{i\uparrow} + n_{i\downarrow}) - m_i(n_{i\uparrow} - n_{i\downarrow})] - \frac{1}{4} U (n_i^2 - m_i^2) \quad (2.40)$$

where

$$n_i = \langle n_{i\uparrow} + n_{i\downarrow} \rangle \quad (2.41)$$

is the average occupancy, and

$$m_i = \langle n_{i\uparrow} - n_{i\downarrow} \rangle, \quad (2.42)$$

is the moment.

The PBE energy functional can be corrected by  $H^{MF}$  term as

$$E_{PBE} = E_{XC}^{PBE} + H^{MF} \quad (2.43)$$

With this correction, the PBE functional is supplemented with the Hubbard-type interaction term in order to circumvent the over-delocalization error of the 3d-electrons in metal oxides and the consequent underestimation of the band gap.

Converged values of the Hubbard  $U$  parameter for the  $Co^{2+}$  and  $Co^{3+}$  ions of  $Co_3O_4$  materials using the linear response approach of Ref. [57] have

been calculated in Selloni’s paper [58], paper used as our reference (in all applications reported in chapters 5, 6). Calculations of the heat of formation ( $\Delta H$ ) at  $T = 298$  K relative to metallic, ferromagnetic Co ions in the hcp structure were performed on various supercells, with volumes ranging from one to four primitive cells. Converged U values are 4.4 and 6.7 eV for  $Co^{2+}$  and  $Co^{3+}$ , respectively. The fact that the value of U is larger for  $Co^{3+}$  than for  $Co^{2+}$  is due to the stronger on-site repulsion in the more contracted  $d$  orbitals of ions with higher oxidation state (such as  $Co^{3+}$ ). To avoid the computational difficulties (more computational time required in the calculations) associated with having two different U values for different Co ions, Selloni *et al.* also performed calculations for  $Co_3O_4$  using a single value of U for both  $Co^{2+}$  and  $Co^{3+}$ , namely, U = 4.4, 5.9, and 6.7 eV. They showed that the value U=5.9 eV (being the average of 4.4 and 6.7 eV) is a good compromise in order to correctly reproduce the electronic properties of  $Co_3O_4$  using only one U value (for both  $Co^{2+}$  and  $Co^{3+}$ ) and hence cut down the computational time required in the calculations.

In our work, the value of U=5.9 eV (for both  $Co^{2+}$  and  $Co^{3+}$  ions) proposed by Selloni *et al.*[58] has been tested and adopted in our calculations as a reliable U value in correctly reproducing electronic properties of bulk  $Co_3O_4$ , such as the band gap (more details in section 5.2).

### 2.7.5 BLYP functional

In the work described from section 8.1 to 8.5 we have used the BLYP exchange and correlation functional (instead of PBE+U) for the sake of compatibility and coherence with previous works done in the group about the same air-water interfacial system. I therefore report below the BLYP exchange and correlation functional.

Becke proposed to correct the exchange functional from LDA (eq. 2.19) with a one parameter expression in the lowest-order gradient correction in order to overcome the traditional underestimation of exchange energies by LDA. The B88 exchange functional [59] is hence expressed as:

$$E_{B88}^X[\rho] = \int \rho \epsilon_{HEG}^X[\rho] \left( 1 + \frac{4}{3} \left( \frac{\pi}{3} \right)^{1/3} a_1 \frac{x^2}{1 + 6a_1 x \sinh^{-1} x} \right) d\mathbf{r}, \quad x = \frac{|\nabla\rho|}{\rho^{4/3}} \quad (2.44)$$

where  $a_1 = 0.0042$  is obtained via a least square fit on the exact HF exchange of noble gases.

The LYP correlation functional has been obtained from a simplification and a reformulation of the Colle-Salvetti formula in terms of  $\rho$  and  $\nabla\rho$ :

$$E_{LYP}^C[\rho] = - \int \frac{b_1}{1 + b_4 \rho^{-1/3}} \left( \rho + b_2 \rho^{-2/3} \left( C_F \rho^{5/3} - 2t_w + \frac{t_w}{9} + \frac{\nabla^2 \rho}{18} \right) e^{-b_3 \rho^{-1/3}} \right) d\mathbf{r}, \quad (2.45)$$

where

$$C_F = \frac{3}{10} (3\pi)^{2/3}, \quad t_w = \frac{1}{8} \left( \frac{|\nabla\rho|^2}{\rho} - \nabla^2 \rho \right). \quad (2.46)$$

$t_w$  is the kinetic energy density, and  $b_1 = 0.04918$ ,  $b_2 = 0.132$ ,  $b_3 = 0.2533$ , and  $b_4 = 0.349$ .

Combining both B88 exchange and LYP correlation functionals gives rise to the BLYP exchange-correlation functional used in this work in BOMD simulations at the electrified air/water interface in chapter 8.

## 2.7.6 Dispersion corrections

Dispersion interactions appear to be much harder to describe than, for instance, electrostatic and exchange parts within DFT. Dispersion originates from quantum fluctuations of the charge distribution, generating instantaneous dipoles that give rise to the well-known  $-\frac{C_6}{R^6}$  law for the energy, where  $R$  represents the intermolecular distance. This is a long range interaction.

Standard LDA, GGA or hybrid DFT functionals, are not able to fully account for dispersion as it arises from long-range electronic correlations, whereas DFT treats more correctly the correlation at short distances. The electronic correlation must be included either through special functionals that take this effect directly into account or through van der Waals corrections added up to the DFT functional.

The Grimme corrections are popular due to the good results provided at a reasonable cost in terms of computational resources. One has to be careful: this correction does not correct the electronic density, it corrects only the associated electronic energy to possibly reproduce the weak van der Waals interactions. In the Grimme method, the dispersion energy is an additional term to the Kohn-Sham energy that does not depend on electron densities but only on atomic coordinates [60], following the general expression:

$$E_{disp}^{DFT-D} = - \sum_{AB} \sum_{n=6,8,10,\dots} s_n \frac{C_n^{AB}}{R_{AB}^n} f_{damp}(R_{AB}) \quad (2.47)$$

In Equation 2.47,  $C_n^{AB}$  are the isotropic  $n$ -th order dispersion coefficients for the pair of atoms A and B, located at a distance  $R_{AB}$ .  $s_n$  is a global scaling factor depending on the repulsive behavior of the functional used.  $f_{damp}$  is a damping function to avoid singularities for small interatomic distances as well as double-counting effects at intermediate distances. In the D2-Grimme dispersion term (that will be used in our works), made only of  $C_6^{AB}$  terms in eq. 2.47, the damping function is chosen as:

$$f_{damp}^{D2}(R_{AB}) = \frac{1}{1 + \exp^{-d(R_{AB}/R_r - 1)}} \quad (2.48)$$

where  $R_r$  corresponds to the sum of atomic vdW radii and  $d$  is an adjustable parameter for corrections at intermediate distances.

In the D2 version, the  $C_6^{AB}$  coefficients come from the geometric mean of single atom coefficients. These atomic  $C_6^A$  coefficients are derived from atomic ionization potentials  $I_p^A$  and static dipole polarizabilities  $\alpha^A$  obtained at the PBE0 level:  $C_6^A = 0.05 N I_p^A \alpha^A$ , where a value of  $N$  is associated to the row in

the periodic table (2, 10, 18, 36 and 54 for the first five rows).

Grimme augmented and refined the D2 method with the D3 version [61]. The purpose of this section is not to go deep in details in the Grimme-D3 version but several improvements of the latter arise from the use of Time-Dependent DFT calculations for the parametrization of  $C_6^{AB}$  coefficients, the inclusion of hybridization states of atoms in the local coordination term, the presence of 3-body interaction terms and the addition of higher order 2-body  $C_8^{AB}$  coefficients (*i.e.* dispersion with decay in  $R^{-8}$ ).

Grimme D2 and D3 dispersion corrections in DFT-MD simulations are the most widely used strategies to correct standard DFT functionals because of their simplicity and broad range of applications, from molecules to condensed phases, and because of their low computational cost [60]. However, due to the additional terms and especially the 3-body terms, the D3 version is more computationally expensive for molecular dynamics simulations: this is why, in all the calculations presented in this thesis, we employ the Grimme-D2 dispersion correction, which is the best compromise between accuracy of the results presented here and computational cost.

## 2.8 Dual GPW representation in CP2K/Quickstep

The CP2K/Quickstep method [62] is characterized by its advantageous mixing of basis sets: the local and atom-centered Gaussians and the uniform delocalized Plane-Waves, giving rise to the dual GPW representation.

For mathematical reasons that ease up and decrease the computational cost, two spaces are used in the CP2K code that we are using for DFT-MD simulations: the real space ( $\vec{r}$ , cartesian coordinates) applied especially with the gaussian basis set and its reciprocal space ( $\vec{G}$ ) applied with the plane waves functions. The two spaces are Fourier transforms of each others.

### 2.8.1 Gaussian basis set

The mono-electronic wavefunctions  $\psi_i$  can be built on a gaussian basis set. The Kohn-Sham spin-orbitals  $\psi_i$  (see the Slater determinant in eq. 2.6.1) are expanded as a linear combination of the gaussian atomic functions  $\phi_\mu(\mathbf{r})$  of the gaussian basis set as:

$$\psi_i(\mathbf{r}) = \sum_{\mu=1}^m c_{i\mu} \phi_\mu(\mathbf{r}) \quad (2.49)$$

with  $m$  the number of gaussian atomic functions (it depends on the gaussian basis set chosen) and  $c_{i\mu}$  a coefficient that determines the participation of the gaussian function  $\phi_\mu(\mathbf{r})$  into the (Kohn-Sham spin-orbital) mono-electronic wavefunction  $\psi_i$ .

The electronic density is obtained from the mono-electronic wavefunctions *via* the equation:

$$\rho(\mathbf{r}) = \sum_i^n |\psi_i(\mathbf{r})|^2 \quad (2.50)$$

By mixing equation 2.49 and 2.50, we have:

$$\rho(\mathbf{r}) = \sum_i^n \sum_{\mu}^m \sum_{\nu}^m c_{i\mu} \phi_{\mu}(\mathbf{r}) c_{i\nu} \phi_{\nu}(\mathbf{r}) = \sum_{\mu}^m \sum_{\nu}^m P^{\nu\mu} \phi_{\mu}(\mathbf{r}) \phi_{\nu}(\mathbf{r}) \quad (2.51)$$

where  $c_{i\mu}$  and  $c_{i\nu}$  are the coefficients of participation of the gaussian atomic functions  $\phi_{\mu}$  and  $\phi_{\nu}$  in the electronic density. Here we write the gaussian functions as real functions. In this equation, we have written  $P^{\nu\mu} = \sum_i^n c_{i\mu} c_{i\nu}$ , the density matrix elements

To reach the "best" wavefunction or electronic density, an infinite basis set would be needed, which would unfortunately lead to an infinite time of calculations. In practice we have to make some compromise on the basis set size and the DZVP(double-zeta valence polarized)-MOLOPT-SR gaussian basis set has been systematically used for our simulations. This is a double-zeta (DZ) type of basis set, with atomic coefficients optimized for the CP2K dual representation in calculating molecular properties in gas and condensed phase. [62].

## 2.8.2 Pseudopotentials

When using plane-waves instead of gaussians, one has to be careful about the core electrons that need a very large plane-wave basis set to be correctly modeled. Pseudopotentials aim at reducing the size of the plane wave basis set by replacing core electrons by approximated potentials and considering together these electrons and the nuclei as rigid non-polarisable ionic cores, taking into account relativistic effects. They have to accurately represent long-range interactions after a given value of a cutoff radius and their construction must give nodeless valence wave functions orthogonal to the core states. It is assumed that non significant overlap between core and valence electrons occurs.

In CP2K, the valence electrons are treated explicitly within the GTH (Goedecker-Tetter-Hutter) pseudopotentials [62, 63] approach. GTH pseudopotentials are part of the norm-conserving pseudopotentials: they conserve the normalization of the pseudo wavefunction inside the core area.

## 2.8.3 Plane Wave basis set

In CP2K, there is a PW (*Plane Wave*) basis set used on top of the gaussian one. This is the dual basis set approach or the GPW scheme (*Gaussian Plane Waves*). The electronic density described in equation 2.51 in the real space is now projected into the reciprocal space using a Fourier transform (*Fast Fourier Transform*). Note that multiple grids (with more or less sparse plane

waves) are used in the reciprocal space. The narrow and large gaussian atomic functions will not be projected on the same grid, in order to speed up the calculations and in order to describe each gaussian atomic function with the same precision. By default, CP2K uses four different grids with a relative energy cut-off of 40 Ry between each successive grid. The density projected on the plane waves is now:

$$\tilde{\rho}(r) = \sum_{\mathbf{G}}^{E_{Cut-off}} \tilde{\rho}_{\mathbf{G}} f_{\mathbf{G}}(\mathbf{r}) \quad (2.52)$$

$\tilde{\rho}_{\mathbf{G}}$  is the expansion coefficient that ensures the following condition:  $\tilde{\rho}(\mathbf{r})=\rho(\mathbf{r})$ ,  $f_{\mathbf{G}}(\mathbf{r})$  is a plane wave written as:

$$f_{\mathbf{G}}(\mathbf{r}) = \frac{e^{i\mathbf{G}\cdot\mathbf{r}}}{\sqrt{V}} \quad (2.53)$$

$V$  is the volume of the simulation box and  $\vec{G}$  a vector of the reciprocal space.

Moreover,  $\mathbf{G}$  and  $\mathbf{r}$  are orthogonal by construction and, as a consequence, do not suffer from basis-set superposition error. They are also independent on nuclei positions. As for the Gaussian basis set, an infinite plane wave basis set would be needed to converge to the "best" wavefunction in the limit of our electronic representation. In practice we have to limit its size for obvious computational reasons, therefore the basis set elements are selected according to:

$$E_{kin} = \frac{1}{2}\|\mathbf{G}\|^2 < E_{kin}^{cut} \quad (2.54)$$

where  $E_{kin}^{cut}$  represents the kinetic energy cutoff. After convergence tests (not discussed here), we chose a value of  $E_{Cut-off}=400$  Ry in all our presented works.

## 2.9 Metadynamics and Collective variables

### 2.9.1 Generalities on metadynamics technique

As stated before, predicting and analyzing chemical reactions requires *ab initio* representations. However, such processes are rare events that necessitate to overcome (possibly large) energy barriers.

Depending on  $\Delta G$  –the free energy barrier to go from one local minimum (A in Fig. 2.2) to another local minimum (B in Fig. 2.2)– and on the actual temperature in the trajectory (or equivalently the total energy of the system), a trajectory started in a local minimum will remain trapped into it for a very long time, before eventually crossing a barrier and reaching another metastable state, see Fig. 2.2.

Following the Eyring formula in the transition state theory [64], the rate constant  $k$  for going from one minimum to the other is:

$$k = \frac{k_B T}{h} \cdot e^{\frac{-\Delta G}{k_B T}} \quad (2.55)$$

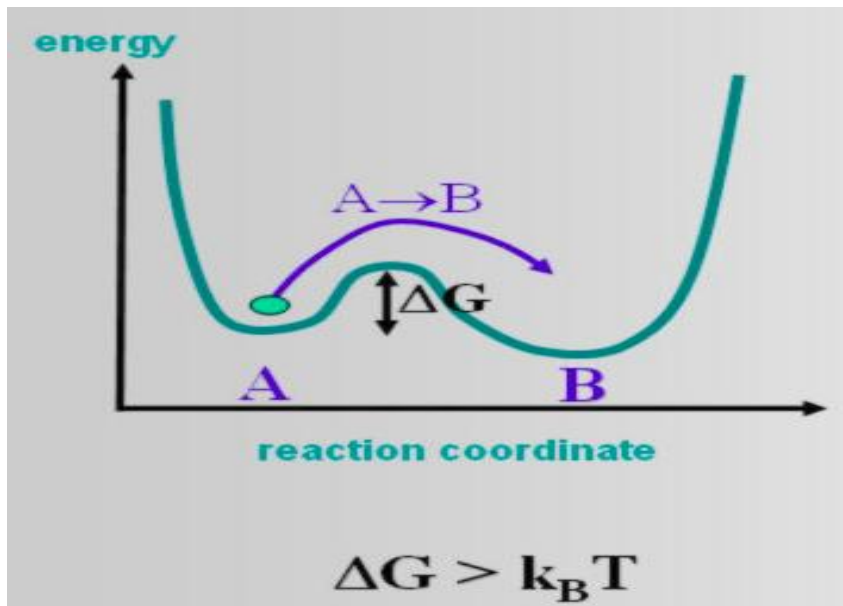


Figure 2.2: Given the reactant and the product, overcome an energy barrier  $\Delta G$  is needed.

here  $T$  is the temperature of the system,  $\Delta G$  is a free energy barrier,  $k_B$  is the Boltzmann's constant,  $\hbar$  the Planck's constant.

Thermodynamically speaking, reactants (A) and products (B) are free energy basins separated by a barrier of free energy  $\Delta G$ . In most cases, such barriers are rather high in energy and thus associated to long time scales (hours/days), that are much larger than those reachable in DFT based molecular dynamics simulations. Biased DFT-MD have therefore to be done, that will force the chemical reaction to occur/proceed. Its effect is to enhance the fluctuations in the basins, accelerating the transitions between reactants and products. There exist a few theoretical and computational methods that are able to sample the free energy surface (FES) representative of a chemical process based on biased DFT-MD simulations. To that end, a pre-choice of collective variables (CVs) has to be done, *i.e* variables that allow sample the FES, also called reaction coordinates. These can be *e.g.* distances, angles, coordination numbers, or more complex variables as we will see in the metadynamics method employed in our work.

As a general presentation of biased MD simulations, let us consider a system in the canonical ensemble for which we introduce a collective variable  $q(\mathbf{R})$  which is a function of the atomic coordinates able to distinguish the relevant metastable states of the system, from reactants to products. The probability in finding the system in a specific configuration characterized by the reaction coordinates (or collective variables) is given by

$$P(s) = \frac{1}{Q} \int e^{-\frac{U(\mathbf{R})}{k_B T}} \delta(q(\mathbf{R}) - s) d^N \mathbf{R} \quad (2.56)$$

where  $Q$  is the partition function from statistical mechanics, and  $U$  is the

potential energy of the system for coordinates  $\mathbf{R}$ . The free energy related to this quantity is

$$F(s) = -k_B T \ln P(s), \quad (2.57)$$

and thus  $P(s) = e^{-\frac{F(s)}{k_B T}}$ .

As a consequence, if it were possible to explore the entire configuration space of a system, in principle feasible by means of an extremely long equilibrium Molecular Dynamics (MD) trajectory, it would be straightforward to reconstruct its FES. Unfortunately, the rates at which chemical reactions evolve (from few picoseconds to hours) makes infeasible the application of even classical MD techniques to efficiently and exhaustively sample the whole FES.

Enhanced sampling algorithms overcome this limitation and reconstruct the FES: in this thesis we employed metadynamics (MetD) [65] to that end. This approach biases the potential energy along a set of collective variables to sample the associated free energy landscape. In metadynamics, the bias is represented by a history dependent function which, during the dynamics evolution, decreases the probability of visiting configurations already explored (history dependent adaptive bias).

In particular, by depositing (typically Gaussian) hills of potential energy centered in the visited points of the collective variables space, metadynamics is able to fill the local free energy minima and escape them when they have been fully explored, and at the end of the dynamics, to reconstruct the underlying FES, see scheme in Fig. 2.3.

At time  $t$ , the bias is

$$W(s, t) = \sum_{i=1}^{N_{\text{hills}}(t)} h e^{-\left(\frac{s-s(t_i)}{\sigma_i}\right)^2}, \quad t_i = i \cdot \tau \quad (2.58)$$

where  $\tau$  is the inverse of the hills deposition rate  $h$  (*i.e.*, the metadynamics time step). Step by step the filling procedure of the "valleys" and of the "mountains" characterizing the FES will lead (in principle in the limit of infinite times) to a "flattening" of this latter once the convergence of the calculation has been achieved. Indeed, a central assumption of metadynamics is that

$$-\lim_{t \rightarrow \infty} W(s, t) \simeq F(s) + \text{const.} \quad (2.59)$$

The statistical convergence of metadynamics is a key aspect in accurately reconstructing the FES. Although in expression 2.59 the concept of infinite limit has been introduced, in practice, time-scales are limited, especially for DFT-metadynamics. Therefore, convergence is achieved when the free energy profile does not evolve anymore with more hills added. Standard metadynamics are done with fixed-height Gaussian hills, while the well-tempered metadynamics variant [66] can be employed. In this latter approach, potential hills of progressively reduced heights are hence deposited when the simulation proceeds, becoming almost negligible once the convergence is achieved.

As briefly stated, the need of the *a priori* choice of the collective variables which drive the chemical reaction limits in a way the applicability and transferability of metadynamics techniques. It is indeed not always straightforward

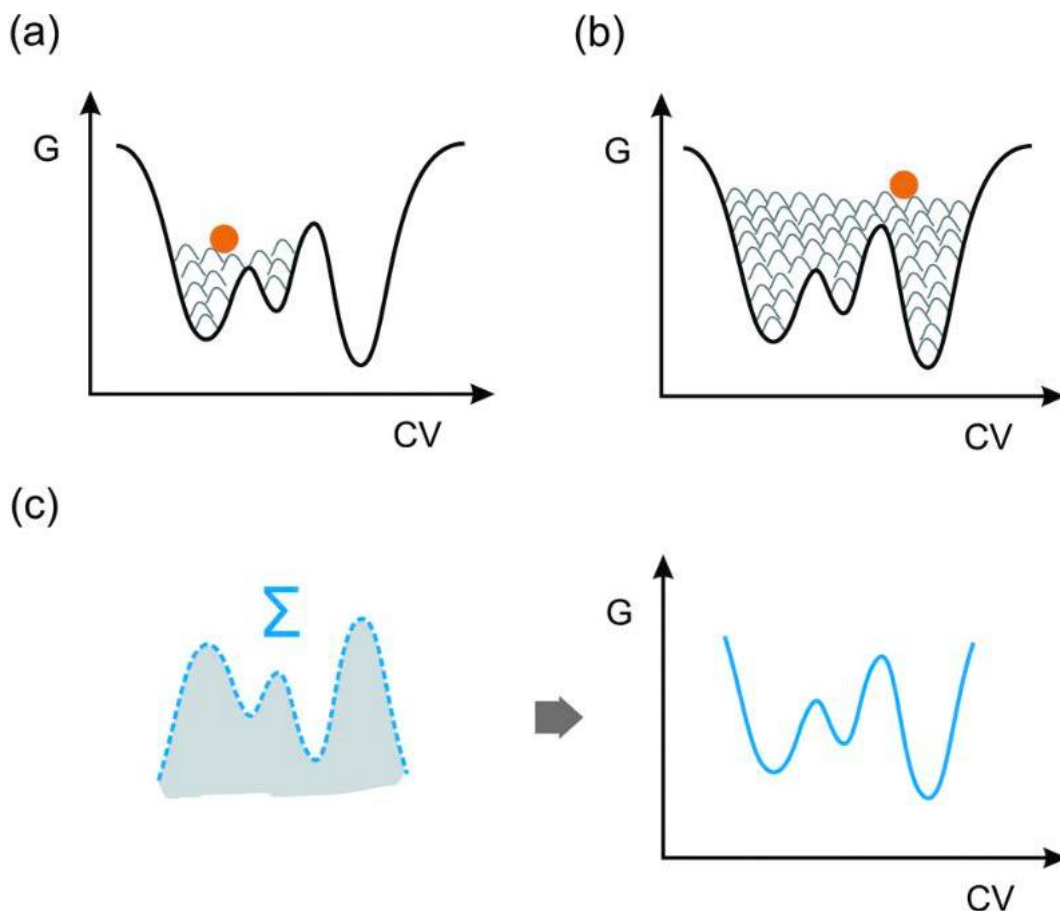


Figure 2.3: Schematic representation of the metadynamics technique. A walker (orange dot) explores the unknown free energy landscape of the system along pre-chosen collective variables (i.e. reaction coordinates). Gaussian hills are added intermittently to allow the walker to overcome high-energy regions and accelerate the sampling of rare events (a). Once the underlying free energy landscape is completely filled (b), the free energy landscape is reconstructed based on the sum of the spawned Gaussians (c).

to predict which is the minimum set of collective variables that are essential in reconstructing the FES for the chemical reaction of interest (which processes and pathways are the unknowns). Moreover, the space of the collective variables grows exponentially with the number of CVs which is computationally more and more expensive.

## 2.9.2 Path collective variables with a new definition of distance metric

Branduardi *et al.* [67] introduced the so-called "path collective variables" to estimate the lower free energy path that connects an initial state  $\mathbf{R}_I$  to a final state  $\mathbf{R}_F$ , where  $\mathbf{R}$  denotes the  $3N$  cartesian coordinates of the given state.

As illustration to the method, in Fig. 2.4, we use the oxygen evolution

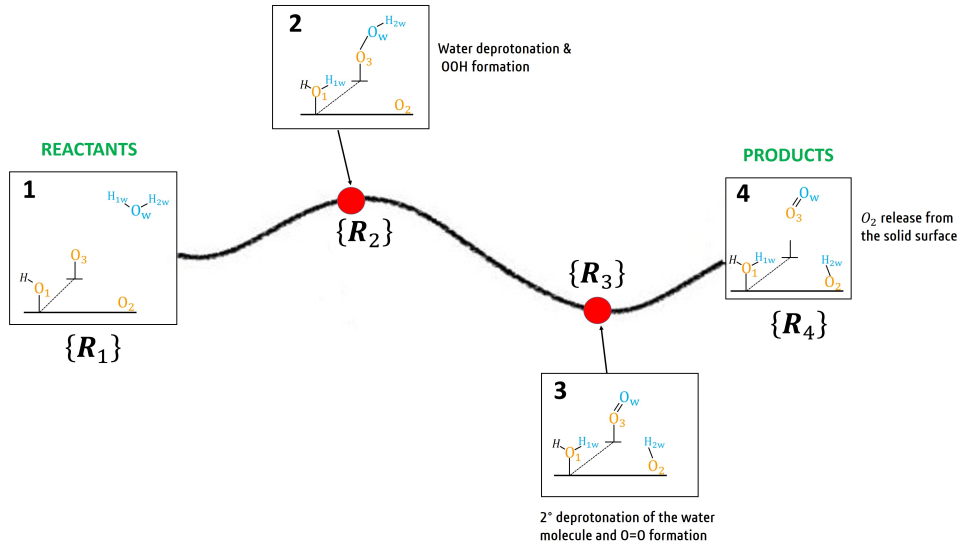


Figure 2.4: Model of the oxygen evolution reaction (OER) in the gas phase based on four *a priori* established reaction steps. 1) reactants: 1 water molecule (in blue color) and oxygens (in orange color) at the catalyst surface. 2) water deprotonation at the catalyst surface and the formation of the intermediate OOH species at the catalyst surface. 3) 2<sup>nd</sup> deprotonation of the water molecule and the O=O formation. 4) O<sub>2</sub> (gas) desorption from the catalyst surface.  $\mathbf{R}_{1-4}$  denote the 3N cartesian coordinates of each given state along the 4-step process.

reaction (OER) as a reaction model (similarly to the mechanism proposed by Rossmeisl, Norskov, and coworkers [29, 31]) which consists of 4 *a priori* established reaction steps. The initial step 1 shows one water molecule (in blue color) and bare oxygens (at the catalyst surface) as reactants, described by the set of cartesian coordinates  $\mathbf{R}_1$ . The final step, labelled 4 with its set of cartesian coordinates ( $\mathbf{R}_4$ ), consists in O<sub>2</sub> desorbed from the catalyst surface, with 2 oxygen atoms non protonated at the surface. The OER proceeds from 1 to 4 through intermediate reaction steps 2 and 3. The intermediate reaction step 2, with its set of cartesian coordinates ( $\mathbf{R}_2$ ), shows the water deprotonation at the catalyst surface and the formation of the intermediate OOH species at the catalyst surface, while reaction step 3, with its set of cartesian coordinates ( $\mathbf{R}_3$ ), shows the 2<sup>nd</sup> deprotonation of the water molecule and the O=O formation.

In a nutshell, the reaction might be very complex and happening with many degrees of freedom and several intermediate steps, as the OER illustrated here.  $\mathbf{R}_{1-4}$  is the ideal path for the chemical reaction to occur. What we now need is a parameter that, given a random cartesian configuration  $\mathbf{R}(t)$  at time  $t$ , just tells how far this configuration is away from the *a priori* established reaction path  $\mathbf{R}_{1-4}$ .

Path collective variables are the extension of this concept in the case one has many intermediate (cartesian) conformations that describe the reaction

path, and therefore, instead of an index that goes from 1 to 2, one needs an index that goes from 1 to  $N$ , where  $N$  is the number of reaction steps described by cartesian configurations  $\mathbf{R}_{i=1,\dots,N}$ . These cartesian configurations  $\mathbf{R}_{i=1,\dots,N}$ , that describe an ideal reaction path with intermediate reaction steps, compose our reference reaction path (as  $\mathbf{R}_1$ ,  $\mathbf{R}_2$ ,  $\mathbf{R}_3$  and  $\mathbf{R}_4$  compose the *a priori* established reference reaction path for the aforementioned OER). From a mathematical point of view, the progress along a given reaction path  $S(\mathbf{R}(t))$  is calculated with the following equation:

$$S(\mathbf{R}(t)) = \frac{\sum_{i=1}^N i \cdot e^{-\lambda|\mathbf{R}(t)-\mathbf{R}_i|}}{\sum_{i=1}^N e^{-\lambda|\mathbf{R}(t)-\mathbf{R}_i|}} \quad (2.60)$$

where in eq. 2.60 the  $\mathbf{R}(t) - \mathbf{R}_i$  represents a distance metric  $D(\mathbf{R}(t), \mathbf{R}_i)$ , in terms of  $3N$  Cartesian coordinates, between the cartesian configuration  $\mathbf{R}(t)$  explored at time  $t$  and the closest cartesian reference configuration  $\mathbf{R}_i$  among the  $\mathbf{R}_{i=1,\dots,N}$  references. The parameter  $\lambda$  is a positive value that is tuned in a way explained later.

An additional parameter  $Z(\mathbf{R}(t))$  is introduced by Branduardi *et al.* [67] in order to take explicitly into account the aforementioned distance  $D(\mathbf{R}(t), \mathbf{R}_i)$  of one configuration  $\mathbf{R}(t)$  at time  $t$  from the closest reference configuration  $\mathbf{R}_i$  that belongs to the reference reaction path  $\mathbf{R}_{i=1,\dots,N}$ :

$$Z(\mathbf{R}(t)) = \lambda^{-1} \log \sum_{i=1}^N e^{-\lambda|\mathbf{R}(t)-\mathbf{R}_i|} \quad (2.61)$$

To summarize, given a reference reaction path described by reference cartesian coordinates  $\mathbf{R}_{i=1,\dots,N}$ ,  $S(\mathbf{R}(t))$  and  $Z(\mathbf{R}(t))$  are descriptors that respectively represent the progress along the reference reaction path and the distance from it. These two variables  $S(\mathbf{R}(t))$  and  $Z(\mathbf{R}(t))$ , put together can be visualized as in Fig. 2.5, for the OER, where the reference path is given by  $\mathbf{R}_{i=1,\dots,N} = \mathbf{R}_{i=1,\dots,4}$

When a reaction path is similar to the *a priori* established reference path  $\mathbf{R}_{i=1,\dots,N}$ , means that what is happening during the reaction is similar (or equal) to the *a priori* established reaction steps, the simulation is thus reliably reproducing the path provided by  $\mathbf{R}_{i=1,\dots,N}$  in input as reference. For this latter case, one thus obtain low values of the  $Z(\mathbf{R}(t))$  parameter.

If by chance, the simulation finds some other pathway, as in Fig. 2.5 where an alternative OER route is depicted in blue dashed line, it is possible to find intermediate reaction steps (as for step  $\mathbf{R}(t)$  in Fig. 2.5) that are rather different from the reference path. For this latter case, one obtain high values of the  $Z(\mathbf{R}(t))$  descriptor.

The path-CV described above is based on the aforementioned distance metric  $D(\mathbf{R}(t), \mathbf{R}_i) = \mathbf{R}(t) - \mathbf{R}_i$  which involves to work with the  $3N$  cartesian coordinates  $\mathbf{R}$  of a given reaction state. Pietrucci and Saitta [33] recently developed a new distance metric  $D(\mathbf{R}(t), \mathbf{R}_i)$  suitable for chemical reactions based not anymore on the  $3N$  cartesian coordinates but based on coordination numbers

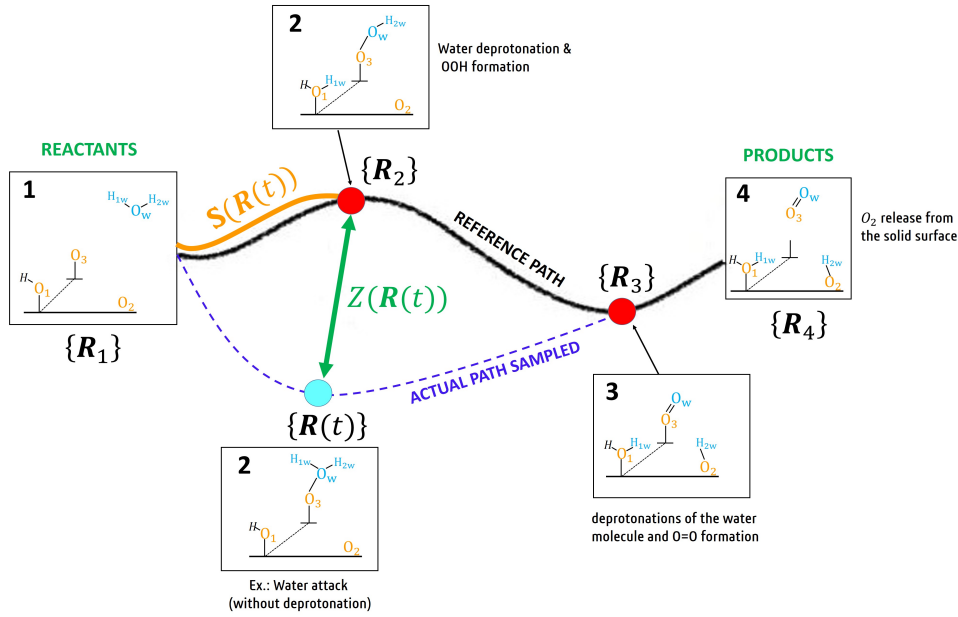


Figure 2.5: The  $S(\mathbf{R}(t))$  variable can be thought as the length of the orange segment, while the  $Z(\mathbf{R}(t))$  variable is the length of the green one. The black line denotes the a priori OER reference path  $\mathbf{R}_{i=1,\dots,4}$ . The blue dashed line denotes the actual path sampled by the metadynamics which becomes an alternative OER reaction route with an intermediate state  $\mathbf{R}(t)$ .

of the atoms involved in the reaction of interest, hence simplifying the calculations. The new distance metric is defined as:

$$D(\mathbf{R}(t), \mathbf{R}_i) = \sum_{IJ} [C_{IJ}(t) - C_{IJ}^{\mathbf{R}_i}]^2, \quad (2.62)$$

where  $C_{IJ}$  is the coordination number of atom  $I$  with all other atoms  $J$  as calculated at time  $t$  of metadynamics, and  $C^{\mathbf{R}_i}$  is its reference value referred to the closest reference configuration/structure  $\mathbf{R}_i$ . In practice the quantity  $C_{IJ}$  is defined by means of the following switching function:

$$C_{IJ}(t) = \sum_J \frac{\left[1 - \left(\frac{\mathbf{R}_{IJ}(t)}{R_{SS'}^0}\right)^N\right]}{\left[1 - \left(\frac{\mathbf{R}_{IJ}(t)}{R_{SS'}^0}\right)^M\right]}, \quad (2.63)$$

where atoms  $I$  and  $J$  are atoms of distinct species  $S$  and  $S'$ ,  $R_{SS'}^0$  takes into account the natural bond lengths between the two distinct atoms (it depends on the two species  $S$  and  $S'$  because, e.g., a C–H bond length is shorter than a C–C bond length.)

The new definitions of the distance metric in eq. 2.62 and the switching function in eq. 2.63, are well-suited to chemical reactions since coordination numbers are permutation invariant with respect to atoms  $I$  belonging to a given species  $S$ : any hydrogen, for instance, can take part in a protonation

event (*i.e.*, it can come from the solvent, from the solute, etc.). Adopting this new definition for the calculation of  $S$  and  $Z$  parameters, we overcome the limit of all the (standard) metadynamics techniques which *a priori* constrain the reactant atoms and hence the reaction path. As already shown in Fig. 2.5, using this new metadynamics framework, it is possible to find alternative reaction pathways (blue dashed lines in Fig. 2.5) completely different from the *a priori* established reference reaction path  $\mathbf{R}_{i=1,\dots,N}$

The coordination numbers of the atoms involved in the reaction path, *i.e.* the coordination numbers of the reactant and product atoms, and possibly atoms in intermediate reaction steps, are arranged in a simple matrix called "contact matrix". As illustration, one contact matrix for the OER reactants and one contact matrix for the OER products are depicted in Fig. 2.6:

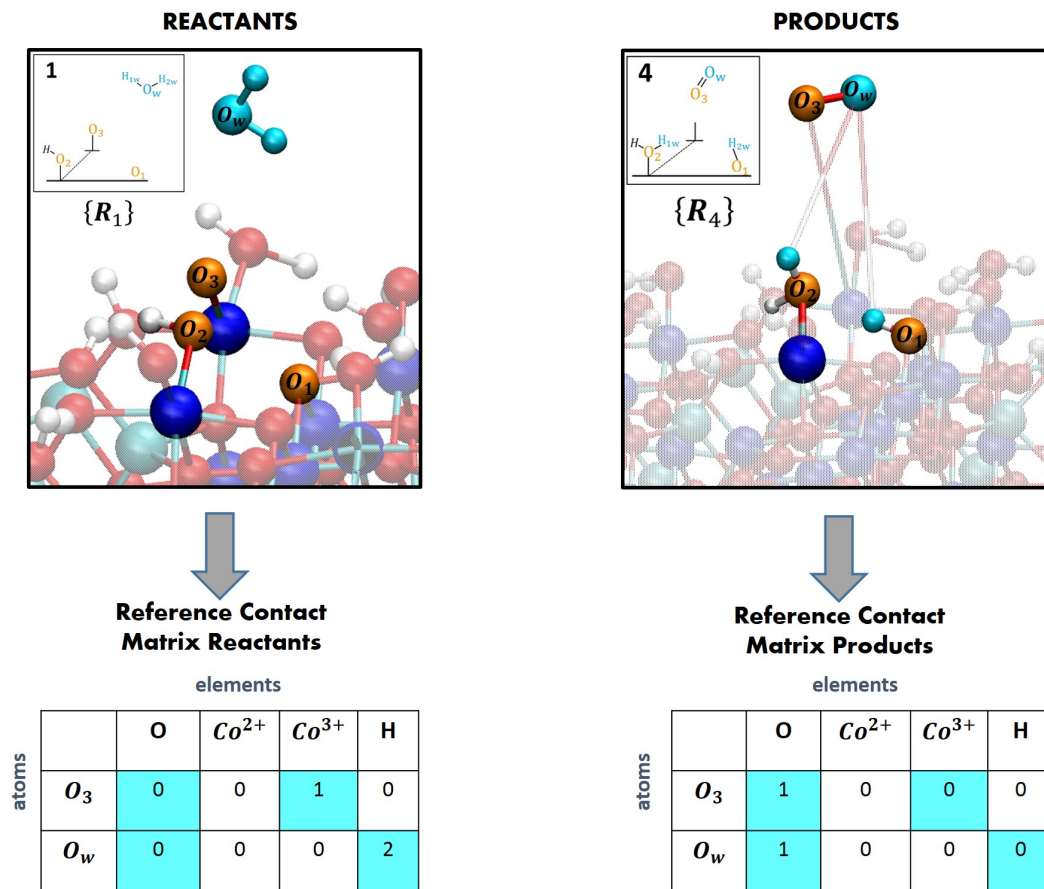


Figure 2.6: a) Construction of the coordination patterns identifying reactants and products for the contact matrix of reactants and products. Top: Reference structure of reactant  $\mathbf{R}_1$  (3 surface oxygen atoms in orange color and 1 water molecule in light blue color) and product  $\mathbf{R}_4$  (desorption of  $O_2$ ). Bottom: contact matrix represented by tables having individual atoms as rows and atomic species as columns. Background colors in matrix elements indicate changes of coordination numbers between reactant and product. All other matrix elements are free to change as well during the phase space exploration thanks to the flexibility of path collective variables. Adapted from ref. [33].

*Contact Matrix Reactants:*  $O_3$  and  $O_w$  are 'chosen' as the main characters for the OER, *i.e.* they will form  $O = O$  at the end of the OER. Hence, we build the contact matrix in terms of coordination numbers of  $O_3$  and  $O_w$  with all the other atoms species, *i.e.*  $O$  (whether they belong to surface or water),  $Co^{2+}$  (surface),  $Co^{3+}$  (surface), and  $H$  (whether they belong to surface or water). At the beginning of the OER, *i.e.* at step/configuration  $\mathbf{R}_1$ ,  $O_3$  is bonded to one  $Co^{3+}$  (in blue color in Fig. 2.6) and hence one has to put 1 in the 4<sup>th</sup> column-2<sup>nd</sup> line (cross-point between  $Co^{3+}$  column and  $O_3$  line) in the contact matrix.  $O_w$  is initially bonded to its 2 hydrogens and hence we put 2 in the 5<sup>th</sup> column-3<sup>rd</sup> line (cross-point between  $H$  column and  $O_w$  line) in the contact matrix.

*Contact Matrix Products:* at the end of the OER,  $O_3$  and  $O_w$  are now bonded to each other and hence we put 1 in the 2<sup>nd</sup> column-2<sup>nd</sup> line (cross-point between  $O$  column and  $O_3$  line) and in the 2<sup>nd</sup> column-3<sup>rd</sup> line (cross-point between  $O$  column and  $O_w$  line) in the contact matrix.

The most striking advantage of this metadynamics technique resides in the fact that, in principle, no insights might be known about the reaction path under investigation, *i.e.* there are no pre-determined trajectories in order to produce a desired (reference) dynamical evolution of the atomic entities. Instead, a simple "contact matrix"/coordination numbers description of the initial and final reaction states is required. Moreover, by its formulation, this new method represents a straightforward way to compute free energy surfaces (FES) in topologically equivalent CV spaces of gas phase and condensed phase chemical reactions. In this way, also a direct comparison between these two situations can be made, highlighting the role of the solvent in possibly assisting complex reactions. That is exactly what has been done in our work.

The aforementioned  $\lambda$  in equations 2.60 and 2.61 is a parameter introduced in order to provide a value of  $S(\mathbf{R}(t))$  and  $Z(\mathbf{R}(t))$  which is continuous (without discontinuity). The authors of the method have shown that the parameter  $\lambda$  has to be tuned following the semi-empirical equation:

$$\lambda = \frac{2.3 \cdot (N - 1)}{\sum_{IJ} C_{IJ}^{(N)} - C_{IJ}^{(1)}} \quad (2.64)$$

where  $C_{IJ}^{(N)} - C_{IJ}^{(1)}$  is new distance metric  $D$  in terms of coordination patterns, between the final configuration  $\mathbf{R}_{i=N}$  and the initial configuration  $\mathbf{R}_{i=1}$  of the reference path.

Therefore, it is possible to construct the free energy landscape of the OER as a 3D plot in terms of the two descriptors  $S$  and  $Z$ , now used as "new reaction coordinates". See Fig. 2.7 for the 3D plot.

To conclude, the "contact matrix" (or officially named the "permutation invariant vector-based path coordinates" [68]) method has been employed in the majority of the free energy calculations presented in this thesis. Once the "map" of the free energy landscape is obtained, it is also possible to perform a series of umbrella sampling [65] simulations in order to refine the sampling of

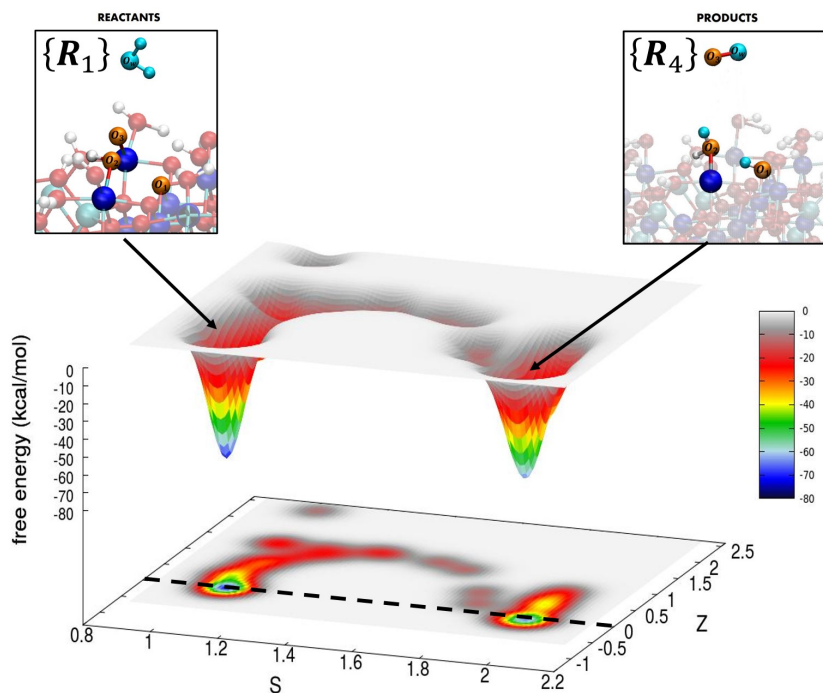


Figure 2.7: *Example of computed free energy surface of the OER (gas phase) with the contact matrix metadynamics method, and plotted in terms of  $S$  and  $Z$  descriptors. Note that there is a free energy path that connects reactants and products and runs very close to the zero distance  $Z$  from the reference path (see black dashed line where reactants and products are at the height of  $Z = 0$ ). This means that the input referential path resembles what is really sampled along the metadynamics. One can see, in this figure, that there are not alternative reaction route different from the 'straight' (reactant to product) reaction pathway sampled.*

the reaction path and hence refine the energetics of the FES, if one wishes. For the sake of completeness, a brief description of the umbrella sampling technique follows.

## 2.10 Umbrella sampling

The sampling probability (2.56) can be modified by virtue of a biased potential added to the system which depends only on the collective variables (CVs). For the sake of simplicity, we will take only one CV but the following treatment can be straightforwardly extended to multi-dimensional FES. The potential energy will be thus modified by the following expression  $U(q) \rightarrow U(q) + V(s(q))$ . Hence the biased distribution of the CV will be:

$$P'(s) \propto \int e^{-\frac{U(q)+V(s(q))}{k_B T}} \delta(s - s(q)) \propto e^{-\frac{V(s(q))}{k_B T}} P(s), \quad (2.65)$$

and the biased free energy  $F'(s)$  is now:

$$F'(s) = -k_B T \ln P'(s) = F(s) + V(s) + \text{const.} \quad (2.66)$$

The additional constant is irrelevant in determining the FES since only energy differences are meaningful. By removing *a posteriori* the bias potential one can simply recover the unbiased FES  $F(s)$

$$F(s) = F'(s) - V(s) + \text{const.} \quad (2.67)$$

In practice, one of the most used bias potential is the harmonic one defined as

$$V(s) = \frac{1}{2} k (s - s_0)^2 \quad (2.68)$$

where  $k$  is the strength of the constant of the harmonic oscillator that constrains the coordinate  $s$  towards the reference  $s_0$ .

In a two-dimensional case - *i.e.*, a FES that would depend on two CVs,  $s$  and  $z$  - the harmonic potential has the form  $V(s, z) = \frac{1}{2} k_s (s - s_0)^2 + \frac{1}{2} k_z (z - z_0)^2$ . In the one-dimensional case, the sampled distribution will be defined by

$$P'(q) \propto P(q) e^{\frac{k(s(q)-s_0)^2}{2k_B T}} \quad (2.69)$$

and the consequent biased free energy can be evaluated by (2.66), while by means of eq. (2.67) one can recover the unbiased free energy.

The bias produces an enhanced sampling in regions close to the minimum  $s_0$  of the bias. In order to sample a large portion of the FES, one has to combine multiple independent umbrella sampling simulations centered on distinct  $s_0$  values. Moreover, for statistical reasons, each sampled window has to overlap with the nearest other sampled region as much as possible.

## 2.11 Static electric fields in *ab initio* simulations

In the work described from section 8.1 to 8.5, electrified air/water interfaces have been simulated, requiring the application of an external electric field during the *ab-initio* molecular dynamics.

The implementation of electric fields in *ab initio* codes is all but trivial. A large literature exists in this field [69, 70, 71, 72, 73]. One of the key points/issues is the PBC in the simulations, and the discontinuities of the electric field  $\mathcal{E}$  at the border of the simulation boxes. At the edges of the boxes, infinite electric fields are found when a linear electrostatic potential is applied within. The periodicity in the presence of a macroscopic electric field  $\mathcal{E}$  will lead to a change in the electronic potential in each replica of the simulation box, as depicted in Fig. 2.8:

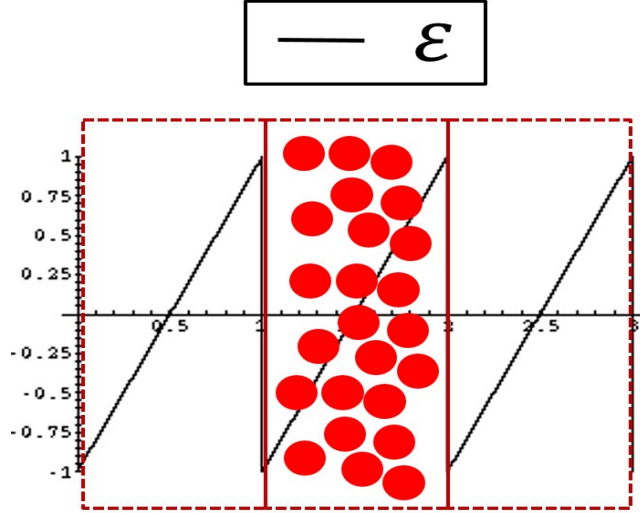


Figure 2.8: *Schematic representation of a sawtooth electrostatic potential in each replica of the simulation box in the presence of a macroscopic electric field  $\mathcal{E}$ .*

The intrinsic problem resides in the non-periodic nature of the position operator. In particular, the electronic potential changes by a factor of  $e\mathcal{E} \cdot \mathbf{R}$  under a translation by a lattice vector  $\mathbf{R}$ . Many perturbative treatments for the application of an electric field have been proposed in the literature but the implementation of an external electric field in numerical codes based on DFT can be achieved by exploiting the *Modern Theory of Polarization* [74, 75] and the *Berry phase* [76] (see *e.g.* ref. [77] for the technical implementation of a static and homogeneous electric field in *ab initio* codes and ref. [78] for a review of several methods that allow for the application of external fields in various simulation frameworks).

Within the *Modern Theory of Polarization* [74, 75] and of the *Berry phase* [76], one can introduce a variational energy functional [77]:

$$E^{\mathcal{E}}[\{\psi_i\}] = E^0[\{\psi_i\}] - \mathcal{E} \cdot P[\{\psi_i\}] \quad (2.70)$$

where  $E^0[\{\psi_i\}]$  is the energy functional of the system in the zero-field approach and  $P[\{\psi_i\}]$  is the polarization along the field  $\mathcal{E}$  direction, as defined by Resta [74]:

$$P[\{\psi_i\}] = -\frac{L}{\pi} \text{Im}(\ln \det S[\{\psi_i\}]) \quad (2.71)$$

where  $L$  is the periodicity of the cell and  $S[\{\psi_i\}]$  is a matrix composed of the following elements

$$S_{i,j} = \langle \psi_i | e^{2\pi i x/L} | \psi_j \rangle \quad (2.72)$$

for doubly occupied wavefunctions  $\psi_i$ . Umari and Pasquarello [77] demonstrated that this variational approach is valid for treating finite homogeneous electric fields in first-principles calculations and that it can be extended to provide atomic forces in first-principles MD simulations by adding the following term to the functional (8.1):

$$E_{ion}^{\mathcal{E}} = -\mathcal{E} \cdot P_{ion}, \quad P_{ion} = \sum_{i=1}^{N_{ion}} Z_i \cdot R_i, \quad (2.73)$$

where  $P_{ion}$  is the ionic polarization,  $R_i$  is the position coordinate in the field direction and  $Z_i$  is the charge of the ionic core, this definition leads to an extra-term on the force acting on the  $i$ -th atom equal to  $F_i = \mathcal{E}Z_i$ .



## Chapter 3

# Oxygen Evolution Reaction (OER): principles of thermodynamics

In the following, we will first provide a general introduction to the basis of the water splitting thermodynamics.

The water splitting chemical process is the decomposition of liquid water into oxygen and hydrogen gas, following the chemical reaction:

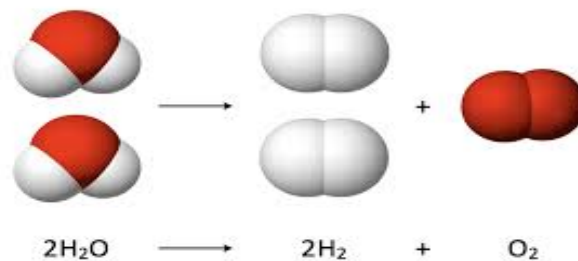
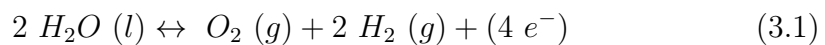
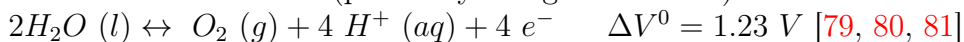


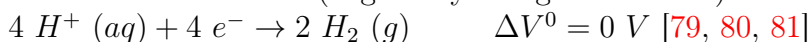
Figure 3.1: *Water splitting reaction.*

where starting from two liquid water molecules, one molecule of oxygen gas and two molecules of hydrogen gas are produced. This process is called water splitting because water molecules ( $2 H_2O (l)$ ) are chemically splitted into their constituent parts, oxygen ( $O_2$ ) and hydrogens ( $2 H_2$ ) via a 4-electron transfer process ( $4 e^-$ ). Note that, the water splitting is a redox chemical reaction, divided into two half-reactions: the oxygen evolution reaction (**OER**) and the hydrogen evolution reaction (**HER**):

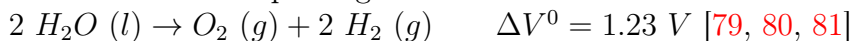
**OER** at the anode (positively charged electrode)



**HER** at the cathode (negatively charged electrode)



The overall water splitting reaction is:



where  $\Delta V^0$  is the theoretical cell potential at standard conditions – *i.e.* at 298 K (temperature) and 1 atm (pressure)– and *vs* SHE (Standard Hydrogen Electrode, *i.e.* used as the reference). The resultant  $\Delta V^0 = 1.23 V$  [79, 80, 81] potential is an ideal and theoretical potential to be applied in an electrochemical cell between the anode and the cathode electrodes for the water splitting to occur (see the following sections 3.1 and 3.2 for all the details about the  $\Delta V^0$  calculation). The theoretical standard cell potential for the overall water splitting reaction of 1.23 V is due only to the energy cost of the OER occurring at the negatively charged anode electrode.

In this chapter we want to go a bit deeper in understanding the thermodynamics and the kinetics behind the OER in electrochemical conditions (electrolysis), and hence understand the operative cell potential for which the water splitting reaction can occur. In general, this thesis has the aim to model the OER electrochemical reaction and the energetics associated to the reaction, especially the OER catalytic performances of the  $Co_3O_4$  and  $CoO(OH)$  cobalt oxides.

### 3.1 Thermodynamics of the Water Splitting Reaction

The cleavage of water in its constituents can occur via two main processes: photocatalytic water splitting, *i.e.* the photolysis process, and electrochemical water splitting, *i.e.* the electrolysis process. The electrolysis of water is the decomposition of liquid water into oxygen and hydrogen gas due to the passage of an electric current generated by an external DC (direct current) electrical power source, see Fig. 3.2-a. In the photolysis of water, by definition, the electric current needed to split water is provided by artificial or natural light, as depicted in Fig. 3.2-b.

We consider the thermodynamics of the water splitting process under standard conditions – *i.e.* at 298 K (temperature) and 1 atm (pressure). The Gibbs reaction energy is:

$$\Delta G_{reaction}^0 = \sum \Delta G_{products}^0 - \sum \Delta G_{reactants}^0 \quad (3.2)$$

where  $\sum \Delta G_{products}^0$  is the standard Gibbs free energy of formation of the products ( $O_2 (g) + 2 H_2 (g)$ ) and  $\sum \Delta G_{reactants}^0$  is the standard Gibbs free energy of formation of the reactants  $2 H_2O (l)$ .

If one refers to tabulated thermodynamic data in the *Lange’s Handbook of Chemistry* [79], *CRC Handbook of Chemistry Physics* [80] and in *NIST JANAF tables* [81] –where the standard Gibbs energy formation of 1 mole of a chemical species from its constituent elements in standard condition are listed– both

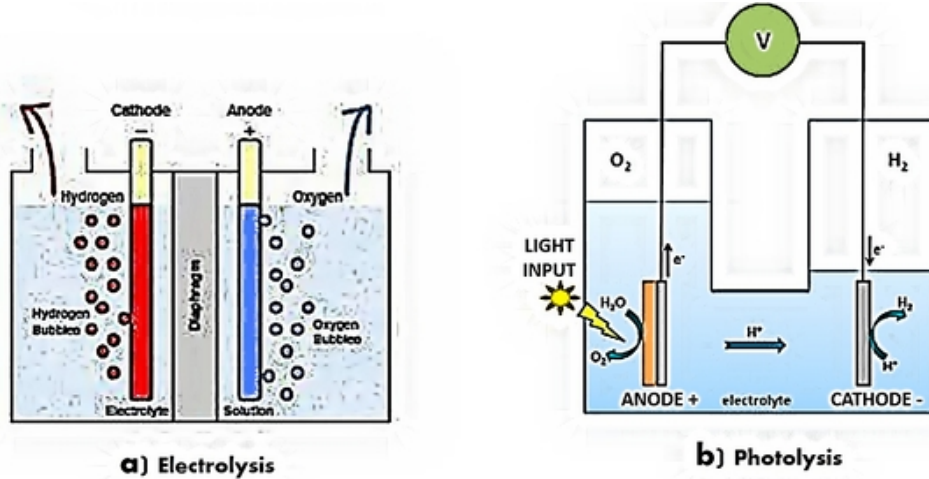


Figure 3.2: Schematic figure of the water splitting via a) electrolysis in an electro-chemical cell b) photolysis in a photo-electrochemical cell.

hydrogen gas and oxygen gas (in their standard gas states) have a Gibbs Free energy of 0 and hence the  $\sum \Delta G_{products}^0$  term in eq. 3.2 is equal to 0 (for the water splitting reaction).

The standard Gibbs free energy of formation of 2  $H_2O(l)$  is however  $-474.26 \text{ kJ} \cdot \text{mol}^{-1}$ , therefore eq. 3.2 becomes:

$$\Delta G_{reaction}^0 = 0 \text{ kJ} \cdot \text{mol}^{-1} - (-474.26 \text{ kJ} \cdot \text{mol}^{-1}) = 474.26 \text{ kJ} \cdot \text{mol}^{-1} \quad (3.3)$$

revealing the endothermic nature of the water splitting reaction (a non-spontaneous reaction, *i.e.* a reaction which needs an energy input to proceed).  $\Delta G_{reaction}^0$  is related to the standard redox potential  $\Delta E^0$  (in volts) required for the occurrence of the reaction by :

$$\Delta G_{reaction}^0 = -n \cdot F \cdot \Delta E^0 \quad (3.4)$$

where  $n$  is the number of electrons involved in the reaction ( $4 e^-$  in our case) and  $F$  is the Faraday constant ( $=96.485 \text{ kJ/V}$ ).

Using the relation in eq. 3.4, we can calculate the theoretical voltage  $\Delta E^0$  (standard redox potential) required for the water splitting reaction to occur as:

$$\Delta E^0 = -\frac{\Delta G_{reaction}^0}{n \cdot F} = -1.23 \text{ V} \quad (3.5)$$

where  $n=4$  is the number of electrons transferred in the overall water splitting reaction.

We remind the reader that a spontaneous redox reaction is characterized by a negative value of  $\Delta G_{reaction}^0$  and a positive value of  $\Delta E^0$ . In our case, the water splitting is a non-spontaneous reaction (endothermic), therefore characterized by a positive value of  $\Delta G_{reaction}^0 = 474.26 \text{ kJ} \cdot \text{mol}^{-1}$  (in eq. 3.3) and a negative value of  $\Delta E^0 = -1.23 \text{ V}$  (in eq. 3.5).

## 3.2 Principles in Water Electrolysis

In this thesis we focus on the electrolysis of water which is thermodynamically disfavored and as such requires an input of energy to drive the process. In the case of the electrolytic splitting of water into hydrogen and oxygen, this energy input is a potential difference  $\Delta V$  between the anode and the cathode of an electrochemical cell. In conventional electrochemical cells (see Fig: 3.3, the OER occurs at the positively charged anode electrode (oxidation chemical process at the anode) and the HER takes place at the negatively charged cathode electrode (reduction chemical process at the cathode), in acidic aqueous solution (*aq*) environment (low pH), as illustrated in Fig. 3.3:

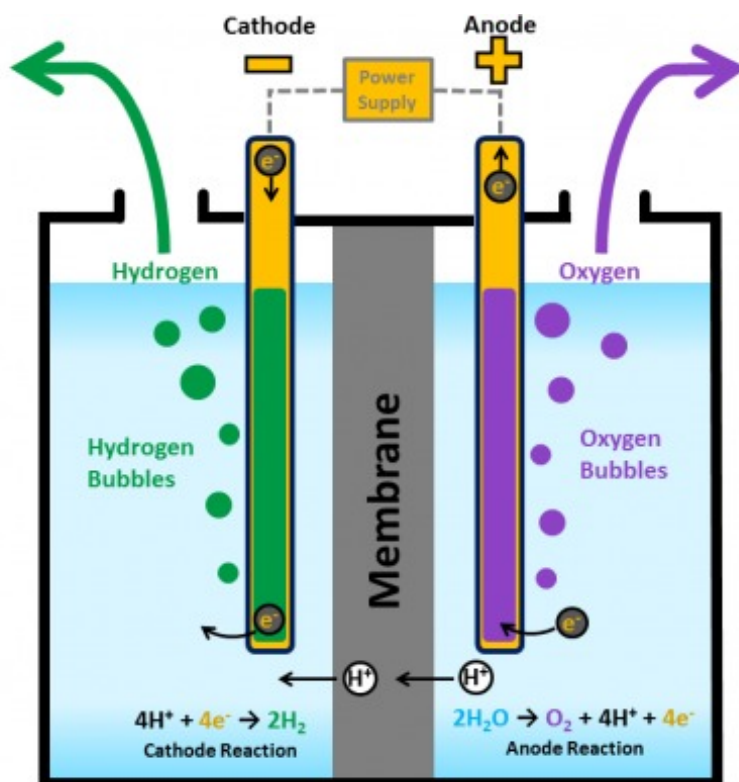
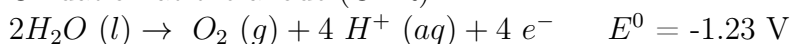
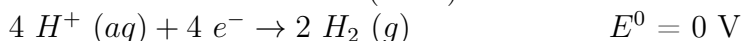


Figure 3.3: Schematic figure of the water splitting reaction via electrolysis in a conventional electrochemical cell.

Oxidation at the anode (OER):



Reduction at the cathode (HER):



where  $E^0$  is the theoretical onset potential of the OER at standard conditions –*i.e.* at 298 K (temperature) and 1 atm (pression)– and *vs* SHE. The Standard Hydrogen Electrode is a platinum electrode, by definition declared to be at zero volt potential at any temperature. The platinum electrode is dipped in an acidic solution where hydrogen gas is bubbled through, following the redox

reaction:  $2 H^+ (aq) + 2 e^- \rightarrow H_2 (g)$ , where the  $H^+$  ions in the acidic solution are assumed to have no interaction with other ions, *i.e.* a theoretical ideal solution analogous to an ideal gas from the point of view of thermodynamics.

Note that, an electrochemical cell will always have a positive voltage. The negative (standard redox) potential  $\Delta E^0 = -1.23 \text{ V}$  of the water splitting reaction we found in eq. 3.5 just means that the electrochemical cell will operate spontaneously (without an applied voltage) in the opposite direction, *i.e.* the reverse reaction of the water splitting  $O_2 (g) + 2 H_2 (g) \rightarrow 2 H_2O (l)$  is thermodynamically favoured (spontaneous reaction). Accordingly, in the electrochemical cell we have to consider the following relation:

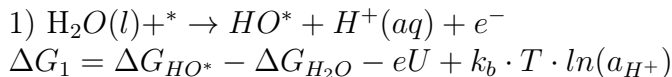
$$|\Delta E^0| = |1.23| \text{ V} = \Delta V^0 \quad (3.6)$$

where  $\Delta V^0$  is the cell potential, *i.e.* the potential difference (between the anode and the cathode of an electrochemical cell) required for the water splitting to occur at standard conditions.

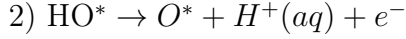
The standard cell potential  $\Delta V^0 = 1.23 \text{ V}$  required in the electrochemical cell is due to the OER only which occurs at the anode electrode (as  $\Delta E^0 = 0 \text{ V}$  for the HER at the cathode). This is a significant potential. Mainly due to this required high potential at the oxygen-evolving anode, extensive research has shown that the potential needed to split water at rates provided for instance by the solar flux (*e.g.*,  $10 \text{ mA/cm}^2$ ) [23] is limited primarily by the sluggish kinetics of the OER [24, 25] being a 4-electrons-transfer process.

At this stage, we remind the reader that the value of  $\Delta V^0 = 1.23 \text{ V}$  is an ideal and theoretical potential value required for the OER process calculated at standard conditions, with an ideal catalyst in an ideal electrochemical cell (in which all chemical species are at unit activity, which essentially means an "effective concentration" of 1 M). In practice, we are so far from these ideal conditions, therefore an additional potential is required for an operative OER (and hence for the occurrence of water splitting). This additional potential is called overpotential and it is possible to determine it by finding the rate-limiting step of the OER (and the associated  $\Delta G_{reaction}$ ).

In order to determine the OER rate-limiting step, Norskov *et al.* [29] proposed, at the molecular scale, that the OER can be modelled as a complex four-steps reaction at the anode electrode as follows (the effect of liquid water was implicitly taken into account as they used liquid water as reference):



a water molecule (in aqueous environment) is dissociated at the anode surface into  $HO^*$  and  $H^+$ . The apex "\*" denotes an anode surface site and  $X^*$  an adsorbed X species.  $a_{H^+}$  is the hydrogen ion activity (closely related to the hydrogen ion concentration ( $[H^+]$ ) and  $eU$  is the shift in the electron energy due to the applied electrode potential  $U$  [29].



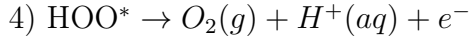
$$\Delta G_2 = \Delta G_{\text{O}^*} - \Delta G_{\text{HO}^*} - eU + k_b \cdot T \cdot \ln(a_{\text{H}^+})$$

the  $\text{HO}^*$  adsorbed species at the anode surface loses one  $\text{H}^+$  to the aqueous environment, leaving the surface adsorbed  $\text{O}^*$  behind.



$$\Delta G_3 = \Delta G_{\text{HOO}^*} - \Delta G_{\text{O}^*} - \Delta G_{\text{H}_2\text{O}} - eU + k_b \cdot T \cdot \ln(a_{\text{H}^+})$$

a water molecule (coming from the aqueous environment) is dissociated into  $\text{HO}^-$  and  $\text{H}^+$  above the anode surface site  $\text{O}^*$ . The  $\text{HO}^-$  reacts with  $\text{O}^*$  to form the surface adsorbed intermediate  $\text{HOO}^*$ .



$$\Delta G_4 = \Delta G_{\text{O}_2} - \Delta G_{\text{HOO}^*} - eU + k_b \cdot T \cdot \ln(a_{\text{H}^+})$$

the surface adsorbed intermediate  $\text{HOO}^*$  loses the  $\text{H}^+$  to the aqueous environment, leaving  $\text{OO}^*$ , free to desorb from the anode surface as molecular gas  $\text{O}_2$ .

In such a mechanistic decomposition, the OER reaction consists of four electrochemical steps, each of which involves one  $\text{H}^+/e^-$  transfer.  $\text{HO}^*$ ,  $\text{O}^*$  and  $\text{HOO}^*$  are denoted as OER intermediates, all adsorbed at the catalyst surface.

The total free energy of the overall OER is determined by the electrochemical step with the highest free energy  $\Delta G$ :

$$G^{\text{OER}} = \max(\Delta G_1, \Delta G_2, \Delta G_3, \Delta G_4) \quad (3.7)$$

This electrochemical step characterized by the highest free energy  $\Delta G$  is called the rate-limiting step (or potential-determining step) and it is the fundamental parameter in order to calculate the overpotential needed for the OER reaction to occur at a measurable rate. The overpotential is defined by:

$$\eta^{\text{OER}} = [(G^{\text{OER}}/e) - 1.23 \text{ V}]. \quad (3.8)$$

The sum of the standard OER cell potential  $\Delta V^0 = 1.23 \text{ V}$  and the OER overpotential  $\eta^{\text{OER}}$  is:

$$\Delta V^0 + \eta^{\text{OER}} = \Delta V^{\text{OER}} \quad (3.9)$$

which determines the minimum operative potential  $\Delta V^{\text{OER}}$  for which all the OER reaction steps 1-4 are downhill in free energy and hence for which the overall water splitting reaction can occur. At this operative voltage  $\Delta V^{\text{OER}}$  applied between both electrodes, also called critical voltage, the electrodes start to produce hydrogen gas at the negatively charged electrode (cathode) and oxygen gas at the positively charged electrode (anode).

### 3.3 History of Photocatalysis and Electrolysis

The earliest mention of photocatalysis dates back to 1911, much later than electrocatalysis that was mentioned for the first time in the 1700' century. In 1911, the german chemist *Eibner* integrated the concept in his research of the illumination of zinc oxide (ZnO) on the bleaching of the dark blue pigment (Prussian blue) [82, 83], while in 1913 Landau published a paper explaining the phenomenon of photocatalysis for the first time [84]. However, it was not until 1938, when Doodeve and Kitchener [85] discovered that  $TiO_2$ , a highly-stable and non-toxic oxide, in the presence of oxygen, could act as a photosensitizer for bleaching dyes, as ultraviolet light absorbed by  $TiO_2$  led to the production of active oxygen species on its surface via photo-oxidation. The concept of photo-oxidation came out for the first time. Research in photocatalysis did not proceed for over 25 years due to lack of interest and absence of practical applications.

A breakthrough in photocatalysis research occurred in 1972, when Akira Fujishima and Kenichi Honda [86] discovered the electrochemical photolysis of water occurring between connected  $TiO_2$  and platinum electrodes, in which ultraviolet light was absorbed by the  $TiO_2$  electrode, and electrons would flow from the platinum electrode (negative cathode; site of reduction reaction) to the  $TiO_2$  electrode (positive anode; site of oxidation reaction) through the external circuit, with hydrogen production occurring at the negative platinum electrode. This was the first time operative water splitting via photo-electro chemistry. Just to mention, in 1977, Nozik [87] discovered that the incorporation of a noble metal in the electrochemical photolysis process, such as platinum and gold, among others, could increase photoactivity, and that an external potential was not required but no particular research interest has been developed further.

Research and development in photocatalysis, especially in electrochemical photolysis of water, continues today, but so far, nothing has been developed for commercial purposes. To conclude, in 2017 Chu *et al.* [88] assessed the future of electrochemical photolysis of water, discussing its major challenge for developing a cost-effective and energy-efficient photoelectrochemical (PEC) cell, which would, "mimic natural photosynthesis", but still involving the presence of electricity (powered by external supply) in the photolysis process leading to electrochemical-photocatalysis process.

The literature reports water electrolysis, *i.e.* the electricity-driven  $2 H_2O \rightarrow O_2 + 2 H_2$  reaction, dating back from 1800', during the first industrial revolution period, by the English scientists William Nicholson (1753-1815) and Anthony Carlisle (1768-1842) [89]. Thus doing, they initiated the science of electrochemistry by discovering the ability of decomposing water. It is also reported that in 1789 the Dutch merchants Jan Rudolph Deiman and Adriaan Paets van Troostwijk were the first able to collect evolving hydrogen (gas) and oxygen (gas) separately using an electrostatic generator to produce an electrostatic discharge between two gold electrodes immersed in water [90]. Later

developments by Johann Wilhelm Ritter exploited Volta’s battery technology and allowed the separation of the product gases [91]. In the same period, Faraday’s 1833 law of electrolysis established the proportional relationship between electrical energy consumption and the amount of gases generated. As a result, researchers began to understand and acknowledge the concepts over the principles of electrolysis of water.

Although the principles of water electrolysis were discovered very early 19-th century, it took almost 100 years before electrolyzers of industrial scale were developed for hydrogen production in countries where hydropower was sufficiently cheap and abundant. Accordingly, a method for the industrial synthesis of hydrogen and oxygen via electrolysis was developed by the Russian engineer Dmitry Lachinov in 1888 [92]. More than 400 industrial water electrolyzers were hence in operation in 1902 [89]. In 1948, the first pressurized industrial electrolyser was manufactured by Zdansky/Lonza. A great turning point was reached in 1966 when the first solid polymer electrolyte system (SPE) was built by General Electric, and in 1972 the first solid oxide water electrolysis unit was developed [89].

The history ends up in our days with the development of proton exchange membranes (PEM) technology (see next section for more details on this technology), first described in the mid-1960s by General Electric as a method for producing electricity for the Gemini Space Program [93], and later adapted for water electrolysis units and fuel cells by Dupont [89]. Due to the developments in the field of high temperature solid oxide technology and by the optimization and reconstruction of alkaline water electrolyzers [94], nowadays a number of companies are active in the manufacture and development of electrolysis technologies, with company such as Proton, Hydrogenics, Giner, and ITM Power being leaders in the field.

### 3.4 Water electrolysis by Proton-Exchange Membranes (PEM)

Nowadays, technological devices able to perform the electrolysis of water are based on three main chemical routes: i) alkaline electrolysis, ii) solid-oxide electrolysis, and ii) proton exchange membrane (PEM) electrolysis.

i) The principle of alkaline water electrolysis is schematically shown in Fig. 3.4. Two water molecules are reduced into one molecule of hydrogen gas  $H_2(g)$  and two hydroxyl ions  $OH^-$  at the negatively charged cathode with the following reaction  $2 H_2O(l) + 2 e^- \rightarrow H_2(g) + 2 OH^-(aq)$  where the hydrogen gas escapes from the surface of the cathode and the hydroxyl ions ( $2 OH^-$ ) move, under the influence of the applied voltage between cathode and anode, through the porous membrane to the positively charged anode, where they form ( $\frac{1}{2}$ ) molecule of oxygen and one molecule of water through the oxidation reaction

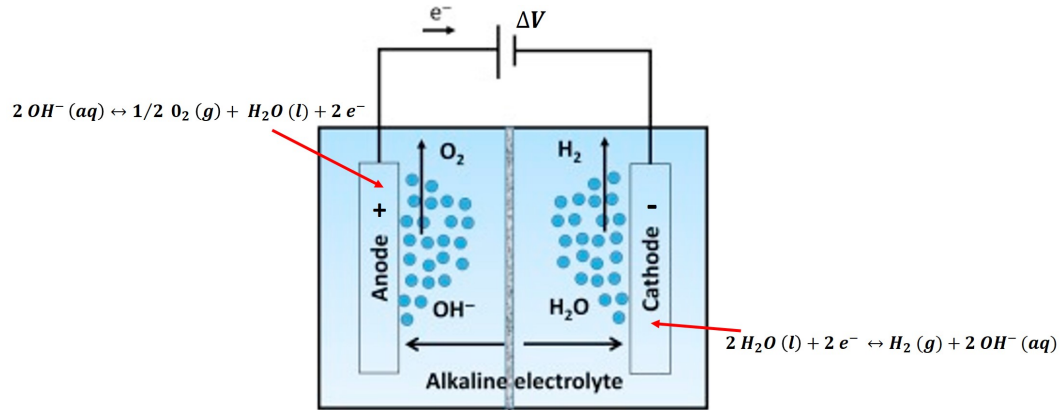


Figure 3.4: Schematic figure of the water splitting reaction via alkaline water electrolysis in a conventional electrochemical cell.

$2 \text{OH}^-(\text{aq}) \rightarrow \text{H}_2\text{O}(\text{l}) + \frac{1}{2} \text{O}_2(\text{g}) + 2 \text{e}^-$  where the oxygen is formed at the anode surface and escapes (like hydrogen) as a gas.

ii) One of the main problem of alkaline electrolyzers is their high electricity consumption. Solid-oxide electrolyzers (SOE) operate at high temperature spanning the range  $800\text{-}1000 \text{ }^\circ\text{C}$  (an order of temperature magnitude greater than other electrolyzers). Intuitively, the high temperatures of the SOE would suggest that the efficiency of operation would be poor because the majority of liquid water is in fact in the form of vapor. This means that not enough water splitting reactant (*i.e.* liquid water) is available, however, this is not the case. The increase in thermal energy demand is compensated for by the decrease in the electrical energy demand and the overall energy demand of the SOE system is largely insensitive to increasing the temperature. At this high temperature, there are numerous problems with cell integrity including poor long-term cell stability, interlayer diffusion, and fabrication and materials problems [95].

Among these electrolyzers, only alkaline have been commercialized while solid-oxide electrolyzers show great technological promise but they are still subject of development [96].

iii) In the following, I focus more on the PEM (Proton Exchange Membrane) technology, because PEM electrolyzers are considered the safest and most effective technology to produce hydrogen from water and it is nowadays the water splitting technology the most employed [97]. PEM electrolyzers were developed for the first time for space and submersible vehicles in the 1960', and PEM remain the most in use for water electrolysis despite the expensive technology behind it. The general features of proton-exchange membrane (PEM) water electrolysis cells are depicted in Fig. 3.5:

The core of an electrolysis unit is an electrochemical cell, which is filled with pure water and has two electrodes connected with an external power supply. In

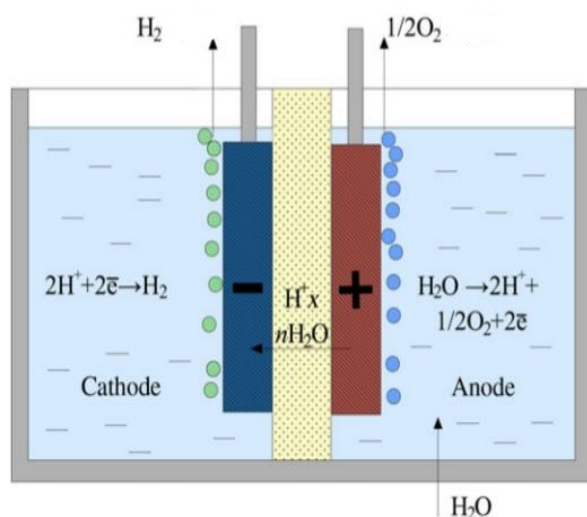


Figure 3.5: Schematic figure of a PEM electrolysis cell.

the PEM, the two electrodes are pressed against a proton-conducting (polymer electrolyte) membrane, thus forming a so-called membrane-electrode assembly (MEA). The MEA is immersed in pure water (no electrolyte in the liquid). A key component of PEM is the proton-conducting membrane made of sulfonated fluorinated polymer (sulfonic acid groups), the most commonly used membrane is Nafion manufactured by DuPont. The acidity of this membrane is equivalent to that of 10% sulfuric aqueous solution.

During the water splitting reaction, the membrane conducts the mobile proton species from the anode (positive) to the cathode (negative) side, this latter process is called electro-osmotic proton transfer through the membrane, hence increasing the water splitting reaction rate. The water splitting reaction starts in the PEM electrolyzers with the oxygen evolution reaction OER (water oxidation) at the positive anode:  $H_2O(l) \rightarrow 1/2 O_2(g) + 2 H^+ + 2 e^-$  the  $H^+$  ions are then attracted by the negative bias of the cathode, they thus move through the proton-conducting membrane. Molecular hydrogen gas is generated at the negative cathode through  $2H^+ + 2 e^- \rightarrow H_2(g)$  The amount of  $H_2$  and  $O_2$  gases produced per unit time is directly related to the voltage applied in the electrochemical cell.

The following advantages of PEM over the alkaline one have been proposed:

- (i) greater safety and reliability are expected since no corrosive electrolyte is circulating in the cell;
- (ii) previous tests made on bare membranes demonstrated that some materials could sustain high differential pressure without damage and were efficient in preventing  $H_2$  and  $O_2$  gases mixing;
- (iii) the possibility of operating cells up to several  $A/cm^2$  with typical thickness of a few millimeters is (theoretically) affordable [98].

However, due to the highly acidic nature of the PEM electrolysis process,

because of the acidic proton-conducting membrane, the choice of electrodes is limited to rare transition metals that are "stable" under acidic conditions, for example, rhodium, ruthenium, platinum, iridium, and their oxides [99]. The current state of the art for electrocatalyst electrodes in PEM water electrolysis is platinum at the cathode for the proton reduction and iridium oxide at the anode for the water oxidation. There has been a large amount of research undertaken to prepare new electrocatalysts for both water oxidation and proton reduction [100, 101, 102, 103], so as to increase the efficiency of the thermodynamically disfavored OER process at the negative anode and to reduce the associated energy cost.

### 3.5 Volcano Plot

In 2011, Man, Rossmeisl, Norskov, *et al.*, showed that is possible to find a universal descriptor for the electrocatalytic activity of an OER catalyst based on the adsorption energies of the surface adsorbed  $HO^*$  (step 1 of the OER, see section 3.2) and  $HOO^*$  (step 3 of the OER, see section 3.2) intermediate species on catalysts surfaces, *i.e.* basically looking at how weak or strong these two intermediate  $HO^*$  and  $HOO^*$  species are bound to the catalyst surface during the OER. In their work, the theoretical OER standard free energy difference  $\Delta G_{1-4}^0$  (see section 3.2 for the definition of  $\Delta G_{1-4}^0$ ) is calculated by applying static density functional theory (DFT) in combination with the computational standard hydrogen electrode (SHE) model.

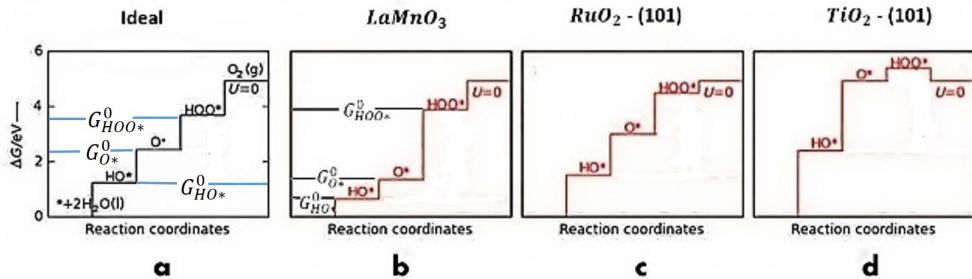


Figure 3.6: Standard Free energy diagrams for the oxygen evolution reaction (OER) calculated at zero potential ( $U = 0$  V) over: a) the ideal catalyst b)  $LaMnO_3$  c)  $RuO_2$  rutile crystal structure with 101 orientation of the surface d)  $TiO_2$  anatase crystal structure with 101 orientation of the surface.

In Figure 3.6, the standard free energy diagrams at  $U = 0$  V for the oxygen evolution reaction are drawn for: a) an ideal catalyst, b)  $LaMnO_3$  (a perovskite), c)  $RuO_2$ -101 (a rutile oxide with the 101 surface orientation), and d)  $TiO_2$ -101 (an anatase phase with the 101 crystallographic orientation).

For an ideal catalyst, shown in the a-panel, the free energy level of  $G_{O^*}^0$  ( $O^*$  appears at step 2 of the OER, see section 3.2) is placed roughly half-way the  $G_{HO^*}^0$  and  $G_{HOO^*}^0$  free energy levels. For  $LaMnO_3$  in the b-panel,  $G_{O^*}^0$  is close

to  $G_{HO^*}^0$  free energy level, while for  $TiO_2$  in the  $d$ -panel,  $G_{O^*}^0$  is very close to  $G_{HOO^*}^0$ .

If the two surface adsorbed intermediates  $HO^*$  and  $HOO^*$  are strongly binded to the catalyst surface, then the  $G_{O^*}^0$  free energy level is placed closer to that of  $G_{HO^*}^0$ , as one can see in the  $b$ -panel for the  $LaMnO_3$ . On the contrary, when the two surface adsorbed intermediates  $HO^*$  and  $HOO^*$  are weakly binded to the catalyst surface, the  $G_{O^*}^0$  free energy level is placed closer to that of  $G_{HOO^*}^0$ , as one can see in the  $d$ -panel for  $TiO_2$ . For the  $RuO_2$ -101 in the  $c$ -panel, we have the optimum binding energies of the OER surface adsorbed intermediates  $HO^*$  and  $HOO^*$ , neither too strong nor too weak, therefore facilitating the formation of the surface intermediate  $HOO^*$  and subsequent desorption of  $O_2$  molecular gas. For this "optimum case" shown in the  $c$ -panel, the  $G_{O^*}^0$  is placed half-way the  $G_{HO^*}^0$  and  $G_{HOO^*}^0$  free energy levels, as in the ideal catalyst (in the  $a$ -panel).

We can evaluate the value of the ratio [104]

$$\frac{\Delta G_2^0}{\Delta G_3^0} = \frac{G_{O^*}^0 - G_{HO^*}^0}{G_{HOO^*}^0 - G_{O^*}^0} \quad (3.10)$$

as universal descriptor of the activity of an OER catalyst. For an ideal catalyst, the ratio should be 1 or as close as possible to 1: this involves that the standard free energy differences  $\Delta G_2^0$  and  $\Delta G_3^0$  are comparable and therefore  $G_{O^*}^0$  is placed roughly half-way the  $G_{HO^*}^0$  and  $G_{HOO^*}^0$  free energy levels, as in the "optimum OER catalyst case" in the  $c$ -panel. If the value of this ratio is closer to 0 or infinity, the catalysts are unsuitable for the oxygen evolution reaction (OER) and the standard free energy of one of these two intermediate steps  $\Delta G_2^0$  and  $\Delta G_3^0$  is most likely to be the rate limiting step from which we can calculate the required operative overpotential  $\eta^{OER}$  for the OER.

From eq. 3.10, we can reasonably consider  $\Delta G_2^0 = G_{O^*}^0 - G_{HO^*}^0$  as a unique descriptor for the OER activity. Therefore, plotting the OER overpotential  $\eta^{OER}$ , as a function of  $\Delta G_2^0 = G_{O^*}^0 - G_{HO^*}^0$  for catalysts, leads to a universal plot, called a volcano plot as reported in Fig. 3.7 for perovskites (in the  $a$ -panel) and for metal oxides (in the  $b$ -panel).

In agreement with eq. 3.10, when the  $OH^*$  intermediate is strongly binded to the catalyst surface, then the  $G_{O^*}^0$  free energy level is placed closer to that of  $G_{HO^*}^0$ , therefore the difference  $\Delta G_2^0 = G_{O^*}^0 - G_{HO^*}^0$  (in the x-axis of the volcano plots) is small. Accordingly, on the left side of the volcano plot are found all the perovskites (in the  $a$ -panel) and metal oxides (in the  $b$ -panel) which make strong bonds with the  $OH^*$  intermediate. When  $\Delta G_2^0 = G_{O^*}^0 - G_{HO^*}^0$  is small, the OER rate-limiting step is  $\Delta G_3^0 = G_{HOO^*}^0 - G_{O^*}^0$ : it is hard for  $O^*$  (strongly binded to the catalyst surface) to go through the chemical reaction that forms the subsequent  $HOO^*$  intermediate.

On the contrary, when the  $OH^*$  intermediate is weakly binded to the catalyst surface, then the  $G_{O^*}^0$  is placed closer to  $G_{HOO^*}^0$  free energy level, therefore the difference  $\Delta G_2^0 = G_{O^*}^0 - G_{HO^*}^0$  (in the x-axis of the volcano plots) is

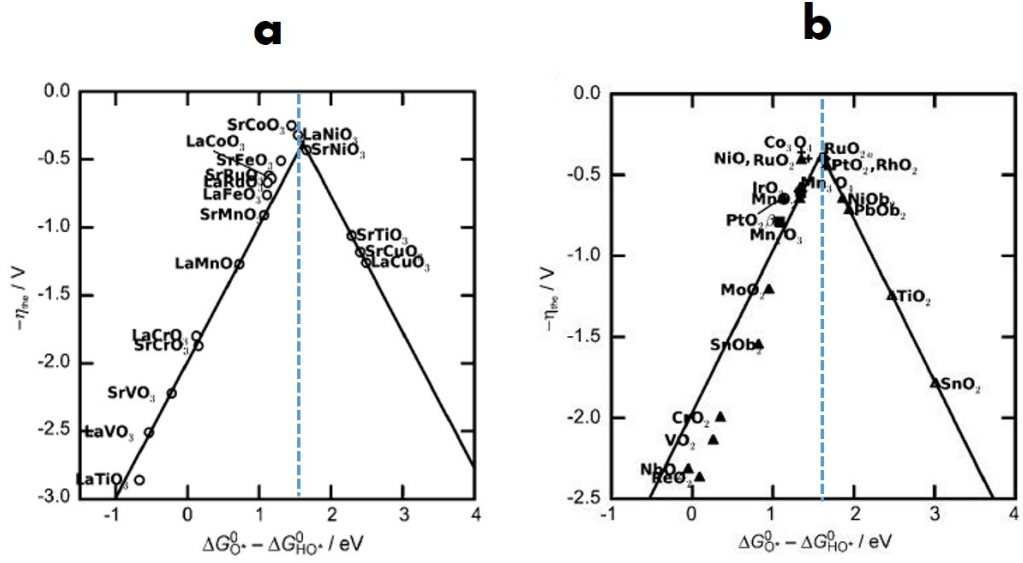


Figure 3.7: Volcano plots for different species of a) perovskites and b) metal oxides.

larger. Accordingly, on the right side of the volcano plot are found all the perovskites (in the *a*-panel) and metal oxides (in the *b*-panel) which make weak bonds with the  $OH^*$  intermediate. In this case, the OER rate-limiting step is  $\Delta G_2^0 = G_{O^*}^0 - G_{HO^*}^0$ : the reaction is limited by the oxidation of  $HO^*$  into  $O^*$ .

When the standard free energy difference  $\Delta G_2^0 = G_{O^*}^0 - G_{HO^*}^0$  in the x-axis of the volcano plots has a value around 1.6, the overpotential has its minimum value (peaks in the plots) and the OER activity is accordingly the highest [31]. Accordingly, the highest activity on the volcano plots is shown for the perovskites (in the *a*-panel) and for metal oxides (in the *b*-panel) able to bind oxygen neither too strongly nor too weakly to the surface.

Focusing on the *b*-panel of Fig. 3.7 for the metal oxides,  $RuO_2$  and  $IrO_2$  have the optimum binding energies for the OER intermediates, *i.e.* neither too strong nor too weak, therefore facilitating the formation of the surface bounded intermediate  $HOO^*$  and subsequent desorption of  $O_2$  molecular gas. Both  $RuO_2$  and  $IrO_2$  are highly active for the OER and precious catalysts which nowadays are the best catalysts employed in facilitating the OER kinetics and showing small values of the overpotential  $\eta^{OER}$ : typically  $RuO_2$  nanoparticles of around 6 nm exhibit an overpotential  $\eta^{OER} = 0.25-0.30$  V in 0.1 M KOH [28], while an overpotential  $\eta^{OER} = 0.7$  V is found using  $IrO_2$ . Therefore, seeing the small values of overpotentials required for the OER using  $RuO_2$  and  $IrO_2$  in comparison with other catalysts,  $RuO_2$  and  $IrO_2$  are considered as the benchmark OER catalysts, and have been widely studied [105, 106, 107, 28]. Just to cite, using  $MnO_2$ , the overpotential  $\eta^{OER}$  could even reach 0.9 V, again an acceptable ("small") experimental  $\eta^{OER}$  value.

However, the surfaces of these noble metal oxides are largely oxidized at the OER potentials and in aggressive and strongly corrosive acidic environments,

leading to an instable OER catalytic performance [108]. This problem can be solved by the addition of other metal oxides. For example, the addition of  $\text{IrO}_2$  to  $\text{RuO}_2$  makes the resultant binary anode 96 % more stable against corrosion than  $\text{RuO}_2$  itself [109]. Co, Cu and Ni are also reported to improve the OER activity of  $\text{RuO}_2$  [110]. Yet, despite their high activity in OER, the very high cost and rareness of Ru and Ir have hindered their large-scale applications. As a result, the development of non-precious metal based catalysts for the OER are needed, which should be able to reduce the overpotential of the OER and simultaneously be stable in the OER operando conditions, with similar final activity as  $\text{RuO}_2$  and  $\text{IrO}_2$  catalysts. This is the key to improve the OER efficiency and to achieve the large-scale production of hydrogen fuel via the electrochemical splitting of water.

Among the most promising cheap OER catalysts, recent experimental investigations have shown that the spinel cobalt oxide  $\text{Co}_3\text{O}_4$  offers effective sites for the water splitting [111, 112, 113, 114], exhibiting a good OER activity and stability, which are slightly lower than those of the noble metal oxides  $\text{RuO}_2$ ,  $\text{IrO}_2$ , and  $\text{PtO}_2$ , with the great advantage that cobalt is an Earth-abundant and eco-friendly element [115, 32]. This will be rediscussed in chapter 4, and it is at the basis of this PhD work

# Chapter 4

## Literature Review for the OER

In the following, I present a review of the literature that summarizes the main results about the electrocatalyzed oxygen evolution reaction (OER) at oxide, metal and graphene based catalysts. We will provide an overview on the experimental (sections 4.1 - 4.12) and theoretical (sections 4.13 - 4.20) literature about OER catalysts for efficient water oxidation. We will underline the reasons behind  $Co_3O_4$  being presumably today's one of the best "low-cost" OER catalyst for large scale applications, comparing and revealing its advantages and its weak points, thus giving us grounds for their modeling for electrocatalysis.

We remind the reader that the precious metal oxides  $RuO_2$  and  $IrO_2$  are considered as the benchmark best OER electro-catalysts with an overpotential range  $\eta^{OER} = 0.3-0.7$  V [116, 117].

We are theoreticians, certainly aware of the underlying experiments done for electrocatalysis and measuring the efficiency of materials for the OER process, thus aware of a certain number of strengths and limitations related to the experiments. However, it is not our purpose here to be too much critical of the measurements done in the literature, if there are criticisms to be stated, as we are not the best positioned to do that. There are indeed a certain number of issues behind the measure of overpotentials  $\eta^{OER}$  in the published papers in the literature, issues that can make comparisons of  $\eta^{OER}$  from one group to the other (for the same material and for different materials) sometimes more tricky than anticipated (from a theorist point of view). We hence propose in our review of the selected papers of experiments in sections 4.1 - 4.12 to provide  $\eta^{OER}$  values as they are reported in these papers, without further comments/criticisms. We however report in the next paragraph one essential issue in the measures of  $\eta^{OER}$ .

The value of the overpotential  $\eta^{OER}$  depends on the current density load into the material and the question of the normalization of the measured current density is admittedly essential in electrocatalysis. From an experimental point of view, characterizing the OER activity of an electrode is "easy" as it is just measuring a current-voltage relation. Comparing the activity of different electrodes (even composed of the same material) is difficult, because the normal-

ization of the current density is a critical issue. In some instances, people normalize with respect to the metal loading, which may make sense from an economical viewpoint. However, (electro)catalysis is (in principle) a pure surface effect. Therefore, a normalization with respect to metal loading is not pertinent if one wishes determining a TOF (turnover frequency: chemical reaction rate measuring the number of reactant molecules converted per minute per catalytic site). One would, at least, need to normalize the current density with the ECSA (electro chemical surface area). However, determining the ECSA is not trivial at all: if methods have been established for nanoparticles of Pt-group metals, there is no good method yet for oxides. Some (Jaramillo and co-workers) proposed measures based on interfaces capacitance, but oxides bulks also have a pseudocapacitance that can lead to overestimated ECSA. Most of the experimental papers here revised adopted the normalization with respect to the metal loading.

Again, the reviews of the experimental papers proposed in this chapter has the focus to give to the reader a general benchmark of the OER overpotential range values, to know which OER catalysts are used nowadays or have been tested, and to have an idea of the possible OER catalyst sites identified in the literature, somehow making abstraction on debates on normalization of  $\eta^{OER}$ . Our choice here is also related to the current theoretical calculation of  $\eta^{OER}$  (chapter 3) that does not take such normalization issues into account either. Presumably this is something to study in future works.

## 4.1 Manganese oxides-Experiments

The  $\mu$ -oxo-bridged tetrameric manganese (Mn) cluster  $CaMn_4O_x$  (see Fig. 4.1) has been shown able to catalyze the OER at a very low overpotential  $\eta$  of 0.16 V at pH 6.5 [118, 119]. The normalization of the current used for the calculation of the value of  $\eta$  was done respect to the metal loading.

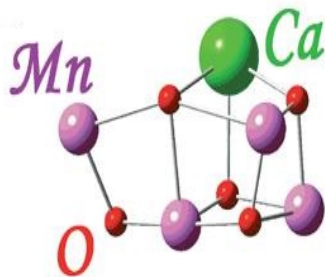


Figure 4.1: *The crystal structure of the manganese tetramer.*

This finding triggered a tremendous amount of research interest in finding efficient water oxidation catalysts based on abundant and inexpensive Mn. Mn is a naturally abundant element with low toxicity, it has therefore become one of the most studied metal in water oxidation catalysis [120, 121, 122].

Jaramillo and co-workers, for instance, prepared nanostructured Mn oxide on the surface of a glassy-carbon (GC) electrode by a simple electrodeposition method [123]. Such deposited Mn oxide nanostructure helped the formation of  $Mn_xO_y$  active sites in OER operando conditions, resulting in an OER activity close to that of the reference  $RuO_2$  or  $IrO_2$  supported on carbon catalysts in alkaline solutions. Promising catalytic activity for the OER was shown also for nanorods of Mn oxides [124] and 3D cross-linked layered Mn oxides [125] (oxides with both mono- and di- $\mu$ -oxo bridged Mn ions).

Among Mn oxides,  $LiMn_2O_4$  is a highly studied material used as a cathode in rechargeable batteries with many nanoscale synthesis procedures. It has a spinel type structure with Mn(III) and Mn(IV) ions in an octahedral geometry with oxygens, while Li ions are in a tetrahedral geometry with oxygens, as depicted in Fig. 4.2:

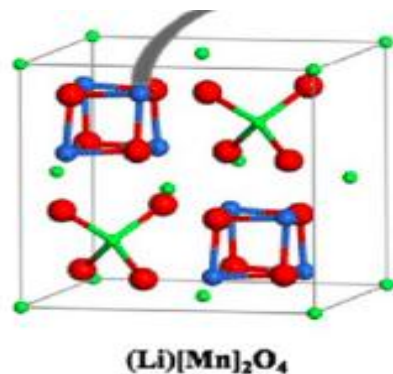


Figure 4.2: (a) unit cell of spinel  $LiMn_2O_4$ . Li, Mn, and O atoms are shown as green, blue, and red color, respectively.

The active structure for the OER in Mn oxides is the  $Mn_4O_4$  cubic subunits [126] and the actual catalytic active sites for OER were shown to be  $Mn^{3+}$  sites, which are pre-oxidised to  $Mn^{4+}$  prior to the onset of the OER [127, 128, 129, 130].

However, the OER catalytic activity of Mn oxides is heavily connected to their chemical composition (*i.e.* presence of enough OER catalyst sites), pH conditions and crystallographic structures, as well as morphologies and pore structures [131, 132, 133]. There exist more than 20 polymorphs for Mn oxides and the multivalent nature and the non-stoichiometric composition of Mn oxides make them more complicated to be synthesized and hence suitable as OER catalysts than oxides with a more simple crystalline structure [134].

## 4.2 Perovskite oxides-Experiments

A potential alternative class of low cost catalysts to the precious metal oxide catalysts (such as  $RuO_2$ ,  $IrO_2$ ) are perovskites, materials with the same crystal structure as calcium titanium oxide ( $CaTiO_3$ ), known as  $A_{1-x}A'_xB_yB'_{1-y}O_3$ , where  $A_{1-x}$  or  $A'_x$  is a rare-earth or alkaline-earth metal and  $B_y$  or  $B'_{1-y}$  is a

transition metal (typically  $Cr$ ,  $Co$ ,  $Cu$ ,  $Fe$  and  $Ni$ ) placed at the center of the oxygen octahedron [135] (see Fig. 4.3-a). Comparing with spinel oxides such as  $Co_3O_4$  and  $MnO_2$ , perovskite oxides show higher conductivity [136] and greater flexibility due to the wide range of ions (and associated valences) present in their structures, hence increasing the number of potential catalyst OER sites [137]. The advantage of perovskites is that they can be used as bifunctional catalysts, *i.e.* as both anode and cathode electrode. This explains their great success in nowadays research interest.

Note that, the degenerate 3d orbitals of the metal oxides (typically in their oxidation states  $Cr^{2+}$ ,  $Co^{2+}$ ,  $Cu^{2+}$ ,  $Fe^{2+}$  and  $Ni^{2+}$ ) which compose the perovskites split into two groups: a doubly degenerate set of two orbitals named  $e_g$  (the  $d_{3z^2-r^2}$  and  $d_{x^2-y^2}$  orbitals) and a lower energy triply degenerate set named  $t_{2g}$  ( $d_{xz}$ ,  $d_{yz}$  and  $d_{xy}$  orbitals), see Fig. 4.3-a.

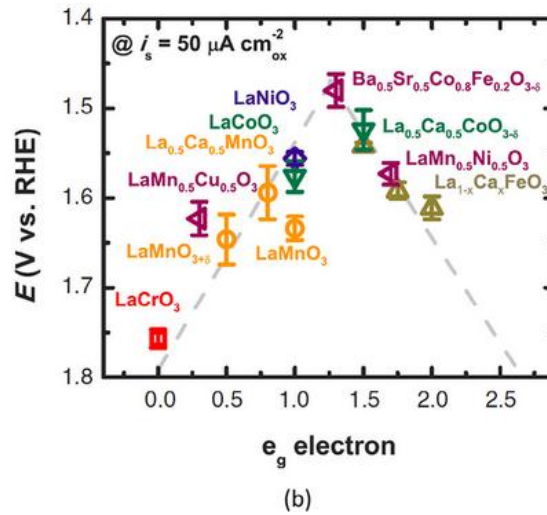
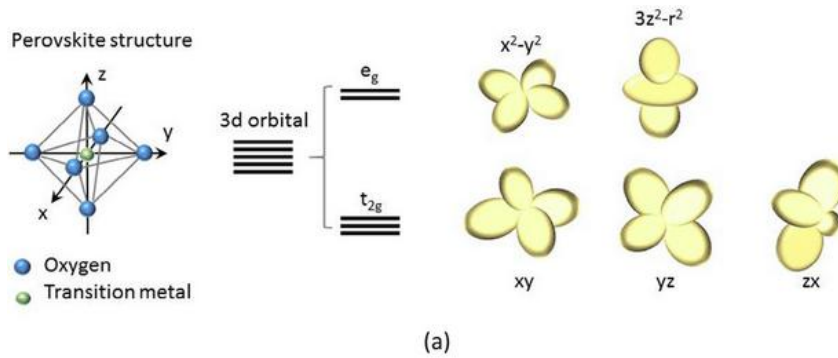


Figure 4.3: a) The  $B_y$  or  $B'_{1-y}$  (transition metals) cations in the  $A_{1-x}A'_x B_y B'_{1-y} O_3$  perovskite structures are at the center of the oxygen octahedron. The 3d orbitals of these atoms are of 2 types, *i.e.*  $e_g$  and  $t_{2g}$  orbitals. The  $t_{2g}$  orbitals have lower overlap with the neighboring 2p orbitals of the oxygen ions, and thus they have lower energy because the Coulomb energy is lower. (b) Volcano plot reporting the OER catalytic activity (OER potential) in the y-axis, defined at  $50 \text{ mA cm}^2$  of OER current, and the occupancy of the  $e_g$ -symmetry electronic orbitals in the x-axis.

Yang and co-workers reported the rational design of a descriptor for a good OER perovskite electrocatalyst [135] based on the  $e_g$  electronic orbitals filling, *i.e.* the intrinsic activity of OER in alkaline solutions can be enhanced when the occupancy of the high energy anti-bonding orbitals  $e_g$  of the transition metal in the perovskite oxides is close to unity. This is because the number of the electrons in the  $e_g$  orbitals of the transition metal can greatly influence the bonding between the oxygen (on the perovskites surface) and the surface adsorbed  $HO^*$  and  $HOO^*$  intermediate species (discussed in section 3.7) during the OER process, and thus optimizing the OER performance.

Based on this rational theory, as shown in Fig. 4.3-b,  $Ba_{0.5}Sr_{0.5}Co_{0.8}Fe_{0.2}O_{3-\delta}$  (BSCF, where  $\delta$  in the O subscript denotes oxygen vacancies) perovskite was found to have one of the highest OER activity due to an optimal (close to unity)  $e_g$  orbital filling [135]. The performing OER activity of BSCF was ascribed to its optimum binding strength of surface adsorbed  $HO^*$  and  $HOO^*$  intermediate species which was found neither too strong nor too weak [135] (as seen in section 3.7). In addition, the diffusion of Ba and Sr (during the amorphisation of BSCF in OER operando conditions) creates pores structures on the BSCF, increasing the exposed active OER sites (Co-O and Fe-O sites), which allowed an easier access of catalytic sites by water and consequently enhance the overall efficiency.

Similar trends were also found with  $SrCo_{0.8}Fe_{0.2}O_{3-\delta}$ , whilst for other perovskite oxides such as  $LaCoO_3$ ,  $LaMnO_3$  and  $LiCo_2O_4$ , the formation of pores structures were not detected [138, 139].

However, the limit of the BSCF perovskites (as OER catalyst) is due to its small specific surface area ( $0.5 \text{ m}^2 \text{ g}^{-1}$ ), *i.e.* not enough OER catalyst sites are available for a sustainable OER rate. This limit clearly hinders the large scale use of BSCF as OER catalyst.

## 4.3 Nickel and Iron based oxides-Experiments

Nickel (Ni) and nickel based oxides have long been known as active catalyst materials for the OER, which require an overpotential around 0.35-0.45 V [140]. Besides, Ni is an earth-abundant first-row transition metal with corrosion resistance and good ductility. The OER reaction mechanism on Ni-based catalysts is complex. The OER pathway includes the evolution from  $NiO_x$  into  $NiO(OH)$  nickel oxo-hydroxide (see Fig. 4.3) in OER operando conditions, and this  $NiO(OH)$  contains highly OER active sites of the type  $Ni^{3+}O$  [141], responsible for the OER.

The OER activity of Ni-based catalysts can be significantly improved by Fe doping. Corrigan et al. [142], in their experimental pioneering work in the 1980s, showed a noticeable decrease in the OER overpotential even at an ultra-low concentration of Fe (0.01%) co-precipitated onto the  $NiO_x$  films, demonstrating that Fe impurities in the  $NiO_x$  catalysts significantly improve its activity [142, 100].

Ni is present as  $Ni^{2+}$  in the  $NiO(OH)$  structure at potentials well below

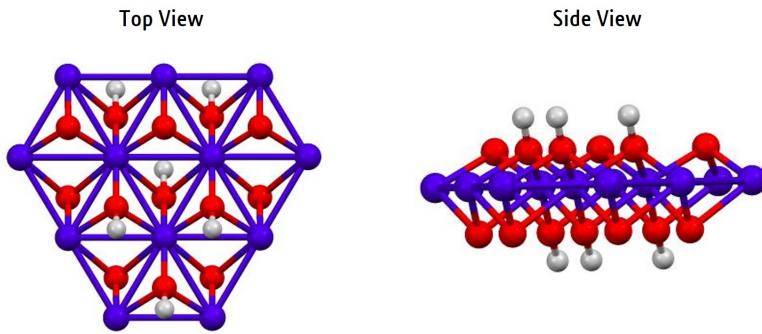


Figure 4.4:  $NiO(OH)$  hexagonal structure. Top and side views. Ni atoms in blue color, oxygens in red color and hydrogens in white color.

the onset of the OER in the presence of Fe. With the potential increasing, the  $Ni^{2+}$  cations undergo oxidation to  $Ni^{3+}$ . The oxidized catalysts can be described as  $Ni_{1-x}Fe_xOOH$ , where Fe sites and Fe-Fe bridge sites at the top surface were identified as highly active Fe sites for the OER.

Gerken *et al.* made an experimental screening of the OER activity for Ni-Fe oxides containing a third metal [143] and the results showed that the presence of *Al*, *Ga* or *Cr* as the third metal provides even higher catalytic performances. For example, amorphous Ni-Fe-Ga and Ni-Fe-Cr oxide nanoparticles show an OER overpotential of 0.28 V. However, a lack of knowledge is still present in understanding the real influence of Fe in improving the OER performances of the NiFe composites in the first place. Electrochemical data, together with XPS results, showed that the presence of iron in the films makes easier the stabilization of higher oxidation states of the metals. Such a change in the preferred oxidation state is believed to improve the OER catalytic activity.

Besides, until recently, most of the Ni-Fe composite catalysts were prepared through electrodeposition, and there are several issues related to this method which forbid an operative use of Ni-Fe composites as OER catalysts:

- (i) first, it can be difficult to control the size of the Ni-Fe films obtained with this preparation technique: the Ni-Fe composite films being rather thick, ranging from several hundred nanometres to many micrometres. However, there are more well-defined deposit experiments that can produce thin or even ultra-thin films, and epitaxy (that controls the facet of the film deposited) is possible if the substrate is a single crystal;
- (ii) in addition, when the experiment is not so well-controlled, the catalyst films are poorly defined, with the presence of pores which inhibit the electron/mass transport properties of these materials during catalytic reactions. As a result, the comparison of OER catalytic activities for these materials can be difficult [144, 145];
- (iii) again if the electrodeposition method is not well-controlled, the ratio of Ni and Fe within the Ni-Fe catalyst films cannot be precisely controlled during electrodeposition [146], which prevents a good control of the material used for

the OER. When more-controlled electrodeposition methods are applied, these issues are not true anymore.

Note that, new methods enabling the fabrication of Ni-Fe composite catalysts with ultrathin film thickness and precise control over the metal compositions are highly demanded. Recently, Boettcher and co-workers synthesized a series of Ni-Fe based thin films with a thickness of merely 2-3 nm [145]. Instead of using the electrodeposition approach, the films were prepared via spin-coating, a mechanism used to deposit uniform thin films onto flat substrates. Usually a small amount of coating material is deposited on the center of the substrate, which is either spinning at low speed or not spinning at all. The substrate is then rotated at high speed in order to spread the coating material by centrifugal force of the metal nitrate solutions onto desired substrates (ITO, Si wafer, etc.) in the presence of surfactants, followed by a brief annealing process at 300 °C. One has however to be aware that spin-coating is not an ideal experimental method either. Solvent evaporation can indeed lead to voids or nanopores. While the films hence produced may have a uniform thickness (which is good), they may be at the same time nanoporous (not too good). Their ECSA (see discussion in the introduction of chapter 4) is thus unclear, and too often is ignored.

An alternative method for the preparation of Ni-Fe films with control on the metal compositions was provided by Berlinguette and co-workers, who employed a photochemical metal-organic deposition (PMOD), a versatile, scalable and low cost technique, to produce amorphous metal oxide films for the OER catalysis [147, 148].

Despite the great interest in improving and controlling the fabrication of Ni-Fe composite catalysts, this subject is an ongoing work with no relevant turn-point yet, therefore Ni-Fe based composites still suffer from fabrication limits listed in i) ii) iii) which hinder the large scale use of Ni-Fe composites as OER catalysts.

## 4.4 Nanocarbon composite OER catalysts -Experiments

To ensure an efficient OER process, high conductivity of catalyst materials is a prerequisite for the rapid transport of electrons and protons during the 4-electrons-transfer OER reaction, but most of the non-precious transition metal oxide-based OER catalysts show a low intrinsic conductivity, which is even worse when they form nanoparticles. With the aim to improve the catalyst conductivity a variety of carbon nanomaterials have been introduced as substrates for transition metal oxides, to obtain composite catalysts for the OER. One of the pioneering composite catalyst is the 'platinum black' (Pt/C) which is typically made of Pt nanoparticles supported on carbon structures/sheets with large surface area and high conductivity [149], see Fig. 4.5.

In particular, it has been shown that adopting carbon nanomaterials as substrates for composite metal catalysts improves the OER catalytic activity

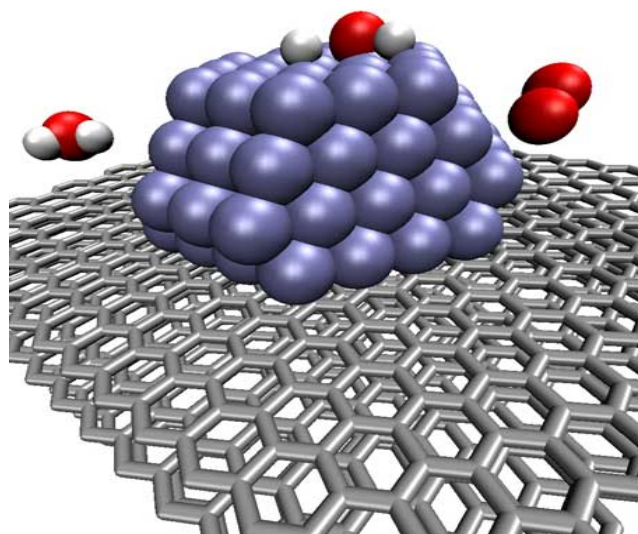


Figure 4.5: A platinum nanoparticle catalyst (in violet) on a graphite carbon sheet support.

for the following reasons:

(i) the stability of the composites is enhanced by the coupling of the metal catalyst with the carbon supports [150];

(ii) the carbon supports make easier the control of the morphologies of the catalysts prepared, resulting in more well-defined nanostructures with narrow size distributions [151];

(iii) the highly conductive carbon supports provide efficient transport pathways for the electrons generated during the OER, which is crucial for the catalysts with low intrinsic conductivity [152];

(iv) carbon substrates reduce the corrosion level of the supported metal catalysts, which can increase the catalytic activity as well as lower the amount of catalysts required for the chemical reaction [152].

However carbon materials usually have a high degree of disorder and defects. In addition carbon materials are unstable, susceptible to corrosion [153] and more vulnerable under the strongly oxidative conditions of the OER [153, 154]. Only graphene and carbon nanotubes, which show a high degree of structural regularity and crystallinity, could be selected as efficient substrates for the preparation of OER composite catalysts. This is a major limitation in the large-scale use of carbon-supported composites as OER catalysts.

## 4.5 Amorphous metal catalysts-Experiments

Amorphous metals have gained increasing interest as potential OER catalysts due to their unique catalytic and electrocatalytic behaviour. Some amor-

phous metal catalysts demonstrated high catalytic activity and stability for the OER [155, 156, 157, 158].

As example, Haber et al. [157] developed experimentally a new family of Ce-rich family of OER catalysts, leading to an array of 5456 discrete oxide compositions containing Ni, Fe, Co and the earth abundant element Ce (see Fig. 4.6). They discovered an unpredicted composition of composites of the type  $Ni_{0.3}Fe_{0.07}Co_{0.2}Ce_{0.43}O_x$ , denoted as high-Ce (in Fig. 4.6-B) of exceptional OER activity with an overpotential of around 0.3 V [157].

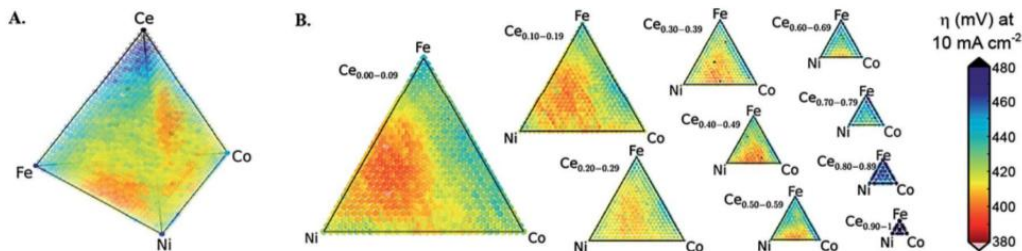


Figure 4.6: Performance map of  $(Ni-Fe-Co-Ce)O_x$  oxygen evolution catalysts. The composition map of the overpotential required for performing oxygen evolution at  $10 \text{ mA cm}^{-2}$  from chronopotentiometry measurements (Chronopotentiometry consists of holding the current of the working electrode constant and measuring the variation of the voltage over time) is shown in (A) in the quaternary composition tetrahedron and (B) as a series of pseudoternary slices through the quaternary space.

More recently, a lot of researches revealed how the amorphous oxides of Co, Ni and Fe showed better catalytic performance than their crystalline counterparts, with amorphous  $CoO_x$  and  $NiO_x$  found better than amorphous  $Fe_2O_3$ , while the mixed oxides of Ni-Co-Fe show, up to now, the best catalytic activity [159]. Same results were obtained for the amorphous Ni-Co.

Yang et al. [158] showed, in their experiments, how the amorphous structures of Ni-Co provide abundant defect sites suitable for the OER, meanwhile the highly porous morphologies provided accessible active surface areas. An overpotential of 325 mV was calculated for the OER (at a  $10 \text{ mA} \times \text{cm}^{-2}$  of density current produced). The excellent electroactivity revealed how amorphous Ni-Co films had better OER activities than their crystalline counterparts.

Despite the great interest in amorphous metal catalysts, they have, by definition, a high level of crystalline disorder which makes harder to experimentally control the size of the OER catalyst surface area. The structure poorly defined with the presence of pores and surface/chemical composition irregularities inhibit the electron transport properties of these materials, preventing a larger use and diffusion of these materials as OER catalysts.

## 4.6 Cobalt-Oxide films as OER catalysts-where it all began

In 2008, a pioneering work [160] about a composite catalyst made of cobalt-phosphate ( $Co_3(PO_4)_2$ ) triggered the currently extensive research interest in finding non-precious metal oxides as efficient OER electrocatalysts like  $MnO_2$ ,  $NiO_2$  and especially  $Co_3O_4$ .

Nocera and co-workers electrodeposited a cobalt-phosphate ( $Co_3(PO_4)_2$ ) amorphous film on the surface of indium tin oxide (ITO) conductive glass from an aqueous solution containing  $Co^{2+}$  and phosphate ions [160]. The deposited  $Co_3(PO_4)_2$  composite coalesced into a thin film of particles up to several micrometers in size (Figure 4.7)



Figure 4.7: SEM image ( $30^\circ$  tilt) of the electrodeposited catalyst after  $30 C/cm^2$  were passed in  $0.1 M KPi$  electrolyte (at  $pH 7.0$ ) which contains  $0.5 mM$  of  $Co^{2+}$ .

Surprisingly, such prepared composite catalyst showed a high catalytic OER activity in neutral solutions in ambient conditions. In particular, the OER started when an overpotential  $\eta$  of merely  $0.28 V$  was applied (overpotential comparable with the one from noble metal oxides). Besides, the composite  $Co_3(PO_4)_2$  catalyst exhibited a long-term stability in the same electrolyte (more than 14 h) with an almost 100% electricity-to-oxygen conversion efficiency. When Co oxides are dissolved in phosphate electrolytes, the P anions are found to stabilize the catalytic domains from Co leaching (percolation), known as self-healing mechanism [160]. It is also reported that the P electrolyte facilitates rapid proton transfers and improves the kinetics of the OER process [161].

A proposed explanation for the unexpected catalyst performances of the composite  $Co_3(PO_4)_2$  films is described as follows. Within the film, both  $Co^{2+}$  and  $Co^{3+}$  sites are present, therefore a dynamic equilibrium can be established between  $Co^{2+}-HPO_4^{2-}$  in solution and  $Co^{3+}-HPO_4^{2-}$  on the anode electrode. As a result, when the water oxidation process leads to the dissolution of a  $Co^{3+}$  site, the dissolution process could be compensated (countered) by continuous catalysts site formation [160, 162]. This design guideline was extended to many other OER catalytic systems including nickel-borate ( $BNiO_3$ ) [163, 164], cobalt-borate (conventionally denoted as  $Co-Bi$ ) [165] and cobalt-methylphosphonate (conventionally denoted as  $Co-MePi$ ) [166].

Among the most promising metal oxide catalysts, the spinel  $Co_3O_4$  has attracted huge interest due to its high catalytic activity, its long-term stability under neutral and alkaline environments and the ability to be used as bifunctional (*i.e.* anode and cathode) electrodes [112]. Henceforth, many strategies have been proposed to further enhance the OER performance of  $Co_3O_4$ : i) using particles of small diameter (nanoparticles), ii) increasing the number of catalytic  $Co^{4+}$  sites combining by *e.g.*  $Co_3O_4$  with electronegative metals such as gold Au.

i) It is generally accepted that larger surface areas have smaller particle sizes without defects or edges, hence leading to more accessible catalytic active sites [113]. Tilley et al. prepared a series of  $Co^{4+}$ -based oxide nanoparticles (NPs) via a hydrothermal reaction [113]. They found that a higher OER activity per unit surface area was achieved with the smaller particle sizes. In their study, the best OER performance was obtained with the 5.9 nm  $Co_3O_4$  NPs (with a nickel substrate) which were the smallest particles available in their experiments. Recently,  $Co_3O_4$  NPs smaller than 5 nm were obtained by using a surfactant-free, size-controllable pulsed-laser ablation in liquids (PLAL) technique [167]. These PLAL prepared  $Co_3O_4$  NPs, have a narrow-size distribution and exhibit one of the highest turnover frequency per cobalt surface site among all the  $Co_3O_4$  based OER electrocatalysts reported so far, with an OER overpotential of 0.32 V.

ii) In addition, electron paramagnetic resonance (EPR) spectroscopy [168], X-ray absorption spectroscopy (XAS) and DFT calculations have confirmed that the  $Co^{4+}$  species are the actual active catalyst sites for the OER [169] on these NPs systems. The electrochemical behaviour of  $Co_3O_4$  layers deposited on titanium supports has been studied by cyclic voltammetry, chronopotentiometry and potential step experiments in alkaline solutions [170]. The authors found that the  $Co_3O_4$  surface is reversibly oxidized prior to oxygen evolution, *i.e.* the complete oxidation to  $Co^{4+}$  of all  $Co^{2+}/Co^{3+}$  ions at the  $Co_3O_4$  surface, at 1.48 V (RHE). Therefore, increasing the amount of catalytic  $Co^{4+}$  active centres in  $Co_3O_4$  materials could be another efficient way to increase its OER catalytic activity. A possible way to achieve this goal is to combine  $Co_3O_4$  with highly electronegative metals, such as Au. In the first attempt, Pyun et al. prepared interconnected  $Co_3O_4$  nanoparticles with Au nanoparticles as the core [171] via colloidal polymerization as depicted in Fig. 4.8. In comparison with the equivalent  $Co_3O_4$  particles, the OER catalytic activity of the interconnected Au/ $Co_3O_4$  NPs has been increased by two-fold. Yeo and Bell electrodeposited a thin film of  $Co_3O_4$  onto the electrochemically roughened surface of gold electrodes, and found that the OER catalytic activity has been enhanced significantly compared with the bulk  $Co_3O_4$  [111]. The enhanced performance was ascribed to the use of Au electrode as electronegative metal support for  $Co_3O_4$ , which creates a strong electric field able to facilitate the O adsorption onto  $Co_3O_4$  surface (on Co species), as supported by DFT calculations and in situ surface enhanced Raman spectroscopy [111, 172], thus

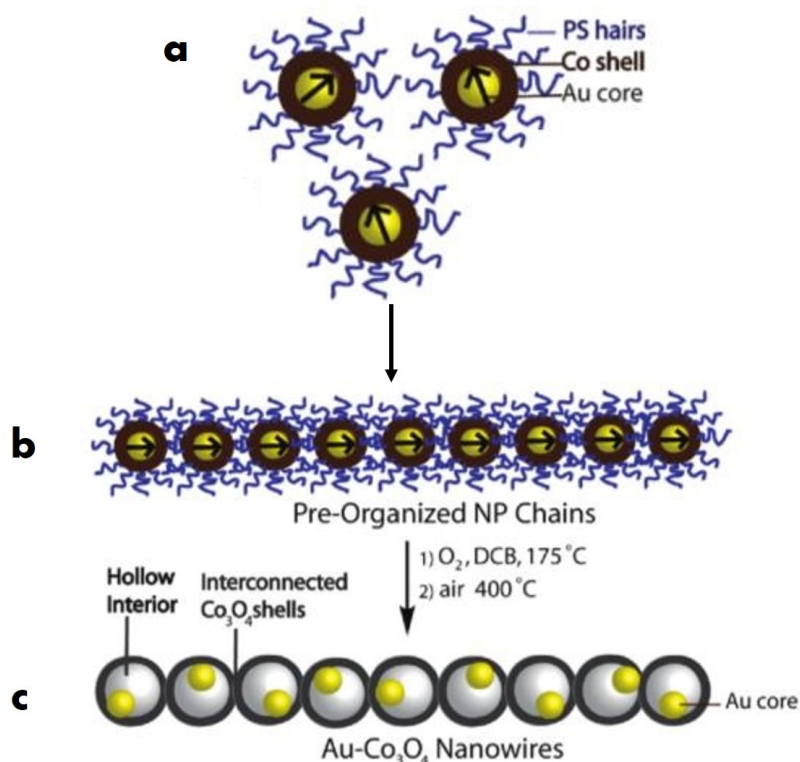


Figure 4.8: Scheme for the synthesis process of Au-Co<sub>3</sub>O<sub>4</sub> nanowires via colloidal polymerization using amine-terminated polystyrene (PS) surfactants.

making the generation of catalytic Co<sup>4+</sup> species easier.

## 4.7 Graphene and Carbon Nanotube as Supports for Co-Oxides-Experiments

The graphene structure, discovered in 2004, exhibits a one-atom-thick planar sheet of *sp*<sup>2</sup> bonded carbon atoms densely packed in a honeycomb lattice [173]. Graphene is the starting material for all carbon nanomaterials including 0D buckyballs, 1D nanotubes and 3D graphite. Due to its large surface area, high mechanical and chemical stability as well as prominent electrical conductivity, graphene has attracted much research interest as a support building material for electrocatalysts. Dai and co-workers grew Co<sub>3</sub>O<sub>4</sub> nanocrystals directly onto the surface of graphene oxide (Co<sub>3</sub>O<sub>4</sub>/rmGO) and doped with nitrogen N in situ to obtain Co<sub>3</sub>O<sub>4</sub>/N-rmGO via a facile two-step technique [174].

The catalytic activity of the Co<sub>3</sub>O<sub>4</sub>/N-rmGO composite for the OER was evaluated and is shown in Fig. 4.9. The Co<sub>3</sub>O<sub>4</sub>/N-rmGO composite is an excellent catalyst for the OER, able to deliver a density current of 10 mA cm<sup>-2</sup> at an overpotential  $\eta$  of merely 0.31 V, much better than Co<sub>3</sub>O<sub>4</sub> or non-N-doped (Co<sub>3</sub>O<sub>4</sub>/rmGO), as shown in Fig. 4.9.

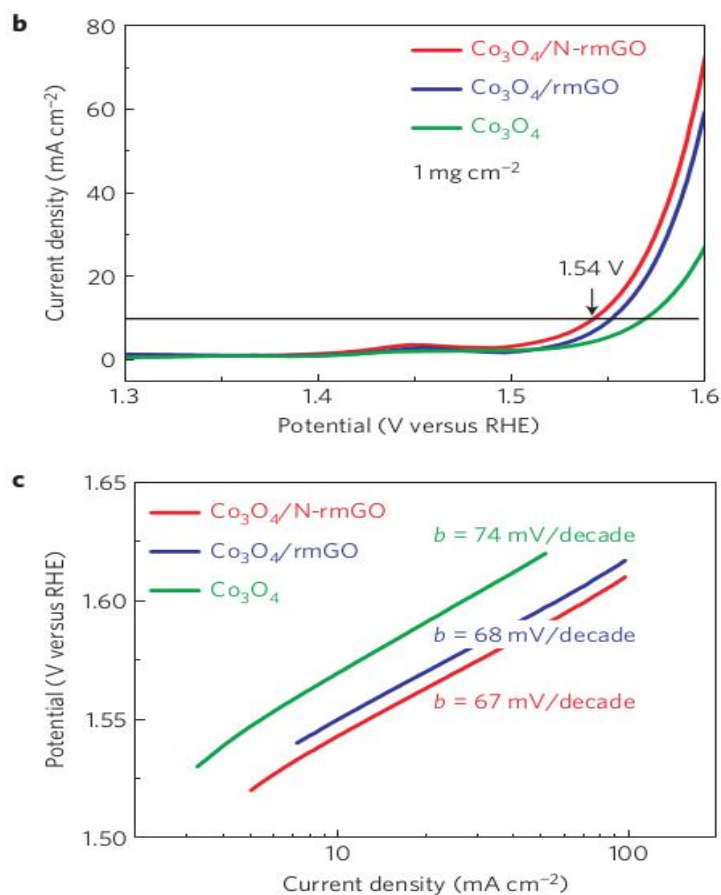


Figure 4.9: *b*)  $\text{Co}_3\text{O}_4/\text{N-rmGO}$ ,  $\text{Co}_3\text{O}_4/\text{rmGO}$  and  $\text{Co}_3\text{O}_4$  nanocrystal loaded onto Ni foam (to reach a high catalyst loading of  $1 \text{ mg} \cdot \text{cm}^2$ ) measured in  $1 \text{ M KOH}$ . *c*) Tafel plots of OER currents in *b*.

A similar preparation strategy has also been extended for the preparation of spinel manganese-cobalt oxide nanoparticles on the surface of N-rmGO ( $\text{MnCo}_2\text{O}_4/\text{N-rmGO}$ ) as well as nickel doped Co-S on N and S co-doped graphene ( $\text{NiCo}_2\text{S}_4@\text{N/S-rGO}$ ) [175, 176]. Both composites displayed significantly enhanced OER activity, compared to their unsupported counterparts.

However, graphene has several limitations as substrate for transition metals catalysts, mainly due to its single layer composition. In order to make easier the anchoring of the metal catalyst and to achieve a strong coupling of catalyst nanoparticles onto the graphene layer, the graphene surface needs to be oxidised, by introducing oxygens containing groups and defects [152]. However, the presence of oxygen groups and defects on graphene greatly decrease its electrical conductivity, resulting in significantly reduced catalytic performances [177]. Dai and coworkers provided a possible remedy by employing mildly oxidised graphene as support for catalyst nanocrystals to balance the dilemma between catalyst-graphene coupling and the electrical conductivity of the hybrid composites [175, 174]. However, the conductivity of the

mildly oxidised graphene of  $169\text{ S}^{-1}$  –this value was obtained by reducing the mildly oxidised graphene with hydrazine, then fabricating it into free-standing paper[178]– is still significantly lower than the unmodified graphene ( $1\text{ MS}^{-1}$ ) [179]. Moreover, same issues affect carbon nanotubes based electrocatalysts, with the addition of a possible disruption of the tube structure –hybridized  $sp^2$  carbon network– when a potential is applied in OER operando conditions [178, 180]. The loss of the tube structure means the loss of reactive surface area and hence a decrease of the probability for the OER to occur.

## 4.8 (110)- $\text{Co}_3\text{O}_4$ as OER catalysts-Experiments

In a recent study by Xie, Shen et al. [181], high-resolution transmission electron microscopy demonstrates that the  $\text{Co}_3\text{O}_4$  nanorods predominantly expose their 110 planes, favouring the presence of active  $\text{Co}^{3+}$  species at the surface. Nanorod-shaped  $\text{Co}_3\text{O}_4$  was prepared by the calcination of a cobalt hydroxide carbonate precursor obtained by the precipitation of cobalt acetate with sodium carbonate in ethylene glycol. Subsequent calcination of this precursor at  $450\text{ }^\circ\text{C}$  in air caused a spontaneous transformation of the morphology, forming  $\text{Co}_3\text{O}_4$  nanorods with diameters of 5–15 nm and lengths of 200-300 nm, showing the preferential growth direction as [110]. The flat top is identified as the (110) atomic plane and the side plane is of (1210) symmetry. The  $\text{Co}_3\text{O}_4$  nanorod exposes four (110) planes among the surface that are rich in  $\text{Co}^{3+}$  sites (identified as active OER sites). In other words, the  $\text{Co}_3\text{O}_4$  nanorod mainly grows along the [110] direction and preferentially exposes (110) planes, the surface area of which are estimated to be 41% of the total surface area, as depicted in Fig. 4.10. Within the (110) cut,  $\text{Co}_3\text{O}_4$  has a spinel structure containing  $\text{Co}^{3+}$  in an octahedral coordination with oxygens and  $\text{Co}^{2+}$  in a tetrahedral coordination with oxygens.

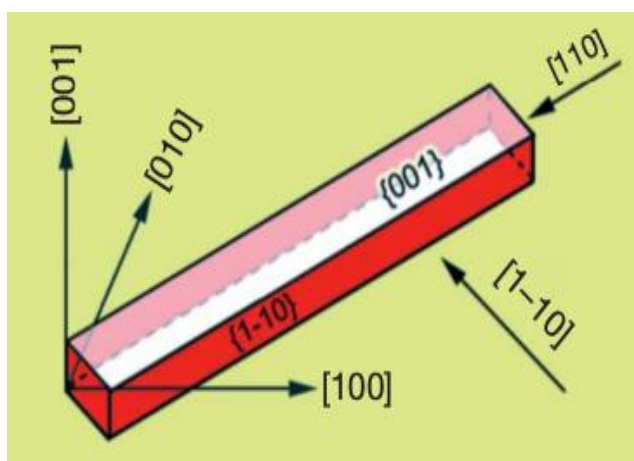


Figure 4.10: Nanorod of  $\text{Co}_3\text{O}_4$ , where red color represents the catalytically active (110) planes.

As said above, the spinel magnetic semiconductor  $\text{Co}_3\text{O}_4$  is a promising

anode material for the electrochemical OER (Oxygen Evolution Reaction) of the water electrolysis reaction [182, 183, 184, 185, 186, 187, 188, 189, 183]  $2 H_2O \rightarrow O_2 + 4 e^- + 4 H^+$ . As a catalyst of gas phase reactions, this cobalt oxide has also typically been successfully applied to CO oxidation [190], Fischer-Tropsch synthesis [191], and oxidation of organic compounds [192].

## 4.9 Oxidation of $Co_3O_4$ in OER operando conditions-Experiments

By combining electron microscopy, linear sweep voltammetry, chronoamperometry, and in situ surface-enhanced Raman spectroscopy, Yeo and Bell [111] showed that  $Co_3O_4$  undergoes progressive oxidation to  $CoO(OH)$  in OER operando conditions, suggesting that the  $Co_3O_4$  electrode is largely covered by  $CoO(OH)$  as the OER proceeds. However, ex-situ XPS analysis on thin film catalysts revealed that the transformation of the spinel  $Co_3O_4$  to a layered hydroxide/oxyhydroxide  $CoO(OH)$  is incomplete, suggesting that in-situ transformation to the layered  $CoO(OH)$  structure is allowed only from the rock salt structure whereas it is inhibited from the spinel structure [145] (investigated in this thesis). This latter is confirmed by other studies [193, 194] present in the literature. Moreover, Liu *et al.* [193] proved why  $Co_3O_4$  appears to be a better OER catalyst than  $CoO(OH)$  due to its higher exchange current density and the lower operative overpotential required for the water oxidation (see section 4.12 in this chapter for the details).

The above observations give rise to several interesting questions, e.g. which is the actual thermodynamic ground state structure of the  $Co_3O_4$  cobalt oxide in OER operando conditions, what is the role of the kinetics during the phase structural transition  $Co_3O_4 \rightarrow CoO(OH)$ , and, more importantly, which surface cut and sites are mainly responsible for the OER activity of  $CoO(OH)$ , if this one is indeed the oxide responsible for the OER at cobalt oxides

In the following, we address these questions by presenting a literature review that summarizes the main results about the  $Co_3O_4 \rightarrow CoO(OH)$  conversion in OER operando conditions.

## 4.10 Surface Reversible Structural Transformation of $Co_3O_4/CoO_x(OH)_y$ -Experiments

In 2015, Bergmann, Strasser *et al.* [195] reported the structural evolution of crystalline  $Co_3O_4$  films (deposited on Ti support) under electrochemical potential control and during the OER, in neutral phosphate-containing electrolyte ( $N_2$ -saturated 0.1 M  $KP_i$  at pH=7) using in situ grazing-incident X-ray diffraction (GIXRD) and quasi-in situ X-ray absorption spectroscopy (XAS). At the onset of OER (1.55 V), the  $Co_3O_4$  structure is maintained, *i.e.* the potential application does not affect the  $Co_3O_4$  coherence structure. As the electrode

potential was increased further to 1.62 V a reversible structural transformation of  $Co_3O_4$  detectable at an electrode potential of 1.62 V occurred, for which the catalytic oxygen evolution proceeded at elevated rates. Thereafter, further increase in the oxygen evolution rate at more anodic electrode potentials resulted in a reversible structural transformation, leading to a lower degree of crystallinity. The X-ray absorption data suggest that in the OER-active state with elevated levels of oxygen evolution (at 1.62 V), tetrahedrally coordinated mono- $\mu$ -oxo-bridged  $Co^{2+}$  ions (*i.e.*  $Co^{2+} - O - Co^{2+}$  sites) are reversibly converted into octahedrally coordinated di- $\mu$ -O(H)-bridged  $Co^{3+}/Co^{4+}$  ions (*i.e.*  $2 Co^{3+/4+} - O - Co^{3+/4+}$  sites). These observations are consistent with a reversible transformation of part of the  $Co_3O_4$  into a  $CoO_x(OH)_y$  surface shell.

In summary, for the first time, the authors uncovered a reversible decrease in structural coherence length at electrochemical potentials, facilitating elevated oxygen evolution, which is coupled to Co oxidation and a change in Co coordination from tetrahedral towards octahedral symmetry. In line with the reversibility, composition and electronic structure of the  $Co_3O_4$  in the bulk volume and in the crystallites near-surface zone remained nearly identical when comparing the catalyst material before and after OER. To explain this reversible process, the authors proposed that the changes in Co coordination at elevated oxygen evolution rates are caused by the formation of a three-dimensional (3D) cross-linked  $CoO_x(OH)_y$  surface shell. Figure 4.11 sketches the structural transformation of the near-surface structure of the crystallites between the resting state (below the Co redox features) and the catalytically active state (at 1.62 V).

However, the authors concluded that the origin of the structural transformation  $Co_3O_4/CoO_x(OH)_y$  of the near-surface described above occurs only when an elevated rate of oxygen evolution reaction (at 1.62 V) is reached. In this case, the participation of lattice surface oxygens in the OER mechanism creates temporary oxygen vacancies at the electrode  $Co_3O_4$  surface [196, 197, 198]. The formation of these surface oxygen vacancies are responsible for a structural relaxation, which leads to the described change in Co coordination and amorphization in the reaction zone: the ex-situ state, after the OER, resembled the as-prepared state in terms of  $\mu$ -oxo Co linking.

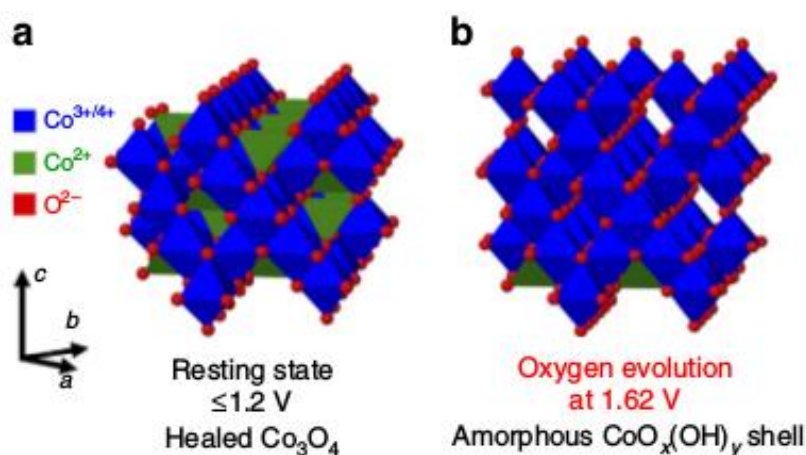


Figure 4.11: Possible near-surface structures on crystalline  $\text{Co}_3\text{O}_4$  core under electrochemical conditions, from ref. [195]. At potentials below Co redox features (a),  $\text{Co}_3\text{O}_4$  is in a healed state at which defects in the near-surface are oxidized. At elevated  $\text{O}_2$  evolution (b), the  $\text{CoO}_x(\text{OH})_y$  grows into the crystalline  $\text{Co}_3\text{O}_4$  core leading to a reversible amorphization of a sub-nanometre shell. This amorphous  $\text{CoO}_x(\text{OH})_y$  shell consists of di- $\mu$ -oxo-bridged  $\text{Co}^{3+}/\text{Co}^{4+}$  ions with arbitrary site occupancy in the ideal cubic close-packed  $\text{O}^{2-}$  lattice. Hydrogen atoms and phosphates are not shown in this representation.

## 4.11 $\text{Co}_3\text{O}_4$ -(111)/ $\text{CoO}(\text{OH})$ -(001) transition -Experiments

In a recent (2019) work by Reikowski, Maroun, Allongue *et al.* [199], the authors have presented operando surface X-ray diffraction studies of two structurally well-defined epitaxial cobalt oxide thin films:  $\text{Co}_3\text{O}_4$ -(111) and  $\text{CoO}(\text{OH})$ -(001) electrodeposited on Au-(111). They monitored the potential-dependent structural changes during potential cycles in the range 0.77 to 1.7 V, always using 1.37 V as rest potential (injection of the 0.1 M NaOH electrolyte at a potential of 1.37 V, which is close to the measured open circuit potential).

The authors found the  $\text{CoO}(\text{OH})$ -(001) film to be smooth and perfectly stable over a wide potential range. On the other hand, in the case of  $\text{Co}_3\text{O}_4$ -(111), fast and fully reversible structural changes are observed. Specifically, the surface region of  $\text{Co}_3\text{O}_4$ -(111) starts restructuring at potentials 300 mV negative of the onset of the OER – pre-OER region above 1.4 V – indicating that the process could be related to the thermodynamically predicted  $\text{Co}_3\text{O}_4$ -(111)/ $\text{CoO}(\text{OH})$ -(001) transition rather than to the catalytic reaction.

The oxyhydroxide  $\text{CoO}(\text{OH})$  forms an amorphous-phase skin layer on top of the  $\text{Co}_3\text{O}_4$ -(111) surface (see Fig. 4.12), it is of defined thickness, which changes linearly with the applied potential, and it is found by the authors to be the OER active phase. Surprisingly, the catalytic activity of the skin layer covered  $\text{Co}_3\text{O}_4$  film and that of the smooth  $\text{CoO}(\text{OH})$ -(001) are almost identi-

cal, if the true microscopic surface area (ECSA) is taken into account for the measurements.

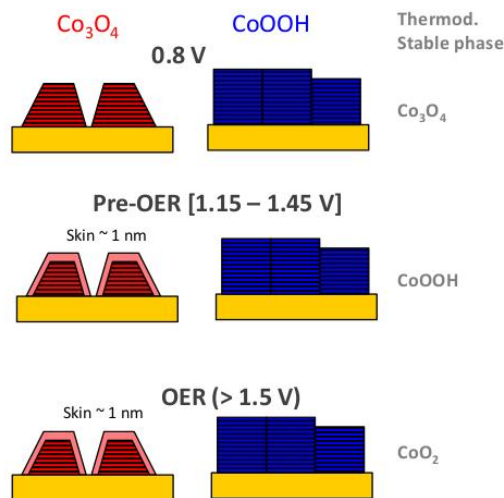


Figure 4.12:  $\text{Co}_3\text{O}_4/\text{Au}(111)$  (red) and  $\text{CoO}(\text{OH})/\text{Au}(111)$  (blue) films, recorded simultaneously in 0.1 M NaOH at 10 mV/s. The out-of-plane and in-plane potential-dependent changes are presented. From ref. [199].

The authors stated that the very similar activity of  $\text{Co}_3\text{O}_4$  and  $\text{CoOOH}$  is difficult to rationalize, due to the fact that previous studies of amorphous CoCat catalyst films [200] identified di- $\mu$ -oxo-bridged site ( $\mu_2 - \text{O}$  site, *i.e.*  $\text{Co} - \text{O} - \text{Co}$  surface structures) as the surface OER active site, but only  $\mu_3 - \text{O}/\text{OH}$  sites exist at the (001) surface of  $\text{CoO}(\text{OH})$ . Indeed, oxygens are 3-fold coordinated to  $\text{Co}^{3+}$  at the (001)- $\text{CoO}(\text{OH})$  surface, and the di- $\mu$ -oxo-bridged ( $\mu_2 - \text{O}$ ) configurations only exist at steps of the  $\text{CoO}(\text{OH})$ -(001) surface or near  $\text{Co}^{3+}$  surface vacancies (defects of the surface structure), as depicted in Fig. 4.13.

The authors concluded that the high catalytic activity of the  $\text{CoO}(\text{OH})$ -(001) surface is not caused by  $\mu_2 - \text{O}/\text{OH}$  sites (identified as active OER surface site in previous studies [200]) alone, but that  $\mu_3 - \text{O}/\text{OH}$  sites significantly contribute to the OER. The fact that the  $\text{Co}_3\text{O}_4$ -(111) and  $\text{CoOOH}$ -(001) have the same activity can indicate that the number of OER active sites on the two oxides is similar, and it is at variance with previous suggestions that di- $\mu$ -oxo bridged Co cations ( $\mu_2 - \text{O}$ , *i.e.*  $\text{Co} - \text{O} - \text{Co}$  sites) are exclusively responsible for the OER activity of Co oxides.

In an atomistic picture, the formation of a skin layer in the pre-OER region (above 1.4 V) plausibly relies on displacements of the  $\text{Co}^{2+}$  cations from tetrahedral to octahedral symmetry (*i.e.* from  $\text{Co}^{2+}$  to  $\text{Co}^{3+}$ ) because of the change in Co oxidation state, [2+] to [3+], for potentials above 1.2 V.

In the OER region, the cobalt redox state increases further from [3+] to [4+] [201, 195] (*i.e.* from  $\text{Co}^{3+}$  to  $\text{Co}^{4+}$ ), but this does not imply further

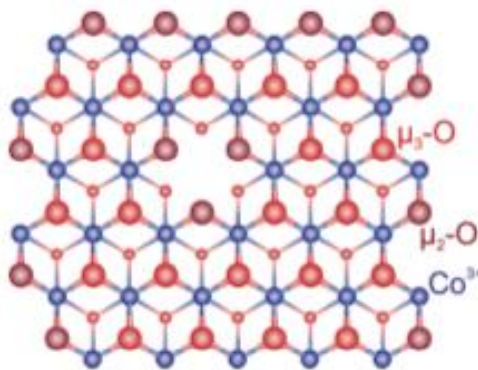


Figure 4.13: Atomic model (top view) of the topmost plane of the  $\text{CoO}(\text{OH})$ -(001) surface. Oxygen atoms are in red and cobalt in blue. O atoms on the ideal surface are 3-fold coordinated ( $\mu_3 - \text{O}$  sites), whereas at steps and next to Co vacancies,  $\mu_2 - \text{O}$  sites (dark red) are found. From ref. [199].

modification of the Co local O-coordination shell, explaining why the skin thickness is only weakly affected by the catalytic reaction.

## 4.12 $\text{CoO}(\text{OH})$ and $\text{Co}_3\text{O}_4$ catalytic OER performances-Experiments

Liu *et al.* [193] experimentally compared the OER catalytic behavior of the  $\text{CoO}(\text{OH})$  and  $\text{Co}_3\text{O}_4$  films by Tafel analysis (which provides insight into the reaction mechanism, while the exchange current density is known as a descriptor of the catalytic activity). This is reported in Fig. 4.14, the experiment is done in an  $\text{O}_2$  saturated 1 M KOH medium, at room temperature. The  $\text{CoO}(\text{OH})$  films grew with a (001) orientation on Au(111), and the  $\text{Co}_3\text{O}_4$  films had a (111) orientation.

Compared with (001)- $\text{CoOOH}$ , (111)- $\text{Co}_3\text{O}_4$  appears to be a better OER catalyst because of its higher exchange current density  $j_0$  and the lower overpotential  $\eta$  for the water oxidation (when the geometric area of the material is used to calculate the current density). (111)- $\text{Co}_3\text{O}_4$  has an exchange current density  $j_0$  of  $6.0 \cdot 10^{-9} \text{ A} \cdot \text{cm}^{-2}$ , see Fig. 4.14, whereas the (001)- $\text{CoOOH}$  has a  $j_0$  of  $1.2 \cdot 10^{-10} \text{ A} \cdot \text{cm}^{-2}$ . The authors concluded that the exchange current densities  $j_0$  suggest that (111)- $\text{Co}_3\text{O}_4$  is 50 times more active than (001)- $\text{CoOOH}$ .

However, if the current densities are corrected based on the measured electrochemically active surface, then the two Tafel plots fall on the same line with the slope of  $60 \text{ mV dec}^{-1}$  and  $j_0$  of  $6.1 \cdot 10^{-11} \text{ A} \cdot \text{cm}^{-2}$  as shown in Fig. 4.14-b. This result suggests that both materials have the same active species, likely  $\text{Co}(\text{IV})$ .

In addition, a more recent (2018) work by Liu *et al.* [194] proved that unlike the rock salt compounds  $\text{CoO}$ , the  $\text{Co}_3\text{O}_4$  catalyst with a spinel struc-

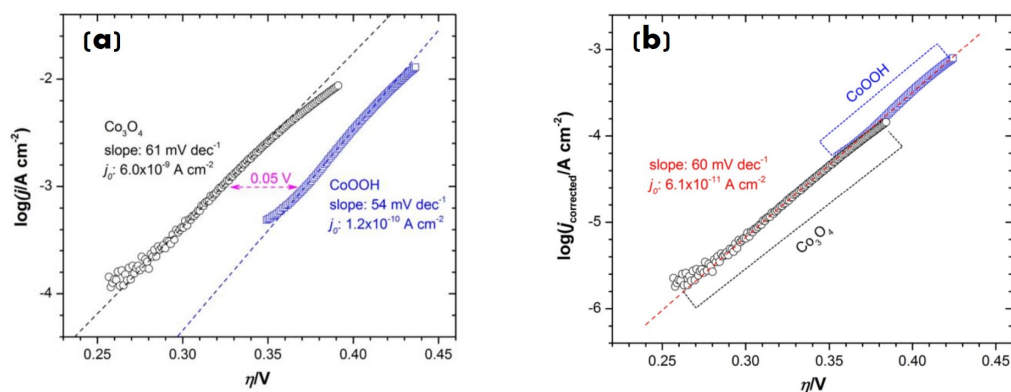


Figure 4.14: a) Tafel plot of the (001)-CoO(OH) and (111)-Co<sub>3</sub>O<sub>4</sub> films. The overpotential  $\eta$  is corrected for the potential drop in the solution (potential drop due to solution resistance). The current density  $j_0$  was calculated using the geometric area of the substrate. b) Tafel plot of the (001)-CoO(OH) and (111)-Co<sub>3</sub>O<sub>4</sub> films with the current density corrected based on the measured surface area estimated from the double-layer capacitance.

ture shows inertness and inhibits the in-situ transformation to layered hydroxide/oxyhydroxide structures during the OER process [202]. To realize the dual modulation of structure and surface on the spinel oxide, electrochemical reduction activation (Fig. 4.15-a) was applied on (311)-Co<sub>3</sub>O<sub>4</sub> nanowires at voltage from 0 V to -0.5 V with different cycles.

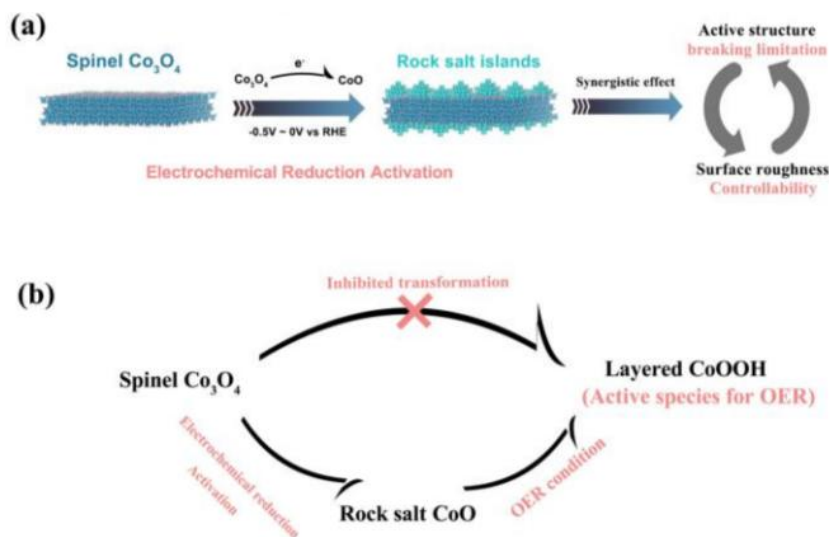


Figure 4.15: (a) Schematic illustration of electrochemical reduction process. (b) Proposed and inhibited transformation in electrochemical process from spinel oxides Co<sub>3</sub>O<sub>4</sub> to the layered oxyhydroxides CoOOH.

The results suggest that the rock salt CoO transfers into layered CoO(OH), which is regarded as the real active oxide during the OER. As for the pristine

(311)- $Co_3O_4$ , the authors could hardly see any  $CoO(OH)$  active species cover the surface in OER operando conditions, as depicted in Figure 4.16).

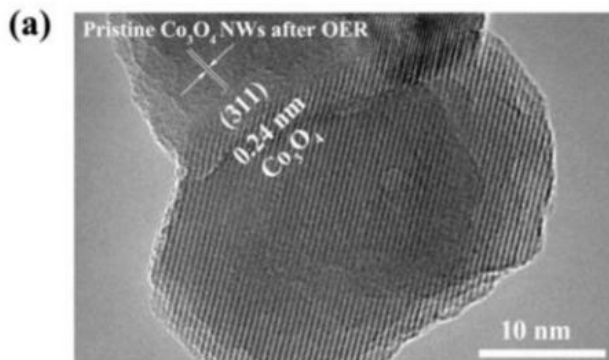


Figure 4.16: (a) HRTEM (High-resolution transmission microscopy) images of Pristine-(311)- $Co_3O_4$  after the OER.

The spinel structure Pristine-(311)- $Co_3O_4$  is found (in this experiment) stable in OER operando conditions, and the applied OER potential does not induce a structural transformation but it increases a charge transfer process for which the exchange current density  $j_0$  of the (111)- $Co_3O_4$  is larger than that of the (001)- $CoOOH$ .

Contrarily, when applying the OER potential on the the rock salt  $CoO$ , the rock salt mainly transfers into  $CoO(OH)$ -(001) or an amorphous phase during the OER process: a significant structural transformation that increases the structural disorder which inhibits the charge transfer processes inside the electrocatalyst, resulted in the exchange current density  $j_0$  smaller than that of (111)- $Co_3O_4$ .

We have seen that  $Co_3O_4$  and  $CoO(OH)$  materials are good candidates as OER catalysts, from experimental data. In the next sections 4.13-4.20, we now report literature on DFT theoretical calculations on the spinel  $Co_3O_4$  and its oxyhydroxide  $CoO(OH)$  in the context of OER. This will indeed be our main systems of investigation in this thesis, we therefore need to summarize previous results.

As introduced in section 3.2, the electrochemical theoretical community is dominated by the approach initiated by Rossmeisl, Norskov, Jonsson and others, based on surface science static DFT calculations of the thermodynamics of surface reaction intermediates [203, 204, 205, 206, 207, 208]. While this approach is successfully providing a wealth of information into the screening of the most promising catalysts, it however lacks some crucial modelling elements in order to get a more detailed atomistic understanding of the electrochemical catalysis processes, and hence it lacks crucial elements to advance further catalyst-materials rational design of the OER in electrochemical conditions.

There follows now an overview of the reference papers, mainly provided by Selloni's group in the USA, about theoretical 'surface science' DFT+U (static) studies on the chemical and physical properties of (110)- $Co_3O_4$ . Its use as OER catalyst and the phase structural transition  $Co_3O_4 \rightarrow CoO(OH)$  in OER operando conditions are now reviewed.

### 4.13 General Insights about $Co_3O_4$ bulk structure-Theory

$Co_3O_4$  crystallizes in the cubic normal spinel structure (space group Fd3m), which contains cobalt ions in two different oxidation states,  $Co^{2+}$  and  $Co^{3+}$ . These are respectively located at the interstitial tetrahedral (8a) and octahedral (16d) sites of the close-packed face centered cubic (fcc) lattice formed by the oxygen ions [209]. An illustration of the unit cell of the  $Co_3O_4$  cobalt-oxide bulk solid is shown in Fig. 4.17-left: 56 atoms, 8  $Co^{2+}$ , 16  $Co^{3+}$ , 32  $O^{2-}$ .

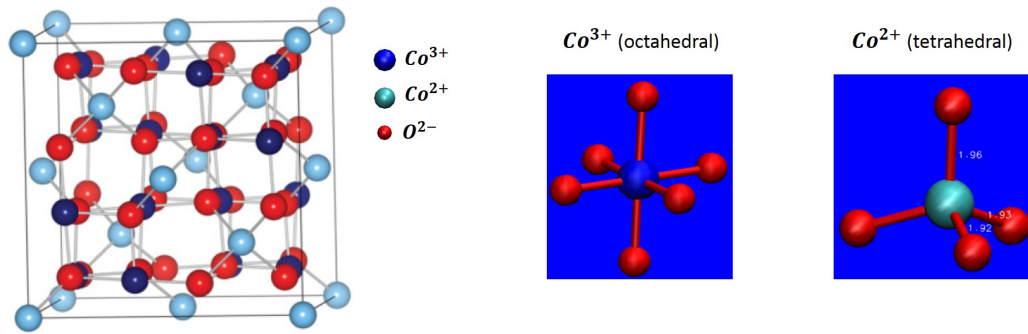


Figure 4.17: Unit cell of  $Co_3O_4$  bulk (on the left) and Co ions arrangement (on the right) in the  $Co_3O_4$  bulk structure. Light cyan and dark blue balls indicate  $Co^{2+}$  and  $Co^{3+}$  ions, red ones indicate  $O^{2-}$  ions.

In a simplified picture, the crystal fields at the 8a and 16d sites split the five degenerate atomic d orbitals of the cobalt ions into two groups, leading to three unpaired d electrons on  $Co^{2+}$ , while all the d electrons of  $Co^{3+}$  are paired (see Fig. 4.18). As a result, the  $Co^{3+}$  ions are not magnetic, whereas the  $Co^{2+}$

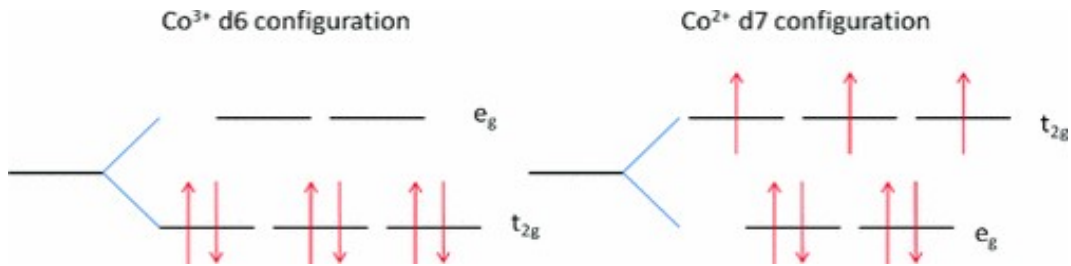


Figure 4.18: Schematic diagram of the electronic structure of  $Co^{3+}$  (left) and  $Co^{2+}$  (right) ions, upon crystal field splitting.

ions carry a magnetic moment which determines the magnetic moment of the whole cobalt oxide. Experimentally,  $Co_3O_4$  is a paramagnetic semiconductor at room temperature. The conductivity is usually of  $p$ -type and measured values of the semi-conductor band gap are around 1.6 eV [210, 211].

## 4.14 Hubbard Term in DFT-calculations for $Co_3O_4$ -Theory

As described in section 2.7.4, the PBE functional in DFT-calculations needs to be supplemented with the Hubbard-type interaction term in order to circumvent the over-delocalization error of the 3d-electrons in metal oxides and the consequent underestimation of the band gap (see section 2.7.4 for more details). Selloni et al. determined the Hubbard U parameter [212] for the  $Co^{2+}$  and  $Co^{3+}$  ions of  $Co_3O_4$  using the linear response approach of Ref. [57] (more details in section 2.7.4). Converged values of the effective U parameter are 4.4 and 6.7 eV for  $Co^{2+}$  and  $Co^{3+}$ , respectively.

Selloni's results [209] for the structural properties of bulk  $Co_3O_4$  are summarized in Table 4.19. Comparison with experimental data shows that the GGA-PBE lattice constant and bond distances are overestimated by about 1.5%. By adopting PBE+U, the bond distances increase further by 2%, as found also in other GGA+U studies of oxide materials [213, 214].

	PBE	PBE+U	Expt.
<b>Lattice constant</b>	8.19	8.27	8.08
<b>Bulk Modulus</b>	199	192	---
<b>Distance <math>Co^{2+}-O^{2-}</math></b>	1.95	1.99	1.93
<b>Distance <math>Co^{3+}-O^{2-}</math></b>	1.93	1.95	1.92

Figure 4.19: *Lattice constant ( $\text{\AA}$ ), bulk modulus (GPa), and bond distances ( $\text{\AA}$ ) of  $Co_3O_4$  from PBE and PBE+U calculations using the primitive 14-atom unit cell and an  $8 \times 8 \times 8$   $k$ -point mesh. From Selloni's paper [209].*

To avoid the computational difficulties (more computational time required in the calculations) associated with having two different U values for Co ions, Selloni's group also performed calculations on  $Co_3O_4$  using a single value of U for both  $Co^{2+}$  and  $Co^{3+}$ , namely U = 4.4, 5.9 and 6.7 eV, the value U = 5.9 eV being the average of 4.4. and 6.7 eV.

The band gap value obtained using the average value of U = 5.9 eV is shown very similar to that obtained using two different values of U (4.4 and 6.7 eV) for the  $Co^{2+}$  and  $Co^{3+}$  ions. Figure 4.20 displays the PBE and PBE+U

projected (electronic) densities of states (PDOS) from Selloni’s results [209] by projecting the Kohn-Sham states onto atomic orbitals centered on the various cobalt and oxygen ions of the  $Co_3O_4$  oxide bulk.

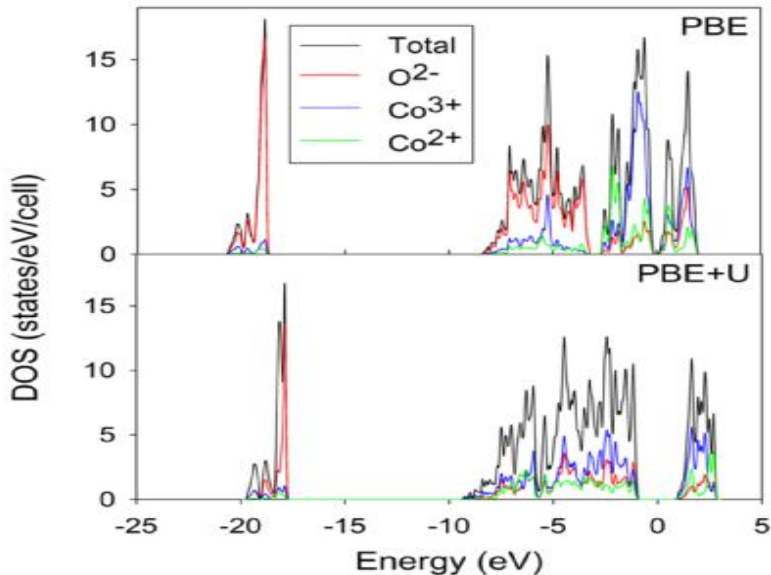


Figure 4.20: Total and projected density of states from PBE (top) and PBE+U (bottom) calculations of the  $Co_3O_4$  oxide bulk. The Fermi energy is set to 0, by construction.

The PBE approach correctly predicts  $Co_3O_4$  to be a semiconductor but the band gap of 0.3 eV is severely underestimated with respect to the experimental value of 1.6 eV [210, 211] (obtained from measurements on films and nanocrystalline samples). The PBE+U method, gives a band gap of 1.96 eV, in “satisfactory” agreement with the experiment. In comparison with the PDOS calculated adopting the PBE approach, however, using the PBE+U no clear splitting of the valence band is present: the contributions from O-2p,  $Co^{3+}$ -d and  $Co^{2+}$ -d states in the PDOS are spread with similar weights throughout the whole valence band, denoting a stronger hybridization of these atoms with respect to the PBE case. The band gap is larger than the one with the PBE calculation, and at the bottom of the conduction band the largest contribution originates from the  $Co^{3+}$ -d states [209], as expected.

Moreover, Selloni’s group performed calculations of bulk  $Co_3O_4$  based on the PBE0 hybrid functional (supposedly being better than a GGA type of functional) for the supercell containing 112 atoms, using the experimental lattice constant (8.08 Å) and experimental geometry parameters, without performing geometry optimization calculations. For a more direct comparison, calculations using the same setup were performed also at the PBE and PBE+U levels. Both the valence bandwidth (9.48 eV) and the band gap (3.42 eV) obtained with the PBE0 functional are larger than those given by PBE (8.41 and 0.33 eV, respectively) and PBE+U (8.35 and 1.94 eV) levels of calculation, a trend observed

for other oxide semiconductors as well, see e.g., Refs. [215, 216]. This trend, however, appears to be amplified in the present case, resulting in a substantial overestimate of the computed band gap with respect to the experiment.

## 4.15 $Co_3O_4$ Bulk Electronic Structure-Theory

To investigate the bonding properties of  $Co_3O_4$  oxide bulk, Selloni's calculations used the Maximally Localized Wannier Functions (MLWFs) at the PBE, PBE+U and PBE0 levels of calculations [209]. They considered the conventional 56-atom cubic supercell and restricted k-space integration to the  $\Gamma$  point only for the calculations. Note that this MLWF method provides a direct measure of the number of electrons localized at a given position in space. One MLWF equals 1 electron (for open shell calculations, as the ones done here).

They found six and seven singly occupied d-type Wannier functions whose centers are very close to each cobalt ion at an octahedral and tetrahedral site, respectively. A neutral Co should have nine valence electrons. This means that the charge states of the cobalt ions at the octahedral and tetrahedral sites, directly calculated from the knowledge of the number of Wannier functions, and therefore number of electrons located at the positions of the cobalt atoms (*i.e.* 6 electrons and 7 electrons in the d-orbitals for 2 types of Co) are thus  $Co^{3+}$  and  $Co^{2+}$ . This is in full agreement with the expected oxidation states of the Co atoms in  $Co_3O_4$  oxide bulk. Similarly, four pairs of Wannier Centers (WCs) are found in proximity of each oxygen ion, indicating an  $O^{2-}$  charge state, in agreement with the formal oxidation state of oxygen ions in  $Co_3O_4$  oxide bulk. All the Wannier centers of bulk  $Co_3O_4$  are shown in Fig. 4.21.

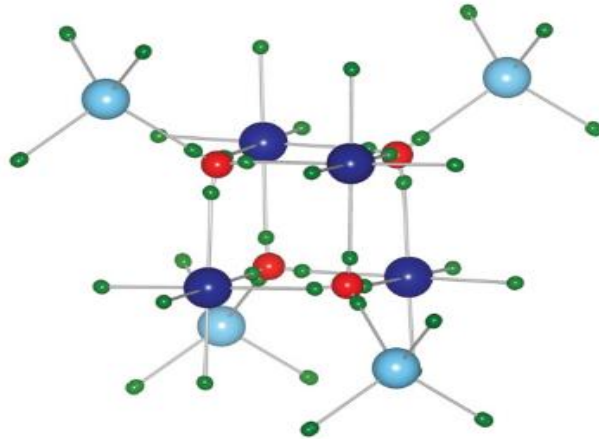


Figure 4.21: *Wannier centers of  $Co_3O_4$  oxide bulk from Selloni's paper [209]. Light cyan, dark blue and red balls indicate  $Co^{2+}$ ,  $Co^{3+}$  and  $O^{2-}$  ions, respectively. Green small balls indicate Wannier centers near the  $O^{2-}$  ions. Wannier centers very close to Co ions are almost overlapping with the Co ions in space so that they can not be seen in this figure.*

Once electrons have been localized in space, one can look at the associated Wannier functions which are (Wannier) orbitals. As depicted in figures 4.22 and 4.23, we can see that the Wannier orbitals of Co ions can be classified in 6 different types. These include d states of  $t_{2g}$  symmetry localized at  $Co^{3+}$  and  $Co^{2+}$  ions, d- $e_g$  states for majority and minority spins (up and down spins) on  $Co^{2+}$  ions, and  $sp^3$ -d types of bonds both between  $Co^{3+}$  and  $O^{2-}$  and between  $Co^{3+}$  and  $O^{2-}$  ions.

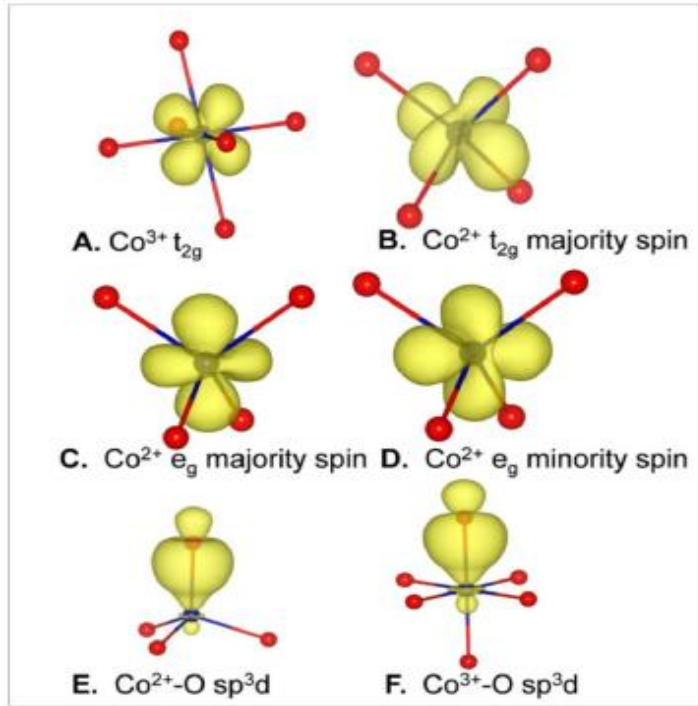


Figure 4.22: Representations of electronic orbitals associated to Co ions in  $Co_3O_4$  oxide bulk. Co and O ions are denoted by blue and red balls respectively.

These MLWF orbitals show that the bonding character of  $Co_3O_4$  oxide bulk, although mainly ionic, has also a small covalent component. This is in agreement with earlier work indicating that covalent bonds are essential to cation ordering in the spinel structure [217].

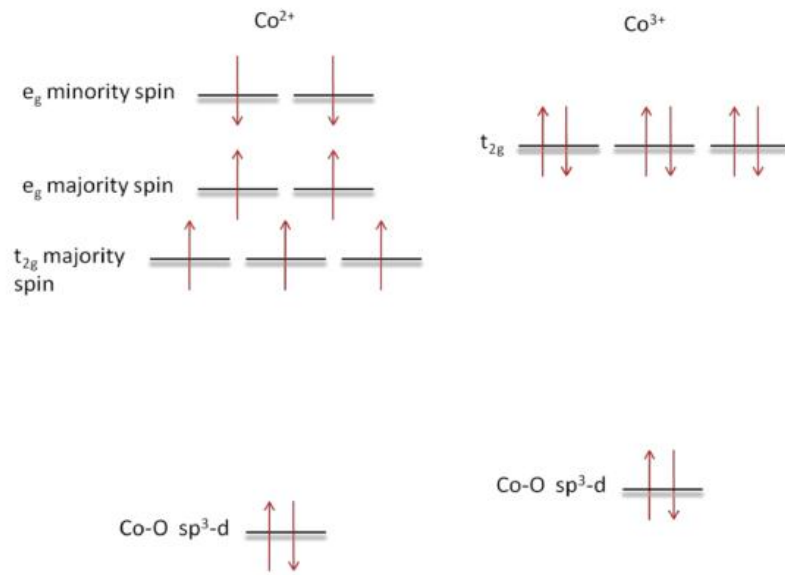


Figure 4.23: Schematic diagram of the electronic spin filling of the Co ions orbitals in  $Co_3O_4$  oxide bulk.

## 4.16 (110)- $Co_3O_4$ Cut of $Co_3O_4$ oxide-Theory

Selloni's group further provided calculations on the (110)- $Co_3O_4$  surface [32]. As already shown in section 4.19, bulk  $Co_3O_4$  contains cobalt ions in two different oxidation states,  $Co^{2+}$  and  $Co^{3+}$  arranged in a cubic spinel structure. These are located at the interstitial tetrahedral (8a) and octahedral (16d) sites, respectively, of the close-packed face centered cubic (fcc) lattice formed by the oxygen ions (see Fig. 4.17) [209]. This gives rise to a  $Fd\bar{3}m$  symmetry (space group  $Fd\bar{3}m$ ) of the  $Co_3O_4$  cobalt oxyde, which shows 9 symmetry planes: 3 glide planes and 6 mirror planes along the diagonal directions of the cubic cell as depicted in Fig. 4.24-right.

As introduced in section 4.8, it is now possible to synthesize  $Co_3O_4$  nanorods that predominantly expose (110) surfaces [181]. These are believed to have a major role in the observed high catalytic activity of the  $Co_3O_4$  oxide [218].

Depending on the height of the (110) cut within the crystal bulk, the (110) surface has two possible terminations, named A and B (see Fig. 4.25), which have cationic and anionic characters, respectively, and the transition between these two terminations can be achieved by controlling the synthetic conditions [219, 220]. The surface (110)-A termination exposes both  $Co^{2+}$  and  $Co^{3+}$  ions at the surface with the air, whereas the surface (110)-B termination has only  $Co^{3+}$  ions at the surface with the air (see Fig. 4.25-right).

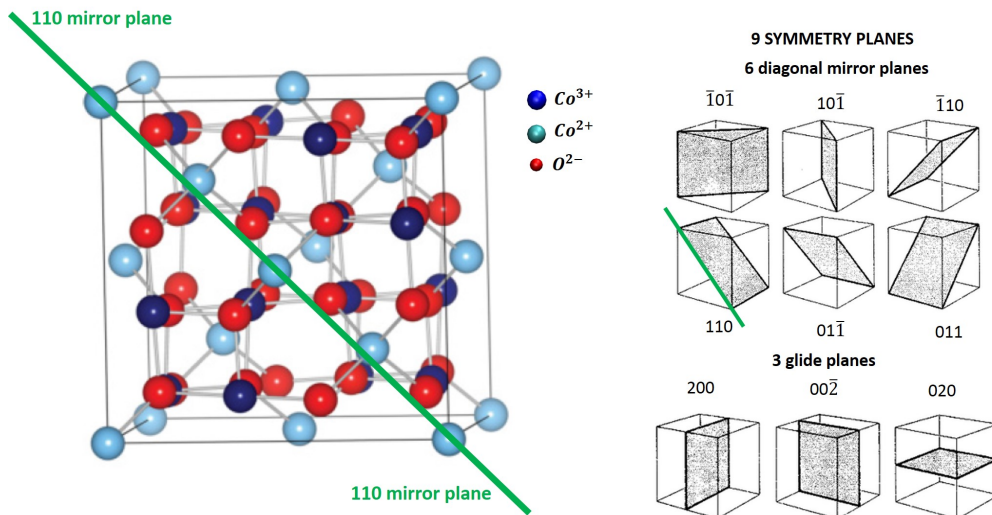


Figure 4.24: Left: FCC unit cell of  $\text{Co}_3\text{O}_4$  oxide bulk: 56 atoms, 8  $\text{Co}^{2+}$ , 16  $\text{Co}^{3+}$ , 32  $\text{O}^{2-}$ . The highlighted green line is a guide for the eye to materialize the 110 direction of the symmetry plane. Right: the 9 symmetry planes of the  $\text{Co}_3\text{O}_4$  cobalt oxyde along which to cut the  $\text{Co}_3\text{O}_4$  ( $Fd\bar{3}m$  symmetry) bulk structure.

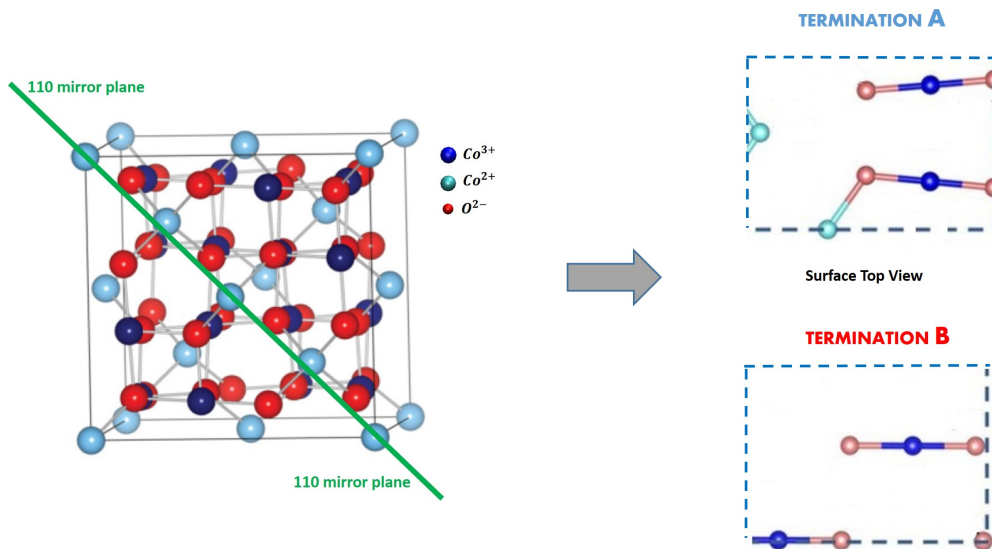


Figure 4.25: Left: FCC unit cell of  $\text{Co}_3\text{O}_4$  oxide bulk: 56 atoms, 8  $\text{Co}^{2+}$ , 16  $\text{Co}^{3+}$ , 32  $\text{O}^{2-}$ . The highlighted green line is a guide for the eye to materialize the 110 direction of the symmetry plane. Right: ball and stick model of the  $\text{Co}_3\text{O}_4$ -(110) surface structure. Surface top views of A and B terminations.

In particular, the (unit cell) surface of the (110)-A termination exposes two  $\text{Co}^{2+}$ , two  $\text{Co}^{3+}$ , and four  $\text{O}^{2-}$  ions (in Fig. 4.25-right) and has a formal charge of  $+2 | e |$ , whereas the (unit cell) surface of the (110)-B termination exposes two  $\text{Co}^{3+}$  and four  $\text{O}^{2-}$  ions (Fig. 4.25-right), and therefore has a formal charge of  $-2 | e |$ . Thus a (110) slab can be viewed as a stack of charged

layers as sketched in Fig. 4.26.

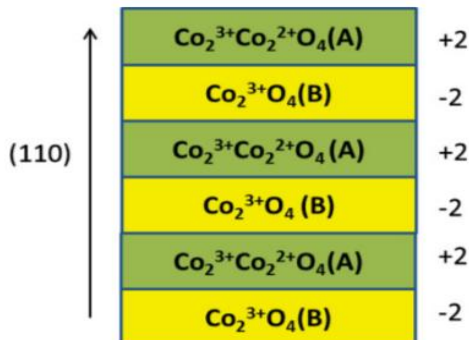


Figure 4.26: Sketch of a  $\text{Co}_3\text{O}_4$ -(110) slab model as a stack of alternating A/B charged layers. (A:  $+2 | e |$ , B:  $-2 | e |$ ).

To study the properties of A or B termination by DFT calculations, Selloni *et al.* considered symmetric slabs with odd numbers of layers, for which the total dipole moment of the cell is zero. These models are non-stoichiometric but neutral in total [221].

## 4.17 Water adsorption on the (110)- $\text{Co}_3\text{O}_4$ surface-Theory

Once the A- and B- terminations are obtained at the surface of the (110)- $\text{Co}_3\text{O}_4$ , and put in contact with water, one has to find out what are the water adsorption modes at the surface, *i.e.* water dissociation or water adsorption and which surface sites lead to any of these events. This is what has been done in the seminal theory work of Selloni *et al.* [32], using density functional theory (DFT) calculations with on-site Coulomb repulsion U term [56].

As shown in Fig. 4.27-left, the A termination exposes both  $\text{Co}^{2+}$  and  $\text{Co}^{3+}$  of Co ions. The bulk  $\text{Co}^{2+}$  (tetrahedral) and  $\text{Co}^{3+}$  (octahedral) ions are 3-fold ( $\text{Co}^{3f}$ ) and 4-fold ( $\text{Co}^{4f}$ ) coordinated with oxygens at the surface, respectively, while all surface oxygens are equivalent and 3-fold coordinated (see Fig. 4.27-left). There are two  $\text{Co}^{3f}$ , two  $\text{Co}^{4f}$  and four oxygen ions per (unit cell) surface. From Selloni's work [32] (and ours, see section 5.5) water is found to adsorb preferentially at bridge sites between either two  $\text{Co}^{3f}$  or two  $\text{Co}^{4f}$  ions, the  $\text{Co}^{3f}$ - $\text{Co}^{3f}$  and  $\text{Co}^{4f}$ - $\text{Co}^{4f}$  distances being 3.10 and 2.85 Å, respectively.

The B-(110) surface (see Fig. 4.27-right) exposes oxygen anions and  $\text{Co}^{3+}$  ions. All  $\text{Co}^{3+}$  ions are equivalent and 4-fold coordinated at the surface with oxygens, whereas there are two different types of surface oxygen ions, one type is 2-fold ( $\text{O}^{2f}$ ) and the other type is 3-fold ( $\text{O}^{3f}$ ) coordinated. There are two cobalt, two  $\text{O}^{2f}$  and two  $\text{O}^{3f}$  ions per surface unit cell. The distance between Co ions is quite large (5.72 Å) on the B termination, and bridge sites are not favorable for water adsorption. It is found instead that each surface  $\text{Co}^{3+}$  ion can bind two water molecules.

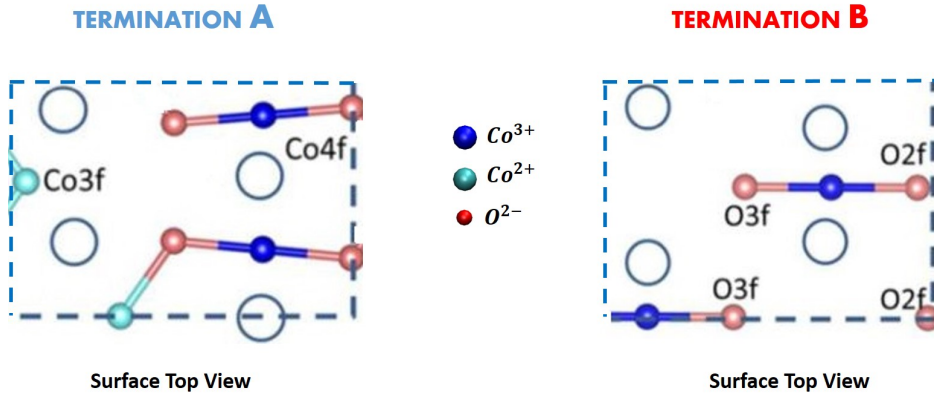


Figure 4.27: Ball and stick model of the  $Co_3O_4$ -(110) surface structure as represented from top views. Left: (unit cell) surface A-termination. Right: (unit cell) surface B-termination. In these top views, empty blue circles indicate water and hydroxyl group ( $-OH$ ) adsorption sites.

Altogether, there are then four adsorption sites per cell (circles in Fig. 4.27) for both terminations [32].

Selloni *et al.* [32] further calculated the water adsorption energy per molecule ( $E_{ads}$ ) as the total energy difference  $E_{ads} = [E_{tot}(0) + nE_{tot}(H_2O) - E_{tot}(n)]/n$ , where the various terms respectively represent the total energy of the bare (*i.e.* no water adsorbed) surface  $E_{tot}(0)$ , the energy of the  $n$  gas-phase water molecules that will be adsorbed  $nE_{tot}(H_2O)$ , and the energy of the surface with  $n$  adsorbed water molecules  $E_{tot}(n)$ .

In a nutshell, water molecules can be surface adsorbed as (entire)  $H_2O$  or can dissociate into surface adsorbed hydroxyl groups ( $-OH$ ) and surface adsorbed hydrogens ( $H$ ). For the A termination, the lowest energy configuration at 1 ML (ML= mono-layer) coverage (*i.e.* full coverage) is composed of all dissociated water, with all bridge sites (between either two  $Co^{2+}$  or two  $Co^{3+}$  ions) occupied by hydroxyl groups ( $-OH$ ) and surface oxygen ions are bound to the hydrogens from the dissociated water molecules, as depicted in Fig. 4.28-A:4D.

On the B termination, the most stable configuration at 1 ML (full coverage) is formed by a mixed molecular-dissociated adsorption of water, *i.e.* with one hydroxyl ( $-OH$ ) and one intact water molecule bound to each surface  $Co^{3+}$  ion (denoted as B:2M+2D-2H@O2f in Fig. 4.28) and the dissociated hydrogens ( $H$ ) adsorbed at  $O^{2f}$  ions.

These results clearly show that, at 1 ML coverage, on both surface terminations dissociative adsorption of water is energetically favored. Moreover, water dissociation energy barriers are very low (0.14 eV at the A-surface, 0.12 eV at the B-surface), indicating that the (110)- $Co_3O_4$  surface is easily hydroxylated, in agreement with the experiment [113]. On the A-(110) surface, dissociation at the  $Co^{3+}$  (4-fold) bridge site is preferred. On the B termination, dissociated H at the  $O^{2f}$  oxygen is more favorable than at  $O^{3f}$  (0.12 eV *vs.* 0.16 eV

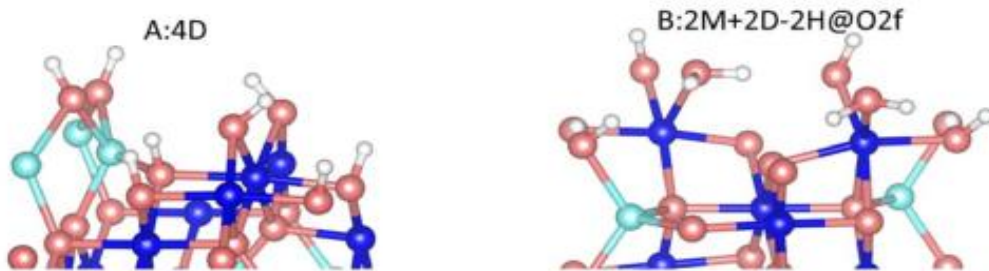
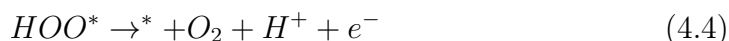
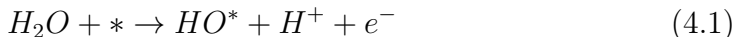


Figure 4.28: Structure of the most stable configurations of the A (left) and B (right) terminations at full coverage (1 ML coverage) of water. From DFT+U calculations by Selloni et al. [32].

dissociation energy).

## 4.18 Oxygen Evolution Reaction at the (110)- $C_{O_3}O_4$ surface-Theory

Once the hydroxylated (1 ML coverage) A- and B- terminations are obtained at the surface of the (110)- $C_{O_3}O_4$ , Selloni's study [32] proceeds with OER investigations following the simplified scheme developed by Norskov et al. [221, 31, 29] for which the OER is (assumed as) a four-steps reaction at the anode electrode. For a better comprehension of the text, we report below the OER four-steps reaction already described in section 3.2:



where \* denotes a surface site and  $X^*$  an adsorbed X species. The authors determined the free energy changes of reactions 1-4 based on DFT+U calculations on the hydroxylated A- and B- terminations at 1 ML coverages (see section 4.17-Fig. 4.28). We remind the reader that all these calculations are done in the gas phase, *i.e.* in absence of liquid water environment.

Free-energy changes calculated in the gas phase with respect to the standard hydrogen electrode (SHE), are plotted in Figure 4.29 (see also section 3.7 where such plots were discussed).

In all investigated cases, the step with the largest free-energy change is the oxidation of  $HO^*$  into  $O^*$  (the 2nd water deprotonation), *i.e.* reaction step 2 of the OER. As shown by the results in Fig. 4.29, the overpotential depends on the reaction site and hence on surface termination. In general, the 1 ML hydroxylated A termination has a smaller overpotential (0.45 V or 0.39 V, depending on the surface reaction site) than the 1 ML hydroxylated B-terminated surface (0.57 V). The authors concluded that the A termination

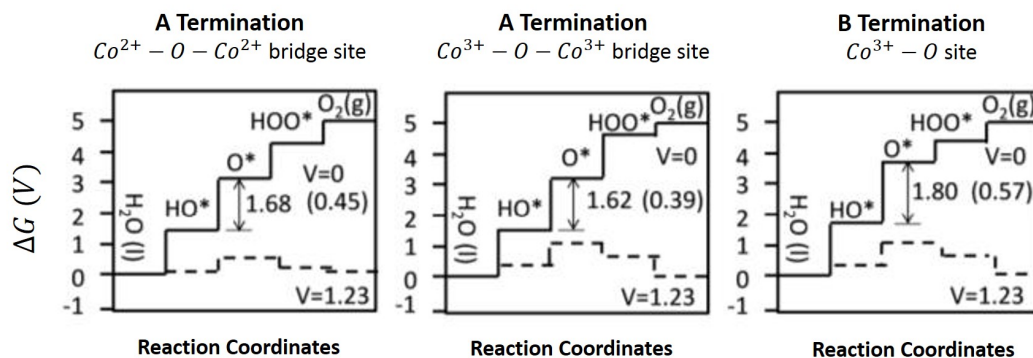


Figure 4.29: Free energy diagrams calculated at  $T=298$  K,  $pH=0$  for the four steps of the OER at  $V=0$  (full line) and at the theoretical OER potential  $V=1.23$  V (dashed line). Results for the hydroxylated A and B terminations at 1 ML water coverage are shown; for the A termination, results for both the  $Co^{2+}-O-Co^{2+}$  ( $Co3f-O-Co3f$ ) and  $Co^{3+}-O-Co^{3+}$  ( $Co4f-O-Co4f$ ) bridge surface sites are given. In each case, the highest free-energy change is indicated by the arrow. Overpotential values are in parentheses.

is more active for the OER than the B-terminated surface, and that the  $Co^{3+}-O-Co^{3+}$  bridge surface sites (also denoted as  $\mu_2-O$  sites) at the A termination are the best OER catalyst sites.

## 4.19 General insights about Cobalt Oxyhydroxide $CoO(OH)$ bulk structure-Theory

$CoO(OH)$  is an example of a metastable phase which can be very hard to synthesize [222]. The mineral of  $CoO(OH)$  is called heterogenite and the most common form of heterogenite is named heterogenite-3R, which belongs to the hexagonal crystal family, trigonal crystal, rhombohedral crystal class, and its space group is R3m [223].

Selloni's DFT theoretical study [224] on  $CoO(OH)$  considered only the more common heterogenite-3R form, whose primitive cell (in Fig. 4.30-a) contains one  $CoO(OH)$  unit, with a lattice constant  $a = 4.6922$  Å, and angle (between the axes)  $\alpha = 35.4503^\circ$  [225].

Theoretical calculations were carried out on the primitive cell (in Fig. 4.30-a) and adopting a value of the Hubbard term  $U=3.0$  eV (see sections 2.7.4 and 4.14 for the Hubbard term in DFT calculations). Selloni's group found a band gap of 2.16 eV, which is higher than the experimental value of 1.7 eV [222]. The calculated projected (electronic) density of states (PDOS) of  $CoO(OH)$  is shown in Fig. 4.31.

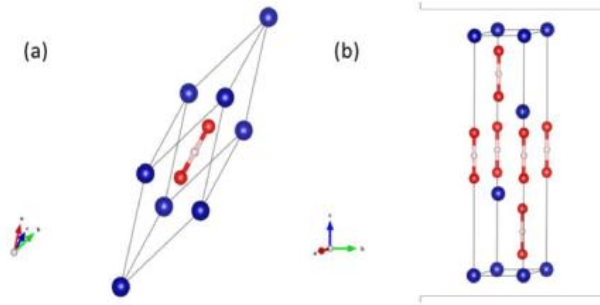


Figure 4.30: a)  $\text{CoO}(\text{OH})$  primitive cell; b)  $\text{CoO}(\text{OH})$  hexagonal unit cell. Blue: cobalt; red: oxygen; pink: hydrogen.

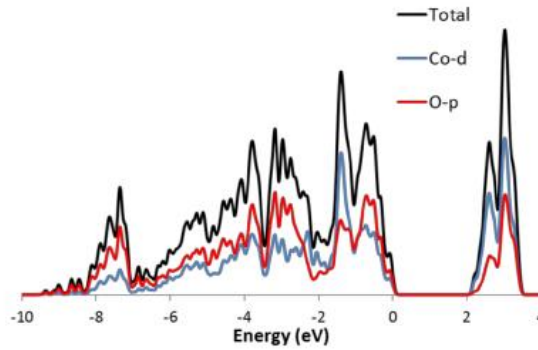


Figure 4.31: Projected density of states of  $\text{CoO}(\text{OH})$ , calculated for the primitive cell, PBE+U representation using  $U=3.0$  eV for the Hubbard term. The zero energy is set at the top of the valence band. From ref. [224].

The natural stable surface is the (0001)- $\text{CoO}(\text{OH})$  (in Fig. 4.32), and there are different surface terminations corresponding to different proton concentrations at the surface. Selloni's group modeled the (0001) surface of  $\text{CoO}(\text{OH})$  using a 7-layer symmetric slab, and they simulated various surface terminations: one with no protons on top (O-terminated surface as in Fig. 4.32), one fully covered by protons (H-terminated surface), and one half-covered by protons (1  $\div$  2 ML coverage surface). They calculated the surface energies of these systems as a function of pH and applied voltage. As a reminder, 1 ML coverage is defined as one H-adsorbed per cobalt surface site.

The resulting surface phase diagram [224] shows that the half-H-covered surface (1  $\div$  2 ML coverage surface) is stable under oxidizing and reducing conditions in a large part of the phase diagram.

Previous PBE+U calculations performed by Selloni *et al.* adopting different values of  $U$ , showed that the electronic structure of the O-terminated (0001)- $\text{CoO}(\text{OH})$  surface, changes from metallic to insulating at  $U=3.5$  eV. Since no experimental information is available on the surface character, insulating *v.s.*

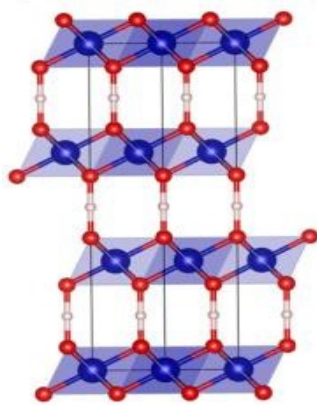
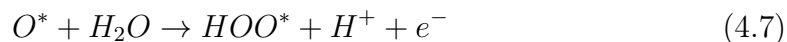
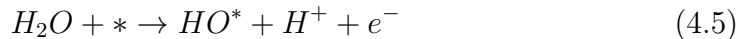


Figure 4.32: Slab used to model the  $\text{CoO(OH)}$  (0001) surface. Only 4 of the 7-layer symmetric slab are depicted in the figure. From ref. [224].

metallic, OER theoretical calculations were performed by Selloni *et al.* for both the metallic ( $U=3.0$  eV) and insulating ( $U=5.0$  eV) cases on the stable half-H-covered (0001)- $\text{CoO(OH)}$  surface.

These OER calculations [224], as already described for the (110)- $\text{Co}_3\text{O}_4$  in section 4.18, refer to the simplified scheme developed by Norskov *et al.* [221, 31?] for which the OER is (assumed as) a four-steps reaction at the anode electrode and the modeling is done in the gas phase, without explicit liquid water environment. For a better comprehension of the text, we report below the OER four-steps reaction already described in section 3.2:



where  $*$  denotes a surface site and  $X^*$  an adsorbed X species. Accordingly, Selloni's gas-phase results [224] about the free energy changes of reactions 1-4 above based on DFT+U calculations over the half-H-covered (0001)- $\text{CoO(OH)}$  surface are presented in Fig. 4.33.

One can see that the OER step 1 (the water molecule dissociation at the anode surface, eq. 4.5 above) is rate limiting and gives rise to a substantial overpotential of 2.94 eV and 3.37 eV for both the metallic ( $U=3.0$  eV) and insulating ( $U=5.0$  eV) cases, respectively.

## 4.20 Theoretical investigation of the OER activity of cobalt oxides $\text{CoO(OH)}$

Bajdich, Norskov *et al.* [226] reported the results of theoretical DFT investigations about the relative stability and the OER activity trends of cobalt

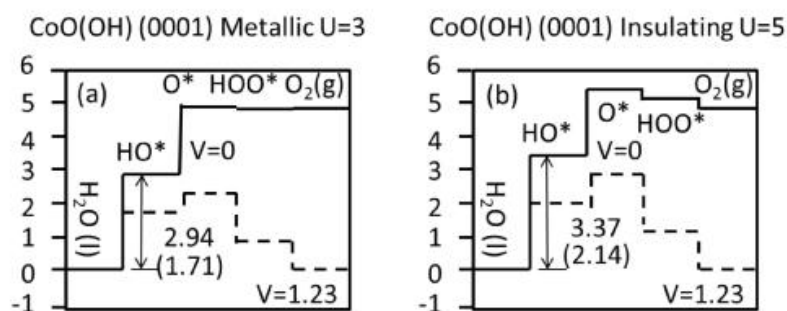


Figure 4.33: Free energy diagrams calculated at  $T=298$  K,  $pH=0$  for the four steps of the OER at  $V=0$  (full line) and at the theoretical OER potential  $V=1.23$  V (dashed line), on (a) metallic ( $U=3$  eV) one half-H-covered (0001)-CoO(OH) surface; (b) insulating ( $U=3$  eV) one half-H-covered (0001)-CoO(OH) surface. In each case, the highest free-energy change is indicated by the arrow. Overpotential values are in parentheses. From ref. [224].

oxides CoO(OH), as well as the stability of selected surfaces as a function of applied potential and pH. The theoretical study is devoted to the following surfaces of CoO(OH): (0001), (01 $\bar{1}2$ ) and (10 $\bar{1}4$ ), depicted in Fig. 4.34.

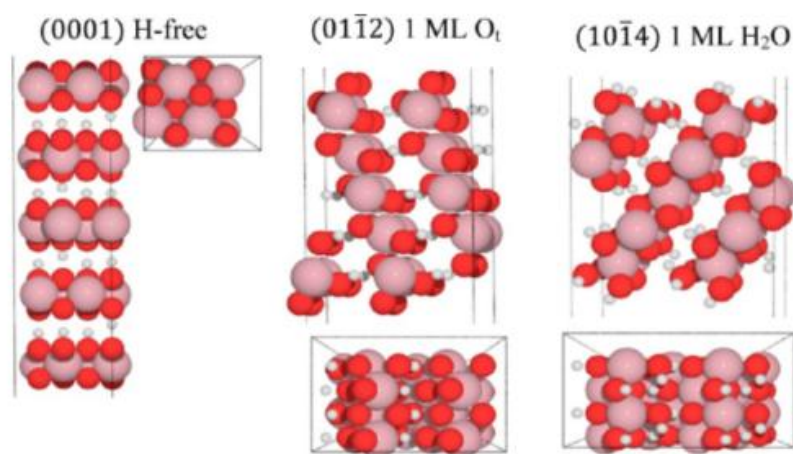


Figure 4.34: Side- and top-views of the optimized geometries for the lowest-energy surfaces of CoOOH represented as 5-layer symmetric slabs. Small white spheres represent H, red spheres represent O, and large pink spheres represent Co atoms. From ref. [226].

These calculations were carried out at the DFT+U level of theory using a single value of the Hubbard term  $U = 3.52$  eV for all Co atoms. The authors model the thermochemistry of the OER in acidic conditions, following the OER reaction steps already described in sections 3.2, 4.19 and in the previous sections.

Comparing the calculated overpotentials  $\eta$  in Fig. 4.35 for all three surfaces,

they find that the  $(10\bar{1}4)$  surface is the most OER active, with an overpotential of  $\eta = 0.48$  V.

surface	$\eta$ [V]
$(01\bar{1}2)$	0.80
$(01\bar{1}4)$	0.48
$(0001)$	0.80

Figure 4.35: Computed overpotentials for the surfaces of  $\text{CoOOH}$ . From ref. [226].

On the basis of the above assignment, the authors note that under OER conditions, the  $(10\bar{1}4)$  surface is best described as having  $\text{Co}^{3+}$  ions, while the  $(0001)$  and the  $(01\bar{1}2)$  surfaces have more  $\text{Co}^{4+}$  ions.

Considering the oxidation states of the Co cations during the OER cycle on the  $(10\bar{1}4)$  surface (oxidation states are in parenthesis in Fig. 4.36) and on the  $(01\bar{1}2)$  surface (oxidation states are in parenthesis in Fig. 4.37), the authors notice that the adsorption of  $\text{OH}$  to form  $\text{OH}^*$  (step 1  $\rightarrow$  2) involves the oxidation of  $\text{Co}^{2+}$  to  $\text{Co}^{3+}$  on the  $(10\bar{1}4)$  surface, while it is oxidation of  $\text{Co}^{3+}$  to  $\text{Co}^{4+}$  on the  $(01\bar{1}2)$  surface.

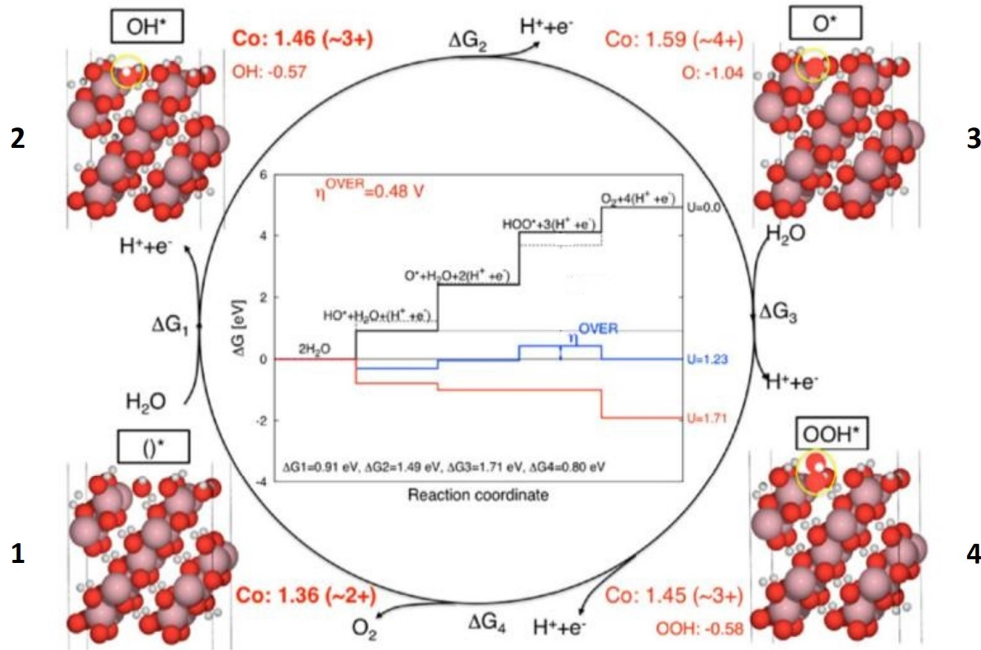


Figure 4.36: Schematic of the OER on the  $(10\bar{1}4)$ - $\text{CoO}(\text{OH})$  surface. The inset shows the free-energy landscape compared to an ideal catalyst (dashed-line) for  $\text{pH}=0$ . Reaction 3 is the potential-limiting step. For  $U > 1.71$  V, all steps are thermodynamically accessible. For each step, there is a list of the measured Bader charges of the Co active site and of the adsorbed species. From ref. [226].

For the  $(10\bar{1}4)$ - $\text{CoO}(\text{OH})$  surface the presence of a majority of  $\text{Co}^{3+}$  sites at the surface (contrary to  $(0001)$  and  $(01\bar{1}2)$  surfaces) increases the OER surface

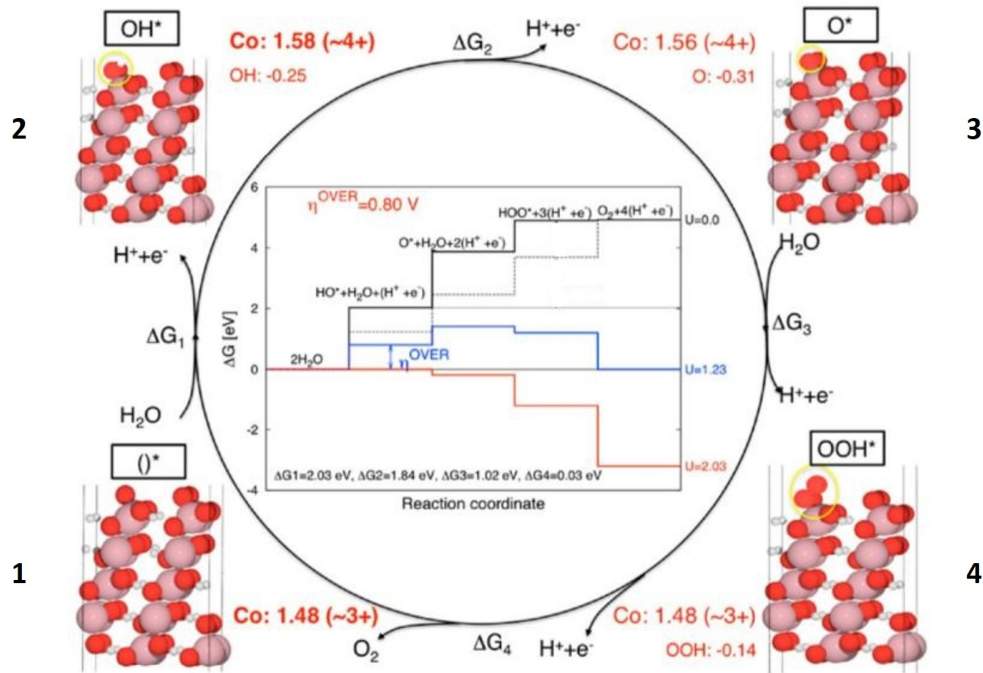


Figure 4.37: Same as Figure 4.36 but for the  $(01\bar{1}2)$ -CoO(OH) surface. For this surface, reaction 1 is the potential-limiting step. For  $U > 2.03$  V, all steps are thermodynamically accessible. For each step, there is a list of the measured Bader charges of the active Co site and of the adsorbed species. From ref. [226].

activity and accordingly it reduces the operative OER overpotential needed, *i.e.* 0.48 V at the  $(10\bar{1}4)$  vs 0.80 V at the  $(01\bar{1}2)$  and  $(0001)$ - CoO(OH) surfaces.

Moreover, in a recent theoretical work by Garcia-Mota, Norskov et al. [227], the OER on (001)- $\text{Co}_3\text{O}_4$  and (01 $\bar{1}$ 2)- $\text{CoO}(\text{OH})$  surfaces has been investigated –see Fig. 4.38 for the top layers representation– using density functional theory (DFT) and DFT+U levels of theory (RPBE for the functional).

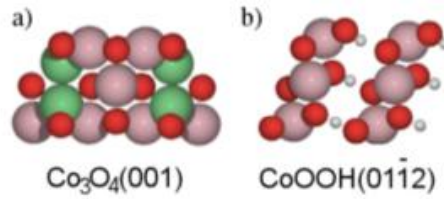


Figure 4.38: Side views of the top layers of the relaxed (001)- $\text{Co}_3\text{O}_4$  and (01 $\bar{1}$ 2)- $\text{CoOOH}$  surface slabs obtained in the DFT and DFT+U calculations. Oxygen atoms and cobalt atoms in tetrahedral ( $\text{Co}^{2+}$ ) and octahedral ( $\text{Co}^{3+}$ ) positions, are colored red, green, and purple, respectively.

The authors found the OER activity on (01 $\bar{1}$ 2)- $\text{CoOOH}$  and (001)- $\text{Co}_3\text{O}_4$  to be comparable as listed in table 4.39 in lines 3-4 (when the Hubbard-U correction term is applied).

		$\eta^{\text{OER}}$
$\text{Co}_3\text{O}_4$	RPBE	0.41
$\beta\text{-CoOOH}$	RPBE	0.27
$\text{Co}_3\text{O}_4$	RPBE+U	0.76
$\beta\text{-CoOOH}$	RPBE+U	0.78

Figure 4.39: Theoretical overpotentials ( $\eta^{\text{OER}}$  in V) associated with the OER on the listed oxygen-covered Co oxide surfaces.

When the Hubbard-U correction is applied (lines 3-4 in table 4.39), the potential determining step (pds) is the formation of  $OH^*$  (reaction step 1, see the red line in Fig. 4.40).

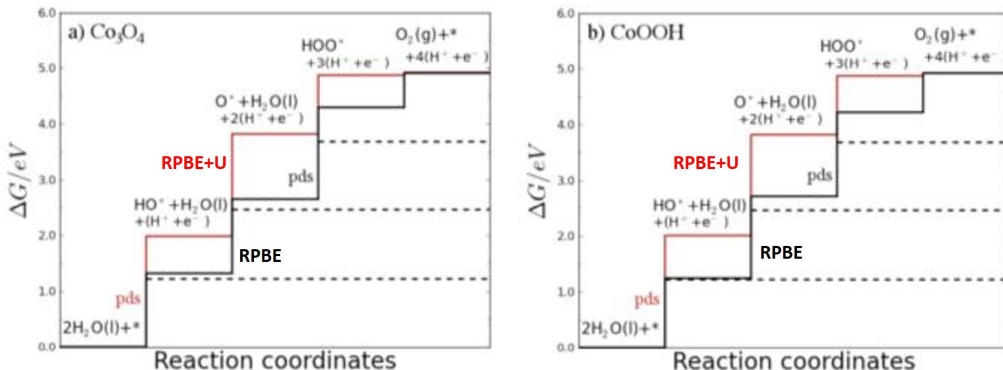


Figure 4.40: *Standard free energy diagram for the oxygen evolution reaction (OER) on oxygen-covered cobalt oxide surfaces calculated with RPBE and with RPBE+U, black and red line, respectively. The dashed lines indicate the free energy diagram for an ideal electrocatalyst. The potential determining steps for the OER on cobalt oxide surfaces calculated with both RPBE and with RPBE+U are marked as pds. From ref. [227].*

The similar theoretical overpotential found on (001)- $Co_3O_4$  and (01 $\bar{1}2$ )-CoOOH (0.76 V vs 0.78 V) can be understood by comparing the local coordination environment of the surface Co active site on (001)- $Co_3O_4$  and (01 $\bar{1}2$ )-CoOOH surfaces. In OER operando conditions, the surface Co active sites of both (001)- $Co_3O_4$  and (01 $\bar{1}2$ )-CoOOH share the same octahedral coordination with oxygens, *i.e.* the surface Co active site is a  $Co^{3+}$  ion (already known in literature as OER catalyst species) with only minor differences in the O-O distances in between the two cobalt oxides.

## 4.21 What simulations do we propose?

One issue in all the theoretical surface science calculations, cited in sections 4.13-4.20, is the lack of explicit water interacting with the surface catalyst and with the chemical compounds involved in the OER reaction. It is not only the explicit presence of the aqueous solvent that matters, *i.e.*, its structural organisation at the interface with the anodic material (metal electrode or semiconductor cobalt oxide of interest here), but the water dynamics at finite temperature also matters (e.g. wriggling of water at the surface, diffusion, dynamical charge transfers). The whole complex structure and dynamicity of the electric double layer (EDL) in the electrochemical conditions has to be accounted for, as well as the presence of adsorbed species at the surface and at the interface for their influence on the EDL structure and hence on the chemical processes occurring at the aqueous interface. With this in mind, it is stating the obvious that electrocatalytic reactions such as the water electrolysis in the

OER are highly complex to model because of the interplay in between the anode material (metal/semiconductor), the electrolyte, the liquid, the adsorbed species, and the material-liquid *vs* liquid-phase reactants and products. The external applied voltage in the electrochemical conditions has also to be taken into account. First principles simulations are therefore mandatory because of the complex interplay in between electronic, structural and dynamics properties at surface-water-electrolyte-EDL interfaces, including the modelling of charge transfers and chemical reactions. These are complex simulations to be achieved at the DFT-MD level, and our work proceeds in incremental steps. Therefore we start by first going beyond the current static "surface science" calculations of the literature, and hence include liquid water and its dynamics at finite temperature into the modeling. This will be shown in chapters 5 (for  $Co_3O_4$ ) and 7 (for  $CoO(OH)$ ) with DFT-MD simulations of these oxides at the interface with liquid water.

As described in section 4.8, Xie, Shen et al. [181] demonstrated that the  $Co_3O_4$  nanorods predominantly expose their (110) planes.  $Co_3O_4$  nanostructures have high surface area and expose largely active (110) planes, therefore (110) is a frequently exposed surface leading to high catalytic activity [228]. Accordingly, in the next chapter 5, following the theoretical reference work provided by Selloni about the (110)- $Co_3O_4$  structure (described in sections 4.16-4.18), we will investigate the (110)- $Co_3O_4$ /liquid water interface by DFT-MD modelling as a preliminary step into the construction of knowledge of the  $Co_3O_4$ -liquid water-electrolyte interface in electrochemical conditions including explicitly the water molecules environment. This latter was never taken into account in the previous cited literature. We model the ideal crystalline  $Co_3O_4$ , without taking into account surface defects that could be relevant in the context of the chemical reactivity at the interface.

The actual controversy in the knowledge of the thermodynamic ground state structure of the  $Co_3O_4$  cobalt oxide in OER operando conditions, is also a subject we need to address. As described in sections 4.9-4.11, progressive oxidation of  $Co_3O_4$  surface onto (0001)- $CoO(OH)$  was detected in OER operando conditions, suggesting that the  $Co_3O_4$  electrode is largely covered by (0001)- $CoO(OH)$ . Accordingly, in chapter 7 we try to rationalize the mechanisms behind the  $Co_3O_4 \rightarrow CoO(OH)$  surface transformation, characterizing the (0001)- $CoO(OH)$  crystalline structures and its surface (OER) activity in gas-phase/liquid-phase conditions, and we compare with the results obtained for the (110)- $Co_3O_4$  structure.

Chapters 5 and 7 will describe in details the interface between  $Co_3O_4$  and  $CoO(OH)$  oxides and liquid water, at zero surface potential, *i.e.* in non operando conditions. In order to shed light into the mechanisms and associated energetics involved in the OER at these two aqueous interfaces, we present in chapters 6 ( $Co_3O_4$ ) and 7 ( $CoO(OH)$ ) novel metadynamics technique (*i.e.* biased DFT-MD with a novel scheme very well adapted for the OER in condensed phase) that are able to catch the role of the explicit water

solvent into the OER mechanisms and catch its influence on the associated energetics. Such dynamics have not been done in the literature up-to-now, as at the best one explicit water only was included in calculations of the OER cycle.

The energetics that will be derived from the metadynamics are the free energy cost for the OER to occur at the aqueous cobalt oxide interfaces, *i.e.* the energy cost for the rate limiting step along the OER, from which the overpotential will be deduced (following equations seen in chapter 3-section 3.2). Note however that these simulations are still done at zero potential on the electrode and still do not account for the electrolytes in the EDL. Both parameters will induce changes in the water organization and dynamics at the interface, and will hence affect the final energetics and overpotential. We believe the results we provide here are thus presumably overestimating the overpotential of the OER at the interfaces we are simulating. The next stage in the DFT-MD will be to include these two parameters, at least, and hence improve the energetics. However the mechanisms shown in our metadynamics are presumably more robust and the final conclusions on the role of the solvent drawn from our current works on the OER by metadynamics will presumably still hold once the more complex environment at the electrode will be introduced in the modeling.



## Chapter 5

# DFT-MD of (110)-Co<sub>3</sub>O<sub>4</sub>/water interface: how the water is organized at this interface in non operando conditions

Within the past decade, first principles simulations of metal-water interfaces have been carried out with different flavors, see e.g. ref. [229] for a recent review. For instance, Gross *et. al.* [230, 231] and Jonsson *et. al.* [232] have included water mono- & bi-layers at metal surfaces in order to take into account the presence of some of the aqueous environment at metal surfaces, through static DFT calculations and DFT-based MD simulations at finite temperature, some of their recent works include bulk liquid water at metallic interfaces [233] (although sometimes implicitly [234]). Jonsson and coworkers have included pH and applied voltage in DFT-MD [232] in an *ad hoc* way, by varying the concentration in H<sub>3</sub>O<sup>+</sup> electrolytes within a few water monolayers at the interface with the surface metal, while Cheng and Sprik [235] have played with the electrolyte concentration in the EDL at a metal-liquid water interface in order to model the interface capacitance and hence indirectly include relevant electrochemical voltage conditions. Imposing the electrochemical voltage is however very challenging in *ab initio* MD simulations, and few theoretical methods have been recently developed to that end [236, 237, 238, 239, 232], without any final consensus for the most relevant methodology.

In the present chapter we focus on one essential aspect of electrochemical interfaces, i.e. the comprehension of the interaction and organisation of liquid water at the (semiconductor) (110)-Co<sub>3</sub>O<sub>4</sub> surface by DFT-MD simulations. This is following the modelling and analyses strategies from recent works of the group on mineral-water interfaces [240, 241, 242, 243, 244, 245].

As reviewed in chapter 4, previous experimental surface science characterization of (110)-Co<sub>3</sub>O<sub>4</sub> have been performed [246], as well as theoretical investigations on the bare surface [247, 248]. As introduced in section 4.17, the group of Selloni has furthermore been the first one to characterize the

hydroxylation state of the (110)-Co<sub>3</sub>O<sub>4</sub> surface, with systematic surface science DFT calculations of phase diagrams as a function of water pressure, pH, and external voltage in electrochemical conditions [249, 250, 251, 252]. These theoretical calculations have provided a clear view of the water monolayer coverage under experimental conditions at the (110)-Co<sub>3</sub>O<sub>4</sub> cobalt oxide surface, but the rest of the liquid water has not been explicitly taken into account.

This is what is achieved in the present thesis, *i.e.*, an explicit consideration of the liquid water in contact with the (110)-Co<sub>3</sub>O<sub>4</sub> cobalt oxide surface, using *ab initio* DFT-based molecular dynamics simulations. A detailed characterization of chemical and physical properties of the aqueous interface is provided (*i.e.* structure, dynamics, electric field, spectroscopy), as a preliminary step into the modelling of the (110)-Co<sub>3</sub>O<sub>4</sub> aqueous surface in more relevant electrochemical conditions. As emphasized by Koper and coworkers, see for instance ref. [253], the efficiency of chemical reactions at material-water interfaces is highly dependent on how much water is easily/not easily reorganized, or in other terms on how much water at the interface has a flexible/rigid structural & dynamical character. This is one key issue into the charge transfers occurring within the double layer as the chemical reactions (such as the OER) proceed. It is thus fundamental to have the knowledge of the intrinsic chemical and physical properties of the material-water-electrolyte interface (at a given pH and electrolyte concentration), before applying the electrochemical voltage.

Of particular interest is how the interfacial water is organised, not only at the direct contact with the semi-conductor cobalt oxide surface, *i.e.* in the BIL (Binding Interfacial Layer, see refs. [241, 242]), but also at slightly larger distances from the aqueous oxide surface, *i.e.* in the DL (Diffuse Layer [241, 242]), the knowledge of the layers' thickness, and at what distance from the surface is bulk liquid water recovered.

The following chapter is organized with the computational methods in section 8.2, the Co<sub>3</sub>O<sub>4</sub> cobalt oxide bulk properties in section 5.2, the surface and hydroxylation properties of the (110) A- and B-terminations in contact with water in 5.3, the water structure at the (110)-Co<sub>3</sub>O<sub>4</sub>-A/B-liquid water interfaces in 5.5, and physical observables such as interfacial electric field, surface work function and SFG (Sum Frequency Generation) vibrational spectroscopy of the oxide-liquid water interface in 5.6. Perspectives in the context of electrochemical reactions are discussed in the conclusions in section 5.7.

Most (but not all) of the data presented in this chapter have been published in our paper [254] *DFT-MD of the (110)-Co<sub>3</sub>O<sub>4</sub> cobalt oxide semiconductor in contact with liquid water, preliminary chemical and physical insights into the electrochemical environment*, *J. Chem. Phys.*, Vol. 150, no. 4, pag. 041721, 2019. This paper has been highlighted by a celebratory press interview in the American Institute of Physics (AIP) Publishing with the title *Simulations provide new insight into water structure and dynamics at the water-cobalt oxide interface*, and it has been selected as part of the Best Paper List and the Most Read List in *J. Chem. Phys.* 2019 (<https://aip-info.org/1XPS-6LEYF->

## 5.1 Computational methods

Unrestricted open shell ab initio DFT-based (Density Functional Theory) molecular dynamics simulations (spin polarized-DFT-MD/spin polarized-AIMD) have been performed on the bulk crystal of  $\text{Co}_3\text{O}_4$ , on the two possible (110)- $\text{Co}_3\text{O}_4$  crystalline surfaces (A- and B- terminations) and on their associated (110)- $\text{Co}_3\text{O}_4$ /liquid water interfaces (details in section 5.3). All simulations have been performed in the Born-Oppenheimer framework with the CP2K package [255, 256], see chapter 2 for all details on DFT and DFT-MD. The PBE [257] functional, that in previous works [58, 258, 259] has been shown as a good description of the properties of both this oxide (and more generally most oxides) and of liquid water, has been adopted in combination with mixed Gaussian-Plane Waves basis sets and GTH pseudopotentials [260], as used in the CP2K software. The DZVP-MOLOPT-SR basis set, augmented with a 400 Ry plane wave basis set have been used, being a good compromise between computational cost and accuracy, as will be shown here. The PBE functional has been supplemented with the Hubbard U term [261, 262] in order to circumvent the overdelocalization of the 3d-electrons in metal oxides (and the consequent underestimation of the band gap). A value of 5.9 eV for the U parameter has been adopted, as proposed by Selloni *et al.* [58], see section 2.7.4. Although U is not universal and depends on the ab initio protocols (typically DFT functional, pseudo-potentials, projection scheme), we decided to stick to this value while checking that electronic properties of the semiconductor are correctly obtained with the DFT-schemes applied in this work (see section 5.2). The Grimme D2 correction [263, 264] for dispersion effects has been taken into account for a better description of van der Waals interactions, especially of importance for liquid water. Default algorithms and convergence criteria in CP2K have been adopted. Periodic boundary conditions (PBC) have been applied in all three spatial directions.

DFT-MD in the flavor of Born-Oppenheimer molecular dynamics have been performed, with the electronic wavefunction being calculated at each time step, the classical nuclei displacements being obtained through the Velocity-Verlet algorithm with a time-step of 0.4 fs. The dynamics are systematically divided into two parts, an equilibration dynamics of 5 ps duration (in the NVE ensemble however allowing rescaling of velocities whenever necessary to reach the target temperature of  $300 \pm 30\text{K}$ ), followed by 20 ps NVE production runs, the latter trajectory being used for all structural and spectroscopic analyses presented here.

$\text{Co}_3\text{O}_4$  crystallizes in a face-centered cubic unit cell called "spinel structure" (Figure 5.1), determined independently by Bragg [265] and Nishikawa [266]. The primitive lattice consists in 2  $\text{Co}^{2+}$ , 4  $\text{Co}^{3+}$  and 8  $\text{O}^{2-}$ , for a total of 14 atoms (Fig. 5.1-left); four primitive lattices form the conventional "spinel" cubic unit cell (Fd3m symmetry space group) which contains 8  $\text{Co}^{2+}$ , 16  $\text{Co}^{3+}$

and 32  $O^{2-}$ , for a total of 56 atoms (Figure 5.1-right) arranged in a face-centered cubic box (the experimental lattice parameter is 8.08 Å [265, 266, 58]).

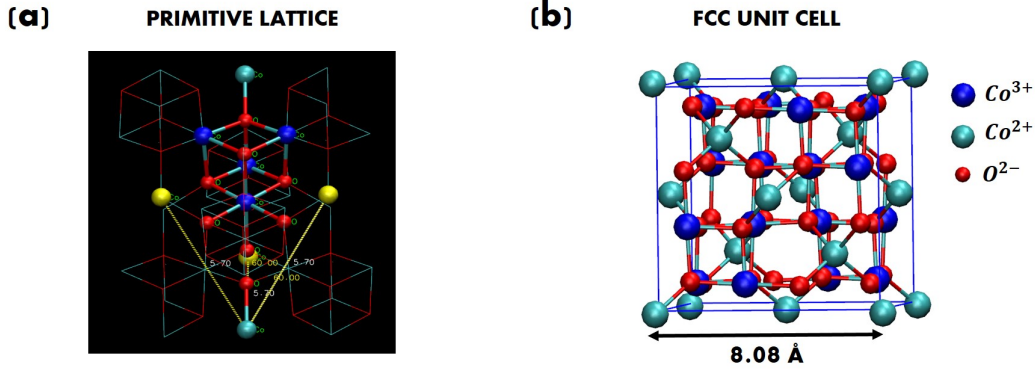


Figure 5.1: a) Primitive lattice of bulk  $Co_3O_4$  spinel structure . b) FCC unit cell of bulk  $Co_3O_4$  spinel: 56 atoms, 8  $Co^{2+}$ , 16  $Co^{3+}$ , 32  $O^{2-}$ .

All our DFT-MD calculations (geometry optimisations and molecular dynamics) are done at the  $\Gamma$  point of the Brillouin zone for the electronic representation, this imposes the use of a supercell (i.e. a certain number of replicas of the unit cell in 3D-space). To find the minimum number of replicas that give an accurate description of the bulk  $Co_3O_4$  crystal, convergence of the lattice parameter of the  $Co_3O_4$  unit cell and of the electronic band gap of the bulk  $Co_3O_4$  oxide have been monitored, see calculations details in section 5.2. To that end, full geometry optimizations (atom positions and cell vectors) and projected densities of states (PDOS) calculations are performed on the unit cell (56 atoms) and on two (112 atoms), four (224 atoms) and eight (448 atoms) replicas of the  $Co_3O_4$  unit cell (in section 5.2). PDOS results (in section 5.2) have been obtained by projecting the Kohn-Sham states onto the atomic orbitals using the standard routine implemented in the CP2K code. Note that the optimisations start from the experimental geometry and are done without imposing symmetry constraints. The  $Fd3m$  symmetry is preserved by the optimizations. Here and for all simulations of the cobalt oxide at the interface with the vacuum or with liquid water, the electronic multiplicity of the system accounts for the number of the open-shell  $Co^{2+}$  atoms in the simulation box, which is of course computationally more expensive.

As PBC are applied in all 3-directions of space, when simulating the (110)-A/B-air interface, a vacuum of 16.5 Å along the z-direction (perpendicular to the surface) has been included in the simulation box to separate the periodic replicas, see Fig. 5.2. This choice allow us to simulate liquid water that is not been squeezed in between the 2 cobalt surface replicas. Liquid water should behave more properly.

A uniform background and the Ewald summation for electrostatics take care of the total charge of the simulation box whenever necessary, as standard

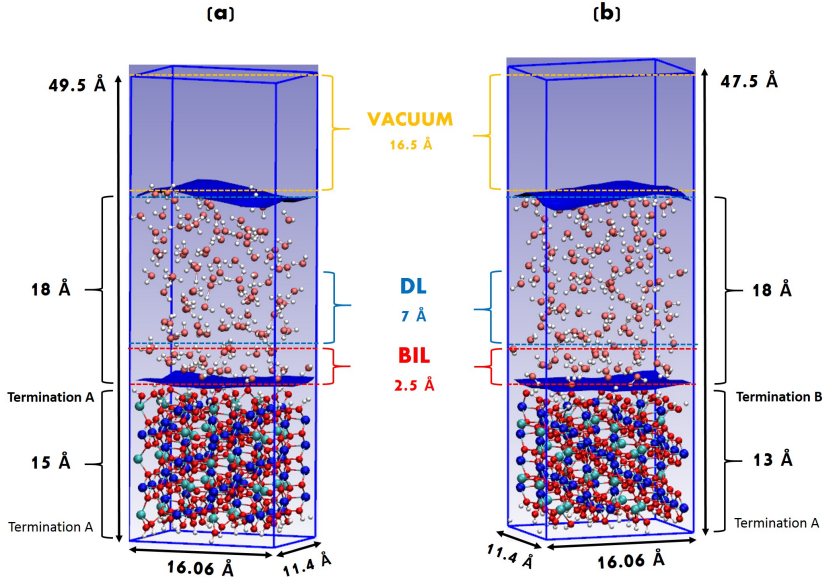


Figure 5.2: *Simulation boxes for the DFT-MD of (110)-A/B-Co<sub>3</sub>O<sub>4</sub>-liquid water interfaces. (a) Co<sub>3</sub>O<sub>4</sub> termination A/liquid water interface (712 atoms): 352 solid atoms, 120 water molecules. (b) Co<sub>3</sub>O<sub>4</sub> termination B/liquid water interface (680 atoms): 320 solid atoms, 120 water molecules. Choice is made here to include a 16.5 Å vacuum above the liquid water in the vertical  $z$ -direction, in order not to simulate confined water due to the PBC applied in all 3-directions of space. Only one surface is put in contact with liquid water in each simulation box. The other hydroxylated surface is in contact with vacuum.*

procedure in DFT-MD simulations.

Electric fields  $\mathbf{E}(z)$  and differences in electric potentials  $\Delta\phi$  have been obtained fully *ab-initio* from the optimized electronic wavefunction and the position of the nuclei, using the standard routine implemented in CP2K. The electronic work function of the (110)-Co<sub>3</sub>O<sub>4</sub> surface, in contact with the air or in contact with liquid water, has been calculated as in refs. [267], *i.e.* it is the difference between the electric potential in the vacuum and the Fermi level (details in section 5.6).

The identification of the water interfacial layers at charged (and non charged) interfaces, namely BIL (Binding Interfacial Layer), DL (Diffuse Layer) and Bulk liquid water, has been obtained following the methodology derived by the group and fully described in ref. [241] on the basis of water structural properties *only*, see section 5.5 below for more details. In the systems investigated here, the BIL is found systematically composed of the first water monolayer, as already shown in several of our investigations on mineral oxide-water interfaces, see e.g. refs. [241, 242].

Spectroscopic analyses are done in terms of non-linear SFG (Sum Frequency Generation) spectroscopy in section 5.6. See past references of the group on various charged and uncharged air-water and oxide-water interfaces on this subject [268, 241, 242, 243]. The SFG (Sum Frequency Generation) signal arises

from both BIL and DL layers, while the subsequent centrosymmetric bulk water layer is not SFG active (this is verified in our calculations). The total resonant electric dipole non-linear susceptibility  $\chi^{(2)}(\omega)$  (real and imaginary components) is calculated following the time-dependent method of Morita and Hynes [269, 270], using the model proposed by Khatib *et al.* [271] for dipole and polarisability derivatives of water. As shown in previous works of the group, this model gives accurate SFG spectra [268, 241, 242, 272]. Only the SFG signal from water is calculated. Briefly, supposing that in the high frequency region ( $> 3000 \text{ cm}^{-1}$ ) only the O-H stretching motions are contributing to the spectrum, and neglecting intermolecular cross-correlation terms, one has:

$$\chi_{PQR}^{(2)}(\omega) = \sum_{m=1}^M \sum_{n_1=1}^2 \sum_{n_2=1}^2 \frac{i}{k_b T \omega} \times \int_0^\infty dt e^{-i\omega t} \langle \dot{\alpha}_{PQ}^{m,n_1}(t) \dot{\mu}_R^{m,n_2}(0) \rangle \quad (5.1)$$

where (P,Q,R) are any  $x, y, z$  direction in the laboratory frame, and  $k_b$  and  $T$  are the Boltzmann constant and temperature of the simulated system.  $\langle \dots \rangle$  is a time-correlation function,  $\alpha_{PQ}(t)$  and  $\mu_R(0)$  are respectively the individual O-H bond contribution to the total polarization and dipole moment of the system and  $\dot{\alpha}_{PQ}(t)$  and  $\dot{\mu}_R(0)$  their time derivatives.  $M$  is the number of water molecules and  $n_1$  and  $n_2$  two indices that identify each of the two O-H oscillators per molecule. We calculate here *ssp* SFG signals, i.e.  $xxz$  directions. Note that the electric-dipole approximation has been used here, electric-quadrupole contributions to the *ssp* signal are neglected. Using the direction cosine matrix (D) projecting the molecular frame ( $x, y, z$ ) onto the laboratory frame ( $P, Q, R$ ), and assuming that the O-H stretching is much faster than the modes involving a bond reorientation, one can write:

$$\dot{\alpha}_{PQ}(t) \simeq \sum_i^{x,y,z} \sum_j^{x,y,z} D_{Pi}(t) D_{Qj}(t) \frac{d\alpha_{ij}}{dr_z} v_z(t) \quad (5.2)$$

$$\dot{\mu}_R(t) \simeq \sum_i^{x,y,z} D_{Ri}(t) \frac{d\mu_i}{dr_z} v_z(t) \quad (5.3)$$

The D matrix and the projection of the velocities on the O-H bond axis ( $v_z$ ) can be readily obtained from the DFT-MD trajectory, while  $\frac{d\alpha_{ij}}{dr_z}$   $\frac{d\mu_i}{dr_z}$  are parametrized [271, 273].

SFG spectra arising from the BIL (resp. from the DL, from the Bulk) are obtained including only the water molecules that belong to BIL/DL/Bulk into the summation in eq. 5.1, known from our decomposition scheme [241] for recognizing these layers.

## 5.2 $\text{Co}_3\text{O}_4$ cobalt oxide bulk properties

We start by considering the solid bulk properties. The ability of the PBE DFT-functional corrected by the Hubbard U term (5.9 eV [58]) in reproducing experimental values for the lattice constant and the electronic band gap of the

bulk solid is tested as a function of the simulation box size, i.e. the number of replicas needed to correctly reproduce experimental values in a supercell approach (calculations at the  $\Gamma$ -point only) is validated.

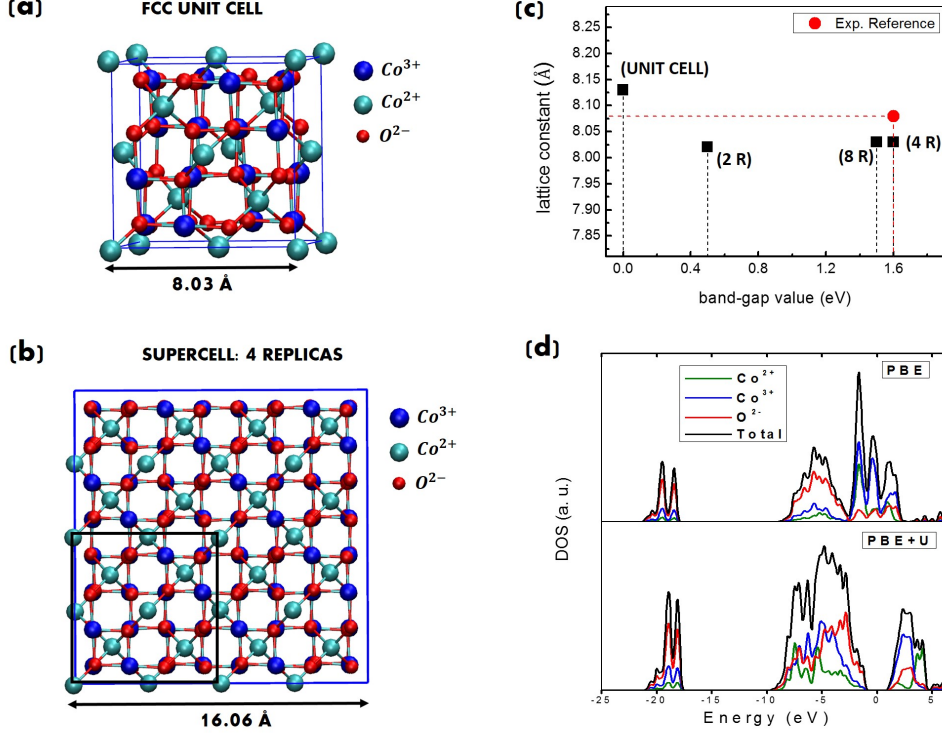


Figure 5.3: (a) FCC unit cell of bulk  $\text{Co}_3\text{O}_4$ : 56 atoms, 8  $\text{Co}^{2+}$ , 16  $\text{Co}^{3+}$ , 32  $\text{O}^{2-}$ . (b) 4-Replicas of the  $\text{Co}_3\text{O}_4$  unit cell: 224 atoms, 32  $\text{Co}^{2+}$ , 64  $\text{Co}^{3+}$ , 128  $\text{O}^{2-}$ . (c): Band gap (x-axis) and lattice constant (y-axis) as obtained from DFT-PBE+U as a function of the simulation box size: unit cell, 2-Replicas of the unit-cell (2R), 4-Replicas (4R), 8-Replicas (8R). The red point in the plot shows the reference experimental values. The value for the band gap is taken from refs.[274, 275] and the one for the lattice constant is from ref.[265, 266, 58]. (d) Projected density of states (PDOS) from PBE (top) and PBE+U (bottom) calculations for the four replicas system. The Fermi energy level is set to 0.

An illustration of the unit cell of the  $\text{Co}_3\text{O}_4$  cobalt-oxide bulk solid is shown in figure 5.3-a (56 atoms). In figure 5.3-c we report a 2D-plot of the lattice constant and band gap values obtained from DFT-PBE+U for different box dimensions (unit cell, 2 replicas (2R), 4 replicas (4R) and 8 replicas (8R)), compared to the experimental values (red circle). Bulk  $\text{Co}_3\text{O}_4$  is a transition metal oxide and a semiconductor at room temperature with an experimental band-gap value of 1.6 eV [274, 275]. While the lattice parameter is already converged (within our numerical error) for the two replicas system, the band gap is more sensitive to finite size effects (*i.e.*, sensitive to Brillouin zone sampling): the unit cell and the 2 replicas system both underestimate the band gap (see figure 5.3-c), while both the four and eight replicas models have a

value of 8.03 Å for the lattice parameter and 1.6 eV and 1.5 eV respectively for the band gap, comparable with the experimental ones (8.06 Å and 1.6 eV, red dot in figure 5.3-c). The 4-replicas system (figure 5.3-b, 224 atoms) is thus the best compromise between accuracy and minimizing computational cost, correctly reproducing both band gap and lattice constant.

Localized wannier functions and charges have been computed for the four replicas system. The correct oxidation states have been found for all  $\text{Co}^{2+}$ ,  $\text{Co}^{3+}$  and  $\text{O}^{2-}$  atoms of the bulk oxide. Same outcome for the shapes of the associated localized wannier orbitals, identical to the results in ref. [58], confirming the correct description of the electronic structure of the system with the here chosen computational set-up.

In figure 5.3-d, we also show the electronic PDOS obtained for the 4-replicas bulk oxide using PBE and PBE+U electronic representations. The comparison highlights that it is essential to include the U correction to correctly represent electronic properties of the bulk solid, as there is no band gap when the PBE representation is used: without the U-term, the system is a conductor.

To conclude, our chosen set-up is sufficient to correctly reproduce structure and electronic properties of the  $\text{Co}_3\text{O}_4$  cobalt oxide crystal bulk, and 4-replicas of the unit cell are enough in a supercell approach (at the electronic  $\Gamma$ -point). This 4-replicas system will thus be used for the next step consisting now in the cut of the bulk oxide along the (110) direction, and ultimately put the hence created surface(s) in contact with liquid water.

Note that previous works [258, 276, 277] have pointed out that the modelling of too small cells (in all 3 directions of space) prevents the correct description of the structure of water at the interface. Some of the recent works in the group [242, 276, 277] give solid bases to trust that lateral dimensions above 15 Å (such as the ones of the cut-surface of the 4 replicas system employed here) are just enough to avoid finite size effects on the structure of interfacial water.

## 5.3 Cutting along the (110) direction: A- and B-terminations in contact with liquid water

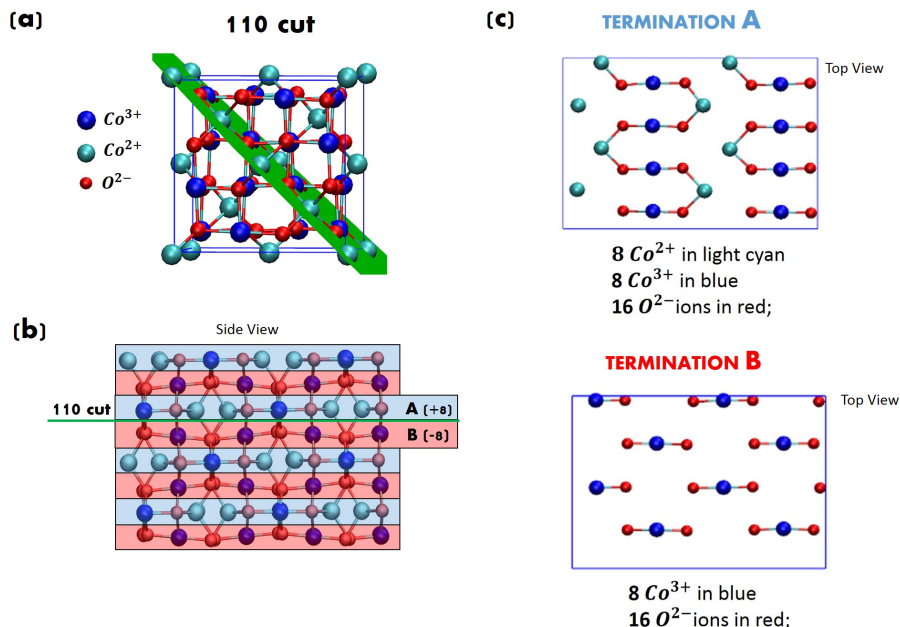


Figure 5.4: (a) FCC unit cell of  $\text{Co}_3\text{O}_4$  cut along the (110) crystallographic plane (in green). (b) Side view of the adopted 4-replicas system (224 atoms) for the (110) cut: positively charged A-layers are in blue background (+8 |e|), negatively charged B-layers are in red background (-8 |e|). See chapter 4-section 4.16 for other details and representation. This figure shows the 8-layers asymmetric slab (A-layer at the top, B-layer at the bottom) used in the simulation box of fig. 5.2-b for the (110)-B-termination in contact with liquid water. (c) Composition and speciation of the A- and B-surfaces after the (110) cut of the 4-replicas system of  $\text{Co}_3\text{O}_4$  (identical to ref.[278]). Top views. Oxygens are in red, Co(II) in light blue, Co(III) in dark blue. See text for details.

When the bulk solid is cut along the (110) crystallographic symmetry plane (Figure 5.4-a), two possible terminations can be obtained (Figure 5.4-c), denoted as A- and B-terminations. Cutting a solid structure along one preferential direction according to the crystallographic planes of symmetry ((110) direction in our case) means that the cut involves the breaking of chemical bonds between atoms, *i.e.* between  $\text{Co}^{2+/3+}$  and  $\text{O}^{2-}$ . Such cleavage can occur in 2 ways, *i.e.* homolytic or heterolytic.

The homolytic cleavage results in each atom of the chemical bond that keeps one of the originally bonding electrons (see Fig. 5.5-left).

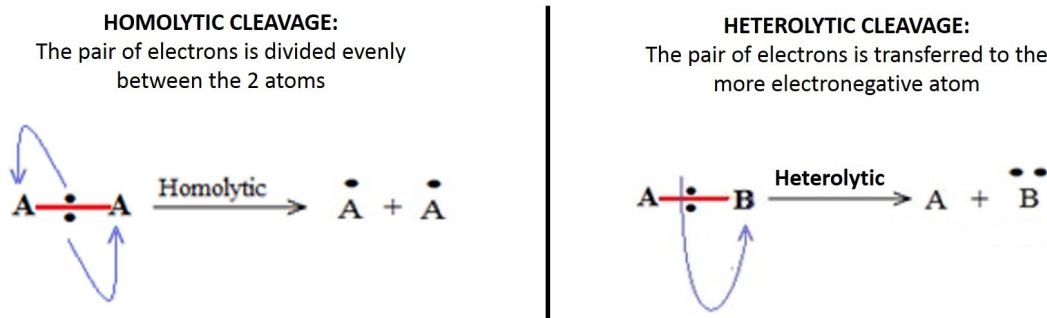


Figure 5.5: Scheme of homolytic and heterolytic cleavage.

The pair of bonding electrons is hence divided equally between Co and O atoms, in our case. For a homolytic cleavage, the charge of each surface Co and O atom does not change, as shown in Fig. 5.6.

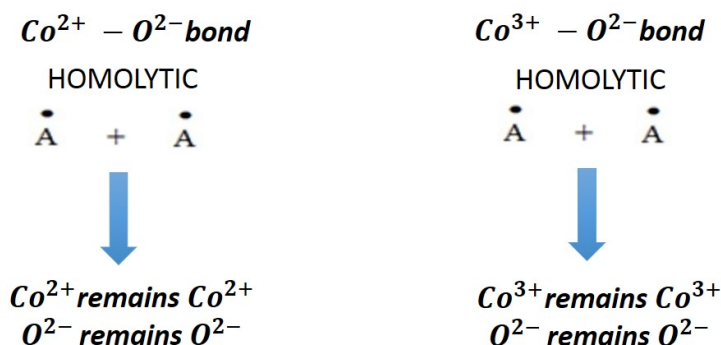


Figure 5.6: Homolytic cleavage for the covalent bonds involved in the (110) cut of  $Co_3O_4$ .

By contrast, the heterolytic cleavage of a covalent bond is a chemical process where only one of the bonding atoms takes both bonding electrons, as depicted schematically in Fig. 5.5-right.

For a heterolytic cleavage, the more electronegative oxygen atom  $O^{2-}$  (in our case) acquires the pair of bonding electrons. In such heterolytic cut, this leads to formal charges on the surface atoms of  $Co^{1+}$  (instead of the initial  $Co^{2+}$ ),  $Co^{2+}$  (instead of the initial  $Co^{3+}$ , and note that  $Co^{3+}$  loses 2 electrons after the cut because it was initially bonded to 2 oxygens), and  $O^{3-}$  (instead of the initial  $O^{2-}$ ), see Fig. 5.7.

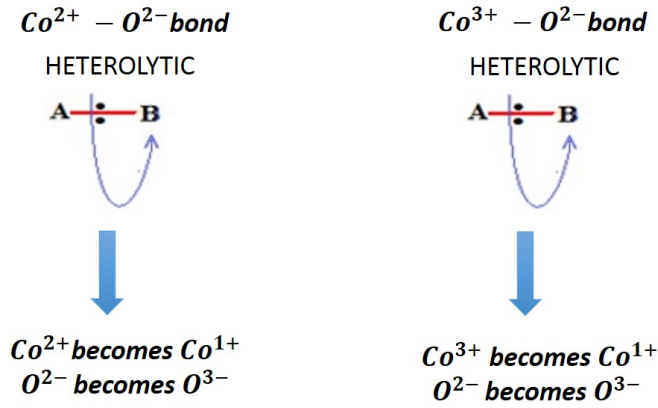


Figure 5.7: *Heterolytic cleavage for the covalent bonds involved in the (110) cut of  $Co_3O_4$ .*

In table 5.8, the surface charge obtained at the (110)-homolytic and at the (110)-heterolytic cleaved  $Co_3O_4$  surfaces is shown.

HOMOLYTIC			HETEROLYTIC		
	A-Termination	B-Termination		A-Termination	B-Termination
$8 Co^{2+}$	$(8 \times 2) = +16$	\	$8 Co^{2+} \rightarrow 8 Co^{1+}$	+8	\
$8 Co^{3+}$	$8 \times (3) = +24$	$8 \times (3) = +24$	$8 Co^{3+} \rightarrow 8 Co^{1+}$	+8	+8
$16 O^{2-}$	$16 \times (-2) = -32$	$16 \times (-2) = -32$	$16 O^{2-} \rightarrow 16 O^{3-}$	-48	-48
SURFACE CHARGE	+8	-8	SURFACE CHARGE	-32	-40

Figure 5.8: *Charge of the surface species involved in the (110) cut of  $Co_3O_4$  and the total surface charge for the A and B terminations. Left: homolytic cleavage, Right: heterolytic cleavage –of the chemical bonds upon the (110) cut of the  $Co_3O_4$  bulk.*

Following previous works from the literature and Selloni’s papers [209, 212, 32], we have chosen to adopt the homolytic cleavage and hence to model the (110)- $Co_3O_4$  with charged surface and layers (+8 | e | for the A-layer and -8 | e | for the B-layer), as shown in Fig. 5.9.

The cationic A-termination surface exposes 8  $Co^{3+}$ , 8  $Co^{2+}$  and 16  $O^{2-}$  in the 4-Replicas box validated in section 5.2 (2  $Co^{3+}$ , 2  $Co^{2+}$  and 4  $O^{2-}$  per unit cell surface), with a formal surface charge of  $4.37 | e | / nm^2$  (+8 | e | in the 4-replicas box). The anionic B-surface instead exposes 8  $Co^{3+}$  and 16  $O^{2-}$  in the adopted 4-Replicas box (2  $Co^{3+}$  and 4  $O^{2-}$  in the unit cell), with formal surface charge of  $-4.37 | e | / nm^2$  (-8 | e | in the 4-replicas box). Interestingly only  $Co^{3+}$  sites are present at the B surface, while both  $Co^{3+}$  and  $Co^{2+}$  sites are exposed at the A surface. This difference together with the opposite surface charge possibly play a role in the reactivity of the two surfaces, thus in their ability to catalyze the water splitting [278, 279]. For the sake

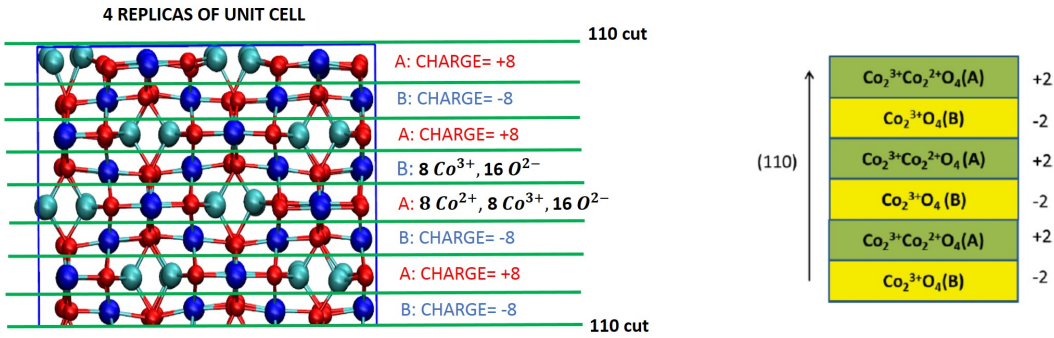


Figure 5.9: Snapshot of modeled (110)- $Co_3O_4$  structure as a stack of charged layers (on the left) in comparison with the model from Selloni's work [212] (on the right) on a smaller size system.

of completeness, each layer is modeled as charged (positively or negatively) but we model the entire system as a neutral system (system total charge=0) using an odd number of layers (see Fig. 5.9) for which the total dipole moment is zero, as also adopted in Selloni's papers reviewed in section 5.12 of this thesis.

Once put in contact with water the two surfaces adsorb water molecules. As will be shown in more details in section 5.6, such surface hydroxylation strongly changes the electronic properties of the Cobalt oxide surface, especially tuning the surface work function. To find the final speciation/hydroxylation state of the A- and B-surfaces in contact with the air, the usual strategy of adsorbing one water molecule at a time and ranking the energetics depending on the surface site adsorption has been adopted, following the strategy by Selloni *et al.* [278] on this same oxide: water molecules have been added one by one at the surface until complete hydroxylation of the surface. This is done through geometry optimizations, and ranking the relative energetics of adsorption of water on each available surface site. See figure 5.10 for top and side views of the hydroxylated A- and B-terminated surfaces obtained (same hydroxylated surface pattern obtained in Selloni's work, in ref. [278]).

Once in contact with water, the A-surface is composed of a total of 16 dissociated water molecules (4 water molecules if one considers the unit cell only), there are no intact water molecules adsorbed: this results in 16  $\mu_2$ -OH sites exposed (at the top surface), systematically bridging 2 identical Cobalt atoms (either  $Co^{2+}$  or  $Co^{3+}$ ), see black and green boxes in fig. 5.10-left, 16  $\mu_3$ -OH inner sites, the initial bulk  $\mu_3$ -O site receiving the dissociated water proton. Once in contact with water, the B-surface is composed of a total of 16 water molecules (4 water molecules if one considers the unit cell only), 8 being dissociated and 8 being intact. This gives rise to the following B-surface speciation, see also fig. 5.10-right: 8  $\mu_1$ -OH<sub>2</sub> exposed sites, 8  $\mu_1$ -OH exposed sites, 8  $\mu_2$ -OH inner sites (the inner  $\mu_2$ -O sites receiving the dissociated water proton), and 8  $\mu_2$ -O inner sites. Both surfaces are not flat anymore after water adsorption, now showing a microscopic rugosity with "inner-channels".

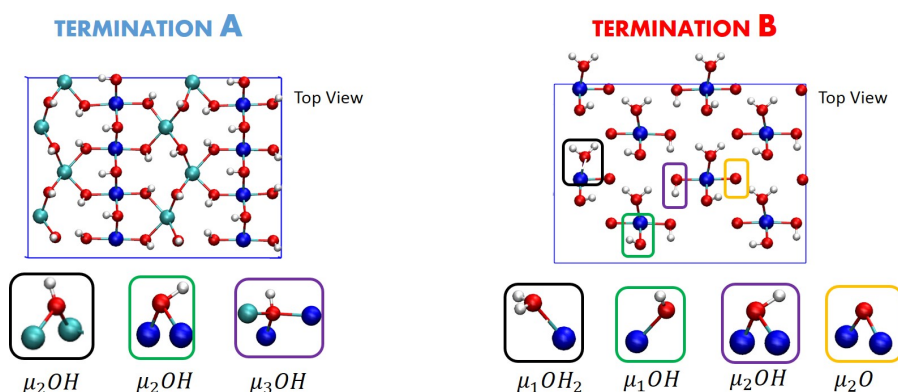


Figure 5.10: *Composition and speciation of the A- and B-surfaces after surface hydroxylation geometry optimizations (identical to ref.[278]). Top and side views. Oxygens are in red, hydrogens in white, Co(II) in light blue, Co(III) in dark blue. See text for details.*

As one can see from the data listed above, the two surfaces are substantially different, and in particular surface B shows a larger variety of chemical species.

Once the surface hydroxylation has been achieved at the oxide-air interface, the next step consists in placing the A- and B-hydroxylated surfaces in contact with bulk water composed of 120 water molecules (liquid water box separately thermally equilibrated), as illustrated by the simulation boxes in figure 5.11. Choice is made here to include a 16.5 Å vacuum above the liquid water in the vertical z-direction (see Figure 5.11 for a scheme). This latter is done in order to avoid to compress the liquid water in between the 2-replicated surfaces in the z-direction, and hence avoid simulate confined water, while keeping the simulation box dimensions reasonable and amenable to large enough time-scales for DFT-MD.

The simulation boxes for the DFT-MD of the (110)-A- $\text{Co}_3\text{O}_4$ -liquid water and of the (110)-B- $\text{Co}_3\text{O}_4$ -liquid water interfaces are illustrated in figure 5.11. One box is composed of 9 layers of bulk cobalt oxide in a symmetric slab model, i.e. with two A-surfaces on each side. Both A-surfaces are hydroxylated, and only one surface is put in contact with liquid water. This is seen in fig. 5.11-a. The other box is composed of 8 layers of bulk cobalt oxide, in an asymmetric slab model, hence displaying the A- and B-surfaces on either side. Both surfaces are hydroxylated and only the B-surface is put in contact with liquid water. This is in fig. 5.11-b. For the asymmetric slab, the thickness of the bulk is such that there is no issue with dipole corrections. The cationic A-layer and anionic B-layer have respectively total charges of  $+8 | e |$  and  $-8 | e |$ , when considering the 4-replicas system used in the simulations (see section 5.2 for details on the choice of the 4-replicas in the supercell approach).

The speciations of the A- and B-surface terminations described above are found to be stable also when the bulk water is explicitly considered in contact with

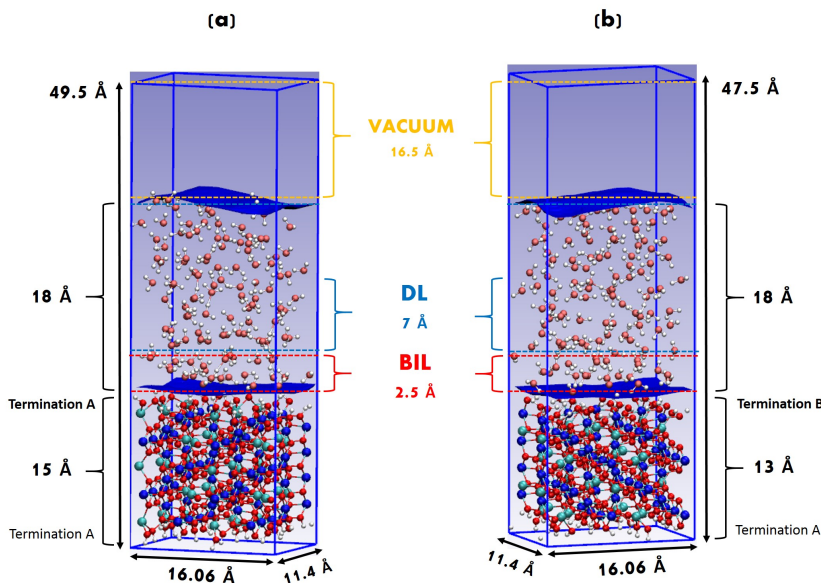


Figure 5.11: *Simulation boxes for the DFT-MD of (110)-A/B- $\text{Co}_3\text{O}_4$ -liquid water interfaces. (a)  $\text{Co}_3\text{O}_4$  termination A/liquid water interface (712 atoms): 352 solid atoms, 120 water molecules. (b)  $\text{Co}_3\text{O}_4$  termination B/liquid water interface (680 atoms): 320 solid atoms, 120 water molecules. Choice is made here to include a 16.5 Å vacuum above the liquid water in the vertical  $z$ -direction, in order not to simulate confined water due to the PBC applied in all 3-directions of space. Only one surface is put in contact with liquid water in each simulation box. The other hydroxylated surface is in contact with vacuum.*

the cobalt hydroxylated surfaces. While this shows that gas phase calculations are enough to get a correct description of the surface speciation, structural and electronic properties of the cobalt oxide-liquid water, such as the work function, are ill-described when not considering the explicit presence of the bulk liquid water. Also, we observe some mobility of protons along the surface, that shows up only when bulk water is introduced.

## 5.4 $\text{Co}_3\text{O}_4$ cobalt surface at the interface with liquid water

We now provide a detailed description of the  $\text{Co}_3\text{O}_4$  cobalt oxide (110)-A/B-liquid water interfaces, with first providing details on the surface sites orientation, on the solid-solid and solid-water H-Bonds. The organization of liquid water is reported in the next section 5.5. While the total number of  $\mu_1/\mu_2/\mu_3$  sites is on average maintained along the trajectories, the aqueous B-surface shows a quite dynamical behaviour with proton hoppings between the surface and bulk water. However the length of our simulations does not allow a more quantitative analysis. Instead the aqueous A-surface is quite static along all the simulation time.

At the aqueous A-surface,  $\mu_2$ -OH sites are found in two possible orientations (on average), with 67% of them being oriented in-plane (IP, forming an angle around  $50^\circ$  with the normal to the surface) and 33% being oriented out-of-plane (OP, forming an angle around  $10^\circ$  with the normal to the surface).

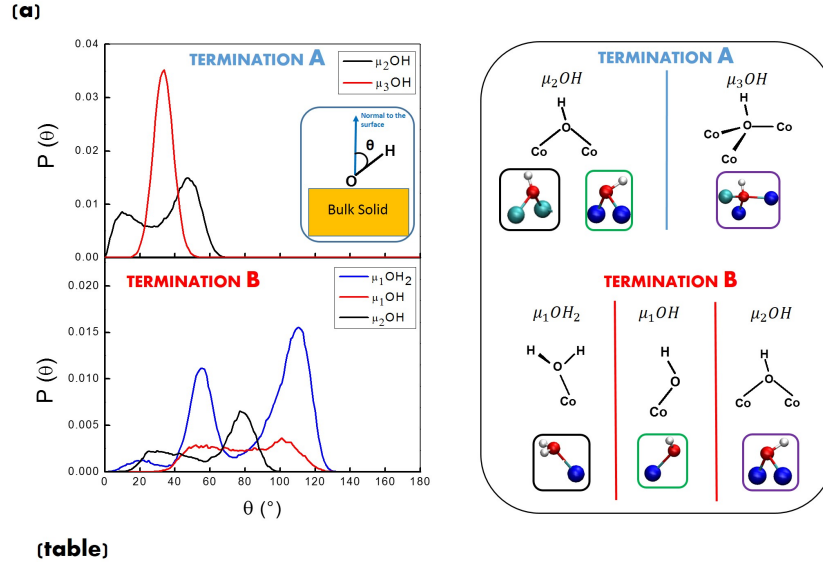


Figure 5.12: (a) Probability distributions of surface O-H sites orientation (left) and speciation of terminations A and B (right). The orientation is calculated as the scalar product of the O-H vector with the normal to the surface (oriented outward the surface). The nomenclature for the surface sites is illustrated on the right side. Table at the bottom: data about the H-Bond arrangements at each interface. Sol=solid, Wat=water, BIL=Binding Interfacial Layer, DL=Diffuse Layer, INTRA-BIL=H-Bonds formed between the water molecules located in the BIL, WA= Water Acceptor, W-W= water-water H-Bond, HBs/mol= hydrogen bonds per water molecule, HBs/nm<sup>2</sup>= hydrogen bonds per nm<sup>2</sup> unit of lateral box dimensions.

The  $\mu_3$ -OH sites are all oriented similarly, with an angle around  $35^\circ$  with the normal to the surface. Neither  $\mu_2$ -OH nor  $\mu_3$ -OH sites form surface-surface H-Bonds, either because of geometrical reasons ( $\mu_2$ -OH) or because of being more buried ( $\mu_3$ -OH) into the material and somehow partially "screened" by adjacent sites. We find that all (93%) surface-liquid water HBs are formed by exposed  $\mu_2$ -OH sites, systematically in the configuration where the  $\mu_2$ -OH sites are donors of HBs and the water is acceptor (see 88% of WA-Water Acceptors in the table in figure 5.12). As a consequence, the aqueous A-surface has a strong HB donor character towards liquid water, certainly compatible with its high positive surface charge.

At the aqueous B-surface,  $\mu_2$ -OH sites are now inner-sites mostly oriented IP (maximum at  $80^\circ$  in Fig. 5.12-a, black line). They are not in direct contact with water, thus forming no HBonds with water molecules, while they contribute to intra-solid H-Bonds as HB-donors to  $\mu_1$  sites. The exposed  $\mu_1$  sites (either  $\mu_1$ -OH<sub>2</sub> or  $\mu_1$ OH, top surface in direct contact with water) are the only ones being H-Bonded to water (91% on average), with the  $\mu_1$ -OH<sub>2</sub> mostly donors of H-Bonds and  $\mu_1$ -OH mostly acceptors of HBs. This goes with their orientation, as the  $\mu_1$ -OH<sub>2</sub> sites always have one proton pointing towards the water, while a broader angular distribution is observed for the  $\mu_1$ -OH sites (red and blue lines in Fig. 5.12-a). The resulting water-solid HB-Network at the aqueous B-surface is roughly equally distributed in HBs with  $\mu_1$ -donors (57%) and  $\mu_1$ -acceptors (43%) (see also the table in Fig. 5.12). The aqueous B-surface therefore is far less of HB donor character towards the liquid water than the aqueous A-surface.

Interestingly the average density of water-solid HBs is higher at the aqueous A-surface than at the aqueous B-surface, showing that, despite both interfaces being strongly hydrophilic (the number of HBs/nm<sup>2</sup> is larger than at the most hydrophilic amorphous silica that the group has investigated in the past [280, 243]), the aqueous A-surface is the most hydrophilic one with a 8.7 water-solid HBs/nm<sup>2</sup>, close to the value of aqueous quartz [240, 244, 241]. At both interfaces, inner sites ( $\mu_3$ -OH for the A-surface and  $\mu_2$ -OH for the B-surface) do not interact with water. Simplified views of the typical solid-water HB patterns obtained at the aqueous A- and B-surfaces can be found in figure 5.13-a,b.

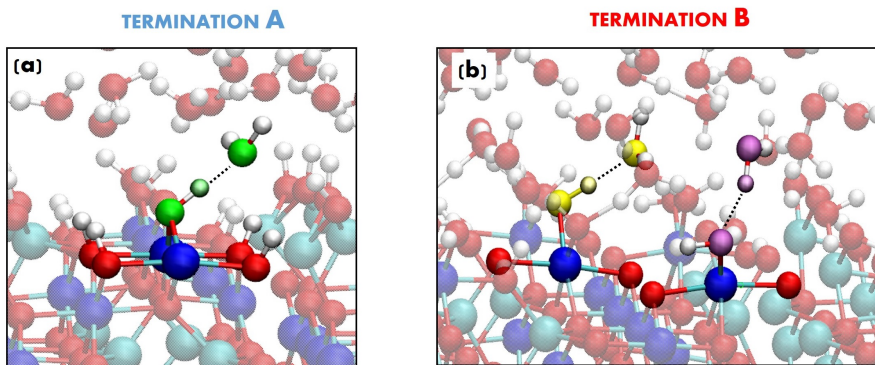


Figure 5.13: (a) and (b) Zooming views of the surface-water HB patterns at the aqueous A-surface (a) and B-surface (b). (a) Hbond donor to water:  $\mu_2$ -OH-water Hbond in green color where  $\mu_2$ -OH acts as a donor at the A-surface. (b) Equally Hbond donor and acceptor to water:  $\mu_1$ -OH-water Hbond where  $\mu_1$ -OH acts either as a donor (yellow) or as an acceptor (violet) at the aqueous B-surface.

## 5.5 Water structure at the $\text{Co}_3\text{O}_4$ cobalt oxide/liquid water interfaces: A- vs B-termination

The group has developed in ref. [241] a procedure to identify the organisation of water, at any charged and isoelectric interfaces, into three universal layers denoted BIL (Binding Interfacial Layer), DL (Diffuse Layer) and Bulk liquid water. These three universal water layers as well as the nomenclature were initially put forward in the experimental work by Tian *et al.* [281]. We apply this strategy here at the (100)- $\text{Co}_3\text{O}_4$ -A/liquid water and (100)- $\text{Co}_3\text{O}_4$ -B/liquid water interfaces. We refer the reader to ref. [241] for all details, we summarize the main ideas hereby. In a nutshell, at any interface water is found organised into BIL, DL and bulk water layers, which relative thickness is system dependent [241]. This statement is especially true for the DL, while we have shown that the BIL is systematically found one water monolayer only, i.e. 3-4 Å in thickness, whatever the surface and charge in regard. See refs. [241, 242, 282]. To reveal BIL, DL and bulk water from molecular dynamics simulations (ab initio and classical MD alike [241, 276, 277]) three theoretical descriptors are used, based *only* on water structural properties. These descriptors are 1) the water density profile (top of figure 5.15) as a function of the vertical z-distance from the surface (the density profile is calculated using Willard and Chandler’s Instantaneous Surface [283]), 2) the water coordination number in each layer identified from the density profile (see table in figure 5.12), for which the reference number is 3.6 for PBE-D2 bulk liquid water (calculated in this work using the set-up used for the interfaces, this value is identical to previous works on liquid water with the PBE & PBE-D2 functionals [259]), and 3) 3D-contour plots for the water-water H-Bond network where the simultaneous probability of a given HB distance and given HB orientation with respect to the surface normal (oriented towards the solid) is recorded (see bottom of figure 5.15). The reference of this latter for bulk liquid water is a homogeneous distribution of HB angles within the 2.6-2.9 Å HB distances, see Fig. 5.14 [276]. Any departing plot from this reference reveals a non isotropic organisation of water in the identified layers.

When all three descriptors correspond to the reference in bulk liquid water, the identified layer(s) is(are) denoted bulk water. When only the 3D-plots depart from the isotropic character of bulk water while the two other descriptors are identical to bulk, the layer(s) is(are) the DL. The DL is indeed bulk liquid water in which the HB network is reoriented by the surface electric field [241, 281]: there is therefore a well-defined direction of the H-Bond network within the contour plot. The DL does not hence exist at isoelectric surfaces. When all three descriptors are different from the reference in bulk water, one is thus in presence of the BIL layer(s).

All these descriptors have been validated in refs. [241, 242] and the methodology is directly applied in the following at the (110)- $\text{Co}_3\text{O}_4$  cobalt oxide-liquid water interfaces. Furthermore, the BIL and DL water layers are the only two ones being vibrationally SFG (Sum Frequency Generation) active at any interface, before probing bulk liquid water which is SFG inactive [241, 242]. One

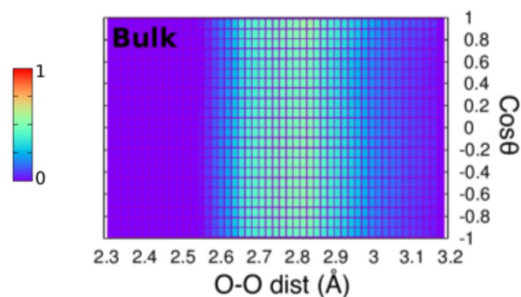


Figure 5.14: 3D-plots of the H-Bond patterns formed on bulk water, calculated from DFT-MD and FF-MD simulations performed in ref. [276]. The x-axis represents the O–O distance (Å) between 2 H-Bonded water molecules and the y-axis provides the angle (cosine value) between the O–O vector (from donor to acceptor) and the normal to the surface (oriented from liquid to vapour phase). The colors represent the probability ( $P$ ) to find one O–H group forming one HB with a given distance and orientation. The probability increases from blue to red.

supplementary proof that the DL is indeed bulk liquid water reoriented by the surface field has been given in ref. [241] where the third order non-linear susceptibility  $\chi_{bulk}^{(3)}(\omega)$  has been extracted from the DL and has been shown identical to the one that is calculated [241] in liquid water subjected to a constant external electric field (that, by construction, reorients the HB network within the liquid water), and also found identical to the measured one. [281]

Let us start by commenting the first descriptor used in the characterization of the three water layers, i.e. the water density profiles at the A- and B-terminations of the  $\text{Co}_3\text{O}_4$  cobalt oxide in contact with liquid water, see the top of fig. 5.15. The density profiles are reported over half of the water box only, the zero in  $r$  is the instantaneous water surface,  $r$  measures the (vertical) distance from the surface (see fig. 5.11 for the simulation boxes). One can observe four layers of water at both interfaces, labelled L0-L3, each of these layers being roughly identically located in space at the two interfaces. While layer L0 systematically has a higher density than in the bulk (e.g.  $\sim 1.5$  higher at the aqueous B-surface), the density of bulk water is on average already recovered in L1-L3 layers.

The oscillations in the density profile around the average bulk value are discussed later in this section, also in relation with the mobility of the water molecules in the different layers.

In the density profiles at the top of fig. 5.15, we have also reported the notation into BIL and DL water layers on top of the notation into L0-L3 layers. Applying the definitions described above for the three descriptors of water, L1-L3 water layers constitute the DL Diffuse Layer (roughly 6 Å thick) at both aqueous A- and B-interfaces. In these layers, the water density is roughly the liquid water’s 1 g/cm<sup>3</sup>, and the water molecules make 3.6 HBs/molecule, equal to bulk liquid water (as obtained from the reference DFT-PBE-D2 MD simulation done in this work on bulk water), which are two necessary descriptor

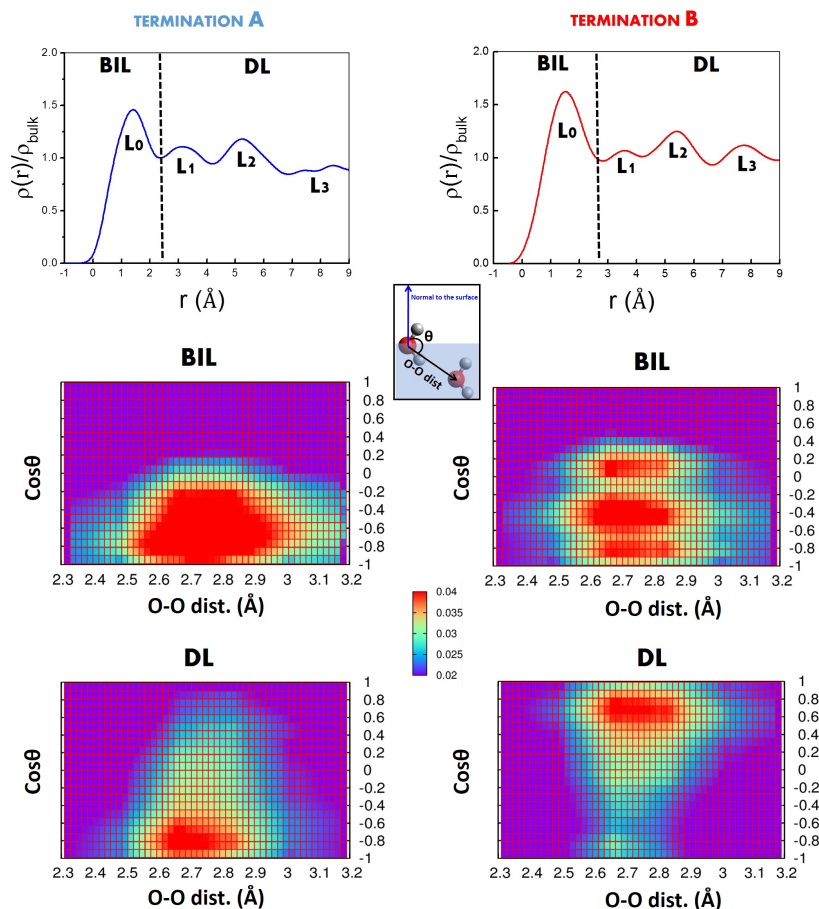


Figure 5.15: *Top: Water density profiles calculated as a function of the distance from the cobalt oxide surface (using Willard & Chandler’s instantaneous surface method [283]). Middle & Bottom: 3D-contour plots of the simultaneous probability for water-water H-Bonds to have a given distance (horizontal axis) and given angle (vertical axis). The convention for the O-O distance and angle  $\theta$  definitions is in the insert scheme. The normal to the surface goes towards the solid. The middle plots are for the water located in the BIL (Binding Interfacial Layer), the bottom plots are for the water located in the DL (Diffuse Layer). See text for correspondence between layers L0-L3 and BIL/DL. See ref. [241] (fig.2) for the reference 3D plot for bulk liquid water (homogeneous distribution of HB angles within the 2.6-2.9 Å HB distances). Left side: (110)- $\text{Co}_3\text{O}_4$ -A cut-liquid water interface, Right side: (110)- $\text{Co}_3\text{O}_4$ -B cut-liquid water interface.*

values for the DL. The other descriptor necessary to reveal the DL is the non-isotropy of the water-water HB network in layers L1-L3, which is shown averaged over all the three L1-L3 layers at the bottom of fig. 5.15 with the 3D-contour plots. One can indeed observe in these plots that there is a certain background of homogeneous distribution of the HB orientations within the 2.6-2.9 Å HB distances that is revealed by the green-blue-ish color, which is reminiscent of bulk liquid water, while the red contour spots reveal a preferred orientation of the HB network in these layers. This corresponds to the HB

network of the liquid water that adapts to the surface field: it is not present in bulk liquid water and it only appears once a field induces a certain direction in the liquid. One hence observes that this preferred orientation of the water in the DL HB network at the aqueous A-surface is on average opposite the positively charged surface (cosine values of the  $\theta$  angle is in the range -0.6/-0.9, see the red spot, for HB distances in between 2.6-2.9 Å), while an opposite net orientation of the water molecules now pointing towards the solid surface is obtained in the DL at the aqueous negatively charged B-surface (red spot for cosine values of the  $\theta$  angle in the range 0.6/1.0 for HB distances in between 2.6-2.9 Å). Our simulation boxes are too small in the vertical direction to see bulk water appear beyond the DL.

Layer L0 at both A- and B-interfaces is the BIL water layer, where all three descriptors differ significantly from bulk liquid water, for the water density (much higher than 1.0), for the number of HBs formed per water molecule (3.4 HBs/mol in the BIL *vs* 3.6 in the bulk), and for the orientation of the HB network, see fig. 5.15 (middle panels). In these contour plots, one can observe that there is no background of homogeneous HB orientations but there is, on the contrary, one single orientation of the HBs, revealing specific hydrogen bonds in between the water molecules (and indirectly possibly revealing HBs between water and the solid surface).

There is one clear single orientation for water-water HBs in the BIL at the aqueous A-surface, with cosine values in the range -0.2/-1.0 for 2.6-2.9 Å HBs distances: the water molecules in the BIL preferentially form water-water HBs with water in the next layer (BIL-DL HBs). There are however two orientations of water-water HBs in the BIL at the aqueous B-surface, as one can distinguish two separate red spots: as already observed at the aqueous A-surface, the red spot at  $\sim$ -0.4/-1.0 cosines corresponds to BIL-DL HBs, while the second one at  $\sim$ +0.0/+0.2 cosines arises from INTRA-BIL HBs (formed between two water molecules in the BIL).

The 3.4 coordination of the water molecules in the BIL is the result of both water-solid and water-water HBs. It is interesting to note that despite both interfaces have a final identical value of this coordination number, the repartition into water-solid HBs and water-water HBs is different at the two interfaces. Hence, there are slightly more water-solid HBs and slightly less water-water HBs that are formed at the more hydrophilic aqueous A-surface compared to the aqueous B-surface (see numbers in the table in figure 5.12). Indeed at the A-liquid water interface, 100% of the water molecules in the BIL are H-Bonded to the solid  $\mu_2$ -OH sites (with also two waters bridging two nearby solid  $\mu_2$ -OH sites, hence being simultaneously HB-acceptor and HB-donor). The percentage decreases at the B-liquid water interface, where 'only' 89% of the water molecules in the BIL are H-Bonded to solid O-H sites ( $\mu_1$ -OH &  $\mu_1$ -OH<sub>2</sub> sites): the decrease in water-solid HBs is compensated by an increase in water-water HBs formed within the BIL, denoted INTRA-BIL HBs in the table in figure 5.12.

Interestingly, water is on average found HB-acceptor with the oxide solid at the B-interface (57% of the water-solid HBs) despite the negatively charged

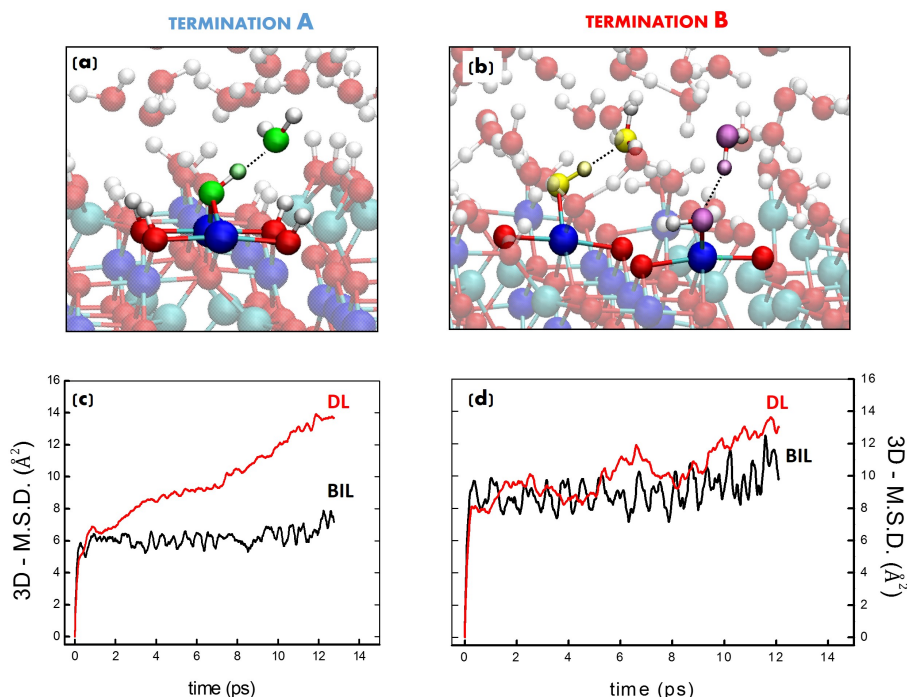


Figure 5.16: (a) and (b) Zooming views of the surface-water HB patterns at the aqueous A-surface (a) and B-surface (b).  $\mu_2$ -OH-water Hbond in green color where  $\mu_2$ -OH acts as a donor at the A-surface.  $\mu_1$ -OH-water Hbond where  $\mu_1$ -OH acts either as a donor (yellow) or as an acceptor (violet) at the aqueous B-surface. (c) and (d): 3-dimensional mean square displacement of BIL-water (black lines) and DL-water (red lines), computed for the aqueous A-surface (c) and B-surface (d).

surface: this reveals that HBs (that we could call 'microscopic interactions') dominate over ('macroscopic') electrostatic interactions. For a negatively charged surface such as the B-termination, one would indeed expect the water molecules located in the BIL to be strongly oriented in response to the surface charge and hence have their dipole moments pointing towards the solid surface, thus being mostly HB-donors to the solid. This would correspond to water being 'good soldiers' as they readily respond to the average surface charge 'driving force'. Water is on the contrary found to be mostly HB-acceptor with the solid, with an orientation of their dipole moments thus found opposite the field generated by the negative surface charge. The water molecules are hence somehow 'undisciplined' and do not respond to the average electrostatic driving force at the direct interface with the solid.

The 'electrostatic undiscipline' stems in the surface chemistry, where the O-H groups are readily available for hydrogen bonds with water molecules approaching the surface. BIL-water hence engage in surface-water HBs that in turn counteract the interactions from the surface electric field. It would certainly be interesting to deconvolve the energetics of the competing interactions (HBs *vs* electrostatic) in order to rationalize more, but this has not been done here. This illustrates the importance of explicit bulk water in simulations of

aqueous solid oxide-water interfaces. An implicit solvent would obviously not provide such a view. A direct consequence of the preferred solid-water HBs over the electrostatic surface-water interactions is of course the organisation of water in the BIL and the associated dielectric constant in the BIL, that again could not be anticipated with implicit solvent. Also, the preference for the oxide-water HBs found here in the BIL at the aqueous B-interface gives a qualitative indication of the underlying acidities of the surface sites. One more remark is that the necessary balance made in between HBs and electrostatic interactions at the interface probably also explains the dynamicity in proton transfers observed at this surface (see below). All these properties will have consequences on the chemical reactivity at this cobalt oxide interface. At the aqueous A-interface, water in the BIL is now found HB-acceptor with the solid (88% of the HBs), which this time goes in line with the positively charged surface. Simplified views of the typical solid-water HB patterns obtained at the aqueous A- and B-surfaces can be found in figure 5.16-a,b.

The oscillations observed earlier in this text in Fig. 5.15 in the water density profile for the layers beyond L0, could very well be due to the finite and limited simulation box-size and time-scale, as already shown for the air-water interface when comparing ab initio and classical MD simulations density profiles [276]. Such oscillations could also be the result of different mobility character of the water in the BIL and DL layers: the 'rather high structuration' of BIL-water in contact with the oxide could indeed induce heterogeneous diffusivity of the water when comparing BIL and DL, which in turn could prevent the establishment of a homogeneous water density beyond the BIL. As shown above, both A and B surfaces are hydrophilic with a high density of water-solid HBs (figure 5.12 and fig. 5.16-a,b for simplified illustrations of the HBs patterns at the two interfaces). These strong water-solid interactions can lead (not so surprisingly) to a reduced mobility of BIL-water molecules as shown in fig. 5.16-c,d, where we report the mean square displacement of the water molecules located in the BIL and in the DL for the aqueous A- and B-interfaces (mean square displacement (MSD) plots obtained as averages over all molecules identified in BIL/DL layers). A word of caution is however needed. Although well-converged diffusion coefficients would require much longer time-scale trajectories than the ones analyzed here, comparing the mobility of the water in the BIL and DL layers through the MSD gives us sufficient insights on their respective diffusivity.

As shown above, there are more solid-water HBs at the aqueous A-termination than at the B-termination, hence resulting into BIL-water being in a more 'static' geometrical arrangement at the A-termination. Water diffusivity is therefore reduced in the BIL as can be seen in figure 5.16-c, where a reduction factor of  $\sim 2$  is found in the mobility of water in the BIL when compared to the DL. Conversely, BIL-water and DL-water have the same diffusivity character at the aqueous B-termination, as shown in fig. 5.16-d, which goes nicely in line with less solid-water HBs being formed at this interface. While it is very interesting to see these differences in the water diffusivity at the two interfaces, this does not seem to provide the sole explanation for the density

profile oscillations, as both profiles display similar oscillations in the DL.

One final important remark. At the two interfaces simulated here, bulk liquid water is never recovered within the  $\sim 18$  Å water thickness. This is not totally surprising as the water in the simulation boxes experiences two interfaces, one with the solid (which has a large surface charge and therefore reorients the water molecules over a large distance, see the  $\sim 6$  Å of the DL revealed here), and one with the neutral air (that the group has fully characterized in a previous work [268] with a 2D-HBond network within the 3.0 Å thickness of the BIL). Note also that the  $\sim 6$  Å thickness of the DL characterized here is presumably underestimated as the liquid water has not been recovered in the box. This is however not an issue for the work done here and for the properties investigated hereby.

## 5.6 Physical observables: electric field, surface work function & SFG vibrational spectroscopy at the interface

Figure 5.17 shows on the left panel the electric field profile (see section 8.2 for the computational details) as a function of the  $z$ -coordinate perpendicular to the (110) bulk oxide surface, comparing the bare A-surface at the interface with vacuum (profile at the top) to the hydroxylated A-surface at the interface with vacuum (profile in the middle) and to the A-liquid water interfacial system (profile at the bottom). These profiles have been calculated extracting many configurations from the DFT-MD simulation and then averaging them, at finite temperature. The first significant peaks in the electric field profile are observed at the height of the surface in contact with the air at the bare surface, with a negative peak located just below the surface layer and a more intense positive peak located at the surface layer. These are sharp and highly localised peaks in the electric field profile. Note that positive/negative fields are the ones taken at the surface at  $z \sim -10$  Å in fig. 5.17, i.e. at the surface that will be put in contact with liquid water. The fields have opposite signs at the second interface ( $z \sim -23$  Å) only because the calculation uses the same convention of direction for the normal to the two surfaces. Once the A-surface has been hydroxylated and is now covered with one water monolayer, one can observe a systematic decrease in intensity of the two peaks in the electric field profile, while the peaks are still rather well localised in space. However, the negative peak penetrates slightly deeper into the bulk oxide, while the initial single positive peak obtained at the bare interface is now divided into two parts with a total larger spreading in the  $z$ -direction into the vacuum. These two oscillations in the field profile at the interface are respectively due to the oxide surface layer and to the adsorbed water layer. The lower intensities of the electric field at the hydroxylated surface are due to screening of the oxide surface field by the water molecules in the adsorbed monolayer. One can also see that  $\sim 3$  Å away from the water monolayer the field is screened, i.e. the underlying surface structure is not visible anymore in the field profile. Once

the hydroxylated surface is in contact with liquid water, the field intensity is screened even more while the region of the field decay is expanded farther away from the surface in the  $z$ -direction perpendicular to the surface. A zero-field is found around 5 Å above the adsorbed water monolayer. Note also that the negative peak inside the oxide just below the cobalt surface is almost non-existent. Similar results are obtained at the (110) B-surface (not presented).

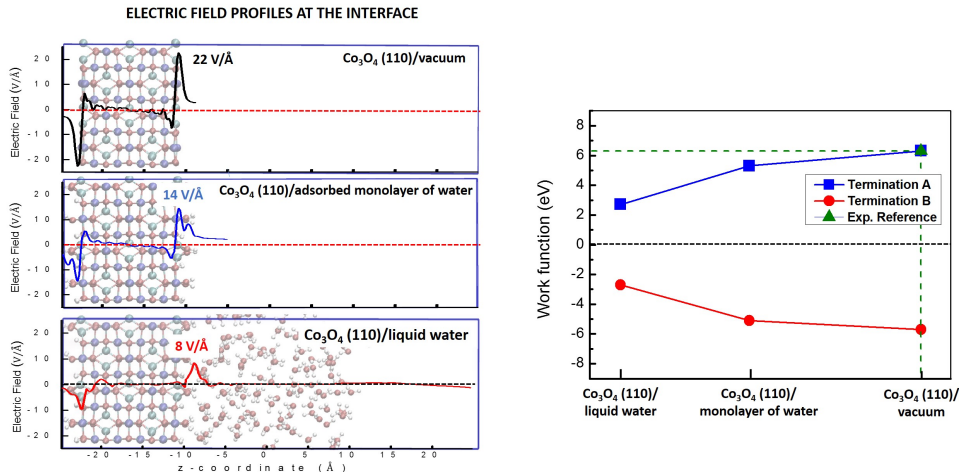


Figure 5.17: *Left side: Electric field profiles for the A-surface. Top: bare A-surface at the interface with vacuum; Middle: hydroxylated A-surface at the interface with vacuum; Bottom: hydroxylated A-surface at the interface with liquid water. Profiles are reported along the  $z$ -direction perpendicular to the (100)  $\text{Co}_3\text{O}_4$  surface. The profile at the bottom for the aqueous interface has been averaged over 35 snapshots statistically extracted from 17 ps dynamics. Right side: Calculated surface work function (eV) reported for the (100)  $\text{Co}_3\text{O}_4$  A- and B-surfaces as a function of the simulation type, i.e. bare surfaces at the interface with vacuum, hydroxylated surfaces at the interface with vacuum, hydroxylated surfaces at the interface with liquid water. The green triangle in the graph is the reference experimental value equal to 6.3 eV from XPS and UPS experimental techniques [284].*

The changes in the intensity of the electric field profile discussed above once a water monolayer and liquid water is added to the bare surface are also directly reflected in the surface work function. The surface work function (see section 8.2 for computational details) is calculated at the (110)  $\text{Co}_3\text{O}_4$  A- and B-terminated surfaces in the three environments investigated here, i.e. bare surfaces at the interface with vacuum, hydroxylated surfaces at the interface with vacuum, hydroxylated surfaces at the interface with liquid water. The value computed here for the bare A-surface at the interface with vacuum compares extremely well with the experimental values from XPS-UPS experiments [284]. The sign of the work function changes from the A-surface to the B-surface, because of the opposite surface charges. When the adsorbed water monolayer is added to the surface, the work function already shows a decrease by around 1 eV, similar at both interfaces. Such decrease has been discussed in the literature [258, 285], and the change obtained here is very similar to this

literature. This decrease is further enhanced when bulk water is in contact with the surface, and one obtains work functions of  $\sim 3$  (-3) eV instead of the  $\sim 6$  (-6) eV at the bare surface. The work needed to remove one electron from the aqueous surface is therefore roughly divided by 2 from the bare surface in contact with the air.

We now turn to a vibrational probe of the interface in terms of non-linear SFG (Sum Frequency Generation) spectroscopy. Details for extracting this complex signal from the DFT-MD simulations have been given in section 8.2. See previous works from the group on theoretical SFG calculation and interpretation [241, 242, 268, 240, 282]. The SFG signals discussed here are calculated for the water, they do not include the solid contribution. Although the cobalt oxide-liquid water interfaces have not yet been spectroscopically characterized by SFG, we provide here theoretical signals that could of course be compared to experiments when they will become available, but our objective here is to show the information contained in the interfacial spectroscopy and how to possibly use these information in the context of chemical reactions that could occur at the interface once put under electrochemical conditions. The signals are discussed in terms of  $\text{Im}\chi^{(2)}(\omega)$  only, as in phase-resolved SFG experiments. The theoretical signal is divided in terms of BIL-SFG signal and DL-SFG signal, i.e. each of these interfacial layers contain distinct information on the organisation of interfacial water that the theory can easily reveal once the two layers are identified, as done in this work in section 5.5.

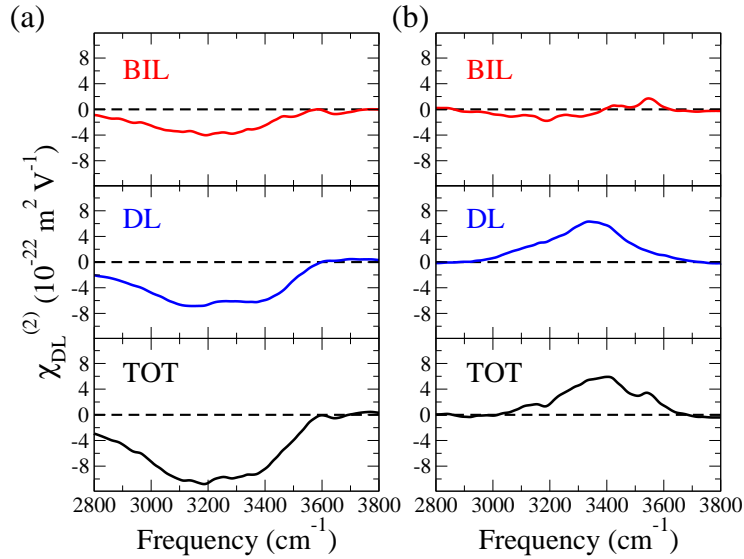


Figure 5.18: Calculated  $\text{Im}\chi^{(2)}(\omega)$  spectra for the (a) (110)  $\text{Co}_3\text{O}_4$ -A-liquid water interface, for the (b) (110)  $\text{Co}_3\text{O}_4$ -B-liquid water interface. Calculated SFG report the water contribution only. The SFG signal is presented as 'total' (TOT) in black, BIL-SFG in red arising from the BIL layer only, DL-SFG in blue arising from the DL layer only.

Figure 5.18 reports  $\text{Im}\chi^{(2)}(\omega)$  spectra calculated for the (110)  $\text{Co}_3\text{O}_4$ -A(left)-/B(right)-liquid water interfaces, the total active SFG spectra (BIL+SFG) are

displayed at the bottom in black, and the decomposition into BIL-SFG and DL-SFG are displayed top and middle of the figures, respectively in red and blue.

The first conclusion that can be extracted from these theoretical spectra is that for both interfaces the SFG spectroscopic response is dominated by the DL third-order contribution:  $I_{DL}/I_{BIL} \sim 4$  for both interfaces, where  $I$  stands for the integral of the  $\text{Im}\chi^{(2)}(\omega)$  signal in the 2800-3800  $\text{cm}^{-1}$  range presented here. The total SFG signals thus directly reflect the signals arising from the water in the DL. The DL-SFG (and thus the total-SFG) signals change sign in between the two interfaces, i.e. from negative at the aqueous A-interface to positive at the aqueous B-interface. As the DL-SFG is proportional to the surface potential [241, 242], the DL-SFG signal directly provides this information.

The BIL signal, despite being a minor contributor to the total SFG response, carries however the information on the structure of water in direct contact with the solid oxide, and therefore directly probes the water-oxide interactions. For the aqueous A-surface, the BIL-SFG has one single negative broad band: this is due to the water molecules located in the BIL being HB donors to the water molecules located in the DL. The water molecules at the aqueous A-surface indeed mostly accept HBs from the solid (section 5.5 and table in figure 5.12) and consequently are oriented such as donating HBs to the water molecules located in the DL. We remind the reader that the BIL is one water monolayer thick. On the contrary, water can be both donor and acceptor of water-solid HBs at the aqueous B-interface, which hence results into the two bands of opposite sign in the BIL-SFG (although of very low absolute amplitudes). The positive band at higher frequencies is due to the weak HB donors to the solid, while the negative broad band (very similar to the aqueous A-surface) is due to the stronger HBs made by the water molecules located in the BIL as HB donors to water molecules located in the DL. The overall less intense SFG-BIL signal at the aqueous B-surface (compared to the aqueous A-surface) is due to the higher number of INTRA-BIL HBs formed at aqueous B-surface, that are SFG-inactive due to their in-plane orientation.

As a final note, it is interestingly also to remark that the DL-SFG absolute intensity is different between the two interfaces, despite the same formal surface charge (same  $4.37 | e | / \text{nm}^2$  in absolute value at both interfaces). Indeed  $I_{DL}$  (as calculated from integration in the 2800-3600  $\text{cm}^{-1}$  region) is 1.4 times higher for the aqueous A-surface than for the B-one. This higher DL-SFG intensity at the aqueous A-interface tells us that there is a higher surface potential at the aqueous A-interface than at the B-one (see ref. [242] for the relationship between DL-SFG intensity and surface potential). This is due to the specific water organization in the BIL (as discussed in the previous section) and specific orientation of surface O-H terminations (see histograms in figure 5.12) at the aqueous A-surface. The surface field does not reflect only the formal surface charge but also the specific organization and orientation of the water molecules in the BIL, which then modulate the field. This again shows how important it is to include explicit water at the interface with the oxide surface in the simulations.

## 5.7 Discussion and perspectives

In this chapter 5, we here provided chemical and physical knowledge of the (110)- $\text{Co}_3\text{O}_4$ -liquid water interface as a preliminary step into the modelling of this interface in the electrochemical conditions of the OER (Oxygen Evolution Reaction) for the electrocatalysis of water. To that end, DFT-based molecular dynamics have been applied at this rather complex oxide interface, explicitly taking into account the liquid water conditions. This work provides the reference knowledge in the interfacial electronic, structural, dynamical, electric and spectroscopic properties needed at this promising interface for the water electrocatalysis. We also described and applied the necessary computational analyses tools for the characterisation of the interfacial water structure (in the BIL layer directly in contact with the oxide surface and in the DL layer at slightly larger distance from the surface), thickness of these layers, rigidity and/or dynamicity of the water in these layers (typically for proton transfers), for the structure of the solid surface in contact with water (e.g. in terms of orientation of the surface sites, their H-Bonding network within the solid and with the water in the BIL), for the electronic interfacial properties, for physical interfacial properties typically in terms of the interfacial electric field and its penetration into the liquid water, the work function, and the vibrational spectroscopy probe of this interface here in the flavor of SFG Sum Frequency Generation. The same modelling could be applied to other facets of the  $\text{Co}_3\text{O}_4$  cobalt oxide in contact with liquid water, also of potential relevance for the OER.

This is the preliminary step into investigating the semiconductor  $\text{Co}_3\text{O}_4$ -water interface in electrochemical conditions and assess its chemical reactivity in the context of the water electrocatalysis. For the electrochemical conditions to be more realistic into the DFT-MD simulations, one has however to include electrolytes and pH conditions. While inclusion of interfacial electrolytes poses no real challenge in DFT-MD simulations, see e.g. some previous works of ours and others at mineral-liquid water interfaces [244, 241, 242, 286, 287], one has however to keep in mind that the lower (nominal bulk liquid) electrolyte concentrations that can reasonably be sustained in DFT-MD are of the order 0.1-0.5 M, for computational reasons due to the simulation box dimensions. This potentially low electrolyte nominal bulk concentration does not preclude a higher electrolyte concentration in the BIL (i.e. in the layer at the direct contact with the oxide surface): depending on the ability of the oxide surface to attract and accommodate the electrolytes in the BIL, larger electrolyte concentrations in the BIL can be obtained, see for instance work from the group in ref. [242] for a related discussion at mineral-water interfaces and the actual measure of the electrolyte concentration at the direct interface. One has also to be aware that in a realistic 'in operando' interface, the BIL accommodates counterions present in the electrolyte, which in turn screen the surface charge, giving rise to the electric double layer. This will certainly have influence on the oxide-water BIL interface, both from structural and dynamical points of view, as well as on the thickness of the subsequent DL. These changes could

then be measured and extracted from the SFG responses of the two layers, following the decomposition and interpretation done in the present work. On the other hand, pH conditions can be monitored through the electrolyte concentration as well as protonation and deprotonation states of the solid surface, although pH is not a trivial quantity to accurately represent within the small DFT-MD simulation boxes. The same analyses tools as the ones described in this work can then be applied in order to extract the fundamental knowledge of e.g. the localisation of the electrolytes within the BIL and DL, the water structure and dynamics in the BIL and DL, dynamical charge transfers between surface and the EDL and within the water layers, the interfacial electric fields and screening by the electrolytes, the work function, the interfacial vibrational spectroscopy. These properties can be compared and put in perspective to the ones obtained at the reference oxide-liquid water interface investigated in this chapter. Any chemical reactivity occurring at the electrolytic aqueous oxide surface, e.g. desorption of water, deprotonation, proton transfers, inner-/outer-sphere adsorption of electrolytes, adsorption of new chemical species, etc, can be followed along the DFT-MD trajectories, providing these are chemical reactive events compatible with the 10<sup>1</sup>-100 ps time-scale of the DFT-MD simulations. Biased DFT-MD can also be run for the chemical reactions to be monitored. Also worth mentioning here, our investigations (as well as most in the literature) take the ideal crystalline structure of the oxide material (Co<sub>3</sub>O<sub>4</sub>) into account in the DFT-MD simulation. Surface defects are probably relevant for the chemical reactivity of these interfaces and should also be included within the modelling.

Imposing the electrochemical applied voltage into the DFT-MD is a more challenging theoretical affair, and only few attempts at developing adequate theoretical methodologies have been presented in the literature [236, 237, 238, 239, 232], without final convergence over the methodology to be applied. Studies of bulk water and of water solutions [288, 289, 290, 291] have shown the ability of a constant external electric field to induce reorientation of the water dipoles along the field direction and an increase in the water dissociation rate. Though such strategy nicely shows that water dissociation can be controlled by constant fields, this is still not simulating electrochemical conditions. One can then rely on more *ad hoc* theoretical ways to include this voltage, following previous attempts in the literature, see for instance refs. [232, 235, 233], playing with H<sub>3</sub>O<sup>+</sup>/OH<sup>-</sup> concentrations and/or electrolyte concentrations in relation with the interfacial capacitance.

We are interested in the OER chemical reaction at such oxide-liquid water electrochemical interface, with the goal of characterizing the mechanisms and the energetics of the underlying chemical reactions. The water oxidation reaction is known to proceed through two general pathways (see e.g. ref [183] for a recent review) known as the water nucleophilic attack (WNA) and the radical oxo coupling (ROC), with the WNA presumably the one occurring at oxide interfaces. Although these reactions are known, their energetics and the actual detailed mechanisms are still unclear, and the role of the whole complex structure and dynamics of the oxide-water-electrolyte-EDL interface has not

been yet elucidated at the atomistic level.

We address some of these questions in the following chapter. In the following chapter, biased metadynamics DFT-MD will be performed in order to assess the chemical processes/mechanisms that can lead to the OER/water splitting at the (110)- $C_3O_4$ /liquid water interfaces as well as measure the associated OER overpotential.



## Chapter 6

# OER at the aqueous (110)- $\text{Co}_3\text{O}_4$ oxide by metadynamics DFT-MD

Chapter 5 has allowed us to fully characterize the (electrode) cobalt oxide (110)- $\text{Co}_3\text{O}_4$ /liquid water interface, both in terms of structures of the solid surface and water in the BIL at the direct interface with the oxide, but also in terms of physical characterizations like diffusion and electrostatic fields at the surface.

With this in hands, we are now in the position to identify how this liquid environment can play roles into the chemistry of the oxygen evolution reaction (OER) at the interface with the (110)- $\text{Co}_3\text{O}_4$  cobalt oxide. We now address such aspects by presenting in this chapter a computational study based on biased DFT-MD simulations of the OER at the (110)- $\text{Co}_3\text{O}_4$ /water interface. To perform DFT simulations in "realistic operando OER conditions" would mean to impose electrochemical voltage at the anode electrode (here, the cobalt oxide) into the DFT-MD, which is still nowadays a very tricky theoretical subject with no clear converged method to be applied [292, 293, 294, 295, 296, 297]. One of the most reliable methods to gain information about a chemical reaction is however the DFT-MD metadynamics, an energetically biased DFT dynamics that will force the chemical reaction to occur/proceed and from which we gain the knowledge of reaction mechanisms and energetics. Accordingly, in this chapter we couple the DFT-MD simulations with a state-of-the-art metadynamics approach able to probe the configurational space and, simultaneously, to reconstruct the underlying free-energy landscape of the OER process [33, 34, 35] through a partially unbiased exploration of both gas-phase and aqueous-phase OER chemical reactions (see section 2.9 for metadynamics details).

The advantages in performing metadynamics investigations instead of a tricky voltage imposed into the DFT-MD are:

- 1) we gain a detailed knowledge on the OER energetics through the reconstruction of the free-energy landscape of the OER process and hence we can know the thermodynamics behind the OER. This is not possible to be so accurate by imposing a voltage into the DFT-MD;

2) we gain a detailed knowledge on the possible OER chemical pathways (*i.e.* the reaction networks) through the novel partially unbiased exploration of the phase space used here (and described in section 2.9.2), and hence we can know the kinetics involved in the OER process. This is again not possible in such details when imposing a voltage into the DFT-MD: one can not have information on the possible or alternative (not predefined) OER pathways.

The biased metadynamics proposed here for the OER chemistry are done both at the oxide-air and oxide-liquid water interfaces, in order not only to evaluate the influence of the liquid water into the OER process and energetics, but also in order to have a reference (*i.e.* the oxide-air interface) that can be compared to the traditional "surface science calculations" of the literature.

As already pointed out a few times in this thesis, our biased metadynamics are performed at zero-voltage on the oxide anode electrode and also without the presence of supported electrolytes. Our results are therefore relevant for these conditions, which are not exactly the ones from the experiments. This is however, at least we believe, as good as the current works from the literature: 1) we indeed include the surrounding water in a "proper way", not done yet in the literature; 2) no calculations on OER have included supported electrolytes either; 3) Selloni's and Norskov's static calculations that included the electrode potential are done in an empirical and indirect way, on solid-air interfaces. The atomistic modifications on the electrode structure as well as on the interfacial water are never taken into account into these modeling.

We therefore trust that the mechanistic processes and associated energetics that we measure in our metadynamics provide a very good first attempt at providing upper limits for the OER. In particular, we suggest a novel reaction route for the multiple-step OER and show how the free-energy landscapes of the OER are deeply dependent on the phase (gas or water) where the reaction occurs. Finally, we identify the catalytic sites associated with the minimum energy pathway which is crucial for a rational design of  $\text{Co}_3\text{O}_4$  catalysts.

## 6.1 Computational methods and application to the OER at the $\text{Co}_3\text{O}_4$ /liquid water interface

Unrestricted open-shell *ab initio*/Density Functional Theory (DFT)-based molecular dynamics (MD) simulations (*i.e.*, spin-polarized DFT-MD/spin-polarized AIMD) coupled with a newly developed metadynamics (MetD) technique within a novel path-Collective Variables (path-CV) enhanced sampling framework [33, 34, 35] (see section 2.9 for all details) have been performed on the two A/B (110)- $\text{Co}_3\text{O}_4$  crystalline surfaces and on their associated (110)- $\text{Co}_3\text{O}_4$ /liquid water interfaces described in chapter 5. We have adopted the computational setup described in section 8.2 (and employed in our recent paper [254]) where we studied the bulk crystal properties of  $\text{Co}_3\text{O}_4$  and the (110)-

Co<sub>3</sub>O<sub>4</sub>/liquid water interfaces.

In a nutshell, all simulations have been performed in the Born-Oppenheimer framework through the CP2K package [255, 256]. The Perdew-Burke-Ernzherof (PBE) [257] functional, which has been shown to be a good descriptor of the properties of this oxide – of most oxides as well – and of liquid water in previous works [58, 254, 258, 259], has been employed in combination with mixed Gaussian-Plane-Waves basis sets and Goedecker-Teter-Hutter (GTH) pseudopotentials. [260] The DZVP-MOLOPT-SR basis set, augmented with a 400 Ry plane-wave basis set, have been used as a good compromise between the computational cost and accuracy. The PBE functional has been supplemented with the Hubbard (U) term [261, 262] in order to circumvent the over-delocalization of 3*d*-electrons in metal oxides and the consequent underestimation of the band gap. A value of 5.9 eV for the U parameter has been used, as proposed by Selloni *et al.* [58]. Dispersion interactions – especially relevant for liquid water – have been taken into account *via* the Grimme D2 correction [298, 299]. Default algorithms and convergence criteria in CP2K have been adopted. Periodic boundary conditions (PBC) have been applied in all three cartesian spatial directions. We remind the reader (see section 5.3) that a vacuum of 16.5 Å is applied on top of the water in the simulation box in order to avoid the too much compression of liquid water in the vertical *z*-direction and its PBCs, see Fig 6.2. During the Born-Oppenheimer MD, the electronic wavefunction has been calculated at each time-step whilst the classical nuclei displacements have been simulated through the velocity Verlet algorithm with a time-step of 0.4 fs. All details are in chapter 2.

We remind the reader that Co<sub>3</sub>O<sub>4</sub> crystallizes in a face-centered cubic (FCC) unit cell known as “spinel structure” (Figure 6.1-a), independently determined by Bragg [265] and Nishikawa [266] (see section 5.2).

The conventional “spinel” cubic unit cell (*Fd3m* symmetry space group) contains 8 Co<sup>2+</sup>, 16 Co<sup>3+</sup> and 32 O<sup>2-</sup>, accounting for a total of 56 atoms (Figure 6.1-a) arranged in a FCC box with an experimentally determined lattice parameter equal to 8.08 Å [265, 266, 58]). Since all the DFT-MD simulations have been performed at the  $\Gamma$  point of the Brillouin zone, the use of a supercell (*i.e.*, a certain number of replicas of the unit cell in the 3D space) was needed. See chapter 5 for all details in setting up and validating this supercell properly. It consists in 4-replicas of the unit cell in the *x* and *y* directions. For all simulations of the cobalt oxide at the interface with the vacuum or with liquid water, the electronic multiplicity of the system accounts for the number of the open-shell Co<sup>2+</sup> atoms in the simulation box (open-shell DFT-MD simulations).

Since PBC were applied along all spatial directions, when simulating the (110)-A/B-air interface (see chapter 5 for the A and B terminations described in details), a vacuum slab of 16.5 Å along the *z* direction (*i.e.*, perpendicular to the surface) has been included in the simulation box to separate the periodic replicas. We remind again that when the bulk solid is cut along the (110) crystallographic plane, as illustrated in Figure 6.1-b, two possible terminations can be obtained (Figure 6.1-c-d), labelled as A- and B-terminations hereafter,

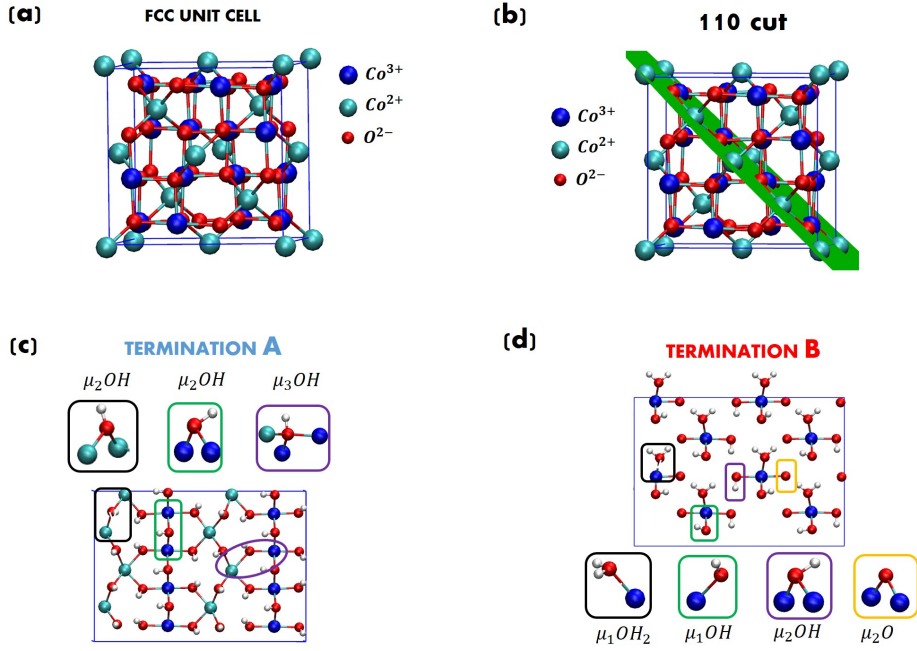


Figure 6.1: (a) FCC unit cell of bulk  $\text{Co}_3\text{O}_4$ : 56 atoms, 8  $\text{Co}^{2+}$ , 16  $\text{Co}^{3+}$ , 32  $\text{O}^{2-}$ . (b) FCC unit cell of  $\text{Co}_3\text{O}_4$  cut along the (110) crystallographic plane (green). (c) and (d) Composition and speciation of the A- and B-surfaces after surface hydroxylation and geometry optimizations (identical to ref.[278]), see chapter 5. Top views. Oxygen atoms are in red, hydrogens in white,  $\text{Co}^{2+}$  in light blue, and  $\text{Co}^{3+}$  in dark blue.

similarly to ref. [58] (see chapter 5). The cationic A-termination surface exposes 8  $\text{Co}^{3+}$ , 8  $\text{Co}^{2+}$  and 16  $\text{O}^{2-}$  in the 4-replicas supercell box (2  $\text{Co}^{3+}$ , 2  $\text{Co}^{2+}$  and 4  $\text{O}^{2-}$  per unit cell surface) [254], with a formal surface charge of  $4.37 |e|/\text{nm}^2$  ( $+8 |e|$ ) in the 4-replicas box. By contrast, the anionic B-surface exposes 8  $\text{Co}^{3+}$  and 16  $\text{O}^{2-}$  in the adopted 4-replicas supercell box (2  $\text{Co}^{3+}$  and 4  $\text{O}^{2-}$  in the unit cell), with a formal surface charge of  $-4.37 |e|/\text{nm}^2$  ( $-8 |e|$ ) in the 4-replicas box. Interestingly, only  $\text{Co}^{3+}$  sites are present at the B surface, while both  $\text{Co}^{3+}$  and  $\text{Co}^{2+}$  sites are available at the A surface.

As already seen in section 5.3, once in contact with water, both terminations adsorb water molecules. In particular, the A-surface is composed of a total of 16 dissociated water molecules (4 water molecules if one considers the unit cell only) and there are no intact adsorbed water molecules: this results in 16  $\mu_2\text{-OH}$  exposed at the top surface sites (Fig. 6.1-c) systematically bridging two identical cobalt atoms (either  $\text{Co}^{2+}$  or  $\text{Co}^{3+}$ ), 16  $\mu_3\text{-OH}$  inner sites, the initial bulk  $\mu_3\text{-O}$  sites receiving the dissociated water proton. On the other hand, the B-surface is composed of a total of 16 water molecules (4 water molecules if one considers the unit cell only), 8 being dissociated and 8 being intact. This gives rise to the B-surface speciation, shown in Fig. 6.1-d, and having 8  $\mu_1\text{-OH}_2$  exposed sites, 8  $\mu_1\text{-OH}$  exposed sites, 8  $\mu_2\text{-OH}$  inner sites (the inner  $\mu_2\text{-O}$  sites receiving the dissociated water proton), and 8  $\mu_2\text{-O}$  inner sites. Once the surface hydroxylation has been achieved, a bulk liquid water

composed of 120 water molecules (thermally equilibrated separately) has been added in the simulation box, keeping the supplementary 16.5 Å vacuum in the  $z$  direction above the liquid (see Fig. 6.2 for a sketch). All has been detailed in chapter 5.

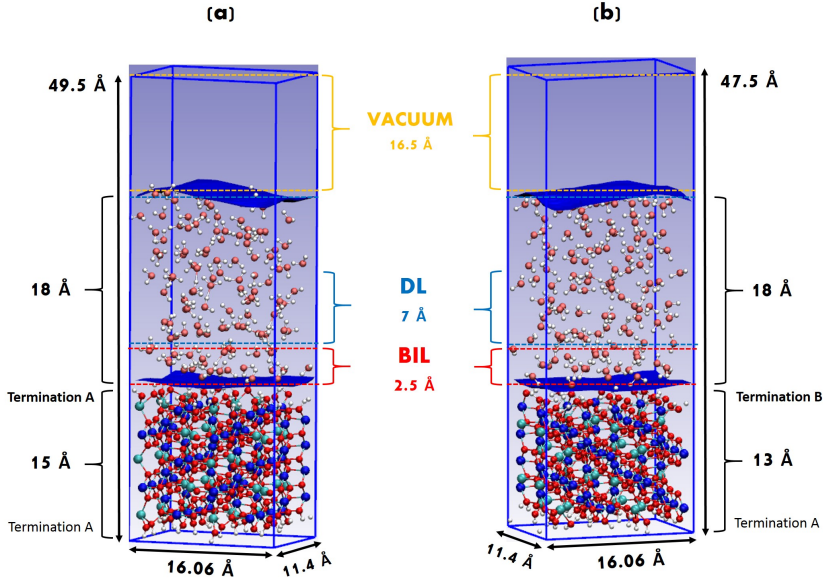


Figure 6.2: *Simulation boxes of the DFT-MD of (110)-A/B-Co<sub>3</sub>O<sub>4</sub>-liquid water interfaces. (a) Co<sub>3</sub>O<sub>4</sub> termination A/liquid water interface (712 atoms): 352 atoms composing the solid oxide and 120 water molecules. (b) Co<sub>3</sub>O<sub>4</sub> termination B/liquid water interface (680 atoms): 320 atoms composing the solid oxide and 120 water molecules. A vacuum slab of 16.5 Å has been placed above the liquid in order to avoid water confinement due to PBC in the  $z$ -direction.*

The simulation boxes for the DFT-MD simulations of the (110)-A-Co<sub>3</sub>O<sub>4</sub>-liquid water and of the (110)-B-Co<sub>3</sub>O<sub>4</sub>-liquid water interfaces are illustrated in Fig. 6.2. One box is composed of 9 layers of bulk cobalt oxide in a symmetric slab model, *i.e.*, with two A-surfaces on each side. Both A-surfaces are hydroxylated, and only one surface is put in contact with liquid water. This is clearly shown in Fig. ??-a. The other box is composed of 8 layers of bulk cobalt oxide – in an asymmetric slab model – hence displaying the A- and B-surfaces on either side. Both surfaces are hydroxylated and only the B-surface is put in contact with liquid water. Such a circumstance is depicted in Fig. ??-b. As far as the asymmetric slab is concerned, the thickness of the bulk has been set in such a way to have no issues with dipole corrections. The cationic A-layer and the anionic B-layer have total charges of  $+8|e|$  and  $-8|e|$ , respectively, when considering the 4-replicas systems used in the simulations (see Ref. [254] for details on the choice of the 4-replicas in the supercell approach). A uniform “jellium” background and the Ewald summation for electrostatics take care of the non-neutral charge of the simulation box whenever necessary, as typical in DFT-MD simulations. The identification of the interfacial layers of water at charged (and not charged) interfaces, namely the Binding Interfacial Layer

(BIL), the Diffuse Layer (DL) and the bulk liquid water, has been achieved *via* our methodology presented in Ref. [241] on the basis of structural properties only. In the systems here investigated, the BIL is found, systematically, to be composed of the first water monolayer, as already shown in other investigations on mineral oxide-water interfaces (see, *e.g.*, Refs. [241, 242]).

The apparently unbridgeable gap between the (long, even very long) time scale of reactive events and the (short) time scale of *ab initio* MD simulations can be effectively handled by employing enhanced sampling techniques, including metadynamics methods [300] and transition path sampling [301]. However, MD simulations in the study of chemical reactions has always been faced to the choice of relevant reaction coordinates for the biased sampling. In particular, the design of coordinates that fully include the role of the solvent degrees of freedom [302, 303, 304] and which are general enough to be applied to a palette of diverse reaction mechanisms is extremely challenging. On the other hand, a novel enhanced sampling approach, able to address in a general way a wide range of chemical reaction mechanisms in condensed phase, is now available, allowing for unveiling reaction networks of remarkable complexity. This method (detailed in section 2.9.2, named MetD) has successfully been applied to the study of the formamide decomposition channels in aqueous solutions [33], to the reconstruction of the liquid methanol reaction network [35, 305], and to reactions in aqueous and aldehydes solutions [306], just to cite a few examples. This is the method applied here in the context of the OER at cobalt oxide/liquid water interfaces.

Gas-phase and liquid-phase OER are here investigated exploiting such novel MetD technique, as implemented in the PLUMED-2.x software package [307]. The free-energy landscape reconstruction has been obtained by exploring the (local) configurational space (*i.e.*, the phase space) and hence probing the relevant (meta)stability basins and the connecting chemical pathways on the space spanned by the two  $S(\mathbf{R}(t))$  and  $Z(\mathbf{R}(t))$  collective variables, as detailed in sections 2.9.2. Such MetD formalism [33] employs the matrices of coordination numbers (also called contact matrices) with the aim to define – and hence render distinguishable – a given molecular state  $S(\mathbf{R}(t))$  that represents the progress along the chemical transformation, whereas  $Z(\mathbf{R}(t))$  is the distance from the predefined (idealized) pathway (see section 2.9.2 and Ref. [33] for details). In our case, only the reactants and the products basins have been chosen to define the OER chemical pathway, allowing the system to explore different potential reaction routes in between.

The present study is novel and we believe it represents a step forward in the theoretical investigations of the OER at  $(\text{Co}_3\text{O}_4)$  surfaces, by treating gas phase and liquid phase environments on the same footing through the definition of simple, intuitive, and transferable reaction coordinates. In combination with state-of-the-art free-energy calculations, those coordinates allow for the exploration of the thermodynamically relevant reaction mechanisms and the reconstruction of the corresponding free-energy landscapes, which can be directly compared between phases and/or at different thermodynamical con-

ditions. As described in section 2.9, in the MetD scheme the hills of potential energy are made of Gaussians with widths  $\sigma_s = 0.02$  and  $\sigma_z = 0.10$ , the heights are of decreasing values down to 0.5 kJ/mol deposited every 40 fs. Since we adopted path-CV MetD in its well-tempered fashion [66], such an initial Gaussian potential height was automatically reduced during the exploration of the configurational space as the filling procedure progressed. The deprotonation reactions  $\text{Co}^{(3+)}\text{OH} \rightarrow \text{Co}^{(4+)}\text{O} + \text{H}^+$  at the (110)- $\text{Co}_3\text{O}_4$  B-surface (the only OER active surface in our simulation time, as will be reviewed in the next sections) in liquid-phase and for its gas-phase counterpart, have been investigated by means of standard metadynamics by choosing as unique reaction coordinate the oxygen-to-hydrogen distance.

## 6.2 Selection of OER active sites at the A- and B- (110)- $\text{Co}_3\text{O}_4$ surfaces for the MetD DFT-MD

Even though it is known that the surface morphology holds a key role in the activity of catalysts and that adsorbed species can further modify the surface structure of the active catalysts, an open question remains about how these effects can affect the activity of electrocatalysts in the OER process.

In section 5.3, we have shown the details of the surface composition and morphology of the semiconductor spinel cobalt oxide  $\text{Co}_3\text{O}_4$  once cut along the (110) crystallographic symmetry plane and placed in contact with water molecules [254]. The geometries of the A- and B-hydroxylated surfaces are also shown in Fig. 6.1-c-d. Such a surface hydroxylation strongly modifies the electronic properties of  $\text{Co}_3\text{O}_4$  as well as the way the water is organised at the interface, as shown in sections 5.5-5.6 in chapter 5, and the difference in the chemical composition of the A- and B surfaces along with the opposite surface charge possibly plays a role in the reactivity of the two surfaces, and thus in their ability to catalyze the water splitting [278, 279].

In the modeling made here by MetD DFT-MD biased trajectories, the OER can occur at the A- and B surfaces through the proposed reaction pathway reported in Fig. 6.3, which is the mechanism proposed by Rossmeisl, Norskov, and co-workers [29, 31] (see section 3.2). It proceeds through the formation of a surface adsorbed intermediate hydroperoxo  $\text{HOO}^*$  and superoxo  $\text{O} = \text{O}^*$ . The reaction mechanism is schematically shown in Figure 6.3.

The overall reaction can be summarized as the dissociation of a water molecule over catalytic active sites on the  $\text{Co}_3\text{O}_4$  surface (step 2), losing two protons (steps 2 and 3) and forming  $\text{O}_2$  with a surface oxygen through the formation of the chemisorbed intermediate hydroperoxo  $\text{HOO}^*$  (step 3). In particular, step 2  $\rightarrow$  3 is the oxidation of the hydroperoxo  $\text{HOO}^*$  (in which  $\text{O} - \text{OH}^*$  is single bonded) into a doubly-bonded superoxo  $\text{O} = \text{O}^*$ . Finally, the superoxo  $\text{O} = \text{O}^*$  desorbs as molecular oxygen (step 4), creating a surface vacancy where a subsequent nucleophilic addition of another water molecule (step 5) can occur, and hence the OER is free to restart and continue. The

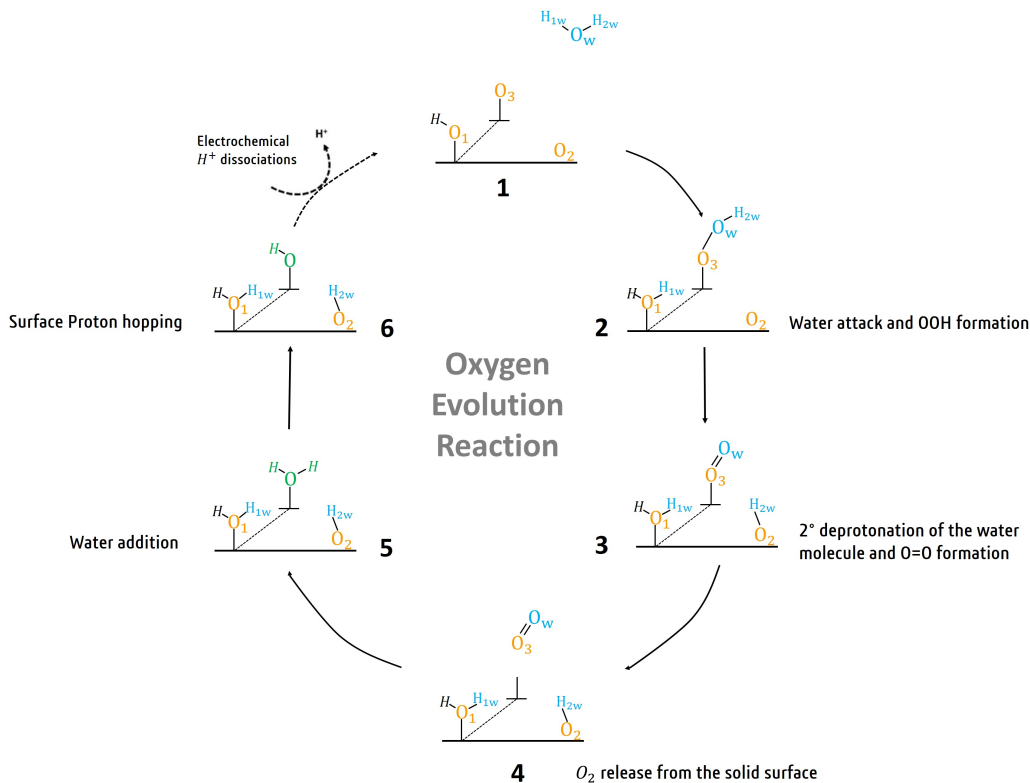


Figure 6.3: Proposed usual mechanism of the OER taking place via a water attack and a surface adsorbed intermediate  $\text{HOO}^*$  and  $\text{O} = \text{O}^*$  superoxo (see section 3.2). Potential catalyst surface oxygens sites are in orange color. The light blue label denotes the reactant water molecule.

existence of a superoxo  $\text{O} = \text{O}^*$  intermediate (step 3) in the water oxidation cycle has been previously detected *in situ* by Zhang and Frei *et al.* by using time-resolved spectroscopy [308]. Step 1 of the OER full cycle, *i.e.* deprotonation of surface sites, is systematically assumed in our simulations, meaning that we impose it from the start. Only the rest of the process is modeled through the novel "contact matrix" metadynamics. However, the energy cost of this step 1 will also be measured in our work.

Previous studies of water oxidation by molecular catalysts have shown that in many cases the O-covered surface shows higher activity than the OH-covered surface, such that the oxygen evolution reaction will only occur on surfaces with a high oxygen coverage [309, 310, 311]. It was also speculated, both experimentally and theoretically, that the oxygen evolution might be generally difficult to achieve at a single Co-O surface catalyst site due to the high localization of the electronic charge [310, 311, 312]. The OER should be easier to occur when, *at the very least*, two active Co-O surface sites are involved. The cooperation of these two neighbors at the surface is able to make (energetically) easier the water dissociation at the catalyst surface (step 2) and to form the desired  $\text{O} = \text{O}^*$  surface adsorbed species (step 3), as provided

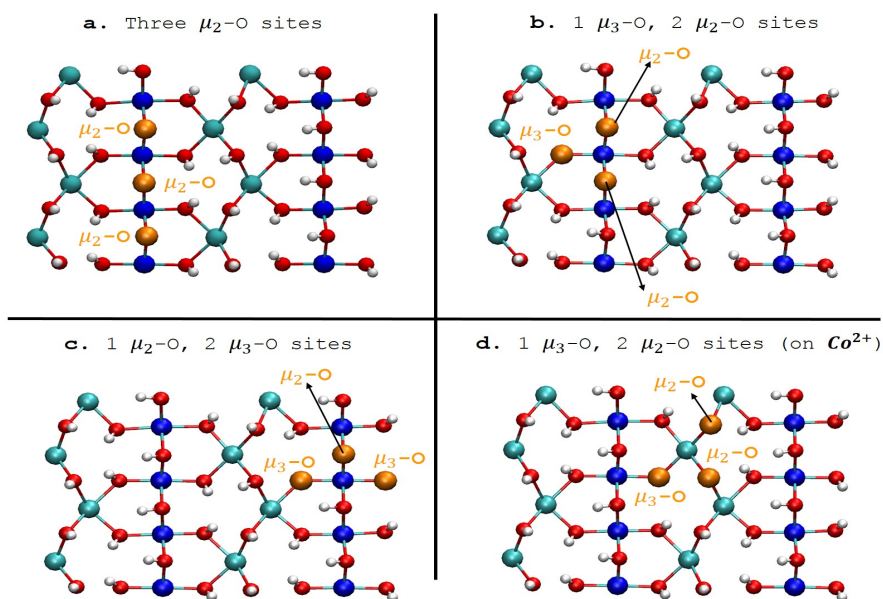
in several theoretical and experimental studies about heterogeneous catalysts [311, 308, 313, 314, 315]. If only one surface  $Co-O$  active site is available for the OER, the repulsion between the electron-rich surface O and the oxygen O of the water molecule would cause a high-energy barrier for the  $O = O^*$  bond formation.

For these highlighted reasons, and for the fact that several chemical species are possible OER catalyst surface sites – such as  $\mu_2-OH$ ,  $\mu_3-OH$  at the A surface and  $\mu_1-OH$ ,  $\mu_1-OH_2$ ,  $\mu_2-O$ ,  $\mu_2-OH$  at the B surface (see Fig. 5.10 in section 5.3 for the hydroxylated surface patterns) –, all metadynamics calculations (in gas and in liquid phase) reported here for the OER investigations at the A- and B- surfaces are performed with the assumption that, *at the very least*, two adjacent  $Co-O$  surface sites are available. The initially hydroxylated sites  $Co-OH$  or  $Co-OHH$  (on A- and B- hydroxylated surfaces) are hence deprotonated in order to have, *at the very least*, two neighbors surface  $Co-O$  sites exposed to the solvent (oxygens sites are in orange color in Fig. 6.3). This way, we have unsaturated exposed oxygen atoms (or unsaturated exposed OH radicals) available to form covalent bonds and hence make the OER (energetically) easier.

One relevant focus is to know whether different OER pathways can occur depending on the different surface location and speciation of the involved surface sites at the A- and B- (110)- $Co_3O_4$  surfaces. By selecting different surface sites and morphology scenarios as possible reactants, both at the A and B surfaces, a complete and thorough evaluation of the mechanistic and thermodynamical aspects of the OER are evaluated by our first-principles biased DFT-MD simulations.

The schematic representations of the chosen surface sites that could be relevant for the water oxidation process at the A and B surfaces and are thus made deprotonated (when they were initially hydroxylated) are shown in Fig. 6.4:

## TERMINATION A



## TERMINATION B

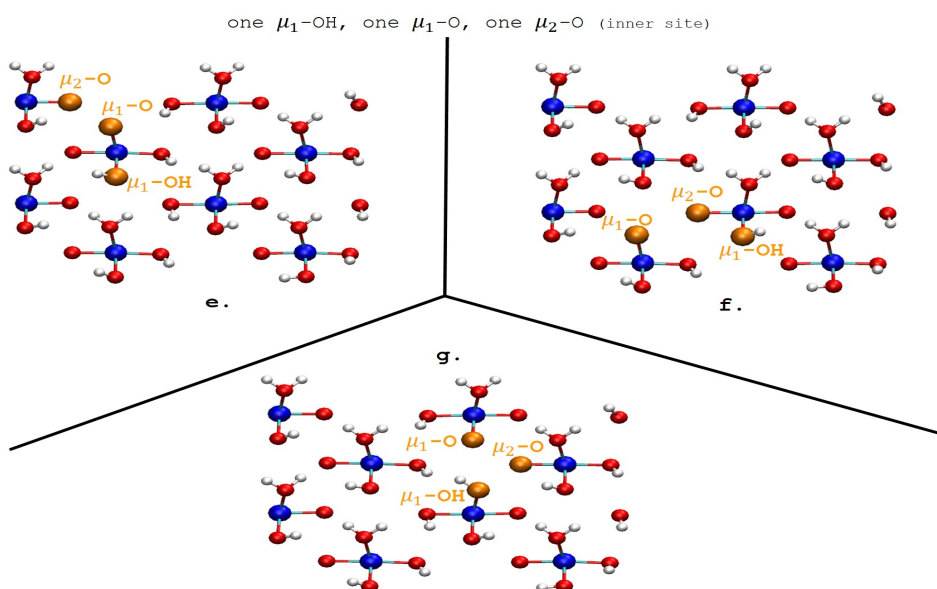


Figure 6.4: Chosen scenario for our metadynamics. Top views of A and B surfaces of aqueous (110)- $Co_3O_4$  with all the possible surface oxygen sites colored in orange chosen as potential OER catalyst sites (potential reactants) upon deprotonation. 3 deprotonated neighbors  $Co-O$  surface sites are chosen at the A surface; 2 deprotonated neighbors  $Co-O$  surface sites and 1  $Co-OH$  surface site are chosen at the B surface.

**Termination A:** a) three  $\mu_2$ -O sites arranged in a row; b) one  $\mu_3$ -O inner sites and two  $\mu_2$ -O site; c) one  $\mu_2$ -O sites and two  $\mu_3$ -O inner site; d) two  $\mu_2$ -O sites and one  $\mu_3$ -O inner site (bonded to  $Co_2^+$ ). **Termination B:** e)

one  $\mu_1$ -OH, one  $\mu_1$ -O, one  $\mu_2$ -O inner site; f) one  $\mu_1$ -OH, one  $\mu_1$ -O, one  $\mu_2$ -O inner site (different surface location from e); g) one  $\mu_1$ -OH, one  $\mu_1$ -O, one  $\mu_2$ -O inner site (different surface location in between e and f). The reactant water molecule, chosen among the BIL-water, is the species just above the selected surface oxygen atoms (or surface -OH) colored in orange, at time=0 of the biased metadynamics. All the other surface sites are not modified and treated as they exist in the hydroxylated state at the interface with the air or with the liquid water.

Note that, the unmodified (not deprotonated) A-surface is composed of 16  $\mu_2$ -OH and 16 inner- $\mu_3$ -OH sites exposed at the top surface and hence all the A-surface sites are initially protonated (hydroxylated), see Fig 5.10-left. Therefore all scenarios for the initial state of surface sites at the A-termination require the initial deprotonation of these sites. The B-surface exposes 8  $\mu_1$ -OH<sub>2</sub>, 8  $\mu_1$ -OH, 8 inner- $\mu_2$ -OH and 8 inner- $\mu_2$ -O sites (see Fig 5.10-right), therefore only the 8 inner- $\mu_2$ -O sites are initially not protonated (not hydroxylated). Thus our scenarios for the initial state of the B-surface deprotonation require only the  $\mu_1$  sites onto which to impose deprotonation, while the  $\mu_2$  inner sites are already naturally deprotonated. That would of course decrease the energetical cost for the whole OER process.

To confirm the need in having, *at the very least*, two adjacent cooperative *Co* – *O* deprotonated surface oxygens and to validate our proposed reaction scheme, we have also considered the fully hydroxylated A and B surfaces, *i.e.* without removing hydrogen (or hydrogens) from the top of surface oxygen atoms (see Fig 6.5). This way, we tested whether the reaction occurs solely when we have unsaturated exposed oxygens as reactants or whether a possible OER reaction pathway can take place at the unmodified hydroxylated A- and B- surfaces.

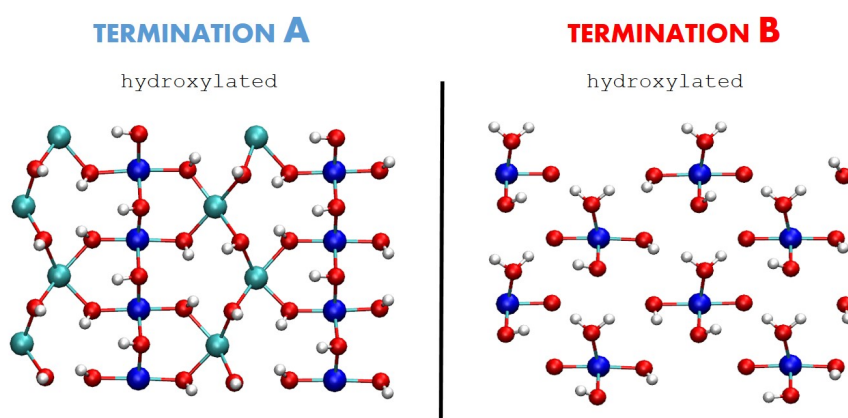


Figure 6.5: Top views of hydroxylated A and B surfaces. No surface sites have been deprotonated for the metadynamics for these surfaces.

## 6.3 OER mechanisms, kinetics and thermodynamics from metadynamics DFT-MD

The main purpose of the present study is to clarify the OER electrocatalytic activity of the A- and B- surfaces of the (110)- $\text{Co}_3\text{O}_4$  cobalt oxide. In this context, understanding the thermodynamics (free energy differences) and a quantitative assessment of the OER mechanisms and kinetics are keys to eventually improve the performance of the aqueous (110)- $\text{Co}_3\text{O}_4$  as a catalyst for the OER. To this aim, metadynamics in the form of a novel MetD path-CV framework, described in section 2.9.2, is coupled with DFT-MD. Within this metadynamics approach, it is sufficient to provide the coordination numbers of the atoms involved in the reaction path, *i.e.* the coordination numbers of the reactant and product atoms, arranged in a simple matrix called "contact matrix". For all details of the construction of the OER contact matrix see section 2.9.2-Fig. 2.6. We report below only the (adapted) Fig. 2.6 for the reading comprehension.

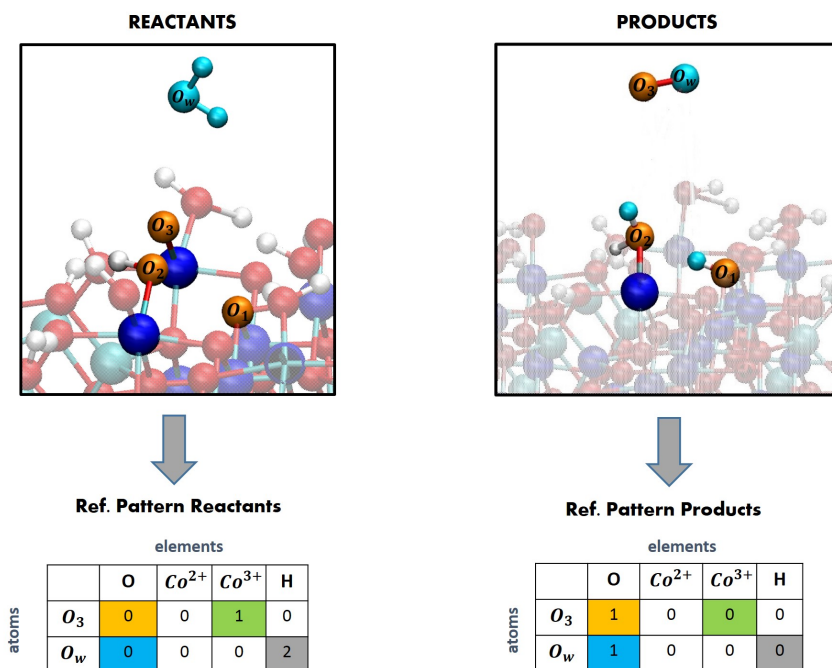


Figure 6.6: a) Construction of the coordination patterns identifying reactants and products for the contact matrix of reactants and products in the MetD-DFT-MD dynamics. Top: Reference structure of reactants (3 surface deprotonated oxygen atoms in orange color and 1 water molecule in light blue color) and products (desorption of  $\text{O}_2$ ). Bottom: contact matrix represented by tables having individual atoms as rows and atomic species as columns. Background colors in the matrix elements indicate changes of coordination numbers between reactants and products. All other matrix elements are free to change as well during the phase space exploration thanks to the flexibility of MetD path collective variables. Adapted from ref. [33]. Liquid water is removed from the snapshots for simplicity of reading.

*Contact Matrix Reactants:*  $O_3$  and  $O_w$  are 'chosen' as the main characters for the OER, *i.e.* they will form  $O = O$  at the end of the OER. Hence, we build the contact matrix in terms of coordination numbers of  $O_3$  and  $O_w$  with all the other atoms species, *i.e.*  $O$  (whether they belong to surface or water),  $Co^{2+}$  (surface),  $Co^{3+}$  (surface), and  $H$  (whether they belong to surface or water). At the beginning of the OER (see panel reactants in Fig. 6.6),  $O_3$  is bonded to one  $Co^{3+}$  at the B-surface (to two  $Co^{3+}$  at the A-surface) and hence one has to put 1 in the 4<sup>th</sup> column-2<sup>nd</sup> line (cross-point between  $Co^{3+}$  column and  $O_3$  line) in the contact matrix.  $O_w$  is initially bonded to its 2 hydrogens and hence we put 2 in the 5<sup>th</sup> column-3<sup>rd</sup> line (cross-point between  $H$  column and  $O_w$  line) in the contact matrix.

*Contact Matrix Products:* at the end of the OER,  $O_3$  and  $O_w$  are now bonded to each other and hence we put 1 in the 2<sup>nd</sup> column-2<sup>nd</sup> line (cross-point between  $O$  column and  $O_3$  line) and in the 2<sup>nd</sup> column-3<sup>rd</sup> line (cross-point between  $O$  column and  $O_w$  line) in the contact matrix.

Reactants and products are free energy basins separated by a barrier of free energy  $\Delta G$ . It is possible to construct the free energy landscape of the OER as a 3D plot in terms of the two collective variables  $S(\mathbf{R}(t))$  and  $Z(\mathbf{R}(t))$ , that respectively represent the progress along the reference reaction path (defined by the coordination patterns in the contact matrix) and the distance from it, see section 2.9.2 for all details. This way, the simulation is able to find (relatively) unbiased reaction pathways, including possible intermediates, as well as off-pathway states. Another crucial feature of such an enhanced sampling method is represented by the possibility to simulate both gas- and condensed-phase reactions (including interfaces, etc.) within a unified formalism. This allows for a one-to-one comparison, highlighting – and fully taking into account – the subtle role played by the entropic contributions due to the phase (gas or water) where the reaction proceeds. With the aim of fully characterizing the OER at the  $Co_3O_4$  (110) aqueous and non aqueous surface, the free-energy activation barrier of the OER and the associated OER overpotential can be calculated from the free-energy landscapes obtained from the MetD dynamics.

### 6.3.1 OER at the B-(110)- $Co_3O_4$ /vacuum interface

We are modeling here the B-(110)- $Co_3O_4$ /vacuum interface, but including one water molecule at the interface in order to have the oxidation (OER) of this particular water. The first result from our MetD simulations is that only the B-(110)- $Co_3O_4$  surface is reactive to the OER over our simulation times of 20 *ps* whether at the air or liquid phase interface. Furthermore, among all the explored potential catalyst surface sites at the B- surface (surfaces in Figure 6.4 and hydroxylated surfaces in Fig. 6.5), only the adjacent  $\mu_1$ -OH,  $\mu_1$ -O, and inner- $\mu_2$  sites placed as in Fig. 6.4-g morphology scenario, led to the OER. Again, this result is true for both OER in the air and the liquid environment. As expected (from the reasons discussed in the previous section

about the need of deprotonated surface sites), in our simulation times of 20 ps no OER occurs at the hydroxylated (not deprotonated) surfaces displayed in Fig. 6.5. Our gas-phase MetD simulations, at the B/vacuum interface have revealed the OER reaction pathway shown in Fig. 6.7.

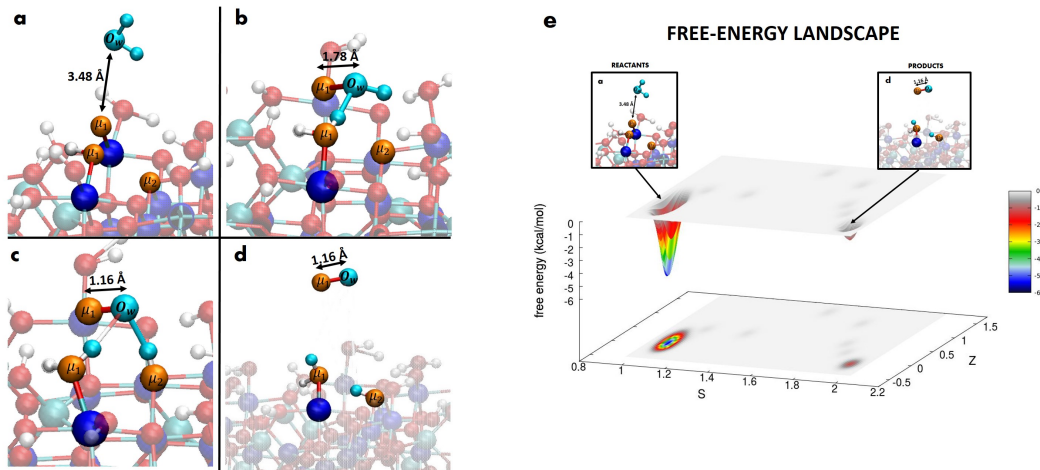


Figure 6.7: Instantaneous snapshots from gas phase MetD-DFT-MD simulations of the  $O_2$  gas formation through the water attack and its dissociation pathway. Orange, blue, and light blue colors refer to catalyst surface O sites,  $Co^{(3+)}$  cations, and water molecule, respectively. Distances (in Å) between the surface oxygen  $\mu_1-O$  ( $Co^{(3+)}-O$ ) and the oxygen of the water molecule are shown using arrows. a) Initial configuration. b) Water attack and its dissociation with the formation of the surface adsorbed  $-OOH^*$ . c) Proton transfer leads to a shortening of the  $\mu_1-O_w$  distance from 1.78 Å to 1.16 Å. d)  $O_2$  desorption. e) Free-energy landscape of the process. The energy scale is in kcal/mol, the S-axis and the Z-axis represent the progress along the reaction and a distance from its ideal path, respectively (see section 2.9.2). Low values of S characterize the reactants whereas high values identify the products. The minimum located at  $S \sim 1$  represents the free-energy barrier (5.8 kcal/mol = 0.25 eV).

The OER multiple-steps reaction starts with the water attack and its dissociation at the  $\mu_1-O$  ( $Co^{(3+)}-O$ ) surface site, to form an active radical group  $Co^{(3+)}-OOH$ , whilst the dissociated hydrogen of the water protonates (hops to) a nearby  $Co^{(3+)}-O$  surface site (Fig. 6.7-b). Once the active radical group  $Co^{(3+)}-OOH$  is formed, the reaction goes through a proton jump from this group to a neighbor  $\mu_2-O$  surface inner-site, leaving  $Co^{(3+)}-OO$  behind (Fig. 6.7-c). In particular, the proton jump induces a significant shortening of the distance between the oxygens of the  $Co^{(3+)}-OO$  group, starting from a distance of  $\sim 1.8$  Å – typical of a single bond – for the  $Co^{(3+)}-OOH$  group (in Fig. 6.7-b) to a distance of 1.2 Å for the  $Co^{(3+)}-OO$  (in Fig. 6.7-c), thus witnessing the formation of a doubly-bonded  $O_2$  species. Consequently, the  $O_2$  species desorbs from the  $Co^{(3+)}-OO$  surface group ( $\mu_1-OO$ ), leading to the expected  $O_2$  gas phase formation.

The associated free-energy surface has been evaluated with the aim of determining the free-energy activation barrier of the overall reaction products from

the reactants (in Fig. 6.7-a) to the product species ( $\text{O}_2$  desorption in Fig. 6.7-d). A free-energy barrier of 5.8 kcal/mol (0.25 eV) has to be overcome in order to convert water into molecular oxygen at this B-(110)- $\text{Co}_3\text{O}_4$ /air interface, see Fig. 6.7-e.

Notwithstanding such a relatively small barrier, the OER rate-limiting step is represented by the deprotonation needed to create the unsaturated sites at the B-(110)- $\text{Co}_3\text{O}_4$  surface, as illustrated in Fig. 6.8-a,b. To evaluate the importance of the free-energy barriers associated to this B-surface deprotonation reaction, the gas phase process  $\text{OH}^* + \text{H}_2\text{O} \rightarrow \text{O}^* + \text{H}^+ + \text{H}_2\text{O}$  has been characterized at a  $\mu_1$ -OH ( $\text{Co}^{3+}$ -OH) B-surface site, as shown in Fig. 6.8, also by MetD-DFT-MD simulations.

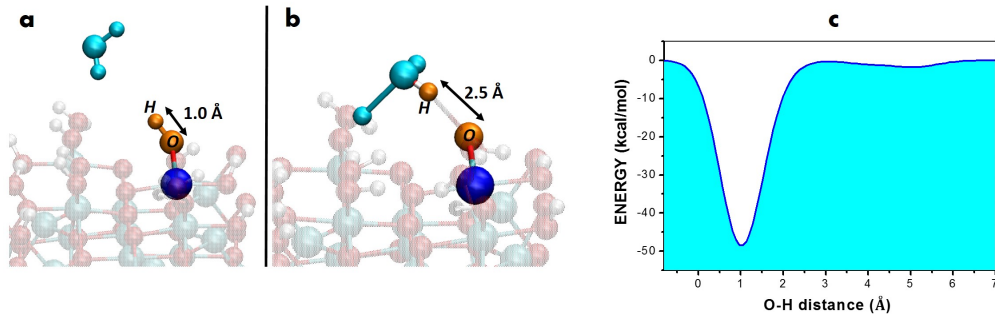


Figure 6.8: *Instantaneous snapshots from MetD simulations of the  $\mu_1$ -OH ( $\text{Co}^{3+}$ -OH) B-surface site deprotonation in contact with one gas-phase water. Distances in Å between the surface oxygen  $\mu_1$  and the hydrogen atoms is shown using arrows. a) Initial configuration. b) Proton transfer event from the surface to one water molecule, necessary for the surface site to be reactive for subsequent OER. c) Associated free-energy barrier in kcal/mol where the abscissa represents the O-H distance track in (a) and (b). The minimum located at  $\sim 1$  Å has a depth of 49.5 kcal/mol (2.14 eV) which corresponds to the free-energy barrier for the deprotonation of the catalyst B-surface site.*

A free-energy barrier larger than 49.5 kcal/mol (2.14 eV) is required to trigger the release of a surface-exposed hydrogen to a water molecule in order to create the catalyst  $\text{Co}^{3+} - \text{O}$  ( $\mu_1$ -O) surface site.

This latter surface deprotonation process is thus the OER rate limiting step. This is thus the free-energy to use for the calculation of the OER overpotential  $\eta$  (see section 3.2). Here it gives rise to an overpotential of  $\eta = [(2.14 \text{ eV}/1 e) - 1.23 \text{ V}] = 0.91 \text{ V}$  to proceed with the OER in the gas phase at the B-(110)- $\text{Co}_3\text{O}_4$  surface catalyst.

On the other hand, MetD simulations have not found any kind of possible OER route at the A surface (with all surface scenarios presented in Figures 6.4 and 6.5) within the simulation times that we systematically applied for the biased dynamics (*i.e.*, 20 ps), also after multiple tests starting from different initial atomic configurations and/or initial atomic velocities. This finding is

not so surprising if one considers that only doubly-triply bridged surface oxygen atoms are present at the A-(110)-Co<sub>3</sub>O<sub>4</sub> surface. Once deprotonated, the A-surface is composed by  $\mu_2 - O^*$  sites and inner  $\mu_3 - O^*$  sites which involve surface oxygen atoms double-bridging two Co<sup>(3+)</sup> ions and triple-bridging three Co<sup>(3+)</sup> ions, respectively. By adsorption and dissociation of the water onto one of these  $Co - O^*$  surface sites, the next step for the OER requires the desorption of the  $O = O^*$  and thus requires that the  $O^*$  desorbs by breaking its covalent bond(s) with the cobalt atom. Thus, even under the best scenario, a possible reaction mechanism at the A-surface should have to break at least two covalent bonds that the  $O^*$  bridging oxygen is making with cobalt. The associated free-energy barrier for the OER at the A-surface should be therefore sizably much larger than the one of the process at the B-surface, which exhibits only singly-bonded  $\mu_1 - O^*$  oxygen atoms at the surface. A similar rationale was given by Norskov and Rossmeisl [316] in the case of TiO<sub>2</sub> metal oxide as catalyst. The authors indeed have not even taken into consideration a possible reaction mechanism involving the doubly-bridged oxygen atoms at the TiO<sub>2</sub> metal oxide surface. Conversely, here we have estimated the free-energy barrier needed to break the two covalent bonds of the doubly-bridged oxygen at the (110) A-surface by the Umbrella sampling method described in section 2.10. We found a free-energy of 83 kcal/mol (3.6 eV) to snatch this doubly bridged oxygen atom from the A-surface, which is indeed enormous and thus prevents the OER to proceed.

Moreover, it is clear that not only the surface oxygen bonds hold a key role in shaping the free-energy surface of the OER, but also the topological arrangement of the catalyst sites at the surface has a prominent contribution in determining the free-energy barrier height. Accordingly, the possible catalyst surface sites chosen at the B-termination consists in  $\mu_1$ -OH,  $\mu_1$ -O, and inner  $\mu_2$ -O sites in all the explored initial configurations (in Fig. 6.4-e,f,g). However, only the geometrical spatial arrangement of these 3 surface sites as depicted in Fig. 6.4-g is able to catalyze the OER at the B-termination. This is due to the fact that such an arrangement (in Fig. 6.4-g), thanks to the closeness of the sites (*i.e.* cobalt catalyst sites are only  $\sim 2.6$  Å apart from each others), is able to provide a restricted catalytic area at the surface and hence inhibits the repulsion between the electron-rich surface O and the oxygen O of the water molecule. The existence of a specific distance between surface sites on a given surface conferring to the latter efficient catalytic properties has also recently been demonstrated at silica surfaces [317].

The oxidation states during the identified OER process found in this work at the B-(110)-Co<sub>3</sub>O<sub>4</sub>-air interface are displayed in Fig. 6.9, calculated by employing the Maximally Localised Wannier Functions (MLWF) [318] analysis (described in section 4.15). This latter is a useful method that characterizes the electronic ground-state properties of a condensed system. One of the key factors that can be extracted from the MLWF are their charge centers which are a sort of quantum equivalent of the classical concept of the localization of an electron pair and thus allows for a direct visualization of the electronic

spatial positions determining the oxidation state of each atomic species, as depicted in Fig. 6.9.

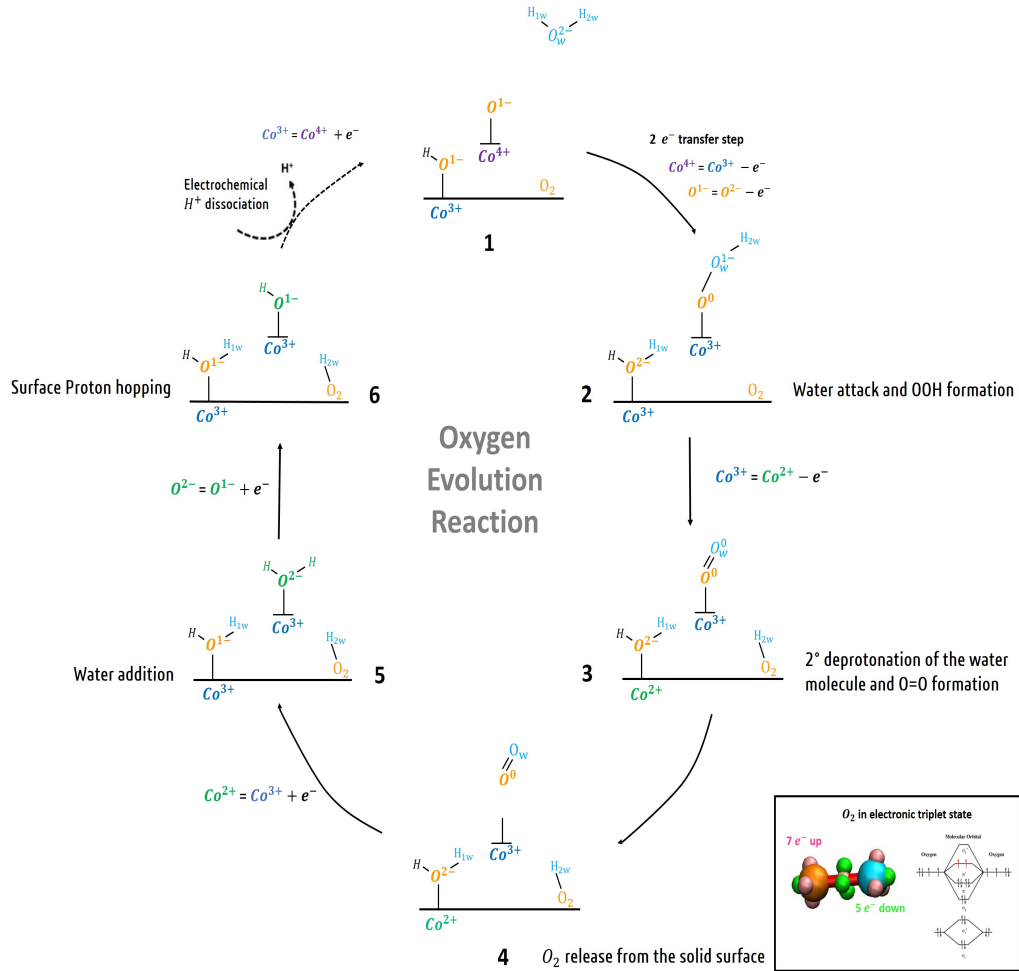


Figure 6.9: Changes of the oxidation states of the atomic species involved in the identified mechanism of the OER at the B-(110)-Co<sub>3</sub>O<sub>4</sub>-air interface. Potential catalyst surface sites are in orange color whereas light blue color identifies the reactant water molecule. The inset displays the calculated electronic configuration of O<sub>2</sub> (gas) in its ground state.

Careful electronic analyses of the B-surface sites as the OER proceeds indicate that the Co<sup>(3+)</sup> cation is oxidized to Co<sup>(4+)</sup> when the deprotonation of the surface Co<sup>(3+)</sup>-OH → Co<sup>(4+)</sup>-O creates the unsaturated surface site (see step 6 → 1 in Fig. 6.9). During the step 1 → 2, which leads to the formation of the radical group Co<sup>(3+)</sup>-OOH, two electrons are transferred from the two reacting oxygens (surface and water oxygens). This way, one electron is reducing Co<sup>(4+)</sup> into Co<sup>(3+)</sup> for the creation of the Co<sup>(3+)</sup>-OOH radical group, while another electron is transferred to a nearby Co<sup>(3+)</sup>-OH<sub>2</sub> (μ<sub>1</sub>-OH<sub>2</sub>) site, reducing the oxygen O<sup>2-</sup> into O<sup>1-</sup>. This is all done simultaneously. Contrarily to the OER model proposed by Norskov *et al.* [29] (described in section 3.2) for which all the OER 4-steps involve one-electron transfer each, we found a

two-electrons transfer process during the step  $1 \rightarrow 2$ , *i.e.* the water attack and its dissociation OER step.

During the further step  $2 \rightarrow 3$ , the O-OH of the radical group  $\text{Co}^{(3+)}\text{-OOH}$  is oxidized and hence a doubly bounded O=O appears by loosing one electron and one proton. The formed superoxo O=O is unstable at the surface site and spontaneously loses one electron to the nearby  $\text{Co}^{(3+)}\text{-OH}_2$  ( $\mu_1\text{-OH}_2$ ) site, reducing  $\text{Co}^{(3+)}\text{-O=O}$  into  $\text{Co}^{(2+)}\text{-O=O}$ . Subsequently, in step 4, the newly formed molecular oxygen  $\text{O}_2$  desorbs from the surface site  $\text{Co}^{(2+)}\text{-O=O}$  creating a surface vacancy where a subsequent nucleophilic addition of another water molecule (step 5) can proceed and hence the OER is free to continue.

In a nutshell, the OER proceeds with the water attack and dissociations at the  $\text{Co}^{(4+)}\text{-O}$  catalyst surface site, this latter identified as the OER catalyst site at the (110)- $\text{Co}_3\text{O}_4$  B-surface. For the sake of completeness, it is worth pointing out that  $\text{O}_2$  (gas) has been found in its electronic ground state, namely the triplet state, as displayed in the inset of Fig 6.9, with two unpaired electrons in the orbital level  $n = 2$ . Note that the two-electrons transfer process found during the step  $1 \rightarrow 2$  (*i.e.* the water attack and its dissociation OER step), has been identified also during the OER step  $1 \rightarrow 2$  at the B-surface/liquid water interface discussed in the next sub-section. However, in Fig. 6.9 we have chosen, for simplicity of reading of the figure, to display the changes of the oxidation states of the atomic species only for the OER which occur in the gas phase.

This was the gas-phase OER pathway (Fig. 6.7) identified at the B-surface (110)- $\text{Co}_3\text{O}_4$ . Starting from now, only the B-surface of (110)- $\text{Co}_3\text{O}_4$  is taken into account for the liquid phase OER.

### 6.3.2 OER at the B-(110)- $\text{Co}_3\text{O}_4$ aqueous interface

Let us now investigate the OER at the B-surface/liquid water interface where the water slab is explicitly considered, overcoming the aforementioned limitation of the current literature in adopting only, at the best, one water molecule or a water monolayer in contact with the catalyst surface. This way, the condensed-phase OER can be investigated. Since the rate-limiting step in the gas phase was the surface  $\mu_1\text{-OH}$  ( $\text{Co}^{3+}\text{-OH}$ ) deprotonation, the same deprotonation reaction ( $\text{OH}^* + \text{H}_2\text{O} \rightarrow \text{O}^* + \text{H}^+ + \text{H}_2\text{O}$ , see Fig. 6.8) has been characterized in the condensed phase by means of the Umbrella Sampling technique [65] (see section 2.10). It turns out that a free-energy barrier of 2.77 kcal/mol (0.12 eV) characterizes such a process at the interface with water. Such free-energy barrier leads to a negative overpotential (*i.e.*,  $\eta = [0.12 \text{ eV}/(1 \text{ e}) - 1.23] \text{ V} = -1.22 \text{ V}$ ) and hence the rate-limiting step is not the surface deprotonation anymore, but is within one of the steps of the OER pathway. Such result already shows how important is explicit liquid water in the modeling of chemical reactions.

In order to analyze the reaction mechanism(s) and the free-energy surface,

the same "contact matrix" MetD technique employed in the gas-phase OER (in the previous sub-section) has been used, but now including the liquid water solvent as a whole in the coordination pattern. As partly expected, we will see in the following that the presence of the interfacial aqueous environment now leads to more possibilities for the reactivity, and two possible reaction pathways for the OER at the  $\text{Co}_3\text{O}_4$  (110) B-surface in contact with water will be identified.

The first OER pathway is similar to the gas-phase one (in Fig. 6.7), as shown in Fig. 6.10:

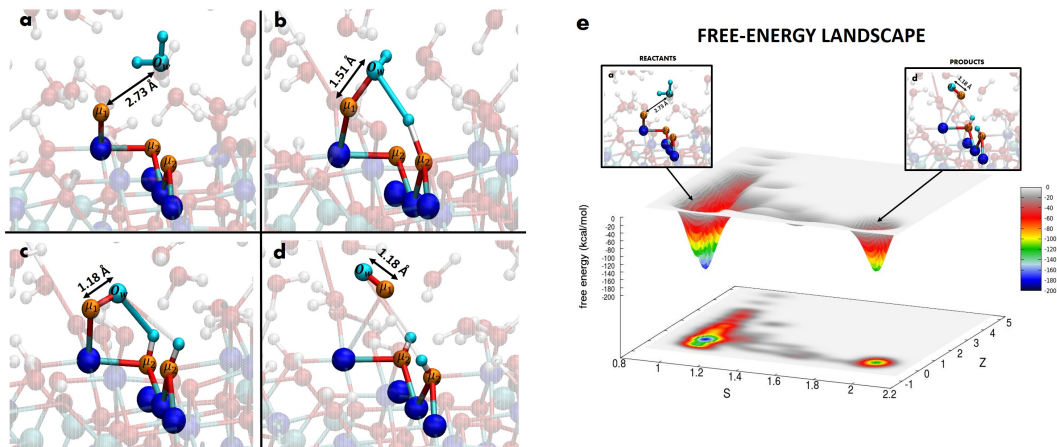


Figure 6.10: *Instantaneous snapshots from MetD-DFT-MD simulations of the  $\text{O}_2$  formation at the  $\text{Co}_3\text{O}_4$  (110) B-surface/liquid water interface via the water attack and its dissociation pathway. Orange, blue, and light blue colors refer to catalyst surface O sites,  $\text{Co}^{(3+)}$  cations, and a water molecule, respectively. Distances (in Å) between the surface oxygen  $\mu_1$  ( $\text{Co}^{(3+)}\text{-O}$ ) and the water oxygen are shown using arrows to better follow the  $\text{O}_2$  formation. a) Initial configuration. b) Water attack and its dissociation with the formation of the surface radical  $\text{-OOH}^*$ . c) Proton transfer event that leads to a shortening of the  $\mu_1\text{-O}_w$  distance from 1.51 Å to 1.18 Å. d)  $\text{O}_2$  desorption. e) Free-energy landscape (in kcal/mol) of  $\text{O}_2$  formation and release in the condensed phase. S-axis and the Z-axis represent the progress along the reaction and a distance from its ideal path, respectively (see section 2.9.2). Low values of S characterize the reactants whereas high values identify the products. The minimum located at  $S \sim 1$  corresponds to a very large free-energy barrier of 180 kcal/mol (7.81 eV).*

Contrarily to the gas-phase reaction process (in Fig. 6.7), the surface catalyst sites at the B-surface are now found as the adjacent  $\mu_1\text{-O}$  and two inner- $\mu_2\text{-O}$  sites arranged as in Fig. 6.10-a (they were adjacent  $\mu_1\text{-OH}$ ,  $\mu_1\text{-O}$ , and inner  $\mu_2\text{-O}$  in the gas phase investigation). As expected, and similarly to the gas phase situation, the OER path is multiple-steps as follows: first, there is the water attack (Fig. 6.10-a) and its dissociation (Fig. 6.10-b) above the  $\mu_1\text{-O}$  ( $\text{Co}^{(3+)}\text{-O}$ ) surface catalyst site, with the following formation of the radical  $\text{Co}^{(3+)}\text{-OO}$  group (Fig. 6.10-c). The hydrogens of the dissociated water molecule are surface adsorbed at the two neighboring  $\mu_2\text{-O}$  inner sites

(Fig. 6.10-c). Finally, the -OO (doubly-bonded O<sub>2</sub>) of the radical Co<sup>(3+)</sup>-OO group desorbs and there is the release of the O<sub>2</sub> molecule from the B-surface, see Fig. 6.10-d.

We remind the reader that the  $S$  parameter in the abscissa axis of the free-energy landscape in Fig. 6.10-e, describes the progress along the OER path (path defined by the coordination patterns in the contact matrix) where  $S = 1$  represents the OER reactants and  $S = 2$  the OER products. This means that the minimum located at  $S \sim 1$  (in Fig. 6.10-e) identifies the first OER reaction step, *i.e.* the water attack and its dissociation (in Fig. 6.10-b) as the OER rate-limiting step. Reactants and products are found separated by a huge free-energy barrier of 180 kcal/mol (7.81 eV), that would lead to an OER overpotential  $\eta = [(7.81 \text{ eV}/2 e) - 1.23 \text{ V}] = 2.68 \text{ V}$  (*vs.*  $\eta = 0.91 \text{ V}$  in the gas phase OER). Here, it seems that the presence of the aqueous environment and the kinetics of the water molecules somehow inhibit the previously gas-phase identified OER route (in Fig. 6.10-a,b,c,d) at the B-(110)-Co<sub>3</sub>O<sub>4</sub>/liquid water interface.

On the other hand, our MetD simulations at the B-(110)-Co<sub>3</sub>O<sub>4</sub>/liquid water interface show an alternative OER reaction route which has a significantly lower free-energy barrier, as shown in Fig. 6.11. This is the strength of the MetD biased metadynamics employed here, to be able to follow alternative pathways to the ideal (or pre-conceived) reaction path.

The surface catalyst sites are now the same ones as the ones detected during the gas-phase OER (Fig. 6.7), consisting in adjacent  $\mu_1$ -OH,  $\mu_1$ -O and inner- $\mu_2$ -O sites arranged as in Fig. 6.4-g. The reaction now proceeds preferentially through a water-assisted one-step mechanism with a proton transfer from a reactant water molecule to a neighbor one (Fig. 6.11-c). More specifically, the reaction starts with the water dissociation above the  $\mu_1$ -O (Co<sup>(3+)</sup>-O) catalyst surface site (see Fig. 6.11-b). However, contrarily to the previously presented OER paths, only one H of this dissociated water molecule is surface adsorbed (at the inner  $\mu_2$ -O site). The other H energetically prefers to hop toward a nearby water molecule (Fig. 6.11-c). The final step of this concerted reaction is represented by the O<sub>2</sub> desorption shown in Fig. 6.11-d. In the described OER pathway, the water molecule does not act as a "spectator" but it plays a crucial role in catalyzing the OER. It is worth to remark that such a water-assisted OER mechanism is different from the OER pathway proposed by Norskov *et al.* [29, 31] for which hydrogens of the dissociated water molecule are systematically surface adsorbed, as in our first OER scenario in Fig. 6.10-a,b,c,d.

Due to the key role of the water molecule as co-reactant found here, this condensed phase OER scenario (see Fig. 6.11) gives rise to an OER activation barrier of 71 kcal/mol (3.08 eV). Equivalently, the OER overpotential needed is  $\eta = [(3.08 \text{ eV}/2 e) - 1.23 \text{ V}] = 0.31 \text{ V}$ , this latter being about nine times smaller than the overpotential required for the previously identified condensed-phase OER ( $\eta = 2.68 \text{ V}$ , Fig. 6.10) and three times smaller than the overpotential found for the gas phase reaction ( $\eta = 0.93 \text{ V}$ , Fig. 6.8). Hence, the catalytic action of the water molecules in the BIL plays a key role

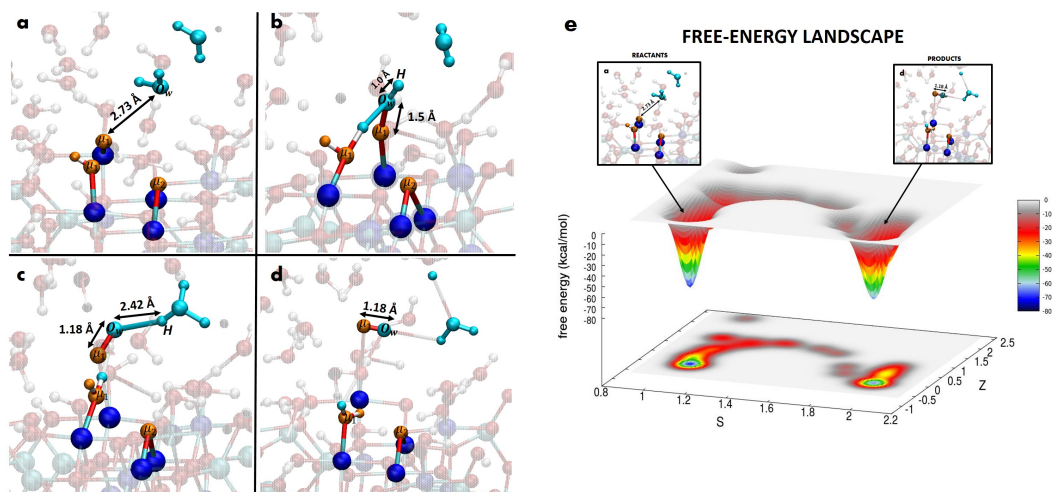


Figure 6.11: *Instantaneous snapshots from MetD simulations of the  $O_2$  formation at the  $Co_3O_4$  (110) B-surface/liquid water interface via a novel proposed water-assisted OER path. Orange, blue, and light blue colors refer to catalyst surface sites,  $Co^{3+}$  cations, and a water molecule, respectively. Distances (in Å) between the surface oxygen  $\mu_1$ -O ( $Co^{3+}$ -O) and the water oxygen are shown using arrows to better follow the  $O_2$  formation. The O-H distance in the reactant water molecule is displayed to highlight the assistance of another water molecule in the c-panel. a) Initial configuration. b) Water attack and its dissociation with the formation of the surface radical  $-OOH^*$ . c) Proton transfer, from the reactant water molecule to an auxiliary one, leads to a shortening of the  $\mu_1$ - $O_w$  distance from 1.5 Å to 1.18 Å. d)  $O_2$  desorption. e) Free-energy landscape, in kcal/mol, of the  $O_2$  formation via the novel water-assisted OER mechanism. S-axis and the Z-axis represent the progress along the reaction and a distance from its ideal path, respectively.  $S = 1$  characterizes the reactants whereas  $S = 2$  describes the products. The minimum located at  $S \sim 1.00$  corresponds to a free-energy barrier equal to 71 kcal/mol (3.08 eV).*

in lowering the OER free-energy barrier. Moreover, the relevance of the presence of the explicit solvent is highlighted, either as discouraging the gas-phase pathway or as showing the water as co-catalyst. By taking into account the drastic different weight of the entropic contributions in gas- and condensed-phase processes, this result is somehow expected and conform to the evidence that condensed-phase reactions are, in general, less demanding in terms of free energy [319, 320, 321].

In addition, the calculated OER overpotential value  $\eta = 0.31$  V found here for the (110)- $Co_3O_4$  B-surface as catalyst is comparable with the range value of  $\eta = [0.3 - 0.9]$  V [28] generally found for the OER when employing the low abundant and very high costly noble earth metal oxides such as  $RuO_2$ ,  $IrO_2$ , and  $PtO_2$  in particular conditions, *i.e.* in 0.1 M  $KOH$ , hence limiting their use as commercially viable OER catalysts.

## 6.4 Discussion and perspectives

In summary, we carried out Density Functional Theory (DFT) with Hubbard corrections (U) molecular dynamics simulations coupled with an *avant-garde* metadynamics (MetD) method in order to characterize – with electronic and atomistic details – the oxygen evolution reaction (OER) at the spinel (110)-Co<sub>3</sub>O<sub>4</sub> surface, either when the latter is exposed to one gas-phase water, or directly at the interface with liquid water.

By investigating the OER on the two possible A and B surface terminations of the spinel (110)-Co<sub>3</sub>O<sub>4</sub>, our simulations indicate that only the B-surface holds OER active catalyst sites, consisting of preferential geometrical motifs of adjacent Co<sup>(3+)</sup>-OH, Co<sup>(3+)</sup>-O, Co<sup>(3+)</sup>-O-Co<sup>(3+)</sup> (respectively  $\mu_1$ -OH,  $\mu_1$ -O<sup>-</sup>, and  $\mu_2$ -O<sup>-</sup> inner site) able to catalyze the OER both in the gas phase as well as at the interfacial liquid water. On the other hand, the composition of the A-surface termination – consisting of surface oxygens doubly/triply-bridged to Co<sup>(3+)</sup> cations – drastically inhibits the onset and the success of the OER due to the sizable energetic cost (here calculated to be around 83 kcal/mol – 3.6 eV) for breaking at least two covalent O-Co<sup>(3+)</sup> bridging bonds that would be necessary for the release of O<sub>2</sub>.

Several scenarios for the surface sites deprotonations have been tested, and we found that the gas-phase reaction between a single water molecule and the B-surface occurs *via* H<sub>2</sub>O dissociation and a subsequent O-O bond formation on a  $\mu_1$ -O<sup>-</sup> surface site whereas the two dissociated protons are adsorbed on the adjacent  $\mu_1$ -OH and  $\mu_2$ -O<sup>-</sup> inner sites of the surface. In such a case, according to the free-energy barriers calculated by means of *ab initio* molecular dynamics and MetD, the rate-limiting step for the overall water splitting reaction is represented by the initial deprotonation of the surface sites which requires an overpotential equal to 0.91 V. A careful analysis of the oxidation states monitored during the OER pathways, in both the gas-phase and the liquid phase, indicates that the Co<sup>(3+)</sup> surface cation is oxidized to Co<sup>(4+)</sup> upon deprotonation (*i.e.*, Co<sup>(3+)</sup>-OH → Co<sup>(4+)</sup>-O). This gives rise to the onset of a  $\mu_1$ -O<sup>-</sup> catalyst surface site and to a detected two-electrons transfer process during the formation of the surface radical Co<sup>(3+)</sup>-OOH group as intermediate OER state. This general pathway/mechanism for the water splitting is the route put forward by Norskov *et al.* [29, 31].

While the same OER route occurs at the interface with liquid water (with slight changes for the surface catalyst sites involved), this route is still high in overpotential. More interestingly, we have obtained an alternative reaction route – taking place when the B-(110) Co<sub>3</sub>O<sub>4</sub> surface is placed in contact with liquid water – where the reaction proceeds preferentially through a water-assisted one-step mechanism, consisting in a proton transfer from the reactant water molecule to a neighbor one instead of a proton adsorbed at the surface. In particular, the catalytic effects carried by the entropic contributions associated with the condensed-phase water environment lower the overpotential required for the OER to  $\eta_{liq} = 0.31$  V, the latter being three times lower than its gas-phase counterpart (*i.e.*,  $\eta_{gas} = 0.91$  V). Therefore, our results strongly

support the importance of the catalytic role of explicit water molecules which play a key role as co-reactant in the electrochemically-driven OER. In addition to the importance of having an explicit water slab in the simulation box, note that the OER product  $O_2$ , once released from the catalyst surface, moves from the BIL region to the DL (or bulk) water environment, preferring to be fully solvated by the DL (or bulk) water molecules, in agreement with the solubility of  $O_2$  in pure water detected in the literature [322, 323, 324].

The present study not only provides an innovative state-of-the-art theoretical/computational strategy for the investigation of the semiconductor (110)  $Co_3O_4$ -water interface under some of the electrochemical conditions, but also quantitatively assesses the thermodynamics underlying the plausible pathways (*i.e.*, the free-energy landscape) composing the reaction network of the OER. Similar modelling can be applied to other facets of the spinel  $Co_3O_4$  cobalt oxide – or other materials relevant for the design of efficient and sustainable heterogeneous catalysts – in contact with liquid water or other solvents, potentially relevant for the OER. The same methodology can also be applied when supported electrolytes would be present in the EDL, which would be required in order to model more relevant electrochemical conditions. The same is true when one adopts one of the very few developed methods from the literature to include the electrode potential into (MetD-) DFT-MD simulations. The finding of a novel – highly efficient – reaction route for the OER strongly also points out the urgency for its experimental characterization.



# Chapter 7

## OER at the aqueous (0001)-CoO(OH) oxide by metadynamics DFT-MD

Despite the aforementioned uncertainties in understanding the thermodynamic ground state structure of the  $Co_3O_4$  cobalt oxide (described in sections 4.9-4.12) and especially if  $Co_3O_4$  transforms into an oxihydroxide like CoO(OH), and in defining the "best" catalyst in between  $Co_3O_4$  and CoO(OH) under OER conditions, main studies [195, 199] proved the  $Co_3O_4$  to CoO(OH) conversion to be due to the elevated oxygen evolution rate [195] which induces structural disorder and hence the conversion from one oxide to the other (section 4.10), other studies showed how the  $Co_3O_4$  to CoO(OH) conversion is inhibited [194, 145] from the spinel structure and hence how the  $Co_3O_4$  comes out as a better catalyst because of its larger exchange current density with respect to CoO(OH) [193] (section 4.12). We address in this chapter some of these questions by DFT+U calculations of the bulk and surface stabilities of (0001)-CoO(OH), extracting the oxygen evolution overpotential of this cobalt (hydr)oxyde under some electrochemical conditions, and compare with the already investigated  $Co_3O_4$ -(110) oxide (in chapters 5-6). Note that we focus on crystalline  $Co_3O_4$ -(110) and crystalline CoO(OH)-(0001) materials without presence of surface defects, edge steps or bulk/surface vacancies, as already pointed out in chapters 5-6.

### 7.1 Computational details

We adopt the same computational setup described in chapters 5 and 6 for the DFT-MD and validated through the previous investigations. The main computational details are here summarized.

DFT-MD have been performed on the (0001)-CoO(OH)-vacuum crystalline surface and on its associated (0001)-CoO(OH)/liquid water interface. All simulations have been performed in the Born-Oppenheimer framework through the CP2K package [255, 256]. The Perdew-Burke-Ernzherof (PBE) [257] functional has been employed in combination with mixed Gaussian-Plane-Waves

basis sets and Goedecker-Teter-Hutter (GTH) pseudopotentials [260]. The DZVP-MOLOPT-SR basis set, augmented with a 400 Ry plane-wave basis set have been used, being a good compromise between the computational cost and accuracy. The PBE functional has been supplemented with the Hubbard (U) term [261, 262] in order to circumvent the over-delocalization of 3d-electrons in metal oxides and the consequent underestimation of the band gap. A value of 6.3 eV for the U parameter has been used, as tested and validated in the following section 7.2. Dispersion interactions *via* the Grimme D2 correction [298, 299], default algorithms and convergence criteria in CP2K have been adopted. Periodic boundary conditions (PBC) have been applied in all three cartesian spatial directions. During the Born-Oppenheimer MD, the electronic wavefunction has been calculated at each time-step while the classical nuclei displacements have been simulated through the velocity Verlet algorithm with a time-step of 0.4 fs.

As already emphasized for  $Co_3O_4$ , since all the DFT-MD simulations have been performed at the  $\Gamma$  point of the Brillouin zone, the use of a supercell (*i.e.*, a certain number of replicas of the CoOOH unit cell in the 3D space) was needed, see section 7.2 for the calculations details. A vacuum slab of 16.5 Å along the vertical  $z$  direction (*i.e.*, perpendicular to the surface) has been included in the simulation box to separate the periodic replicas. This choice allows us to simulate liquid water that is not being squeezed in between the 2 cobalt surface replicas. The identification of the interfacial layers of water at charged (and not charged) interfaces, namely the Binding Interfacial Layer (BIL), the Diffuse Layer (DL) and the bulk liquid water, has been achieved *via* the methodology developed in the group, presented in Ref. [241] and already described in section 5.5, on the basis of structural properties of water only.

For the gas-phase and liquid-phase OER metadynamics investigations, we show in this chapter the results obtained using a standard metadynamics technique (as implemented in the PLUMED-2.x software package [307]). Here we could not use the newly developed "contact matrix" metadynamics (MetD) technique [33, 34, 35], described in section 2.9 and validated in chapter 6 for  $Co_3O_4$  surfaces/interfaces. This is due to the fact that the "contact matrix" metadynamics method (as implemented in the PLUMED-2.x software package [307]) is not optimized/suitable when having non-orthorhombic simulation cells, as is our case for the CoO(OH) (see next section for CoO(OH) cell details). To remedy to that issue by ourselves was beyond the time-scale of our work. The only solution to overcome this issue (for the time being) is to sample each single reaction step (which compose the entire 4-multiple-step OER described in section 3.2) by means of the standard enhanced sampling DFT metadynamics technique based not anymore on the definition of the "contact matrix" (seen in chapter 6) but on the choice of a proper reaction coordinate(s) able to span the relevant reaction phase-space for each OER step. The choice of the reaction coordinate(s) for each OER step is showed and discussed in section 7.5. In the here adopted metadynamics scheme, the hills of potential energy are made of Gaussians with widths  $\sigma_s = 0.02$  and  $\sigma_z = 0.10$  and having heights of decreasing values from 15 kJ/mol to 1 kJ/mol deposited every 40 fs.

Since we adopted CV (collective variables) metadynamics in its well-tempered fashion [66], the Gaussian potential height was automatically reduced during the exploration of the configurational space as the filling procedure progressed.

## 7.2 CoO(OH) cobalt oxide bulk properties

Following the theoretical reference study provided by Selloni *et al.* [224] and described in section 4.19, we consider the more common CoO(OH) heterogenite-3R form, whose trigonal unit cell exhibits a total of 12 atoms, 3  $Co^{3+}$ , 6  $O^{2-}$  and 3 H, as depicted in Fig. 7.1-a. Within this heterogenite 3R structure, the CoO(OH) trigonal unit cell (R3m space group) is identified with sides  $a = b = 2.85 \text{ \AA}$ ,  $c = 13.15 \text{ \AA}$  [199], and angles  $\alpha = \beta = 90^\circ$ ,  $\gamma = 120^\circ$  (see Fig. 7.1-a).

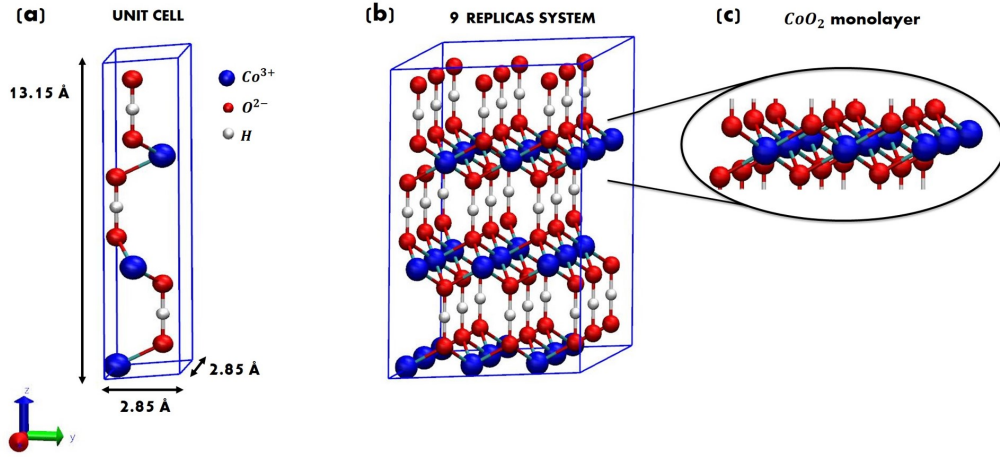


Figure 7.1: (a)  $CoO(OH)$  trigonal unit cell: 12 atoms, 3  $Co^{3+}$ , 6  $O^{2-}$  and 3 H. (b) 9-Replicas of the  $CoO(OH)$  unit cell along x-y directions: 108 atoms, 27  $Co^{3+}$ , 54  $O^{2-}$ , 27 H. (c) Monolayer of  $CoO_2$ : each  $O^{2-}$  ion is 3-fold coordinated to  $Co^{3+}$  ions

In particular, the trigonal geometry shows  $Co^{3+}$  ions sandwiched between two (upper and lower) layers of  $O^{2-}$  ions as depicted in Fig. 7.1-c. Each  $O^{2-}$  ion is 3-fold coordinated to  $Co^{3+}$  ions, leading to a  $\mu_3$ -O site. This sandwich structure is identified as a monolayer of  $CoO_2$ , wherein oxygen ions undergo hydroxylation, resulting in H-atoms located between the  $CoO_2$  layers, to finally form the CoO(OH) structure (in Fig. 7.1-a,b), with an hexagonal pattern called Heterogenite-3R structure [223, 325].

We start by considering the CoO(OH) solid bulk properties. Since all the DFT-MD calculations (geometry optimization and molecular dynamics) have been done here in a supercell approach (calculations at the  $\Gamma$ -point only), we follow the scheme already described in section 5.2 to define the supercell dimensions, *i.e.* the number of unit cell replicas (in the 3D space) needed to correctly reproduce experimental values, here evaluated as a function of lattice parameters and electronic band gap (as for bulk  $Co_3O_4$ , see section 5.2).

The geometry optimizations of the cell parameters (lattice and angles) and the CoO(OH) bulk structures give us an optimized trigonal unit cell having dimensions  $a=b= 2.78 \text{ \AA}$ ,  $c= 13.11 \text{ \AA}$  and  $\alpha = \beta = 90^\circ$ ,  $\gamma = 120^\circ$ , in very good agreement with the aforementioned experimental data  $a=b= 2.85 \text{ \AA}$ ,  $c= 13.15 \text{ \AA}$  [199], angles  $\alpha = \beta = 90^\circ$ ,  $\gamma = 120^\circ$  (see Fig. 7.1-a).

Subsequently, projected density of (electronic) states (PDOS) have been obtained on the optimized unit cell (12 atoms), 9 replicas (108 atoms), 16 replicas (192 atoms), 25 replicas (300 atoms) and 36 replicas (432 atoms) of the optimized unit cell, respectively. The PDOS convergence to the experimental band-gap value of 1.7 eV [222] is tested as a function of the number of replicas as well as different values of the Hubbard U term (DFT+U framework): results are reported in Fig. 7.2.  $U = 3.0 \text{ eV}$  and  $U = 5.0 \text{ eV}$  are chosen following the reference paper by Selloni *et al.* [224], which shows PDOS calculations for both the metallic ( $U=3.0 \text{ eV}$ ) and insulating ( $U=5.0 \text{ eV}$ ) cases on the CoO(OH) primitive cell (described in section 4.19).  $U = 6.3 \text{ eV}$  is chosen as the converged U value for which we obtain the expected semi-conductor band-gap value of 1.7 eV for the CoO(OH) (16 and 25) replicas systems.

	BAND GAP (eV) (U= 3 eV)	BAND GAP (eV) (U= 5 eV)	BAND GAP (eV) (U= 6.3 eV)
<b>UNIT CELL</b> (12 ATOMS) [2.78 x 2.78 x 13.11] Å	UNCORRECT BAND-GAP ( $\vec{k}$ -points would be needed)	NO-CONVERGENCE ( $\vec{k}$ -points would be needed)	NO-CONVERGENCE ( $\vec{k}$ -points would be needed)
<b>9 REPLICAS</b> (108 ATOMS) [8.34 x 8.34 x 13.11] Å	0.7	1.4	1.8
<b>16 REPLICAS</b> (192 ATOMS) [11.12 x 11.12 x 13.11] Å	0.4	1.2	1.7
<b>25 REPLICAS</b> (300 ATOMS) [13.9 x 13.9 x 13.11] Å	0.85	1.2	1.7
<b>36 REPLICAS</b> (432 ATOMS) [16.68 x 16.68 x 13.11] Å	0.7	1.3	1.6

Figure 7.2: Table: band gap values of bulk CoO(OH) as a function of Hubbard U values in the DFT+U framework computed for the CoO(OH) unit cell system and its replicas (supercells). The experimental band-gap is 1.7 eV [222].

While the lattice parameter of the unit cell is already converged (within our numerical error) in our geometry optimizations, the band gap is more sensitive to finite size effects (*i.e.*, sensitive to the Brillouin zone sampling), and to the U value employed. For each U value, the 9 replicas and the 36 replicas systems systematically respectively overestimate and underestimate the band gap value, while the 16 and the 25 replicas systems have the expected band-gap value of 1.7 eV only when using a U value equal to 6.3 eV. The 25-replicas system (see Figure 7.3-a, 300 atoms) is thus the best compromise between accuracy, minimizing computational cost and minimum lateral area required to carefully simulate bulk liquid water above the CoO(OH) solid structure, cor-

rectly reproducing both experimental band gap (see Figure 7.3-b) and lattice constants.

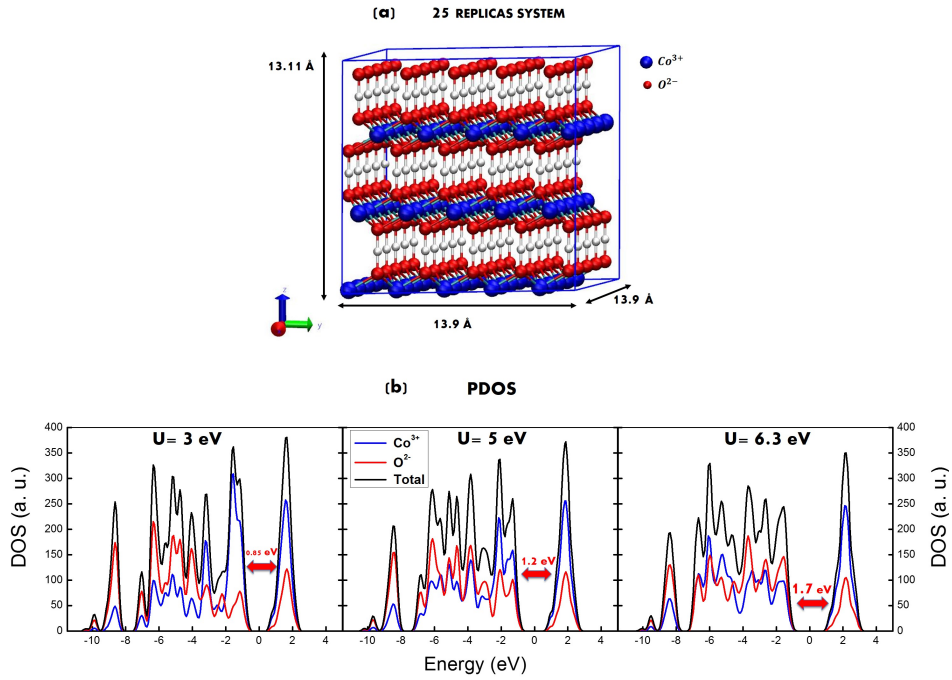


Figure 7.3: (a) 25 replicas model of bulk  $\text{CoO}(\text{OH})$  supercell: 300 atoms, 75  $\text{Co}^{3+}$ , 150  $\text{O}^{2-}$  and 75 H. (b) Projected density of states (PDOS) from PBE+U calculations for this 25 replicas bulk  $\text{CoO}(\text{OH})$ . The Fermi energy level is set to 0, by construction. The experimental band-gap value of 1.7 eV [222] is correctly reproduced using a value of  $U=6.3$  eV (Fig. 7.2).

Accordingly, Maximally Localised Wannier Functions (MLWF) [318] analyses (described in section 4.15 and already adopted in section 6.3) have been performed on the 25 replicas system ( $a=b=13.9$  Å,  $c=13.1$  Å, and  $\alpha = \beta = 90^\circ$ ,  $\gamma = 120^\circ$ ) to ensure that we have the correct electronic states for all the  $\text{Co}^{3+}$ ,  $\text{O}^{2-}$  and H species of the  $\text{CoO}(\text{OH})$  bulk oxide, confirming the correct description of the electronic structure of the system in using the adopted computational set-up.

### 7.3 (0001)-CoO(OH) Cut of CoO(OH) oxide

The 25-replicas bulk supercell (in Fig. 7.4-a) will thus be used as our CoO(OH) bulk model for the next steps, consisting first in cutting the bulk CoO(OH) oxide along the (0001) direction, and ultimately put the hence created surface in contact with liquid water.

When the CoO(OH) bulk solid is cut along the (0001) crystallographic symmetry plane (Figure 7.4-a), the surface exposes 25  $\mu_3$ -OH sites, as depicted in Fig. 7.4-b, where each surface O forms 3 covalent bonds (3-fold coordinated) with  $Co^{3+}$  ions. We chose this surface hydroxylation instead of the bare-oxygen surface, as the surface will be in contact with liquid water and hence the oxygens will become hydroxylated. Note that we chose to also do the following in the construction of the box: the cutted (surfacial) O-layer is transferred at the bottom of the box as a bottom O-layer (Fig. 7.4-b), to maintain the charge neutrality of the simulation box.

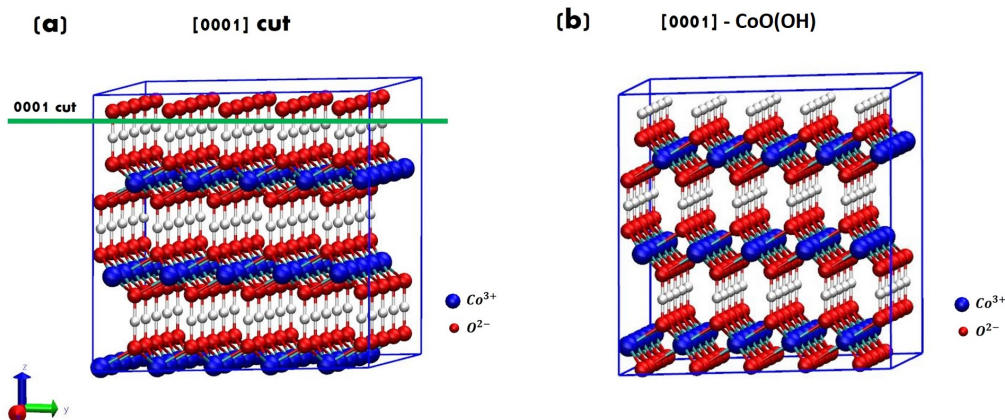


Figure 7.4: (a) *CoO(OH)*-25 replicas bulk supercell cut along the (0001) crystallographic plane (in green). (b) The (0001)-*CoO(OH)* is composed of a 12-layers asymmetric slab (H-layer at the top, O-layer at the bottom) in the simulation box. Oxygens are in red, hydrogens in white, Co(III) in blue.

We are now interested in evaluating the real proton surface coverage and accordingly, we model slabs of (0001)-CoO(OH) corresponding to different proton concentrations at the surface in contact with the air: one fully covered (100%) by protons (H-terminated surface)- Fig. 7.5-a, one half-covered (50%) by protons (1  $\div$  2 ML coverage surface)- Fig. 7.5-b, one 1  $\div$  4 (25%) covered by protons- Fig. 7.5-c, and finally one with no protons (0 %) on top (bare O-terminated surface)- Fig. 7.5-d. The number of hydrogen atoms is maintained equal in all boxes by putting the "removed" H atoms from top surface to the bottom surface. Moreover, we remove the H atoms from the top surface in order to create surface areas exposing 3-deprotonated neighbor sites (*i.e.* neighbor  $\mu_3$ -O sites), a mandatory precondition (see section 6.2) for the OER to occur at the (0001)-CoO(OH) (section 7.5).

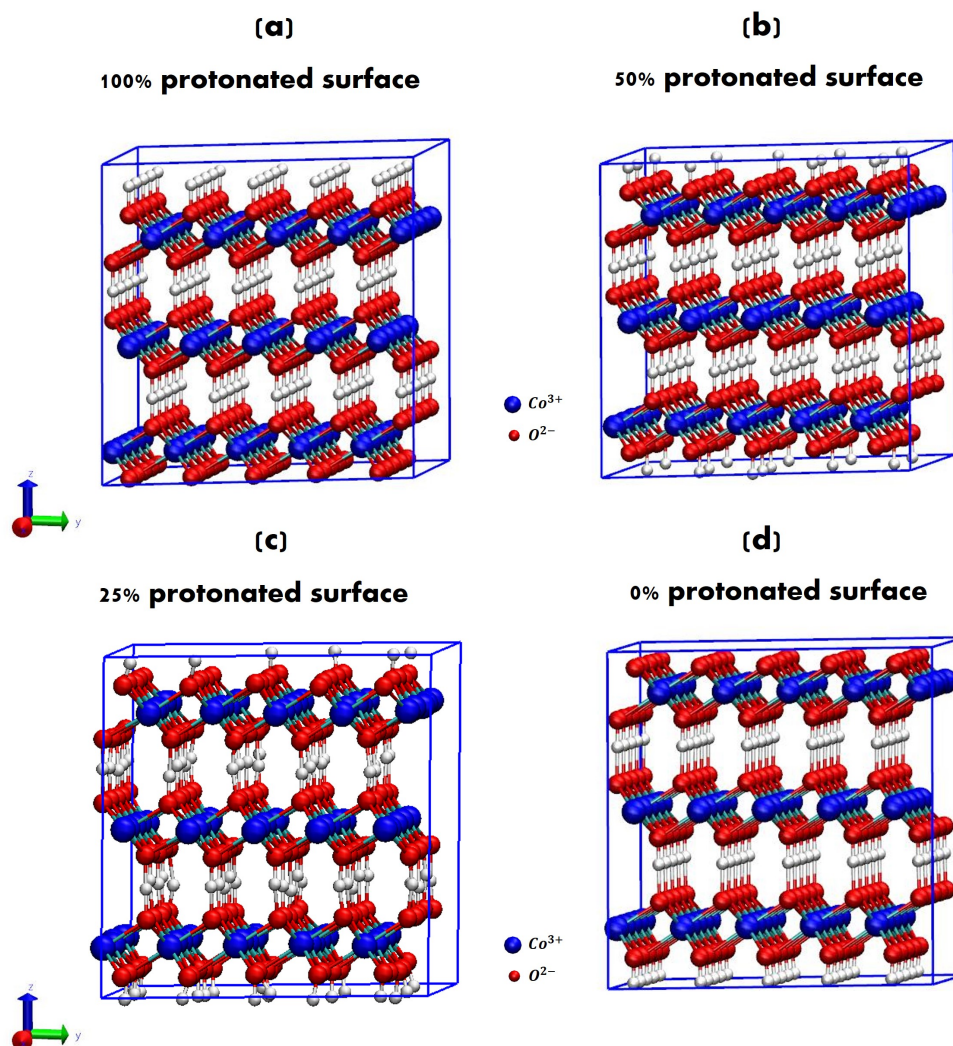


Figure 7.5: Side views of  $(0001)\text{-CoO(OH)-air-interfaces}$  modeled with different  $H$ -surface coverages. Follow the top surface for its correspondance to the % of  $H$ -coverages.

We next put these slabs in contact with liquid water, see Fig. 7.6 for an illustration of the typical simulation box. Each  $H$ -covered  $(0001)\text{-CoO(OH)}$  system (in Fig. 7.5) is now put in contact with bulk liquid water and hence an entire slab of 120 water molecules is added into the simulation box, as depicted in Fig. 7.6, with the focus of finding the stable surface speciation/hydroxylation. For the reasons already explained in sections 5.3 and 6.1, a choice is made here to include a  $17 \text{ \AA}$  vacuum above the liquid water in the vertical  $z$ -direction, illustrated by the simulation box in Fig. 7.6.

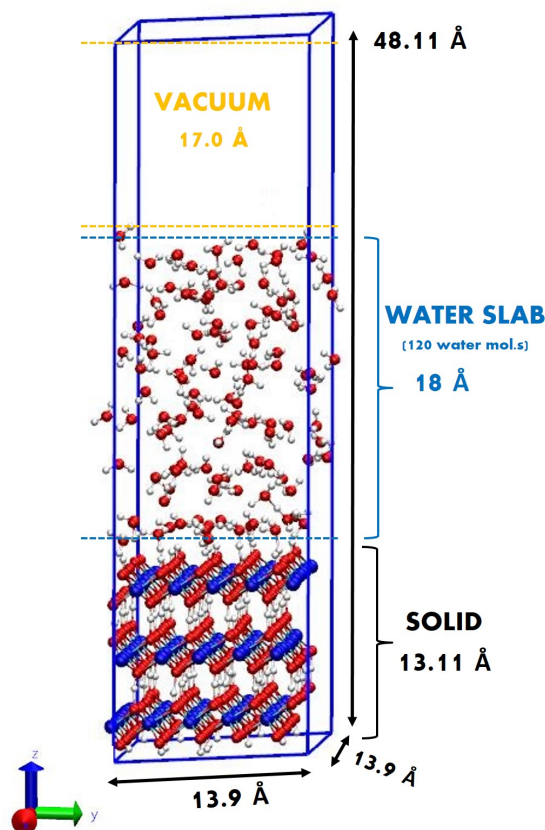


Figure 7.6: Illustration of a simulation box for the DFT-MD of (0001)-CoO(OH)-liquid water interface: 300 solid atoms, 120 water molecules. Choice is made here to include a 17 Å vacuum above the liquid water in the vertical z-direction, in order not to simulate confined water due to the PBC applied in all 3-directions of space. Only one surface is put in contact with liquid water. The other surface (at the bottom) is in contact with vacuum.

As depicted in the table in Fig. 7.7, only the one-half (50%) H-covered surface is stable during the DFT-MD simulation time of around 30 ps –same result obtained in Selloni’s work [224] on CoO(OH), described in section 4.19. The other modeled H-covered surfaces (100%, 25%, 0 % H-coverage) are undergoing interface reactions such as proton hoppings from water to the surface, and surface oxygen desorptions which deeply modify not only the initial H-coverage (described in Fig. 7.7) but also the surface patterns and hence the chemistry of the surface. As example, the DFT-MD simulation of the 25% H-coverage shows that this surface remains more or less unmodified in terms of H-coverage when exposed to liquid water (see 25% coverage that becomes 28% in table 7.7), but surface oxygen desorption events deeply modify the initial chemistry of the surface, hence exhibiting the instability of this surface.

Thus, we infer from these DFT-MD simulations that the most stable (0001)-CoO(OH) surface is the one with 50% H-coverage, which speciation/hydroxylation hence exposes 12  $\mu_3$ -OH sites and 13  $\mu_3$ -O sites in our simulation box,

H- Surface Coverage	 + $H_2O$ liquid water in the box	Final H- Surface coverage	Final no. of surface $\mu_3$ -OH sites
0% (zero H)		28% (7 H)	7 $\mu_3$ -OH
25% (6 H)		28% (7 H)	7 $\mu_3$ -OH
50% (12 H)		50% (12 H)	12 $\mu_3$ -OH
100% (25 H)		90% (23 H)	23 $\mu_3$ -OH

Figure 7.7: Table: H-surface coverage for the (0001)-CoO(OH) models in the absence (on the left) and in the presence (on the right) of liquid water.

as depicted in the surface pattern shown in Fig. 7.8. Note that these surface patterns might change in time with surface-surface proton hopping, leaving the 50% H-coverage percentage unmodified.

[0001]- CoO(OH)  $\frac{1}{2}$  ML H-covered surface

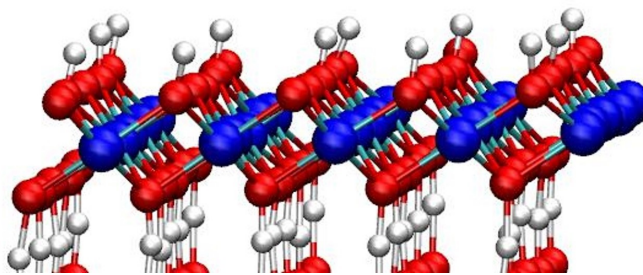


Figure 7.8: Surface motif of the 50% H-covered (0001)-CoO(OH) surface at the interface with liquid water (liquid water not shown in the picture for clarity).

## 7.4 Water structure at the (0001)-CoO(OH)/liquid water interface

We now work with the (0001)-CoO(OH) surface 50% H-coverage, and we follow the procedure already explained in section 5.5 to identify the organization of water into the three universal layers denoted BIL (Binding Interfacial Layer), DL (Diffuse Layer) and Bulk liquid water. To reveal BIL, DL and bulk water from molecular dynamics simulations (ab initio and classical MD alike [241, 276, 277]) three theoretical descriptors are used, based *only* on water structural properties (more details in section 5.5). The procedure and the descriptors were already tested and validated in previous works of the group for several water interfaces [241, 242, 276, 277]. We refer the reader to ref. [241] for all details and to section 5.5 for the main ideas. Thus, the methodology is here directly applied at the 50% H-coverage (0001)-CoO(OH)/liquid water interface. The DFT-MD trajectories used here for this analysis are 30 ps in time length. The first descriptor used in the characterization of the three water layers is the water density profiles at the 50% H-coverage (0001)-CoO(OH)

surface in contact with liquid water, calculated as a function of the vertical z-distance from the surface (the density profile is calculated using Willard and Chandler’s Instantaneous Surface [283]), see the top of Fig. 7.9.

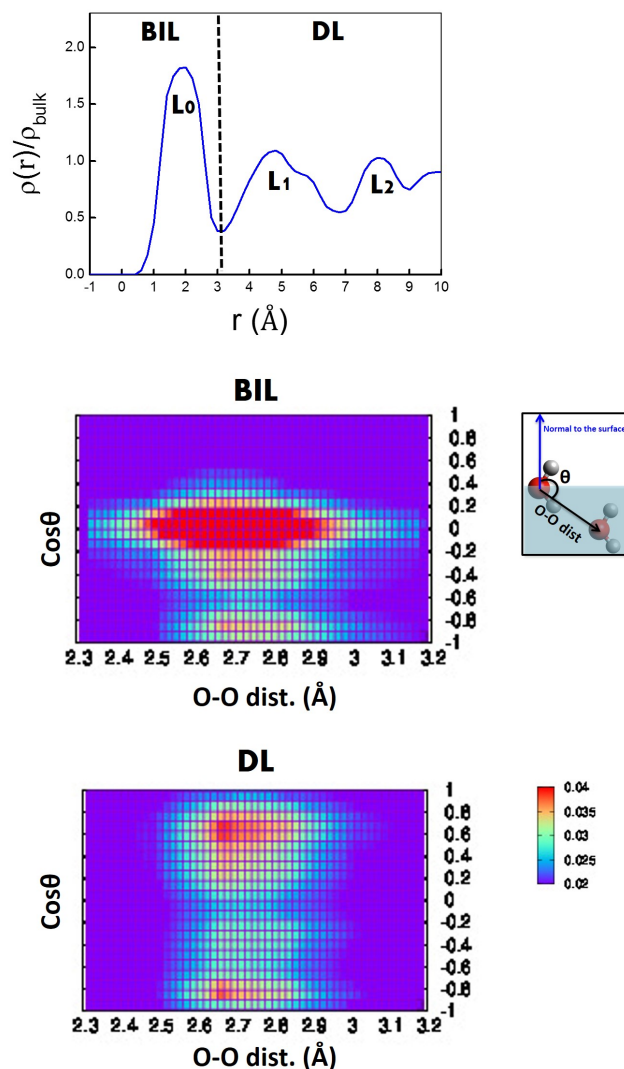


Figure 7.9: Top: Water density profiles calculated as a function of the distance from the 50% H-covered (0001)-CoO(OH) cobalt oxide surface (using Willard & Chandler’s instantaneous surface method [283]). Middle & Bottom: 3D-contour plots of the simultaneous probability for water-water H-Bonds to have a given distance (horizontal axis) and given angle (vertical axis). The convention for the O-O distance and angle  $\theta$  definitions is in the inset scheme. The normal to the surface goes towards the solid. The middle plot is for the water located in the BIL (Binding Interfacial Layer), the bottom plot is for the water located in the DL (Diffuse Layer). See text for correspondence between layers L0-L2 and BIL/DL. See ref. [241] for the reference 3D plot for bulk liquid water (homogeneous distribution of HB angles within the 2.6-2.9 Å HB distances).

The 1st descriptor density profile is reported over half of the water box

only, the zero in  $r$  is the instantaneous water surface,  $r$  measures the (vertical) distance from the surface (see Fig. 7.6 for the simulation box). One can observe 3 layers of water, labelled L0-L2. While layer L0 systematically has a higher density than in the bulk (e.g.  $\sim 1.8$  higher), the density of bulk water is on average already recovered in L1-L2 layers.

Applying the definitions described in section 5.5 for the three descriptors of water, L1-L2 water layers constitute the DL Diffuse Layer (roughly 6 Å thick). In these layers, the water density is roughly the liquid water's 1 g/cm<sup>3</sup>, and the water molecules make 3.6 HBs/molecule, equal to bulk liquid water (as obtained from the reference DFT-PBE-D2 MD simulation done in this work on bulk water), which are two necessary descriptor values for the identification of the DL water layer.

The other descriptor necessary to reveal the DL is the non-isotropicity of the water-water HB network in this region of space, which is indeed shown in the bottom of Fig. 7.9 with the 3D-contour plots averaged over L1 and L2 layers. One can indeed observe in these plots that there is a certain background of homogeneous distribution of the HB orientations within the 2.6-2.9 Å HB distances that is revealed by the green-blue-ish color, which is reminiscent of bulk liquid water, while the red contour spots reveal a preferred orientation of the HB network in these layers. This corresponds to the HB network of the liquid water which exhibits an in-plane preferred orientation (cosine values of the  $\theta$  angle is in the range  $-0.6/+0.4$ , see the red spot, for HB distances in between 2.6-2.9 Å). Layer L0 is the BIL water layer, for which the calculated water density is much higher than 1.0, and in the related 3D contour plot one can observe that there is no background of homogeneous HB orientations but there is, on the contrary, one single strongly preferred orientation of the HBs, revealing specific hydrogen bonds in between the water molecules (and indirectly possibly revealing HBs between water and the solid surface).

There is one clear single orientation for water-water HBs in the BIL with cosine values in the range  $-0.2/0.2$  for 2.6-2.9 Å HBs distances: the water molecules in the BIL preferentially form in-plane water-water HBs within themselves, so called INTRA-BIL HBs pointing out a highly connected HB water wire in the BIL plane. This should be analysed further, but this BIL-water seems reminiscent of the 2D-HB-Network that we already found at hydrophobic interfaces, especially at the air water [326] and at the (0001)-Al<sub>2</sub>O<sub>3</sub>-water interface [PhD manuscript of L. Poitier [327]]. However, for both BIL and DL contour plots in Fig. 7.9 one can distinguish a minority presence of red spots at  $\sim -0.4/-1.0$  cosines that correspond to BIL-DL HBs, *i.e.* inter-layers HBs formed between water molecules in the BIL and water in the subsequent DL. We have not analyzed yet further the structure of the BIL.



H-coverage (0001)-CoO(OH) surface, we removed the other initial 50% of H atoms from the top surface in order to create surface areas, hence exposing 3-deprotonated neighbor sites (*i.e.* neighbor  $\mu_3$ -O sites). Therefore, the here chosen  $\mu_3$ -O surface sites as potential OER surface catalytic sites, are naturally deprotonated in our 50% H-coverage (0001)-CoO(OH) surface. No deprotonation processes are thus needed, which removes one possible limiting step for the whole OER cycle (see chapter 6 for  $Co_3O_4$ ). The schematic representation of the chosen  $\mu_3$ -O surface sites that could be relevant for the water oxidation process at the (0001)-CoO(OH) surface is shown in Fig. 7.11.

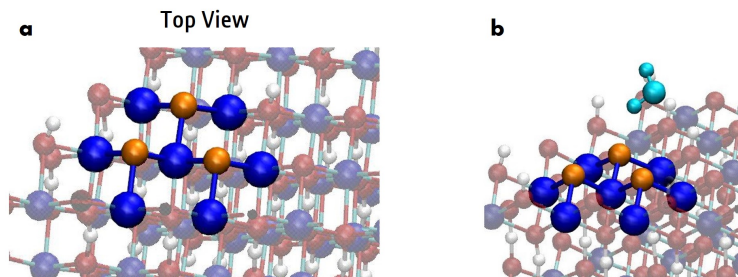


Figure 7.11: *Three neighbor  $\mu_3$ O surface sites chosen as possible potential OER catalyst sites at the (0001)-CoO(OH) surface (50% H-covered). Oxygen atoms O are in orange color.  $Co^{(3+)}$  atoms are in blue color. Light blue color identifies the reactant water molecule.*

Note that, the first results from our OER metadynamics simulations is that adjacent  $\mu_3$ -O sites (Fig 7.11), *i.e.* the naturally deprotonated surface sites present at the (50% H-covered) (0001)-CoO(OH) surface, are indeed reactive OER catalyst sites whether at the air or liquid phase interface.

Once we have chosen the  $\mu_3$ -O surface sites (Fig. 7.11), we follow the methodology described below for the OER metadynamics:

- 1) we consider the OER steps 2-4 shown in the OER scheme in Fig. 7.10, *i.e.* step 2= water deprotonation and -OOH formation; step3 = 2<sup>nd</sup> water deprotonation and O=O formation; step 4=  $O_2$  desorption from the catalyst surface;
- 2) each OER step 2-4 is now investigated using a standard metadynamics technique (implemented in the PLUMED-2.x software package [307]) both in the gas-phase and the liquid-phase, see point 4 hereafter for details;
- 3) we perform different metadynamics for each OER step 2-4 (Fig. 7.10). Note that we divided the reaction step 2, *i.e.* water deprotonation and -OOH formation, into 2 sub-steps called 2-a and 2-b as depicted in Fig. 7.12: 2-a for the water deprotonation and 2-b for the -OOH formation;
- 4) in order to sample each single reaction step 2-4 (Fig. 7.10) via DFT metadynamics, we need to choose one or several reaction coordinate(s) able to span the relevant reaction phase-space for each OER step. We have chosen one single interatomic distance for each reaction step 2-4. Hence, for each metadynamics of step 2-4, we change the selected interatomic distance depending

on the reactants involved in the reaction step. The selected atomic distance for each OER step 2-4 is depicted and discussed in Fig. 7.12 (follow the red arrows).

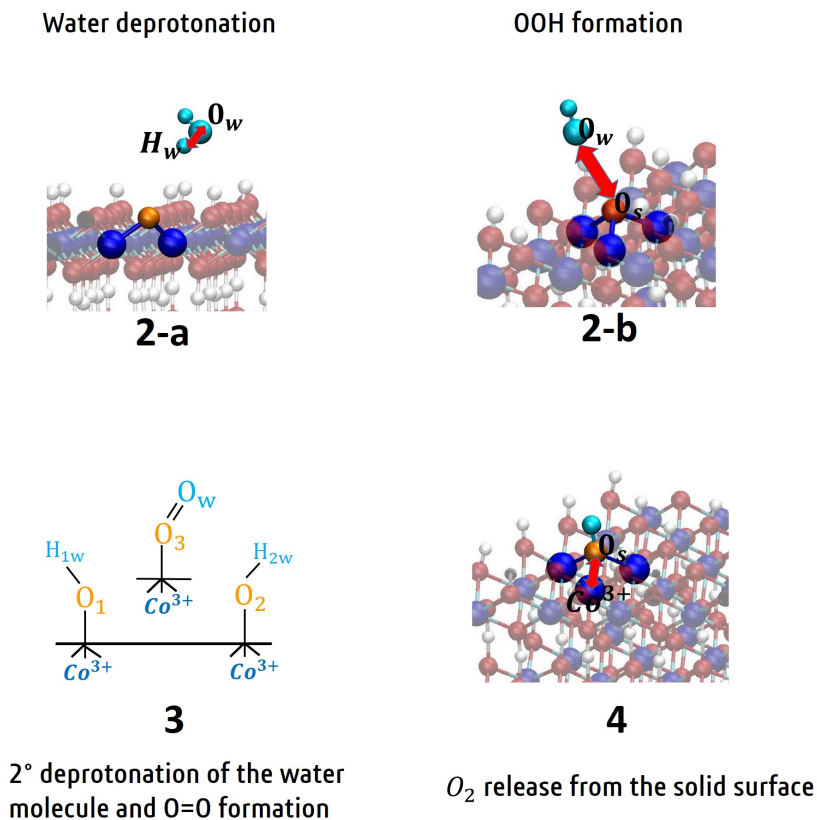


Figure 7.12: Snapshots from metadynamics simulations of the  $O_2$  gas formation through the water attack and its dissociation pathway (see Fig. 7.10). Orange, blue, and light blue colors refer to O catalyst surface sites,  $Co^{(3+)}$  cations, and the water molecule, respectively. The red arrow identifies the interatomic distance chosen as reaction coordinate at each OER reaction step 2-4.

2-a) deprotonation of the reactant water molecule above a  $\mu_3O$  surface site: the chosen reaction coordinate is the distance between the  $O_w$  and the  $H_w$  of the reactant water molecule.

2-b) -OH surface attack with the formation of the surface radical  $Co^{(3+)}-OOH$  group: the chosen reaction coordinate is the distance between the -OH and the surface oxygen  $O_s$  of the  $\mu_3-O$  site.

3) 2<sup>nd</sup> water deprotonation, i.e. a proton jump from the  $Co^{(3+)}-OOH$  radical group to a neighbor  $\mu_3-O$  surface site: note that we skip this step 3 from the metadynamics investigation only because, from previous investigation on the  $Co_3O_4$  (chapter 6), we have learned that the energy barrier of this step 3 is comparable to the energy barrier already investigated in step 1 for the water deprotonation.

4)  $O_2$  desorption from the catalyst surface: the chosen reaction coordinate is the distance between the  $Co^{(3+)}$  and the  $O=O$  radical of the  $Co^{(3+)}-OO$  surface group.

With the aim to fully characterize the OER at the (0001)- $CoO(OH)$  surface

(50% H-covered), the free-energy activation barrier and the associated overpotential are therefore calculated for each OER step 2-a, 2-b and 4 shown in Fig. 7.12. The OER gas-phase metadynamics free energy profiles for the reaction steps 2-a, 2-b and 4 are shown in Fig. 7.13.

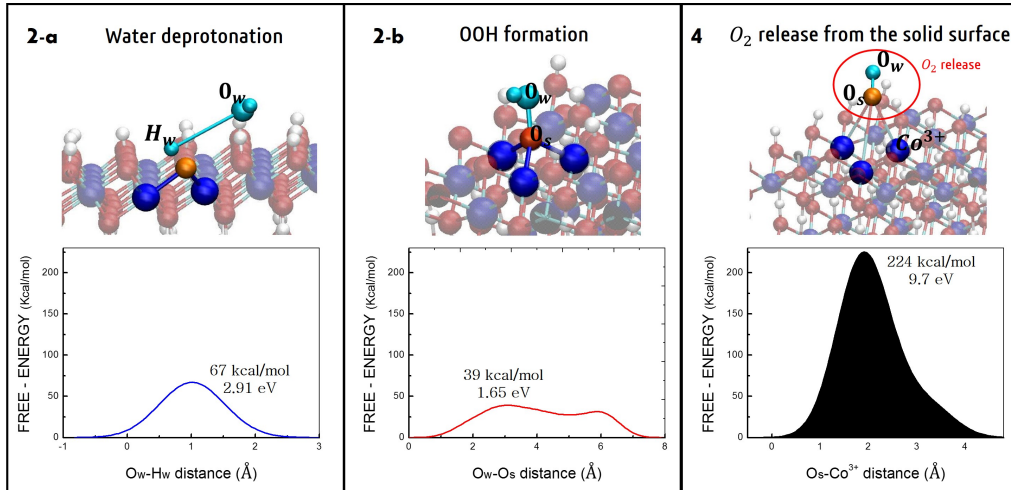


Figure 7.13: *Instantaneous snapshots from metadynamics simulations of the successive events for the OER at the (0001)-CoO(OH)-air surface (50 % H-coverage) and the associated free-energy profiles of the OER reaction steps. 2-a) deprotonation of the water molecule above a  $\mu_3$ -O surface site and the associated free-energy landscape at the bottom. 2-b) -OH attack with the formation of the surface radical  $\text{Co}^{(3+)}\text{-OOH}$  group and the associated free-energy landscape at the bottom. 4)  $\text{O}_2$  desorption from the catalyst surface and the associated free-energy landscape at the bottom. Orange, blue, and light blue coloring refer to O catalyst surface sites,  $\text{Co}^{(3+)}$  cations, and the reactant water molecule, respectively. The free-energy scale is in kcal/mol. The values on the free-energy profiles are the barriers expressed in kcal/mol and in eV.*

The rate-limiting step of the gas-phase OER at the (0001)-CoO(OH) is given by step 4, *i.e.* the  $\text{O}_2$  desorption process from the surface (Fig. 7.13-4): a huge free-energy barrier of 224 kcal/mol (9.7 eV) has to be overcome in that step. With such a large energy for this limiting step, a huge overpotential  $\eta = [(9.7 \text{ eV}/1 e) - 1.23 \text{ V}] = 8.47 \text{ V}$  has to be applied for the OER to occur at the (0001)-CoO(OH) surface (50% H-covered) in gas-phase conditions, making the CoO(OH) a non relevant OER catalyst.

As already done for the OER at the (110)- $\text{Co}_3\text{O}_4$  B-surface in section 6.3, we now evaluate the OER free-energy barrier and the OER rate-limiting step (and hence the OER overpotential) in presence of explicit liquid water at the (50% H-covered) (0001)-CoOOH/liquid water interface. In order to analyze the OER kinetics and the associated free-energy profiles, the metadynamics setup shown in Fig. 7.12 (with the already chosen reaction coordinates for each OER step 2-a, 2-b, 4), has been re-adopted in the here investigated OER in the condensed phase. The OER liquid-phase metadynamics results for reaction steps 2-a, 2-b and 4 are shown in Fig. 7.14, with the same illustrative

snapshots and associated free-energy profiles as in Fig. 7.13.

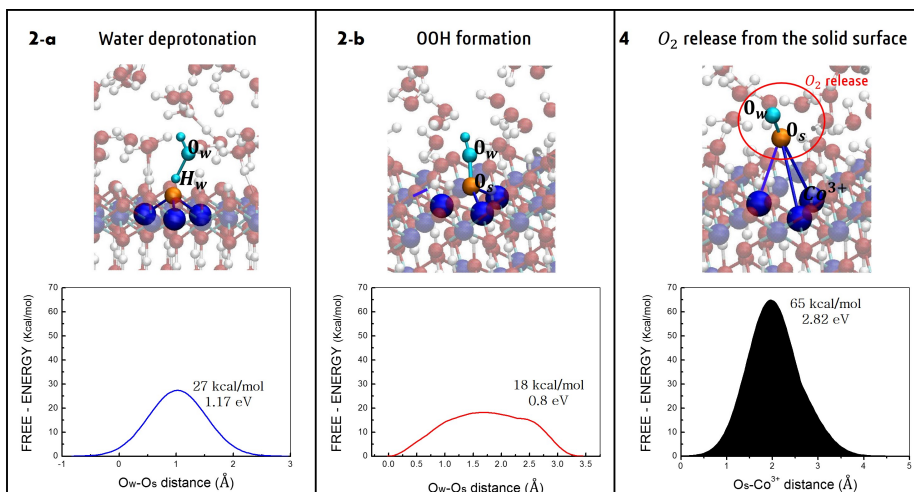


Figure 7.14: *Instantaneous snapshots from metadynamics simulations of the successive events for the OER at the (0001)-CoOOH/liquid water interface and the associated free-energy profiles of each OER step. 2a) deprotonation of the water molecule above a  $\mu_3\text{O}$  surface site and the associated free-energy landscape at the bottom. 2b)  $-\text{OH}$  attack with the formation of the surface radical  $\text{Co}^{(3+)}-\text{OOH}$  group and the associated free-energy landscape at the bottom. 4)  $\text{O}_2$  desorption from the catalyst surface and the associated free-energy landscape at the bottom. Orange, blue, and light blue coloring refer to O catalyst surface sites,  $\text{Co}^{(3+)}$  cations, and the reactant water molecule, respectively. The free-energy scale is in kcal/mol. The values on the free-energy profiles are the barriers expressed in kcal/mol and in eV.*

As already seen for the gas-phase OER investigation at this  $\text{CoO}(\text{OH})$  oxide, the liquid phase OER rate-limiting step is still identified as step 4, *i.e.* the  $\text{O}_2$  desorption process from the surface (in Fig. 7.14-4). However, the explicit presence of the interfacial aqueous environment leads to a lower free-energy barrier than in the gas phase situation, now equal to 65 kcal/mol (2.82 eV), and thus the overpotential  $\eta = [(2.82 \text{ eV}/1 e) - 1.23 \text{ V}] = 1.59 \text{ V}$ . It is around five times lower than the OER overpotential required in the gas-phase counterpart ( $\eta = 8.47 \text{ V}$ ) for the same  $\text{O}_2$  desorption process in step 4, but it is still very high.

Note that, for (110)- $\text{Co}_3\text{O}_4$  (chapter 6), we identified a pathway of lowest energy (Fig. 6.11) that involved water as co-catalyst. This is not the process measured here for  $\text{CoO}(\text{OH})$ , because the standard metadynamics technique adopted does not allow this process here. Contrarily to the "contact matrix" metadynamics method, described in section 2.9 and adopted in chapter 6 for  $\text{Co}_3\text{O}_4$ , the standard metadynamics technique used here (for the reasons explained in section 7.1) does not allow the knowledge of possible/alternative (not predefined) OER pathways at the  $\text{CoO}(\text{OH})$  surface/interface. We would need to explicitly include the alternative scenario in the choice of the reaction coordinate(s) to see it appears. This has not been done yet.

The larger OER overpotential values ( $\eta_{gas} = 8.47$  V,  $\eta_{liquid} = 1.59$  V) found at the (0001)-CoO(OH) 50% H-coverage surface in comparison with the values ( $\eta_{gas} = 0.91$  V,  $\eta_{liquid} = 0.31$  V) at the (110)-Co<sub>3</sub>O<sub>4</sub> B-surface, can be mainly ascribed to the identified OER catalyst surface sites. In particular,  $\mu_1$ -O site ( $O^*$  singly covalently bonded) is the OER catalyst surface site at the (110)-Co<sub>3</sub>O<sub>4</sub> whereas a  $\mu_3$ -O site ( $O^*$  triply covalently bonded) is found as the only possible OER catalyst site at the crystalline (no defects) (0001)-CoO(OH) surface. By adsorption and dissociation of the water onto one of these  $Co - O^*$  surface sites, the next step for the OER requires the desorption of the  $O = O^*$  and thus requires that the  $O^*$  desorbs by breaking its covalent bond(s) with the cobalt atom. Thus, the OER mechanism should have to break only one covalent bond at  $\mu_1 - O^*$  sites at the (110)-Co<sub>3</sub>O<sub>4</sub> B-surface, whereas it involves the breaking of 3 covalent bonds at  $\mu_3 - O^*$  sites to release  $O = O^*$  at the (0001)-CoO(OH) surface, as depicted for example in Fig. 7.14-4. The associated free energy barrier for the OER at the (0001)-CoOOH surface is therefore sizably much larger than the one of the process at the (110)-Co<sub>3</sub>O<sub>4</sub> B-surface, which exhibits only catalyst singly-bonded  $\mu_1 - O^*$  oxygen atoms at the surface.

Accordingly, we found an energy barrier of 120 kcal/mol (5.2 eV) to break the 3 covalent bonds of  $\mu_3 - O^*$  at the (0001)-CoO(OH) surface, see Fig. 7.15-top. However, an energy barrier of 'just' 28 kcal/mol (1.2 eV) is enough to break the single bond  $\mu_1 - O^*$  at the (110)-Co<sub>3</sub>O<sub>4</sub> B-surface, see Fig. 7.15-bottom.

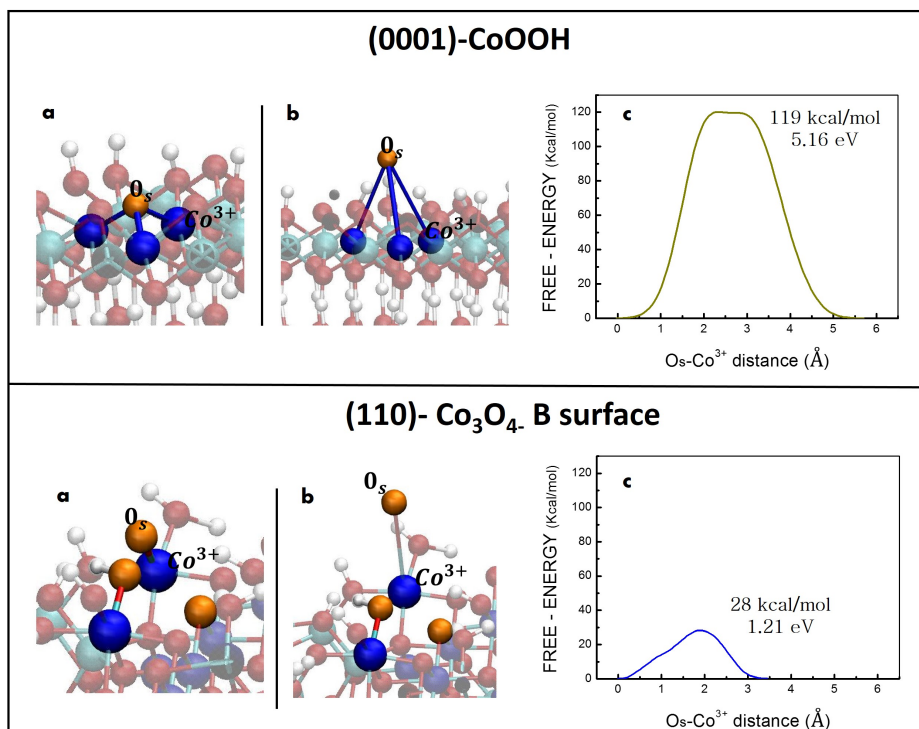


Figure 7.15: *Instantaneous snapshots from metadynamics simulations for measuring the free-energy of a surface O desorption at the (0001)-CoO(OH) surface, in the top, and at the (110)-Co<sub>3</sub>O<sub>4</sub> B-surface, in the bottom. Associated free-energy profiles of the process in panels c. a) Initial configuration. b) O desorption from the surface. c) Free-energy barriers. The free-energy scale is in kcal/mol. The values on the free-energy profiles are the barriers expressed in kcal/mol and in eV. The abscissa identifies the interatomic distance (in Å) chosen as reaction coordinate.*

## 7.6 Conclusions and Comparison between the (110)-Co<sub>3</sub>O<sub>4</sub> and (0001)-CoO(OH) oxides

To summarize, in the following table in Fig. 7.16 we compare the OER rate-limiting steps, the OER free-energy barriers and OER overpotential values calculated at the Co<sub>3</sub>O<sub>4</sub> (110) B-surface (chapter 6) and at the (0001)-CoOOH surface (50% H-covered) (chapter 7), when both surfaces are exposed to either one gas-phase water or to full liquid water.

<b>(110)- Co<sub>3</sub>O<sub>4</sub> B-surface</b>			
	<b>OER Rate Limiting Step</b>	<b>Free Energy Barrier</b>	<b>Overpotential <math>\eta</math></b>
<b>GAS PHASE</b>	Surface Deprotonation of $\mu_1\text{OH}$ site	49 kcal/mol 2.14 eV	<b>0.91 V</b>
<b>LIQUID PHASE-Path 1</b> (lowest energy pathway with water as co-catalyst)	Water Attack & Dissociation (2 $e^-$ process) at $\mu_1\text{OH}$ site	71 kcal/mol 3.08 eV (2 $e^-$ process)	<b>0.31 V</b>
<b>LIQUID PHASE-Path 2</b> (OER pathway <b>without</b> water as co-catalyst)	Water Attack & Dissociation (2 $e^-$ process) at $\mu_1\text{OH}$ site	180 kcal/mol 7.81 eV (2 $e^-$ process)	<b>2.68 V</b>

<b>(0001)-CoOOH , 50% H-coverage</b>			
	<b>OER Rate Limiting Step</b>	<b>Free Energy Barrier</b>	<b>Overpotential <math>\eta</math></b>
<b>GAS PHASE</b>	$\text{O}_2$ release from the solid surface (from $\mu_3\text{O}$ site)	224 kcal/mol 9.7 eV	<b>8.47 V</b>
<b>LIQUID PHASE</b>	$\text{O}_2$ release from the solid surface (from $\mu_3\text{O}$ site)	65 kcal/mol 2.82 eV	<b>1.59 V</b>

Figure 7.16: Computed OER rate limiting steps and associated free-energy barriers/overpotentials in the gas phase and in the liquid phase for both Co<sub>3</sub>O<sub>4</sub> (110) B-surface (chapter 6) and (0001)-CoO(OH) surface (chapter 7). Note that the surface of CoO(OH) is already deprotonated by half, thus there is no rate-limiting step associated to such process.

Firstly, looking at the overpotential values, we note that Co<sub>3</sub>O<sub>4</sub> (110) B-surface is definitely a better OER catalyst than the (0001)-CoOOH surface

(50%H-covered) in both gas-phase and liquid-phase environments –  $\eta_{Co_3O_4} = 0.91$  V *vs.*  $\eta_{CoOOH} = 8.47$  V in the gas phase and  $\eta_{Co_3O_4} = 0.31$  V *vs.*  $\eta_{CoOOH} = 1.59$  V in the liquid phase – with an OER overpotential 9 times less and 5 times less than CoOOH, in gas and in liquid phases, respectively. The exception is with the  $\eta_{Co_3O_4} = 2.68$  V (path-2 in Fig. 7.16) obtained for the OER pathway in the liquid phase, that if compared with the liquid phase  $\eta_{CoOOH} = 1.59$  V, shows that the  $\eta_{Co_3O_4}$  is larger than  $\eta_{CoOOH}$ . However, we remind the reader that the  $\eta_{Co_3O_4} = 2.68$  V was obtained for an OER pathway that is not the minimum energy path (see Fig. 6.10 to remind), and that the low  $\eta_{Co_3O_4} = 0.31$  V is obtained because water acts as co-catalyst.

Moreover, we remark again that the OER overpotential  $\eta_{Co_3O_4} = 0.31$  V, associated to the pathway of lowest energy found in the liquid phase (path-1 in Fig. 7.16), is comparable with the range value of  $\eta = [0.3 - 0.9]$  V [28] generally found for the OER when employing a high cost noble earth metal oxide such as RuO<sub>2</sub>, IrO<sub>2</sub>, and PtO<sub>2</sub> in particular conditions, *i.e.* in 0.1 M KOH. Here, the value of  $\eta_{Co_3O_4} = 0.31$  V was obtained at the neat interface. In addition, if we now look at the free energy barriers and the OER overpotential values obtained in the liquid phase (see Fig. 7.16), they are systematically lower than the values calculated in the gas phase, for both cobalt oxides investigated in this thesis, with the aforementioned exception of *path* – 2 (see table). This result strongly supports the importance of the explicit presence of liquid water as additional catalyst in the electrochemically-driven OER modeling. This is in agreement with the evidence that condensed-phase reactions are, in general, less demanding in terms of free energy [319, 320, 321].

We remind the reader that the present study not only provides an innovative state-of-the-art theoretical/computational strategy for the investigation of the OER, but it also quantitatively assesses the thermodynamics and the kinetics underlying the "minimum free-energy pathways" and it identifies the possible catalyst sites without ambiguity. In this context, we found 3 neighbor  $\mu_3$ -O sites ( $\mu_3$ -O: O 3-fold coordinated to Co<sup>(3+)</sup> ions) as OER catalyst sites at the (0001)-CoO(OH) surface (50% H-covered), as depicted in Fig. 9.3-left, while adjacent Co<sup>(3+)</sup>-OH, Co<sup>(3+)</sup>-O, Co<sup>(3+)</sup>-O-Co<sup>(3+)</sup> surface sites (respectively  $\mu_1$ -OH,  $\mu_1$ -O<sup>-</sup>, and inner  $\mu_2$ -O<sup>-</sup> sites) are able to catalyze the OER both in gas phase and in liquid water at the Co<sub>3</sub>O<sub>4</sub> (110) B-surface (see Fig. 9.3-right). Note that, a novel OER pathway –*i.e.* a water-assisted OER pathway (see section 6.3)– was found, for which water is explicitly involved in the OER mechanism at the B-surface (110)-Co<sub>3</sub>O<sub>4</sub>/liquid water interface (see Fig. 9.3-right).

We rationalized the increased OER overpotential values at the (0001)-CoO(OH) surface showing that we need a larger free energy barrier to break 3 covalent bonds in the catalyst surface site  $\mu_3$ -O (at the (0001)-CoO(OH) surface) than for breaking one single covalent bond in the  $\mu_1$ -O site at the Co<sub>3</sub>O<sub>4</sub> (110) B-surface: 120 kcal/mol (5.2 eV) *vs.* 28 kcal/mol (1.2 eV) free energy barrier values, respectively.

## OER - CATALYST SITES:

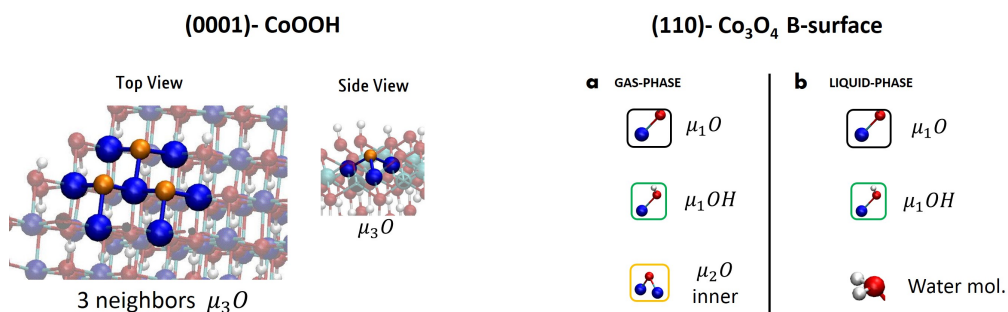
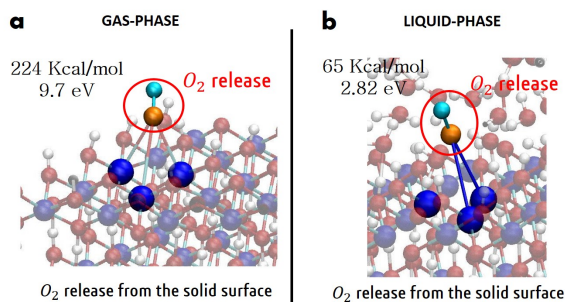


Figure 7.17: OER surface catalyst sites comparison between (0001)-CoO(OH) surface (chapter 7) –panels on the left– and Co<sub>3</sub>O<sub>4</sub> (110) B-surface (chapter 6) –panels on the right–. Oxygen atoms O are in orange color in the left panels and in red color in the right panels. Co<sup>(3+)</sup> ions are in blue color.

Accordingly, the O<sub>2</sub> desorption from the cobalt surface is systematically found as the rate limiting step at the (0001)-CoO(OH) surface in both gas-phase and liquid phase OER metadynamics, see Fig. 7.18-Top. Conversely, for the Co<sub>3</sub>O<sub>4</sub> (110) B-surface two different OER rate-limiting steps are found: the surface deprotonation in the gas phase condition and the water attack/dissociation reaction step at the interface with liquid water, see Fig. 7.18-bottom.

## OER-RATE LIMITING STEP:

### (0001)- CoOOH



### (110)- $Co_3O_4$ B-surface

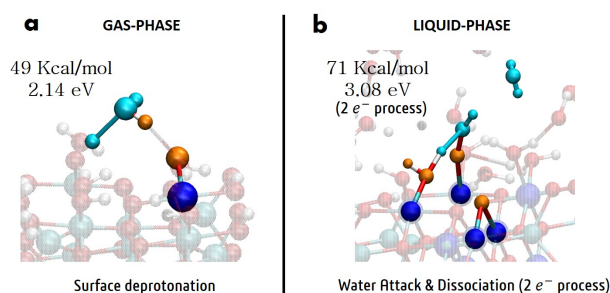


Figure 7.18: Comparison of the OER rate-limiting steps between (0001)-CoO(OH) surface –panels at the top– and  $Co_3O_4$  (110) B-surface –panels at the bottom–. Oxygen atoms O are in orange color.  $Co^{3+}$  ions are in blue color. Light blue color identifies the reactant water molecules. Free energy barrier is in kcal/mol and eV.

To conclude, we went beyond the OER gas-phase investigations from the literature [29, 31] introducing interfacial water in contact with the cobalt oxides (overcoming the modeling limits described in chapter 5), and in this context we found an unpublished OER pathway at the  $Co_3O_4$  (110) B-surface, where the explicit presence of liquid water is not only an additional catalyst able to decrease the OER free-energy barrier but water is directly involved in the OER acting as a reactant/co-catalyst in the electrochemically-driven OER. Only in this case, *i.e* when the water is explicitly involved in the OER pathway, one can reach the low value of the OER overpotential of  $\eta_{Co_3O_4} = 0.31$  V, which is comparable with the overpotential values obtained when using costly-noble-metals (denoted as our OER benchmark).

We do not exclude that the presence of  $\mu_2$ -O or  $\mu_1$ -O sites as possible surface defects at the (0001)-CoO(OH) surface (as pointed out in section 4.11 [199]) could decrease the energy of the rate-limiting step of the OER at the (0001)-CoO(OH) surface and thus make the OER easier, leading the (0001)-CoO(OH) surface to be a better OER catalyst than what we have found in this thesis. This should definitely be investigated, but we did not have time to investigate this issue in this PhD.

# Chapter 8

## Electrified H-bonded systems

In this last chapter, we change gears a little bit and we analyze the effects of a constant electric field on liquid water and other H-bonded liquid systems (see section 8.7) as well as on the air-water interface (see section 8.1).

The reason for each of these investigations are pointed at the start of each section. The investigation in section 8.1 for the air-water interface is done in the UEVE group in relation with other investigations achieved on this particular interface in the group, while the other investigations for H-bonded liquids are done in collaboration with Prof. A. M. Saitta at Sorbonne University-Paris, where such theme research started with an Erasmus internship in 2015, and is also pursued with Dr. F. Saija at CNR-IPCF in Messina-Italy. I have continued these collaborations during my PhD period at UEVE.

Though these investigations might appear disconnected from my main PhD subject of the OER at aqueous cobalt oxide interface, they are not totally disconnected. In particular, all of them rely on the application of an electric field to a medium, *i.e.* liquids and air-water interface, and the transformations onto the structures, chemistry, dynamics, proton transfers, conductivity, that thus field can induces. Applying an electric field is also part of electrochemistry, although this is not a constant field applied in all the simulation box as done in this chapter but rather it is a surface potential applied at the electrode that in turn gives rise to a complex field in the simulation box. Therefore these simulations presented in this chapter pave the way to the characterization of interfaces and liquids once we will be able to apply a constant surface potential on the electrode in the *ab initio* molecular dynamics simulations. We will come back to that issue in chapter 9 with our perspectives.

To the best of our knowledge, the following studies establish the current state-of-the-art on theoretical/*ab initio* simulations on H-bonded systems under extreme conditions, such as high electric fields.

## 8.1 Electric field applied on the air/water interface - Introduction

This has been published in our paper [328] *Enhanced conductivity of water at the electrified air–water interface: a DFT-MD characterization*, *Phys. Chem. Chem. Phys.*, 22, 10438, 2020.

The structure of liquid water at the interface with the air is an essential key to rationalize and characterize chemical and physical phenomena observed at such an interface, among which proton trapping and hopping along "water wires" [329], charge separation/recombination processes [330, 331], change in acidity/basicity with respect to bulk water [332, 333], the atypical Pockels effect [334], and surface tension [335].

Hassanali *et al.* [329] reported the high affinity of protons for the interface especially in terms of specific proton hopping pathways at the air-water (AW) interface, with protons exchanged between water molecules belonging to the first interfacial layer, via water wires running parallel to the surface. This result strongly suggests that a certain ordering of the water molecules within the surface plane is present at the AW interface. In a recent paper [326] of the group – combining Density Functional Theory-based molecular dynamics simulations (DFT-MD) and non-linear vibrational Sum Frequency Generation (vSFG) spectroscopy – is shown that such an order consists of a two-dimensional (2D) H-bonded network (denoted hereafter as "2DN"), connecting the vast majority of the interfacial water molecules (on average more than 90%) through water-water H-bonds/wires oriented parallel to the instantaneous water surface [336, 337]. Furthermore, due to the additional constraint imposed by the preferential H-bonds orientation, water molecules in the 2DN have less degrees of freedom for rotation and libration, which were shown to result in a slower orientational dynamics of the interfacial water molecules and, at the same time, to more dynamical H-bond breaking/reforming processes than in bulk liquid water [336]. The structure and dynamics of the 2DN thus provide a framework for the preferential direction of the above-mentioned proton hopping reported in refs.[329, 338] Interestingly, a recent MD simulation of the AW interface has shown that the application of an electric field perpendicular to the interface induces a less efficient reorientation of water molecules than a field applied parallel to the surface [339]. However, the way in which the local structure of interfacial water changes in response to an external static electric field, and how this can affect proton hoppings, remains poorly understood both at the molecular and macroscopic levels.

We hence report here on the first, to the best of our knowledge, *ab initio* MD study of the microscopic effects produced by an external static and homogeneous electric field applied at the AW interface and oriented parallel to the water surface (*i.e.* along the  $-x$  direction in the simulation box). We reveal the possible perturbations in the 2DN at the AW interface under the influence of an external electric field and the consequence on proton hoppings at the

electrified interface. Beyond proton hopping, we also characterize the electric conditions for the protolysis reaction  $2H_2O \rightleftharpoons OH^- + H_3O^+$  to occur, where formally a proton transfer between two water molecules gives rise to the formation of hydroxide ( $OH^-$ ) and hydronium ( $H_3O^+$ ) ions. The protolysis reaction is however a rare event, and interestingly Saitta *et al.* [340, 341] have shown that it is possible to stimulate the proton transfer process in bulk (liquid and ice) water – and hence, to investigate protolysis in a more systematic fashion – by applying a static external electric field. Based on ref. [340] for liquid water, the electrostatic coupling of interfacial water with an external electric field is expected to perturb the interfacial H-bonded network, hence possibly affecting proton transfers, water dissociation and protolysis at the AW interface.

An information that can be readily gained upon applying sufficiently strong electric fields are the effective thresholds associated respectively with the onset of proton transfers and with the onset of molecular dissociation. In liquid water, fields of  $\sim 0.25$  V/Å are needed to induce proton transfers and molecular dissociations of water along the 3D H-bonded network [342, 340, 343, 344], whereas a field intensity of at least 0.35 V/Å has to be applied in order to establish a measurable protonic current [340]. A further and correlated consequence of the application of static electric fields to liquid water is the gradual alignment of an increasing fraction of molecular dipole moments along the field direction [345]. Moreover, as very recently demonstrated by monitoring the IR and Raman spectra of electrified liquid water via *ab initio* MD [346], static electric fields of intensities beneath the molecular dissociation threshold induce structural changes in the H-bonded network and in the water tetrahedrality, in that the water structure becomes more ice-like.

In the following, we show how the proton conductivity is enhanced by the presence of the specific 2DN at the air-water (AW) interface under external fields. The following is organized as follows. In section 8.2 we present the methodology, sections 8.3-8.5 report results on the protonic current density-voltage diagram and the structural effects introduced by the external field applied parallel to the air-water 2DN interfacial network. We provide a detailed analysis of the H-bond network, water dissociation and proton conduction properties under increasing field strengths. Concluding remarks are in section 8.6.

## 8.2 Computational methods

Density Functional Theory (DFT)-based Molecular Dynamics (MD) simulations (DFT-MD) have been carried out with the CP2K package [255, 256], consisting in Born-Oppenheimer MD by means of the DFT-BLYP [347, 348] exchange-correlation functional including the Grimme D2 correction for dispersion interactions [263, 264], GTH pseudopotentials [349] for the oxygen and hydrogen atoms, and a combined Plane-Wave (400 Ry density cutoff) and TZV2P basis set. The simulation box of  $19.734 \times 19.734 \times 35$  Å<sup>3</sup> is composed by a liquid phase made of 256 water molecules, periodically repeated in the  $x$  &  $y$  directions and separated by a vacuum layer of 15 Å from the replica in the vertical  $z$  direction. See Fig. 8.1-a for a snapshot.

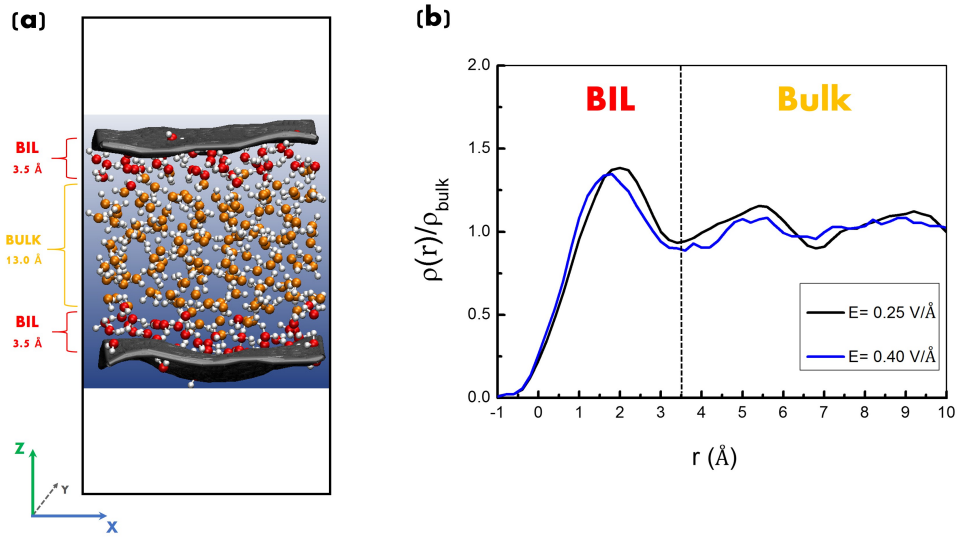


Figure 8.1: (a) Snapshot extracted from DFT-MD simulations showing the simulation box composed by 256 water molecules. The Willard and Chandler instantaneous surface [283] is shown in grey sheets, the identified water layers (BIL and bulk water) are color-coded and discussed in the text. A large slab of 15.0 Å of vacuum is used in order to separate the simulation box from its replicas along the vertical  $z$ -direction. (b) Electrified air-water interface: time averaged water density profiles normalized with respect to bulk liquid water obtained for applied electric fields of 0.25 V/Å (5 V potential) in black line and 0.40 V/Å (8 V potential) in blue line. The density is plotted as a function of the distance from the instantaneous Willard and Chandler surface [331].

The 256 neutral air-water (AW) trajectory is the one presented in ref. [326] while the other trajectories in presence of an external electric field applied parallel to the  $-x$  axis have been generated for the present investigation. The non-zero-field regime was explored in the range [0.05 ; 0.70] V/Å, the electric field being gradually increased with a step increment of about 0.05 V/Å. The implementation of an external electric field in numerical codes based on DFT can be achieved by exploiting the modern theory of polarization and the Berry phase [76] (see *e.g.* ref. [77] for the technical implementation of a static and homogeneous electric field in *ab initio* codes and ref. [78] for a review of several methods that allow for the application of external fields in various simulation frameworks). In a nutshell, the difficulty in treating finite electric fields in first principles periodic systems is the non-periodic nature of the position operator, see details in section 2.11. Within the Modern Theory of Polarization [74, 75] and of the Berry phase [76], one can introduce a variational energy functional [77]

$$E^{\mathcal{E}}[\{\psi_i\}] = E^0[\{\psi_i\}] - \mathcal{E} \cdot P[\{\psi_i\}], \quad (8.1)$$

where  $E^0[\{\psi_i\}]$  is the energy functional of the system in the zero-field approach and  $P[\{\psi_i\}]$  is the polarization along the field  $\mathcal{E}$  direction, as defined by Resta

[74]:

$$P[\{\psi_i\}] = -\frac{L}{\pi} \text{Im}(\ln \det S[\{\psi_i\}]), \quad (8.2)$$

where  $L$  is the periodicity of the cell and  $S[\{\psi_i\}]$  is a matrix composed of the following elements

$$S_{i,j} = \langle \psi_i | e^{2\pi i x/L} | \psi_j \rangle \quad (8.3)$$

for doubly occupied wavefunctions  $\psi_i$ . Umari and Pasquarello [77] demonstrated that this variational approach is valid for treating finite homogeneous electric fields in first-principles calculations and that it can be extended to provide atomic forces in first-principles MD simulations.

We performed simulations at the nominal temperature of 300 K, kept fixed through the coupling of the system with a Nosé-Hoover thermostat. The molecular systems were kept in an isothermal-isochoric (NVT) ensemble and the classical Newton's equations of motion for the nuclei are integrated through the Velocity Verlet algorithm with a time-step of 0.4 fs. For each electric field strength, the dynamics was followed for time lengths up to about 30 ps, extending to about 100 ps in the absence of the field. Hence, we globally cumulated a total simulation time of approximately 400 ps.

Analyses of the DFT-MD trajectories into instantaneous surface and water layers (Fig. 8.1) follow the derivation, respectively, by Willard and Chandler [283] and Pezzotti *et al.* [350]. Water-water H-bonds are defined through Galli and coworkers criteria [351]:  $\text{O}(-\text{H}) \cdots \text{O} \leq 3.2 \text{ \AA}$  and  $\text{O}-\text{H} \cdots \text{O}$  angle in the range  $[140-220]^\circ$ .

The identification of the water interfacial layers at the neutral AW interface, namely BIL (Binding Interfacial Layer) and bulk liquid water, has been done following the methodology developed by the group and described in chapter 5 on the basis of water structural descriptors only [350]. As already validated in previous works of the group [350, 352, 254, 338, 336] and confirmed by the present results at the electrified AW interface, the BIL is systematically composed of the topmost water molecules located within  $3.5 \text{ \AA}$  from the instantaneous water surface [283], forming less water-water H-bonds (2.9 H-bonds/mol) and being 1.4 times denser than water in the bulk. These water molecules form H-bonds preferentially oriented parallel to the surface plane, resulting in the formation of a collective and extended 2D-Hbond-Network (2DN for short notation) in the BIL [326]. This leads to the breaking of centrosymmetry and consequent SFG activity of the BIL [326, 338]. Further away than  $3.5 \text{ \AA}$  from the surface, centrosymmetric bulk water is recovered (with hence no SFG activity).

One of the three descriptors used to define the BIL [350], namely the water density profile as a function of the vertical distance from the instantaneous water surface, is shown in Fig. 8.1-b for two electrified air-water interfaces (respectively, homogeneous static electric field intensities of  $0.25 \text{ V/\AA}$  (5 V potential) and  $0.40 \text{ V/\AA}$  (8 V potential) applied along the  $-x$ -axis/surface plane). As will become clear in the discussion in the following sections, they correspond to crucial field values for the water conductivity in the BIL and

bulk regions. The plots reveal that the water density profile is only slightly affected by the increase in the field, and in particular that the first peak (position and intensity, as well as following minimum position) is maintained in the 0.25-0.40 V/Å field-regime. The thickness of the BIL is thus not changed in this regime. One can see the onset of small modifications to the second peak and following bulk region in the density profiles with the increase in the field intensity, showing that the field-induced rearrangement kicks-in the 3D-HB-Network of bulk water before it affects the 2D-HB-Network of the BIL interface. This will be discussed in more details later in this manuscript.

According to Ohm's law, the current density is related to the number of charge carriers  $\Delta N$  flowing through a section area  $a^2$  orthogonal to the direction of the electric field within a time interval  $\Delta t$ . With  $a$  the side of the simulation box orthogonal to the field direction and  $q$  the elementary charge ( $1.6 \cdot 10^{-19}$  C), the current density is:

$$J = \frac{q \Delta N}{a^2 \Delta t} \quad (8.4)$$

expressed in  $\mu\text{A}/\text{nm}^2$ . The protonic conductivity is then calculated as

$$\sigma = \frac{J}{E} \quad (8.5)$$

expressed in S/cm.

### 8.3 Enhanced conductivity of water at the electrified air-water interface

Although it is now established that applying static electric fields of the order of 0.30 V/Å to liquid water favours molecular dissociations [340, 343], theoretical modeling of the microscopic behaviour at the air/liquid water (AW) electrified interface carries fundamental insights on the conductivity properties of the interfacial H-bonded network that, to the best of our knowledge, has not been explored so far. From liquid water modelling, the application of an external static field is known to alter the H-bond environment in the bulk, triggering the cleavage of some oxygen-hydrogen (O-H) covalent bonds and thus promoting the hopping of protons along intermolecular H-bonds, resulting in the formation of new ionic complexes such as hydronium ( $H_3O^+$ ) and hydroxide ( $OH^-$ ) in liquid water. This is due to at least two cooperative roles played by the field, which (i) aligns the water molecules dipole moment vectors along the field direction [345] and (ii) elongates/weakens their covalent O-H bonds [336]. In neat bulk water the lowest field intensity able to induce a measurable net proton flow/current has been quantified theoretically to a value of 0.35 V/Å [340, 343] (obtained from DFT-MD using the PBE exchange-correlation functional; note that a change in the functional might induce a slight change in the absolute value of the field threshold), while a lower field strength of 0.25 V/Å triggers a series of ordered and correlated proton jumps via the Grotthuss mechanism in electrolytic aqueous solutions [345, 343, 353].

In the case of the AW electrified interface here investigated, the first significant molecular dissociation events have been recorded for field strengths equal to  $0.30 \text{ V}/\text{\AA}$  applied parallel to the air-water surface plane. Moreover, as shown in the protonic current density-voltage diagram plotted in Fig. 8.2, such a field intensity, that corresponds to the application of a voltage of 6 V at the edges of the employed simulation box, is not only able to trigger water dissociations but also to give rise to a net proton flow both at the AW interface (*i.e.*, in the BIL) and in the bulk liquid.

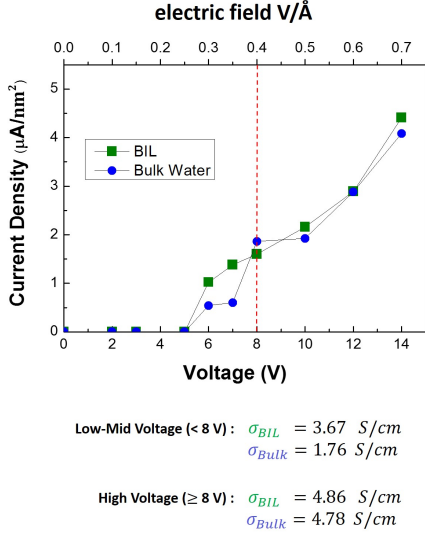


**Table:**

Electric Field (V/Å)	Voltage (V)	Current density BIL ( $\mu\text{A}/\text{nm}^2$ )	Current density Bulk Water ( $\mu\text{A}/\text{nm}^2$ )
0.30	6.0	1.02	0.54
0.35	7.0	1.38	0.60
0.40	8.0	1.60	1.86
0.50	9.9	2.16	1.92
0.60	11.8	2.89	2.88
0.70	13.8	4.41	4.08

Figure 8.2: *Left: protonic current density-voltage diagram calculated in the BIL (green squares) and in bulk water (blue circles). The corresponding electric field strength is given with the top axis. The dotted red line highlights the conductivity threshold discussed in the text.  $\sigma_{BIL}$  and  $\sigma_{bulk}$  are the conductivity calculated in the BIL and in bulk water, respectively. Table: for each electric field strength applied (and the related voltage for a cell side of  $19.734 \text{ \AA}$ ) list of protonic current density values calculated in the BIL and bulk water. Data highlighted in red represent the conductivity ( $\sigma$ ) threshold discussed in the text.*

Molecular dissociation processes (BIL and bulk alike) already start at  $0.25 \text{ V}/\text{\AA}$  (corresponding to a voltage of 5 V). However, similarly to bulk liquid water [340], these events are rare enough, the created hydronium and hydroxide ions are short-lived (*i.e.*, their lifetime is  $\leq 20 - 30 \text{ fs}$ ), this is not enough to give rise to a measurable protonic current. Once a field intensity of  $0.30 \text{ V}/\text{\AA}$  is applied, the BIL-AW slab shows a Ohmic behaviour, as already observed in refs. [340, 345, 343, 353] for bulk water and electrolytic aqueous solutions. In order to extract the current density contributions arising separately from the BIL and from the bulk liquid, respectively, these two regions have been systematically identified in the simulations based on the procedure presented in refs. [337, 338, 350]. As discussed in the methods section, the BIL includes all water molecules within a slab having a thickness equal to  $3.5 \text{ \AA}$  from the instantaneous water surface, while all remaining water molecules are assigned to the bulk region, as depicted in Fig. 8.1, independently of the field

strength. Importantly, as will be demonstrated later in the text, the water-water BIL-2DN specific 2-Dimensional H-bond network is maintained at the electrified AW interfaces, which is of high relevance for the rationalization of our findings for the protonic current densities presented and discussed below.

As shown in Fig. 8.2, two conductivity regimes can be identified, one for the BIL and one for the bulk liquid. In particular, as displayed in Fig. 8.2 and in the Table included in this figure, when an electric field strength equal to  $0.30 \text{ V/\AA}$  (corresponding to 6 V potential) is applied parallel to the water surface, protons start to flow along the field direction, with a higher current density along the water-water 2D-Hbond-Network than in the bulk. While there is also a protonic flow in the liquid, the protonic current density measured in the BIL ( $1.02 \mu\text{A}/\text{nm}^2$ ) is roughly twice larger than that of the bulk ( $0.54 \mu\text{A}/\text{nm}^2$ ), up to  $0.40 \text{ V/\AA}$  fields. Correspondingly, the protonic conductivity in the BIL ( $\sigma_{BIL} = 3.67 \text{ S/cm}$ ) is twice the one of the bulk ( $\sigma_{bulk} = 1.76 \text{ S/cm}$ ). Thus, in the  $[0.30 - 0.40] \text{ V/\AA}$  field intensity range (corresponding to 6-8 V potentials), the electrified AW interface (*i.e.*, the BIL) is a much better protonic conductor than the electrified bulk water.

On the other hand, beyond an electric field strength of  $0.40 \text{ V/\AA}$  (corresponding to about 8 V potential), the protonic current densities in the BIL and in the bulk liquid become roughly identical. Under such a high-voltage regime (*i.e.*,  $\geq 8 \text{ V}$ ), the BIL and the bulk protonic conductivities are equal to an average value of  $\sim 4.8 \text{ S/cm}$  (Fig. 8.2, bottom). The lower absolute bulk protonic conductivity found here in comparison to that of the pioneering work of Saitta *et al.* [340] (*i.e.*,  $7.8 \text{ S/cm}$ ) is presumably due to a combination of differences in the adopted theoretical frameworks between our works (*i.e.*, Born-Oppenheimer vs. Car-Parrinello MD, dispersion-corrected BLYP XC functional vs. PBE, etc.) and to different statistics (*i.e.*, box sizes and simulation timescales).

The rationale behind the significant difference in the conduction properties of the BIL and of the bulk for fields below  $0.40 \text{ V/\AA}$ , can be ascribed to the specific organization of the interfacial water molecules in the BIL, creating the already mentioned 2DN that connects more than 90% of the water molecules belonging to the BIL within a unique extended and collective network via H-bonds all oriented parallel to the surface plane [326] and surviving the application of a static electric field, as demonstrated now.

## 8.4 The 2-dimensional network (2DN) at the electrified air-water interface

With the aim of providing a statistical and quantitative analysis of the 2DN in the BIL, Fig. 8.3 shows the probability distribution  $P_n(\%)$  of the number of BIL-water molecules ( $n$ , x-axis) inter-connected by H-bonds through a non-interrupted 2-dimensional interfacial network. The probability distribution  $P_n(\%)$  is presented for the zero-field case in Fig. 8.3-a, it is the reference for the two other probability distributions presented here for electric fields

of  $0.25 \text{ V}/\text{\AA}$  and  $0.30 \text{ V}/\text{\AA}$  (Figs. 8.3-(b)-(c)), this latter being the electric field threshold able to dissociate water molecules and to establish a protonic current.

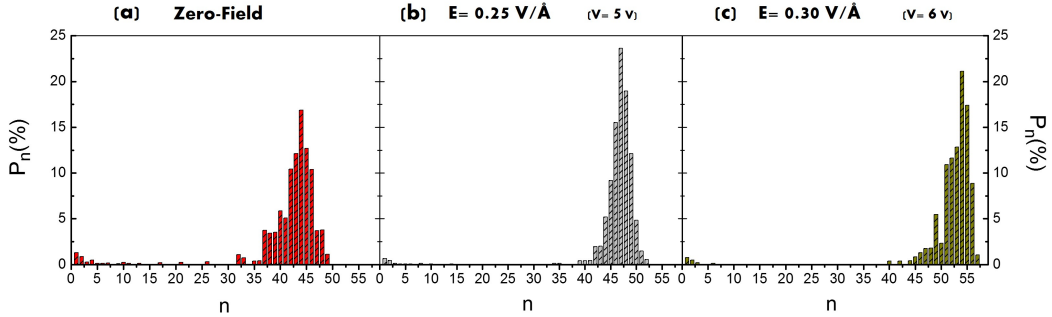


Figure 8.3: Probability distribution  $P_n(\%)$  of the possible structure of water molecules located in the interfacial layer (BIL),  $3.5 \text{ \AA}$  thickness.  $n$  ( $x$ -axis) is the number of BIL water molecules connected by non-interrupted H-bonds. (a) Zero-field case. (b) Electric field strength of  $0.25 \text{ V}/\text{\AA}$  ( $5 \text{ V}$  potential). (c) Electric field strength of  $0.30 \text{ V}/\text{\AA}$  ( $6 \text{ V}$  potential).

As depicted in Fig. 8.3-(a) (and already discussed in refs. [336, 337]), the vast majority of the water molecules (*i.e.* more than 90%) located in the BIL (Binding Interfacial Layer) form one single collective and extended H-bond structure, *i.e.*, the 2DN – as described in previous work of the group [336]. Less than 5% of interfacial water molecules are found either isolated ( $n=1$ ), or involved in dimers ( $n=2$ ) or in other small H-bonded structures ( $n \leq 5$ ), on average.

Similar considerations hold at  $0.25 \text{ V}/\text{\AA}$  and  $0.30 \text{ V}/\text{\AA}$  (Figs. 8.3-(b)-(c)), where the 2DN is not only still present, but is even enforced by the electric field applied parallel to the surface. One can indeed see that the main peak in the  $P_n(\%)$  distribution is shifted towards a higher central value of water molecules ( $n$ ) forming the extended and collective 2DN, while the peak distribution is also less broad than in the zero-field case. At both fields shown here, the minimum size of the continuous 2DN motif is obtained for  $n \sim 42$ -45. Not surprisingly, this reveals that the 2DN collectivity benefits from the alignment of the water dipoles under the influence of the external electric field applied along the direction parallel to the water surface (*i.e.* parallel to the 2DN H-bonds direction). Let us also stress here that the current-density in the BIL (Fig. 8.2) is entirely due to the 90% water molecules that build the special 2DN network at the interface.

Besides, the 2DN is composed of H-bonded water rings, as already emphasized in refs.[336, 329] These rings are quantified here, following the same method as in ref. [336] for the non electrified air-water interface. Fig. 8.4 hence reports the probability distribution  $P_n(\%)$  of finding ring structures of given sizes in the interfacial BIL-2DN, in absence of the electric field (8.4-(a)), and in presence of the  $0.25 \text{ V}/\text{\AA}$  (8.4-(b)) and  $0.30 \text{ V}/\text{\AA}$  (8.4-(c)) fields. As far as the zero-field case is concerned, rings composed of four, five, and six H-bonded

water molecules are the most likely structural motifs that build the collective 2DN. The more likelihood for the rings sizes are 4, 5 and 6, by decreasing order of probability. There are also probabilities to observe rings composed by up to nine water molecules.

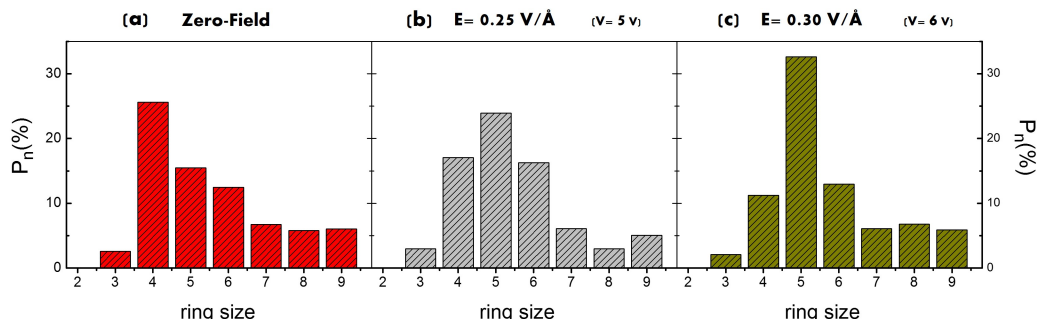


Figure 8.4: Probability distribution  $P_n(\%)$  of the size of the ring structures formed by the interfacial water molecules within the 2DN. (a) Zero-field. (b) Electric field strength of  $0.25 \text{ V/\AA}$  ( $5 \text{ V}$  potential). (c) Electric field strength of  $0.30 \text{ V/\AA}$  ( $6 \text{ V}$  potential).

For the two external fields reported in Fig. 8.4-(b)-(c), one can see that the distribution of ring sizes in between 4-6 is still the most probable one, however with a global distribution that now clearly shifts towards the ring size of 5 as the most probable/favored, especially for the  $0.30 \text{ V/\AA}$  field applied. The formation of H-bonded rings in the BIL-water with the H-bonds oriented parallel to the water surface plane is the fingerprint of the 2DN at the air-water interface, maintained and even strengthened once the interface is electrified, as shown here.

## 8.5 The role of the electrified BIL-water in the proton hopping water wires

For proton transfers to occur, protons have to move from one water molecule to the neighbouring one along H-bonded chains of molecules known as "water wires" [329, 354]. Because of the reduced number of available spatial configurations in the collective BIL-2DN, water molecules within the 2DN have less degrees of freedom for rotation and libration, which leads to a slower timescale for the orientational dynamics of the interfacial water molecules [337]. Somehow counter-intuitively, however, those interfacial water molecules exhibit an H-bond breaking/reforming dynamics that is faster than for the water molecules in the bulk liquid [337]. The BIL-2DN and its rings of H-bonded molecules connected to each others through this network of H-bonds formed parallel to the surface (at both zero-field and at the electrified interfaces) indeed create preferential water wires that can favor proton hoppings along these wires. The BIL-2DN furthermore leads to an increase of the residence time of protons at the interface, as already reported in refs. [329, 338] Moreover, the preferential

H-bonds orientation naturally present in the 2DN along with the fast H-bonds dynamics within the surface plane, as reported in ref.[336], makes easier the alignment of the water molecules in the BIL in response to an electric field applied along a direction parallel to the surface plane. All these properties highly favor proton hoppings along the BIL-2Dimensional-Hbond-wires, more efficiently than along the 3D H-bonded network of the liquid bulk, and also favor more efficient water dissociation and hence higher protonic flows within the BIL, which is indeed what is observed in this work.

A good illustration of these points can be found in Fig. 8.5 where 3D-plots report the probability of the combined O-O H-bonded distances and O-O orientation of the water-water H-bonds with respect to the applied  $\vec{E}$  field vector ( $\theta$  in the insert scheme), comparing the results for the water molecules in the BIL (left) and for water in the liquid bulk (right), for the electric field strengths of  $0.25 \text{ V/\AA}$  (Fig. 8.5-a, electric field condition before the onset of detectable water dissociations and protonic currents) and  $0.40 \text{ V/\AA}$  (figure-b). The probability coding is given by the scaling from blue (lower probabilities) to red (higher probabilities) values. Very interestingly and in line with our discussion above, one can see immediately that the  $0.25 \text{ V/\AA}$  field-induced re-orientation of the H-bonded water molecules measured through  $\theta$  is more efficient in the BIL-2DN (see Fig. 5-a), where the maximum probability (red spots) is observed for values of  $\cos \theta$  between 0.6 and 1.0, than in the liquid bulk where the red spots are found between 0.4 and 0.9. For a field intensity of  $0.40 \text{ V/\AA}$  ( $8 \text{ V}$  potential), both BIL-2D and bulk-3D H-bonded networks become equally oriented by the electrostatic driving force. One can indeed see that the 3D-plots presented in Fig. 8.5-b for the BIL and Bulk regions are very similar when such a higher field is applied, with the same final net HB-orientation of the water in the two regions. The only appreciable difference is found in the length of the HBs forming the 2D-HB-Network in the BIL, which are slightly longer than the HBs formed in between the bulk water molecules. This was already found at the non-electrified air-water interface [336] or at the lower  $0.25 \text{ V/\AA}$  in Fig. 8.5-a.

The water wires in the BIL are consequently found more oriented along the field direction than the water wires in the bulk, at least at the  $0.25 \text{ V/\AA}$  low-field strength. This can also be seen by eyes in Fig. 8.6-(b), and in Fig. 8.6-(c) at the slightly higher  $0.30 \text{ V/\AA}$  field strength. As furthermore highlighted in Fig. 8.6-(c), the water wires in the bulk retain their 3D-structure, resulting in proton motions that explore a larger 3D portion of space in the re-oriented bulk than in the re-oriented 2DN, as illustrated by the two wires in Fig. 8.6-(c). It follows that, in order to move any proton from a position  $A$  to a position  $B$  under an external field applied parallel to the AW surface, a lower number of proton jumps are required along the more aligned water wires in the BIL than along the more spatially spread water wires in the bulk. This leads to the higher conductivity of the BIL in the low-to-moderate field regime, as reported in Fig. 8.2. Moreover, as shown in Fig. 8.5-a for the  $0.25 \text{ V/\AA}$  field strength, the re-orientation of the interfacial water molecules in the BIL along the field

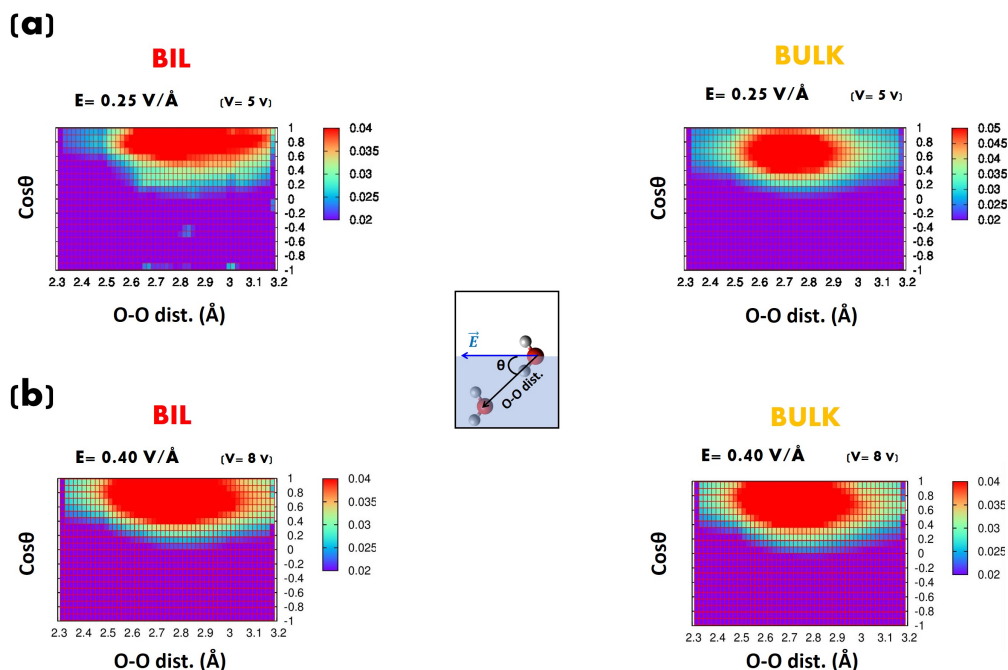


Figure 8.5: 3D plots of the H-bonds patterns between the water molecules in the interfacial layer-BIL (on the left) and between the water molecules in the bulk water (on the right) when an electric field of  $0.25 \text{ V}/\text{\AA}$  ( $5 \text{ V}$  potential) –fig-a at the top– and  $0.40 \text{ V}/\text{\AA}$  ( $8 \text{ V}$  potential) –fig-b at the bottom– is applied. The x-axis reports the O-O distance ( $\text{\AA}$ ) between 2 H-bonded water molecules and the y-axis provides the angle (cosine value) between the O-O vector (from donor to acceptor) and the direction ( $-x$  axis) of the applied electric field (see scheme). The colors represent the probability ( $P$ ) to find one O-H group forming one H-bond with a given distance and orientation. The probability increases from blue to red, see the scaling.

direction ( $-x$  axis) leads to longer and hence weaker H-bonds than in the liquid, which also favors and enhances the proton conductivity.

It is important to note that a few H-bonds present in the BIL are naturally weaker (and thus more dynamical) also under the zero-field condition, as a way to satisfy the finite temperature geometrical constraints on the water-water H-bonds and on the rings that thus maintain the extended 2DN structure. The further increase of the number of such weaker H-bonds with increasing the field strength is the direct consequence of the additional 1D constraint imposed by the application of the field along one direction only. Those weaker H-bonds have an influence on the lifetime of the water wires formed at the interface, which are hence expected to be shorter-lived than the water wires of the bulk due to the increased H-bonds dynamics within the 2DN [337]. It is well-known that autoionization in water is generated by fluctuations of the water dipole moments and is hence connected to librations and to more dynamical water wires that ultimately favour water dissociation [355]. The efficient separation of hydronium and hydroxide ions is also due to short-lived water wires, which in turn also reduce the probability of ionic recombination. All these effects play

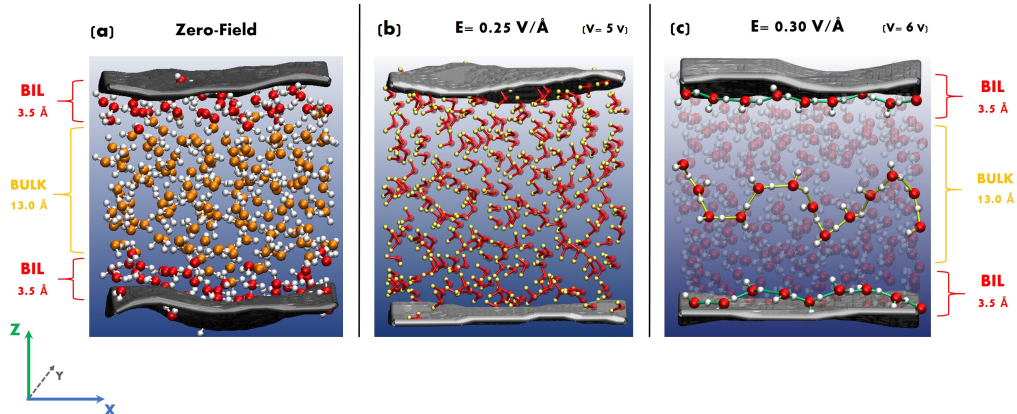


Figure 8.6: Snapshots extracted from the DFT-MD simulations representing the instantaneous surface in grey sheets and the two water layers (BIL and bulk water) identified and discussed in the text. Oxygen atoms are colored in red and hydrogen atoms are in white (hydrogen in yellow only in panel (b)). (a) Zero-field. (b) Oriented water molecules along the field direction ( $-x$  axis) by an electric field strength equal to  $0.25 \text{ V}/\text{\AA}$  (corresponding to  $5 \text{ V}$  potential). (c) Illustration of proton hopping water wires in the BIL and in bulk water under the action of a field intensity of  $0.30 \text{ V}/\text{\AA}$  ( $6 \text{ V}$ ) along the  $-x$  axis.

a role for field strengths slightly higher than the water dissociation threshold ( $0.25 \text{ V}/\text{\AA}$ ). At larger intensities ( $\geq 0.40 \text{ V}/\text{\AA}$ ) however, the limited size of the BIL likely leads to the saturation of the 2DN conductivity which cannot be further enhanced by the action of the field. In other words, any differences in structures that exist between the BIL-2DN and the 3D H-bonded network in the bulk are washed out at higher fields, simply because both networks are then equally and completely oriented by the electrostatic driving force.

## 8.6 Conclusions

Based on state-of-the-art *ab initio* molecular dynamics simulations, we have characterized proton transfers and water dissociations at the air-water interface, triggered by intense static and homogeneous electric fields applied parallel to the air-water surface plane. Those results have been directly compared with those measured in the bulk portion of the liquid.

We have found that the onset of water dissociation (*i.e.*, the minimum field intensity capable to ionize water) is not affected by the specific 2-Dimensional Hbond network formed by water at the air-water interface. The first formation of hydronium ( $\text{H}_3\text{O}^+$ ) and hydroxide ( $\text{OH}^-$ ) ions has been recorded at the Binding Interfacial Layer (BIL) and in the bulk at the same field strength (*i.e.*,  $0.30 \text{ V}/\text{\AA}$ ). However, the proton transfer activity at low-to-moderate field regimes ( $\leq 0.40 \text{ V}/\text{\AA}$ ) is differently influenced in the two regions of the liquid. The response of the current density-voltage diagrams is Ohmic in both cases (provided that a conduction regime has been achieved), the protonic

conductivity of the BIL ( $\sigma_{BIL} = 3.67$  S/cm) is twice the one recorded in the bulk ( $\sigma_{bulk} = 1.76$  S/cm). By monitoring the behaviour of the H-bond networks in the BIL and in the bulk liquid, respectively, we showed such difference in conductivity to be due to the specifically organised 2-Dimensional Hbond network (2DN) shaping the water at the air-water interface, which was shown to enhance the proton transfer events under low-to-moderate ( $0.30$  V/Å -  $0.40$  V/Å) electric field strengths applied along the interface plane (*i.e.* along the 2DN). The reduced dimensionality of the intermolecular network has a clear influence on the behaviour of the water wires responsible for the proton conduction. The better aligned and shorter-lived water wires, as existing in the BIL, lead to more efficient spatially (and temporal) correlated proton hoppings than in the 3D liquid bulk. On the other hand, for more intense fields ( $\geq 0.40$  V/Å), both BIL and bulk protonic conductivities converge to the same value ( $\sim 4.8$  S/cm), because the 1D direction constraint imposed by the stronger electrostatic field now aligns both BIL and bulk water in a similar way and hence reduces the structural differences between the BIL and the bulk H-bonded networks. The insights gained from this investigation certainly could have more practical implications, typically in relation with the water splitting in confined electrified/electrocatalytic solid/water environments. According to the present study, any confined environment exhibiting the 2DN structural arrangement of water at the interface would indeed be favorable for the water dissociation/splitting, especially under electrified conditions applied parallel to the BIL-2DN surface.

## 8.7 Other works performed during this PhD/ Electric field applied on monovalent and di- valent electrolyte water solutions

We report hereafter the 4 published works performed during my PhD period, as a result of a personal scientific collaboration with Prof. A. M. Saitta at Sorbonne University-Paris and Dr. F. Saija at CNR-IPCF in Messina-Italy. I have continued these collaborations during my PhD period at UEVE.

1. Ab-initio molecular dynamics study of NaCl water solutions under an external electric field.  
G. Cassone, F. Creazzo, P. V. Giaquinta, F. Saija, A. M. Saitta.  
*Phys. Chem. Chem. Phys.*, 18, 23164-23173, **2016**;
2. Ionic diffusion and proton transfer in aqueous solutions of alkali metal salts.  
G. Cassone, F. Creazzo, P. V. Giaquinta, J. Sponer, F. Saija.  
*Phys. Chem. Chem. Phys.*, 19, 20420-20429, **2017**;
3. Ionic Diffusion and Proton Transfer in Aqueous Solutions under an Electric Field: State-of-The-Art.  
F. Creazzo.  
*Editorial in J. Mol. Sci.* Vol. 1, No. 1:2, **2017**;
4. Ionic diffusion and proton transfer of  $MgCl_2$  and  $CaCl_2$  aqueous solutions: an ab initio study under electric field.  
G. Cassone, F. Creazzo, F. Saija.  
*Mol. Simul.*, Special Issue 1-8, Vol. 40, **2018**.

Please, read paper no. 4 for a summary of the main results from papers 1-3.



Cite this: *Phys. Chem. Chem. Phys.*,  
2016, **18**, 23164

## *Ab initio* molecular dynamics study of an aqueous NaCl solution under an electric field

Giuseppe Cassone,<sup>a</sup> Fabrizio Creazzo,<sup>b</sup> Paolo V. Giaquinta,<sup>c</sup> Franz Saija\*<sup>d</sup> and A. Marco Saitta<sup>e,f</sup>

We report on an *ab initio* molecular dynamics study of an aqueous NaCl solution under the effect of static electric fields. We found that at low-to-moderate field intensity regimes chlorine ions have a greater mobility than sodium ions which, being a sort of “structure makers”, are able to drag their own coordination shells. However, for field strengths exceeding  $0.15 \text{ V \AA}^{-1}$  the mobility of sodium ions overcomes that of chlorine ions as both types of ions do actually escape from their respective hydration cages. The presence of charged particles lowers the water dissociation threshold (*i.e.*, the minimum field strength which induces a transfer of protons) from  $0.35 \text{ V \AA}^{-1}$  to  $0.25 \text{ V \AA}^{-1}$ ; moreover, a protonic current was also recorded at the estimated dissociation threshold of the solution. The behaviour of the current–voltage diagram of the protonic response to the external electric field is Ohmic as in pure water, with a resulting protonic conductivity of about  $2.5 \text{ S cm}^{-1}$ . This value is approximately one third of that estimated in pure water ( $7.8 \text{ S cm}^{-1}$ ), which shows that the partial breaking of hydrogen bonds induced by the solvated ions hinders the migration of protonic defects. Finally, the conductivity of  $\text{Na}^+$  and  $\text{Cl}^-$  ions ( $0.2 \text{ S cm}^{-1}$ ) is in fair agreement with the available experimental data for a solution molarity of 1.7 M.

Received 6th June 2016,  
Accepted 29th July 2016

DOI: 10.1039/c6cp03926j

www.rsc.org/pccp

### 1. Introduction

Water is ubiquitous and represents one of the most studied molecular compounds in condensed matter physics. Although the investigation of pure liquid water has so far produced an impressive amount of fundamental insights on its microscopic and macroscopic behaviour, neat water does not actually exist. Indeed, the presence of some ions cannot be avoided even in ultrapure water samples and the role played by such ions is indisputable since most biological functions are mediated, if not completely driven, by a few types of charged atomic species such as  $\text{Na}^+$ ,  $\text{Cl}^-$ ,  $\text{K}^+$ ,  $\text{Ca}^{2+}$ , *etc.* In fact, these ions are responsible for the specific selectivity of cell membranes.<sup>1–3</sup> Of particular relevance is the subtle role played by ions and their aqueous

hydration shells in specifying, by means of the associated local electric fields, the peculiar character of a given ionic channel. Despite the fact that a plasma membrane cannot be simulated in its entirety *via ab initio* approaches, first-principles methods are mandatory in this field in order to model the behaviour of an electrolyte solution in an appropriate way.

Definitely, one of the most important and largely studied ionic pair in natural water is that formed by sodium and chlorine. Although the effects of these ions on the macroscopic properties of an aqueous solution have already been extensively explored, some microscopic details on this topic are still undisclosed. About sixty years ago it was argued that the inclusion of ionic species in “pure” water might produce important local changes in its microscopic structure.<sup>4,5</sup> These assumptions have led to concepts such as “structure maker” – *i.e.*, kosmotrope – and “structure breaker” – *i.e.*, chaotrope –, which characterize the type of perturbation produced by a specific ion on the hydrogen-bond (H-bond) network of water. Nowadays, such notions are rather strongly supported by dozens of classical molecular dynamics simulations,<sup>6–8</sup> however, they have been recently blunted by an *ab initio* molecular dynamics study.<sup>9</sup> In particular, it seems that at low-to-moderate concentrations the ions may replace water molecules in the aqueous H-bonded structure, by following the same “water rules”.<sup>9</sup> This example proves that classical molecular dynamics may fail in dealing with delicate local electrostatic balances and that first-principles approaches are necessary not only for a correct microscopic

<sup>a</sup> Institute of Biophysics – Czech Academy of Sciences, Královopolská 135, 61265 Brno, Czech Republic. E-mail: giuseppe.cassone@impmc.upmc.fr

<sup>b</sup> Laboratoire Analyse et Modélisation pour la Biologie et l'Environnement, UMR8587 (CHARMMAT), Université d'Evry val d'Essonne, Blvd. F. Mitterrand, 91025 Evry, France. E-mail: fabrizio.creazzo@pec.it

<sup>c</sup> Università degli Studi di Messina, Dipartimento di Scienze Matematiche e Informatiche, Scienze Fisiche e Scienze della Terra, Contrada Papardo, 98166 Messina, Italy. E-mail: paolo.giaquinta@unime.it

<sup>d</sup> CNR-IPCF, Viale Ferdinando Stagno d'Alcontres 37, 98158 Messina, Italy. E-mail: saiija@ipcf.cnr.it

<sup>e</sup> Sorbonne Universités, Université Pierre et Marie Curie Paris 06, Institut de Minéralogie, de Physique des Matériaux et de Cosmochimie, Unité Mixte de Recherche 7590, 75005 Paris, France. E-mail: saitta@impmc.upmc.fr

<sup>f</sup> CNRS, UMR 7590, IMPMC, 75005 Paris, France

characterization of these phenomena but also in order to improve the models on which classical force fields rely.

When an external electric field is applied, the situation is even more tough. A classical molecular dynamics attempt at ascertaining the role of external electric fields in enhancing the ionic mobility in an aqueous electrolyte solutions has been carried out by Murad.<sup>10,11</sup> Notwithstanding some interesting insights, the added fictitious force that mimics the field does not lead to a quantitative assessment of the involved field intensities. Fortunately, a classical molecular dynamics study of an electrolyte NaCl solution performed by Sellner *et al.*,<sup>12</sup> in which, perhaps, the classical trajectories have been re-sampled by means of the Quantum Theory of Atoms in Molecules – better known as Bader analysis–,<sup>13</sup> has provided the order of magnitude of local electric fields present in the investigated sample. In fact, albeit this kind of investigation has the drawback of the lack of a correct dynamical molecular evolution of the system, the *ab initio* resampling of the trajectories has produced an important result: field intensities of the order of  $1 \text{ V \AA}^{-1}$  and even stronger were detected at the atomic sites.

The application of static electric fields on H-bonded systems has several consequences which are strongly dependent on the field strength.<sup>14–20</sup> Indeed, as far as liquid water is concerned, above certain field thresholds it is possible to induce molecular dissociation and proton transfers along the H-bonded network<sup>14,21</sup> *via* the following well-known reaction:



where two water molecules ionize upon transferring one proton. This process, which in liquid water is known as (auto)protolysis, plays a crucial role in many disparate domains, from neurobiology to electrolytic batteries and hydrogen-based technology.<sup>22,23</sup> Although these phenomena have been studied in pure liquid water,<sup>14,24–27</sup> to the best of our knowledge they have never been investigated in aqueous solutions under an electric field. Thus, in order to catch the most relevant features which characterize the complex interplay between intermolecular interactions and field effects, we report here on the first *ab initio* molecular dynamics study of an aqueous solution with solvated  $\text{Na}^+$  and  $\text{Cl}^-$  ions at room conditions and under a static electric field. The presence “from scratch” of strong electric fields acting on the atomic sites of the water molecules leads to significant changes in the molecular dissociation and proton transfer properties with respect to the neat water case. It turns out that, despite the expected enhancement of the dynamical properties of the alkali and halide ions when an external electric field has been switched on, the protonic conductivity is manifestly altered by the presence of other ionic species.

The present article is structured as follows. In Section II we illustrate the methodology of our investigation. Section III is divided into three subsections: in the first one we present the results involving radial distribution functions, H-bonds, and dipole moment orientation responses to an external electric field; in the following subsection we illustrate a detailed analysis of the dynamical properties of the “free” ions, whereas in the third subsection we present our results on water dissociation

and proton conduction properties. Section IV is finally devoted to concluding remarks.

## II. Computational method

We carried out a series of computer simulations on a system containing two NaCl ion pairs (*i.e.*, 4 ions) solvated by 64 water molecules. The molecules were arranged in a cubic box with side  $a = 12.5 \text{ \AA}$ , corresponding to a solution molarity of  $1.7 \text{ M}$  (*i.e.*,  $\rho = 1.071 \text{ g cm}^{-3}$  and solute concentration  $\sim 10\%$  in mass). Periodic boundary conditions were thoroughly applied. The study was conducted with QUANTUM ESPRESSO,<sup>28</sup> a well-known open-source package for DFT calculations. In particular, the Car–Parrinello<sup>29</sup> approach was employed in order to perform *ab initio* molecular dynamics under a static electric field applied along a given direction (corresponding to the  $z$ -axis).

The implementation of an external electric field in *ab initio* codes can be achieved within the modern theory of polarization and Berry’s phases.<sup>30</sup> All the calculations were performed at the nominal temperature of  $315 \text{ K}$ , kept fixed through the coupling of the system with a Nosé–Hoover thermostat whose frequency was set at  $13.5 \text{ THz}$ . The non-zero-field regime was explored in the range  $[0.05; 0.70] \text{ V \AA}^{-1}$ , the electric field being gradually increased with a step increment of about  $0.05 \text{ V \AA}^{-1}$ . The dynamics of ions was simulated classically within a constant number, volume, and temperature ( $NVT$ ) ensemble using the Verlet algorithm; for each electric field strength the ions dynamics was followed for times up to about 8 or 9 ps, extending to about 28 ps in the absence of the field. Hence, we globally cumulated a simulation time of approximately 140 ps.

The fictitious electronic mass was set to a value of  $300 \text{ a.u.}$ , with a cutoff energy of  $45 \text{ Rydberg (Ry)}$  for the wavefunctions and a cutoff energy of  $360 \text{ Ry}$  for the charge density, which allowed us to adopt a timestep of  $0.075 \text{ fs}$ . With such cutoff values, the sample could be described in a sufficiently realistic way, the core electronic structure interaction being depicted through ultrasoft pseudopotentials (USPP).

Exchange and correlation effects were taken into account through the Perdew–Burke–Ernzerhof (PBE) functional, which belongs to the generalized gradient approximation (GGA) class.<sup>31</sup> In fact, the PBE functional has been found to be quite reliable in the case of H-bonded systems,<sup>32</sup> thanks to an adequate description of polarization effects.<sup>33</sup> Indeed, the results obtained by Saitta *et al.*<sup>14</sup> with this functional for dealing with the phenomenon of protolysis in liquid water under the action of a static electric field were successfully tested against the available experimental data.<sup>15–17</sup>

The conductivities were obtained from Ohm’s law. The current intensity is related to the number of charge carriers flowing in a time interval  $\Delta t$  through a section area  $a^2$  orthogonal to the direction of the electric field,  $a$  being the side of the simulation box. The conductivity was then calculated as

$$\sigma = \left( \frac{q\Delta N}{\Delta t a^2} \right) \cdot \frac{1}{E}, \quad (2)$$

where  $q$  is the elementary charge.

### III. Results

#### A. Structural properties

The structural correlations in a liquid solution can be quantified through the evaluation of the atomic radial distribution functions (RDFs). As far as the microscopic structure of water at zero field is concerned, it is clear from the oxygen–oxygen (O–O) and oxygen–hydrogen (O–H) RDFs, shown in Fig. 1, that sodium and chlorine ions do not alter in a significant way the average local aqueous environment around each water molecule. In fact, at least for the relatively moderate salt concentration which we have investigated, one recovers the same typical oscillations of the RDFs characterizing the short-range water–water interactions that are also present in neat water modeled with the same<sup>14,34</sup> or similar *ab initio* techniques.<sup>35–37</sup>

This aspect is further emphasized by the evidence that the first peak of the O–O RDF falls at 2.71 Å, whereas the first extramolecular peak of the O–H RDF is located at 1.72 Å, corresponding to the typical H-bond length in liquid water.

In order to analyze the hydration-shell structures of the solvated ions, a direct assessment of their respective RDFs is needed. As shown in Fig. 2, despite the limited number of sodium and chlorine ions employed in our simulation study, the average local structure around the ions is very well defined as shown by the sharp first peaks in both RDF pairs.

As expected, the first peak of the Cl–O RDF falls in a range delimited by the positions of the first two maxima of the Cl–H RDF (see Fig. 2). This clearly indicates that one of the hydrogen atoms of each water molecule in the ion solvation shell points toward the chlorine ion. In another study,<sup>3</sup> performed at the same salt molarity, the authors provided thorough benchmarks of several exchange and correlation functionals in reproducing the hydration structure of Na<sup>+</sup> and Cl<sup>−</sup>. As far as the location of the first maximum of the water–ions atomic RDFs is concerned, the agreement between the just cited study and the present simulations is excellent (see Table 1).

An important property which can be extracted from each pair RDF is the coordination number  $n_{\alpha,\beta}(r)$ . Upon integrating the RDF up to the position of the first minimum, we calculated

the average number of oxygen and hydrogen atoms belonging to water molecules in the first solvation shell (see Table 2).

It turns out that, on average, 5.6 and 4.9 water molecules surround a Na<sup>+</sup> ion and a Cl<sup>−</sup> ion, respectively. Moreover, since the average number of hydrogen atoms that are first neighbours of sodium ions is equal to 12.9, the geometrical arrangement of the water molecules within the Na<sup>+</sup> hydration shell is characterized by a prevalent molecular orientation toward the solvent. Of course, for electrostatic reasons this circumstance is almost reversed in a chlorine hydration shell, as also emerges from the Cl–O and the Cl–H radial distribution functions. In particular, 4.9 hydrogen atoms point, on average, towards a chlorine ion.

van der Waals effects are significant in *ab initio* study of water under several conditions.<sup>37,43,44</sup> Since we are dealing with charged particles, dispersion interactions are expected to play an important role. However, the results obtained by Bankura *et al.*<sup>3</sup> show that the coordination numbers obtained with the dispersion-corrected variant of the PBE exchange and correlation functional are very close to those obtained in the present simulations, except for  $n_{\text{NaH}}$  (*viz.*, 12.9 vs. 15.1). Moreover, the estimated Na–O coordination number (5.6) is the same as that obtained through a different QM/MM calculation.<sup>45</sup> These considerations, in addition to the fact that electric fields likely suppress van der Waals contributions to several properties of water, make us confident on the reliability of the present results.

The accuracy of the data produced by the PBE functional in the absence of an external field is a good premise for testing the changes in the average local structure of the system that this functional accounts for when a static and uniform electric field has been switched on. We first run a zero-field Car–Parrinello dynamics about 28 ps long at 315 K, and then applied a field of increasing intensity. As shown in Fig. 3, density correlations between pairs of oxygen atoms and between oxygen and hydrogen atoms get weaker and weaker as the field strength increases. In fact, the maxima of both O–O and O–H RDFs are depressed whereas the first minima rise; in other words, the aqueous solvent becomes more disordered at short and medium distances, as also shown for neat water by Saitta *et al.*<sup>14</sup>

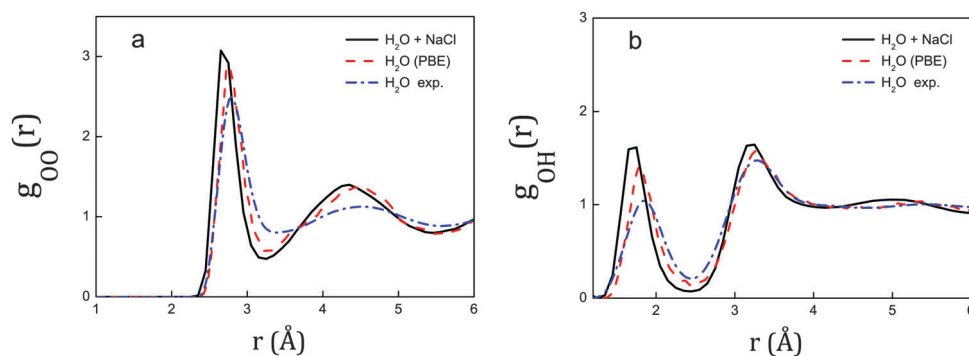


Fig. 1 Zero-field oxygen–oxygen (a) and oxygen–hydrogen (b) radial distribution functions of a NaCl solution at  $T = 315$  K with a saline molarity of 1.7 M as obtained through the present calculations (continuous black lines) are compared with the corresponding curves for neat water as modelled through the same PBE functional (red dashed lines) at  $T = 350$  K<sup>14</sup> and with the experimental data for pure water (blue dotted-dashed lines) at  $T = 298$  K.<sup>38</sup> We have plotted only the extramolecular part of the oxygen–hydrogen radial distribution functions.

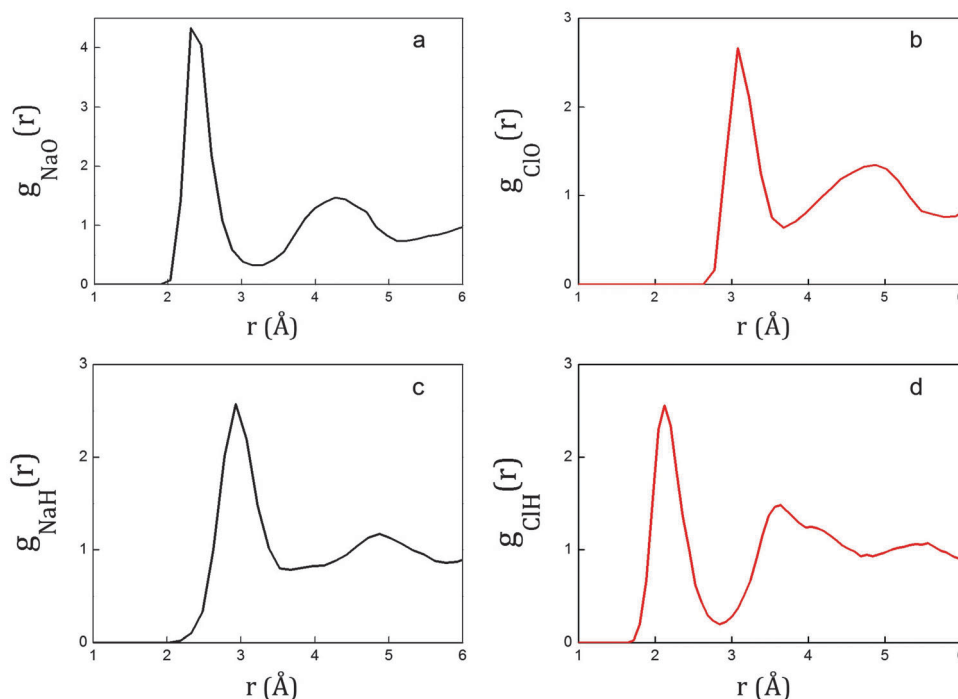


Fig. 2 Sodium–oxygen (a), chlorine–oxygen (b), sodium–hydrogen (c), and chlorine–hydrogen (d) radial distribution functions plotted as a function of the interatomic radial separation for zero electric field.

Table 1 Positions (Å) of the first peaks of the atomic radial distribution functions for zero electric field; column 2: present estimates obtained with the PBE exchange and correlation functional; column 3: values obtained with the PBE exchange and correlation functional documented in ref. 3

$R_{1st\ peak}$	PBE	PBE <sup>3</sup>
Na–O	2.38	2.37
Cl–O	3.12	3.11
Na–H	2.92	2.93
Cl–H	2.14	2.15

Table 2 Comparison between the atomic coordination numbers calculated in the present study (column 2), in a similar *ab initio* simulation carried out with the PBE (column 3) and BLYP (column 4) exchange and correlation functionals,<sup>3</sup> and the corresponding values extracted from neutron and X-ray diffraction experiment<sup>39–42</sup>

$n(r)$	PBE	PBE <sup>3</sup>	BLYP <sup>3</sup>	Exp. <sup>39–42</sup>
Na–O	5.6	4.9	5.5	4.3–5.3
Cl–O	5.8	5.9	6.3	5.3–6.9
Na–H	12.9	13.3	14.0	11.6–13.9
Cl–H	4.9	5.2	5.5	5.3–6.4

As far as the local structural environment of the ions is concerned, it is clear that even for feeble field strengths sodium and chlorine ions may become more mobile than water. Despite this evidence, the location of the first peak of all the RDFs shown in Fig. 4 does not appreciably change upon applying a field strength of  $0.25\ \text{V}\ \text{\AA}^{-1}$ . Only a decrease of the mentioned peak heights can be appreciated, except for the Cl–O RDF.

As it will be further explained in the next section, for such a field intensity the sodium ion has a larger mobility than the

chlorine ion. This fact is consistent with the decrease of the height of the first Na–O RDF peak upon increasing the field intensity. The slightly less structured situation also shown by the ion–H RDFs is also a consequence of the increase of the fraction of water molecules which align, on average, with the field direction. Upon increasing the field strength also some hydrogen atoms belonging to the first ionic hydration shells start to point along the field orientation.

In particular, the maximum of the angular distribution  $P(\theta)$  displayed in Fig. 5, where  $\theta$  is the angle formed by the water dipole moment vector with the electric field ( $z$ -axis), progressively shifts towards lower values of the angle, which implies that an increasing fraction of water molecules tends to align with the field as its intensity grows.

## B. Dynamical properties

Since very long simulations are needed in order to obtain well-converged estimates of the diffusion coefficients,<sup>9</sup> we first focus our attention on the mean square displacement (MSD) and on the drift of  $\text{Na}^+$  and  $\text{Cl}^-$  ions along the field direction (see Fig. 6). Despite the trivial evidence that charges with opposite sign flow towards opposite directions (see the  $z$ -axis drift in Fig. 6a), more important insights can be gained through the evaluation of the MSD. In particular, chlorine ions appear to be slightly more mobile than sodium ions for field strengths up to  $0.15\ \text{V}\ \text{\AA}^{-1}$ ; however, above this threshold intensity, the relative mobilities are completely reversed.

In fact, sodium ions gradually acquire a mobility which, even at  $0.25\ \text{V}\ \text{\AA}^{-1}$ , largely exceeds that of chlorine ions (see Fig. 6b). Such a different behaviour in a low-to-moderate field

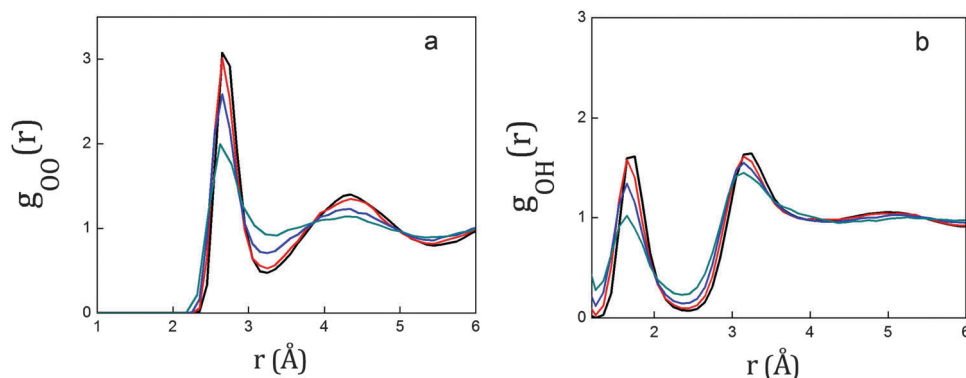


Fig. 3 Oxygen–oxygen (a) and oxygen–hydrogen (b) radial distribution functions calculated for increasing values of the electric field; black solid lines:  $E = 0 \text{ V } \text{Å}^{-1}$ ; red solid lines:  $E = 0.15 \text{ V } \text{Å}^{-1}$ ; blue solid lines:  $E = 0.25 \text{ V } \text{Å}^{-1}$ ; green solid lines:  $E = 0.35 \text{ V } \text{Å}^{-1}$ . The response of the average local water structure to the field is the same as that documented in ref. 14.

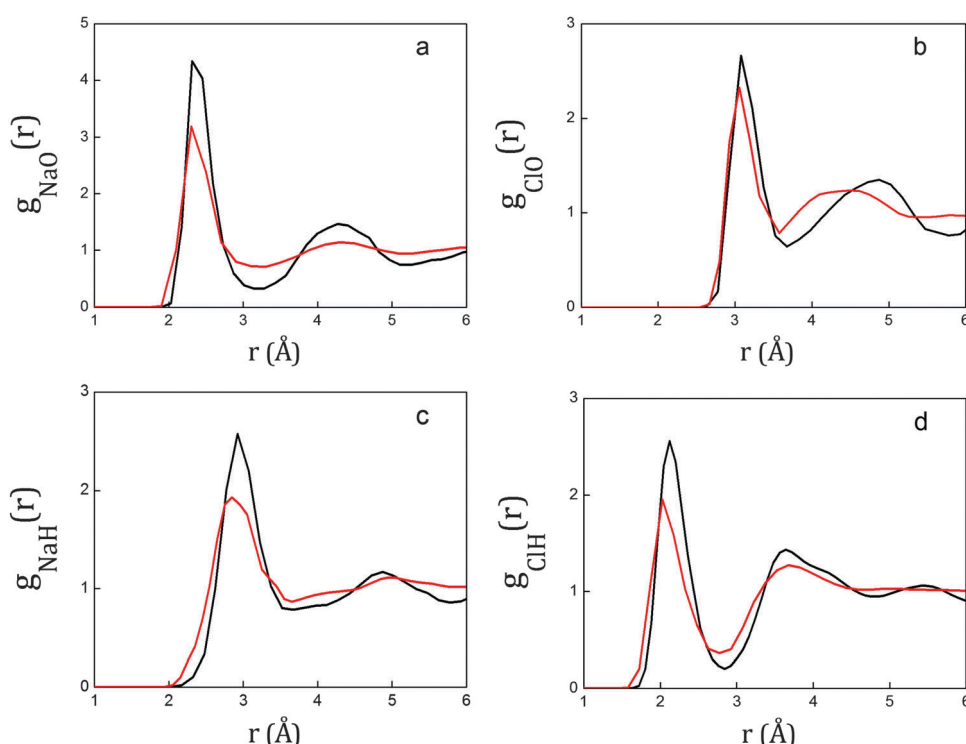


Fig. 4 Sodium–oxygen (a), chlorine–oxygen (b), sodium–hydrogen (c), and chlorine–hydrogen (d) radial distribution functions plotted as a function of the radial separation for zero electric field (black solid lines) and for  $E = 0.25 \text{ V } \text{Å}^{-1}$  (red solid lines).

regime as compared with a regime of higher field strengths, can also be interpreted by resorting to the concepts of “structure maker” and “structure breaker” ions. In particular, cations, which are relatively small, do behave as structure formers whereas all the halide anions, except for  $\text{F}^-$ , are structure breakers.<sup>4,5,9</sup> This evidence accounts for the slightly greater mobility which the external field confers to chlorine ions in the low-to-moderate field regime. This finding is consistent with the experimental evidence on the limit ionic conductivities of  $\text{Cl}^-$  ( $\lambda_{-}^0 \approx 7.6 \text{ mS m}^2 \text{ mol}^{-1}$ ) and  $\text{Na}^+$  ( $\lambda_{+}^0 \approx 5.0 \text{ mS m}^2 \text{ mol}^{-1}$ ), according to Kohlraush’s law of independent migration of ions.<sup>46</sup> However, when the intensity of the external field increases,

the intermolecular interactions between the ions and the surrounding water molecules become almost negligible with respect to the electrostatic coupling of the ions with the field. Indeed, at the presently investigated molar concentration (but these results are almost concentration-independent) sodium and chlorine ions carry charges of  $0.91 e$  and  $-0.69 e$ , respectively.<sup>12</sup> Moreover, it is well-known that the ionic radius and the ionic mass of sodium are equal to  $1.16 \text{ Å}$  and  $22.99 \text{ a.u.}$ , respectively, whereas the corresponding values for chlorine ions are  $1.67 \text{ Å}$  and  $35.45 \text{ a.u.}$  The higher effective charge of  $\text{Na}^+$  obviously implies a stronger electrostatic coupling of the ion with its hydration shell than in the case of  $\text{Cl}^-$ .

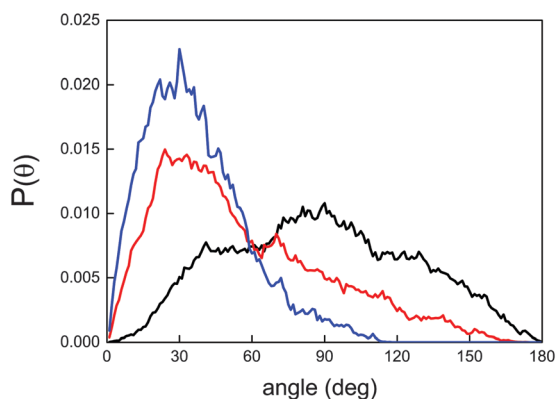


Fig. 5 Distribution of the angle  $\theta$  formed by the water dipole moment vector with the electric field ( $z$ -axis); black curve:  $E = 0 \text{ V } \text{\AA}^{-1}$ ; red curve:  $E = 0.15 \text{ V } \text{\AA}^{-1}$ ; blue curve:  $E = 0.25 \text{ V } \text{\AA}^{-1}$ .

Hence, for moderate field intensities (*viz.*, up to  $0.15 \text{ V } \text{\AA}^{-1}$ ), the free motion of the sodium ions is somewhat inhibited by the coordinated water molecules. Actually, as shown in Fig. 7a, the hydrated  $\text{Na}^+$  complexes move as unique entities until when the alkalis succeed in escaping from their water “cages”. More specifically, the sodium ions are initially able to drag at least part of their first solvation shells but after approximately 4 ps of concerted dynamics at  $0.15 \text{ V } \text{\AA}^{-1}$  one observes a decoupling of their respective motions. On the contrary, Fig. 7b shows that the motion of  $\text{Cl}^-$  is not correlated, for the same field intensity, with that of its surrounding water molecules; as a result, the anions can then diffuse almost freely throughout the sample.

As already shown above while commenting Fig. 6, for higher field intensities the electrostatic coupling of the cation with the field becomes more relevant. Moreover, being smaller and lighter than the chlorine ion, steric and inertial effects are greatly reduced with respect to the halogen ion; hence,  $\text{Na}^+$  starts diffusing more freely, as also shown in Fig. 8. Above the field threshold of  $0.15 \text{ V } \text{\AA}^{-1}$ , the ions acquire, at the presently investigated length and time scales, such a great mobility that a sort of dehydration phenomenon is recorded. In particular, for a field intensity of  $0.45 \text{ V } \text{\AA}^{-1}$  we have estimated an average residence time of the first solvation shells of approximately 0.3 ps,

a value two orders of magnitude lower than that evaluated at standard conditions.<sup>3</sup>

### C. Electrical properties

Applying static electric fields of intensities of the order of  $0.3 \text{ V } \text{\AA}^{-1}$  on H-bonded systems induces molecular dissociations.<sup>14–19</sup> In fact, the external field can trigger the cleavage of O–H covalent bonds, thus stimulating the migration of protons along H-bonds and the consequent formation of new covalent bonds. As a result, new ionic complexes do form, such as hydronium  $\text{H}_3\text{O}^+$  and hydroxide  $\text{OH}^-$  in liquid water.

Ions generate in condensed systems electric fields of the order of  $1 \text{ V } \text{\AA}^{-1}$ .<sup>47,48</sup> In the case of  $\text{Na}^+$  and  $\text{Cl}^-$ , the associated electric field distributions show strength peaks of almost  $0.5 \text{ V } \text{\AA}^{-1}$ .<sup>12</sup> In turn, such fields unexpectedly produce on the atomic sites of the hydration water molecules rather intense local fields of about  $2 \text{ V } \text{\AA}^{-1}$ ; this circumstance does not appear to depend on the concentration of the solvated ions.<sup>12</sup>

In an aqueous electrolyte solution field-induced effects such as molecular ionization are expected to occur for lower field intensities than in pure liquid water.<sup>14</sup> Indeed, it was found that field strengths of about  $0.35 \text{ V } \text{\AA}^{-1}$  are needed to induce molecular dissociations in neat water, whereas in a solution the first permanent ionization events were already recorded under the action of fields as intense as  $0.25 \text{ V } \text{\AA}^{-1}$ . Actually, molecular dissociations have been observed even at  $0.20 \text{ V } \text{\AA}^{-1}$ , but these events are rare and incomplete, the rattling of a proton between the donor and the acceptor water molecules being the most likely circumstance. Such events produce extremely short-lived ( $\sim 10 \text{ fs}$ )  $\text{H}_3\text{O}^+ - \text{OH}^-$  ionic pairs, similar to those observed at  $0.25 \text{ V } \text{\AA}^{-1}$  in neat water.<sup>14</sup> A careful check of whether water dissociation has a maximum probability to occur at a specific distance from the ions revealed that this is not apparently the case.

Another striking difference with respect to the pure case resides in the protonic current thresholds. In neat water the lowest field intensity that is able to trigger a measurable net proton flow again is  $0.35 \text{ V } \text{\AA}^{-1}$ , whereas in the electrolyte solution even a field strength of  $0.25 \text{ V } \text{\AA}^{-1}$  is able to induce a series of ordered and correlated proton jumps *via* the Grotthuss

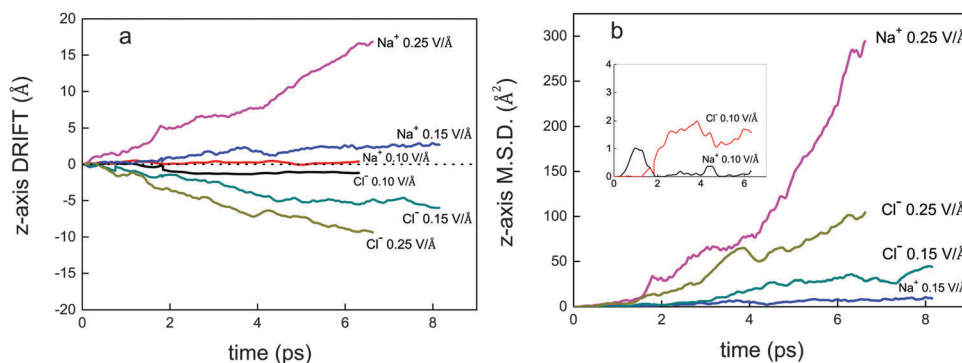


Fig. 6 Drift (a) and mean square displacement (b) of sodium and chlorine ions along the  $z$ -axis. Sodium: red, blue, and magenta curves refer to field strengths of  $0.10 \text{ V } \text{\AA}^{-1}$ ,  $0.15 \text{ V } \text{\AA}^{-1}$ , and  $0.25 \text{ V } \text{\AA}^{-1}$ , respectively. Chlorine: black, dark cyanide, and dark yellow curves refer to field strengths of  $0.10 \text{ V } \text{\AA}^{-1}$ ,  $0.15 \text{ V } \text{\AA}^{-1}$ , and  $0.25 \text{ V } \text{\AA}^{-1}$ , respectively. The inset in (b) shows the results for a field intensity of  $0.10 \text{ V } \text{\AA}^{-1}$ .

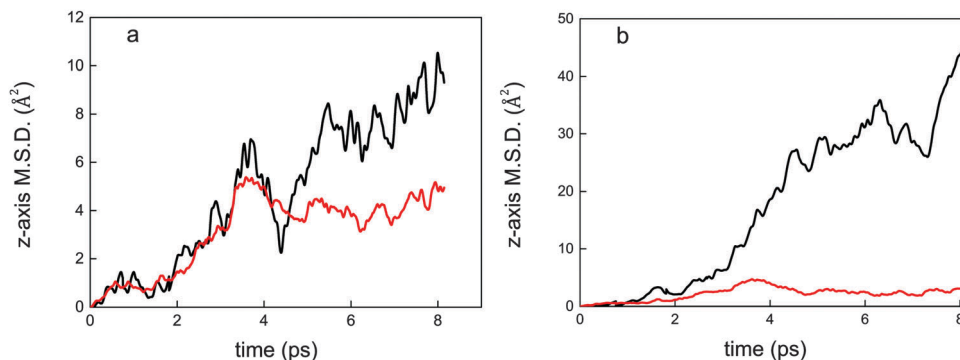


Fig. 7 Mean-square displacement along the z-axis of (a) sodium ions (black curve) and of their solvated oxygen atoms (red curve) and of (b) chlorine ions (black curve) and of their solvated oxygen atoms (red curve) for a field strength of  $0.15 \text{ V } \text{Å}^{-1}$ .

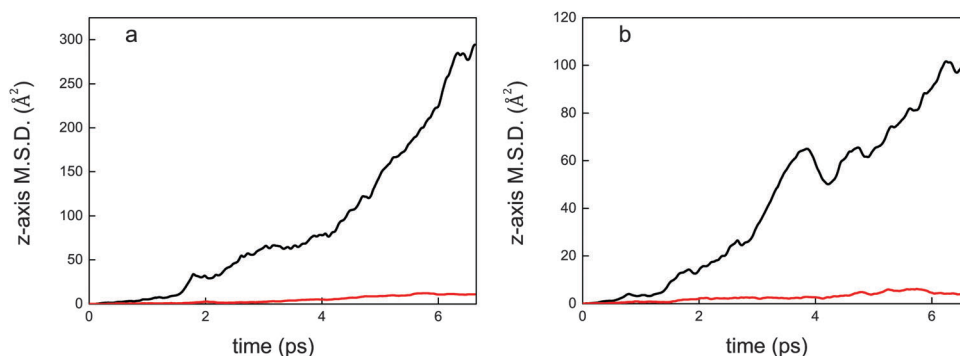


Fig. 8 Mean-square displacement along the z-axis of (a) sodium ions (black curve) and of their solvated oxygen atoms (red curve) and of (b) chlorine ions (black curve) and of their solvated oxygen atoms (red curve) for a field strength of  $0.25 \text{ V } \text{Å}^{-1}$ .

mechanism. Such one-stage process, in which the formation of new ionic species readily leads to a conductive regime, was not observed in neat water.

The protonic current-voltage diagram in Fig. 9 shows that, once the electric field as intense as  $0.25 \text{ V } \text{Å}^{-1}$  has stabilized a few fractions of hydronium and hydroxide ions, protons do start flowing in the sample as well. The protonic component of the total ionic current of the aqueous solution shows an Ohmic behaviour provided that the molecular dissociation threshold has been surpassed.

The presence of  $\text{Na}^+$  and  $\text{Cl}^-$  species triggers the dissociation of the water molecules for perceptibly lower field strengths than those needed in pure water. On the other hand, the estimated protonic conductivity is  $2.5 \text{ S cm}^{-1}$ , approximately one third of that observed in neat water ( $7.8 \text{ S cm}^{-1}$ ).

Hence, although the chlorine ion participates in the collective proton transfer phenomenon *via* the formation of hydrogen chloride (HCl) for field intensities equal to or greater than  $0.30 \text{ V } \text{Å}^{-1}$ , a break of the H-bond network in proximity of the ions hinders the Grotthuss mechanism. As shown in Fig. 10, since protons of most water molecules surrounding chlorine point toward this ion, chlorine may actually act as a sort of pit, thus accepting protons; but, once the recombination process of  $\text{H}^+$  with  $\text{Cl}^-$  has taken place, the amount of available H-bond paths is extremely limited for a successive proton migration.

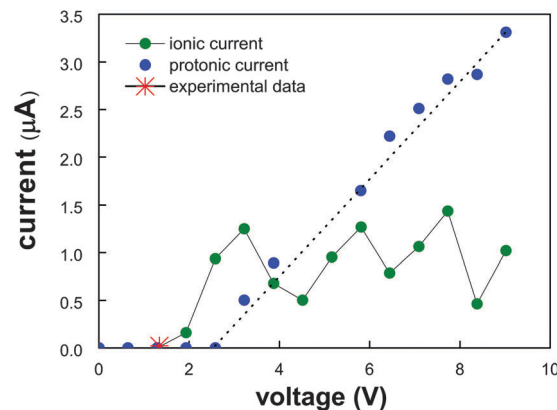
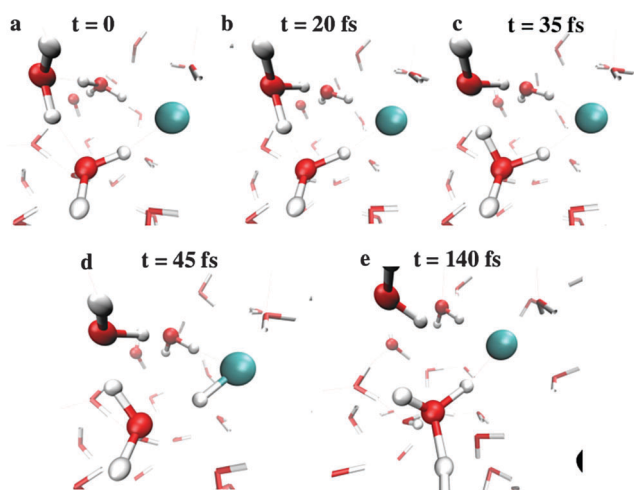


Fig. 9 Current-voltage diagram of the protonic (blue dots) and ionic (green dots) contributions to the total electrical response. The dotted black line which highlights the Ohmic behaviour of the protonic current is a guide for the eye. Notwithstanding the very low statistics of the ionic part (*i.e.*, only 2 NaCl ion pairs are present in the sample), this contribution exhibits a similar behaviour over a smaller range, *i.e.*, approximately between 2 and 3.5 V. At higher voltages the ionic response is seen to saturate.

In addition, other electrostatic effects may be relevant. Indeed, although the formation of the hydroxide ion in the first solvation shell of  $\text{Na}^+$  has been observed, the hydronium ion has never been found in this region. The diffusion of the sodium ion, being positively charged, clearly inhibits the propagation of protonic



**Fig. 10** Formation of hydrogen chloride (HCl) at  $0.45 \text{ V } \text{\AA}^{-1}$ . Red, white, and cyan atoms represent oxygen, hydrogen, and chlorine, respectively. Within a few tens of fs several proton transfers, involving some of the chlorine hydration molecules, occur (a–c). When an hydronium ion ( $\text{H}_3\text{O}^+$ ) forms in the chlorine hydration shell (a and c), a proton ( $\text{H}^+$ ) can be transferred to a nearby  $\text{Cl}^-$  (d). The just formed HCl molecule will likely prefer to give the excess proton back to the donor species (e), as most of the hydrogen atoms of the solvation water molecules point toward it. The newly (re)formed hydronium ion makes another attempt of transferring a proton to a nearby acceptor water molecule (e). Note that the lifetime of HCl is of the order of 100 fs, whereas in 35 fs proton transfers between three adjacent water molecules (a–c) are often observed for such field intensities.

defects in the space spanned by its motion. Hence, when cations move almost freely, neighbouring hydronium ions have statistically lower chances to diffuse. These effects account for the lower protonic conductivity of the solution with respect to that of neat water. Of course, in addition to protons also ions contribute to the total conductivity of our sample. Although the ionic contribution ( $0.2 \text{ S cm}^{-1}$ ) is in fairly good agreement with the available experimental data at the sampled molarity (*i.e.*,  $0.14 \text{ S cm}^{-1}$ <sup>49,50</sup>), the ionic current achieves saturation in our *ab initio* size-limited simulation at  $0.25 \text{ V } \text{\AA}^{-1}$  (see Fig. 9). Indeed, for this latter field strength all the four ions have had enough mobility to cross half a side of the simulation box during the simulation time window. Finally, time limitations are also responsible for the impossibility to measure any ionic current beneath a field strength of  $0.15 \text{ V } \text{\AA}^{-1}$ . In fact, by evaluating the ionic velocities in this regime, a time longer than the explored 8–9 ps would have been necessary in order to record an albeit feeble ionic current intensity.

## IV. Conclusions

In this paper we have studied the response of an aqueous NaCl solution to an external static electric field of varying intensity by means of *ab initio* molecular dynamics simulations. We first checked the reliability of our *ab initio* setup in the absence of the field, by calculating the radial distribution functions (RDFs) and coordination numbers of the ionic hydration shells.

Upon switching on the field, the mean-square displacement of the ions and of their respective solvation shells along the

direction of the field revealed that for low-to-moderate field intensities (up to  $0.15 \text{ V } \text{\AA}^{-1}$ ) chlorine ions are more mobile than sodium ions. The motion of the cations, which have stronger intermolecular interactions with their first neighbours, is first hindered. For field intensities exceeding the cited threshold, the mobility of sodium ions overcomes that of chlorine ions both because of a stronger electrostatic coupling with the external field and of lower inertial and steric effects acting on this ionic species.

The possibility of dissociating the water molecule through the application of static electric fields is very well known.<sup>14–17</sup> We have carried out a detailed comparison of the molecular dissociation phenomenon and of protonic current thresholds in the aqueous solution with the pure water case. We have found that the presence of charged particles in the electrolyte solution anticipates the ionization of the water molecules and the stabilization of a net proton flow. However, the measured protonic conductivity appears to be smaller than that recorded in the pure water sample, *i.e.*,  $2.5 \text{ S cm}^{-1}$  vs.  $7.8 \text{ S cm}^{-1}$ . We explained this finding by considering the interruption of the hydrogen bond network in proximity of ions and the impossibility of the formation of hydronium in the first solvation shell of the very mobile cation, two circumstances which clearly hinder the migration of protons. In particular, although for high field intensities we have observed the formation of HCl which participates in the collective transfer of protons, the formation of the hydronium  $\text{H}_3\text{O}^+$  in the solvation shell of sodium has never been detected. This means that sodium ions, which move almost freely for field strengths higher than  $0.15 \text{ V } \text{\AA}^{-1}$ , discourage the proton migration over wide spatial regions spanning the sample. Finally, we have obtained an estimate of the ionic conductivity ascribable to  $\text{Na}^+$  and  $\text{Cl}^-$  species ( $\sim 0.2 \text{ S cm}^{-1}$ ) which is in fair agreement with the available experimental data performed at similar conditions.

## Acknowledgements

G. C., F. C. and A. M. S. thank Fabio Pietrucci for useful discussions and insight. F. C. thanks IMPMC/UPMC for hospitality during his Master Internship. We acknowledge the GENCI-IDRIS French National Supercomputing Facility for CPU time under projects x2015091387 and x2016091387.

## References

- 1 B. Hille, *Ion Channels of Excitable Membranes*, Sinauer Associates, Inc. Publishers, Sunderland, Massachusetts USA, 2001.
- 2 Y. Zhou and R. MacKinnon, The Occupancy of Ions in the  $\text{K}^+$  Selectivity Filter: Charge Balance and Coupling of Ion Binding to a Protein Conformational Change Underlie High Conduction Rates, *J. Mol. Biol.*, 2003, **333**, 965.
- 3 A. Bankura, V. Carnevale and M. L. Klein, Hydration structure of salt solution from *ab initio* molecular dynamics, *J. Chem. Phys.*, 2013, **138**, 014501.

- 4 R. W. Gurney, *Ionic Processes in Solution*, McGraw-Hill, New York, 1953.
- 5 H. S. Frank and W. Y. Wen, Structural Aspects of Ion-Solvent Interaction in Aqueous Solutions: a Suggested Picture of Water Structure, *Discuss. Faraday Soc.*, 1957, **24**, 133.
- 6 N. Galamba, On the Effects of Temperature, Pressure, and Dissolved Salts on the Hydrogen-Bond Network of Water, *J. Phys. Chem. B*, 2013, **117**, 589.
- 7 M. T. Reagan, J. G. Harris and J. W. Tester, Molecular Simulations of Dense Hydrothermal NaCl-H<sub>2</sub>O Solutions deom Subcritical to Supercritical Conditions, *J. Phys. Chem. B*, 1999, **103**, 7935.
- 8 R. Renou, M. Ding, H. Zhu, A. Szymczyk, P. Malfreyt and A. Ghoufi, Concentration Dependence of the Dielectric Permittivity, Structure, and Dynamics of Aqueous NaCl Solutions: Comparison between the Drude Oscillator and Electronic Continuum Models, *J. Phys. Chem. B*, 2014, **118**, 3931.
- 9 Y. Ding, A. Hassanali and M. Parrinello, Anomalous Water Diffusion in Salt Solutions, *Proc. Natl. Acad. Sci. U. S. A.*, 2014, **111**, 3310.
- 10 S. Murad, The Role of the External Electric Fields in Enhancing Ion Mobility, Drift Velocity, and Drift-Diffusion Rates in Aqueous Electrolyte Solutions, *J. Chem. Phys.*, 2011, **134**, 114504.
- 11 S. Murad, Note: The Role of the External Electric Fields in Enhancing Ion Mobility, Drift Velocity, and Drift-Diffusion Rates in Aqueous Electrolyte Solutions, *J. Chem. Phys.*, 2012, **136**, 076101.
- 12 B. Sellner, M. Valiev and S. M. Kathman, Charge and Electric Field Fluctuations in Aqueous NaCl Electrolytes, *J. Phys. Chem. B*, 2013, **117**, 10869.
- 13 R. F. W. Bader, *Atoms in Molecules – A Quantum Theory*, Oxford University Press, Oxford, 1990.
- 14 A. M. Saitta, F. Saija and P. V. Giaquinta, *Ab Initio* Molecular Dynamics Study of Dissociation of Water under an Electric Field, *Phys. Rev. Lett.*, 2012, **108**, 207801.
- 15 E. M. Stuve, Ionization of Water in Interfacial Electric Fields: an Electrochemical View, *Chem. Phys. Lett.*, 2012, **519–520**, 1.
- 16 C. J. Rothfuss, V. K. Medvevev and E. M. Stuve, The influence of the Surface Electric Field on Water Ionization: a Two Step Dissociative Ionization and Desorption Mechanism for Water Ion Cluster Emission from a Platinum Field Emitter Tip, *J. Electroanal. Chem.*, 2003, **554–555**, 133.
- 17 Z. Hammadi, M. Descoins, E. Salanon and R. Morin, Proton and light ion nanobeams from field ionization of water, *J. Appl. Lett.*, 2013, **101**, 243110.
- 18 G. Cassone, P. V. Giaquinta, F. Saija and A. M. Saitta, Proton Conduction in Water Ices under an Electric Field, *J. Phys. Chem. B*, 2014, **118**, 4419.
- 19 G. Cassone, P. V. Giaquinta, F. Saija and A. M. Saitta, Liquid Methanol under a Static Electric Field, *J. Chem. Phys.*, 2015, **142**, 054502.
- 20 A. M. Saitta and F. Saija, Miller Experiments in Atomistic Computer Simulations, *Proc. Natl. Am. Soc.*, 2014, **111**, 13768.
- 21 C. J. T. Grotthus, Sur la décomposition de l'eau et des corps qu'elle tient en dissolution à l'aide de l'électricité galvanique, *Ann. Chim.*, 1806, **LVIII**, 54.
- 22 K. Kaila and B. R. Ransom, in *pH and Brain Function*, ed. K. Kaila and B. R. Ransom, Wiley, New York, 1998.
- 23 E. I. Zoulias and N. Lymberopoulos, *Hydrogen-Based Autonomous Power Systems*, Springer, London, 2008.
- 24 M. Tuckerman, K. Laasonen, M. Sprik and M. Parrinello, *Ab Initio* Molecular Dynamics Simulation of the Solvation and Transport of H<sub>3</sub>O<sup>+</sup> and OH<sup>-</sup> Ions in Water, *J. Phys. Chem.*, 1995, **99**, 5749.
- 25 P. I. Geissler, C. Dellago, D. Chandler, J. Hutter and M. Parrinello, Autoionization in Liquid Water, *Science*, 2001, **291**, 2121.
- 26 A. Hassanali, M. K. Prakash, H. Eshet and M. Parrinello, On the Recombination of Hydronium and Hydroxide Ions in Water, *Proc. Natl. Acad. Sci. U. S. A.*, 2011, **108**, 20410.
- 27 A. Hassanali, F. Giberti, J. Cuny, T. D. Kühne and M. Parrinello, Proton Transfer Through the Water Gossamer, *Proc. Natl. Acad. Sci. U. S. A.*, 2013, **110**, 142237.
- 28 P. Giannozzi, *et al.* QUANTUM ESPRESSO: A Modular and Open-Source Software Project for Quantum Simulation of Materials, *J. Phys.: Condens. Matter*, 2009, **21**, 395502.
- 29 R. Car and M. Parrinello, Unified Approach for Molecular Dynamics and Density-Functional Theory, *Phys. Rev. Lett.*, 1985, **55**, 2471.
- 30 M. V. Berry, Quantal Phase Factors Accompanying Adiabatic Changes, *Proc. R. Soc. London, Ser. A*, 1984, **392**, 45.
- 31 J. P. Perdew, K. Burke and M. Ernzerhof, Generalized Gradient Approximation Made Simple, *Phys. Rev. Lett.*, 1996, **77**, 3865–3868 (*Phys. Rev. Lett.*, 1997, **78**, 1396).
- 32 C. Fiolhais, F. Nogueira and M. Marques, *A Primer in Density Functional Theory*, Springer-Verlag, Berlin Heidelberg, 2010.
- 33 N. Marom, A. Tkatchenko, M. Rossi, V. G. Gobre, O. Hod, M. Scheffler and L. Kronik, Dispersion Interactions with Density-Functional Theory: Benchmarking Semiempirical and Interatomic Pairwise Corrected Density Functionals, *J. Chem. Theory Comput.*, 2011, **7**, 3944.
- 34 J. C. Grossman, E. Schwegler, E. W. Draeger, F. Gygi and G. Galli, Towards an Assessment of the Accuracy of Density Functional Theory for First Principles Simulations of Water, *J. Chem. Phys.*, 2003, **120**, 300.
- 35 B. Chen, I. Ivanov, M. L. Klein and M. Parrinello, Hydrogen Bonding in Water, *Phys. Rev. Lett.*, 2003, **91**, 215503.
- 36 M. Sprik, J. Hutter and M. Parrinello, *Ab Initio* Molecular Dynamics Simulation of Liquid Water: Comparison of Three Gradient-Corrected Density Functional, *J. Chem. Phys.*, 1996, **105**, 1142.
- 37 I.-C. Lin, A. P. Seitsonen, I. Tavernelli and U. Rothlisberger, Structure and Dynamics of Liquid Water from *Ab Initio* Molecular Dynamics – Comparison of BLYP, PBE, and revPBE Density Functionals with and without van der Waals Corrections, *J. Chem. Theory Comput.*, 2012, **8**, 3902.
- 38 A. K. Soper, The Radial Distribution Functions of Water as Derived from Radiation Total Scattering Experiments: Is There Anything we can Say for Sure?, *ISRN Phys. Chem.*, 2013, **2013**, 279463.

- 39 S. Cummings, J. E. Enderby, G. W. Neilson, J. R. Newsome, R. A. Howe, W. S. Howells and A. K. Soper, Chloride Ions in Aqueous Solutions, *Nature*, 1980, **287**, 714.
- 40 T. Megyes, S. Bálint, T. Grósz, T. Radnai, I. Bakó and P. Sipos, The Structure of Aqueous Sodium Hydroxide Solutions: a Combined Solution X-ray Diffraction and Simulation study, *J. Chem. Phys.*, 2008, **128**, 044501.
- 41 R. Mancinelli, A. Botti, F. Bruni, M. A. Ricci and A. K. Soper, Hydration of Sodium, Potassium, and Chloride Ions in Solution and the Concept of Structure Maker/Breaker, *J. Phys. Chem. B*, 2007, **111**, 13570.
- 42 D. H. Powell, G. W. Neilson and J. E. Enderby, The Structure of  $\text{Cl}^-$  in Aqueous Solution: an Experimental Determination of  $g_{\text{ClH}}(r)$  and  $g_{\text{ClO}}(r)$ , *J. Phys.: Condens. Matter*, 1993, **5**, 5723.
- 43 R. Jonchiere, A. P. Seitsonen, G. Ferlat, A. M. Saitta and R. Vuilleumier, van der Waals Effects in *Ab Initio* Water at Ambient and Supercritical Conditions, *J. Chem. Phys.*, 2011, **135**, 154503; *Erratum: J. Chem. Phys.*, 2015, **143**, 209902.
- 44 J. Schmidt, J. VandeVondele, I.-F. W. Kuo, D. Sebastiani, J. I. Siepmann, J. Hutter and C. J. Mundy, Isobaric-Isothermal Molecular Dynamics Simulations Utilizing Density Functional Theory: An Assessment of the Structure and Density of Water at Near-Ambient Conditions, *J. Phys. Chem. B*, 2009, **113**, 11959.
- 45 A. Tongraar, K. R. Liedl and B. M. Rode, Born Oppenheimer *Ab Initio* QM/MM Dynamics Simulations of  $\text{Na}^+$  and  $\text{K}^+$  in Water: From Structure Making to Structure Breaking Effects, *J. Phys. Chem. A*, 1998, **102**, 10340.
- 46 M. R. Wright, *An Introduction to Aqueous Electrolyte Solutions*, Wiley, Chichester, England, 2007.
- 47 B. Reischl, J. Köfinger and C. Dellago, The Statistics of Electric Field Fluctuations in Liquid Water, *Mol. Phys.*, 2009, **107**, 495.
- 48 Y. Bronstein, P. Depondt, L. E. Bove, R. Gaal, A. M. Saitta and F. Finocchi, Quantum versus Classical Protons in Pure and Salty Ice under Pressure, *Phys. Rev. B: Condens. Matter Mater. Phys.*, 2016, **93**, 024104.
- 49 *CRC Handbook of Chemistry and Physics*, ed. R. C. Weast and D. R. Lide, CRC Press, Boca Raton, FL, 1989, p. D-221.
- 50 A. V. Wolf, *Aqueous Solutions and Body Fluids*, Harper and Row, New York, 1966.



Cite this: *Phys. Chem. Chem. Phys.*,  
2017, 19, 20420

## Ionic diffusion and proton transfer in aqueous solutions of alkali metal salts

Giuseppe Cassone,<sup>a</sup> Fabrizio Creazzo,<sup>b</sup> Paolo V. Giaquinta,<sup>c</sup> Jiri Sponer<sup>a</sup> and Franz Saija<sup>d</sup>

We report on a series of *ab initio* molecular dynamics investigations on LiCl, NaCl, and KCl aqueous solutions under the effect of static electric fields. We have found that although in low-to-moderate field intensity regimes the well-known sequence of cationic mobilities  $\mu(\text{K}^+) > \mu(\text{Na}^+) > \mu(\text{Li}^+)$  (i.e., the bigger the cation the higher the mobility) is recovered, from intense field strengths this intuitive rule is no longer verified. In fact, field-induced water molecular dissociations lead to more complex phenomena regulating the standard migration properties of the simplest monovalent cations. The water dissociation threshold is lowered from  $0.35 \text{ V \AA}^{-1}$  to  $0.25 \text{ V \AA}^{-1}$  by the presence of charged species in all samples. However, notwithstanding a one-stage process of water ionization and proton conduction takes place at  $0.25 \text{ V \AA}^{-1}$  in the electrolyte solutions where “structure maker” cations are present (i.e., LiCl and NaCl), the KCl aqueous solution shows some hindrance in establishing a proton conductive regime, which is characterized by the same proton conduction threshold of neat water (i.e.,  $0.35 \text{ V \AA}^{-1}$ ). In addition, it turns out that protons flow easily in the LiCl ( $\sigma_p = 3.0 \text{ S cm}^{-1}$ ) solution and then – in descending order – in the NaCl ( $\sigma_p = 2.5 \text{ S cm}^{-1}$ ) and KCl ( $\sigma_p = 2.3 \text{ S cm}^{-1}$ ) electrolyte solutions. The protonic conduction efficiency is thus inversely proportional to the ionic radii of the cations present in the samples. Moreover,  $\text{Cl}^-$  anions act as a sort of “protonic well” for high field intensities, further lowering the overall proton transfer efficiency of the aqueous solutions. As a consequence, all the recorded protonic conductivities are lower than that for neat water ( $\sigma_p = 7.8 \text{ S cm}^{-1}$ ), which strongly indicates that devices exploiting the proton transfer ability should be designed so as to minimize the presence of ionic impurities.

Received 31st May 2017,  
Accepted 12th July 2017

DOI: 10.1039/c7cp03663a

rsc.li/pccp

### 1. Introduction

Most of the properties and anomalies describing the behaviour of water are somehow related to the hydrogen bonded (H-bonded) network.<sup>1–3</sup> Albeit the features of H-bonds have been investigated and depicted by an impressive amount of research, the way in which some external conditions – such as the inclusion of ionic species – affect the three-dimensional H-bonds arrangement is wrapped up in a high degree of uncertainty.

If, on one hand, the presence of solvated ions cannot be avoided even in ultra-pure water samples, on the other hand, the lack of scientific consensus about the ion-induced microscopic effects on the water structure is representative of the

practical challenges faced when investigating electrolyte solutions.<sup>4,5</sup> However, the indisputable role played by a few atomic charged species both in biology (i.e.,  $\text{Na}^+$ ,  $\text{K}^+$ ,  $\text{Cl}^-$ ,  $\text{Mg}^{2+}$ ,  $\text{Ca}^{2+}$ , etc.)<sup>6–8</sup> and in industry (e.g.,  $\text{Li}^+$  batteries)<sup>9</sup> requires impelling and massive scientific efforts. In fact, besides the well-known Hofmeister series,<sup>10</sup> hydrated ionic species finely rule the selectivity of cell membranes,<sup>6,7</sup> which is thus responsible for complex processes such as nerve pulse generation. On the other hand, aqueous solutions represent the prototype of electrolytic batteries.

In all cases, a subtle balance between electrostatics, quantum mechanics (i.e., partial orbital sharing), and thermodynamics governs the delicate behaviour of the hydration process. The complexity of the problem is witnessed, *inter alia*, by the fact that there is no general consensus on the spatial extent of the effects induced by the inclusion of an ion in bulk water.<sup>11–13</sup> Recent *ab initio* calculations<sup>14</sup> have shown that the presence of a chaotrope species such as  $\text{Cl}^-$  does not have any effect on the orientation of water dipoles beyond the first hydration shell, whereas detectable perturbations – perhaps extremely small and unable to affect biological phenomena – have been observed in the polarizability of the water molecules at longer distances.

<sup>a</sup> Institute of Biophysics, Czech Academy of Sciences, Královopolská 135, 61265 Brno, Czech Republic. E-mail: cassone@ibp.cz, sponer@ncbr.muni.cz

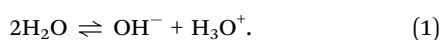
<sup>b</sup> Université d'Evry val d'Essonne-Université Paris-Saclay, Blvd. F. Mitterrand, 91025 Evry, France. E-mail: fabrizio.creazzo@univ-evry.fr

<sup>c</sup> Università degli Studi di Messina, Dipartimento di Scienze Matematiche e Informatiche, Scienze Fisiche e Scienze della Terra, Contrada Papardo, 98166 Messina, Italy. E-mail: paolo.giaquinta@unime.it

<sup>d</sup> CNR-IPCF, Viale Ferdinando Stagno d'Alcontres 37, 98158 Messina, Italy. E-mail: saija@ipcf.cnr.it

Additionally, the lack of a wide consensus on the typical coordination numbers characterizing the ionic first solvation shell is thoroughly recorded in the literature.<sup>4</sup> From an experimental perspective, the identification of this quantity is a very hard task for small ions such as Li<sup>+</sup> and, recently, new ionic radii for this species and for Na<sup>+</sup> have been proposed<sup>4</sup> by joining the advantages stemming from large angle X-ray scattering (LAXS) and double difference infrared spectroscopy (DDIR). In this respect, *ab initio* Molecular Dynamics (AIMD)<sup>8,14</sup> and QM/MM<sup>15</sup> computational techniques have proven their reliability in reproducing the ion-induced structural changes in aqueous solutions, thus becoming an invaluable tool for the characterization of electrolyte solutions at a molecular level. Indeed, although sixty years ago concepts such as kosmotrope and chaotrope have been introduced to characterize the perturbation produced by a given ion on the H-bond network of water,<sup>16,17</sup> and notwithstanding the fact that these notions were supported by classical molecular dynamics simulations,<sup>18–20</sup> they have recently been blunted by an AIMD study.<sup>21</sup>

Ionic conductivities are determined by applying an oriented external static electric field to electrolyte solutions. In the low field strength regime and within the Kohlrausch's law of independent migration of ions (*i.e.*, in the limit of infinite dilution), the mobilities of the alkali metal cations are well-established and can be easily related to their respective ionic sizes:<sup>22</sup> the bigger the cation the larger the mobility. However, at finite molarities and for stronger field intensity regimes the overall situation may dramatically change. Field intensities of the order of 1 V Å<sup>-1</sup> and even stronger were detected at the atomic sites of the water molecules hydrating Na<sup>+</sup> and Cl<sup>-</sup> ions,<sup>23</sup> suggesting that for moderate-to-intense field strengths more complicated phenomena may be relevant in describing the ionic diffusion. Moreover, field intensities of about 0.30 V Å<sup>-1</sup> are able to induce the molecular dissociation of water and proton transfers along the H-bonded network<sup>24–27</sup> *via* the well-known protolysis reaction:



This latter process plays a crucial role in many disparate domains, from neurobiology to electrolytic batteries and hydrogen-based technology.<sup>28,29</sup> Thus, it can be expected that a subtle interplay between the two deeply different mechanisms of protonic migration, on one hand, and of standard ionic diffusion, on the other, rules the complex dynamics of electrolytic solutions subjected to intense field strengths.

The present article is structured as follows. In Section II we illustrate the methodology of our investigation. Section III is divided into three subsections: in the first one we present the results involving radial distribution functions and the structural effects introduced by the inclusion of the ions in the H-bonded network of water; in the following subsection we illustrate a detailed analysis of the dynamical properties of the ions under the action of progressively increasing field strengths, whereas in the third subsection we present our results on water dissociation and proton conduction properties. Section IV is finally devoted to concluding remarks.

## II. Methods

First-principles Molecular Dynamics simulations were carried out on KCl and LiCl water solutions. In addition, these simulations have been compared with a recent study on an electrolyte NaCl aqueous solution, performed exactly under the same conditions,<sup>26</sup> in order to characterize both the ionic mobilities of the three simplest alkali metal cations and the different proton conduction efficiencies. Each of our numerical samples was represented by two ionic pairs solvated by 64 water molecules arranged in a cubic cell with the side length equal to 12.93 Å and 12.72 Å for the KCl and the LiCl water solutions, respectively, corresponding to the molarities of 1.7 M. As usual, periodic boundary conditions were thoroughly applied.

We used the software package Quantum ESPRESSO,<sup>30</sup> based on the Car–Parrinello (CP) approach,<sup>31</sup> to perform AIMD simulations of all the above-mentioned samples under the action of static and homogeneous electric fields applied along a given direction (corresponding to the *z*-axis). The implementation of an external electric field in numerical codes based on density functional theory (DFT) can be achieved by exploiting the modern theory of polarization and Berry's phases<sup>32</sup> (see, *e.g.*, ref. 33 for the technical implementation of a static and homogeneous electric field in *ab initio* codes and ref. 34 for a review of several methods that allow for the application of external fields in disparate simulation frameworks).

As for exchange and correlation effects, we adopted the gradient-corrected Perdew–Burke–Ernzerhof (PBE)<sup>35</sup> functional within the plane-wave/pseudopotential framework. The PBE functional and its adequate description of polarization effects<sup>36</sup> are known to provide a reasonably accurate structure in the case of H-bonded systems.<sup>37</sup> Moreover, although its employment is justified by the already tested adherence of some computational results<sup>25,26,38</sup> to many experimental data (*e.g.*, see ref. 39), we thoroughly and carefully checked the reliability of the current results by means of a direct comparison with the available experimental and computational data (see the “Structural properties” section). In addition, as far as the PBE accuracy and reliability in mimicking the phenomenon of the protolysis in liquid water is concerned, a pioneering study<sup>25</sup> performed using PBE predicted the experimental field-induced dissociation threshold of the water molecule,<sup>27</sup> confirming thus some preliminary<sup>24</sup> and rather up-to-date<sup>40</sup> experimental data.

All the AIMD simulations have been carried out at the nominal temperature of 315 K after equilibration runs of 5 ns performed by means of typical classical force fields in order to prepare suitable initial atomic configurations. In the AIMD simulations we gradually increased the intensity of the electric field from zero up to a maximum of 0.50 V Å<sup>-1</sup> (0.70 V Å<sup>-1</sup> in the case of the NaCl water solution) with a step increment of about 0.05 V Å<sup>-1</sup>. The temperature was kept fixed through the coupling of the system using a Nosé–Hoover thermostat whose frequency was set at 13.5 THz. The systems were kept in an isothermal–isochoric (*NVT*) ensemble and the dynamics was classically treated using the Verlet algorithm; for each electric field intensity the dynamics was propagated for time-lengths up

to about 7 or 8 ps, extending to about 25 ps in the zero-field regime. Hence, a simulation time of approximately 100 ps has been cumulated for the KCl and the LiCl aqueous solutions, whereas a trajectory of about 140 ps was previously collected for the NaCl electrolyte solution.<sup>26</sup>

The fictitious electronic mass was set to a value of 300 a.u., and a plane-wave kinetic energy cutoff of 40 Ry and a cutoff energy of 320 Ry for the charge density were chosen, which allowed us to adopt a timestep of 0.096 fs. With such cutoff values the sample can be described in a reliable way since the core electronic interaction is being depicted through Ultrasoft Pseudopotentials (USPP) generated *via* the Rappe–Rabe–Kaxiras–Joannopoulos (RRKJ) method.<sup>41</sup>

A Löwdin population analysis<sup>42</sup> has been performed by projecting the wavefunctions onto their standard (pseudo)atomic basis sets. By using a simple Gaussian broadening with spread equal to 0.002 Ry, the projected density of states and the Löwdin valence electron populations have been thus evaluated.

The conductivities were obtained from Ohm's law. The current intensity is related to the number of charge carriers flowing in a time interval  $\Delta t$  through a section area  $a^2$  orthogonal

to the direction of the electric field, with  $a$  being the side of the simulation box. The protonic conductivity  $\sigma_p$  was then calculated as

$$\sigma_p = \left( \frac{q\Delta N}{\Delta t a^2} \right) \cdot \frac{1}{E}, \quad (2)$$

where  $q$  is the elementary charge.

### III. Results and discussion

#### A. Structural properties

Averaged molecular correlations can be quantified by means of the evaluation of the atomic radial distribution functions (RDF). As shown in Fig. 1, a molarity of 1.7 M does not significantly alter the overall water structure which is delineated by the oxygen–oxygen (O–O) and oxygen–hydrogen (O–H) RDFs. In fact, the typical oscillations characterizing the structural correlations present in neat water modelled using the same<sup>25,38</sup> or similar *ab initio* techniques<sup>43–45</sup> also appear in all the investigated aqueous solutions (*i.e.*, NaCl, KCl, and LiCl). Notwithstanding the slight and well-known over-structuring of the water arrangement

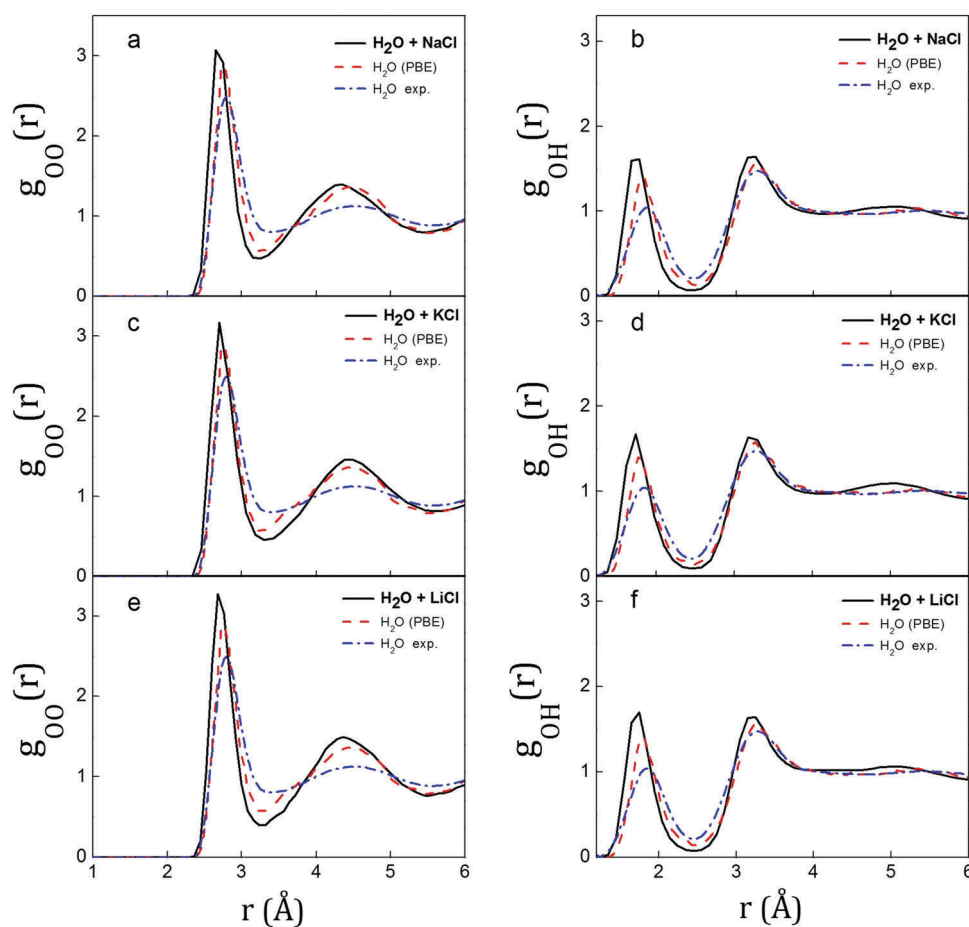


Fig. 1 Zero-field oxygen–oxygen (a, c and e) and oxygen–hydrogen (b, d and f) radial distribution functions of NaCl (a and b), KCl (c and d), and LiCl (e and f) water solutions at  $T = 315$  K with a saline molarity of 1.7 M (*i.e.*, from the current calculations and for the NaCl case from ref. 26) (black curves), of neat water modeled with the same PBE exchange and correlation functional at  $T = 350$  K of ref. 25 (red dashed curves), and from experiment at  $T = 298$  K<sup>39</sup> (blue dot-dashed curves); we have plotted only the extramolecular part of the oxygen–hydrogen radial distribution functions.

typically introduced by the PBE functional, the locations of the first peak of both O–O and O–H RDFs fall at 2.7 Å and 1.7 Å, indicating that the typical H-bond length is finely reproduced.

As far as the alkali metal cations are concerned, the cation–oxygen ( $\alpha$ -O) RDFs indicate the different roles played by each cation in the aqueous H-bonded network. As shown in Fig. 2, the potassium ion–oxygen (K–O) RDF shows the smallest peaks heights. In addition, also the locations of the K–O RDF maxima fall at longer distances, indicating less structured hydration shells with respect to those established by the water molecules with Li<sup>+</sup> and Na<sup>+</sup>. The first solvation shell is not sharply separate from the second one and several exchange events take place between the first and the second hydration shell. As is well-known, K<sup>+</sup> is in fact considered a structure breaker, inducing the formation of regions in the water network to which an increase of entropy is associated with respect to the pure water case.<sup>16,17</sup>

On the contrary, the other RDFs shown in Fig. 2 are characterized by highly-defined peaks and dips. By comparison of these latter curves with the O–O RDFs shown in Fig. 1, it is clear that the heights of the first peak of the Na–O and Li–O RDFs depict more structured water arrangements around each cation with respect to that characterizing the typical water molecule solvation. These ionic species can in fact be regarded as structure makers, introducing water regions to which a loss of entropy can be associated with respect to the neat bulk water case.<sup>16,17</sup> In addition, the Li–O RDF clearly shows a further oscillation beyond the second solvation shell.

The only anionic species here investigated is the chlorine ion Cl<sup>-</sup>. Although the overall arrangement of its hydration water molecules shows a preferential orientation (*i.e.*, solvating water molecules tend to point one hydrogen atom toward the ion) as can be noticed by the locations of the first peaks of the Cl–O and Cl–H RDFs shown in Fig. 3, it is well-known that all

the halide anions are structure breaker species with the exception of F<sup>-</sup>.<sup>16,17</sup>

A useful property characterizing the solvation properties of a given ion in solution is the coordination number. The average number of water molecules surrounding a given cationic species has been calculated by choosing a distance cutoff equal to the spatial location of the first dip of the respective cation–oxygen ( $\alpha$ -O) RDF (see Fig. 2). In the Cl<sup>-</sup> case, an equivalent criterion applies to both the Cl–O and the Cl–H coordination numbers. It turns out that Na<sup>+</sup> and K<sup>+</sup> ions are on average solvated by 5.9 and 6.0 water molecules, respectively. Bankura *et al.*,<sup>8</sup> in a similar study performed with the same salt molarity, have found values of 4.9 and 6.1 whereas Rowley and Roux,<sup>15</sup> by employing more advanced computational techniques, have shown coordination numbers falling in the ranges 5.7–5.8 and 6.9–7.0 for sodium and potassium cations, respectively. These coordination numbers are in fairly good agreement with the (reliable) experimentally determined estimates of 6 and 7 for Na<sup>+</sup> and K<sup>+</sup>, respectively.<sup>4</sup> However, wide ranges of values have been proposed both for Na<sup>+</sup> (*i.e.*, 4,<sup>46</sup> 4.6,<sup>47</sup> 5.3,<sup>48</sup> 5.5,<sup>49</sup> 5.6–6.5,<sup>50</sup> 6,<sup>51</sup> 6.5,<sup>52</sup> 8<sup>4</sup>) and K<sup>+</sup> (*i.e.*, 5.6,<sup>47</sup> 6,<sup>53</sup> 6.2–6.8,<sup>49</sup> 7.8–8.3<sup>50</sup>), rendering the coordination number evaluation of typical electrolyte solutions somehow strictly dependent on the technique and on the cutoff distance employed for the counting.

Notwithstanding the fact that experiments leading to the precise knowledge of the average number of water molecules hydrating small ions are quite difficult and thus not very reliable,<sup>4</sup> the coordination number of Li<sup>+</sup> is usually considered to be 4,<sup>4,54,55</sup> a value which is in fairly good agreement with that obtained from the current *ab initio* investigation: 3.6.

As far as the atomic coordination numbers of Cl<sup>-</sup> species are concerned, the estimates found among the investigated samples (*i.e.*, LiCl, NaCl, and KCl) lead to values equal to 5.8 and 4.9 for the Cl–O and for the Cl–H coordination numbers, respectively. These latter values are in good agreement with those reported in ref. 8 (*i.e.*, 5.9 and 5.2, respectively) and with the corresponding values extracted from several neutron and X-ray diffraction experiments.<sup>48,56–58</sup>

## B. Dynamical properties

Although the relative mobilities of monovalent cations are well-established within the Kohlrausch limit of infinite dilution,<sup>22</sup> at finite concentrations more complex phenomena may reside behind the diffusive properties of simple ions. Since estimates of well-converged ionic diffusion coefficients require extremely long trajectories,<sup>21</sup> their careful evaluation in first-principles simulations in the presence of an electric field is beyond the capabilities of the most powerful supercomputers within a reasonably brief (human) time. However, the mean square displacement (MSD) and the drift carry fundamental insights into the diffusion properties of any species. Whereas in the low-field intensity regime (*i.e.*, up to 0.10 V Å<sup>-1</sup>) a fully Brownian motion rules the dynamics of the investigated alkali metal within the accessible time-scale, a field strength of 0.15 V Å<sup>-1</sup> marks the transition to a slightly diffusive regime for the Na<sup>+</sup> species. As shown in Fig. 4a and b, at this field threshold

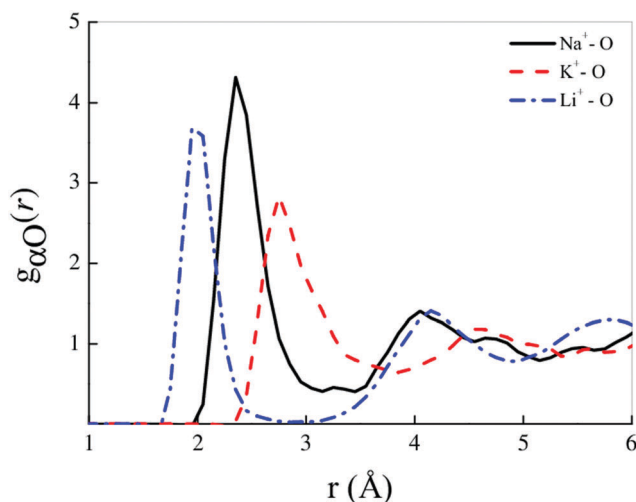


Fig. 2 Cation–oxygen ( $\alpha$ -O) radial distribution functions for Na<sup>+</sup> (black solid line), K<sup>+</sup> (red solid line), and Li<sup>+</sup> (blue solid line) in the zero-field regime. Whereas sodium and lithium cations are clearly structure maker species (*i.e.*, sharp first peaks and dips fall at short distances), potassium can be regarded as a (mild) structure breaker cation.

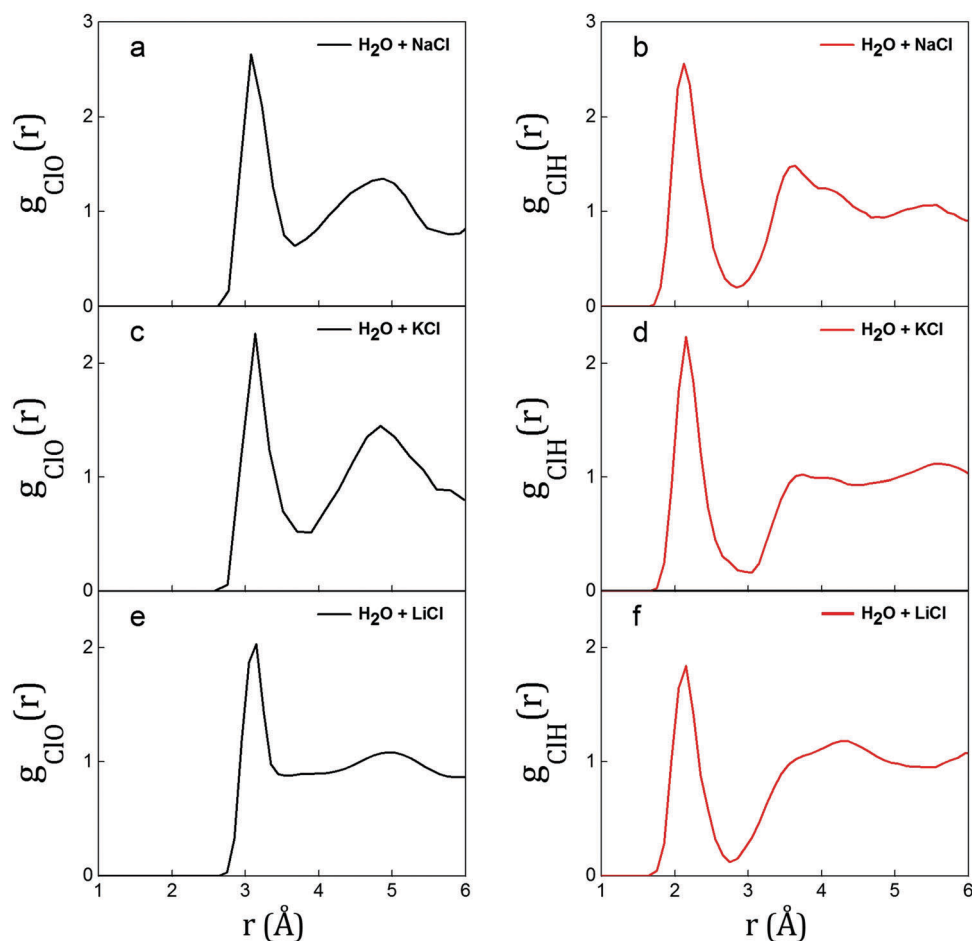


Fig. 3 Chloride–oxygen (black solid lines) (a, c and e) and chloride–hydrogen (red solid lines) (b, d and f) radial distribution functions of NaCl (a and b),<sup>26</sup> KCl (c and d), and LiCl (e and f) aqueous solutions in the zero-field regime.

sodium cations have the tendency to slightly – but neatly – migrate along the field direction. In other words, the  $z$ -axis represents the privileged direction along which the motion of sodium ions takes place. However, even a structure breaker species such as  $K^+$  is not able to escape from its own hydration shell. A Löwdin population analysis shows that sodium cations, at this field intensity, hold on average a higher charge than  $K^+$ , as shown in Fig. 5. In fact, the valence electron population of this cation (*i.e.*, 8.6) is larger than that of  $Na^+$  (*i.e.*, 8.3). Therefore, a smaller local (positive) charge surrounds, on average, potassium cations than that of sodium ions. This finding suggests that  $Na^+$  ions can stabilize a better coupling with the external electrostatic field than that established by  $K^+$  cations at a field strength of  $0.15 \text{ V \AA}^{-1}$ .

As shown in Fig. 4c–h, a noticeable diffusive regime is achieved by all the cations for stronger field intensities. In particular, as shown by the drift and the MSD in Fig. 4c and d,  $Li^+$  starts to (almost freely) diffuse just after about 2 ps at a field strength of  $0.25 \text{ V \AA}^{-1}$ . This strong structure maker species has indeed the capability of initially maintaining a coupled dynamics with its own first solvation shell even in this field regime before escaping from its hydration “cage”, as shown in Fig. 6c. On the other hand, a structure breaker species such as

$K^+$  acquires such a high mobility that, in practice, it is almost free to diffuse through the aqueous environment. Because of the local charge characterizing  $Na^+$  cations, this species – which is commonly considered as a structure maker – is able to diffuse more similarly to a structure breaker such as  $K^+$  than to a structure maker such as  $Li^+$ , as shown in Fig. 4c and d for a field strength of  $0.25 \text{ V \AA}^{-1}$  and in Fig. 4e and f for an intensity of  $0.35 \text{ V \AA}^{-1}$ . After all, sodium cations are located in a borderline position within the first-column elements, marking indeed the ideal passage from the structure maker to the structure breaker species.

Albeit the surprisingly high mobility of  $Na^+$  ions,  $K^+$  species have – in a low-to-moderate field intensity regime – the highest mobility among the investigated cations, as it is visible from the slopes of the curves shown in Fig. 4c–f. This trend has been recorded up to a field strength of  $0.40 \text{ V \AA}^{-1}$ . Above this threshold, the capability of  $Na^+$  and  $K^+$  to neatly migrate achieves saturation: an increase of the external field intensity does not induce enhancements on the mobilities of these cations. On the contrary, a slight decrease of the transport properties of sodium and potassium ions has been detected, as is visible from a direct comparison of Fig. 4e with Fig. 4g or, similarly, of Fig. 4f with Fig. 4h. As we shall point out in the next

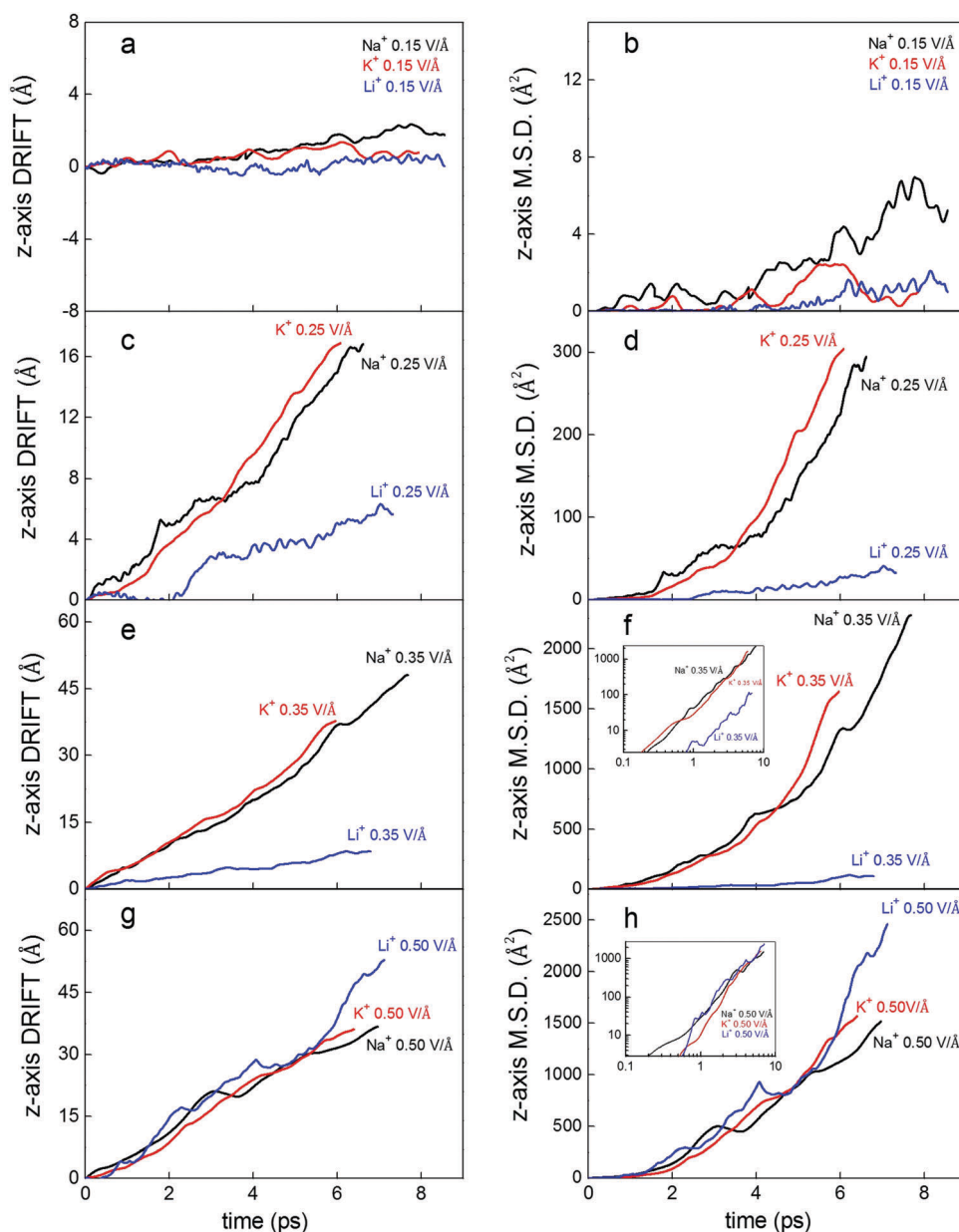


Fig. 4 Drift (a, c, e and g) and mean square displacement (b, d, f and h) along the field direction (*i.e.*, *z*-axis) of Na<sup>+</sup> (black solid lines), K<sup>+</sup> (red solid lines), and Li<sup>+</sup> (blue solid lines) for four field strengths: 0.15 V Å<sup>-1</sup> (a and b), 0.25 V Å<sup>-1</sup> (c and d), 0.35 V Å<sup>-1</sup> (e and f), and 0.50 V Å<sup>-1</sup> (g and h). In the inset of panels (f) and (h) the mean square displacement of the three cations has been plotted in a log–log scale for 0.35 V Å<sup>-1</sup> and 0.50 V Å<sup>-1</sup>, respectively.

section, such strong fields are indeed able to dissociate measurable fractions of water molecules and to sustain protonic currents, rendering the overall ionic conduction process a very complex phenomenon. In addition, also steric and inertial effects may play important roles in the saturation process characterizing the conductive regime of sodium and potassium cations. In fact, for these intense-field regimes (*i.e.*, between 0.40 and 0.50 V Å<sup>-1</sup>) the very small and light lithium cations are able to achieve and overcome the Na<sup>+</sup> and K<sup>+</sup> mobilities, as shown in Fig. 4g and h.

### C. Electrical properties

It is nowadays well-established that solvated ions produce intense local electric fields stronger than 1 V Å<sup>-1</sup>.<sup>23,59–61</sup>

In particular, field strengths up to 2 V Å<sup>-1</sup> have been detected on the atomic sites of the water molecules hydrating sodium and chlorine ions.<sup>23</sup> In addition, this result appears to be somewhat independent – within a reasonable range of concentrations – of the specific molarity of the solution.<sup>23</sup> On the other hand, more feeble field intensities are able to lead to the cleavage of some OH covalent bonds in neat liquid water at ambient temperature. In fact, the production of hydronium H<sub>3</sub>O<sup>+</sup> and hydroxide OH<sup>-</sup> ions has been achieved for a minimum field intensity threshold of 0.35 V Å<sup>-1</sup> in pure water.<sup>24,25,27</sup> A previous investigation of ours<sup>26</sup> concluded that the presence of sodium and chlorine ions in the aqueous environment allows for the decrease of the water dissociation threshold to a value of

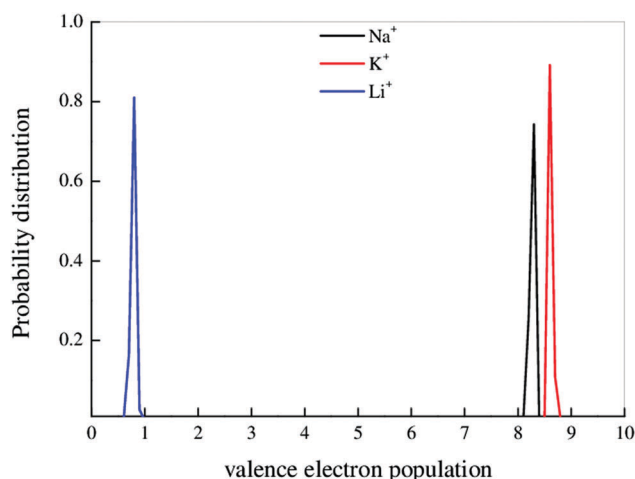


Fig. 5 Probability distributions of the averaged Löwdin valence electron populations of  $\text{Na}^+$  (black solid line),  $\text{K}^+$  (red solid line), and  $\text{Li}^+$  (blue solid line) in aqueous solutions under a field strength of  $0.15 \text{ V \AA}^{-1}$ . Although  $\text{Na}^+$  and  $\text{K}^+$  are nominally characterized by the same ideal valence population (*i.e.*, 8), solvation and thermodynamic properties give rise to larger valence electron populations of potassium ions than those identified in sodium cations. For the sake of completeness, also the distribution of the naturally smaller valence electron populations of  $\text{Li}^+$  is shown.

$0.25 \text{ V \AA}^{-1}$ . Exactly the same threshold holds for both the KCl and the LiCl water electrolytes here investigated. Indeed, although in all the simulated samples the appearance of the water counter-ions  $\text{H}_3\text{O}^+$  and  $\text{OH}^-$  has been revealed even at  $0.20 \text{ V \AA}^{-1}$ , their life-times were too short (*i.e.*,  $\sim 10 \text{ fs}$  or even shorter) to be considered as ascribable to entities uncorrelated from statistical fluctuations. *A posteriori* this finding suggests that also species such as  $\text{Li}^+$  and  $\text{K}^+$  generate local fields of the order of  $\sim 1 \text{ V \AA}^{-1}$ , rendering thus the water molecular dissociation feasible for lower external field intensities than those needed in the neat water case.

If the presence of such local fields leads to the same molecular dissociation thresholds for the water molecules in different electrolyte solutions, the very different sizes of the alkali metal cations lead to disparate protonic current thresholds. Although a field strength of  $0.25 \text{ V \AA}^{-1}$ , which is able to induce the first (non-negligible) dissociative events, is also capable of

establishing a net proton transfer both in the NaCl and in the LiCl water solutions, no detectable protonic current has been observed in the KCl electrolyte solution under these conditions. In order to reach a conductive regime, protons in this sample have to be irradiated by means of a field intensity of  $0.35 \text{ V \AA}^{-1}$ . Incidentally, this latter strength identifies the same threshold that is necessary to sustain an ordered (net) proton flow in neat water.<sup>25</sup> This finding is not so surprising if one considers that the basic mechanism of proton transfer involves the formation of a transient Zundel ion which is marked by the approach of a hydronium ion and a water molecule to an oxygen–oxygen distance of  $2.42 \text{ \AA}$ <sup>62</sup> before the typical Grotthuss mechanism of migration can take place. At  $0.25 \text{ V \AA}^{-1}$   $\text{Na}^+$ ,  $\text{K}^+$ , and  $\text{Li}^+$  have enough mobility to be able to escape from their own initial hydration “cage” and temporarily jump onto new solvation shells, as shown in Fig. 6. By spanning over the space, structure maker cations such as  $\text{Na}^+$  and  $\text{Li}^+$  are able to transiently let water molecules explore intermolecular distances shorter than those typically sampled in neat water or in the KCl aqueous solution, thus making the triggering of proton conduction easier.

In Fig. 7, the protonic current–voltage diagrams of the NaCl, KCl, and LiCl water solutions are shown. The just mentioned “delay” of the KCl solution in establishing a conductive regime of the protonic subsystem is visible from the fact that the first measurable current occurs at  $0.35 \text{ V \AA}^{-1}$  which corresponds to a nominal voltage of  $4.53 \text{ V}$  for this system size. All the investigated solutions show an Ohmic behaviour of the protonic component of the current, provided that a regime of net proton flow has been achieved. By exploiting Ohm’s law, it turns out that protons flow easily in the LiCl aqueous solution and therefore, in descending order, in the NaCl and in the KCl electrolyte solutions. In fact, protonic conductivities equal to  $3.0 \text{ S cm}^{-1}$ ,  $2.5 \text{ S cm}^{-1}$ , and  $2.3 \text{ S cm}^{-1}$  characterize the LiCl, NaCl, and KCl solutions, respectively. Thus, the protonic conduction efficiency is inversely proportional to the ionic radii of the cations present in the different solutions; in practice, the smaller the cation, the smaller the hindrance between the two distinct migration processes of standard and Grotthuss diffusion. Upon reversing the perspective, one recognizes that the enhanced proton transfer established in the LiCl water solution does not hamper the diffusion of  $\text{Li}^+$ , a process manifestly observed for the bigger cations  $\text{Na}^+$  and  $\text{K}^+$ , as shown in Fig. 4.

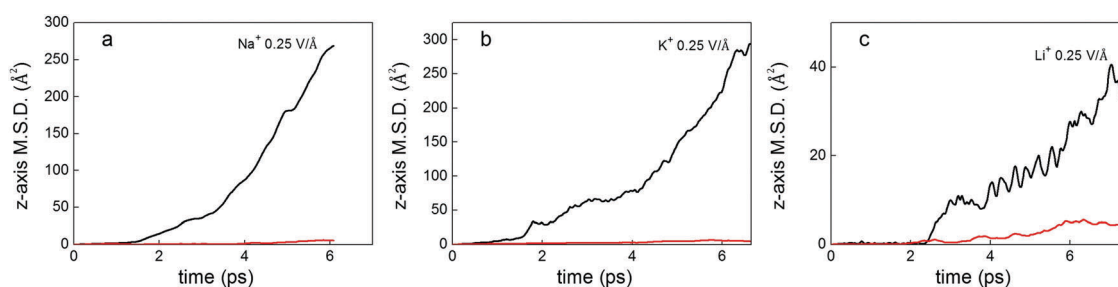


Fig. 6 Mean square displacement along the field direction (*i.e.*,  $z$ -axis) of  $\text{Na}^+$  (a),  $\text{K}^+$  (b), and  $\text{Li}^+$  (c) (black solid curves) and of their respective solvating oxygen atoms (red solid curves) for a field strength of  $0.25 \text{ V \AA}^{-1}$ . Whereas the motion of  $\text{Na}^+$  ions is initially coupled to that of their own solvation shells for about  $1.5 \text{ ps}$  and that of  $\text{Li}^+$  for more than  $2 \text{ ps}$ ,  $\text{K}^+$  cations, being structure breakers, are statistically able to escape from their own solvation “cages” in less than  $1 \text{ ps}$  at this field intensity.

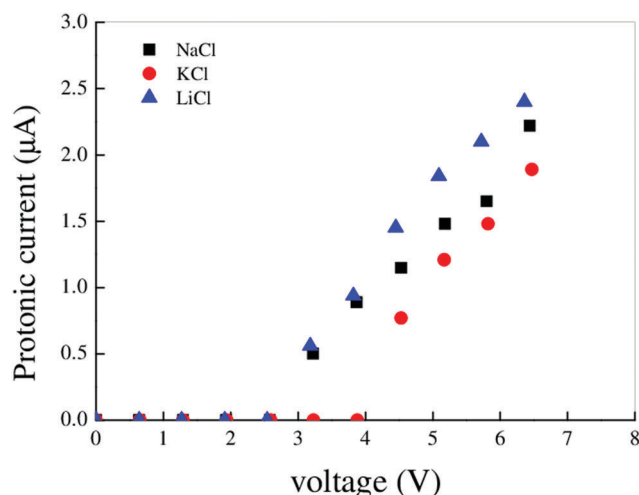


Fig. 7 Protonic current–voltage diagrams of NaCl (black squares), KCl (red dots), and LiCl (blue triangles) aqueous solutions. Once a conductive regime is established in all the systems, an Ohmic behaviour characterizes the protonic response (*i.e.*, the current) to an increment of the external field strength (*i.e.*, the voltage).

Finally, all the evaluated conductivities are smaller than that recorded in neat water (*i.e.*,  $7.8 \text{ S cm}^{-1}$ ).<sup>25</sup> This evidence can be explained by considering a twofold phenomenon. On one hand, as just mentioned, charges of the same sign repel each other hindering the mutual motion; this hindrance is of course enhanced by bigger and bigger cations. On the other hand,  $\text{Cl}^-$  species act, at strong field intensities, as a sort of “protonic well” by attracting some protons  $\text{H}^+$  and transiently forming hydrogen chloride HCl species, as shown in Fig. 8. Because of the typical arrangement of the solvation water molecules of  $\text{Cl}^-$ , each one having on average one hydrogen pointed toward the anion, the further release of the proton from the chlorine ion to a water molecule represents a sizable hurdle to the proton transfer efficiency of a water solution. This process represents a

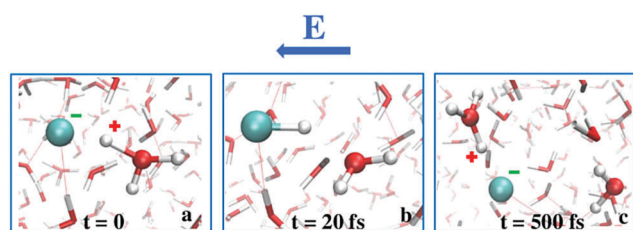


Fig. 8 Hydrogen chloride (HCl) formation mechanism. Red, white, and cyanide atoms represent oxygen, hydrogen, and chlorine, respectively. At high field strengths (*i.e.*, above  $0.35 \text{ V \AA}^{-1}$ ) the formation of an hydronium cation  $\text{H}_3\text{O}^+$  in the first solvation shell of  $\text{Cl}^-$  species (a) is thoroughly detected in all the electrolyte solutions. After an ultra-fast proton transfer, the neutralization process leads to the transient synthesis of HCl (b). The formation of this latter represents the rate-limiting step for the collective net proton flow since HCl has to wait for the re-orientation of another water molecule of its hydration shell in order to release the proton along the field direction (c). In another possible mechanism,<sup>26</sup> the only choice HCl has is to return the proton to the initial donor water molecule. Both mechanisms significantly slow down the overall proton transfer process in electrolyte solutions.

common feature of all the investigated solutions, clearly suggesting that high-performance proton transfer-based devices should be designed in such a way so as to minimize the presence of other ionic impurities.

## IV. Conclusions

By performing *ab initio* molecular dynamics simulations of three different electrolyte solutions (*i.e.*, LiCl, NaCl, and KCl) at a molarity of 1.7 M, we have studied their response to external static electric fields of varying intensities. As far as the cationic mobilities are concerned, we have found that although in low-to-moderate field intensity regimes the bigger the cation the higher the mobility (*i.e.*,  $\mu(\text{K}^+) > \mu(\text{Na}^+) > \mu(\text{Li}^+)$ ), at stronger fields this is no longer true. Up to a field strength of  $0.40 \text{ V \AA}^{-1}$ , the potassium ions are slightly more mobile than sodium ions which in turn have a sizeably greater freedom of migration across the water environment than lithium cations. Above this field threshold, whereas both  $\text{Na}^+$  and  $\text{K}^+$  ionic mobilities achieve saturation,  $\text{Li}^+$  cations are still able to increase their own diffusion properties, slightly overcoming the sodium and potassium mobilities. This counterintuitive finding is related to the formation of other ionic species in the samples. In fact, in those field intensity regimes, water molecular dissociations and sustained proton transfers occur in all the investigated electrolyte solutions.

The presence of solvated charged species anticipates the well-known water dissociation threshold from  $0.35 \text{ V \AA}^{-1}$  to  $0.25 \text{ V \AA}^{-1}$ . However, if on one hand “structure maker” cations present in the NaCl and LiCl electrolyte solutions give rise to a one-stage process in that water ionizations are rapidly followed by a net collective proton flow, on the other hand, “structure breaker” ions composing the KCl solution hamper the initial proton conduction which starts only at  $0.35 \text{ V \AA}^{-1}$ , as in neat water.<sup>24,25,27</sup> Although all the protonic subsystems of the investigated samples show an Ohmic response to the external field, the estimated protonic conductivities are dependent on the nature of the present alkali metal cations. Indeed, the LiCl, NaCl, and KCl water solutions show protonic conductivities equal to  $3.0 \text{ S cm}^{-1}$ ,  $2.5 \text{ S cm}^{-1}$ , and  $2.3 \text{ S cm}^{-1}$ , respectively, a series that inversely follows the trend of the ionic radii of  $\text{Li}^+$ ,  $\text{Na}^+$ , and  $\text{K}^+$  species. Moreover, these values are noticeably lower than that estimated for pure water (*i.e.*,  $7.8 \text{ S cm}^{-1}$ ).<sup>25</sup> We show that in addition to the trivial repulsion between charged species of the same sign – such as protons  $\text{H}^+$  and the solvated alkali metal cations, other processes take place that reduce the ability of electrolyte solutions in transferring protons. The most relevant phenomenon is in fact the involvement of the  $\text{Cl}^-$  anions that, acting as a sort of “protonic well” at high field intensities, slow down the overall process of proton transfer by means of the formation of hydrogen chloride (HCl).

By summarizing, at high field intensities, the relative mobilities of the simplest alkali metal cations are no longer the same as those recorded for low-to-moderate field regimes because of a delicate balance with the activated proton transfer. *Vice versa*, the proton

conduction efficiencies of the different electrolyte solutions are inversely proportional to the ionic radii of the solvated cationic species.

## Acknowledgements

J. S. acknowledges the support by Preamium Academiae. F. C. thanks LAMBE UMR8587 (Charmmmat), Laboratoire Analyse et Modélisation pour la Biologie et l'Environnement and, in particular, Prof. Marie-Pierre Gaigeot for support.

## References

- 1 P. G. Debenedetti, *Metastable Liquids – Concepts and Principles*, Princeton University Press, Princeton, New Jersey U. S. A., 2006.
- 2 F. Franks, *Water: A Matrix of Life*, Royal Society of Chemistry, Cambridge, 2nd edn, 2000.
- 3 I. Brovchenko and A. Oleinikova, Multiple Phases of Liquid Water, *ChemPhysChem*, 2008, **9**, 2660–2675.
- 4 J. Mähler and I. Persson, A Study of the Hydration of the Alkali Metal Ions in Aqueous Solution, *Inorg. Chem.*, 2012, **51**, 425–438.
- 5 P. R. Smirnov and V. N. Trostin, Structure of the Nearest Surrounding of the Li<sup>+</sup> Ion in Aqueous Solution of its Salts, *Russ. J. Gen. Chem.*, 2006, **76**, 175–182.
- 6 B. Hille, *Ion Channels of Excitable Membranes*, Sinauer Associates, Inc. Publishers, Sunderland, Massachusetts U.S.A., 3rd edn, 2001.
- 7 Y. Zhou and R. MacKinnon, The Occupancy of Ions in the K<sup>+</sup> Selectivity Filter: Charge Balance and Coupling of Ion Binding to a Protein Conformational Change Underlie High Conduction Rates, *J. Mol. Biol.*, 2003, **333**, 965–975.
- 8 A. Bankura, V. Carnevale and M. L. Klein, Hydration structure of salt solution from *ab initio* molecular dynamics, *J. Chem. Phys.*, 2013, **138**, 014501.
- 9 J.-M. Tarascon and M. Armand, Issues and Challenges facing Rechargeable Lithium Batteries, *Nature*, 2001, **414**, 359–367.
- 10 W. Kunz, J. Henle and B. W. Ninham, Zur Lehre von der Wirkung der Salze (About the Science of the Effects of Salts): Franz Hofmeister's historical papers, *Curr. Opin. Colloid Interface Sci.*, 2004, **9**, 19–37.
- 11 L. Stryer and R. P. Haugland, Energy Transfer: A Spectroscopic Ruler, *Proc. Natl. Acad. Sci. U. S. A.*, 1967, **68**, 719–726.
- 12 J. E. Enderby, Ion Solvation via Neutron-Scattering, *Chem. Soc. Rev.*, 1995, **24**, 159–168.
- 13 K. D. Collins, G. W. Neilson and J. E. Enderby, Ions in Water: Characterizing the Forces that Control Chemical Processes and Biological Structure, *Biophys. Chem.*, 2007, **128**, 95–104.
- 14 A. P. Gaiduk and G. Galli, Local and Global Effects of Dissolved Sodium Chloride on the Structure of Water, *J. Phys. Chem. Lett.*, 2017, **8**, 1496–1502.
- 15 C. N. Rowley and B. Roux, The Solvation Structure of Na<sup>+</sup> and K<sup>+</sup> in Liquid Water Determined from High Level *ab initio* Molecular Dynamics Simulations, *J. Chem. Theory Comput.*, 2012, **8**, 3526–3535.
- 16 R. W. Gurney, *Ionic Processes in Solution*, McGraw-Hill, New York, 1953.
- 17 H. S. Frank and W. Y. Wen, Structural Aspects of Ion-Solvent Interaction in Aqueous Solutions: A Suggested Picture of Water Structure, *Discuss. Faraday Soc.*, 1957, **24**, 133–140.
- 18 N. Galamba, On the Effects of Temperature, Pressure, and Dissolved Salts on the Hydrogen-Bond Network of Water, *J. Phys. Chem. B*, 2013, **117**, 589–601.
- 19 M. T. Reagan, J. G. Harris and J. W. Tester, Molecular Simulations of Dense Hydrothermal NaCl-H<sub>2</sub>O Solutions deom Subcritical to Supercritical Conditions, *J. Phys. Chem. B*, 1999, **103**, 7935–7941.
- 20 R. Renou, M. Ding, H. Zhu, A. Szymczyk, P. Malfreyt and A. Ghoufi, Concentration Dependence of the Dielectric Permittivity, Structure, and Dynamics of Aqueous NaCl Solutions: Comparison between the Drude Oscillator and Electronic Continuum Models, *J. Phys. Chem. B*, 2014, **118**, 3931–3940.
- 21 Y. Ding, A. Hassanali and M. Parrinello, Anomalous Water Diffusion in Salt Solutions, *Proc. Natl. Acad. Sci. U. S. A.*, 2014, **111**, 3310–3315.
- 22 M. R. Wright, *An Introduction to Aqueous Electrolyte Solutions*, Wiley, Chichester, England, 2007.
- 23 B. Sellner, M. Valiev and S. M. Kathman, Charge and Electric Field Fluctuations in Aqueous NaCl Electrolytes, *J. Phys. Chem. B*, 2013, **117**, 10869–10882.
- 24 E. M. Stuve, Ionization of Water in Interfacial Electric Fields: an Electrochemical View, *Chem. Phys. Lett.*, 2012, **519–520**, 1–17.
- 25 A. M. Saitta, F. Saija and P. V. Giaquinta, *Ab Initio* Molecular Dynamics Study of Dissociation of Water under an Electric Field, *Phys. Rev. Lett.*, 2012, **108**, 207801.
- 26 G. Cassone, F. Creazzo, P. V. Giaquinta, F. Saija and A. M. Saitta, *Ab initio* Molecular Dynamics Study of an Aqueous NaCl Solution under an Electric Field, *Phys. Chem. Chem. Phys.*, 2016, **18**, 23164–23173.
- 27 Z. Hammadi, M. Descoins, E. Salanon and R. Morin, Proton and light ion nanobeams from field ionization of water, *Appl. Phys. Lett.*, 2013, **101**, 243110.
- 28 K. Kaila and B. R. Ransom, in *pH and Brain Function*, ed. K. Kaila and B. R. Ransom, Wiley, New York, 1998.
- 29 E. I. Zoulias and N. Lymberopoulos, *Hydrogen-Based Autonomous Power Systems*, Springer, London, 2008.
- 30 P. Giannozzi, *et al.*, QUANTUM ESPRESSO: A Modular and Open-Source Software Project for Quantum Simulation of Materials, *J. Phys.: Condens. Matter*, 2009, **21**, 395502.
- 31 R. Car and M. Parrinello, Unified Approach for Molecular Dynamics and Density-Functional Theory, *Phys. Rev. Lett.*, 1985, **55**, 2471.
- 32 M. V. Berry, Quantal Phase Factors Accompanying Adiabatic Changes, *Proc. R. Soc. London, Ser. A*, 1984, **392**, 45.
- 33 P. Umari and A. Pasquarello, *Ab initio* Molecular Dynamics in a Finite Homogeneous Electric Field, *Phys. Rev. Lett.*, 2002, **89**, 157602.

- 34 N. J. English and C. J. Waldron, Perspectives on External Electric Fields in Molecular Simulation: Progress, Prospects and Challenges, *Phys. Chem. Chem. Phys.*, 2015, **17**, 12407–12440.
- 35 J. P. Perdew, K. Burke and M. Ernzerhof, Generalized Gradient Approximation Made Simple, *Phys. Rev. Lett.*, 1996, **77**, 3865–3868; J. P. Perdew, K. Burke and M. Ernzerhof, Generalized Gradient Approximation Made Simple, *Phys. Rev. Lett.*, 1997, **78**, 1396.
- 36 N. Marom, A. Tkatchenko, M. Rossi, V. G. Gobre, O. Hod, M. Scheffler and L. Kronik, Dispersion Interactions with Density-Functional Theory: Benchmarking Semiempirical and Interatomic Pairwise Corrected Density Functionals, *J. Chem. Theory Comput.*, 2011, **7**, 3944–3951.
- 37 C. Fiolhais, F. Nogueira and M. Marques, *A Primer in Density Functional Theory*, Springer-Verlag, Berlin, Heidelberg, 2010.
- 38 J. C. Grossman, E. Schwegler, E. W. Draeger, F. Gygi and G. Galli, Towards an Assessment of the Accuracy of Density Functional Theory for First Principles Simulations of Water, *J. Chem. Phys.*, 2003, **120**, 300.
- 39 A. K. Soper, The Radial Distribution Functions of Water as Derived from Radiation Total Scattering Experiments: Is There Anything we can Say for Sure?, *ISRN Phys. Chem.*, 2013, **2013**, 279463.
- 40 J. R. Choudhuri, D. Vanzo, P. A. Madden, M. Salanne, D. Bratko and A. Luzar, Dynamic Response in Nanoelectrowetting on a dielectric, *ACS Nano*, 2016, **10**, 8536–8544.
- 41 A. M. Rappe, K. M. Rabe, E. Kaxiras and J. D. Joannopoulos, Optimized Pseudopotentials, *Phys. Rev. B: Condens. Matter Mater. Phys.*, 1990, **44**, 13175.
- 42 P.-O. Löwdin, On the Nonorthogonality Problem, *Adv. Quantum Chem.*, 1970, **5**, 185–199.
- 43 B. Chen, I. Ivanov, M. L. Klein and M. Parrinello, Hydrogen Bonding in Water, *Phys. Rev. Lett.*, 2003, **91**, 215503.
- 44 M. Sprik, J. Hutter and M. Parrinello, *Ab Initio* Molecular Dynamics Simulation of Liquid Water: Comparison of Three Gradient-Corrected Density Functional, *J. Chem. Phys.*, 1996, **105**, 1142.
- 45 I.-C. Lin, A. P. Seitsonen, I. Tavernelli and U. Rothlisberger, Structure and Dynamics of Liquid Water from *Ab Initio* Molecular Dynamics – Comparison of BLYP, PBE, and revPBE Density Functionals with and without van der Waals Corrections, *J. Chem. Theory Comput.*, 2012, **8**, 3902–3910.
- 46 S. Bouazzizi and S. Nasr, Local Order in Aqueous Lithium Chloride Solutions as Studied by X-ray Scattering and Molecular Dynamics Simulations, *J. Mol. Struct.*, 2007, **837**, 206–213.
- 47 H. Ohtaki and N. Fukushima, A Structural Study of Saturated Aqueous Solutions of Some Alkali Halides by X-ray Diffraction, *J. Solution Chem.*, 1992, **21**, 23–28.
- 48 R. Mancinelli, A. Botti, F. Bruni, M. A. Ricci and A. K. Soper, Hydration of Sodium, Potassium, and Chloride Ions in Solution and the Concept of Structure Maker/Breaker, *J. Phys. Chem. B*, 2007, **111**, 13570–13577.
- 49 S. S. Azam, T. S. Hofer, B. R. Randolph and B. M. Rode, Hydration of Sodium (I) and Potassium (I) Revisited: A Comparative QM/MM and QMCF MD Simulation Study of Weakly Hydrated Ions, *J. Phys. Chem. A*, 2009, **113**, 1827–1834.
- 50 A. Tongraar, K. R. Liedl and B. M. Rode, Born Oppenheimer *Ab Initio* QM/MM Dynamics Simulations of Na<sup>+</sup> and K<sup>+</sup> in Water: From Structure Making to Structure Breaking Effects, *J. Phys. Chem. A*, 1998, **102**, 10340–10347.
- 51 V. I. Chizhik, V. I. Mikhailov and P. C. Su, NMR Relaxation Data on the Microstructure of Aqueous Solutions of Alkali-Metal Salts and Hydroxides, *Theor. Exp. Chem.*, 1987, **22**, 480–483.
- 52 G. Heinje, W. Luck and K. Heinzinger, Molecular Dynamics Simulation of an Aqueous Sodium Perchlorate Solution, *J. Phys. Chem.*, 1987, **91**, 331–338.
- 53 A. K. Soper and K. Weckstrom, Ion Solvation and Water Structure in Potassium Halide Aqueous Solutions, *Biophys. Chem.*, 2006, **124**, 180–191.
- 54 G. Palinkas, T. Radnai and F. Z. Hajdu, Ion-Solvent and Solvent-Solvent Interactions. X-ray Study of Aqueous Alkali Chloride Solutions, *Z. Naturforsch., A: Phys. Sci.*, 1980, **35**, 107–114.
- 55 H. Loeffler and B. Rode, The Hydration Structure of the Lithium Ion, *J. Chem. Phys.*, 2002, **117**, 110–117.
- 56 S. Cummings, J. E. Enderby, G. W. Neilson, J. R. Newsome, R. A. Howe, W. S. Howells and A. K. Soper, Chloride Ions in Aqueous Solutions, *Nature*, 1980, **287**, 714–716.
- 57 T. Megyes, S. Bálint, T. Grósz, T. Radnai, I. Bakó and P. Sipos, The Structure of Aqueous Sodium Hydroxide Solutions: A Combined Solution X-ray Diffraction and Simulation study, *J. Chem. Phys.*, 2008, **128**, 044501.
- 58 D. H. Powell, G. W. Neilson and J. E. Enderby, The Structure of Cl<sup>-</sup> in Aqueous Solution: An Experimental Determination of  $g_{\text{ClH}}(r)$  and  $g_{\text{ClO}}(r)$ , *J. Phys.: Condens. Matter*, 1993, **5**, 5723.
- 59 S. Laporte, F. Finocchi, L. Paulatto, M. Blanchard, E. Balan, F. Guyot and A. M. Saitta, Strong Electric Fields at a Prototypical Oxide/Water Interface Probed by *ab initio* Molecular Dynamics: MgO(001), *Phys. Chem. Chem. Phys.*, 2015, **17**, 20382–20390.
- 60 Y. Bronstein, P. Depondt, L. E. Bove, R. Gaal, A. M. Saitta and F. Finocchi, Quantum Versus Classical Protons in Pure and Salty Ice under Pressure, *Phys. Rev. B*, 2016, **93**, 024104.
- 61 G. Cassone, F. Pietrucci, F. Saija, F. Guyot and A. M. Saitta, One-step Electric-Field Driven Methane and Formaldehyde Synthesis from Liquid Methanol, *Chem. Sci.*, 2017, **8**, 2329–2336.
- 62 M. Dagrada, M. Casula, A. M. Saitta, S. Sorella and F. Mauri, Quantum Monte Carlo Study of the Protonated Water Dimer, *J. Chem. Theory Comput.*, 2014, **10**, 1980–1993.

# Ionic Diffusion and Proton Transfer in Aqueous Solutions under an Electric Field: State-of-The-Art

**Fabrizio Creazzo\***

University of Paris-Saclay, France

**Received:** August 22, 2017; **Accepted:** August 23, 2017; **Published:** August 31, 2017**\*Corresponding author:**

Fabrizio Creazzo

✉ [fabrizio.creazzo@univ-evry.fr](mailto:fabrizio.creazzo@univ-evry.fr)Researcher, University of Paris-Saclay,  
France.**Tel:** +33 637250092**Citation:** Creazzo F (2017) Ionic Diffusion and Proton Transfer in Aqueous Solutions under an Electric Field: State-of-The-Art. J Mol Sci. Vol. 1 No. 1: 2.

Most of the properties and anomalies describing the behavior of water are somehow related to the hydrogen bonded (H-bonded) network [1-3]. Albeit the features of H-bonds have been investigated and depicted by an impressive amount of research, the way in which some external conditions—such as the inclusion of ionic species—affect the three-dimensional H-bonds arrangement is wrapped up in a high degree of uncertainty.

If, on one hand, the presence of solvated ions cannot be avoided even in ultra-pure water samples, on the other hand, the lack of scientific consensus about the ion-induced microscopic effects on the water structure is representative of the practical challenges faced when investigating electrolyte solutions [4,5]. However, the indisputable role played by a few atomic charged species both in biology (i.e.,  $\text{Na}^+$ ,  $\text{Cl}^-$ ,  $\text{Mg}^{2+}$ ,  $\text{Ca}^{2+}$ , etc.) [6-8] and in industry (e.g.,  $\text{Li}^+$  batteries) [9] requires impelling and massive scientific efforts. In fact, besides the well-known Hofmeister series [10], hydrated ionic species finely rule the selectivity of cell membranes [6,7], being thus responsible of complex processes such as the nerve pulse generation. On the other hand, aqueous solutions represent the prototype of electrolytic batteries.

In all cases, a subtle balance between electrostatics, quantum mechanics (i.e., partial orbital sharing), and thermodynamics governs the delicate behaviour of the hydration process. The complexity of the problem is witnessed, inter alia, by the fact that there is no general consensus on the spatial extent of the effects induced by the inclusion of an ion in bulk water [11-13].

Recent ab initio calculations [14] have shown that the presence of a chaotrope species such as  $\text{Cl}^-$  does not have any effect on the orientation of water dipoles beyond the first hydration shell, whereas detectable perturbations—perhaps extremely small and unable to affect biological phenomena—have been observed in the polarizability of the water molecules at longer distances.

Additionally, the lack of a wide consensus on the typical coordination numbers characterizing the ionic first solvation shell is thoroughly recorded in the literature [4]. From an experimental perspective, the identification of this quantity is a very hard task for small ions such as  $\text{Li}^+$  and, recently, new ionic radii for this species and for  $\text{Na}^+$  have been proposed [4] by joining the advantages stemming from Large Angle X-ray Scattering (LAXS) and double Difference Infrared Spectroscopy (DDIR). In this respect, ab initio Molecular Dynamics (AIMD)

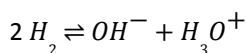
[8,14] and QM/MM [15] computational techniques have proven their reliability in reproducing the ion-induced structural changes in aqueous solutions, thus becoming an invaluable tool for the characterization of electrolyte solutions at a molecular level.

In particular, it seems that at low-to-moderate concentrations the ions may replace water molecules in the aqueous H-bonded structure, by following the same “water rules”. This example proves that classical molecular dynamics may fail in dealing with delicate local electrostatic balances and that first-principles approaches are necessary not only for a correct microscopic characterization of these phenomena but also in order to improve the models on which classical force fields rely.

Indeed, although sixty years ago concepts such as kosmotrope and chaotrope have been introduced to characterize the perturbation produced by a given ion on the H-bond network of water [16,17], and notwithstanding the fact that these notions were supported by classical molecular dynamics simulations [18-20], they have recently been blunted by an AIMD study [21]. Ionic conductivities are determined by applying an oriented external static electric field to electrolyte solutions. When an external electric field is applied, the situation is even tougher.

In the low field strength regime and within the Kohlrausch’s law of independent migration of ions (i.e., in the limit of infinite dilution), the mobilities of the alkali metal cations are well-established and can be easily related to their respective ionic sizes [22] i.e. the bigger the cation the larger the mobility. However, at finite molarities and for stronger field intensity regimes the overall situation may dramatically change. Field intensities of the order

of  $1 \text{ V}/\text{\AA}$  and even stronger were detected at the atomic sites of the water molecules hydrating  $\text{Na}^+$  and  $\text{Cl}^-$  ions [23], suggesting that for moderate-to-intense field strengths more complicated phenomena may be relevant in describing the ionic diffusion. Moreover, field intensities of about  $0.30 \text{ V}/\text{\AA}$  are able to induce the molecular dissociation of water and proton transfers along the H-bonded network [24-27] via the well-known proteolysis reaction:



This latter process plays a crucial role in many disparate domains, from neurobiology to electrolytic batteries and hydrogen-based technology [28,29]. Thus, it can be expected that a subtle interplay between the two deeply different mechanisms of protonic migration, on one hand, and of standard ionic diffusion, on the other, rules the complex dynamics of electrolytic solutions subjected to intense field strengths.

## References

- 1 Debenedetti PG (2006) *Metastable liquids-concepts and principles*. Princeton University Press, Princeton, NJ, USA.
- 2 Franks F (2000) *Water: a matrix of life* (2nd edn.). Royal Society of Chemistry, Cambridge.
- 3 Brovchenko I, Oleinikova A (2008) Multiple phases of liquid water. *ChemPhysChem* 9: 2660-2675.
- 4 Mahler J, Persson I (2012) A study of the hydration of the alkali metal ions in aqueous solution. *Inorg Chem* 51: 425-438.
- 5 Smirnov PR, Trostin VN (2006) structure of the nearest surrounding of the  $\text{Li}^+$  ion in aqueous solution of its salts. *Russ. J Gen Chem* 76: 175-182.
- 6 Hille B (2001) *ion channels of excitable membranes* (3rd edn.). Sinauer Associates, Inc. Publishers, Sunderland, MA, USA.
- 7 Zhou Y, MacKinnon R (2003) the occupancy of ions in the  $\text{K}^+$  selectivity filter: charge balance and coupling of ion binding to a protein conformational change underlie high conduction rates. *J Mol Bio* 333: 965-975.
- 8 Bankura A, Carnevale V, Klein ML (2013) Hydration structure of salt solution from ab initio molecular dynamics. *J Chem Phys* 138: 014501.
- 9 Tarascon JM, Armand M (2001) issues and challenges facing rechargeable lithium batteries. *Nature* 414: 359-367.
- 10 Kunz W, Henle J, Ninham BW (2004) "Zur Lehre von der Wirkung der Salze" (About the Science of the Effects of Salts): Franz Hofmeister's historical papers. *Curr Opin Colloid Interface Sci* 9: 19-37.
- 11 Stryer L, Haugland RP (1967) Energy transfer: a spectroscopic ruler. *Proc Natl Acad Sci USA* 68: 719-726.
- 12 Enderby JE (1995) Ion solvation via neutron-scattering. *Chem Soc Rev* 24: 159-168.
- 13 Collins KD, Neilson GW, Enderby JE (2007) Ions in water: characterizing the forces that control chemical processes and biological structure. *Biophys Chem* 128: 95-104.
- 14 Gaiduk AP, Galli G (2017) Local and global effects of dissolved sodium chloride on the structure of water. *J Phys Chem Lett* 8: 1496-1502.
- 15 Rowley CN, Roux B (2012) The solvation structure of  $\text{Na}^+$  and  $\text{K}^+$  in liquid water determined from high level ab initio molecular dynamics simulations. *J Chem Theo Comp* 8: 3526-3535.
- 16 Gurney RW (1953) *Ionic Processes in Solution*. McGraw-Hill: NY, USA.
- 17 Frank HS, Wen WY (1957) Structural aspects of ion-solvent interaction in aqueous solutions: a suggested picture of water structure. *Discuss Farad Soc* 24: 133-140.
- 18 Galamba N (2013) On the effects of temperature, pressure, and dissolved salts on the hydrogen-bond network of water. *J Phys Chem B* 117: 589-601.
- 19 Reagan MT, Harris JG, Tester JW (1999) Molecular simulations of dense hydrothermal  $\text{NaCl-H}_2\text{O}$  solutions deom subcritical to supercritical conditions. *J Phys Chem B* 103: 7935-7941.
- 20 Renou R, Ding M, Zhu H, Szymczyk A, Malfreyt P, et al. (2014) concentration dependence of the dielectric permittivity, structure, and dynamics of aqueous  $\text{NaCl}$  solutions: comparison between the drude oscillator and electronic continuum models. *J Phys Chem B* 118: 3931-3940.
- 21 Ding Y, Hassanali A, Parrinello M (2014) Anomalous water diffusion in salt solutions. *Proc Natl Acad Sci USA* 111: 3310-3315.
- 22 Wright MR (2007) *An Introduction to aqueous electrolyte solutions*. Wiley: Chichester, England.
- 23 Sellner B, Valiev M, Kathman SM (2013) Charge and electric field fluctuations in aqueous  $\text{NaCl}$  electrolytes. *J Phys Chem B* 117: 10869-10882.
- 24 Stuve EM (2012) Ionization of water in interfacial electric fields: an electrochemical view. *Chem Phys Lett* pp: 519-520, 1-17.
- 25 Saitta AM, Saija F, Giaquinta PV (2012) Ab Initio molecular dynamics study of dissociation of water under an electric field. *Phys Rev Lett*.
- 26 Cassone G, Creazzo F, Giaquinta PV, Saija F, Saitta AM (2016) Ab initio molecular dynamics study of an aqueous  $\text{NaCl}$  solution under an electric field. *Phys Chem Chem Phys* 18: 3164-23173.
- 27 Hammadi Z, Descoins M, Salanon E, Morin R (2013) Proton and light ion nanobeams from field ionization of water. *J Appl Lett* 101: 110-243.
- 28 Kaila K, Ransom BR (1998) pH and brain function; In: Kaila K, Ransom BR (eds.) Wiley, NY, USA.
- 29 Zoulias EI (2008) *Lymberoupolos, N. hydrogen based autonomous power systems*. Springer, London.



# Ionic diffusion and proton transfer of $\text{MgCl}_2$ and $\text{CaCl}_2$ aqueous solutions: an *ab initio* study under electric field

Giuseppe Cassone<sup>a</sup>, Fabrizio Creazzo<sup>b</sup> and Franz Saija<sup>c</sup>

<sup>a</sup>Institute of Biophysics of the Czech Academy of Sciences, Brno, Czech Republic; <sup>b</sup>Université d'Evry val d'Essonne-Université Paris-Saclay, Evry, France; <sup>c</sup>CNR-IPCF, Messina, Italy

## ABSTRACT

We report on a series of *ab initio* molecular dynamics simulations on  $\text{MgCl}_2$  and  $\text{CaCl}_2$  aqueous solutions subjected to the effect of static electric fields. The diffusion properties of the solvated cationic species have been investigated both in the low-to-moderate field regime and for intense field strengths, where correlated proton transfers between the water molecules take place. Albeit the Grotthuss-like motion of the protons  $\text{H}^+$  dramatically affects the standard relative mobility of monovalent cations such as  $\text{Li}^+$ ,  $\text{Na}^+$ , and  $\text{K}^+$  [Phys Chem Chem Phys 2017;19:20420], here we demonstrate that the rule 'the bigger the cation the higher its mobility' is preserved for divalent cations – such as  $\text{Mg}^{2+}$  and  $\text{Ca}^{2+}$  – even when a sustained protonic current is established by the field action. Notwithstanding the presence of charged particles anticipates the field threshold of the molecular dissociation of water from 0.35 V/Å to 0.25 V/Å, such a shift does not depend on the *nominal* charge the cations hold. Protons flow more easily in the  $\text{MgCl}_2$  solution ( $\sigma_p=2.3$  S/cm) rather than in the  $\text{CaCl}_2$  ( $\sigma_p=1.7$  S/cm) electrolyte solution because of a twofold reason. Firstly,  $\text{Ca}^{2+}$ , being larger than  $\text{Mg}^{2+}$ , more strongly hampers the propagation of a charge defect of the same sign (i.e.  $\text{H}^+$ ). Secondly, we demonstrate that the mobility of  $\text{Ca}^{2+}$  is sizably higher than that of  $\text{Mg}^{2+}$ . This way, by spanning more efficiently the aqueous environment,  $\text{Ca}^{2+}$  further inhibits the proton transfers along the H-bonded network. Finally, the protonic conduction efficiency is inversely proportional both to the ionic radii and to the nominal charge of the cations present in solution.

## ARTICLE HISTORY

Received 11 May 2018  
Accepted 10 August 2018

## KEYWORDS

Aqueous solutions; *ab initio* molecular dynamics; proton transfer

## 1. Introduction

Ion-water interactions play a key role in sustaining life as we know it as well as in the fundamental and industrial physical-chemical realm [1]. Despite the enormous amount of research focussed on the microscopic properties of electrolyte solutions, understanding the perturbations induced by the inclusion of common ionic species on the typical hydrogen-bonded (H-bonded) network of water is still an open debate [2,3]. A few atomic charged species (i.e.  $\text{Na}^+$ ,  $\text{K}^+$ ,  $\text{Cl}^-$ ,  $\text{Mg}^{2+}$ ,  $\text{Ca}^{2+}$ , etc.) [1,3,4] are responsible for the specific selectivity of the cell membranes [1,3,4]. In fact, the subtle role played by ions and their aqueous hydration shells specifies, by means of the associated local electric fields, the peculiar chemical permeability of a given ionic channel, determining thus the nature of crucial biochemical phenomena such as, *inter alia*, the nerve pulse generation.

On the other hand, sixty years ago it was argued that the inclusion of ionic species in 'pure' water might produce important local changes in the aqueous microscopic structure [5,6]. The tetrahedral H-bond arrangement of water can be indeed distorted not only by modifications in temperature and pressure, but also by the presence of solutes [7]. Gurney [5] introduced the concepts of 'structure maker' (i.e. kosmotrope) and 'structure breaker' (i.e. chaotrope) according to the ion's ability to induce structuring or under-structuring of the local water environment, respectively. Although these notions have

been strongly supported by dozens of classical molecular dynamics simulations [7–9], they have been recently blunted by an *ab initio* molecular dynamics study [10]. In particular, it seems that at low-to-moderate concentrations the ions may physically replace the water molecules in the H-bonded network by following the same 'water rules' [10]. Effectively, *ab initio* calculations are mandatory in order to fully describe the complex behaviour of an electrolyte solution which ultimately depends on a delicate interplay between thermodynamical, quantum chemical, and electrostatic interactions [11,12].

Magnesium ( $\text{Mg}^{2+}$ ) is the fourth most abundant mineral in living organisms (and the third most abundant dissolved ions in seawater) playing a key biochemical role in the appropriate bone formation and for the immune system. In addition,  $\text{Mg}^{2+}$  kinetics drives the synthesis of the RNA polymerase. Calcium ( $\text{Ca}^{2+}$ ) is the fifth most abundant ion in living organisms and it plays an important role in the signal transduction pathways and in the release of neurotransmitters from neurons. Moreover,  $\text{Ca}^{2+}$  is central in mining and as binding and deoxidiser agent in the production of many ferrous alloys.

Because of their importance and ubiquitous nature, *ab initio* and classical molecular dynamics simulations have been used to study divalent electrolyte solutions such as  $\text{MgCl}_2$  and  $\text{CaCl}_2$  [13–16] in terms of their hydration structure and kinetic properties. However, several microscopic details remain undisclosed and the fine characterisation of their response upon electric

field exposure has never been investigated, to the best of our knowledge. The latter aspect represents a serious limitation to our comprehension of a plethora of biological phenomena since (intense and local) electric fields ultimately rule the behaviour of condensed systems at the molecular level.

It is well-established that H-bonded systems are deeply influenced by the application of static electric fields and several consequences are strongly dependent on the field strength [17–23]. Moreover, for intense field regimes the *autoprotolysis* of water can be induced in aqueous solutions:



where two water molecules ionise to produce hydronium cations ( $\text{H}_3\text{O}^+$ ) and hydroxide anions ( $\text{OH}^-$ ). In neat water, field strengths of  $0.35 \text{ V/\AA}$  are necessary to induce frequent molecular dissociations [17]. However, it has been proven that the presence of solvated charged species stemming from, e.g. NaCl and LiCl, anticipates the water dissociation threshold to  $0.25 \text{ V/\AA}$  [11].

In order to catch the most relevant features characterising the complex interplay between intermolecular interactions and field effects, we report here on the first *ab initio* molecular dynamics study of two aqueous solutions (i.e.  $\text{MgCl}_2$  and  $\text{CaCl}_2$ ) at room conditions and under static electric fields. Furthermore, we compare them with very recent *ab initio* data stemming from aqueous solutions of alkali metal salts [11,24]. This way, we unveil the intrinsic differences between structure maker and structure breaker agents and – incidentally – between aqueous solutions with monovalent and divalent dissolved cations in responding to the application of intense electric fields.

## 2. Methods

First-principles molecular dynamics simulations were carried out on  $\text{MgCl}_2$  and  $\text{CaCl}_2$  water solutions. In addition, these simulations have been compared with recent studies on electrolyte aqueous solutions of metal alkali salts, performed exactly at the same conditions [11,24]. Each of our numerical samples was represented by two ionic pairs solvated by 64 water molecules arranged in a cubic cell with side length equal to  $13.07 \text{ \AA}$  and  $13.17 \text{ \AA}$  for the  $\text{MgCl}_2$  and the  $\text{CaCl}_2$  water solutions, respectively, corresponding to molarities of  $1.7 \text{ M}$ . The specific choice of working with 64 water molecules has not been merely dictated by a balanced compromise between accuracy and computational efficiency, but also by extensive testing performed by our group in the past [21,25], where the protonic conduction properties have been investigated *inter alia* as a function of the sample’s size. In particular, it turned out that in the range between 32 and 128 water molecules, the results were size-independent [21,25]. As usual, periodic boundary conditions were thoroughly applied.

We used the software package Quantum ESPRESSO [26], based on the Car-Parrinello (CP) approach [27], to perform CPMD simulations of all the above-mentioned samples under the action of static and homogeneous electric fields applied along a given direction (corresponding to the  $z$ -axis). The implementation of an external electric field in numerical codes based on density functional theory (DFT) can be achieved by exploiting the modern theory of polarisation and

Berry’s phases [28] (see, e.g. Ref. [29] for the technical implementation of a static and homogeneous electric field in *ab initio* codes and Ref. [30] for a review of several methods that allow for the application of external fields in disparate simulation frameworks).

As for exchange and correlation effects, we adopted the gradient-corrected Perdew-Burke-Ernzerhof (PBE) [31] functional within the plane-wave/pseudopotential framework. The PBE functional and its adequate description of polarisation effects [32] is known to provide a reasonably accurate structure in the case of H-bonded systems [33]. Moreover, although its employment is justified by the already tested adherence of some computational results [11,17,24,34] to many experimental data (e.g. see Ref. [35]), we thoroughly and carefully checked the reliability of the current results by means of a direct comparison with the available experimental and computational data (see the ‘Structural properties’ section). In addition, as far as the PBE accuracy and reliability in mimicking the phenomenon of the *protolysis* in liquid water, a pioneering study [17] performed with PBE predicted the experimental field-induced dissociation threshold of the water molecule [20], confirming thus some preliminary [18] and rather up-to-date [36] experimental data.

All the CPMD simulations have been carried out at the nominal temperature of  $315 \text{ K}$  after equilibration runs of  $5 \text{ ns}$  performed by means of typical classical force fields in order to prepare suitable initial atomic configurations. In the CPMD simulations we gradually increased the intensity of the electric field from zero up to a maximum of  $0.50 \text{ V/\AA}$  with a step increment of about  $0.05 \text{ V/\AA}$ . The temperature was kept fixed through the coupling of the system with a Nosé-Hoover thermostat whose frequency was set at  $13.5 \text{ THz}$ . The systems were kept in an isothermal-isochoric (NVT) ensemble and the dynamics was classically treated using the Verlet algorithm; for each electric field intensity the dynamics was propagated for time-lengths up to  $10 \text{ ps}$ , extending to about  $25 \text{ ps}$  in the zero-field regime. Hence, a simulation time of approximately  $125 \text{ ps}$  has been cumulated for the  $\text{MgCl}_2$  and the  $\text{CaCl}_2$  aqueous solutions, whereas trajectories of about  $100 \text{ ps}$  were previously collected for the metal alkali electrolyte solutions [11].

The fictitious electronic mass was set to a value of  $300 \text{ a.u.}$ , and a plane-wave kinetic energy cutoff of  $40 \text{ Ry}$  and a cutoff energy of  $320 \text{ Ry}$  for the charge density were chosen, which allowed us to adopt a timestep of  $0.096 \text{ fs}$ . The choice of the latter has been achieved after extensive testing by following the methodology reported in Ref. [37]. With such cutoff values the samples can be described in a reliable way since the core electronic interaction is being depicted through Ultrasoft Pseudopotentials (USPP) generated *via* the Rappe-Rabe-Kaxiras-Joannopoulos (RRKJ) method [38].

The conductivities were obtained from Ohm’s law. The current intensity is related to the number of charge carriers flowing in a time interval  $\Delta t$  through a section area  $a^2$  orthogonal to the direction of the electric field,  $a$  being the side of the simulation box. The protonic conductivity  $\sigma_p$  was then calculated as

$$\sigma_p = \left( \frac{q \Delta N}{\Delta t a^2} \right) \cdot \frac{1}{E}, \quad (2)$$

where  $q$  is the elementary charge.

### 3. Results and discussion

#### 3.1. Structural properties

It is well-known that water molecules in salt solutions differently re-orient around cations and anions. Generally speaking they form hydration shells where both hydrogen atoms point away from the cation and where a single hydrogen atom points toward the anion to form a water-anion H-bond. A more detailed knowledge on the microscopic interactions can be gathered from the atomistic pair radial distribution functions (RDFs), which bring informations about the statistical (i.e. averaged) local structural properties. The presence of charged particles in aqueous environment does not sizably modify the local water structure. Indeed, the oxygen-oxygen (O-O) RDFs shown in Figure 1, for both monovalent [11] and divalent ions in water, display a well defined first peak located at around 2.76 Å, similarly to that typical of the neat water case. It means that the overall water H-bond structure and the water density profile are not affected – at the investigated molarity of 1.7 M – by the inclusion of common monovalent and divalent ions. Notwithstanding Leberman and Soper have recently suggested that the effects induced by the inclusion of some ions in the water structure can be qualitatively interpreted as pressure-induced effects [39], at the investigated molarity such a

phenomenon is strictly confined to the first solvation shell, as it will be shown later.

The fact that the water structure is preserved upon the salt inclusion is further demonstrated by the fact that the second peak of the O-O RDF is located around 4.5 Å. The latter value represents the signature of the tetrahedral structure of water, confirming thus that ions may replace water molecules in the three-dimensional H-bonded network by following the same ‘water rules’, as suggested by Ding et al. [10] for two ionic species. Our data – stemming from a wider selection of solutions – strongly indicate that this behaviour is essentially independent of the type of the electrolyte solution, extending thus this specific evidence to a more general feature.

As far as the alkali metal ( $\text{Na}^+$ ,  $\text{K}^+$ ,  $\text{Li}^+$ ) and the alkaline-earth metal ( $\text{Mg}^{2+}$ ,  $\text{Ca}^{2+}$ ) cations are concerned, the cation-oxygen ( $\alpha$ -O) RDFs unveil the peculiar role played by the inclusion of each cation in the aqueous H-bonded network. As shown in Figure 2 (a), the location of the K-O RDF peaks falls at longer distances than in the  $\text{Na}^+$  and  $\text{Li}^+$  cases indicating the presence of sizably less structured hydration shells with respect to those around the cations of NaCl and LiCl aqueous solutions. It is well-known that monovalent potassium cations increase the local entropy in their proximity upon water solvation. Moreover, the activation energy related to the water exchange between the first and second

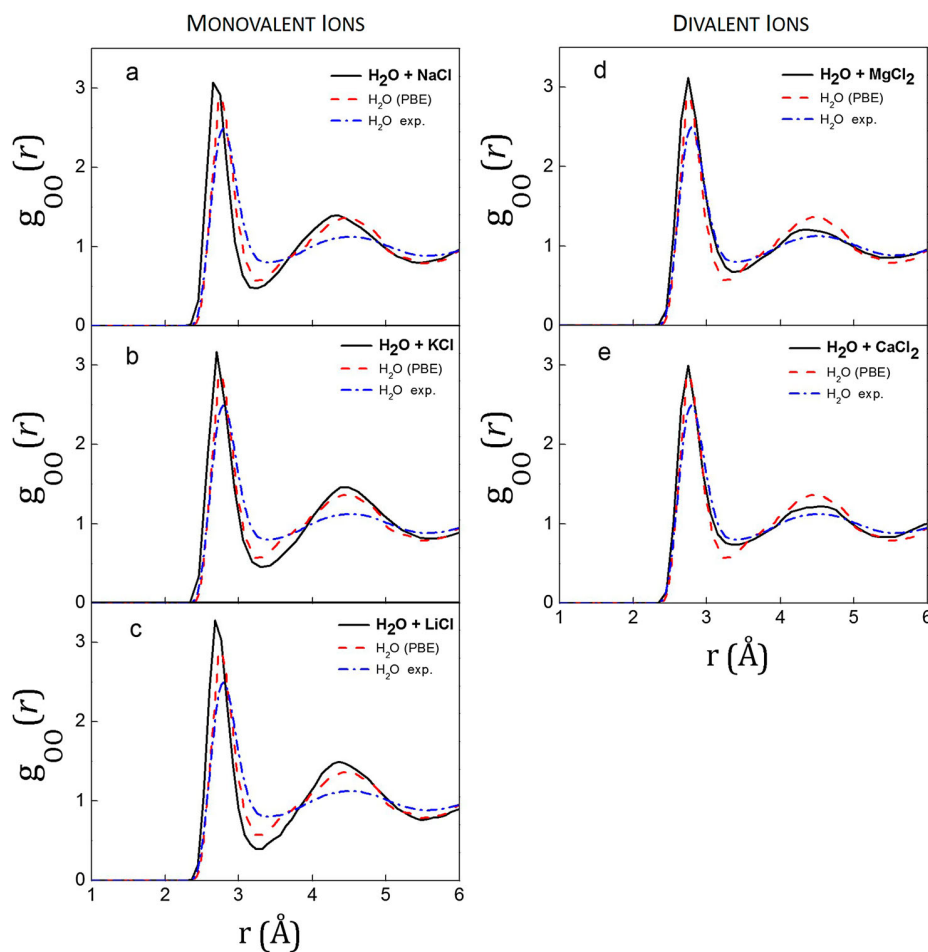


**Figure 1.** (Colour online) Zero-field oxygen-oxygen radial distribution functions of NaCl (a), KCl (b), LiCl (c),  $\text{MgCl}_2$  (d) and  $\text{CaCl}_2$  (d) water solutions at  $T=315$  K with a salt concentration of 1.7 M (i.e. from the current calculations and for the NaCl, KCl and LiCl case from Ref. [24]) (black curves), of neat water modelled with the same PBE exchange and correlation functional at  $T=350$  K of Ref. [17] (red dashed curves), and from experiment at  $T=298$  K [35] (blue dot-dashed curves).

hydration shell is significantly lowered by the presence of such a cation. Because of the perturbation induced on the H-bonded water network by the inclusion of potassium cations, they are defined as structure breaker (i.e. chaotrope) species [5,6]. This evidence can be further and easily visualised by considering that both the peaks and the dips of the K-O RDF are located at larger distances than those typical of the O-O RDF in neat water. On the other hand,  $\text{Na}^+$  and  $\text{Li}^+$  are a moderate and a strong structure maker (i.e. kosmotrope) species, respectively. They tend indeed to induce a local – both orientational and positional – over-structuring of the water environment to which can be associated a decrease of the local entropy.

Divalent cations  $\text{Mg}^{2+}$  and  $\text{Ca}^{2+}$  in water solutions behave similarly to sodium and lithium cations, respectively. As shown in Figure 2(b), the magnesium-oxygen (Mg-O) RDF exhibits a well-defined peak centered at a distance of about 2.2 Å whereas a second smaller peak is located around 4.2 Å. The former value clearly indicates a very well-defined first hydration shell consisting of six water molecules placed – on average – between 2.0 Å and 2.4 Å. This way, no water molecular exchanges have been recorded during the zero-field molecular dynamics indicating longer residence times than the sampled time-scale. Notwithstanding the functional shape of the calcium-oxygen (Ca-O) RDF displayed in Figure 2(b) resembles the Mg-O RDF, the first two peaks are shifted to 2.5 Å and 4.5 Å. However, the coordination number partially describing

the solvation properties of  $\text{Ca}^{2+}$  is the same as for  $\text{Mg}^{2+}$  (i.e. 6). Albeit the latter evidence may in principle suggest similar entropic (topologically-induced) contributions introduced by the inclusion of  $\text{Mg}^{2+}$  and  $\text{Ca}^{2+}$ , it must be stressed here that their interactions with the aqueous environment are deeply different. In fact, the interaction  $\text{Mg}^{2+}$  establishes with the water molecules of the first solvation shell is clearly stronger than that characterising the  $\text{Ca}^{2+}$ -water one. This results into more ordered and rigid octahedral-type water arrangements around the magnesium cation than those found in the calcium cation case. Due to the smaller radius of  $\text{Mg}^{2+}$  ion (i.e. 0.86 Å) with respect to that estimated for  $\text{Ca}^{2+}$  (i.e. 1.14 Å), water molecules are more tightly bound to the denser electronic cloud around the magnesium cation. This phenomenon, revealed both by experiments [40] and, more recently, by *ab initio* investigations [41], indicates that  $\text{Mg}^{2+}$  and  $\text{Ca}^{2+}$  can be considered as a strong and a moderate structure maker species, respectively.

### 3.2. Dynamical properties

Several theoretical approaches focussed on the ionic mobility [42–46] have long been proposed to explain the ionic diffusion properties at infinite dilution regimes (i.e. within the Kohlrausch's limit). In particular, such theories explain somehow counter-intuitive evidences related to the increase of the ionic mobility with the ionic size – for alkali and halide ions – which are in net contrast with the Stokes' law [42].

The essential features of the diffusion mechanisms of solvated species in aqueous electrolyte solutions reside behind their diffusive properties which emerge – within a limited time-scale exploration – under the action of intense static electric fields. Although it is well-established that estimates of well-converged ionic diffusion coefficients would require extremely long trajectories, the single-particle dynamics evaluated by means of the atomistic mean-square-displacement (MSD), shown in Figure 3, carries fundamental insights on the capabilities the species hold in migrating across the aqueous environment. For relatively low field intensity regimes (i.e. up to 0.10 V/Å) the dynamics of the investigated ionic species follows the rules of Brownian motion. Of course, it is simply related to the unavoidable narrowness of the time-scales affordable by state-of-the-art *ab initio* molecular dynamics techniques performed under electric field. On the other hand, a field strength of 0.15 V/Å marks the transition to a (very feeble) diffusive regime both for monovalent and divalent ionic species, as displayed in Figure 3(a–e). In particular, it has been proven that  $\text{Na}^+$  cations are able to establish a stronger coupling with the external electrostatic potential by means of a higher electron population present on its own nuclei upon solvation [11]. This feature, assisted by the fact that sodium cations are only weak-to-moderate structure maker species, confers higher diffusion capabilities to  $\text{Na}^+$  with respect not only to the remainder monovalent cations (Figure 3(a)) but also to the divalent cations (Figure 3(e)), at least at this regime. In fact, if on the one hand  $\text{Mg}^{2+}$  and  $\text{Ca}^{2+}$  are characterised by an higher (more positive) electric charge on their proximity, on the other, they are more efficiently solvated – and thus electrically screened and their inertia increased – by their denser water first-solvation shells.

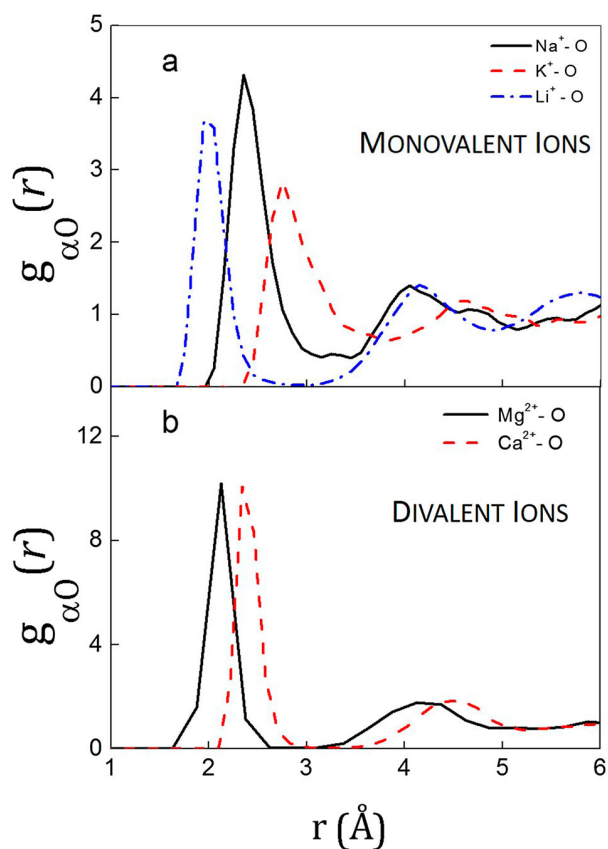


**Figure 2.** (Colour online) Cation-oxygen ( $\alpha$ -O) radial distribution functions in the zero-field regime for  $\text{Na}^+$  (black solid line),  $\text{K}^+$  (red dashed line), and  $\text{Li}^+$  (blue dashed-dotted line) in the (a) panel (from Ref. [24]) and for  $\text{Mg}^{2+}$  (black solid line), and  $\text{Ca}^{2+}$  (red dashed line) in the (b) panel.



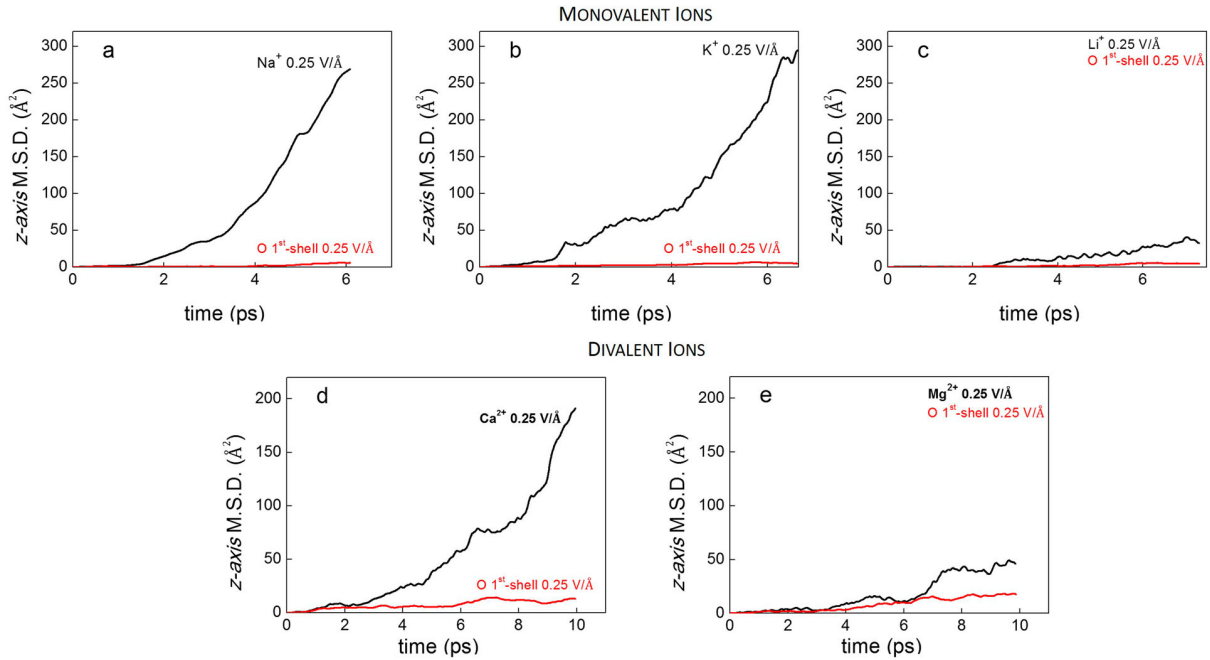


**Figure 4.** (Colour online) Mean-square-displacement (MSD) along the field direction (i.e. z-axis) of  $\text{Na}^+$  (a),  $\text{K}^+$  (b), and  $\text{Li}^+$  (c) (black solid curves) and of their respective solvating oxygen atoms (red solid curves) for a field strength of  $0.25 \text{ V}/\text{\AA}$  from Ref. [24]. MSD of  $\text{Ca}^{2+}$  (d) and  $\text{Mg}^{2+}$  (e) (black solid curves) and of their respective solvating oxygen atoms (red solid curves) for a field intensity of  $0.25 \text{ V}/\text{\AA}$ .

that, in practice, it is almost free to diffuse through the aqueous environment. According to the fact that  $\text{Na}^+$  and  $\text{Ca}^{2+}$  are weak-to-moderate structure maker species due to a larger entropy of hydration than the smaller  $\text{Li}^+$  and  $\text{Mg}^{2+}$  ions, they are initially able to diffuse more similarly to a structure breaker entity, escaping away from their hydration ‘cages’ just after 2 ps (Figure 4(d)).

Once the most extreme field regime is achieved (i.e.  $0.50 \text{ V}/\text{\AA}$ ), other considerations qualitatively rule the behaviour of the cations of the dissolved salts here investigated. At those intensities, the field-activated proton transfer leads to a complex interplay between two deeply different types of charge transport: the simple ionic diffusion treated up to this point and the cooperative Grotthuss-like proton transfer along the H-bonded network. In fact, starting from a field threshold of  $0.20 \text{ V}/\text{\AA}$  all the investigated samples exhibit sporadic events of water ionisation leading to the transient release of  $\text{H}_3\text{O}^+$  and  $\text{OH}^-$  species. However, the latter ions have appreciable lifetimes higher than few femtoseconds (fs) only starting from a field intensity of  $0.25 \text{ V}/\text{\AA}$ . The presence of solvated charged species anticipates the molecular dissociation threshold of neat water from  $0.35 \text{ V}/\text{\AA}$  [17] to  $0.25 \text{ V}/\text{\AA}$ . With the exception of the structure-breaker-containing sample (i.e. the KCl water solution), all the electrolytes give rise to a one-stage process in that water ionisation events are followed – within the same field strength – by correlated and ordered proton transfers establishing a protonic conductive regime. On the contrary, both in neat water [17,18,20] and in the potassium chloride aqueous solution, field strengths of at least  $0.35 \text{ V}/\text{\AA}$  have to be applied in order to measure a protonic current.

As far as the motion of the monovalent ions is concerned, it has been recently demonstrated [11] that although at low-to-moderate field intensity regimes the bigger the cation the

higher the mobility (i.e.  $\mu(\text{K}^+) > \mu(\text{Na}^+) > \mu(\text{Li}^+)$ ), at stronger fields this is no longer true. In particular, as shown in Figure 3(d),  $\text{Li}^+$  cations are sizably more mobile than  $\text{K}^+$  and  $\text{Na}^+$  under the influence of a field intensity of  $0.50 \text{ V}/\text{\AA}$ . This is almost entirely ascribable to the fact that lithium, being the smallest among the investigated cations, is the least affected by the proton migration process that takes place along the H-bonded network. *Vice-versa*, also the distinct protonic responses that the respective protonic subsystems exhibit are dependent on the ionic radii of the cations dissolved in a given sample, as shown in Figure 5(a); as expected, protons migrate more easily in presence of smaller cations. As a consequence, the systems where monovalent cations are present display protonic conductivities equal to  $3.0 \text{ S/cm}$  (LiCl),  $2.5 \text{ S/cm}$  (NaCl), and  $2.3 \text{ S/cm}$  (KCl) [11]. Moreover, these values are noticeably lower than that estimated for pure water (i.e.  $7.8 \text{ S/cm}$ ) [17], further indicating that the proton conduction efficiencies of the different electrolyte solutions are inversely proportional to the ionic radii of the solvated cationic species. As far as the  $\text{MgCl}_2$  and the  $\text{CaCl}_2$  water solutions are concerned, the same rules hold, as shown in Figure 5(b). In particular,  $\text{Mg}^{2+}$  being smaller and a stronger structure maker species than  $\text{Ca}^{2+}$ , offers a lower hindrance to the migration of the protonic defects. The effects due to the local cationic charge are indeed more confined in the  $\text{MgCl}_2$  electrolyte rather than in the  $\text{CaCl}_2$  one. This way, the protonic conductivity recorded in the former sample is equal to  $2.3 \text{ S/cm}$  whereas that of the latter is  $1.7 \text{ S/cm}$ . Albeit it can appear somehow counter-intuitive that  $\text{MgCl}_2$  water solution exhibits the same efficiency ( $\sigma_p = 2.3 \text{ S/cm}$ ) in transferring protons of the aqueous mixture with a bigger and monovalent cation (i.e. KCl), it can be easily taken into account. In fact, if on the one hand,  $\text{Mg}^{2+}$  – being more charged than  $\text{K}^+$  – should offer an higher

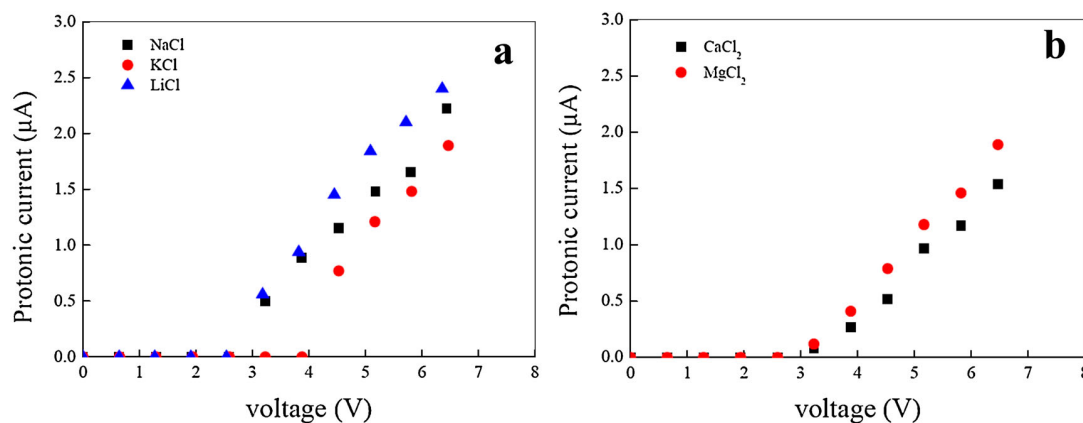


**Figure 5.** (Colour online) Protonic current-voltage diagrams of NaCl (black squares), KCl (red dots), and LiCl (blue triangles) aqueous solutions (a) taken from Ref. [11]. (b) Protonic current-voltage diagrams of CaCl<sub>2</sub> (black squares) and MgCl<sub>2</sub> (red dots) aqueous solutions at the same molarity of 1.7 M. Once a conductive regime is established, the protonic response of all the samples is Ohmic.

hindrance to the proton transport by means of a direct electrostatic repulsion, on the other, it is at the same time smaller and sizably less mobile than the potassium cation, as shown in Figure 3(d–h).

Finally, Figure 3(h) indicates *inter alia* that Ca<sup>2+</sup> is significantly more mobile than Mg<sup>2+</sup> at the highest field intensity explored. It means that, at a given instant, the probability that a calcium cation and a migrating proton directly interacts (i.e. repel each other) is sizably higher than that between a smaller and less mobile cation such as Mg<sup>2+</sup>. This way, protonic migrations in the CaCl<sub>2</sub> aqueous solution – being a sample where large and divalent cations are solvated – are the most hampered among the investigated electrolytes, leading thus to the least proton transfer efficiency.

#### 4. Conclusions

By performing *ab initio* molecular dynamics simulations of two different electrolyte solutions (i.e. MgCl<sub>2</sub> and CaCl<sub>2</sub>) at a molarity of 1.7 M, we have studied their response to external static electric fields of varying intensities. Their data have been also thoroughly compared with those stemming from common electrolyte solutions such as LiCl, NaCl, and KCl [11]. We have found that although a drastic change of the relative cationic mobilities is recorded for monoatomic cations at very intense field regimes with respect their ranking in the low-to-moderate field regimes (i.e.  $\mu(\text{K}^+) > \mu(\text{Na}^+) > \mu(\text{Li}^+)$ ), divalent cations – such as Mg<sup>2+</sup> and Ca<sup>2+</sup> – follow the well-known rule ‘the bigger the cation the higher the mobility’ at all the explored intensities.

The presence of solvated charged species anticipates the well-known water dissociation threshold from 0.35 V/Å to 0.25 V/Å. However, in this respect, no measurable differences have been detected between the monovalent-cations- and the divalent-cations-containing samples, indicating *a posteriori* that the *nominal* charge of the specific cation is greatly screened by its own solvation shells. Whereas structure maker cations present in all the electrolyte solutions (i.e. Li<sup>+</sup>, Na<sup>+</sup>, Mg<sup>2+</sup>, and Ca<sup>2+</sup>) give rise to a one-stage process in that water ionizations are rapidly followed by a net collective proton flow, structure breaker cations composing the KCl solution (i.e. K<sup>+</sup>) hamper the trigger of the

proton conduction, which starts only at 0.35 V/Å, as in neat water [17,18,20]. Although all the protonic subsystems of the investigated samples show an Ohmic response to the external field, the estimated protonic conductivities are dependent on the nature of the present alkali metal cations. Indeed, it has been recently proven that the LiCl, NaCl, and KCl water solutions exhibit protonic conductivities equal to 3.0 S/cm, 2.5 S/cm, and 2.3 S/cm, respectively, a series that inversely follows the trend of the ionic radii of Li<sup>+</sup>, Na<sup>+</sup>, and K<sup>+</sup> species [11]. Here we show that the MgCl<sub>2</sub> and CaCl<sub>2</sub> aqueous solutions are characterised by protonic conductivities of 2.3 S/cm and 1.7 S/cm, respectively, in agreement with the respective cationic radii. It is clear that Ca<sup>2+</sup> – being larger and a more moderate structure maker than Mg<sup>2+</sup> – more strongly hampers the proton migration along the water H-bonded network. Moreover, since we demonstrate that the mobility of Ca<sup>2+</sup> is sizably higher than that of Mg<sup>2+</sup> at all the field regimes, also the probability that Ca<sup>2+</sup> and H<sup>+</sup> directly (negatively) interact is larger, at a given instant, than that characterising the interaction between the smaller and less mobile Mg<sup>2+</sup> with protons.

By summarising, at high field intensities, the relative mobilities of simple divalent cations preserve those recorded for low-to-moderate field regimes, indicating a compensating balance with the activated proton transfer. *Vice-versa*, the proton conduction efficiencies of the different electrolyte solutions are inversely proportional both to the ionic radii and to the nominal charge of the solvated cationic species.

#### Disclosure statement

No potential conflict of interest was reported by the authors.

#### References

- [1] Hille B. Ion channels of excitable membranes. 3rd Ed. Sunderland, Massachusetts U.S.A.: Sinauer Associates, Inc.; 2001.
- [2] Gaiduk AP, Galli G. Local and global effects of dissolved sodium chloride on the structure of water. *J Phys Chem Lett.* 2017;8:1496–1502.
- [3] Bankura A, Carnevale V, Klein ML. Hydration structure of salt solution from *ab initio* molecular dynamics. *J Chem Phys.* 2013;138:014501.

- [4] Zhou Y, MacKinnon R. The occupancy of ions in the K<sup>+</sup> selectivity filter: charge balance and coupling of ion binding to a protein conformational change underlie high conduction rates. *J Mol Biol.* **2003**;333:965–975.
- [5] Gurney RW. Ionic processes in solution. New York: McGraw-Hill; **1953**.
- [6] Frank HS, Wen WY. Structural aspects of ion-solvent interaction in aqueous solutions: a suggested picture of water structure. *Discuss Farad Soc.* **1957**;24:133.
- [7] Galamba N. On the effects of temperature, pressure, and dissolved salts on the hydrogen-bond network of water. *J Phys Chem B.* **2013**;117:589.
- [8] Reagan MT, Harris JG, Tester JW. Molecular simulations of dense hydrothermal NaCl-H<sub>2</sub>O solutions deom subcritical to supercritical conditions. *J Phys Chem B.* **1999**;103:7935–7941.
- [9] Renou R, Ding M, Zhu H, et al. Concentration dependence of the dielectric permittivity, structure, and dynamics of aqueous NaCl solutions: comparison between the drude oscillator and electronic continuum models. *J Phys Chem B.* **2014**;118:3931–3940.
- [10] Ding Y, Hassanali A, Parrinello M. Anomalous water diffusion in salt solutions. *Proc Natl Acad Sci.* **2014**;111:3310–3315.
- [11] Cassone G, Creazzo F, Giaquinta PV, et al. Ionic diffusion and proton transfer in aqueous solutions of alkali metal salts. *Phys Chem Chem Phys.* **2017**;19:20420–20429.
- [12] Pye CC, Rudolph WW. An ab initio and Raman investigation of magnesium (II) hydration. *J Phys Chem A.* **1998**;102:9933–9943.
- [13] Ikeda T, Boero M, Terakura K. Hydration properties of magnesium and calcium ions from constrained first principles molecular dynamics. *J Chem Phys.* **2007**;127:074503.
- [14] Hartkamp R, Coasne B. Structure and transport of aqueous electrolytes: from simple halides to radionuclide ions. *J Chem Phys.* **2014**;141:124508.
- [15] Sammalkorpi M, Karttunen M, Haataja M. Ionic surfactant aggregates in saline solutions: sodium dodecyl sulfate (SDS) in the presence of excess sodium chloride (NaCl) or calcium chloride (CaCl<sub>2</sub>). *J Phys Chem B.* **2009**;113:5863–5870.
- [16] Kohagen M, Lepsik M, Jungwirth P. Calcium binding to calmodulin by molecular dynamics with effective polarization. *J Phys Chem Lett.* **2014**;5:3964–3969.
- [17] Saitta AM, Saija F, Giaquinta PV. Ab initio molecular dynamics study of dissociation of water under an electric field. *Phys Rev Lett.* **2012**;108:207801.
- [18] Stuve EM. Ionization of water in interfacial electric fields: an electrochemical view. *Chem Phys Lett.* **2012**;1:519–520.
- [19] Rothfuss CJ, Medvevev VK, Stuve EM. The influence of the surface electric field on water ionization: a two step dissociative ionization and desorption mechanism for water ion cluster emission from a platinum field emitter tip. *J Electroanal Chem.* **2003**;133:554–555.
- [20] Hammadi Z, Descoins M, Salanon E, et al. Proton and light ion nanobeams from field ionization of water. *Appl Phys Lett.* **2013**;101:243110.
- [21] Cassone G, Giaquinta PV, Saija F, et al. Proton conduction in water ices under an electric field. *J Phys Chem B.* **2014**;118:4419–4424.
- [22] Cassone G, Giaquinta PV, Saija F, et al. Liquid methanol under a static electric field. *J Chem Phys.* **2015**;142:054502.
- [23] Saitta AM, Saija F. Miller experiments in atomistic computer simulations. *Proc Natl Acad Sci.* **2014**;111:13768–13773.
- [24] Cassone G, Creazzo F, Giaquinta PV, et al. *Ab initio* molecular dynamics study of an aqueous NaCl solution under an electric field. *Phys Chem Chem Phys.* **2016**;18:23164–23173.
- [25] Cassone G, Giaquinta PV, Saija F, et al. Effect of electric field orientation on the mechanical and electrical properties of water ices: an ab-initio study. *J Phys Chem B.* **2014**;118:12717–12724.
- [26] Giannozzi P, Baroni S, Bonini N, et al. Quantum ESPRESSO: a modular and open-source software project for quantum simulation of materials. *J Phys Condens Matter.* **2009**;21:395502.
- [27] Car R, Parrinello M. Unified approach for molecular dynamics and density-functional theory. *Phys Rev Lett.* **1985**;55:2471–2474.
- [28] Berry MV. Quantal phase factors accompanying adiabatic changes. *Proc R Soc Lond A.* **1984**;392:45.
- [29] Umari P, Pasquarello A. *Ab initio* molecular dynamics in a finite homogeneous electric field. *Phys Rev Lett.* **2002**;89:157602.
- [30] English NJ, Waldron CJ. Perspectives on external electric fields in molecular simulation: progress, prospects and challenges. *Phys Chem Chem Phys.* **2015**;17:12407–12440.
- [31] Perdew JP, Burke K, Ernzerhof M. Generalized gradient approximation made simple. *Phys Rev Lett.* **1996**;77:3865–3868. and *Phys Rev Lett.* **1997**;78:1396–1396.
- [32] Marom N, Tkatchenko A, Rossi M, et al. Dispersion interactions with density-functional theory: benchmarking semiempirical and interatomic pairwis corrected density functionals. *J Chem Theory Comput.* **2011**;7:3944–3951.
- [33] Fiolhais C, Nogueira F, Marques M. A primer in density functional theory. Berlin Heidelberg: Springer-Verlag; **2010**.
- [34] Grossman JC, Schwegler E, Draeger EW, et al. Towards an assessment of the accuracy of density functional theory for first principles simulations of water. *J Chem Phys.* **2003**;120:300.
- [35] Soper AK. The radial distribution functions of water as derived from radiation total scattering experiments: is there anything we can say for sure? *ISRN Phys Chem.* **2013**;2013:ID 279463.
- [36] Choudhuri JR, Vanzo D, Madden PA, et al. Dynamic response in nanoelectrowetting on a dielectric. *ACS Nano.* **2016**;10:8536–8544.
- [37] Tassone F, Mauri F, Car R. Acceleration schemes for ab initio molecular-dynamics simulations and electronic-structure calculations. *Phys Rev B.* **1994**;50:10561–10573.
- [38] Rappe AM, Rabe KM, Kaxiras E, et al. Optimized pseudopotentials. *Phys Rev B.* **1990**;44:13175.
- [39] Leberman R, Soper AK. Effect of high salt concentrations on water structure. *Nature.* **1995**;378:364–366.
- [40] Helm L, Merbach AE. Water exchange on metal ions: experiments and simulations. *Coord Chem Rev.* **1999**;187:151–181.
- [41] Mehandzhiyski AY, Riccardi E, van Erp TS, et al. Ab initio molecular dynamics study on the interactions between carboxylate ions and metal ions in water. *J Phys Chem B.* **2015**;119:10710–10719.
- [42] Bagchi B, Biswas R. Ionic mobility and ultrafast solvation: control of a slow phenomenon by fast dynamics. *Acc Chem Res.* **1998**;31:181.
- [43] Wolyne PG. Dynamics of electrolyte solutions. *Annu Rev Phys Chem.* **1980**;31:345–376.
- [44] Biswas R, Bagchi B. Limiting ionic conductance of symmetrical, rigid ions in aqueous solutions: temperature dependence and solvent isotope effects. *J Amer Chem Soc.* **1997**;119:5946–5953.
- [45] Biswas R, Bagchi B. Ionic mobility in alcohols: from dielectric friction to the solvent-berg model. *J Chem Phys.* **1997**;106:5587–5598.
- [46] Biswas R, Roy S, Bagchi B. Anomalous ion diffusion in dense dipolar liquids. *Phys Rev Lett.* **1995**;75:1098–1101.



# Chapter 9

## Summary, conclusions, perspectives

In this thesis, DFT-MD simulations, coupled with state-of-the-art metadynamics techniques, have been applied to gain a global understanding of  $\text{Co}_3\text{O}_4$  and  $\text{CoO}(\text{OH})$  cobalt oxide aqueous interfaces in catalyzing the oxygen evolution reaction (OER) and hence possibly help in the design of novel catalysts based on non-precious materials.

The design of catalysts cannot be done entirely from experiments, as it is complicated to individually tune the relevant microscopic parameters that enter into a catalyst and ascribe them directly to the cell performance. An atomistic probing is required, methods to tune one-by-one the parameters are required, none of these are obvious from experiments alone, while one would like to avoid costly "trial and errors" experiments.

These represent significant hurdle toward the development of improved catalysts, which could be overcome by employing methods able to track the catalytic features of the OER at the atomistic scale. Atomistic simulations are the way to get these informations. Disclosing the detailed mechanisms of water oxidation on cobalt oxide surfaces – as well as the surface chemical reactivity and the involved reaction pathways – would have a crucial role in improving the efficiency of the catalyst and thus help for a better design. This thesis discusses some of the parameters affecting the catalysis for the electrochemical conversion of water into oxygen within the hypotheses of our simulations. The slow kinetics for the oxygen evolution reaction (OER) is one of the major bottlenecks in the water-oxygen conversion process, which reduces the efficiency of the electrochemical fuels generation. This sluggish OER kinetics and the exorbitant cost of the precious metal OER catalysts such as  $\text{RuO}_2$ ,  $\text{IrO}_2$ , and  $\text{PtO}_2$  are two main obstacles for the large-scale application of water electrolyzers. In this thesis, a series of OER cobalt-based electrocatalysts are discussed, and the influence of morphologies, substrates and compositions of these catalysts upon their OER performance are thoroughly investigated by DFT-MD simulations. Moreover, in this thesis, we step-by-step revealed the OER mechanisms on spinel  $\text{Co}_3\text{O}_4$  and  $\text{CoO}(\text{OH})$  cobalt aqueous electrocatalysts carefully and rationally via novel metadynamics techniques.

As already pointed out a few times in this thesis, our biased metadynamics are performed at zero-voltage on the oxide anode electrode and also without the presence of supported electrolytes. Our results are therefore relevant for these conditions, which are not including all conditions from the experiments. However, we include the surrounding water in a "proper way", not done yet in the literature; no calculations on OER have included supported electrolytes either; Selloni's and Norskov's static calculations that included the electrode potential were done in an empirical and indirect way, on solid-air interfaces. The atomistic modifications on the electrode structure as well as on the interfacial water are never taken into account into these modeling. Despite our DFT-MD and associated DFT-MD metadynamics are not including all conditions of the OER electrochemical experiments, they advance the field and pave the way for more complex systems to be modeled soon.

We have shown how important it is to take into consideration the presence of the water environment in the structural characterization of catalyst surfaces, *i.e.* (110)-Co<sub>3</sub>O<sub>4</sub> and (0001)-CoO(OH) in this work. The hydroxylation of the (110)-Co<sub>3</sub>O<sub>4</sub> and (0001)-CoO(OH) surfaces plays a key role in the reactivity of the surfaces, thus in their ability to catalyze the water splitting. Such surface hydroxylation strongly changes the electronic properties of the cobalt oxide surfaces and thus their capability in chemistry. In the present thesis we firstly focused on this essential aspect of electrochemical interfaces, *i.e.* the comprehension of the interaction and organization of liquid water at the (110)-Co<sub>3</sub>O<sub>4</sub> and (0001)-CoO(OH) water interfaces by DFT-MD simulations. This is what is firstly achieved in the present thesis, *i.e.*, an explicit consideration of the liquid water, and of its dynamics, in contact with the (110)-Co<sub>3</sub>O<sub>4</sub> and (0001)-CoO(OH) cobalt oxide surfaces, using *ab initio* DFT-based molecular dynamics simulations, not done before in the literature where water is at the best modeled as implicit solvent or only by few water molecules that are included in static DFT calculations [29, 30, 31, 32] ('surface science calculations'). A detailed characterization of chemical and physical properties of the aqueous interfaces is provided in this work (*i.e.* structure, dynamics, spectroscopy, electric field), for the (110)-Co<sub>3</sub>O<sub>4</sub> and (0001)-CoO(OH) aqueous surfaces. We have seen how the water in the Binding Interfacial Layer-BIL, *i.e.* the "true" interfacial layer, is the most relevant for the chemical and physical description of these interfaces, and how important it is to take these water explicitly into account in the modelling, as well as the successive (Diffuse Layer-DL and bulk) liquid water

What we report in Fig. 9.1 is the surface speciation of the aqueous (110)-Co<sub>3</sub>O<sub>4</sub> and (0001)-CoO(OH) surfaces, just to remind the reader how the different speciation/hydroxylation that occur at these electrochemical surfaces can affect the OER discussed hereafter.

Most of the theoretical and experimental attempts to understand the factors affecting the kinetics for the electrochemical water oxidation into oxygen focus only in the properties of the catalysts. Those research efforts concentrate on developing catalysts able to reduce the intrinsic overpotential needed at

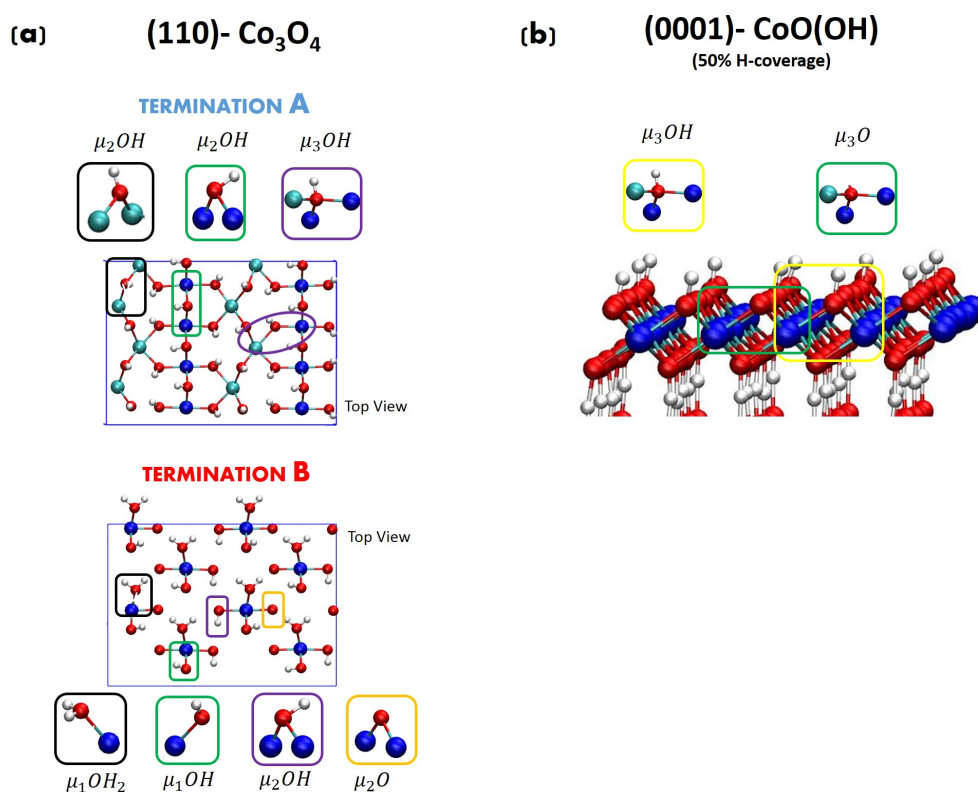


Figure 9.1: a) Aqueous (110)-Co<sub>3</sub>O<sub>4</sub>: composition and speciation of the A- and B-surfaces. Top views. b) Surface motif of the 50% H-covered (0001)-CoO(OH) surface at the interface with liquid water (liquid water not shown in the picture for clarity). Oxygens are in red, hydrogens in white, Co(II) in light blue, Co(III) in dark blue.

the anode inherent to the oxygen evolution reaction. Only few research efforts have been devoted to understand the role of an explicit water environment in the water electrocatalysis, which can however strongly affect the OER activity.

In this thesis, for the first time, a study of the OER was presented not only by looking at the catalysts, but also by addressing the role of the water environment in the catalytic process. Accordingly, both gas-phase and liquid-phase OER were here investigated at the (110)-Co<sub>3</sub>O<sub>4</sub> and (0001)-CoO(OH) adopting a novel enhanced sampling metadynamics approach able to address a wide range of chemical reaction mechanisms and to fully include the role of the solvent degrees of freedom, allowing to unveil reaction networks of remarkable complexity. The energetics, kinetics and thermodynamics behind the OER are therefore found at these cobalt oxide surfaces.

The power of this novel metadynamics technique here adopted resides in the fact that it allows the knowledge of possible/alternative (not predefined) OER pathways, overcoming the limits of the (standard) metadynamics techniques which *a priori* constrain the reactant atoms and hence the reaction path. This is possible by adopting new collective variables  $S$  and  $Z$  (see section 2.9), which define a new configurational space and, simultaneously, allow to reconstruct

the free-energy landscape of the OER process through a partially unbiased exploration of both gas-phase and aqueous-phase OER. Moreover, an additional striking advantage of this metadynamics technique is that, in principle, no insights might be known about the reaction path under investigation: one only needs the knowledge of the coordination numbers of the atoms involved in the reaction path, *i.e.* the coordination numbers of the reactant and product atoms arranged in a simple matrix called "contact matrix", in order to identify pathway(s) of lowest energy and associated energetics/kinetics. All of these, together with the DFT-MD simulations, should give us a strategy for materials design to improve heterogeneous catalysis processes.

An overview of the OER energetics at the (110)-Co<sub>3</sub>O<sub>4</sub> B-surface (chapter 6) and at the (0001)-CoOOH surface (50% H-covered) (chapter 7), when both surfaces are exposed to either one gas-phase water or to full liquid water, is presented in Fig. 9.2.

The first result from our metadynamics simulations is that only the B-(110)-Co<sub>3</sub>O<sub>4</sub> surface and the 50% H-covered (0001)-CoOOH are reactive to the OER over our simulation times of 20 *ps* whether at the air or liquid phase interface.

Looking at the overpotential values, our results show that the (110)-Co<sub>3</sub>O<sub>4</sub> B-surface is definitely a better OER catalyst than the (0001)-CoOOH surface (50% H-coverage) in both gas-phase and liquid-phase environments. We indeed found overpotentials of  $\eta_{Co_3O_4} = 0.91$  V *vs.*  $\eta_{CoOOH} = 8.47$  V in the gas phase and  $\eta_{Co_3O_4} = 0.31$  V *vs.*  $\eta_{CoOOH} = 1.59$  V in the liquid phase, with an OER overpotential for Co<sub>3</sub>O<sub>4</sub> B-surface that is 9 times less and 5 times less than CoOOH, in gas and in liquid phases, respectively. The exception is with the  $\eta_{Co_3O_4} = 2.68$  V (path-2 in Fig. 9.2) obtained for the OER pathway in the liquid phase, that if compared with the liquid phase  $\eta_{CoOOH} = 1.59$  V, shows that the  $\eta_{Co_3O_4}$  is larger than  $\eta_{CoOOH}$ . However, we remind the reader that the  $\eta_{Co_3O_4} = 2.68$  V was obtained for an OER pathway that is not the minimum energy path (see Fig. 6.10 as reminder), and that the low  $\eta_{Co_3O_4} = 0.31$  V is obtained because water acts as co-catalyst.

The noticeable OER pathway of lowest energy found in the liquid phase (path-1 in Fig. 9.2) at the B-Co<sub>3</sub>O<sub>4</sub> (110)/water interface leads to a striking low OER overpotential  $\eta_{Co_3O_4} = 0.31$  V, hence comparable with the range value of  $\eta = [0.3 - 0.9]$  V [28] generally found for the OER when employing a high cost noble earth metal oxide such as RuO<sub>2</sub>, IrO<sub>2</sub>, and PtO<sub>2</sub>. Here, the value of  $\eta_{Co_3O_4} = 0.31$  V was obtained at the interface with water and it is associated to a new identified water-assisted OER mechanism different from the OER pathway proposed by Norskov *et al.* [29, 31] (for which hydrogens of the dissociated water molecule are systematically surface adsorbed). Water molecules thus do not act as a "spectators" but they are explicitly involved in the lowest energy OER mechanism.

We have identified, for the first time, that water act as OER co-reactant and

<b>(110)- Co<sub>3</sub>O<sub>4</sub> B-surface</b>			
	<b>OER Rate Limiting Step</b>	<b>Free Energy Barrier</b>	<b>Overpotential <math>\eta</math></b>
<b>GAS PHASE</b>	Surface Deprotonation of $\mu_1\text{OH}$ site	49 kcal/mol 2.14 eV	<b>0.91 V</b>
<b>LIQUID PHASE-Path 1</b> (lowest energy pathway with water as co-catalyst)	Water Attack & Dissociation (2 $e^-$ process) at $\mu_1\text{OH}$ site	71 kcal/mol 3.08 eV (2 $e^-$ process)	<b>0.31 V</b>
<b>LIQUID PHASE-Path 2</b> (OER pathway without water as co-catalyst)	Water Attack & Dissociation (2 $e^-$ process) at $\mu_1\text{OH}$ site	180 kcal/mol 7.81 eV (2 $e^-$ process)	<b>2.68 V</b>

<b>(0001)-CoOOH , 50% H-coverage</b>			
	<b>OER Rate Limiting Step</b>	<b>Free Energy Barrier</b>	<b>Overpotential <math>\eta</math></b>
<b>GAS PHASE</b>	$\text{O}_2$ release from the solid surface (from $\mu_3\text{O}$ site)	224 kcal/mol 9.7 eV	<b>8.47 V</b>
<b>LIQUID PHASE</b>	$\text{O}_2$ release from the solid surface (from $\mu_3\text{O}$ site)	65 kcal/mol 2.82 eV	<b>1.59 V</b>

Figure 9.2: Computed OER rate limiting steps and associated free-energy barriers/overpotentials in the gas phase and in the liquid phase for both  $\text{Co}_3\text{O}_4$  (110) B-surface (chapter 6) and (0001)-CoO(OH) surface (chapter 7). Note that the surface of CoO(OH) is already deprotonated by half, thus there is no rate-limiting step associated to such process.

co-catalyst, and hence this coupled water behaviour is crucial in lowering the OER free-energy barrier. We strongly believe that the synergistic effect between surface catalyst and water environment is the basis for a rational design of novel catalysts based on non-precious materials for the electrochemically-driven OER. We also found that the OER product  $\text{O}_2$ , once released from the catalyst surface, moves from the BIL region to the DL (or bulk) water environment, preferring to be fully solvated by the DL (or bulk) water molecules (in agreement with the large solubility of  $\text{O}_2$  in pure water detected in the literature [322, 323, 324]), highlighting again the importance of having an explicit water slab in the simulation box to have relevant events modeled.

These hopefully clearly demonstrate the relevance of *ab initio* molecular dynamics simulations coupled with the here adopted metadynamics technique in the rationalization of several interfacial properties and in the comprehension of reactions occurring at electrochemical solid/water interfaces, also showing the importance of explicit water in the modeling of the OER.

In addition, the present study not only provided an innovative state-of-the-art theoretical/computational strategy for the investigation of the OER, but it also identifies the possible catalyst sites without ambiguity. In this context, we found 3 neighbor  $\mu_3$ -O sites ( $\mu_3$ -O: O 3-fold coordinated to  $\text{Co}^{(3+)}$  ions) as OER catalyst sites at the (0001)- $\text{CoO}(\text{OH})$  surface (50% H-covered), as depicted in Fig. 9.3-left, while adjacent  $\text{Co}^{(3+)}\text{-OH}$ ,  $\text{Co}^{(3+)}\text{-O}$ ,  $\text{Co}^{(3+)}\text{-O-Co}^{(3+)}$  surface sites (respectively  $\mu_1\text{-OH}$ ,  $\mu_1\text{-O}^-$ , and inner  $\mu_2\text{-O}^-$  sites) are able to catalyze the OER both in gas phase and in liquid water at the  $\text{Co}_3\text{O}_4$  (110) B-surface (see Fig. 9.3-right). Note again that, for the novel OER pathway – *i.e.* the water-assisted OER pathway (see section 6.3)– the water is explicitly involved in the OER mechanism at the B-surface (110)- $\text{Co}_3\text{O}_4$ /liquid water interface (see Fig. 9.3-right).

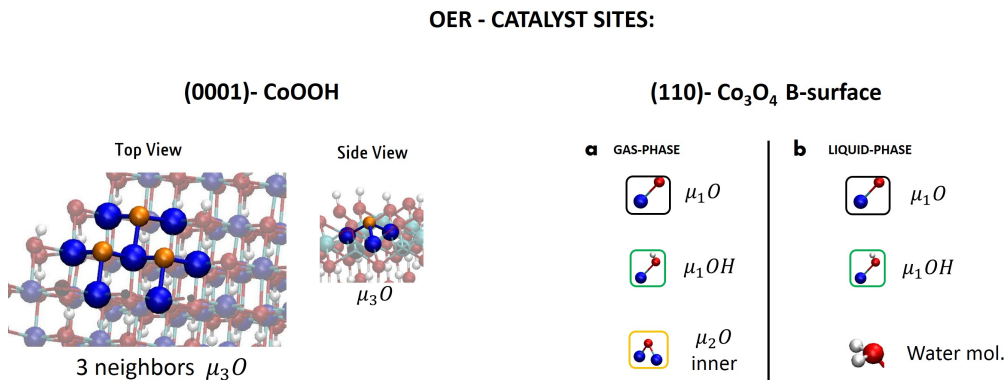
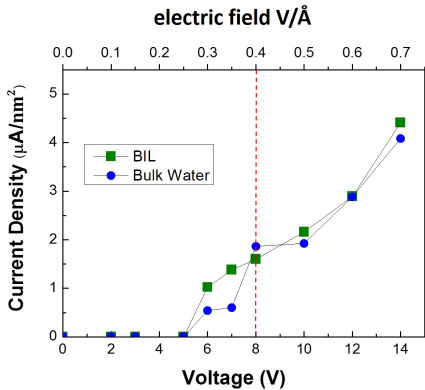


Figure 9.3: OER surface catalyst sites comparison between (0001)- $\text{CoO}(\text{OH})$  surface (chapter 7) –panels on the left– and  $\text{Co}_3\text{O}_4$  (110) B-surface (chapter 6) –panels on the right–. Oxygen atoms O are in orange color in the left panels and in red color in the right panels.  $\text{Co}^{(3+)}$  ions are in blue color.

Furthermore, in this thesis, the water dissociation and the proton transfer phenomena have been investigated in different H-bonded systems. We reported here on the first, to the best of our knowledge, *ab initio* MD results of the microscopic effects produced by an external static and homogeneous electric field applied at the air-liquid water interface and on monovalent ( $\text{NaCl}$ ,  $\text{KCl}$ ,  $\text{LiCl}$ ) and divalent ( $\text{MgCl}_2$  and  $\text{CaCl}_2$ ) electrolyte solutions (chapter 8), by means of proton hopping mechanisms, protonic conductivity and ion-water interactions.

Not surprisingly, when considering the 2D-Hbond-Network formed in the BIL-water at the air-water interface, we found that electric fields applied parallel to the air-water surface plane are able to trigger water dissociations and proton transfers very efficiently. We found that the first formation of hydronium ( $\text{H}_3\text{O}^+$ ) and hydroxide ( $\text{OH}^-$ ) ions has been recorded at the same field strength (*i.e.*,  $0.30 \text{ V}/\text{\AA}$ ), both at the Binding Interfacial Layer (BIL) and in the bulk water, in good agreement with previous work in the literature.

The more surprising result concerns the proton transfer activity at low-to-moderate field regimes ( $\leq 0.40 \text{ V}/\text{\AA}$ ). Two proton conductivity regimes have hence been identified, one for the BIL and one for the bulk liquid: when  $0.30 \text{ V}/\text{\AA}$  (corresponding to  $6 \text{ V}$  potential) is applied parallel to the water surface, protons start to flow along the field direction, with a higher protonic current density along the water network than in the bulk, leading to a protonic conductivity of the BIL ( $\sigma_{BIL} = 3.67 \text{ S/cm}$ ) twice the one recorded in the bulk ( $\sigma_{bulk} = 1.76 \text{ S/cm}$ ). See Fig. 9.4.



**Table:**

Electric Field (V/Å)	Voltage (V)	Current density BIL ( $\mu\text{A}/\text{nm}^2$ )	Current density Bulk Water ( $\mu\text{A}/\text{nm}^2$ )
0.30	6.0	1.02	0.54
0.35	7.0	1.38	0.60
0.40	8.0	1.60	1.86
0.50	9.9	2.16	1.92
0.60	11.8	2.89	2.88
0.70	13.8	4.41	4.08

Figure 9.4: *Left: protonic current density-voltage diagram calculated in the BIL (green squares) and in bulk water (blue circles). The corresponding electric field strength is given with the top axis. The dotted red line highlights the conductivity threshold discussed in the text.  $\sigma_{BIL}$  and  $\sigma_{bulk}$  are the conductivity calculated in the BIL and in bulk water, respectively. Table: for each electric field strength applied (and the related voltage for a cell side of  $19.734 \text{ \AA}$ ) list of protonic current density values calculated in the BIL and bulk water. Data highlighted in red represent the conductivity ( $\sigma$ ) threshold discussed in the text.*

We rationalized the significant difference in the conduction properties of the BIL and of the bulk for fields below  $0.40 \text{ V}/\text{\AA}$ , showing the existence of the specific organization of the interfacial water molecules in the BIL, *i.e.* the 2-Dimensional-Network (2DN) that connects more than 90% of the water molecules belonging to the BIL within a unique extended and collective network via H-bonds all oriented parallel to the surface plane [326], thus favouring

the dissociation of water molecules and the associated proton transfer phenomena (and hence the protonic current) in this direction parallel to the surface.

Beyond a field intensity of  $0.40 \text{ V/\AA}$  (8 V potential), both BIL-2D and bulk-3D H-bonded networks become equally oriented by the electrostatic driving force and the protonic current densities in the BIL and in the bulk liquid become roughly identical. Under such a high-voltage regime (*i.e.*,  $\geq 8 \text{ V}$ ), the BIL and the bulk protonic conductivities are equal to an average value of  $\sim 4.8 \text{ S/cm}$  (Fig. 9.4, bottom).

By performing Car-Parrinello molecular dynamics (CPMD) [356] simulations of monovalent *NaCl*, *KCl*, *LiCl* and divalent  $\text{MgCl}_2$  and  $\text{CaCl}_2$  electrolyte water solutions at a molarity of 1.7 M, we have studied their response to external static electric fields of varying intensities. Their data have been also thoroughly compared. We have found that although a drastic change of the relative cationic mobilities in solutions is recorded for monoatomic cations at very intense field regimes with respect to their ranking in the low-to-moderate field regimes (*i.e.*,  $\mu(\text{K}^+) > \mu(\text{Na}^+) > \mu(\text{Li}^+)$ ), divalent cations – such as  $\text{Mg}^{2+}$  and  $\text{Ca}^{2+}$  – follow the well-known rule of "the bigger the cation the higher the mobility" at all the explored field intensities.

Although all the protonic subsystems of the investigated samples show an Ohmic response to the external field, *i.e.* the estimated protonic conductivities are dependent on the nature of the present alkali metal cations. Accordingly, we proved that the *LiCl*, *NaCl*, and *KCl* water solutions exhibit protonic conductivities equal to  $3.0 \text{ S/cm}$ ,  $2.5 \text{ S/cm}$ , and  $2.3 \text{ S/cm}$ , respectively, a series that inversely follows the trend of the ionic radii of  $\text{Li}^+$ ,  $\text{Na}^+$ , and  $\text{K}^+$  species.  $\text{MgCl}_2$  and  $\text{CaCl}_2$  aqueous solutions are characterized by protonic conductivities of  $2.3 \text{ S/cm}$  and  $1.7 \text{ S/cm}$ , respectively, in agreement with the respective cationic radii. All the aforementioned conductivities values are noticeably lower than the one of pure water, *i.e.*  $7.8 \text{ S/cm}$  [340].

## Perspectives

As said in the previous section and in other instances in this manuscript, there are a few relevant and important things missing in our DFT-MD simulations and associated DFT-MD metadynamics, that have to be included now that we have developed one relevant theory strategy for the OER at cobalt oxide aqueous interfaces.

i) First of all, the influence of the supported electrolytes in the cobalt oxides-water interactions and in the OER is certainly one goal for the near future. We have already started this modelling on the  $\text{B-Co}_3\text{O}_4$ -(110)/water interface by including the  $\text{K}^+$  species in the BIL-water, see Fig. 9.5 for an illustration. Only the cations of the *KOH* electrolyte are introduced for the time-being at the anode cobalt surface. In particular we are interested in understanding how the presence of  $\text{K}^+$  species can affect the BIL water structure and the

cobalt surface reactivity, and again, how the presence of electrolytes can affect the OER energetics and kinetics. Is the OER energetically favored when electrolytes are included? Is it possible to find lower OER pathways in which electrolytes play a direct role? All these questions need answers.

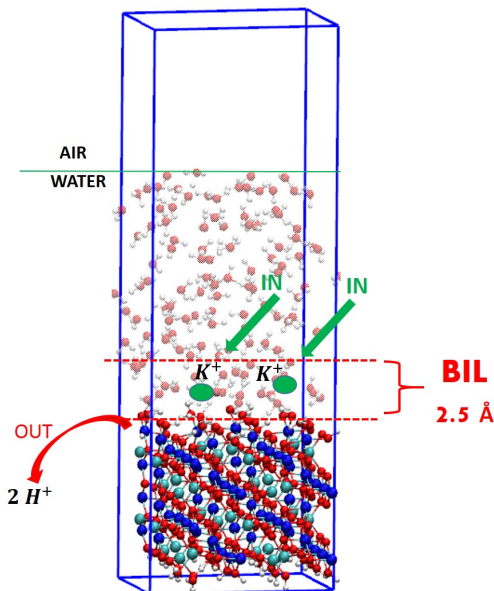


Figure 9.5: Simulation box for the DFT-MD of (110)-B-Co<sub>3</sub>O<sub>4</sub>-liquid water interface, including K<sup>+</sup> in the BIL water. 680 atoms: 320 solid atoms, 120 water molecules. For each K<sup>+</sup> ions introduced, one H at the surface is removed in order to maintain the neutrality of the simulation box. Just like for all simulations in this thesis, there is a 16.5 Å vacuum included above the liquid water in the vertical z-direction, in order not to simulate confined water due to the PBC applied in all 3-directions of space. Only one surface is put in contact with liquid water in each simulation box. The other hydroxylated surface is in contact with vacuum. Oxygens are in red, hydrogens in white, Co(III) in dark blue.

ii) Furthermore and importantly, including electrolytes at the cobalt interface, *i.e.* in the BIL-water, will change the work function of the cobalt surface, thus inducing a change in the surface field produced at the surface. This is one way used in the literature [232, 235, 233] to indirectly model a surface potential at an electrode in *ab initio* calculations. This is another direction into which our simulations should proceed in order to include "realistic" surface potential conditions for electrochemistry in AIMD. There are other AIMD methods currently developed to take into account a constant surface potential applied at the anode, none with still maturity. See the review of A. Gross [357]. Comparisons of benefits and drawbacks of each of these methods should be done in the near future.

iii) Modeling cobalt oxides doped structures and defects at their surface. An interesting future work is to leave out the actual ideal crystalline structures

and introduce defects like bulk/surface vacancies, bond vacancies, edge steps, or introduce doping atoms like  $Fe$  ions in the here investigated cobalt structures. The goal is to fill up the lack of knowledge about the role of defects in the OER mechanisms and assess if they can lower the overpotential. In chapter 4, we have already stated how the presence of defects in the  $CoO(OH)$  surface, *i.e.* the presence of surface site  $\mu_2 - O/OH$  sites instead of  $\mu_3 - O/OH$ , might be crucial for a rational design of an efficient OER catalyst based on  $CoO(OH)$  electrodes [199].

iv) Improve the "contact matrix" metadynamics, making it suitable when using non-orthorhombic boxes and for more complex reactions where hundreds of atomic species can be involved. The reader can easily understand that including the coordination patterns of hundreds of atoms in the "contact matrix" and performing such a kind of metadynamics is a tricky affair due to the large number of variables: such development should be possible by adopting Machine Learning techniques.

v) One further future work would be to investigate the thermodynamic properties of the BIL-water in terms of entropy and enthalpy using the fancy method based on "spatially resolved thermodynamic properties in a voxel" (a sort of grid) developed by Persson R., Heyden M., *et al.* [358]. This method should allow us to determine structural and thermodynamic properties, free energy contributions of the water environment which surround a chemical species and the relevance of these contributions into the OER. Such method has already been applied in the group in the case of hydrophobicity of solutes [359].

The idea would be to quantify these properties for the surface adsorbed OER intermediates  $HO^*$ ,  $O^*$ ,  $HOO^*$  and  $O_2$  product, solvated by water. This way, we should be able to *a priori* know which surface sites are OER reactive, rank them, without doing AIMD simulations of the OER. We could hence even obtain insights on the kinetics of the lower energy OER pathways, without performing any kind of computationally expensive metadynamics investigations.

However, for sampling reasons (both size and time-scale samplings), this method is suitable for classical molecular simulations in which force fields are required. To the best of our knowledge, force fields for cobalt oxides do not exist yet. Such investigation could instead be conducted on titanium oxide  $TiO_2$ , which is actually thought a good alternative to cobalt oxides for OER, for which a wide range of force fields have been developed [360]. Such modeling has already started.

# Appendix

We report hereafter 3 published papers related to my thesis: paper no. 1 is discussed in chapter 5, paper no. 2 is discussed in chapter 8, and paper no. 3 has been achieved in this PhD work in collaboration with other PhD students in the Gageot group and in the Borguet group at Temple University in the USA.

1. DFT-MD of the (110)-Co<sub>3</sub>O<sub>4</sub> cobalt oxide semiconductor in contact with liquid water, preliminary chemical and physical insights into the electrochemical environment.  
F. Creazzo, D. Galimberti, S. Pezzotti, M. P. Gageot.  
*J. Chem. Phys.*, 150, 041721, **2019**;
2. Enhanced conductivity of water at the electrified air-water interface: a DFT-MD characterization.  
F. Creazzo, S. Pezzotti, S. Bougueroua, A. Serva, J. Sponer, F. Saija, G. Cassone, and M. P. Gageot.  
*Phys. Chem. Chem. Phys.*, 22, 10438, **2020**;
3. Ions Tune Interfacial Water Structure and Modulate Hydrophobic Interactions at Silica Surfaces.  
A. Tuladhara, S. Dewana, S. Pezzotti, F. S. Brigiano, F. Creazzo, M.-P. Gageot and Eric Borguet.  
*J. Am. Chem. Soc.*, 142, 15, 6991-7000, **2020**;

# DFT-MD of the (110)-Co<sub>3</sub>O<sub>4</sub> cobalt oxide semiconductor in contact with liquid water, preliminary chemical and physical insights into the electrochemical environment



Cite as: J. Chem. Phys. 150, 041721 (2019); doi: 10.1063/1.5053729

Submitted: 25 August 2018 • Accepted: 10 October 2018 •

Published Online: 26 December 2018



View Online



Export Citation



CrossMark

Fabrizio Creazzo,<sup>a)</sup> Daria Ruth Galimberti, Simone Pezzotti, and Marie-Pierre Gaigeot<sup>a)</sup>

## AFFILIATIONS

LAMBE UMR8587, Univ Evry, Université Paris-Saclay, CNRS, 91025 Evry, France

<sup>a)</sup> Authors to whom correspondence should be addressed: [fabrizio.creazzo@univ-evry.fr](mailto:fabrizio.creazzo@univ-evry.fr) and [mgaigeot@univ-evry.fr](mailto:mgaigeot@univ-evry.fr)

## ABSTRACT

Within the general context of the electrochemical oxygen evolution reaction of the water oxidation/electrolysis, we focus on one essential aspect of electrochemical interfaces, i.e., the comprehension of the interaction and organisation of liquid water at the (semiconductor) (110)-Co<sub>3</sub>O<sub>4</sub> surface using density functional theory-molecular dynamics simulations. A detailed characterization of the chemical and physical properties of the aqueous interface is provided in terms of structure, dynamics, electric field, work function, and spectroscopy, as a preliminary step into the modelling of the (110)-Co<sub>3</sub>O<sub>4</sub> aqueous surface in more relevant electrochemical conditions. The water at the aqueous B-termination is, in particular, shown more dynamical than that at the A-termination and more “undisciplined”: the water is indeed mostly an HB-acceptor with the solid, with an orientation of their dipole moments found opposite the field generated by the negative surface charge. At both aqueous interfaces, the work function is twice lower than that at the bare (non-hydroxylated) surfaces. The SFG (Sum Frequency Generation) spectroscopy is shown dominated by the water in the diffuse layer, while the SFG signal from the binding interfacial layer reflects the single orientation of water at the aqueous A-termination and the two orientations of water at the aqueous B-termination.

Published under license by AIP Publishing. <https://doi.org/10.1063/1.5053729>

## I. INTRODUCTION

The spinel Co<sub>3</sub>O<sub>4</sub> magnetic semiconductor is a promising anode material for the electrochemical OER (Oxygen Evolution Reaction) of water oxidation/electrolysis<sup>1-8</sup>  $2\text{H}_2\text{O} \rightarrow \text{O}_2 + 4\text{e}^- + 4\text{H}^+$ . As a catalyst of gas phase reactions, this cobalt oxide has also typically been successfully applied to CO oxidation,<sup>9</sup> Fischer-Tropsch synthesis,<sup>10</sup> and oxidation of organic compounds.<sup>11</sup> The splitting of water to produce molecular hydrogen and oxygen could be one key process in the quest for future green technology, addressing climate change issues and the ever growing sustainable green/renewable energy demand. The success of the hydrogen economy is closely related to the efficiency of the hydrogen production and its use in energy conversion systems, and is dependent on the development of cost-effective and

efficient materials catalysing both the OER and the HER (Hydrogen Evolution Reaction) half-cell chemical reactions and operating at low overpotential. This still remains a challenge partly because of the lack of detailed atomistic understanding of the electrocatalysis mechanisms, especially at the anode side (for the OER).<sup>12,13</sup> Therefore, there is a need for theoretical rationalization and characterization at the atomistic level.

The electrochemical theoretical community is dominated by the approach initiated by Rossmeisl, Norskov, Jonsson, and others, based on the surface science static density functional theory (DFT) calculations of the thermodynamics of surface reaction intermediates.<sup>14-19</sup> While this approach is successfully providing a wealth of information into the screening of the most promising catalysts, it however lacks some crucial

modelling elements in order to get a more detailed atomistic understanding of the electrochemical catalysis processes and hence advance further the catalyst-material rational design of the OER in electrochemical conditions.

One issue in these surface science calculations is the lack of explicit water interacting with the surface catalyst and with the chemical compounds involved in the OER reaction. It is not only the explicit presence of the aqueous solvent that matters, i.e., its structural organisation at the interface with the anodic material (metal electrode or semiconductor cobalt oxide of interest here), but the water dynamics at finite temperature also matters (e.g., wriggling of water at the surface, diffusion, and dynamical charge transfers). The whole complex structure and dynamicity of the electric double layer (EDL) in the electrochemical conditions have to be accounted for, as well as the presence of adsorbed species at the surface and at the interface for their influence on the EDL structure and hence on the chemical processes occurring at the aqueous interface. With this in mind, it is obvious that electrocatalytic reactions such as the water electrolysis in the OER are highly complex to model because of the interplay in between the anode material (metal/semiconductor), the electrolyte, the liquid, the adsorbed species, and the material-liquid vs liquid-phase reactants and products. The external applied voltage in the electrochemical conditions also has to be taken into account. First principles simulations are therefore mandatory because of the complex interplay in between electronic, structural, and dynamics properties at surface-water-electrolyte-EDL interfaces, including the modelling of charge transfers and chemical reactions.

Within the past decade, first principles simulations of metal-water interfaces have been carried out with different flavors, see, e.g., Ref. 20 for a recent review. For instance, Gross *et al.*<sup>21,22</sup> and Jonsson *et al.*<sup>23</sup> have included water mono- and bi-layers at metal surfaces in order to take into account the presence of some of the aqueous environment at metal surfaces, through static DFT calculations and DFT-based molecular dynamics (MD) simulations at finite temperature; some of their recent studies include bulk liquid water at metallic interfaces<sup>24</sup> (although sometimes implicitly<sup>25</sup>). Jonsson and co-workers have included pH and applied voltage in DFT-MD<sup>23</sup> in an *ad hoc* way, by varying the concentration in  $\text{H}_3\text{O}^+$  electrolytes within a few water monolayers at the interface with the surface metal, while Cheng and Sprik<sup>26</sup> have played with the electrolyte concentration in the EDL at a metal-liquid water interface in order to model the interface capacitance and hence indirectly include relevant electrochemical voltage conditions. Imposing the electrochemical voltage is however very challenging in *ab initio* MD simulations, and a few theoretical methods have been recently developed to this end.<sup>23,27-30</sup>

In the present work, we focus on one essential aspect of electrochemical interfaces, i.e., the comprehension of the interaction and organisation of liquid water at the (semiconductor) (110)- $\text{Co}_3\text{O}_4$  surface using DFT-MD simulations. This is following the modelling and analyses strategies from our

recent studies on mineral-water interfaces.<sup>31-36</sup> Other facets of this cobalt oxide [e.g., (100), (111), and (311)] are certainly also of interest in the context of water electrocatalysis. Previous experimental surface science characterization of (110)- $\text{Co}_3\text{O}_4$  has been performed,<sup>37</sup> as well as theoretical investigations on the bare surface.<sup>38,39</sup> The group of Selloni has furthermore been the first one to characterize the hydroxylation state of the (110)- $\text{Co}_3\text{O}_4$  surface, with systematic surface science DFT calculations of phase diagrams as a function of water pressure, pH, and external voltage in electrochemical conditions.<sup>40-43</sup> These theoretical calculations have provided a clear view of the water monolayer coverage under experimental conditions at the (110)- $\text{Co}_3\text{O}_4$  cobalt oxide surface, but the rest of the liquid water has not been explicitly taken into account.

This is what is achieved in the present work, i.e., an explicit consideration of the liquid water in contact with the (110)- $\text{Co}_3\text{O}_4$  cobalt oxide surface, using *ab initio* DFT-based molecular dynamics simulations. A detailed characterization of the chemical and physical properties of the aqueous interface is provided (i.e., structure, dynamics, electric field, and spectroscopy), as a preliminary step into the modelling of the (110)- $\text{Co}_3\text{O}_4$  aqueous surface in more relevant electrochemical conditions. As emphasized by Koper and co-workers, see, for instance, Ref. 44, the efficiency of chemical reactions at material-water interfaces is highly dependent on how much water is easily/not easily reorganized, or in other terms on how much water at the interface has a flexible/rigid structural and dynamical character. This is one key issue into the charge transfers occurring within the double layer as the chemical reactions (such as the OER) proceed. It is thus fundamental to have the knowledge of the intrinsic chemical and physical properties of the material-water-electrolyte interface (at a given pH and electrolyte concentration), before applying the electrochemical voltage.

Here we investigate the material (110)- $\text{Co}_3\text{O}_4$ -liquid water interface by DFT-MD modelling as a preliminary step into the construction of knowledge of the  $\text{Co}_3\text{O}_4$ -liquid water-electrolyte interface in electrochemical conditions (i.e., including electrolytes, external voltage, and pH). We also model the ideal crystalline  $\text{Co}_3\text{O}_4$  without taking into account surface defects that could be relevant in the context of the chemical reactivity at the interface. Of particular interest is how the interfacial water is organised, not only at the direct contact with the semi-conductor cobalt oxide surface, i.e., in the BIL (Binding Interfacial Layer, see Refs. 32 and 33), but also at slightly larger distances from the aqueous oxide surface, i.e., in the DL (Diffuse Layer<sup>32,33</sup>), the knowledge of the layers' thickness, and at what distance from the surface is bulk liquid water recovered.

Our paper presents the computational methods in Sec. II, the  $\text{Co}_3\text{O}_4$  cobalt oxide bulk properties in Sec. III A, the surface and hydroxylation properties of the (110) A- and B-terminations in contact with water in Sec. III B, the water structure at the (110)- $\text{Co}_3\text{O}_4$ -A/B-liquid water interfaces in Sec. III C, and physical observables such as the interfacial

electric field, surface work function, and SFG (Sum Frequency Generation) vibrational spectroscopy of the oxide-liquid water interface in Sec. III D. Perspectives in the context of electrochemical reactions are discussed in the conclusions in Sec. IV.

## II. COMPUTATIONAL METHODS

Unrestricted open shell *ab initio* DFT (Density Functional Theory)-based molecular dynamics simulations [spin polarized-DFT-MD/spin polarized-AIMD (*Ab Initio* Molecular Dynamics)] have been performed on the bulk crystal of  $\text{Co}_3\text{O}_4$ , on two possible (110)- $\text{Co}_3\text{O}_4$  crystalline surfaces and on their associated (110)- $\text{Co}_3\text{O}_4$ /liquid water interfaces. All simulations have been performed in the Born-Oppenheimer framework with the CP2K package.<sup>45,46</sup> The PBE<sup>47</sup> functional, which in previous studies<sup>42,48,49</sup> has been shown as a good description of the properties of both this oxide (and more generally most oxides) and of liquid water, has been adopted in combination with mixed Gaussian-plane wave basis sets and GTH (Goedecker-Tetter-Hutter) pseudopotentials.<sup>50</sup> The DZVP-MOLOPT-SR basis set, augmented with a 400 Ry plane wave basis set, has been used, being a good compromise between computational cost and accuracy, as will be shown here. The PBE functional has been supplemented with the Hubbard U term<sup>51,52</sup> in order to circumvent the overdelocalization of the 3d-electrons in metal oxides (and the consequent underestimation of the bandgap). A value of 5.9 eV for the U parameter has been adopted, as proposed by Selloni *et al.*<sup>42</sup> Although U is not universal and depends on the *ab initio* protocol (typically DFT functional, pseudo-potentials, and projection scheme), we decided to stick to this value while checking that the electronic properties of the semiconductor are correctly obtained with the DFT-schemes applied in this work (see Sec. III A). The Grimme D2 correction<sup>53,54</sup> for dispersion effects has been taken into account for a better description of van der Waals interactions, especially of importance for liquid water. Default algorithms and convergence criteria in CP2K have been adopted. Periodic boundary conditions (PBC) have been applied in all three spatial directions.

DFT-MD in the flavor of Born-Oppenheimer molecular dynamics have been performed, with the electronic wavefunction being calculated at each time step and the classical nuclei displacements being obtained through the velocity-Verlet algorithm with a time step of 0.4 fs. The dynamics are systematically divided into two parts, an equilibration dynamics of 5 ps duration (in the NVE ensemble however allowing rescaling of velocities whenever necessary to reach the target temperature of  $300 \pm 30$  K), followed by 20 ps NVE production runs, the latter trajectory being used for all structural and spectroscopic analyses presented here.

$\text{Co}_3\text{O}_4$  crystallizes in a face-centered cubic unit cell called “spinel structure” [Figs. 1(a) and 1(b)], determined independently by Bragg<sup>55</sup> and Nishikawa.<sup>56</sup> The primitive

lattice consists in 2  $\text{Co}^{2+}$ , 4  $\text{Co}^{3+}$ , and 8  $\text{O}^{2-}$ , for a total of 14 atoms; four primitive lattices form the conventional “spinel” cubic unit cell (Fd3m symmetry space group) which contains 8  $\text{Co}^{2+}$ , 16  $\text{Co}^{3+}$ , and 32  $\text{O}^{2-}$ , for a total of 56 atoms [Fig. 1(a)] arranged in a face-centered cubic box (the experimental lattice parameter is 8.08 Å<sup>42,55,56</sup>).

All our DFT-MD calculations (geometry optimizations and molecular dynamics) are done at the  $\Gamma$  point of the Brillouin zone for the electronic representation; this imposes the use of a supercell (i.e., a certain number of replicas of the unit cell in 3D-space). To find the minimum number of replicas that give an accurate description of the bulk  $\text{Co}_3\text{O}_4$  crystal, convergence of the lattice parameter of the  $\text{Co}_3\text{O}_4$  unit cell and convergence of the electronic bandgap of the bulk  $\text{Co}_3\text{O}_4$  oxide have been monitored. To this end, full geometry optimizations (atom positions and cell vectors) and projected densities of states (PDOS) calculations are performed on the unit cell (56 atoms) and on two (112 atoms), four (224 atoms), and eight (448 atoms) replicas of the  $\text{Co}_3\text{O}_4$  unit cell. PDOS results have been obtained by projecting the Kohn-Sham states onto the atomic orbitals using the standard routine implemented in the CP2K code. Note that the optimizations start from the experimental geometry and are done without imposing symmetry constraints. The Fd3m symmetry is preserved by the optimizations. Here and for all simulations of the cobalt oxide at the interface with vacuum or with liquid water, the electronic multiplicity of the system accounts for the number of the open-shell  $\text{Co}^{2+}$  atoms in the simulation box.

When the bulk solid is cut along the (110) crystallographic plane, two possible terminations can be obtained (as illustrated in Fig. 2), labelled A- and B-terminations in the rest of this work as in Ref. 42. As PBC are applied in all 3-directions of space, when simulating the (110)-A/B-air interface, a vacuum of 16.5 Å along the z-direction (perpendicular to the surface) has been included in the simulation box to separate the periodic replicas. Once put in contact with water, there is adsorption of water molecules at the surfaces. This has been investigated at the A- and B-terminations in contact with vacuum, following the procedure proposed by Selloni *et al.*:<sup>40</sup> water molecules have been added one by one at the surface until complete hydroxylation of the surface. This is done through geometry optimizations and ranking the relative energetics of adsorption of water on each available surface site. Note that these calculations were done with adsorbates on one side only. Once the surface hydroxylation has been achieved at the oxide-air interface, a bulk liquid water composed of 120 water molecules (liquid water box separately thermally equilibrated) has been added in the simulation box, keeping the supplementary 16.5 Å vacuum in the z-direction above the liquid (see Fig. 3 for a scheme). This latter is done in order to avoid the liquid water to be compressed in between the 2-replicated surfaces in the z-direction, and hence avoid simulate confined water, while keeping the simulation box dimensions reasonable and amenable to large enough time scales (for DFT-MD).

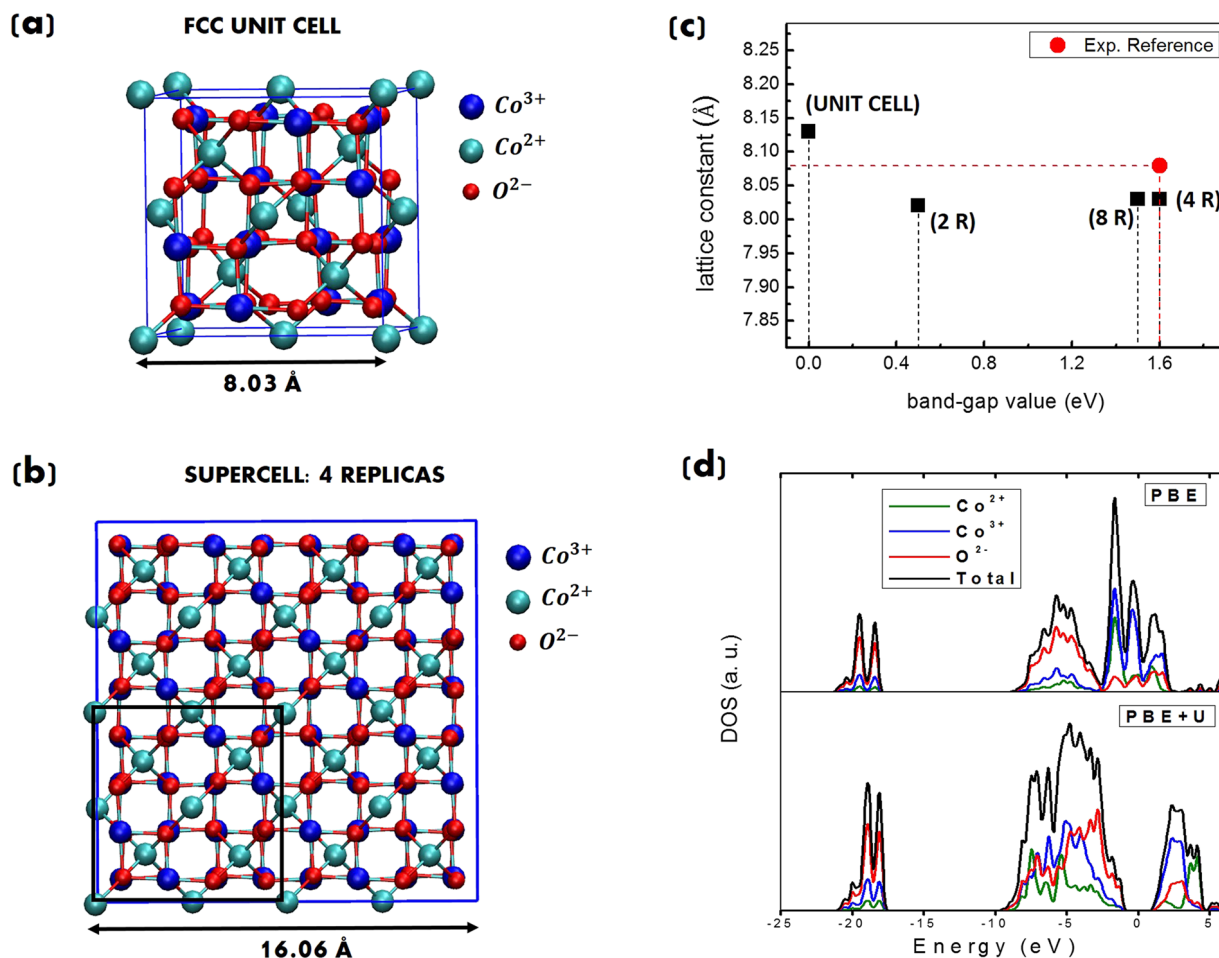


**FIG. 1.** (a) FCC unit cell of bulk  $\text{Co}_3\text{O}_4$ : 56 atoms, 8  $\text{Co}^{2+}$ , 16  $\text{Co}^{3+}$ , and 32  $\text{O}^{2-}$ ; (b) 4-replicas of the  $\text{Co}_3\text{O}_4$  unit cell: 224 atoms, 32  $\text{Co}^{2+}$ , 64  $\text{Co}^{3+}$ , and 128  $\text{O}^{2-}$ ; (c) bandgap (x-axis) and lattice constant (y-axis) as obtained from DFT-PBE + U as a function of the simulation box size: unit cell, 2-replicas of the unit-cell (2R), 4-replicas (4R), and 8-replicas (8R). The red point in the plot shows the reference experimental values. The value for the bandgap is taken from Refs. 63 and 64 and the one for the lattice constant is taken from Refs. 42, 55, and 56. (d) Projected density of states (PDOS) from PBE (top) and PBE + U (bottom) calculations for the four replicas system. The Fermi energy level is set to 0.

The simulation boxes for the DFT-MD of the (110)-A- $\text{Co}_3\text{O}_4$ -liquid water and of the (110)-B- $\text{Co}_3\text{O}_4$ -liquid water interfaces are illustrated in Fig. 3. One box is composed of 9 layers of bulk cobalt oxide in a symmetric slab model, i.e., with two A-surfaces on each side. Both A-surfaces are hydroxylated, and only one surface is put in contact with liquid water. This is shown in Fig. 3(a). The other box is composed of 8 layers of bulk cobalt oxide, in an asymmetric slab model, hence displaying the A- and B-surfaces on either side. Both surfaces are hydroxylated and only the B-surface is put in contact with liquid water. This is shown in Fig. 3(b). For the asymmetric slab, the thickness of the bulk is such that there is no issue with dipole corrections. The cationic A-layer and anionic B-layer have total charges of  $+8|e|$  and  $-8|e|$ , respectively, when considering the 4-replicas system used in the simulations (see Sec. III A for details on the choice of the

4-replicas in the supercell approach). A uniform background and the Ewald summation for electrostatics take care of the total charge of the simulation box whenever necessary, as a standard procedure in DFT-MD simulations.

Electric fields  $\mathbf{E}(z)$  and differences in electric potentials  $\Delta\phi$  have been obtained fully *ab initio* from the optimized electronic wavefunction and the position of the nuclei, using the standard routine implemented in CP2K. The electron work function of the (110)- $\text{Co}_3\text{O}_4$  surface, in contact with air or in contact with liquid water, has been calculated as in Ref. 57, i.e., it is the difference between the electric potential in the vacuum and the Fermi level.

The identification of the water interfacial layers at charged (and non-charged) interfaces, namely, BIL (Binding Interfacial Layer), DL (Diffuse Layer), and bulk liquid

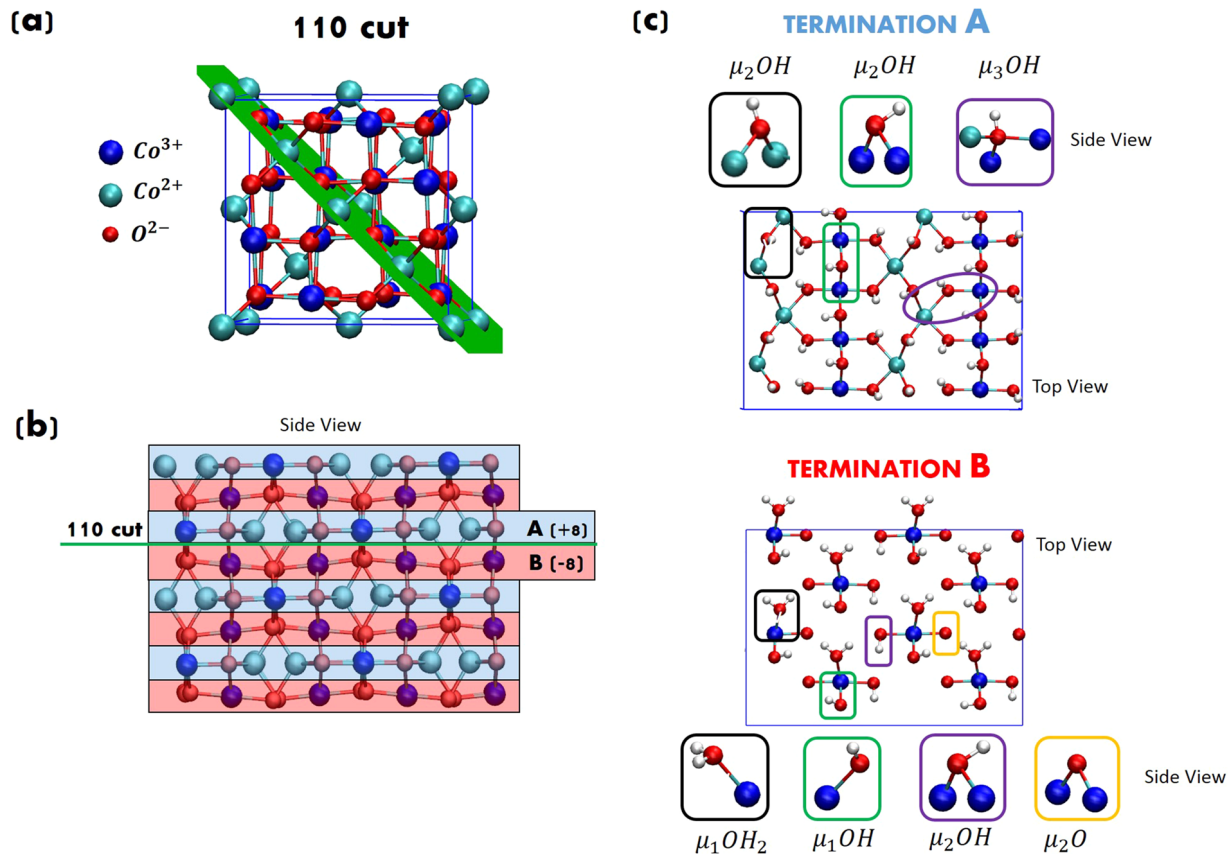


**FIG. 2.** (a) FCC unit cell of  $Co_3O_4$  cut along the (110) crystallographic plane (in green). (b) Side view of the adopted 4-replica system (224 atoms) for the (110) cut: positively charged A-layers are in blue background (+8|e|) and negatively charged B-layers are in red background (-8|e|). This figure shows the 8-layers asymmetric slab (A-layer at the top and B-layer at the bottom) used in the simulation box of Fig. 3(b) for the (110)-B-termination in contact with liquid water. (c) Composition and speciation of the A- and B-surfaces after surface hydroxylation geometry optimizations (identical to Ref. 40). Top and side views: Oxygens are in red, hydrogens in white, Co(II) in light blue, and Co(III) in dark blue. See the text for details.

water, has been done following our methodology derived and fully described in Ref. 32 on the basis of water structural properties only. In the systems investigated here, the BIL is found systematically composed of the first water monolayer, as already shown in several of our investigations on mineral oxide-water interfaces, see, e.g., Refs. 32 and 33.

Spectroscopic analyses are done in terms of non-linear SFG (Sum Frequency Generation) spectroscopy. See our past references on various charged and uncharged air-water and oxide-water interfaces on this subject.<sup>32-34,58</sup> The SFG (Sum Frequency Generation) signal arises from both BIL and DL layers only, while the subsequent centrosymmetric bulk water layer is not SFG active (this is verified in our calculations). The total resonant electric dipole non-linear susceptibility  $\chi^{(2)}(\omega)$  (real and imaginary components) is calculated following the time-dependent method of Morita and Hynes,<sup>59,60</sup> using the model proposed by Khatib *et al.*<sup>61</sup> for dipole and polarisability derivatives of water. As shown in our previous

studies, this model gives accurate SFG spectra.<sup>32,33,58</sup> Only the SFG signal from water is calculated. In brief, supposing that in the high frequency region ( $>3000\text{ cm}^{-1}$ ) only the O-H stretching motions are contributing to the spectrum, and neglecting intermolecular cross correlation terms, one has

$$\chi_{PQR}^{(2)}(\omega) = \sum_{m=1}^M \sum_{n_1=1}^2 \sum_{n_2=1}^2 \frac{i}{k_b T \omega} \times \int_0^\infty dt e^{-i\omega t} \langle \dot{\alpha}_{PQ}^{m,n_1}(t) \dot{\mu}_R^{m,n_2}(0) \rangle, \quad (1)$$

where (P, Q, R) are any x, y, z direction in the laboratory frame, and  $k_b$  and T are the Boltzmann constant and temperature of the simulated system, respectively.  $\langle \dots \rangle$  is a time-correlation function,  $\alpha_{PQ}(t)$  and  $\mu_R(0)$  are the individual O-H bond contribution to the total polarization and dipole moment of the system, respectively, and  $\dot{\alpha}_{PQ}(t)$  and  $\dot{\mu}_R(0)$  are their time derivatives. M is the number of water molecules, and  $n_1$  and  $n_2$  are two indices that identify each of the two O-H oscillators per molecule. Here we calculate ssp SFG signals, i.e., xxx directions. Note that the electric-dipole approximation has

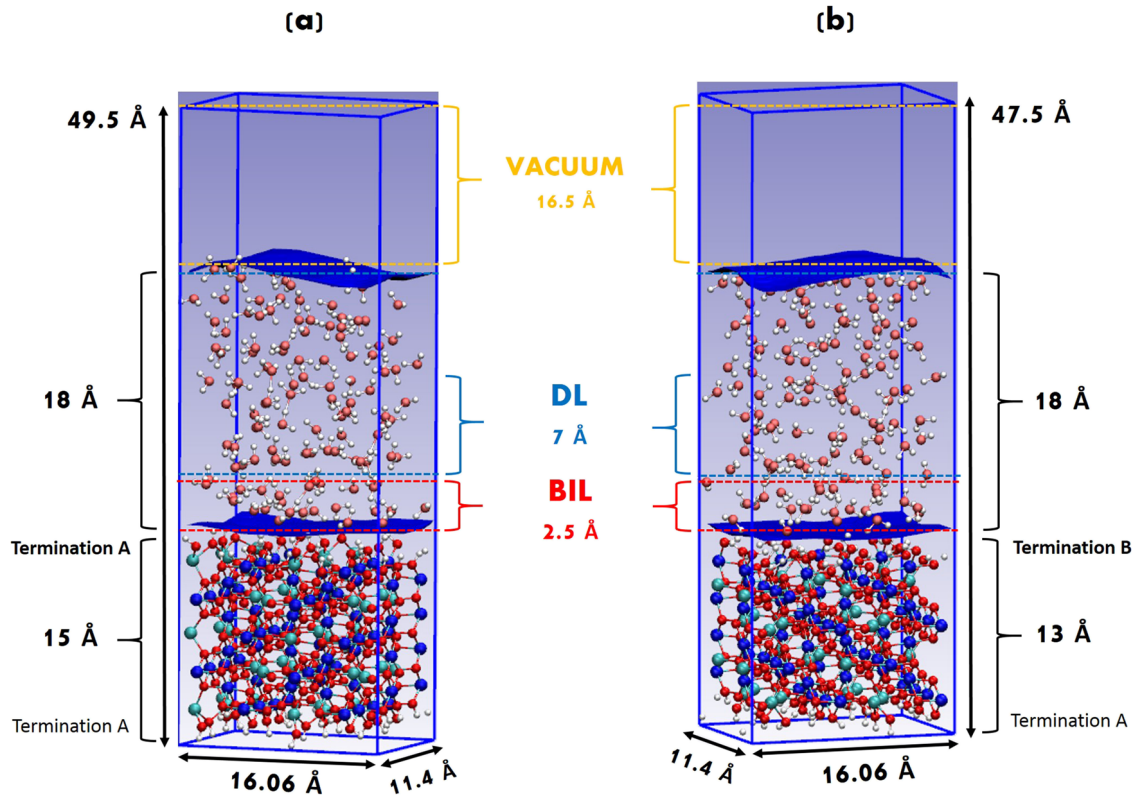


**FIG. 3.** Simulation boxes for the DFT-MD of (110)-A/B- $\text{Co}_3\text{O}_4$ -liquid water interfaces. (a)  $\text{Co}_3\text{O}_4$  termination A/liquid water interface (712 atoms): 352 solid atoms and 120 water molecules. (b)  $\text{Co}_3\text{O}_4$  termination B/liquid water interface (680 atoms): 320 solid atoms and 120 water molecules. Choice is made here to include a 16.5 Å vacuum above the liquid water in the vertical  $z$ -direction, in order not to simulate confined water due to the PBC applied in all 3-directions of space. Only one surface is put in contact with liquid water in each simulation box. The other hydroxylated surface is in contact with vacuum.

been used here, and electric-quadrupole contributions to the ssp signal are neglected. Using the direction cosine matrix ( $D$ ) projecting the molecular frame ( $x, y, z$ ) onto the laboratory frame ( $P, Q, R$ ) and assuming that the O–H stretching is much faster than the modes involving a bond reorientation, one can write

$$\dot{\alpha}_{PQ}(t) \approx \sum_i^{x,y,z} \sum_j^{x,y,z} D_{Pi}(t) D_{Qj}(t) \frac{d\alpha_{ij}}{dr_z} v_z(t), \quad (2)$$

$$\dot{\mu}_R(t) \approx \sum_i^{x,y,z} D_{Ri}(t) \frac{d\mu_i}{dr_z} v_z(t). \quad (3)$$

The  $D$  matrix and the projection of the velocities on the O–H bond axis ( $v_z$ ) can be readily obtained from the DFT-MD trajectory, while  $\frac{d\alpha_{ij}}{dr_z}$  and  $\frac{d\mu_i}{dr_z}$  are parametrized.<sup>61,62</sup>

The SFG spectra arising from the BIL (respectively, from the DL, from the bulk) are obtained including only the water molecules that belong to BIL/DL/bulk into the summation in Eq. (1), known from our decomposition scheme<sup>32</sup> for recognizing these layers.

### III. RESULTS AND DISCUSSIONS

#### A. $\text{Co}_3\text{O}_4$ cobalt oxide bulk properties

We start by considering the solid bulk properties. The ability of the PBE DFT-functional corrected by the Hubbard  $U$  term (5.9 eV<sup>42</sup>) in reproducing the experimental values for the lattice constant and the electronic bandgap of the bulk solid is tested as a function of the simulation box size, i.e., the number of replicas needed to correctly reproduce experimental values in a supercell approach (calculations at the  $\Gamma$ -point only) is validated.

An illustration of the unit cell of the  $\text{Co}_3\text{O}_4$  cobalt-oxide bulk solid is shown in Fig. 1(a) (56 atoms). In Fig. 1(c), we report a 2D-plot of the lattice constant and bandgap values obtained from DFT-PBE +  $U$  for different box dimensions [unit cell, 2 replicas (2R), 4 replicas (4R), and 8 replicas (8R)], compared to the experimental values (red circle). Bulk  $\text{Co}_3\text{O}_4$  is a transition metal oxide and a semiconductor at room temperature with an experimental bandgap value of 1.6 eV.<sup>63,64</sup> While the lattice parameter is already converged (within our numerical error) for the two replicas system, the bandgap is more sensitive to finite size effects (i.e., sensitive to Brillouin zone sampling): the

unit cell and the 2 replicas system both underestimate the bandgap [see Fig. 1(c)], while both the four and eight replicas systems have a value of 8.03 Å for the lattice parameter and 1.6 eV and 1.5 eV, respectively, for the bandgap, comparable with the experimental ones [8.06 Å and 1.6 eV, red dot in Fig. 1(c)]. The 4-replicas system [Fig. 1(b), 224 atoms] is thus the best compromise between accuracy and minimizing computational cost, correctly reproducing both the bandgap and lattice constant.

Localized Wannier functions and charges have been computed for the four replicas system. The correct oxidation states have been found for all  $\text{Co}^{2+}$ ,  $\text{Co}^{3+}$ , and  $\text{O}^{2-}$  atoms of the bulk oxide. The same outcome for the shapes of the associated localized Wannier orbitals, identical to the results in Ref. 42, confirms the correct description of the electronic structure of the system with the here chosen computational setup.

In Fig. 1(d), we also show the electronic PDOS obtained for the 4-replicas bulk oxide using PBE and PBE + U electronic representations. The comparison highlights that it is essential to include the U correction to correctly represent the electronic properties of the bulk solid, as there is no bandgap when the PBE representation is used: without the U-term, the system is a conductor.

To conclude, our chosen setup is sufficient to correctly reproduce the structure and electronic properties of the  $\text{Co}_3\text{O}_4$  cobalt oxide crystal bulk, and 4-replicas of the unit cell are enough in a supercell approach (at the electronic  $\Gamma$ -point). This 4-replicas system will thus be used for the next step consisting now in the cut of the bulk oxide along the (110) direction and ultimately put the hence created surface(s) in contact with liquid water. Note that previous studies<sup>48,65,66</sup> have pointed out that the modelling of very small cells (in all 3 directions of space) prevents the correct description of the structure of water at the interface. Some of our recent studies<sup>33,65,66</sup> give solid bases to trust that lateral dimensions above 15 Å (such as the ones of the cut-surface of the 4 replicas system employed here) are just enough to avoid finite size effects on the structure of interfacial water.

## B. Cutting along the (110) direction: A- and B-terminations in contact with water

When the bulk solid is cut along the (110) crystallographic symmetry plane [Fig. 2(a)], two possible terminations can be obtained [Fig. 2(b)] and are denoted A- and B-terminations. The cationic A-termination surface exposes 8  $\text{Co}^{3+}$ , 8  $\text{Co}^{2+}$ , and 16  $\text{O}^{2-}$  in the 4-replicas box validated in Sec. III A (2  $\text{Co}^{3+}$ , 2  $\text{Co}^{2+}$ , and 4  $\text{O}^{2-}$  per unit cell surface), with a formal surface charge of 4.37  $|e|/\text{nm}^2$  (+8 $|e|$  in the 4-replicas box). The anionic B-surface instead exposes 8  $\text{Co}^{3+}$  and 16  $\text{O}^{2-}$  in the adopted 4-replicas box (2  $\text{Co}^{3+}$  and 4  $\text{O}^{2-}$  in the unit cell), with a formal surface charge of -4.37  $|e|/\text{nm}^2$  (-8 $|e|$  in the 4-replicas box). Interestingly, only  $\text{Co}^{3+}$  sites are present at the B surface, while both  $\text{Co}^{3+}$  and  $\text{Co}^{2+}$  sites are exposed

at the A surface. This difference together with the opposite surface charge possibly play a role in the reactivity of the two surfaces, thus in their ability to catalyze water splitting.<sup>40,43</sup>

Once put in contact with water the two surfaces adsorb water molecules. As described in more detail in Sec. III D, such surface hydroxylation strongly changes the electronic properties of the cobalt oxide, especially tuning the surface work function. To find the final speciation/hydroxylation state of the A- and B-surfaces in contact with air, the usual strategy of adsorbing one water molecule at a time and ranking the energetics depending on the surface site adsorption has been adopted, following the strategy by Selloni *et al.*<sup>40</sup> on this same oxide. We obtain the same results as in Ref. 40. See Fig. 2(c) for top and side views of the final A- and B-terminated surfaces.

Once in contact with water, the A-surface is composed of a total of 16 dissociated water molecules (4 water molecules if one considers the unit cell only), there are no intact water molecules adsorbed: this results in 16  $\mu_2$ -OH exposed (i.e., at the top surface) sites systematically bridging 2 identical cobalt atoms (either  $\text{Co}^{2+}$  or  $\text{Co}^{3+}$ ), see the black and green boxes in Fig. 2(c), 16  $\mu_3$ -OH inner sites, and the initial bulk  $\mu_3$ -O site receiving the dissociated water proton. Once in contact with water, the B-surface is composed of a total of 16 water molecules (4 water molecules if one considers the unit cell only), with 8 being dissociated and 8 being intact. This gives rise to the following B-surface speciation, see also Fig. 2(c): 8  $\mu_1$ -OH<sub>2</sub> exposed sites, 8  $\mu_1$ -OH exposed sites, 8  $\mu_2$ -OH inner sites (the inner  $\mu_2$ -O sites receiving the dissociated water proton), and 8  $\mu_2$ -O inner sites. Both surfaces are not flat anymore after water adsorption, now showing a microscopic rugosity with “inner-channels.” As one can see from the data listed above, the two surfaces are substantially different, and, in particular, surface B shows a larger variety of chemical species.

The next step consists in placing the A- and B-hydroxylated surfaces in contact with bulk water, as illustrated by the simulation boxes in Fig. 3. Choice is made here to include a 16.5 Å vacuum above the liquid water in the vertical z-direction, in order not to simulate confined water due to the PBC applied in all 3-directions of space. The speciations of the A- and B-surface terminations described above are found to be stable also when the bulk water is explicitly considered in contact with the cobalt hydroxylated surfaces. While this shows that gas phase calculations are enough to get a correct description of the surface speciation, the structural and electronic properties of the cobalt oxide-liquid water systems, such as the work function, are ill-described when not considering the explicit presence of the bulk liquid water (see Secs. III C and III D). Also, we observe some mobility of protons along the surface, which shows up only when bulk water is introduced.

We now provide a detailed description of the  $\text{Co}_3\text{O}_4$  cobalt oxide-(110)-A/B-liquid water interfaces, with details on the surface sites' orientation and on the solid-solid

and solid-water H-bonds. While the total number of  $\mu_1/\mu_2/\mu_3$  sites is on average maintained along the trajectories, the aqueous B-surface shows a quite dynamical behaviour with proton hoppings between the surface and bulk water. However, the length of our simulations does not allow a more quantitative analysis. Instead, the aqueous A-surface is quite static along all the simulation time.

At the aqueous A-surface,  $\mu_2$ -OH sites are found in two possible orientations (on average), with 67% of them being oriented in-plane (IP, forming an angle around  $50^\circ$  with the normal to the surface) and 33% being oriented out-of-plane (OP, forming an angle around  $10^\circ$  with the normal to the surface). The  $\mu_3$ -OH sites are all oriented similarly, with an angle around  $35^\circ$  with the normal to the surface. Neither  $\mu_2$ -OH nor  $\mu_3$ -OH sites form surface-surface H-bonds, either because of geometrical reasons ( $\mu_2$ -OH) or because of being more buried ( $\mu_3$ -OH) into the material and somehow partially “screened” by adjacent sites. We find that all (93%) surface-liquid water HBs are formed by exposed  $\mu_2$ -OH sites, systematically in the configuration where the  $\mu_2$ -OH sites are donors of HBs and the water is an acceptor (see 88% of WA-water acceptors in the table in Fig. 4). Consequently, the aqueous A-surface has a strong HB donor character towards liquid water, certainly compatible with its high positive surface charge.

At the aqueous B-surface,  $\mu_2$ -OH sites are now inner-sites mostly oriented IP [maximum at  $80^\circ$  in Fig. 4(a), black line]. They are not in direct contact with water, thus forming no H-bonds with water molecules, while they contribute to intra-solid H-bonds as HB-donors to  $\mu_1$  sites. The exposed  $\mu_1$  sites (either  $\mu_1$ -OH<sub>2</sub> or  $\mu_1$ -OH, top surface in direct contact with water) are the only ones being H-bonded to water (91% on average), with the  $\mu_1$ -OH<sub>2</sub> being mostly donors of H-bonds and  $\mu_1$ -OH being mostly acceptors of HBs. This goes with their orientation, as the  $\mu_1$ -OH<sub>2</sub> sites always have one proton pointing towards the water, while a broader angular distribution is observed for the  $\mu_1$ -OH sites [red and blue lines in Fig. 4(a)]. The resulting water-solid HB-network at the aqueous B-surface is roughly equally distributed in HBs with  $\mu_1$ -donors (57%) and  $\mu_1$ -acceptors (43%) (see also the table in Fig. 4). The aqueous B-surface therefore is far less of HB donor character towards the liquid water than the aqueous A-surface.

Interestingly, the average density of water-solid HBs is higher at the aqueous A-surface than at the aqueous B-surface, showing that, despite both interfaces being strongly hydrophilic (the number of HBs/nm<sup>2</sup> is larger than that at the most hydrophilic amorphous silica that we have investigated in the past<sup>34,67</sup>), the aqueous A-surface is the most hydrophilic one with 8.7 water-solid HBs/nm<sup>2</sup>, close to the value of aqueous quartz.<sup>31,32,35</sup> At both interfaces, the inner sites ( $\mu_3$ -OH for the A-surface and  $\mu_2$ -OH for the B-surface) do not interact with water. Simplified views of the typical solid-water HB patterns obtained at the aqueous A- and B-surfaces can be found in Figs. 6(a) and 6(b).

### C. Water structure at the Co<sub>3</sub>O<sub>4</sub> cobalt oxide/liquid water interfaces: A- vs B-termination

We have developed in Ref. 32 a procedure to identify the organisation of water, at any charged and isoelectric interfaces, into three universal layers denoted BIL (Binding Interfacial Layer), DL (Diffuse Layer), and bulk liquid water. These three universal water layers as well as the nomenclature were initially put forward in the experimental work by Tian *et al.*<sup>68</sup> We apply this strategy at the (110)-Co<sub>3</sub>O<sub>4</sub>-A/liquid water and (110)-Co<sub>3</sub>O<sub>4</sub>-B/liquid water interfaces. We refer the reader to Ref. 32 for all details, and we hereby summarize the main ideas. In a nutshell, at any interface, water is found organised into BIL, DL, and bulk water layers, in which relative thickness is system dependent.<sup>32</sup> This statement is especially true for the DL, while we have shown that the BIL is systematically found to be one water monolayer only, i.e., 3–4 Å in thickness, whatever the surface in regard. See Refs. 32 and 33. To reveal BIL, DL, and bulk water from molecular dynamics simulations (*ab initio* and classical MD alike<sup>32,65,66</sup>), three theoretical descriptors are used, based only on water structural properties. These descriptors are (1) the water density profile (top of Fig. 5) as a function of the z-distance from the surface (the density profile is calculated using Willard and Chandler’s instantaneous surface<sup>69</sup>), (2) the water coordination number in each layer identified from the density profile (see the table in Fig. 4), for which the reference number is 3.6 for PBE-D2 bulk liquid water (calculated in this work using the setup used for the interfaces; this value is identical to previous studies on liquid water with the PBE and PBE-D2 functionals<sup>49</sup>), and (3) 3D-contour plots for the water-water H-bond network where the simultaneous probability of a given HB distance and a given HB orientation with respect to the surface normal (oriented towards the solid) is recorded (see the bottom of Fig. 5). The reference of this latter for bulk liquid water is a homogeneous distribution of HB angles within the 2.6–2.9 Å HB distances (see Fig. 2 of Ref. 32). Any departing plot from this reference reveals a non-isotropic organisation of water in the identified layers.

When all three descriptors correspond to the reference in bulk liquid water, the identified layer(s) is(are) denoted bulk water. When only the 3D-plots depart from the isotropic character of bulk water, while the two other descriptors are identical to bulk, the layer(s) is(are) the DL. The DL is indeed bulk liquid water in which the HB network is reoriented by the surface electric field<sup>32,68</sup> (or put in other words, this is liquid water under the influence of a surface field): there is therefore a well-defined direction of the H-bond network within the contour plot. The DL does not hence exist at isoelectric surfaces. When all three descriptors are different from the reference in bulk water, one is thus in the presence of the BIL layer(s). All these descriptors have been validated in Refs. 32 and 33, and the methodology is directly applied in the following at the (110)-Co<sub>3</sub>O<sub>4</sub> cobalt oxide-liquid water interfaces. Furthermore, the BIL and DL water layers are the only two being vibrationally SFG (Sum Frequency Generation) active at any interface, before probing bulk liquid water which is SFG inactive.<sup>32,33</sup> One supplementary proof that the DL is indeed bulk liquid water

(a)

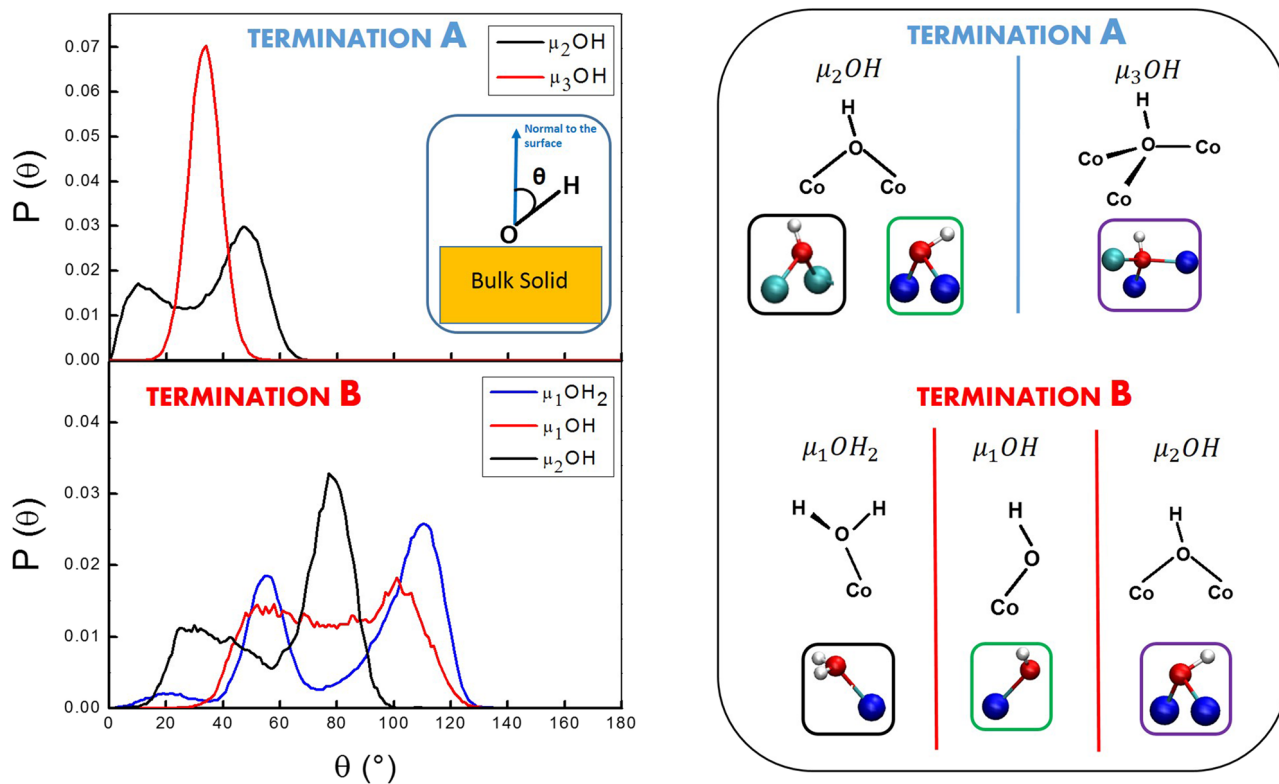


(table)

TERMINATION	Sol-Sol HBs/nm <sup>2</sup>	Wat-Sol HBs/nm <sup>2</sup>	HBs/mol - BIL	HBs/mol - DL	INTRA-BIL HBs/mol
A	0.0	8.7 (88% WA)	3.4 (2.3 W-W)	3.7	1.2
B	6.0	7.7 (57% WA)	3.4 (2.5 W-W)	3.7	1.4

**FIG. 4.** (a) Probability distributions of surface O—H sites orientation (left) and speciation of terminations A and B (right). The orientation is calculated as the scalar product of the O—H vector with the normal to the surface (oriented outward the surface). The nomenclature for the surface sites is illustrated on the right side. Table at the bottom: data about the H-bond arrangements at each interface. Sol = solid, Wat = water, BIL = Binding Interfacial Layer, DL = Diffuse Layer, INTRA-BIL = H-bonds formed between the water molecules located in the BIL, WA = Water Acceptor, W-W = water-water H-bond, HBs/mol = hydrogen bonds per water molecule, and HBs/nm<sup>2</sup> = hydrogen bonds per nm<sup>2</sup> unit of lateral box dimensions.

reoriented by the surface field has been given in Ref. 32 where the third order non-linear susceptibility  $\chi_{\text{bulk}}^{(3)}(\omega)$  has been extracted from the DL and has been shown identical to the one that is calculated<sup>52</sup> in liquid water subjected to a constant external electric field (which, by construction,

reorients the HB network within the liquid water) and also found identical to the measured one.<sup>68</sup>

Let us start by commenting the first descriptor used in the characterization of the three water layers, i.e., the water density profiles at the A- and B-terminations of the Co<sub>3</sub>O<sub>4</sub>

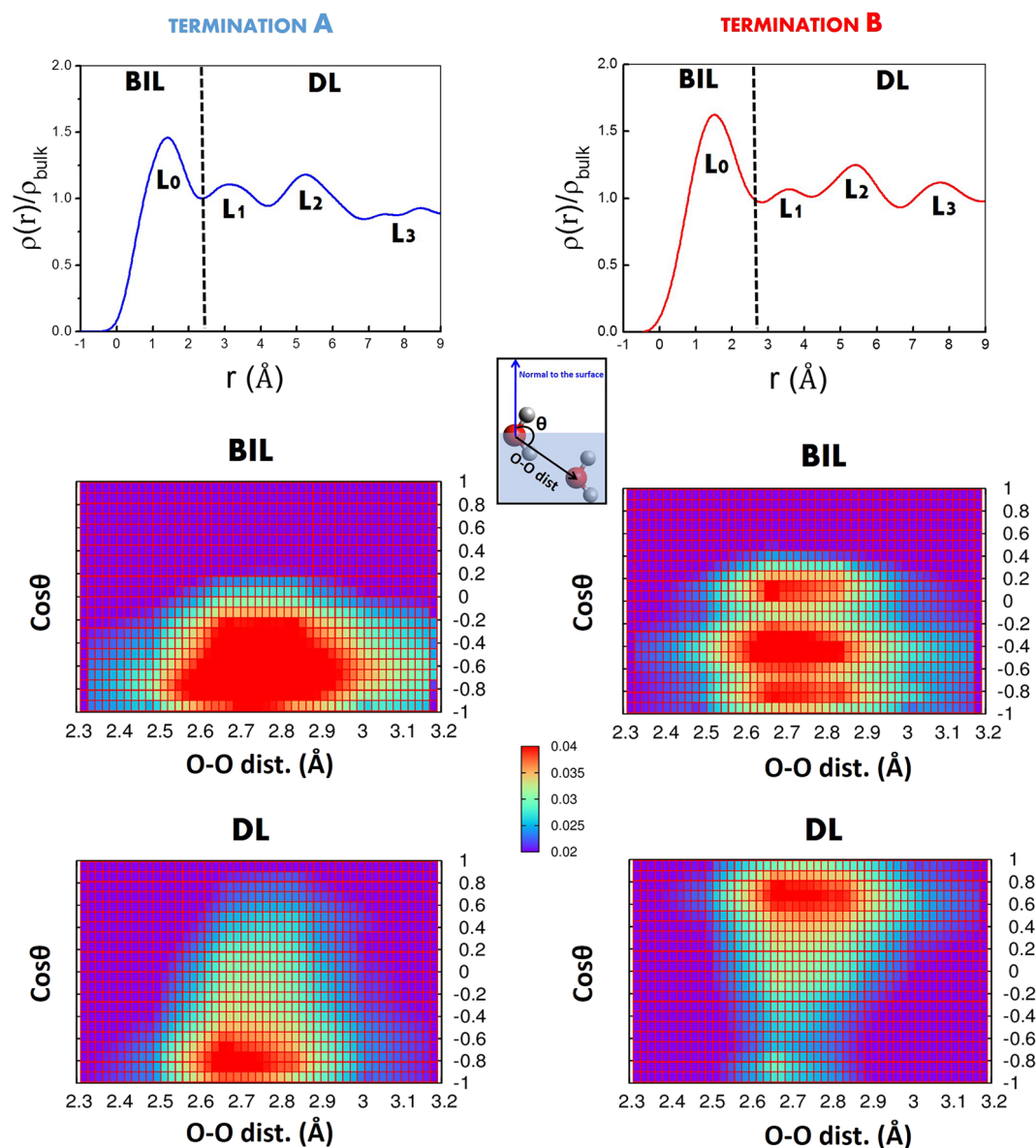


**FIG. 5.** (Top) Water density profiles calculated as a function of the distance from the cobalt oxide surface (using Willard and Chandler's instantaneous surface method<sup>69</sup>). (Middle and bottom) 3D-contour plots of the simultaneous probability for water-water H-bonds to have a given distance (horizontal axis) and a given angle (vertical axis). The convention for the O—O distance and angle  $\theta$  definitions is in the inset scheme. The normal to the surface goes towards the solid. The middle plots are for the water located in the BIL (Binding Interfacial Layer), and the bottom plots are for the water located in the DL (Diffuse Layer). See the text for correspondence between layers L0–L3 and BIL/DL. See Fig. 2 of Ref. 32 for the reference 3D plot for bulk liquid water (homogeneous distribution of HB angles within the 2.6–2.9 Å HB distances). Left side: (110)-Co<sub>3</sub>O<sub>4</sub>-A cut-liquid water interface. Right side: (110)-Co<sub>3</sub>O<sub>4</sub>-B cut-liquid water interface.

cobalt oxide in contact with liquid water, see the top of Fig. 5. The density profiles are reported over half of the water box only, the zero in  $r$  is the instantaneous water surface, and  $r$  measures the (vertical) distance from the surface (see Fig. 3 for the simulation boxes). One can observe four layers of water at both interfaces, labelled L0–L3, each of these layers being roughly identically located in space at the two interfaces.

While layer L0 systematically has a higher density than in the bulk (e.g.,  $\sim 1.5$  higher at the aqueous B-surface), the density of bulk water is on average already recovered in L1–L3 layers. The oscillations in the density profile around the average bulk value are discussed later in this section, also in relation with the mobility of the water molecules in the different layers.

In the density profiles at the top of Fig. 5, we have also reported the notation of BIL and DL water layers on top of the notation of L0-L3 layers. Applying the definitions described above for the three descriptors of water, L1-L3 water layers constitute the DL (roughly 6 Å thick) at both aqueous A- and B-interfaces. In these layers, the water density is roughly the liquid water's 1 g/cm<sup>3</sup>, and the water molecules make 3.6 HBs/molecule, equal to bulk liquid water (as obtained from the reference DFT-PBE-D2 MD simulation done in this work on bulk water), which are two necessary descriptor values for the DL. The other descriptor necessary to reveal the DL is the non-isotropicity of the water-water HB network in layers L1-L3, which is shown averaged over all the three L1-L3 layers at the bottom of Fig. 5 with the 3D-contour plots. One can indeed observe in these plots that there is a certain background of homogeneous distribution of the HB orientations within the 2.6-2.9 Å HB distances that is revealed by the greenish-blue color, which is reminiscent of bulk liquid water, while the red contour spots reveal a preferred orientation of the HB network in these layers. This corresponds to the HB network of the liquid water that adapts to the surface field: it is not present in bulk liquid water and it only appears once a field induces a certain direction in the liquid. One hence observes that this preferred orientation of the water in the DL HB network at the aqueous A-surface is on average opposite the positively charged surface (the cosine values of the  $\theta$  angle are in the range  $-0.6/-0.9$ , see the red spot, for HB distances in between 2.6 and 2.9 Å), while an opposite net orientation of the water molecules now pointing towards the solid surface is obtained in the DL at the aqueous negatively charged B-surface (red spot for cosine values of the  $\theta$  angle in the range  $0.6/1.0$  for HB distances in between 2.6 and 2.9 Å).

Layer L0 at both A- and B-interfaces is the BIL water layer, where all three descriptors differ significantly from bulk liquid water, for the water density (much higher than 1.0), for the number of HBs formed per water molecule (3.4 HBs/mol in the BIL vs 3.6 in the bulk), and for the orientation of the HB network; see Fig. 5 (middle panels). In these contour plots, one can observe that there is no background of homogeneous HB orientations, but there is, on the contrary, one single orientation of the HBs, revealing specific hydrogen bonds in between the water molecules (and indirectly possibly revealing HBs between water and the solid surface). There is one clear single orientation for water-water HBs in the BIL at the aqueous A-surface, with the cosine values in the range  $-0.2/-1.0$  for 2.6-2.9 Å HBs distances: the water molecules in the BIL preferentially form water-water HBs with water located in the next layer (BIL-DL HBs). There are however two orientations of water-water HBs in the BIL at the aqueous B-surface, as one can distinguish two separate red spots: as already observed at the aqueous A-surface, the red spot at  $\sim -0.4/-1.0$  cosines corresponds to BIL-DL HBs, while the second red spot at  $\sim +0.0/+0.2$  cosines arises from INTRA-BIL HBs (formed in between water molecules in the BIL).

The 3.4 coordination of the water molecules in the BIL is the result of both water-solid and water-water HBs. It is interesting to note that despite both interfaces have a final identical value of this coordination number, the repartition into water-solid HBs and water-water HBs is different at the two interfaces. Hence, there are slightly more water-solid HBs and slightly less water-water HBs that are formed at the more hydrophilic aqueous A-surface compared to the aqueous B-surface (see the numbers in the table in Fig. 4). Indeed at the A-liquid water interface, 100% of the water molecules in the BIL are H-bonded to the solid  $\mu_2$ -OH sites (with also two waters bridging two nearby solid  $\mu_2$ -OH sites, hence being simultaneously HB-acceptor and HB-donor). The percentage decreases at the B-liquid water interface, where "only" 89% of the water molecules in the BIL are H-bonded to solid O-H sites ( $\mu_1$ -OH and  $\mu_1$ -OH<sub>2</sub> sites): the decrease in water-solid HBs is compensated by an increase in water-water HBs formed within the BIL, denoted INTRA-BIL HBs in the table in Fig. 4.

Interestingly, water is on average found to be HB-acceptors with the oxide solid at the B-interface (57% of the water-solid HBs) despite the negatively charged surface: this reveals that HBs (that we could call "microscopic interactions") dominate over ("macroscopic") electrostatic interactions. For a negatively charged surface such as the B-termination, one would indeed expect the water molecules located in the BIL to be strongly oriented in response to the surface charge and hence have their dipole moments pointing towards the solid surface, thus being mostly HB-donors to the solid. This would correspond to water being "good soldiers" as they readily respond to the average surface charge "driving force." Water is on the contrary found to be mostly HB-acceptors with the solid, with an orientation of their dipole moments thus found opposite to the field generated by the negative surface charge. The water molecules are hence somehow "undisciplined" and do not respond to the average electrostatic driving force at the direct interface with the solid. The "electrostatic undiscipline" stems in the surface chemistry, where the O-H groups are readily available for hydrogen bonds with water molecules approaching the surface. BIL-water hence engages in surface-water HBs that in turn counteract the interactions from the surface electric field. It would certainly be interesting to deconvolve the energetics of the competing interactions (HBs vs electrostatic) in order to rationalize more, but this has not been done here. This illustrates the importance of explicit bulk water in simulations of aqueous solid oxide-water interfaces. An implicit solvent would obviously not provide such a view. A direct consequence of the preferred solid-water HBs over the electrostatic surface-water interactions is of course the organisation of water in the BIL and the associated dielectric constant in the BIL, which again could not be anticipated with implicit solvent. Also, the preference for the oxide-water HBs found here in the BIL at the aqueous B-interface gives a qualitative indication of the underlying acidities of the surface sites. One more remark is that the necessary balance made in between HBs and electrostatic interactions at the interface probably

also explains the dynamicity in proton transfers observed at this surface (see below). All these properties will have consequences on the chemical reactivity at this cobalt oxide interface. At the aqueous A-interface, water in the BIL is now found be HB-acceptor with the solid (88% of the HBs), which this time goes in line with the positively charged surface. Simplified views of the typical solid-water HB patterns obtained at the aqueous A- and B-surfaces can be found in Figs. 6(a) and 6(b).

The oscillations observed earlier in the text and in Fig. 5 in the water density profile for the layers beyond L0 could very well be due to the finite and limited simulation box-size and time scale, as already shown for the air-water interface when comparing *ab initio* and classical MD simulation density profiles.<sup>65</sup> Such oscillations could also be the result of different mobility characters of the water in the BIL and

DL layers: the “rather high structuration” of BIL-water in contact with the oxide could indeed induce heterogeneous diffusivity of the water when comparing BIL and DL, which in turn could prevent the establishment of a homogeneous water density beyond the BIL. As shown above, both A and B surfaces are hydrophilic with a high density of water-solid HBs [Fig. 4 and Figs. 6(a) and 6(b) for simplified illustrations of the HBs patterns at the two interfaces]. These strong water-solid interactions can lead (not so surprisingly) to a reduced mobility of BIL-water molecules as shown in Figs. 6(c) and 6(d), where we report the mean square displacement of the water molecules located in the BIL and in the DL for the aqueous A- and B- interfaces (MSD plots obtained as averages over all molecules identified in BIL/DL layers). A word of caution is however needed. Although well-converged diffusion coefficients would require much longer time scale trajectories than the ones analyzed here,

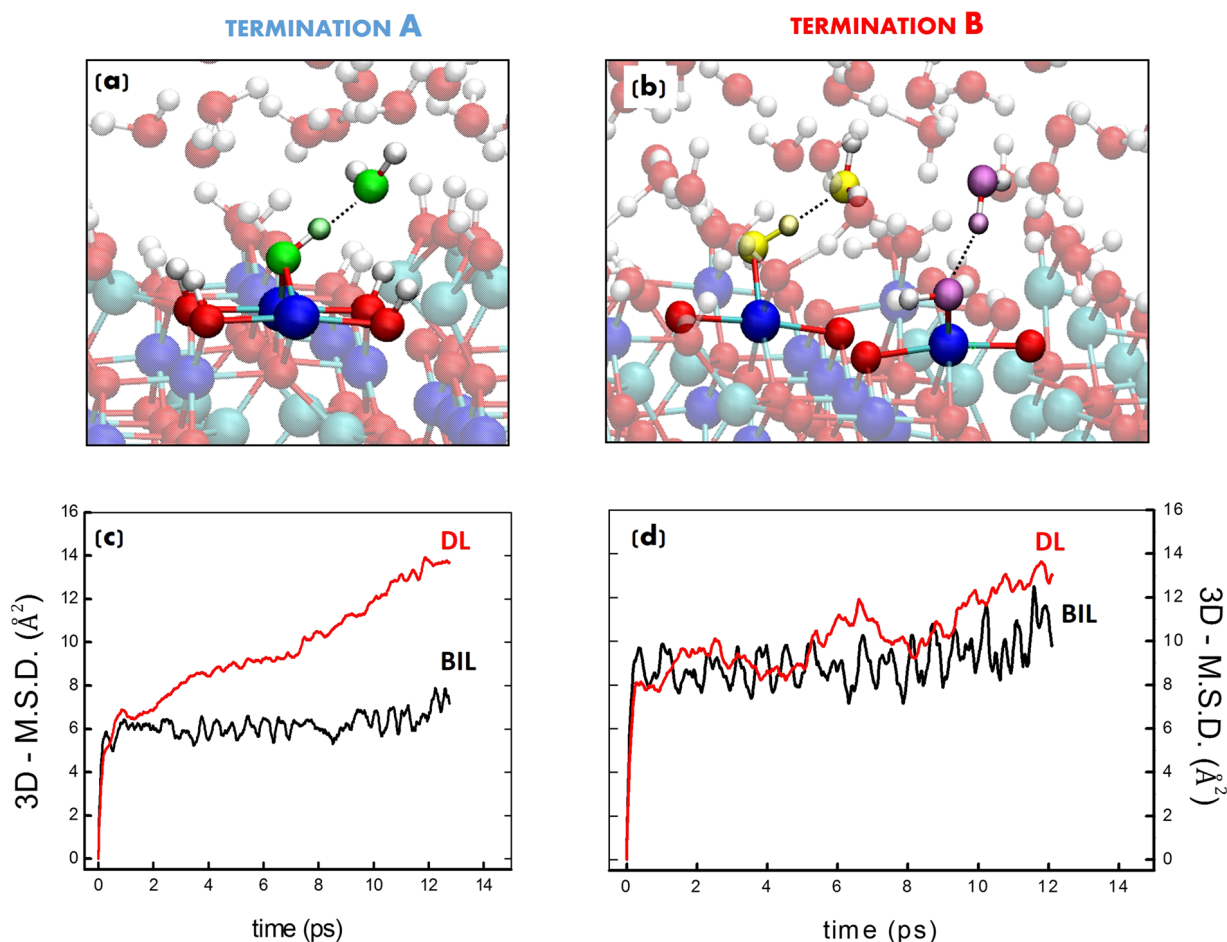


**FIG. 6.** [(a) and (b)] Zoomed-in views of the surface-water HB patterns at the aqueous A-surface (a) and B-surface (b).  $\mu_2$ -OH-water H-bond in green color where  $\mu_2$ -OH acts as a donor at the A-surface.  $\mu_1$ -OH-water H-bond where  $\mu_1$ -OH acts either as a donor (yellow) or as an acceptor (violet) at the aqueous B-surface. [(c) and (d)] 3-dimensional mean square displacement of BIL-water (black lines) and DL-water (red lines), computed for the aqueous A-surface (c) and B-surface (d).

comparing the mobility of the water in the BIL and DL layers through the MSD gives us sufficient insights on their respective diffusivity.

As shown above, there are more solid-water HBs at the aqueous A-termination than at the B-termination, hence resulting into BIL-water being in a more “static” geometrical arrangement at the A-termination. Water diffusivity is therefore reduced in the BIL as can be seen in Fig. 6(c), where a reduction factor of  $\sim 2$  is found in the mobility of water in the BIL when compared to the DL. Conversely, BIL-water and DL-water have the same diffusivity character at the aqueous B-termination, as shown in Fig. 6(d), which goes nicely in line with less solid-water HBs being formed at this interface. While it is very interesting to see these differences in the water diffusivity at the two interfaces, this does not seem to provide the sole explanation for the density profile oscillations, as both profiles display similar oscillations in the DL.

One final important remark is as follows: At the two interfaces simulated here, bulk liquid water is never recovered within the  $\sim 18$  Å water thickness. This is not totally surprising as the water in the simulation boxes experiences two interfaces, one with the solid (which has a large surface charge and therefore reorients the water molecules over a large distance, see the  $\sim 6$  Å of the DL revealed here) and one with the neutral air (which we have fully characterized in a previous work<sup>58</sup> with a 2D-H-bond network within the 3.0 Å thickness of the BIL). Note also that the  $\sim 6$  Å thickness of the DL characterized

here is presumably underestimated as the liquid water has not been recovered in the box. This is however not an issue for the work done here and for the properties investigated hereby.

#### D. Physical observables: Electric field, surface work function, and SFC vibrational spectroscopy at the interface

The left panel of Figure 7 shows the electric field profile (see Sec. II for the computational details) as a function of the  $z$ -coordinate perpendicular to the (110) bulk oxide surface, comparing the bare A-surface at the interface with vacuum (profile at the top) to the hydroxylated A-surface at the interface with vacuum (profile in the middle) and to the A-liquid water interfacial system (profile at the bottom). These profiles have been calculated for one single configuration extracted either from geometry optimisations (for the bare and one water monolayer systems) or from the DFT-MD simulation at finite temperature when the liquid water is in contact with the A-hydroxylated surface. The first significant peaks in the electric field profile are observed at the height of the surface in contact with air at the bare surface, with a negative peak located just below the surface layer and a more intense positive peak located at the surface layer. These are sharp and highly localised peaks in the electric field profile. Note that the positive/negative fields are the ones taken at the surface at  $z \sim -10$  Å in Fig. 7, i.e., at the surface which will be put in contact with liquid water. The fields have opposite signs at the second interface

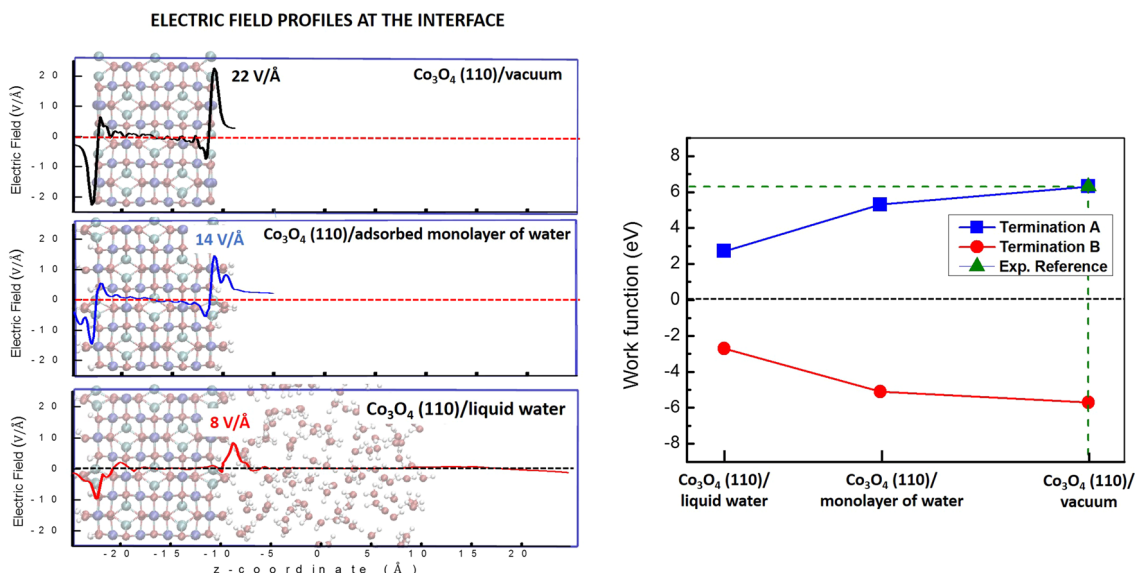


**FIG. 7.** (Left side) Electric field profiles for the A-surface. Top: bare A-surface at the interface with vacuum; middle: hydroxylated A-surface at the interface with vacuum; bottom: hydroxylated A-surface at the interface with liquid water. Profiles are reported along the  $z$ -direction perpendicular to the (110)  $\text{Co}_3\text{O}_4$  surface. The profile at the bottom for the aqueous interface has been averaged over 35 snapshots statistically extracted from 17 ps dynamics. (Right side) Calculated surface work function (eV) reported for the (110)  $\text{Co}_3\text{O}_4$  A- and B-surfaces as a function of the simulation type, i.e., bare surfaces at the interface with vacuum, hydroxylated surfaces at the interface with vacuum, and hydroxylated surfaces at the interface with liquid water. The green triangle in the graph is the reference experimental value equal to 6.3 eV from XPS and UPS experimental techniques.<sup>70</sup>

( $z \sim -23 \text{ \AA}$ ) only because the calculation uses the same convention of direction for the normal to the two surfaces. Once the A-surface has been hydroxylated and is now covered with one water monolayer, one can observe a systematic decrease in intensity of the two peaks in the electric field profile, while the peaks are still rather well localised in space. However, the negative peak penetrates slightly deeper into the bulk oxide, while the initial single positive peak obtained at the bare interface is now divided into two parts with a total larger spreading in the  $z$ -direction into the vacuum. These two oscillations in the field profile at the interface are, respectively, due to the oxide surface layer and the adsorbed water layer. The lower intensities of the electric field at the hydroxylated surface are due to screening of the oxide surface field by the water molecules in the adsorbed monolayer. One can also see that  $\sim 3 \text{ \AA}$  away from the water monolayer the field is screened, i.e., the underlying surface structure is not visible anymore in the field profile. Once the hydroxylated surface is in contact with liquid water, the field intensity is screened even more while the region of the field decay is expanded farther away from the surface in the  $z$ -direction perpendicular to the surface. A zero-field is found around  $5 \text{ \AA}$  above the adsorbed water monolayer. Note also that the negative peak inside the oxide just below the cobalt surface almost non-exists. Similar results are obtained at the (110) B-surface (not presented).

The changes in the intensity of the electric field profile discussed above once a water monolayer and liquid water is added to the bare surface are also directly reflected in the surface work function. The surface work function (see Sec. II for computational details) is calculated at the (110)  $\text{Co}_3\text{O}_4$  A- and B-terminated surfaces in the three environments investigated here, i.e., bare surfaces at the interface with vacuum, hydroxylated surfaces at the interface with vacuum, and hydroxylated surfaces at the interface with liquid water. The value computed here for the bare A-surface at the interface with vacuum compares extremely well with the experimental values from XPS-UPS experiments.<sup>70</sup> The sign of the work function changes from the A-surface to the B-surface because of the opposite surface charges. When the adsorbed water monolayer is added to the surface, the work function already shows a decrease by around 1 eV, similar at both interfaces. Such a decrease has been discussed in the literature,<sup>48,71</sup> and the change obtained here is very similar to the literature. This decrease is further enhanced when bulk water is in contact with the surface, and one obtains work functions of  $\sim 3$  (–3) eV instead of the  $\sim 6$  (–6) eV at the bare surface. The work needed to remove one electron from the aqueous surface is therefore roughly divided by 2 from the bare surface in contact with air.

We now turn to a vibrational probe of the interface in terms of non-linear SFG (Sum Frequency Generation) spectroscopy. The details for extracting this complex signal from the DFT-MD simulations have been given in Sec. II. For our previous studies on theoretical SFG calculation and interpretation, see Refs. 31–33 and 58. The SFG signals discussed here are calculated for the water, and they do not include the solid

contribution. Although the cobalt oxide-liquid water interfaces have not yet been spectroscopically characterized by SFG, we provide here theoretical signals that could of course be compared to experiments when they will become available, but our objective here is to show the information contained in the interfacial spectroscopy and how to possibly use this information in the context of chemical reactions that could occur at the interface once put under electrochemical conditions. The signals are discussed in terms of  $\text{Im}\chi^{(2)}(\omega)$  only, as in phase-resolved SFG experiments. The theoretical signal is divided in terms of the BIL-SFG signal and DL-SFG signal, i.e., each of these interfacial layers contain distinct information on the organisation of interfacial water that the theory can easily reveal once the two layers are identified, as done in this work in Sec. III C.

Figure 8 reports the  $\text{Im}\chi^{(2)}(\omega)$  spectra calculated for the (110)  $\text{Co}_3\text{O}_4$ -A(left)/B(right)-liquid water interfaces, the total active SFG spectra (BIL + SFG) are displayed at the bottom in black, and the decomposition into BIL-SFG and DL-SFG are displayed top and middle of the figures, respectively, in red and blue.

The first conclusion that can be extracted from these theoretical spectra is that for both interfaces the SFG spectroscopic response is dominated by the DL third-order contribution:  $I_{\text{DL}}/I_{\text{BIL}} \sim 4$  for both interfaces, where  $I$  stands for the integral of the  $\text{Im}\chi^{(2)}(\omega)$  signal in the  $2800$ – $3800 \text{ cm}^{-1}$  range presented here. The total SFG signals thus directly reflect the signals arising from the water in the DL. The DL-SFG (and thus the total-SFG) signals change sign in between the two interfaces, i.e., from negative at the aqueous A-interface to positive at the aqueous B-interface. As the DL-SFG is proportional to the surface potential,<sup>32,33</sup> the DL-SFG signal directly provides this information.

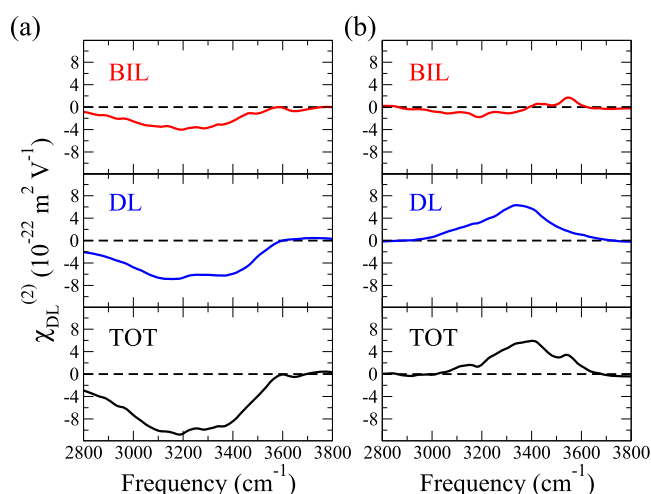


**FIG. 8.** Calculated  $\text{Im}\chi^{(2)}(\omega)$  spectra for the (a) (110)  $\text{Co}_3\text{O}_4$ -A-liquid water interface and (b) (110)  $\text{Co}_3\text{O}_4$ -B-liquid water interface. Calculated SFG report the water contribution only. The SFG signal is presented as “total” (TOT) in black, BIL-SFG in red arising from the BIL layer only, and DL-SFG in blue arising from the DL layer only.

The BIL signal, despite being a minor contributor to the total SFG response, carries however the information on the structure of water in direct contact with the solid oxide and therefore directly probes the water-oxide interactions. For the aqueous A-surface, the BIL-SFG has one single negative broad band: this is due to the water molecules located in the BIL being HB donors to the water molecules located in the DL. The water molecules at the aqueous A-surface indeed mostly accept HBs from the solid (see Sec. III C and table in Fig. 4) and consequently are oriented such as donating HBs to the water molecules located in the DL. We remind the reader that the BIL is one water monolayer thick. On the contrary, water can be both donors and acceptors of water-solid HBs at the aqueous B-interface, which hence results into the two bands of opposite sign in the BIL-SFG (although of very low absolute amplitudes). The positive band at higher frequencies is due to the weak HB donors to the solid, while the negative broad band (very similar to the aqueous A-surface) is due to the stronger HBs made by the water molecules located in the BIL as HB donors to water molecules located in the DL. The overall less intense SFG-BIL signal at the aqueous B-surface (compared to the aqueous A-surface) is due to the higher number of INTRA-BIL HBs formed at the aqueous B-surface, which are SFG-inactive due to their in-plane orientation.

As a final note, it is also interesting to remark that the DL-SFG absolute intensity is different between the two interfaces, despite the same formal surface charge (the same  $4.37 |e|/\text{nm}^2$  in absolute value at both interfaces). Indeed  $I_{\text{DL}}$  (as calculated from integration in the  $2800\text{--}3600 \text{ cm}^{-1}$  region) is 1.4 times higher for the aqueous A-surface than for the B-one. This higher DL-SFG intensity at the aqueous A-interface tells us that there is a higher surface potential at the aqueous A-interface than that at the B-one (see Ref. 33 for the relationship between DL-SFG intensity and surface potential). This is due to the specific water organization in the BIL (as discussed in Sec. III C) and specific orientation of surface O-H terminations [see the histograms in Fig. 4(a)] at the aqueous A-surface. The surface field reflects not only the formal surface charge but also the specific organization and orientation of the water molecules in the BIL, which then modulates the field. This again shows how important it is to include explicit water at the interface with the oxide surface in the simulations.

#### IV. DISCUSSION AND PERSPECTIVES

This work provides chemical and physical knowledge of the (110)- $\text{Co}_3\text{O}_4$ -liquid water interface as a preliminary step into the modelling of this interface in the electrochemical conditions of the OER (Oxygen Evolution Reaction) for electrocatalysis of water. To this end, DFT-based molecular dynamics have been applied at this rather complex oxide interface, explicitly taking into account the liquid water conditions. This work provides the reference knowledge in the interfacial electronic, structural, dynamical, electric, and spectroscopic properties needed at this promising interface for the water electrocatalysis. This work also describes and applies

the necessary computational analysis tools for the characterisation of the interfacial water structure (in the BIL layer directly in contact with the oxide surface and in the DL layer at a slightly larger distance from the surface), thickness of these layers, rigidity and/or dynamism of the water in these layers (typically for proton transfers), for the structure of the solid surface in contact with water (e.g., in terms of orientation of the surface sites and their H-bonding network within the solid and with the water in the BIL), for the electronic interfacial properties, for physical interfacial properties typically in terms of the interfacial electric field and its penetration into the liquid water, the work function, and the vibrational spectroscopy probe of this interface here in the flavor of SFG. The same modelling could be applied to other facets of the  $\text{Co}_3\text{O}_4$  cobalt oxide in contact with liquid water, also of potential relevance for the OER.

This is the preliminary step into investigating the semiconductor  $\text{Co}_3\text{O}_4$ -water interface in electrochemical conditions and assessing its chemical reactivity in the context of the water electrocatalysis. For the electrochemical conditions to be more realistic into the DFT-MD simulations, one has however to include electrolytes and pH conditions. While inclusion of interfacial electrolytes poses no real challenge in DFT-MD simulations, see, e.g., some previous studies of ours and others at mineral-liquid water interfaces,<sup>32,33,35,72,73</sup> one has however to keep in mind that the lower (nominal bulk liquid) electrolyte concentrations that can reasonably be sustained in DFT-MD are of the order 0.1-0.5 M, for computational reasons due to the simulation box dimensions. This potentially low electrolyte nominal bulk concentration does not preclude a higher electrolyte concentration in the BIL (i.e., in the layer at the direct contact with the oxide surface): depending on the ability of the oxide surface to attract and accommodate the electrolytes in the BIL, larger electrolyte concentrations in the BIL can be obtained, see, for instance, our work in Ref. 33 for a related discussion at mineral-water interfaces and the actual measure of the electrolyte concentration at the direct interface. One has also to be aware that in a realistic “in operando” interface, the BIL accommodates counterions present in the electrolyte, which in turn screens the surface charge, giving rise to the electric double layer. This will certainly have influence on the oxide-water BIL interface, both from structural and dynamical points of view, as well as on the thickness of the subsequent DL. These changes could then be measured and extracted from the SFG responses of the two layers, following the decomposition and interpretation done in the present work. On the other hand, pH conditions can be monitored through the electrolyte concentration, although pH is not a trivial quantity to accurately represent within the small DFT-MD simulation boxes.

The same analysis tools as the ones described in this work can then be applied in order to extract the fundamental knowledge of, e.g., the localisation of the electrolytes within the BIL and DL, the water structure and dynamics in the BIL and DL, dynamical charge transfers between surface and

the EDL and within the water layers, the interfacial electric fields, and screening by the electrolytes, the work function, and interfacial vibrational spectroscopy. These properties can be compared and put in perspective to the ones obtained at the reference oxide-liquid water interface investigated in this work. Any chemical reactivity occurring at the electrolytic aqueous oxide surface, e.g., desorption of water, deprotonation, proton transfers, inner-/outer-sphere adsorption of electrolytes, and adsorption of new chemical species, can be followed along the DFT-MD trajectories, providing that these are chemical reactive events compatible with the 10<sup>3</sup>-100 ps time scale of the DFT-MD simulations. Biased DFT-MD can also be run for the chemical reactions to be monitored. Also worth mentioning here, our investigations (as well as most in the literature) take the ideal crystalline structure of the oxide material (Co<sub>3</sub>O<sub>4</sub>) into account in the DFT-MD simulation. Surface defects are probably relevant for the chemical reactivity of these interfaces and should also be included within the modelling.

Imposing the electrochemical applied voltage into the DFT-MD is a more challenging theoretical affair, and only few attempts at developing adequate theoretical methodologies have been presented in the literature.<sup>23,27-30</sup> Studies of bulk water and of water solutions<sup>74-77</sup> have shown the ability of a constant external electric field to induce reorientation of the water dipoles along the field direction and an increase in the water dissociation rate. Although such a strategy nicely shows that water dissociation can be controlled by constant fields, this is still not simulating electrochemical conditions. One can then rely on more *ad hoc* theoretical ways to include this voltage, following previous attempts in the literature, see, for instance, Refs. 23, 24, and 26, playing with H<sub>3</sub>O<sup>+</sup>/OH<sup>-</sup> concentrations and/or electrolyte concentrations in relation with the interfacial capacitance.

We are interested in the OER chemical reaction at such an oxide-liquid water-electrolyte electrochemical interface, with the goal of characterizing the mechanisms and the energetics of the underlying chemical reactions. The water oxidation reaction is known to proceed through two general pathways (see, e.g., Ref. 2 for a recent review) known as the water nucleophilic attack (WNA) and the radical oxo coupling (ROC), with the WNA presumably the one occurring at oxide interfaces. Although these reactions are known, their energetics and the actual detailed mechanisms are still unclear, and the role of the whole complex structure and dynamics of the oxide-water-electrolyte-EDL interface has not been yet elucidated at the atomistic level. This is where our DFT-MD simulations are heading.

## ACKNOWLEDGMENTS

This work was performed under Grant No. LABEX CHARMA<sub>3</sub>T 11-LABX-0039/ANR-11-IDEX-0003-02 "Excellence Laboratory" program of the University Paris-Saclay and Grant No. ANR DYNAWIN ANR-14-CE35-0011-01 (ANR Agence Nationale de la Recherche), and using HPC resources from GENCI-France Grant No. 072484 (CINES/IDRIS/TGCC). Louis

Potier in the group is gratefully acknowledged for sharing some codes for the structural analyses. This work is part of a collaborative consortium within the LABEX CHARMA<sub>3</sub>T "Excellence Laboratory" program with Professor Ph. Allongue and F. Maroun at the Ecole Polytechnique, University Paris-Saclay.

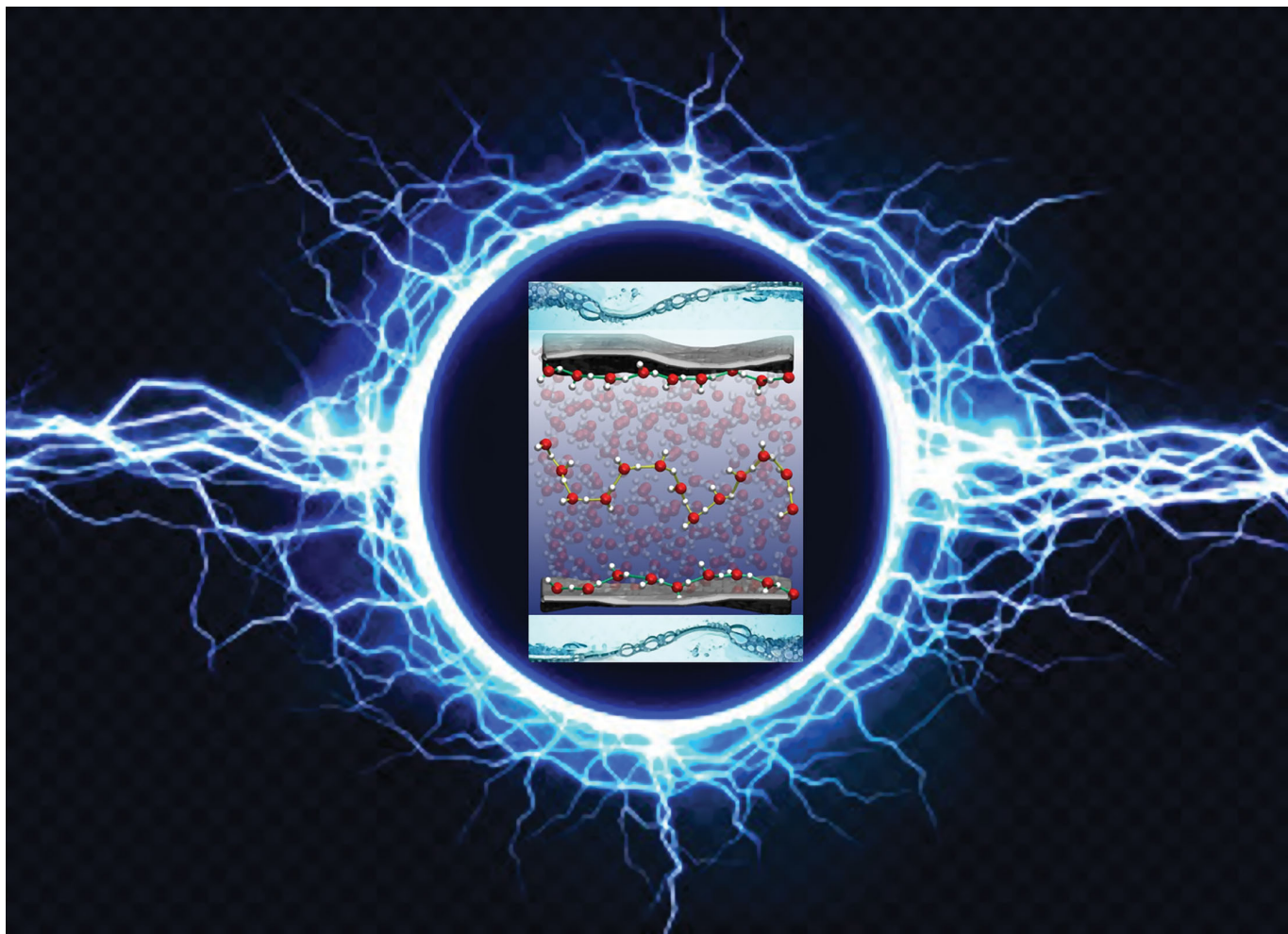
There are no conflicts of interest to declare.

## REFERENCES

- 1S. Anantharaj, K. Karthick, and S. Kundu, "Evolution of layered double hydroxides (LDH) as high performance water oxidation electrocatalysts: A review with insights on structure, activity and mechanism," *Mater. Today Energy* **6**, 1-26 (2017).
- 2J. Hessels, R. J. Detz, M. T. M. Koper, and J. N. H. Reek, "Rational design rules for molecular water oxidation catalysts based on scaling relationships," *Chem.-Eur. J.* **23**, 16413-16418 (2017).
- 3B. S. Yeao and A. T. Bell, "Enhanced activity of gold-supported cobalt oxide for the electrochemical evolution of oxygen," *J. Am. Chem. Soc.* **133**, 5587-5593 (2011).
- 4M. Hamdani, R. N. Singh, and P. Chartier, "Co<sub>3</sub>O<sub>4</sub> and Co-based spinel oxides bifunctional oxygen electrodes," *Int. J. Electrochem. Sci.* **5**, 556-577 (2010).
- 5F. Jiao and H. Frei, "Nanostructured cobalt oxide clusters in mesoporous silica as efficient oxygen-evolving catalysts," *Angew. Chem., Int. Ed.* **48**, 1841-1844 (2009).
- 6M. Zhang, M. de Respinis, and H. Frei, "Time-resolved observations of water oxidation intermediates on a cobalt oxide nanoparticle catalyst," *Nat. Chem.* **6**, 362-367 (2014).
- 7M. W. Kanan and D. G. Nocera, "In situ formation of an oxygen-evolving catalyst in neutral water containing phosphate and Co<sup>2+</sup>," *Science* **321**, 1072-1075 (2008).
- 8Z. Cai, Y. Bi, E. Hu, W. Liu, N. Dwarica, Y. Tian, X. Li, Y. Kuang, Y. Li, X. Q. Yang, H. Wang, and X. Sun, "Single-crystalline ultrathin Co<sub>3</sub>O<sub>4</sub> nanosheets with massive vacancy defects for enhanced electrocatalysis," *Adv. Energy Mater.* **8**, 1701694 (2018).
- 9X. Xie, Y. Li, Z. Q. Liu, M. Haruta, and W. Shen, "Low-temperature oxidation of CO catalysed by Co<sub>3</sub>O<sub>4</sub> nanorods," *Nature* **458**, 746-749 (2009).
- 10A. Y. Khodakov, J. Lynch, D. Bazin, B. Rebours, N. Zanier, B. Moisson, and P. Chaumette, "Reducibility of cobalt species in silica-supported Fischer-Tropsch catalysts," *J. Catal.* **168**, 16-25 (1997).
- 11S. Zafeirotos, T. Dintzer, D. Teschner, R. Blume, M. Havecker, A. Knop-Gericke, and R. Schlögl, "Methanol oxidation over model cobalt catalysts: Influence of the cobalt oxidation state on the reactivity," *J. Catal.* **269**, 309-317 (2010).
- 12M. Yagi and M. Kaneko, "Molecular catalysts for water oxidation," *Chem. Rev.* **101**, 21-35 (2001).
- 13W. Ruttiger and G. C. Dismukes, "Synthetic water-oxidation catalysts for artificial photosynthetic water oxidation," *Chem. Rev.* **97**, 1-24 (1997).
- 14A. Kulkarni, S. Siahrostami, A. Patel, and J. Nørskov, "Understanding catalytic activity trends in the oxygen reduction reaction," *Chem. Rev.* **118**, 2302-2312 (2018).
- 15E. Skulason and H. Jonsson, "Atomic scale simulations of heterogeneous electrocatalysis: Recent advances," *Adv. Phys.: X* **2**, 481-495 (2017).
- 16J. Hussain, H. Jonsson, and E. Skulason, "Faraday efficiency and mechanism of electrochemical surface reactions: CO<sub>2</sub> reduction and H<sub>2</sub> formation on Pt(111)," *Faraday Discuss.* **195**, 619-636 (2016).
- 17J. Rossmeisl, Z. W. Qu, H. Zhu, G. J. Kroes, and J. Nørskov, "Electrolysis of water on oxide surfaces," *J. Electroanal. Chem.* **607**, 83-89 (2007).
- 18J. Nørskov, J. Rossmeisl, A. Lagodttr, L. Lindqvist, J. R. Kitchin, T. Bligaard, and H. Jonsson, "Origin of the overpotential for oxygen reduction at a fuel-cell cathode," *J. Phys. Chem. B* **108**, 17886-17892 (2004).
- 19J. Nørskov, T. Bligaard, J. Rossmeisl, and C. H. Christensen, "Towards the computational design of solid catalysts," *Nat. Chem.* **1**, 37-46 (2009).

- <sup>20</sup>O. Bjorneholm, M. Hansen, A. Hodgson, L. Liu, D. Limmer, A. Michaelides, P. Pedevilla, J. Rossmeisl, H. Shen, G. Tocci, E. Tyrode, M. Walz, J. Werner, and H. Blum, "Water at interfaces," *Chem. Rev.* **116**, 7698–7726 (2016).
- <sup>21</sup>T. Roman and A. Gross, "Structure of water layers on hydrogen-covered Pt electrodes," *Catal. Today* **202**, 183–190 (2013).
- <sup>22</sup>F. Gossenberger, T. Roman, and A. Gross, "Hydrogen and halide co-adsorption on Pt(111) in an electrochemical environment: A computational perspective," *Electrochim. Acta* **216**, 152–159 (2016).
- <sup>23</sup>J. Hussain, H. Jonsson, and E. Skulason, "Calculations of product selectivity in electrochemical CO<sub>2</sub> reduction," *ACS Catal.* **8**, 5240–5249 (2018).
- <sup>24</sup>S. Sakong, K. Forster-Tonigold, and A. Gross, "The structure of water at a Pt(111) electrode and the potential of zero charge studied from first principles," *J. Chem. Phys.* **144**, 194701–194709 (2016).
- <sup>25</sup>S. Sakong, M. Nadarian, K. Mathew, R. G. Hennig, and A. Gross, "Density functional theory study of the electrochemical interface between a Pt electrode and an aqueous electrolyte using an implicit solvent method," *J. Chem. Phys.* **142**, 234107–234118 (2015).
- <sup>26</sup>J. Cheng and M. Sprik, "The electric double layer at a rutile TiO<sub>2</sub> water interface modelled using density functional theory based molecular dynamics simulation," *J. Phys.: Condens. Matter* **26**, 244108–244118 (2014).
- <sup>27</sup>A. Bouzid and A. Pasquarello, "Atomic-scale simulation of electrochemical processes at electrode/water interfaces under referenced bias potential," *J. Phys. Chem. Lett.* **9**, 1880–1884 (2018).
- <sup>28</sup>S. Surendralal, M. Todorova, M. W. Finnis, and J. Neugebauer, "First-principles approach to model electrochemical reactions: Understanding the fundamental mechanisms behind Mg corrosion," *Phys. Rev. Lett.* **120**, 246801–246905 (2018).
- <sup>29</sup>C. Zhang, "Computing the Helmholtz capacitance of charged insulator-electrolyte interfaces from the supercell polarization," *J. Chem. Phys.* **149**, 031103–031107 (2018).
- <sup>30</sup>C. Zhang and M. Sprik, "Finite field methods for the supercell modeling of charged insulator/electrolyte interfaces," *Phys. Rev. B* **94**, 245309–245326 (2016).
- <sup>31</sup>M. Sulpizi, M.-P. Gaigeot, and M. Sprik, "The silica-water interface: How the silanols determine the surface acidity and modulate the water properties," *J. Chem. Theory Comput.* **8**, 1037–1047 (2012).
- <sup>32</sup>S. Pezzotti, D. R. Galimberti, Y. R. Shen, and M.-P. Gaigeot, "Structural definition of the BIL and DL: A new universal methodology to rationalize non-linear  $\chi^{(2)}(\omega)$  SFG signals at charged interfaces, including  $\chi^{(3)}(\omega)$  contributions," *Phys. Chem. Chem. Phys.* **20**, 5190–5199 (2018).
- <sup>33</sup>S. Pezzotti, D. R. Galimberti, Y. R. Shen, and M.-P. Gaigeot, "What the diffuse layer (DL) reveals in non-linear SFG spectroscopy," *Minerals* **8**, 305–321 (2018).
- <sup>34</sup>M. Pfeiffer-Laplaud, M. Gaigeot, and M. Sulpizi, "Electrolytes at the hydroxylated (0001)  $\alpha$ -quartz/water interface: Location and structural effects on interfacial silanols by DFT-based MD," *J. Phys. Chem. Lett.* **7**, 3229 (2016).
- <sup>35</sup>M. Pfeiffer-Laplaud and M. Gaigeot, "Electrolytes at the hydroxylated (0001)  $\alpha$ -quartz/water interface: Location and structural effects on interfacial silanols by DFT-based MD," *J. Phys. Chem. C* **120**, 14034 (2016).
- <sup>36</sup>M. Pfeiffer-Laplaud and M. Gaigeot, "Adsorption of singly-charged ions at the hydroxylated (0001)  $\alpha$ -quartz/water interface," *J. Phys. Chem. C* **120**, 4866 (2016).
- <sup>37</sup>S. C. Petitto, E. M. Marsh, G. A. Carson, and M. A. Langell, "Cobalt oxide surface chemistry: The interaction of CoO(100), Co<sub>3</sub>O<sub>4</sub>(110) and Co<sub>3</sub>O<sub>4</sub>(111) with oxygen and water," *J. Mol. Catal. A: Chem.* **281**, 49–58 (2008).
- <sup>38</sup>F. Zasada, W. Pirkorz, S. Cristol, J. F. Paul, A. Kotarba, and Z. Sojka, "Periodic density functional theory and atomistic thermodynamic studies of cobalt spinel nanocrystals in wet environment: Molecular interpretation of water adsorption equilibria," *J. Phys. Chem. C* **114**, 22245–22253 (2010).
- <sup>39</sup>X. L. Xu and J. Li, "DFT studies on H<sub>2</sub>O adsorption and its effect on CO oxidation over spinel Co<sub>3</sub>O<sub>4</sub>(110) surface," *Surf. Sci.* **605**, 1962–1967 (2011).
- <sup>40</sup>J. Chen and A. Selloni, "Water adsorption and oxidation at the Co<sub>3</sub>O<sub>4</sub>(110) surface," *J. Phys. Chem. Lett.* **3**, 2808–2814 (2012).
- <sup>41</sup>S. Selcuk and A. Selloni, "DFT+U study of the surface structure and stability of Co<sub>3</sub>O<sub>4</sub>(110): Dependence on U," *J. Phys. Chem. C* **119**, 9973–9979 (2015).
- <sup>42</sup>J. Chen, X. Wu, and A. Selloni, "Electronic structure and bonding properties of cobalt oxide in the spinel structure," *Phys. Rev. B* **83**, 245204 (2011).
- <sup>43</sup>J. Chen, X. Wu, and A. Selloni, "First principles study of cobalt (hydr)oxides under electrochemical conditions," *J. Phys. Chem. C* **117**, 20002–20006 (2013).
- <sup>44</sup>I. Ledezma-Yanez, W. D. Z. Wallace, P. Sebastian-Pascual, V. Climent, J. M. Feliu, and M. T. M. Koper, "Interfacial water reorganization as a pH-dependent descriptor of the hydrogen evolution rate on platinum electrodes," *Nat. Energy* **2**, 17031–17036 (2017).
- <sup>45</sup>J. Hutter, M. Iannuzzi, F. Schiffmann, and J. VandeVondele, "CP2K: Atomistic simulations of condensed matter systems," *Wiley Interdiscip. Rev.: Comput. Mol. Sci.* **4**, 15–25 (2014).
- <sup>46</sup>J. VandeVondele, M. Krack, F. Mohamed, M. Parrinello, T. Chassaing, and J. Hutter, "Quickstep: Fast and accurate density functional calculations using a mixed Gaussian and plane waves approach," *Comput. Phys. Commun.* **167**, 103–128 (2005).
- <sup>47</sup>K. Burke, J. Perdew, and M. Ernzerhof, "Generalized gradient approximation made simple [Phys. Rev. Lett. 77, 3865 (1996)]," *Phys. Rev. Lett.* **78**, 1396 (1997).
- <sup>48</sup>S. Schnur and A. Groß, "Properties of metal–water interfaces studied from first principles," *New J. Phys.* **11**, 125003 (2009).
- <sup>49</sup>E. Schwegler, J. C. Grossman, F. Gygi, and G. Galli, "Towards an assessment of the accuracy of density functional theory for first principles simulations of water. II," *J. Chem. Phys.* **121**, 5400–5409 (2004).
- <sup>50</sup>S. Goedecker, M. Teter, and J. Hutter, "Separable dual-space Gaussian pseudopotentials," *Phys. Rev. B* **54**, 1703–1710 (1996).
- <sup>51</sup>J. Hubbard, "Electron correlations in narrow energy bands," *Proc. R. Soc. A* **276**, 238–257 (1963).
- <sup>52</sup>V. I. Anisimov, J. Zaanen, and O. K. Andersen, "Band theory and Mott insulators: Hubbard U instead of stoner I," *Phys. Rev. B* **44**, 943 (1991).
- <sup>53</sup>S. Grimme, "Accurate description of van der waals complexes by density functional theory including empirical corrections," *J. Comput. Chem.* **25**, 1463–1473 (2004).
- <sup>54</sup>S. Grimme, "Semiempirical GGA-type density functional constructed with a long-range dispersion correction," *J. Comput. Chem.* **27**, 1787–1799 (2006).
- <sup>55</sup>W. H. Bragg, "XXX. The structure of the spinel group of crystals," *London, Edinburgh, Dublin Philos. Mag. J. Sci.* **30**, 305–315 (1915).
- <sup>56</sup>S. Nishikawa, "Structure of some crystals of spinel group," in *Proceedings of the Tokyo Mathematico-Physical Society. 2nd Series* (The Physical Society of Japan and The Mathematical Society of Japan, 1915), Vol. 8, pp. 199–209\_1.
- <sup>57</sup>S. Laporte, F. Finocchi, L. Paulatto, M. Blanchard, E. Balan, F. Guyot, and A. M. Saitta, "Strong electric fields at a prototypical oxide/water interface probed by *ab initio* molecular dynamics: MgO(001)," *Phys. Chem. Chem. Phys.* **17**, 20382–20390 (2015).
- <sup>58</sup>S. Pezzotti, D. R. Galimberti, and M.-P. Gaigeot, "2D H-bond network as the topmost skin to the air–water interface," *J. Phys. Chem. Lett.* **8**, 3133–3141 (2017).
- <sup>59</sup>A. Morita and J. T. Hynes, "A theoretical analysis of the SFG spectrum of the water surface. II. Time dependent approach," *J. Phys. Chem. B* **106**, 673–685 (2002).
- <sup>60</sup>A. Morita and T. Ishiyama, "Recent progress in theoretical analysis of vibrational sum frequency generation spectroscopy," *Phys. Chem. Chem. Phys.* **10**, 5801–5816 (2008).
- <sup>61</sup>R. Khatib, E. H. G. Backus, M. Bonn, M.-J. Perez-Haro, M.-P. Gaigeot, and M. Sulpizi, "Water orientation and hydrogen-bond structure at the fluoride/water interface," *Sci. Rep.* **6**, 24287 (2016).
- <sup>62</sup>S. A. Corcelli and J. L. Skinner, "Infrared and Raman line shapes of dilute HOD in liquid H<sub>2</sub>O and D<sub>2</sub>O from 10 to 90 C," *J. Phys. Chem. A* **109**, 6154–6165 (2005).

- <sup>63</sup>V. Shinde, S. Mahadik, T. Gujar, and C. Lokhande, "Supercapacitive cobalt oxide (Co<sub>3</sub>O<sub>4</sub>) thin films by spray pyrolysis," *Appl. Surf. Sci.* **252**, 7487–7492 (2006).
- <sup>64</sup>K. J. Kim and Y. R. Park, "Optical investigation of charge-transfer transitions in spinel Co<sub>3</sub>O<sub>4</sub>," *Solid State Commun.* **127**, 25–28 (2003).
- <sup>65</sup>S. Pezzotti, A. Serva, and M.-P. Gaigeot, *J. Chem. Phys.* **148**, 174701 (2018).
- <sup>66</sup>A. Serva, S. Pezzotti, S. Bougueroua, D. R. Galimberti, and M.-P. Gaigeot, "Combining *ab-initio* and classical molecular dynamics simulations to unravel the structure of the 2D-HB-network at the air-water interface," *J. Mol. Struct.* **1165**, 71–78 (2018).
- <sup>67</sup>A. Cimas, F. Tielens, M. Sulpizi, M. Gaigeot, and D. Costa, "The amorphous silica-liquid water interface studied by *ab initio* molecular dynamics (AIMD): Local organisation in global disorder," *J. Phys.: Condens. Matter* **26**, 244106 (2014).
- <sup>68</sup>Y.-C. Wen, S. Zha, X. Liu, S. Yang, P. Guo, G. Shi, H. Fang, Y. R. Shen, and C. Tian, "Unveiling microscopic structures of charged water interfaces by surface-specific vibrational spectroscopy," *Phys. Rev. Lett.* **116**, 016101 (2016).
- <sup>69</sup>A. Willard and D. Chandler, "Instantaneous liquid interfaces," *J. Phys. Chem. B* **114**, 1954–1958 (2010).
- <sup>70</sup>M. T. Greiner, L. Chai, M. G. Helander, W.-M. Tang, and Z.-H. Lu, "Transition metal oxide work functions: The influence of cation oxidation state and oxygen vacancies," *Adv. Funct. Mater.* **22**, 4557–4568 (2012).
- <sup>71</sup>J. Filhol and M. Bocquet, "Charge control of the water monolayer/Pd interface," *Chem. Phys. Lett.* **438**, 203 (2007).
- <sup>72</sup>F. Bellucci, S. S. Lee, J. D. Kubicki, A. Bandura, Z. Zhang, D. J. Wesolowski, and P. Fenter, "Rb<sup>+</sup> adsorption at the quartz(101)-aqueous interface: Comparison of resonant anomalous x-ray reflectivity with *ab initio* calculations," *J. Phys. Chem. C* **119**, 4778–4788 (2015).
- <sup>73</sup>M. J. DelloStritto, J. Kubicki, and J. O. Sofo, "Density functional theory simulation of hydrogen-bonding structure and vibrational densities of states at the quartz(101)-water interface and its relation to dissolution as a function of solution pH and ionic strength," *J. Phys.: Condens. Matter* **26**, 244101–244112 (2014).
- <sup>74</sup>A. M. Saitta, F. Saija, and P. V. Giaquinta, "*Ab initio* molecular dynamics study of dissociation of water under an electric field," *Phys. Rev. Lett.* **108**, 207801 (2012).
- <sup>75</sup>G. Cassone, F. Creazzo, P. V. Giaquinta, F. Saija, and A. M. Saitta, "*Ab initio* molecular dynamics study of an aqueous NaCl solution under an electric field," *Phys. Chem. Chem. Phys.* **18**, 23164–23173 (2016).
- <sup>76</sup>G. Cassone, F. Creazzo, P. V. Giaquinta, J. Sponer, and F. Saija, "Ionic diffusion and proton transfer in aqueous solutions of alkali metal salts," *Phys. Chem. Chem. Phys.* **19**, 20420–20429 (2017).
- <sup>77</sup>G. Cassone, F. Creazzo, and F. Saija, "Ionic diffusion and proton transfer of MgCl<sub>2</sub> and CaCl<sub>2</sub> aqueous solutions: An *ab initio* study under electric field," *Mol. Simul.* (published online).

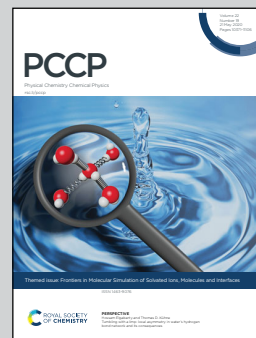


Showcasing research from the group of Fabrizio Creazzo and Marie-Pierre Gaijeot at LAMBE UMR8587 Laboratory.

Enhanced conductivity of water at the electrified air-water interface: a DFT-MD characterization

DFT-based molecular dynamics simulations of the electrified air-liquid water interface show the importance of the 2D-Hbond-network (2DN) in the binding interfacial layer (BIL) for the proton conductivity being twice that of the bulk liquid for fields up to  $0.40 \text{ V \AA}^{-1}$  applied parallel to the surface. Beyond this, water in the BIL and in the liquid are aligned in the same way by the fields, hence leading to the same proton conductivity in both BIL and bulk water.

As featured in:



See Fabrizio Creazzo, Giuseppe Cassone, Marie-Pierre Gaijeot *et al.*, *Phys. Chem. Chem. Phys.*, 2020, **22**, 10438.



Cite this: *Phys. Chem. Chem. Phys.*,  
2020, 22, 10438

Received 26th December 2019,  
Accepted 12th February 2020

DOI: 10.1039/c9cp06970d

rsc.li/pccp

## Enhanced conductivity of water at the electrified air–water interface: a DFT-MD characterization

Fabrizio Creazzo,<sup>a</sup> Simone Pezzotti,<sup>a,b</sup> Sana Bougueroua,<sup>a</sup>  
Alessandra Serva,<sup>c</sup> Jiri Sponer,<sup>d</sup> Franz Saija,<sup>e</sup> Giuseppe Cassone<sup>d,e</sup> and  
Marie-Pierre Gaigeot<sup>a</sup>

DFT-based molecular dynamics simulations of the electrified air–liquid water interface are presented, where a homogeneous field is applied parallel to the surface plane. We unveil the field intensity for the onset of proton transfer and molecular dissociation; the protonic current/proton conductivity is measured as a function of the field intensity/voltage. The air–water interface is shown to exhibit a proton conductivity twice the one in the liquid water for field intensities below  $0.40 \text{ V \AA}^{-1}$ . We show that this difference arises from the very specific organization of water in the binding interfacial layer (BIL, *i.e.* the air–water interface region) into a 2D-HBond-network that is maintained and enforced at the electrified interface. Beyond fields of  $0.40 \text{ V \AA}^{-1}$ , water in the BIL and in the bulk liquid are aligned in the same way by the rather intense fields, hence leading to the same proton conductivity in both BIL and bulk water.

### 1 Introduction

The structure of liquid water at the interface with the air is an essential key to rationalize and characterize chemical and physical phenomena observed at such an interface, among which are proton trapping and hopping along “water wires”,<sup>1</sup> charge separation/recombination processes,<sup>2,3</sup> changes in acidity/basicity with respect to bulk water,<sup>4,5</sup> the atypical Pockels effect,<sup>6</sup> and surface tension.<sup>7</sup>

Hassanali *et al.*<sup>1</sup> reported the high affinity of protons for the interface especially in terms of specific proton hopping pathways at the air–water (AW) interface, with protons exchanged between water molecules belonging to the first interfacial layer, *via* water wires running parallel to the surface. This result strongly suggests that a certain ordering of the water molecules within the surface plane is present at the AW interface. In our recent paper<sup>8</sup> – where we have combined density functional theory-based molecular dynamics simulations (DFT-MD) and non-linear vibrational sum frequency generation (vSFG) spectroscopy – we have shown that such an order consists of a two-dimensional (2D) H-bonded network (denoted hereafter as “2DN”), connecting the

vast majority of the interfacial water molecules (on average more than 90%) through water–water H-bonds/wires oriented parallel to the instantaneous water surface.<sup>9,10</sup> Furthermore, due to the additional constraint imposed by the preferential H-bond orientation, water molecules in the 2DN have fewer degrees of freedom for rotation and libration, which was shown to result in a slower orientational dynamics of the interfacial water molecules and, at the same time, to more dynamical H-bond breaking/reforming processes than in bulk liquid water.<sup>9</sup> The structure and dynamics of the 2DN thus provide a framework for the preferential direction of the above-mentioned proton hopping reported in ref. 1 and 11. Interestingly, a recent MD simulation of the AW interface has shown that the application of an electric field perpendicular to the interface induces a less efficient reorientation of water molecules than a field applied parallel to the surface.<sup>12</sup> However, the way in which the local structure of interfacial water changes in response to an external static electric field, and how this can affect proton hopping remain poorly understood both at the molecular and macroscopic levels.

We hence report here for the first time, to the best of our knowledge, an *ab initio* MD study of the microscopic effects produced by an external static and homogeneous electric field applied at the AW interface and oriented parallel to the water surface (*i.e.* along the  $-x$  direction in the simulation box). We reveal the possible perturbations in the 2DN at the AW interface under the influence of an external electric field and the consequence on proton hopping at the electrified interface. Beyond proton hopping, we also characterize the electric conditions for the protolysis reaction  $2\text{H}_2\text{O} \rightleftharpoons \text{OH}^- + \text{H}_3\text{O}^+$  to occur, where formally a proton transfer between two water molecules gives

<sup>a</sup> LAMBE UMR8587, Univ Evry, Université Paris-Saclay, CNRS, 91025 Evry, France.  
E-mail: fabrizio.creazzo@univ-evry.fr, mpgaigeot@univ-evry.fr

<sup>b</sup> Lehrstuhl für Physikalische Chemie II, Ruhr-Universität Bochum, 44780 Bochum, Germany

<sup>c</sup> Sorbonne Université, CNRS, Physico-chimie des électrolytes et nano-systèmes interfaciaux, PHENIX, 75005, Paris, France

<sup>d</sup> Institute of Biophysics of the Czech Academy of Sciences, Královopolská 135, 61265 Brno, Czech Republic. E-mail: giuseppe.cassone@ipcf.cnr.it

<sup>e</sup> CNR-IPCF, Viale Ferdinando Stagno d'Alcontres 37, 98158 Messina, Italy

rise to the formation of hydroxide ( $\text{OH}^-$ ) and hydronium ( $\text{H}_3\text{O}^+$ ) ions. The protolysis reaction is however a rare event, and interestingly, Saitta *et al.*<sup>13,14</sup> have shown that it is possible to stimulate the proton transfer process in bulk (liquid and ice) water – and hence, to investigate protolysis in a more systematic fashion – by applying a static external electric field. Based on ref. 13 for liquid water, the electrostatic coupling of interfacial water with an external electric field is expected to perturb the interfacial H-bonded network, hence possibly affecting proton transfer, water dissociation and protolysis at the AW interface.

Some information that can be readily gained upon applying sufficiently strong electric fields is the effective thresholds associated, respectively, with the onset of proton transfer and with the onset of molecular dissociation. In liquid water, fields of  $\sim 0.25 \text{ V \AA}^{-1}$  are needed to induce proton transfers and molecular dissociations of water along the 3D H-bonded network,<sup>13,15–17</sup> whereas a field intensity of at least  $0.35 \text{ V \AA}^{-1}$  has to be applied in order to establish a measurable protonic current.<sup>13</sup> A further and correlated consequence of the application of static electric fields to liquid water is the gradual alignment of an increasing fraction of molecular dipole moments along the field direction.<sup>18</sup> Moreover, as very recently demonstrated by monitoring the IR and Raman spectra of electrified liquid water *via ab initio* MD,<sup>19</sup> static electric fields of intensities beneath the molecular dissociation threshold induce structural changes in the H-bonded network and in the water tetrahedrality, in that the water structure becomes more ice-like.

Here, we show how the proton conductivity is enhanced by the presence of the specific 2DN at the air–water (AW) interface under external fields. This paper is organized as follows.

In Section 2, we present the methodology, and Section 3 reports results on the protonic current density–voltage diagram and the structural effects introduced by the external field applied parallel to the air–water 2DN interfacial network. We provide a detailed analysis of the H-bond network, water dissociation and proton conduction properties under increasing field strengths. Concluding remarks are in Section 4.

## 2 Computational methods

Density functional theory (DFT)-based molecular dynamics (MD) simulations (DFT-MD) have been carried out with the CP2K package,<sup>20,21</sup> consisting of Born–Oppenheimer MD by means of the DFT-BLYP<sup>22,23</sup> exchange–correlation functional including the Grimme D2 correction for dispersion interactions,<sup>24,25</sup> GTH pseudopotentials<sup>26</sup> for the oxygen and hydrogen atoms, and a combined Plane-Wave (400 Ry density cutoff) and TZV2P basis set. The simulation box of  $19.734 \times 19.734 \times 35 \text{ \AA}^3$  is composed of a liquid phase made of 256 water molecules, periodically repeated in the  $x$  and  $y$  directions and separated by a vacuum layer of  $15 \text{ \AA}$  from the replica in the vertical  $z$  direction. See Fig. 1a for a snapshot.

The 256 neutral air–water (AW) trajectory is the one presented in ref. 8, while the other trajectories in the presence of an external electric field applied parallel to the  $-x$  axis have been generated for the present investigation. The non-zero-field regime was explored in the range  $[0.05; 0.70] \text{ V \AA}^{-1}$ , the electric field being gradually increased with a step-increment of about  $0.05 \text{ V \AA}^{-1}$ . The implementation of an external electric field in

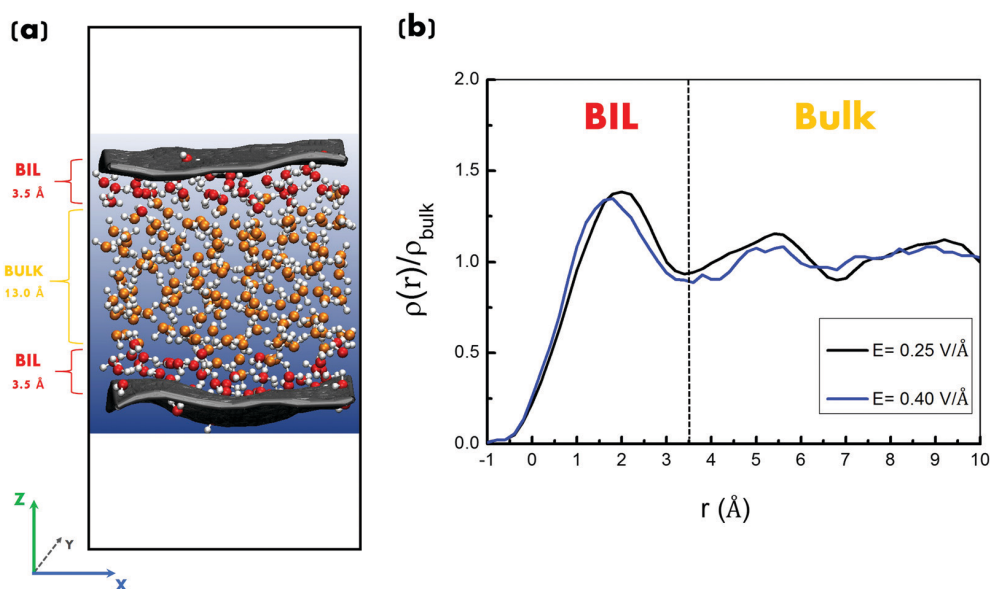


Fig. 1 (a) Snapshot extracted from DFT-MD simulations showing the simulation box composed of 256 water molecules. The Willard and Chandler instantaneous surface<sup>27</sup> is shown in grey sheets, the identified water layers (BIL and bulk water) are color-coded and discussed in the text. A large slab of  $15.0 \text{ \AA}$  of vacuum is used in order to separate the simulation box from its replicas along the vertical  $z$ -direction. (b) Electrified air–water interface: time averaged water density profiles normalized with respect to bulk liquid water obtained for applied electric fields of  $0.25 \text{ V \AA}^{-1}$  ( $5 \text{ V}$  potential) in black line and  $0.40 \text{ V \AA}^{-1}$  ( $8 \text{ V}$  potential) in blue line. The density is plotted as a function of the distance from the instantaneous Willard and Chandler surface.<sup>27</sup>

numerical codes based on DFT can be achieved by exploiting the modern theory of polarization and the Berry phase<sup>28</sup> (see *e.g.* ref. 29 for the technical implementation of a static and homogeneous electric field in *ab initio* codes and ref. 30 for a review of several methods that allow for the application of external fields in various simulation frameworks). In a nutshell, the difficulty in treating finite electric fields in first principles periodic systems is the non-periodic nature of the position operator. Within the modern theory of polarization<sup>31,32</sup> and of the Berry phase,<sup>28</sup> one can introduce a variational energy functional<sup>29</sup>

$$E^{\mathcal{E}}[\{\psi_i\}] = E^0[\{\psi_i\}] - \mathcal{E} \cdot P[\{\psi_i\}], \quad (1)$$

where  $E^0[\{\psi_i\}]$  is the energy functional of the system in the zero-field approach and  $P[\{\psi_i\}]$  is the polarization along the field  $\mathcal{E}$  direction, as defined by Resta.<sup>31</sup>

$$P[\{\psi_i\}] = -\frac{L}{\pi} \text{Im}(\ln \det S[\{\psi_i\}]), \quad (2)$$

where  $L$  is the periodicity of the cell and  $S[\{\psi_i\}]$  is a matrix composed of the following elements

$$S_{i,j} = \langle \psi_i | e^{2\pi i x/L} | \psi_j \rangle \quad (3)$$

for doubly occupied wavefunctions  $\psi_i$ . Umari and Pasquarello<sup>29</sup> demonstrated that this variational approach is valid for treating finite homogeneous electric fields in first-principles calculations and that it can be extended to provide atomic forces in first-principles MD simulations.

We performed simulations at the nominal temperature of 300 K, kept fixed through the coupling of the system with a Nosé–Hoover thermostat. The molecular systems were kept in an isothermal–isochoric (*NVT*) ensemble and the classical Newton's equations of motion for the nuclei are integrated through the velocity Verlet algorithm with a time-step of 0.4 fs. For each electric field strength, the dynamics was followed for time lengths up to about 30 ps, extending to about 100 ps in the absence of the field. Hence, we globally cumulated a total simulation time of approximately 400 ps.

Analyses of the DFT-MD trajectories into instantaneous surface and water layers (Fig. 1) follow the derivation, respectively, by Willard and Chandler<sup>27</sup> and Pezzotti *et al.*<sup>33</sup> Water–water H-bonds are defined through Galli and coworkers' criteria:<sup>34</sup>  $\text{O}(\text{H}) \cdots \text{O} \leq 3.2 \text{ \AA}$  and  $\text{O}-\text{H} \cdots \text{O}$  angle in the range  $[140-220]^\circ$ .

The identification of the water interfacial layers at the neutral AW interface, namely the BIL (binding interfacial layer) and bulk liquid water, has been done following our methodology described in ref. 33 on the basis of water structural descriptors only. As already validated in our previous works<sup>9,11,33,35,36</sup> and confirmed by the present results at the electrified AW interface, the BIL is systematically composed of the topmost water molecules located within 3.5 Å from the instantaneous water surface,<sup>27</sup> forming less water–water H-bonds (2.9 H-bonds per mol) and being 1.4 times denser than water in the bulk. These water molecules form H-bonds preferentially oriented parallel to the surface plane, resulting in the formation of a collective and extended 2D-Hbond-Network (2DN for short notation) in the BIL.<sup>8</sup> This leads to the breaking of centrosymmetry and

consequent SFG activity of the BIL.<sup>8,11</sup> Further away than 3.5 Å from the surface, centrosymmetric bulk water is recovered (with hence no SFG activity).

One of the three descriptors used to define the BIL,<sup>33</sup> namely the water density profile as a function of the vertical distance from the instantaneous water surface, is shown in Fig. 1b for two electrified air–water interfaces (respectively, homogeneous static electric field intensities of  $0.25 \text{ V \AA}^{-1}$  (5 V potential) and  $0.40 \text{ V \AA}^{-1}$  (8 V potential) applied along the  $-x$ -axis/surface plane). As will become clear in the discussion in the following Section 3, they correspond to crucial field values for the water conductivity in the BIL and bulk regions. The plots reveal that the water density profile is only slightly affected by the increase in the field, and in particular that the first peak (position and intensity, as well as following minimum position) is maintained in the  $0.25-0.40 \text{ V \AA}^{-1}$  field-regime. The thickness of the BIL is thus not changed in this regime. One can see the onset of small modifications to the second peak and following bulk region in the density profiles with the increase in the field intensity, showing that the field-induced rearrangement kicks-in in the 3D-HB-network of bulk water before it affects the 2D-HB-network of the BIL interface. This will be discussed in more detail later in this manuscript.

According to Ohm's law, the current density is related to the number of charge carriers  $\Delta N$  flowing through a section area  $a^2$  orthogonal to the direction of the electric field within a time interval  $\Delta t$ . With  $a$  being the side of the simulation box orthogonal to the field direction and  $q$  being the elementary charge ( $1.6 \times 10^{-19} \text{ C}$ ), the current density is:

$$J = \frac{q\Delta N}{a^2\Delta t} \quad (4)$$

expressed in  $\mu\text{A nm}^{-2}$ . The protonic conductivity is then calculated as

$$\sigma = \frac{J}{E} \quad (5)$$

expressed in  $\text{S cm}^{-1}$ .

## 3 Results

Although it is now established that applying static electric fields of the order of  $0.30 \text{ V \AA}^{-1}$  to liquid water favours molecular dissociations,<sup>13,16</sup> theoretical modeling of the microscopic behaviour at the air/liquid water (AW) electrified interface provides fundamental insights on the conductivity properties of the interfacial H-bonded network that, to the best of our knowledge, has not been explored so far. From liquid water modelling, the application of an external static field is known to alter the H-bond environment in the bulk, triggering the cleavage of some oxygen–hydrogen (O–H) covalent bonds and thus promoting the hopping of protons along intermolecular H-bonds, resulting in the formation of new ionic complexes such as hydronium ( $\text{H}_3\text{O}^+$ ) and hydroxide ( $\text{OH}^-$ ) in liquid water. This is due to at least two cooperative roles played by the field, which (i) aligns the water molecule dipole moment vectors

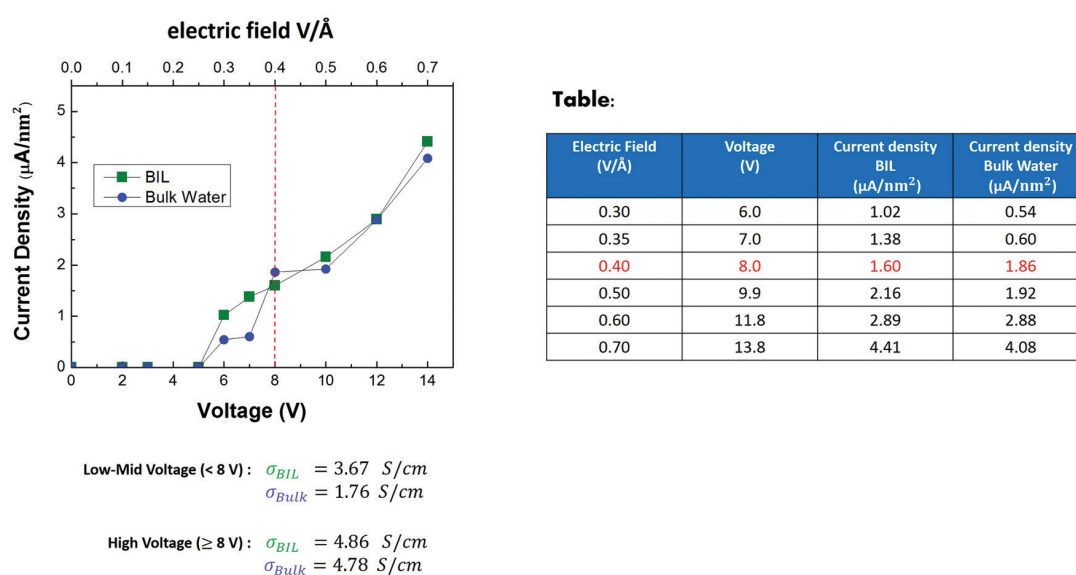


Table:

Electric Field (V/Å)	Voltage (V)	Current density BIL ( $\mu\text{A}/\text{nm}^2$ )	Current density Bulk Water ( $\mu\text{A}/\text{nm}^2$ )
0.30	6.0	1.02	0.54
0.35	7.0	1.38	0.60
0.40	8.0	1.60	1.86
0.50	9.9	2.16	1.92
0.60	11.8	2.89	2.88
0.70	13.8	4.41	4.08

**Fig. 2** Left: Protonic current density–voltage diagram calculated in the BIL (green squares) and in bulk water (blue circles). The corresponding electric field strength is given with the top axis. The dotted red line highlights the conductivity threshold discussed in the text.  $\sigma_{\text{BIL}}$  and  $\sigma_{\text{bulk}}$  are the conductivity values calculated in the BIL and in bulk water, respectively. Table: for each electric field strength applied (and the related voltage for a cell side of 19.734 Å), a list of protonic current density values calculated in the BIL and bulk water. Data highlighted in red represent the conductivity ( $\sigma$ ) threshold discussed in the text.

along the field direction<sup>18</sup> and (ii) elongates/weaken their covalent O–H bonds.<sup>9</sup> In neat bulk water, the lowest field intensity able to induce a measurable net proton flow/current has been quantified theoretically to a value of  $0.35 \text{ V } \text{\AA}^{-1}$ <sup>13,16</sup> (obtained from DFT-MD using the PBE exchange–correlation functional; note that a change in the functional might induce a slight change in the absolute value of the field threshold), while a lower field strength of  $0.25 \text{ V } \text{\AA}^{-1}$  triggers a series of ordered and correlated proton jumps *via* the Grotthuss mechanism in electrolytic aqueous solutions.<sup>16,18,37</sup>

In the case of the AW electrified interface here investigated, the first significant molecular dissociation events have been recorded for field strengths equal to  $0.30 \text{ V } \text{\AA}^{-1}$  applied parallel to the air–water surface plane. Moreover, as shown in the protonic current density–voltage diagram plotted in Fig. 2, such a field intensity, which corresponds to the application of a voltage of 6 V at the edges of the employed simulation box, is not only able to trigger water dissociations but also to give rise to a net proton flow both at the AW interface (*i.e.*, in the BIL) and in the bulk liquid.

Molecular dissociation processes (BIL and bulk alike) already start at  $0.25 \text{ V } \text{\AA}^{-1}$  (corresponding to a voltage of 5 V). However, similar to bulk liquid water,<sup>13</sup> these events are rare enough, and the created hydronium and hydroxide ions are short-lived (*i.e.*, their lifetime is  $\leq 20$ –30 fs), which is not enough to give rise to a measurable protonic current. Once a field intensity of  $0.30 \text{ V } \text{\AA}^{-1}$  is applied, the BIL–AW slab shows Ohmic behaviour, as already observed in ref. 13, 16, 18 and 37 for bulk water and electrolytic aqueous solutions. In order to extract the current density contributions arising separately from the BIL and from the bulk liquid, respectively, these two

regions have been systematically identified in the simulations based on the procedure presented in ref. 10, 11 and 33. As discussed in the methods section, the BIL includes all water molecules within a slab having a thickness equal to  $3.5 \text{ \AA}$  from the instantaneous water surface, while all remaining water molecules are assigned to the bulk region, as depicted in Fig. 1, independent of the field strength. Importantly, as will be demonstrated later in the text, the water–water BIL–2DN specific 2-dimensional H-bond network is maintained at the electrified AW interfaces, which is of high relevance for the rationalization of our findings for the protonic current densities presented and discussed below.

As shown in Fig. 2, two conductivity regimes can be identified, one for the BIL and one for the bulk liquid. In particular, as displayed in Fig. 2 and in the table included in this figure, when an electric field strength equal to  $0.30 \text{ V } \text{\AA}^{-1}$  (corresponding to 6 V potential) is applied parallel to the water surface, protons start to flow along the field direction, with a higher current density along the water–water 2D-Hbond-network than that in the bulk. While there is also a protonic flow in the liquid, the protonic current density measured in the BIL ( $1.02 \mu\text{A nm}^{-2}$ ) is roughly twice larger than that of the bulk ( $0.54 \mu\text{A nm}^{-2}$ ), up to  $0.40 \text{ V } \text{\AA}^{-1}$  fields. Correspondingly, the protonic conductivity in the BIL ( $\sigma_{\text{BIL}} = 3.67 \text{ S cm}^{-1}$ ) is twice the one of the bulk ( $\sigma_{\text{bulk}} = 1.76 \text{ S cm}^{-1}$ ). Thus, in the  $[0.30\text{--}0.40] \text{ V } \text{\AA}^{-1}$  field intensity range (corresponding to 6–8 V potentials), the electrified AW interface (*i.e.*, the BIL) is a much better protonic conductor than the electrified bulk water.

On the other hand, beyond an electric field strength of  $0.40 \text{ V } \text{\AA}^{-1}$  (corresponding to about 8 V potential), the protonic current densities in the BIL and in the bulk liquid become

roughly identical. Under such a high-voltage regime (*i.e.*,  $\geq 8$  V), the BIL and the bulk protonic conductivities are equal to an average value of  $\sim 4.8$  S cm $^{-1}$  (Fig. 2, right). The lower absolute bulk protonic conductivity found here in comparison to that of the pioneering work of Saitta *et al.*<sup>13</sup> (*i.e.*, 7.8 S cm $^{-1}$ ) is presumably due to a combination of differences in the adopted theoretical frameworks between our works (*i.e.*, Born–Oppenheimer *vs.* Car–Parrinello MD, dispersion-corrected BLYP XC functional *vs.* PBE, *etc.*) and to different statistics (*i.e.*, box sizes and simulation timescales).

The rationale behind the significant difference in the conduction properties of the BIL and of the bulk for fields below  $0.40$  V Å $^{-1}$  can be ascribed to the specific organization of the interfacial water molecules in the BIL, creating the already mentioned 2DN that connects more than 90% of the water molecules belonging to the BIL within a unique extended and collective network *via* H-bonds all oriented parallel to the surface plane<sup>8</sup> and surviving the application of a static electric field, as demonstrated now.

With the aim of providing a statistical and quantitative analysis of the 2DN in the BIL, Fig. 3 shows the probability distribution  $P_n(\%)$  of the number of BIL–water molecules ( $n$ ,  $x$ -axis) inter-connected by H-bonds through a non-interrupted 2-dimensional interfacial network. The probability distribution  $P_n(\%)$  is presented for the zero-field case in Fig. 3a; it is the reference for the two other probability distributions presented here for electric fields of  $0.25$  V Å $^{-1}$  and  $0.30$  V Å $^{-1}$  (Fig. 3(b) and (c)), the latter being the electric field threshold able to dissociate water molecules and to establish a protonic current.

As depicted in Fig. 3(a) (and already discussed in ref. 9 and 10), the vast majority of the water molecules (*i.e.* more than 90%, as obtained by integration of  $P_n(\%)$  for values  $n \geq 38$ ) located in the BIL (binding interfacial layer) form one single collective and extended H-bond structure – *i.e.*, the 2DN – as described in our previous works.<sup>9</sup> Less than 5% of interfacial water molecules are found either isolated ( $n = 1$ ), or involved in dimers ( $n = 2$ ) or in other small H-bonded structures ( $n \leq 5$ ), on average.

Similar considerations hold at  $0.25$  V Å $^{-1}$  and  $0.30$  V Å $^{-1}$  (Fig. 3(b) and (c)), where the 2DN is not only still present, but is

even enforced by the electric field applied parallel to the surface. One can indeed see that the main peak in the  $P_n(\%)$  distribution is shifted towards a higher central value of water molecules ( $n$ ) forming the extended and collective 2DN, while the peak distribution is also less broad than in the zero-field case. At both fields shown here, the minimum size of the continuous 2DN motif is obtained for  $n \sim 42$ –45. Not surprisingly, this reveals that the 2DN collectivity benefits from the alignment of the water dipoles under the influence of the external electric field applied along the direction parallel to the water surface (*i.e.* parallel to the 2DN H-bond direction). Let us also stress here that the current-density in the BIL (Fig. 2) is entirely due to the 90% water molecules that build the special 2DN network at the interface.

Besides, the 2DN is composed of H-bonded water rings, as already emphasized in ref. 1 and 9. These rings are quantified here, following the same method as in ref. 9 for the non-electrified air–water interface. Fig. 4 hence reports the probability distribution  $P_n(\%)$  of finding ring structures of given sizes in the interfacial BIL–2DN, in the absence of the electric field (Fig. 4(a)), and in the presence of the  $0.25$  V Å $^{-1}$  (Fig. 4(b)) and  $0.30$  V Å $^{-1}$  (Fig. 4(c)) fields. As far as the zero-field case is concerned, rings composed of four, five, and six H-bonded water molecules are the most likely structural motifs that build the collective 2DN. The most likely ring sizes are 4, 5 and 6, with decreasing order of probability. There are also probabilities to observe rings composed of up to nine water molecules.

For the two external fields reported in Fig. 4(b) and (c), one can see that the distribution of ring sizes between 4 and 6 is still the most probable, however with a global distribution that now clearly shifts towards the ring size of 5 as the most probable/favored, especially for the  $0.30$  V Å $^{-1}$  field applied. The formation of H-bonded rings in the BIL – water with the H-bonds oriented parallel to the water surface plane is the fingerprint of the 2DN at the air–water interface, maintained and even strengthened once the interface was electrified, as shown here.

For proton transfers to occur, protons have to move from one water molecule to the neighbouring one along H-bonded chains of molecules known as “water wires”.<sup>1,38</sup> Because of the reduced number of available spatial configurations in the

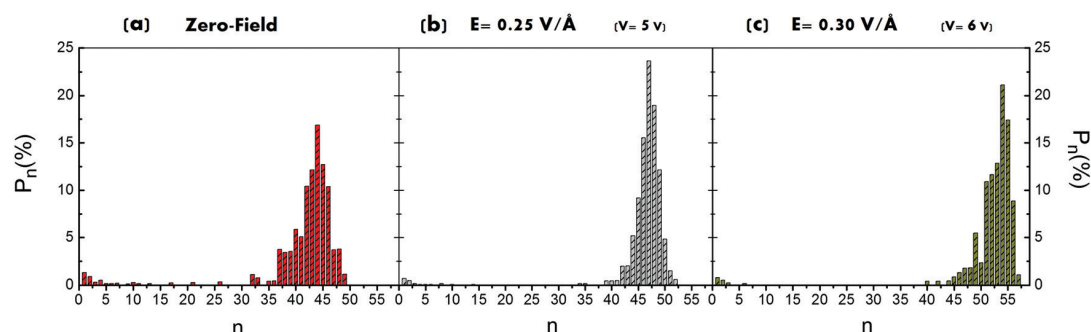


Fig. 3 Probability distribution  $P_n(\%)$  of the possible structure of water molecules located in the interfacial layer (BIL), 3.5 Å thickness.  $n$  ( $x$ -axis) is the number of BIL water molecules connected by non-interrupted H-bonds. (a) Zero-field case. (b) Electric field strength of  $0.25$  V Å $^{-1}$  (5 V potential). (c) Electric field strength of  $0.30$  V Å $^{-1}$  (6 V potential).

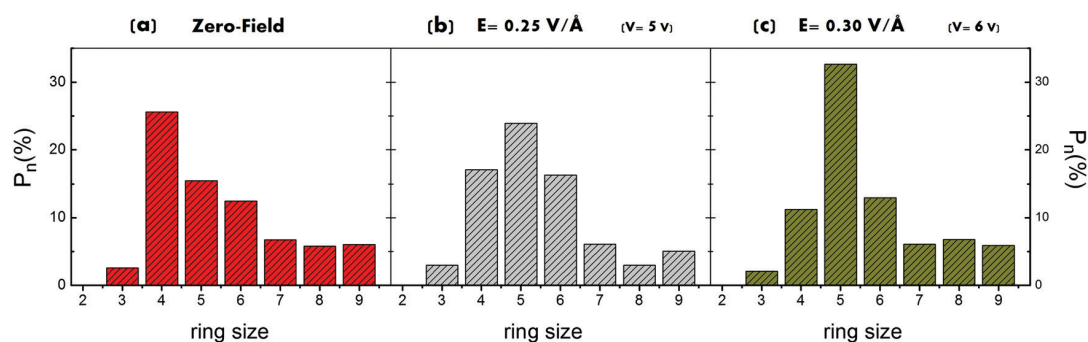


Fig. 4 Probability distribution  $P_n(\%)$  of the size of the ring structures formed by the interfacial water molecules within the 2DN. (a) Zero-field. (b) Electric field strength of  $0.25 \text{ V } \text{\AA}^{-1}$  (5 V potential). (c) Electric field strength of  $0.30 \text{ V } \text{\AA}^{-1}$  (6 V potential).

collective BIL-2DN, water molecules within the 2DN have lower degrees of freedom for rotation and libration, which leads to a slower timescale for the orientational dynamics of the interfacial water molecules.<sup>10</sup> Somehow counter-intuitively, however, these interfacial water molecules exhibit a H-bond breaking/reforming dynamics that is faster than for the water molecules in the bulk liquid.<sup>10</sup> The BIL-2DN and its rings of H-bonded molecules connected to each other through this network of H-bonds formed parallel to the surface (at both zero-field and at the electrified interfaces) indeed create preferential water wires that can favor proton hopping along these wires. The BIL-2DN furthermore leads to an increase of the residence time of protons at the interface, as already reported in ref. 1 and 11. Moreover, the preferential H-bond orientation naturally present in the 2DN along with the fast H-bond dynamics within the surface plane, as reported in ref. 9, enables easier alignment of the water molecules in the BIL in response to an electric field applied along a direction parallel to the surface plane. All these properties highly favor proton hopping along the BIL-2-dimensional-Hbond-wires, more efficiently than along the 3D H-bonded network of the liquid bulk, and also favor more efficient water dissociation and hence higher protonic flows within the BIL, which is indeed what is observed in this work.

A good illustration of these points can be found in Fig. 5, where 3D-plots report the probability of the combined O–O H-bonded distances and O–O orientation of the water–water H-bonds with respect to the applied  $\vec{E}$  field vector ( $\theta$  in the inset scheme), comparing the results for the water molecules in the BIL (left) and for water in the liquid bulk (right), for the electric field strengths of  $0.25 \text{ V } \text{\AA}^{-1}$  (Fig. 5a, electric field condition before the onset of detectable water dissociations and protonic currents) and  $0.40 \text{ V } \text{\AA}^{-1}$  (Fig. 5b). The probability coding is given by the scale from blue (lower probability) to red (higher probability). Very interestingly and in line with our discussion above, one can see immediately that the  $0.25 \text{ V } \text{\AA}^{-1}$  field-induced reorientation of the H-bonded water molecules measured through  $\theta$  is more efficient in the BIL-2DN (see Fig. 5a), where the maximum probability (red spots) is observed for values of  $\cos \theta$  between 0.6 and 1.0, compared to those in the liquid bulk where the red spots are found between 0.4 and 0.9.

For a field intensity of  $0.40 \text{ V } \text{\AA}^{-1}$  (8 V potential), both BIL-2D and bulk-3D H-bonded networks become equally oriented by the electrostatic driving force. One can indeed see that the 3D-plots presented in Fig. 5b for the BIL and bulk regions are very similar when such a higher field is applied, with the same final net HB-orientation of the water in the two regions. The only appreciable difference is found in the length of the HBs forming the 2D-HB-network in the BIL, which are slightly longer than those of the HBs formed between the bulk water molecules. This was already found at the non-electrified air–water interface<sup>9</sup> or at the lower  $0.25 \text{ V } \text{\AA}^{-1}$  field in Fig. 5a.

The water wires in the BIL are consequently found to be more oriented along the field direction than the water wires in the bulk, at least at the  $0.25 \text{ V } \text{\AA}^{-1}$  low-field strength. This can also be seen by the eye in Fig. 6(b), and in Fig. 6(c) at the slightly higher  $0.30 \text{ V } \text{\AA}^{-1}$  field strength. As furthermore highlighted in Fig. 6(c), the water wires in the bulk retain their 3D-structure, resulting in proton motions that explore a larger 3D portion of space in the reoriented bulk than in the reoriented 2DN, as illustrated by the two wires in Fig. 6(c). It follows that in order to move any proton from a position A to a position B under an external field applied parallel to the AW surface, a lower number of proton jumps are required along the more aligned water wires in the BIL than along the more spatially spread water wires in the bulk. This leads to the higher conductivity of the BIL in the low-to-moderate field regime, as reported in Fig. 2. Moreover, as shown in Fig. 5a for the  $0.25 \text{ V } \text{\AA}^{-1}$  field strength, the reorientation of the interfacial water molecules in the BIL along the field direction ( $-x$  axis) leads to longer and hence weaker H-bonds than in the liquid, which also favors and enhances the proton conductivity.

It is important to note that a few H-bonds present in the BIL are naturally weaker (and thus more dynamical) also under the zero-field condition, as a way to satisfy the finite temperature geometrical constraints on the water–water H-bonds and on the rings that thus maintain the extended 2DN structure. The further increase of the number of such weaker H-bonds with increasing field strength is a direct consequence of the additional 1D constraint imposed by the application of the field along one direction only. These weaker H-bonds have an influence on the lifetime of the water wires formed at the

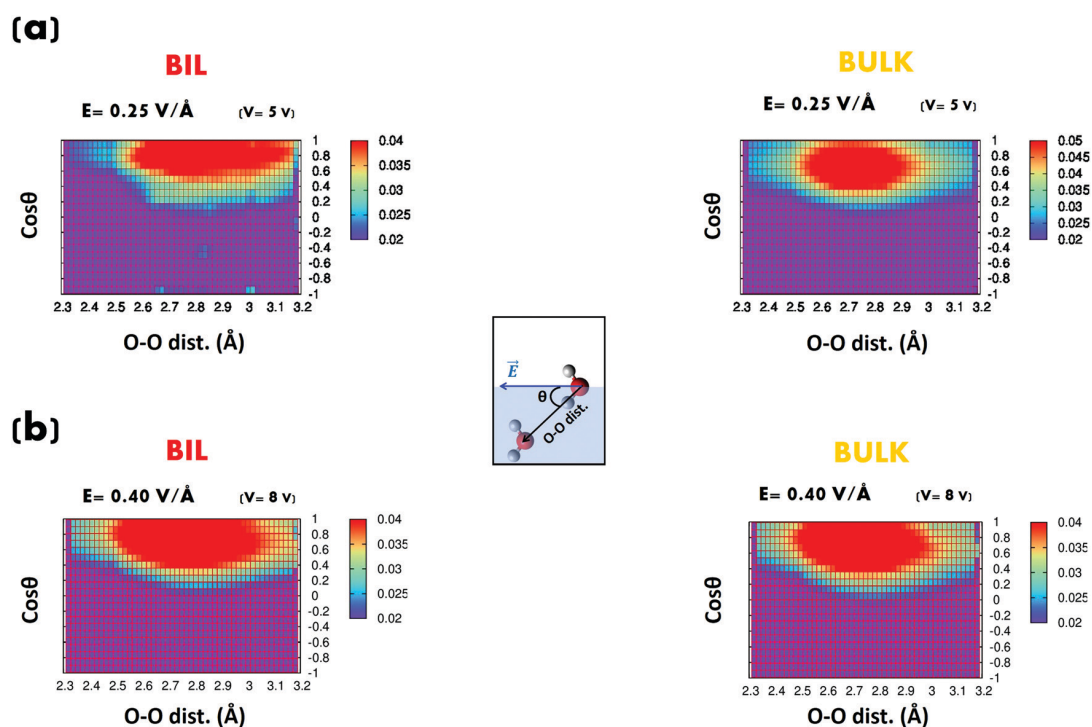


Fig. 5 3D plots of the H-bond patterns between the water molecules in the interfacial layer-BIL (on the left) and between the water molecules in the bulk water (on the right) when an electric field of  $0.25 \text{ V } \text{Å}^{-1}$  (5 V potential) – (a) at the top – and  $0.40 \text{ V } \text{Å}^{-1}$  (8 V potential) – (b) at the bottom – is applied. The x-axis reports the O–O distance (Å) between 2 H-bonded water molecules and the y-axis provides the angle (cosine value) between the O–O vector (from donor to acceptor) and the direction ( $-x$  axis) of the applied electric field (see inset scheme). The colors represent the probability ( $P$ ) to find one O–H group forming one H-bond with a given distance and orientation. The probability increases from blue to red, see the scale.

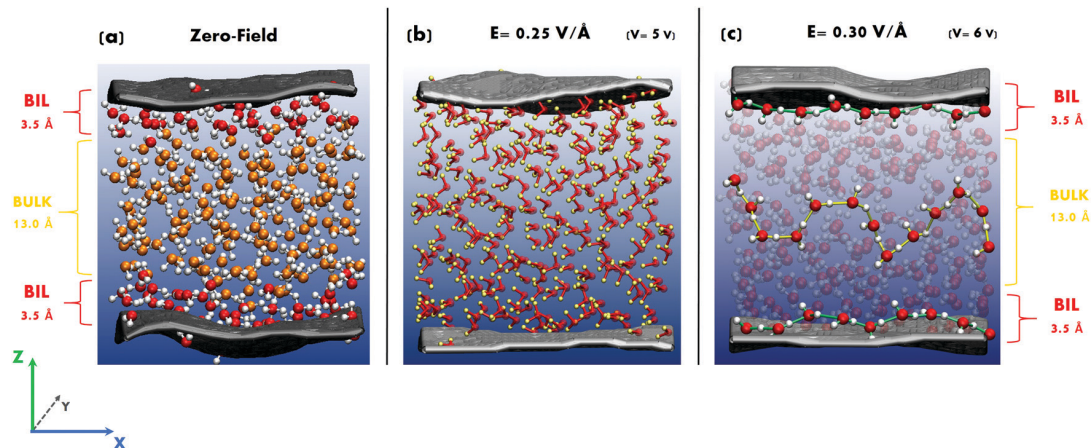


Fig. 6 Snapshots extracted from the DFT-MD simulations representing the instantaneous surface in grey sheets and the two water layers (BIL and bulk water) identified and discussed in the text. Oxygen atoms are colored in red and hydrogen atoms are in white (hydrogen in yellow only in panel (b)). (a) Zero-field. (b) Oriented water molecules along the field direction ( $-x$  axis) by an electric field strength equal to  $0.25 \text{ V } \text{Å}^{-1}$  (corresponding to 5 V potential). (c) Illustration of proton hopping water wires in the BIL and in bulk water under the action of a field intensity of  $0.30 \text{ V } \text{Å}^{-1}$  (6 V) along the  $-x$  axis.

interface, which are hence expected to be shorter-lived than the water wires of the bulk due to the increased H-bond dynamics within the 2DN.<sup>10</sup> It is well known that autoionization in water is generated by fluctuations of the water dipole moments and is hence connected to librations and to more dynamical water wires that ultimately favour water dissociation.<sup>39</sup> The efficient

separation of hydronium and hydroxide ions is also due to short-lived water wires, which in turn also reduce the probability of ionic recombination. All these effects play a role for field strengths slightly higher than the water dissociation threshold ( $0.25 \text{ V } \text{Å}^{-1}$ ). At larger intensities ( $\geq 0.40 \text{ V } \text{Å}^{-1}$ ), however, the limited size of the BIL likely leads to saturation

of the 2DN conductivity, which cannot be further enhanced by the action of the field. In other words, any differences in structures that exist between the BIL-2DN and the 3D H-bonded network in the bulk are washed out at higher fields, simply because both networks are then equally and completely oriented by the electrostatic driving force.

## 4 Conclusions

Based on state-of-the-art *ab initio* molecular dynamics simulations, we have characterized proton transfer and water dissociation at the air–water interface, triggered by intense static and homogeneous electric fields applied parallel to the air–water surface plane. These results have been directly compared with those measured in the bulk portion of the liquid.

We have found that the onset of water dissociation (*i.e.*, the minimum field intensity capable of ionizing water) is not affected by the specific 2-dimensional Hbond network formed by water at the air–water interface. The first formation of hydronium ( $\text{H}_3\text{O}^+$ ) and hydroxide ( $\text{OH}^-$ ) ions has been recorded at the binding interfacial layer (BIL) and in the bulk at the same field strength (*i.e.*,  $0.30 \text{ V \AA}^{-1}$ ). However, the proton transfer activity at low-to-moderate field regimes ( $\leq 0.40 \text{ V \AA}^{-1}$ ) is differently influenced in the two regions of the liquid. The response of the current density–voltage diagrams is Ohmic in both cases (provided that a conduction regime has been achieved), the protonic conductivity of the BIL ( $\sigma_{\text{BIL}} = 3.67 \text{ S cm}^{-1}$ ) is twice the one recorded in the bulk ( $\sigma_{\text{bulk}} = 1.76 \text{ S cm}^{-1}$ ). By monitoring the behaviour of the H-bond networks in the BIL and in the bulk liquid, respectively, we showed this difference in conductivity to be due to the specifically organised 2-dimensional Hbond network (2DN) shaping the water at the air–water interface, which was shown to enhance the proton transfer events under low-to-moderate ( $0.30\text{--}0.40 \text{ V \AA}^{-1}$ ) electric field strengths applied along the interface plane (*i.e.* along the 2DN). The reduced dimensionality of the intermolecular network has a clear influence on the behaviour of the water wires responsible for the proton conduction. The better aligned and shorter-lived water wires, as existing in the BIL, lead to more efficient spatially (and temporally) correlated proton hoppings than those in the 3D liquid bulk. On the other hand, for more intense fields ( $\geq 0.40 \text{ V \AA}^{-1}$ ), both BIL and bulk protonic conductivities converge to the same value ( $\sim 4.8 \text{ S cm}^{-1}$ ), because the 1D direction constraint imposed by the stronger electrostatic field now aligns both BIL and bulk water in a similar way and hence reduces the structural differences between the BIL and the bulk H-bonded networks. The insights gained from this investigation certainly could have more practical implications, typically in relation with water splitting in confined electrified/electrocatalytic solid/water environments. According to the present work, any confined environment exhibiting the 2DN structural arrangement of water at the interface would indeed be favorable for water dissociation/splitting, especially under electrified conditions applied parallel to the BIL-2DN surface.

## Conflicts of interest

There are no conflicts of interest to declare.

## Acknowledgements

This work was performed under Grants LABEX CHARMA<sub>3</sub>T 11-LABEX-0039/ANR-11-IDEX-0003-02 ‘Excellence Laboratory’ program of the University Paris-Saclay and ANR DYNAWIN ANR-14-CE35-0011-01 (ANR Agence Nationale de la Recherche), and using HPC resources from GENCI-France Grant 072484 (CINES/IDRIS/TGCC). Discussions with Dr D. R. Galimberti are gratefully acknowledged.

## References

- 1 A. Hassanali, F. Giberti, J. Cuny, T. D. Kühne and M. Parrinello, *Proc. Natl. Acad. Sci. U. S. A.*, 2013, **110**, 13723–13728.
- 2 V. Venkateshwaran, S. Vembanur and S. Garde, *Proc. Natl. Acad. Sci. U. S. A.*, 2014, **111**, 8729–8734.
- 3 J. A. Kattirtzi, D. T. Limmer and A. P. Willard, *Proc. Natl. Acad. Sci. U. S. A.*, 2017, **114**, 13374–13379.
- 4 X. Zhao, S. Subrahmanyam and K. B. Eisenthal, *Chem. Phys. Lett.*, 1990, **171**, 558–562.
- 5 R. Bianco, S. Wang and J. T. Hynes, *J. Phys. Chem. A*, 2008, **112**, 9467–9476.
- 6 Y. Suzuki, K. Osawa, S. Yukita, T. Kobayashi and E. Tokunaga, *Appl. Phys. Lett.*, 2016, **108**, 191103.
- 7 R. C. Tolman, *J. Chem. Phys.*, 1949, **17**, 333–337.
- 8 S. Pezzotti, D. R. Galimberti and M.-P. Gaigeot, *J. Phys. Chem. Lett.*, 2017, **8**, 3133–3141.
- 9 A. Serva, S. Pezzotti, S. Bougueroua, D. R. Galimberti and M.-P. Gaigeot, *J. Mol. Struct.*, 2018, **1165**, 71–78.
- 10 S. Pezzotti, A. Serva and M.-P. Gaigeot, *J. Chem. Phys.*, 2018, **148**, 174701.
- 11 S. Pezzotti and M.-P. Gaigeot, *Atmosphere*, 2018, **9**, 396.
- 12 M. Nikzad, A. R. Azimian, M. Rezaei and S. Nikzad, *J. Chem. Phys.*, 2017, **147**, 204701.
- 13 A. M. Saitta, F. Saija and P. V. Giaquinta, *Phys. Rev. Lett.*, 2012, **108**, 207801.
- 14 G. Cassone, P. V. Giaquinta, F. Saija and A. M. Saitta, *J. Phys. Chem. B*, 2014, **118**, 4419–4424.
- 15 E. M. Stuve, *Chem. Phys. Lett.*, 2012, **519**, 1–17.
- 16 G. Cassone, F. Creazzo, P. V. Giaquinta, J. Sponer and F. Saija, *Phys. Chem. Chem. Phys.*, 2017, **19**, 20420–20429.
- 17 Z. Hammadi, M. Descoins, E. Salançon and R. Morin, *Appl. Phys. Lett.*, 2012, **101**, 243110.
- 18 G. Cassone, F. Creazzo, P. V. Giaquinta, F. Saija and A. M. Saitta, *Phys. Chem. Chem. Phys.*, 2016, **18**, 23164–23173.
- 19 G. Cassone, J. Sponer, S. Trusso and F. Saija, *Phys. Chem. Chem. Phys.*, 2019, **21**, 21205–21212.
- 20 J. Hutter, M. Iannuzzi, F. Schiffmann and J. VandeVondele, *WIREs Comput. Mol. Sci.*, 2014, **4**, 15–25.
- 21 J. VandeVondele, M. Krack, F. Mohamed, M. Parrinello, T. Chassaing and J. Hutter, *Comput. Phys. Commun.*, 2005, **167**, 103–128.

- 22 A. D. Becke, *Phys. Rev. A: At., Mol., Opt. Phys.*, 1988, **38**, 3098–3100.
- 23 C. Lee, W. Yang and R. G. Parr, *Phys. Rev. B: Condens. Matter Mater. Phys.*, 1988, **37**, 785–789.
- 24 S. Grimme, *J. Comput. Chem.*, 2004, **25**, 1463–1473.
- 25 S. Grimme, *J. Comput. Chem.*, 2006, **27**, 1787–1799.
- 26 S. Goedecker, M. Teter and J. Hutter, *Phys. Rev. B: Condens. Matter Mater. Phys.*, 1996, **54**, 1703.
- 27 A. Willard and D. Chandler, *J. Phys. Chem. B*, 2010, **114**, 1954–1958.
- 28 M. V. Berry, *Proc. R. Soc. London*, 1984, **392**, 45–57.
- 29 P. Umari and A. Pasquarello, *Phys. Rev. Lett.*, 2002, **89**, 157602.
- 30 N. J. English and C. J. Waldron, *Phys. Chem. Chem. Phys.*, 2015, **17**, 12407–12440.
- 31 R. Resta, *Rev. Mod. Phys.*, 1994, **66**, 899–915.
- 32 R. D. King-Smith and D. Vanderbilt, *Phys. Rev. B: Condens. Matter Mater. Phys.*, 1993, **47**, 1651–1654.
- 33 S. Pezzotti, D. R. Galimberti, Y. R. Shen and M.-P. Gaigeot, *Phys. Chem. Chem. Phys.*, 2018, **20**, 5190–5199.
- 34 J. A. White, E. Schwegler, G. Galli and F. Gygi, *J. Chem. Phys.*, 2000, **113**, 4668–4673.
- 35 S. Pezzotti, D. Galimberti, Y. Shen and M.-P. Gaigeot, *Minerals*, 2018, **8**, 305.
- 36 F. Creazzo, D. R. Galimberti, S. Pezzotti and M.-P. Gaigeot, *J. Chem. Phys.*, 2019, **150**, 041721.
- 37 G. Cassone, F. Creazzo and F. Saija, *Mol. Simul.*, 2019, **45**, 373–380.
- 38 T. von Grotthuß, *Mémoire sur la décomposition de l'eau et des corps qu'elle tient en dissolution à l'aide de l'électricité galvanique*, 1805.
- 39 P. L. Geissler, C. Dellago, D. Chandler, J. Hutter and M. Parrinello, *Science*, 2001, **291**, 2121–2124.

# Ions Tune Interfacial Water Structure and Modulate Hydrophobic Interactions at Silica Surfaces

Aashish Tuladhar,<sup>||</sup> Shalaka Dewan,<sup>||</sup> Simone Pezzotti,<sup>||</sup> Flavio Siro Brigiano, Fabrizio Creazzo, Marie-Pierre Gaigeot,<sup>\*</sup> and Eric Borguet<sup>\*</sup>

Cite This: *J. Am. Chem. Soc.* 2020, 142, 6991–7000

Read Online

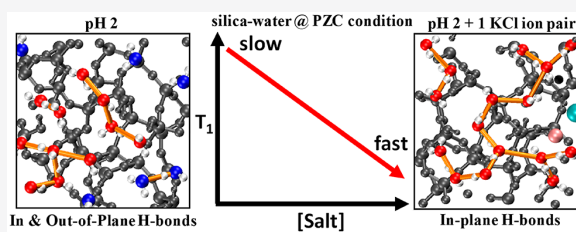
ACCESS |

Metrics & More

Article Recommendations

Supporting Information

**ABSTRACT:** The structure and ultrafast dynamics of the electric double layer (EDL) are central to chemical reactivity and physical properties at solid/aqueous interfaces. While the Gouy–Chapman–Stern model is widely used to describe EDLs, it is solely based on the macroscopic electrostatic attraction of electrolytes for the charged surfaces. Structure and dynamics in the Stern layer are, however, more complex because of competing effects due to the localized surface charge distribution, surface–solvent–ion correlations, and the interfacial hydrogen bonding environment. Here, we report combined time-resolved vibrational sum frequency generation (TR-vSFG) spectroscopy with ab initio DFT-based molecular dynamics simulations (AIMD/DFT-MD) to get direct access to the molecular-level understanding of how ions change the structure and dynamics of the EDL. We show that innersphere adsorbed ions tune the hydrophobicity of the silica–aqueous interface by shifting the structural makeup in the Stern layer from dominant water–surface interactions to water–water interactions. This drives an initially inhomogeneous interfacial water coordination landscape observed at the neat interface toward a homogeneous, highly interconnected in-plane 2D hydrogen bonding (2D-HB) network at the ionic interface, reminiscent of the canonical, hydrophobic air–water interface. This ion-induced transformation results in a characteristic decrease of the vibrational lifetime ( $T_1$ ) of excited interfacial O–H stretching modes from  $T_1 \sim 600$  fs to  $T_1 \sim 250$  fs. Hence, we propose that the  $T_1$  determined by TR-vSFG in combination with DFT-MD simulations can be widely used for a quantitative spectroscopic probe of the ion kosmotropic/chaotropic effect at aqueous interfaces as well as of the ion-induced surface hydrophobicity.



## INTRODUCTION

Water is critical to sustaining life on Earth, and knowledge about its chemistry and physics is central to a vast range of subjects.<sup>1–11</sup> However, the organization of water in inhomogeneous environments remains controversial, owing to water's many anomalous properties.<sup>12</sup> A simple question such as how far away ions can affect the physical and the chemical properties of water is still rigorously debated.<sup>13–20</sup> To make matters worse, understanding the behavior of water and solvated ions at an interface is an even more arduous task. Intuitively, it is fairly obvious that when ions approach an interface, they screen the surface charge (if present) and also (most likely) reorganize the interfacial environment by restructuring the original surface–solvent and solvent–solvent interactions since competing ion–solvent, ion–surface, and ion–ion interactions are introduced. Therefore, a quantitative and molecular-level understanding of these interactions is essential to understand and predict ion activity at interfaces and their influence on chemical reactivity.

The mineral oxide–electrolyte aqueous interface provides an excellent platform to investigate surface–ion–solvent interactions as a function of surface charge by manipulating the pH

of the bulk aqueous solution across the point of zero charge (PZC) of the mineral, hence tuning the electrostatic attraction between the surface and the ions. The silica–water interface represents the most widely studied mineral–aqueous interface. Therefore, many spectroscopic and imaging techniques have been used extensively to study the electric double layer (EDL) at the silica–electrolyte interface.<sup>21–26</sup> The EDL can be broadly subdivided into a Stern layer located within the first one/two aqueous monolayers from the solid surface where ions accumulate, followed by a diffuse layer consisting of solvated ions that screen the remaining surface charge.<sup>27,28</sup> While the energetics of the diffuse layer is reasonably well approximated by the Gouy–Chapman (GC) model, the understanding of the Stern layer is still limited. This is largely because the structure and dynamics of the Stern layer are

Received: December 10, 2019

Published: April 1, 2020



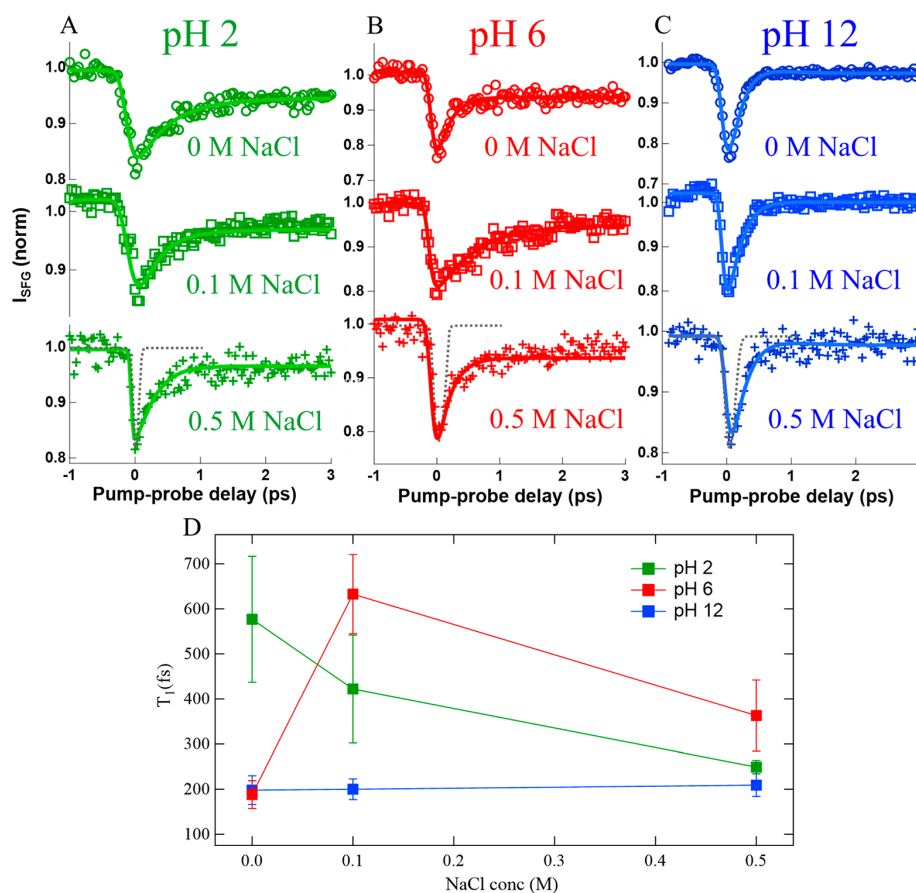


**Figure 1.** Effect of ions on the vibrational dynamics of the O–H stretch in  $\text{H}_2\text{O}$  at the silica–water interface at (A) pH 2, (B) pH 6, and (C) pH 12. The gray dotted line represents the cross-correlation of the IR pump, IR probe, and visible pulses, i.e., the instrument response function, indicating a fwhm of  $\sim 120$  fs. The solid lines are the best fits with a four-level system, described in the Supporting Information. (D)  $T_1$  (O–H vibrational lifetime) vs NaCl concentration. The  $T_1$  values reported are the average  $T_1$  from separate measurements repeated at least 3 times, and in some cases up to 5 times. The error bars indicate the standard deviation for all the individual  $T_1$  values obtained on different days.

directly sensitive to the competing effects of the surface charge distribution, surface–solvent–ion correlations, and the interfacial hydrogen bonding environment, which are all extremely difficult to probe experimentally. Hence, the detailed understanding of these interfacial properties is not accounted for in the most commonly used Stern–Gouy–Chapman (SGC) model. Therefore, experimental tools that can provide quantitative and molecular understanding of the EDL are key to the development of more sophisticated models that can accurately describe its structure, composition, and energetics.

Vibrational sum frequency generation (vSFG) spectroscopy, a laser-based second-order nonlinear optical technique, has played a key role in the last few decades in advancing our understanding of the EDL structure at the silica–electrolyte interface.<sup>21,22,24,29–33</sup> In a typical vSFG experiment, an infrared (IR) laser beam which is in resonance with a molecular vibration is temporally and spatially overlapped with a visible laser at an interface of interest, resulting in the generation of sum frequency (SF) photons whose frequency is the sum of the IR and visible frequencies. Within the dipole approximation, only noncentrosymmetric molecules and environments generate a vSFG signal. Centrosymmetry is inherently broken at any interface between two bulk media, thus making vSFG spectroscopy an exclusive probe of molecular vibrations

at the interface and hence an ideal tool for probing the EDL. Moreover, vSFG can be employed in both the frequency domain (steady-state (SS) vSFG) and the time-domain (time-resolved (TR) vSFG) to extract structural and dynamics information on the EDL. Despite a plethora of investigations of the silica–electrolyte interface using SS-vSFG<sup>31,34–40</sup> and TR-vSFG,<sup>21,22,41,42</sup> a complete molecular picture of the silica–electrolyte EDL is still lacking. This mainly stems from two critical shortcomings in past vSFG studies.

The first issue is due to the ambiguity of the probing depth of vSFG at charged interfaces (the silica–water interface is habitually charged except at its PZC, around pH 2–4) where the surface electric field can break the centrosymmetry of bulklike water residing further than the first few interfacial layers and hence contributing to, or even dominating, the vSFG signal. This has greatly complicated the interpretation of vSFG studies of silica–water interfaces and has impeded a definitive rationalization of the structure and dynamics of the EDL, since it is unclear which populations (interfacial water or electric field-oriented bulklike water) are probed. However, recent experimental<sup>43</sup> and computational<sup>44</sup> studies have developed methodologies to separate vSFG spectra into contributions originating from the first few layers [binding interfacial layer (BIL)] and from the electric field oriented

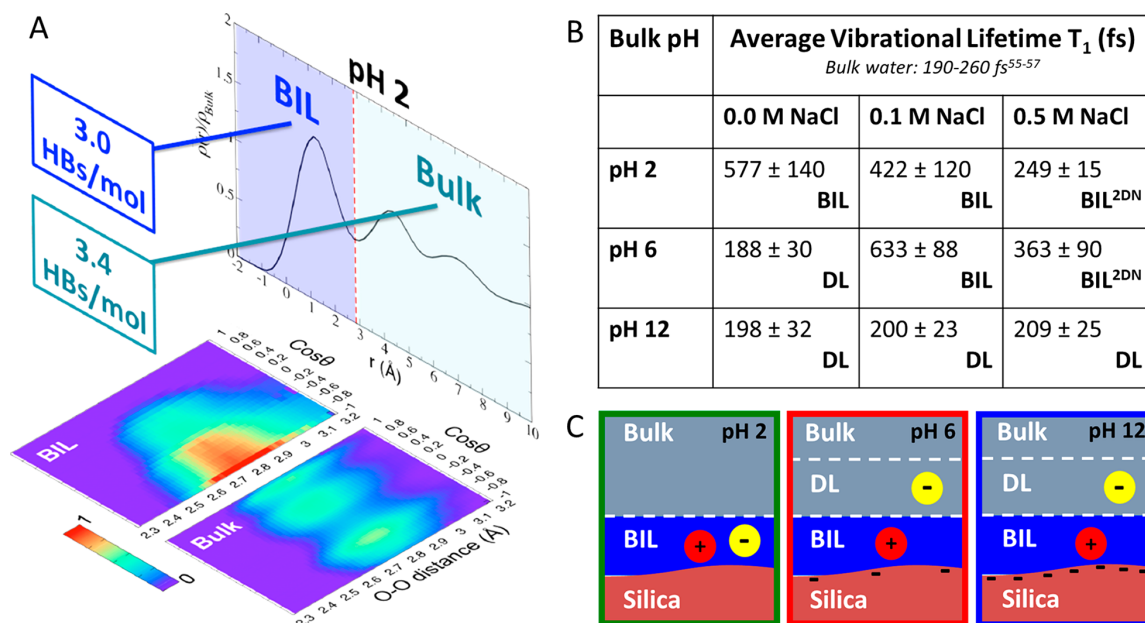


**Figure 2.** (A) Three descriptors used for characterizing and determining water BIL/DL/Bulk layers at the neat silica–water interface at pH 2. They are (see refs 44, 54, and 55) the water density profile with respect to the distance from the surface ( $r$ ), the average water coordination (HBs/molecule), and the 3D-plots evaluating the probability for water–water HBs formed in each layer with a given HB (O–O) distance and orientation with respect to the normal to the surface (red regions correspond to the maximum probability to find water with preferential HB distances and orientations; see Section S6 in the SI for details). See all details in Section S5 of the SI. (B) Average vibrational lifetime  $T_1$  at different bulk pH and NaCl concentrations, obtained from 4 level model fits (described in the SI) to TR-vSFG traces. The error bars indicate the standard deviation for all the individual  $T_1$  values obtained on different days. The labels “BIL” (binding interfacial layer), “BIL<sup>2DN</sup>” (2DN stands for the 2D–H bond-network formed by the BIL water), and “DL” (diffuse layer) refer to the interfacial region that dominates the vSFG response in each aqueous environment, as described in the text. (C) Schemes of the structural organization of water and ions at the 1 M electrolytic amorphous silica–water interface (pH = 2, 6, 12) extracted from the AIMD/DFT-MD simulations. Red/yellow balls with +/- signs represent the cations/anions and their distribution at the interface (BIL vs DL).

bulklike contribution [diffuse layer (DL)]. The BIL water region is analogous to the Stern layer in the double layer theory from the aspect of the spatial distribution of the ions.<sup>43</sup> Only recently, this methodology has been applied to vSFG studies of the fused silica–aqueous interface revealing important insight on its chemical and physical properties (for example, microscopic hydrophobicity).<sup>29,74</sup>

The second shortcoming stems from the lack of understanding of how the presence of ions affects the vSFG signal. Historically, the ion associated attenuation of the vSFG signal at the silica–aqueous interface has been assigned to the Debye screening effect (as predicted by GC theory); i.e., ions reduce the thickness of the non-centrosymmetric diffuse layer probed by vSFG. It is also obvious that ions can rearrange the interfacial hydrogen-bonding environment due to ion–solvent and ion–surface interactions. However, it is unclear how ion-induced screening and ion-induced solvent rearrangement affect the vSFG signal. The need to look beyond the GC/SGC models to understand the silica–electrolyte EDL, in order to disclose the more complex molecular-level rearrangements occurring in the BIL, is the missing ingredient for the development of next-generation models describing ion activity at interfaces. The need for such development was, for instance, recently pointed out in nonlinear spectroscopy studies by Borguet et al.,<sup>35</sup> Gibbs et al.,<sup>25</sup> and Geiger et al.<sup>23</sup> where they provided evidence for highly pH-dependent specific ion effects, whose understanding is beyond the GC/SGC models. Here, we report a joint effort, combining time-resolved vibrational

sum frequency generation (TR-vSFG) spectroscopy with ab initio DFT-based molecular dynamics simulations (AIMD/DFT-MD), to reveal novel molecular details on how ions change the interfacial water structure in the BIL and consequently affect its ultrafast vibrational dynamics. TR-vSFG spectroscopy, measuring the vibrational relaxation time-scale of the O–H stretching vibrations, provides an excellent quantifiable probe of the hydrogen bonding environments of the silica–electrolyte EDL, allowing us to experimentally detect ion-induced changes in the BIL, which may otherwise be too subtle or nonexistent in the SS-vSFG signal.<sup>24,35</sup> Complementarily, DFT-MD simulations provide a detailed understanding of the microscopic mechanism(s) resulting in the ion-induced effects on the TR-vSFG measurements. Our results clearly show that the GC/SGC models are insufficient in describing the ion activity at silica surfaces, and the molecular insights provided by this study could be significant in the development of more accurate and sophisticated EDL models that would account for the interface specific chemistry, surface charge and ion distribution, and the resulting hydrogen bonding environment.

## RESULTS AND DISCUSSION

**Time-Resolved Sum Frequency Generation.** The vibrational dynamics of the silica–water interface, measured using TR-vSFG spectroscopy (experimental and sample preparation details are provided in the SI), is clearly a function of both bulk pH and ionic strength (Figures 1 and 2B). More

precisely, the water OH stretch  $T_1$  lifetime is found to strongly depend on the ion concentration at pH 2 and 6, while a constant  $T_1$  of  $\sim 200$  fs is observed for pH 12 in the 0–0.5 M NaCl range. At pH  $\sim 12$ , the silica surface is dehydroxylated by  $\sim 25\%$ ,<sup>45</sup> inducing a rather high surface charge density of  $\sim -0.2$  C/m<sup>2</sup>, thus resulting in a surface potential of  $\sim 170$  mV, as calculated using the silica deprotonation ratio and the GC model (described in Section S3 of the SI, see also Figures S4 and S5). There is therefore a strong water DL impact to vSFG due to the surface field-oriented bulklike water (see, e.g., refs 21, 22, 44, 46, and 47). Both the BIL and the DL impact the vSFG response, and their relative weighted contributions to the final TR-vSFG measurements can be qualitatively estimated from the surface potential by using the framework described hereafter. See Section S5 in the SI for the BIL/DL definition. The vSFG signal in the DL is due to the potential drop across the DL ( $\Delta\varphi_{\text{DL}}$ , assumed here as equal to the surface potential; see Table S2 for a comparison with other choices) through  $\chi_{\text{DL}}^{(2)}(\omega) = \chi_{\text{bulk}}^{(3)}(\omega) \Delta\varphi_{\text{DL}}$ ,<sup>43,44,46</sup> where  $\chi_{\text{bulk}}^{(3)}(\omega)$  is the third-order susceptibility of bulk liquid water (this expression is here written without interference contributions<sup>48,49</sup> which are only important at low ionic strength and hence trivial at pH 12 which has an ionic strength of 10 mM).  $\chi_{\text{bulk}}^{(3)}(\omega)$  is known.<sup>43,44</sup> In the present experiments,  $|\chi_{\text{DL}}^{(2)}(\omega)|^2$  signals are measured to deduce  $T_1$  relaxation times; thus,  $|\chi_{\text{DL}}^{(2)}(\omega)|^2 = |\chi_{\text{bulk}}^{(3)}(\omega)|^2 (\Delta\varphi_{\text{DL}})^2$ . Defining  $I_{\text{BIL}}$  and  $I_{\text{DL}}$  as the integral of  $\chi_{\text{BIL}}^{(2)}(\omega)$  and  $\chi_{\text{DL}}^{(2)}(\omega)$  in the O–H stretching region, one finds that  $I_{\text{DL}}/I_{\text{BIL}} \propto (\Delta\varphi_{\text{DL}})^2$ , i.e., the ratio of DL/BIL intensities, is proportional to the square of the surface potential. According to previous works on silica–water interfaces,<sup>44,46</sup> values of  $I_{\text{DL}}/I_{\text{BIL}} \sim 10$  were found for  $\Delta\varphi_{\text{DL}} \sim 10$  mV. Taking  $\Delta\varphi_{\text{DL}} \sim 10$  mV as the reference ( $(\Delta\varphi_{\text{DL}})_{\text{ref}}$ ), we can estimate the  $I_{\text{DL}}/I_{\text{BIL}}$  ratio at any other  $\Delta\varphi_{\text{DL}}$  value as  $I_{\text{DL}}/I_{\text{BIL}}(\Delta\varphi_{\text{DL}}) = I_{\text{DL}}/I_{\text{BIL}}(\Delta\varphi_{\text{DL}})_{\text{ref}} \times (\Delta\varphi_{\text{DL}}/(\Delta\varphi_{\text{DL}})_{\text{ref}})^2 = 10(\Delta\varphi_{\text{DL}}/10 \text{ mV})^2$ . See Sections S9 and S10 for more details. Therefore,  $I_{\text{DL}}/I_{\text{BIL}} \sim 2960$  is expected here for  $\Delta\varphi_{\text{DL}} \sim 172$  mV at pH  $\sim 12$  (see Table S2). The vSFG response at the neat pH  $\sim 12$  silica–water interface is consequently dominated by the water in the DL, i.e., by bulklike oriented liquid, and indeed one measures  $T_1 = 198 \pm 32$  fs (Figures 1 and 2B), typical of the 190–260 fs<sup>50–52</sup> relaxation measured in bulk liquid water. When adding 0.1 and 0.5 M salt, the surface potential is reduced but is still of the order  $\sim 100$  mV (see Table S2), thus giving rise to the same DL-dominated fast interfacial relaxation. These results suggest that higher concentrations than 0.5 M are needed to screen the silica surface potential and hence suppress the DL contribution to vSFG at pH  $\sim 12$ . This is indeed the conclusion of the recent vSFG measurements by Tahara’s group,<sup>40</sup> where 2 M NaCl is needed to measure only the BIL contribution at pH 12.

When lowering the pH to 6, the silica surface is now only  $\sim 1\%$  dehydroxylated.<sup>45</sup> A smaller surface potential ( $\sim 80$  mV) is hence created, and in the absence of additional ions,  $\Delta\varphi_{\text{DL}} \sim 80$  mV (Figure S5 in the SI). Correcting for interference effects, which now need to be considered for the neat pH 6 condition (where the ionic strength is  $10^{-6}$ ), an  $I_{\text{DL}}/I_{\text{BIL}}$  ratio of 26 is obtained (see Sections S9 and S10 and Table S2 in the SI), still large enough to conclude that the measured relaxation time is dominated by the DL contribution. Consistently, we measure  $T_1 = 188 \pm 30$  fs (Figures 1 and 2B), similar to pH 12 conditions. A recent study from Hore-Tyrodé<sup>32</sup> reported a surface potential of  $\sim 200$  mV for the same neat pH 6

conditions (i.e., no excess salt). Taking this larger surface potential value leads to an even larger  $I_{\text{DL}}/I_{\text{BIL}}$  ratio, making our conclusion on dominant DL contributions even stronger.

Adding 0.1 or 0.5 M salt at pH  $\sim 6$  results in an accumulation of cations at the negatively charged surface, hence reducing the surface potential by more than 1 order of magnitude (Figure S5 and Table S2, SI). We note here that addition of ions is known to increase the percentage of deprotonated sites.<sup>32,45,53</sup> Despite the increase in deprotonation, the surface potential is lower than in the case of no salt (Figure S5B), as shown in a recent study.<sup>32</sup> This is possibly due to the counterion screening the surface potential by directly interacting with the deprotonated SiO<sup>−</sup> sites, as shown by a previous study.<sup>53</sup> Moreover, the surface potential is observed to decay exponentially away from the surface when salt is present (Figure S5) so that it is only 4 and 1 mV at 1 nm away from surface for 0.1 and 0.5 M NaCl, respectively. Due to the lower surface potential and rapid decay (see Figure S5 and Table S2 in the SI), the DL contribution to the vSFG signal is largely suppressed at pH 6 when salt is added.

In agreement with these estimates, we find that the presence of 0.1 M NaCl initially slows down  $T_1$  to 633 fs, which is similar to the  $T_1$  at neat pH 2. This means that the 0.1 M NaCl at pH 6 is mainly only responsible for screening surface charge, hence excluding the DL water contribution to  $T_1$  lifetime, as one would expect from the GC model and consistent with a previous study.<sup>22</sup> However, when the salt concentration is further increased to 0.5 M,  $T_1$  becomes faster (363 fs), deviating from the behavior expected from GC theory. Since the surface potential is very low at pH 6 with 0.5 M [NaCl], the  $T_1$  decrease has to arise from ion-induced changes in the BIL.

In analogy with the findings at pH 6, a similar BIL-specific effect is also observed for pH 2, point of zero charge (PZC) conditions, where the measured  $T_1$  lifetimes (Figures 1 and 2B) show that the vibrational relaxation of water is accelerated by increasing the bulk ionic concentration. In the absence of salt, the surface potential is close to zero (Figure S5A and Table S2, SI) and we can consequently assume that the silica surface is neutral and that the vSFG probing depth and the  $T_1$  lifetimes reflect the water structure in the BIL alone. When ions are introduced, the  $T_1$  lifetime decreases from 577 fs for the neat interface to 422 fs for 0.1 M [NaCl] and to 249 fs for 0.5 M [NaCl], while the surface potential remains close to zero (Figure S5 and Table S2, SI). The BIL is thus expected to be solely responsible for the measured  $T_1$  lifetime in the entire investigated concentration range at pH = 2, meaning that there is no preferential adsorption of cations over anions or vice versa, and both ionic species have the same probability to populate the BIL layer.

Here, it is important to consider the possibility of cations preferentially accumulating at the neutral silica surface compared to anions (as is known to occur at higher pH values, above PZC), resulting in a slightly positive surface so that the vSFG probes DL (“bulklike”) water via the  $\chi^{(3)}$  effect and causing an acceleration of the  $T_1$ . However, this scenario would manifest in a large DL-water contribution to the total SS-vSFG spectra. This was indeed reported in a recent vSFG study<sup>24</sup> which showed a significant increase in the vSFG signal at pH 2 when the NaCl concentration was raised from 10 to 100 mM, which was interpreted as an overcharging effect. However, the overcharging effect was mostly apparent for the ssp-vSFG signal and not for the ppp-vSFG signal. We use the

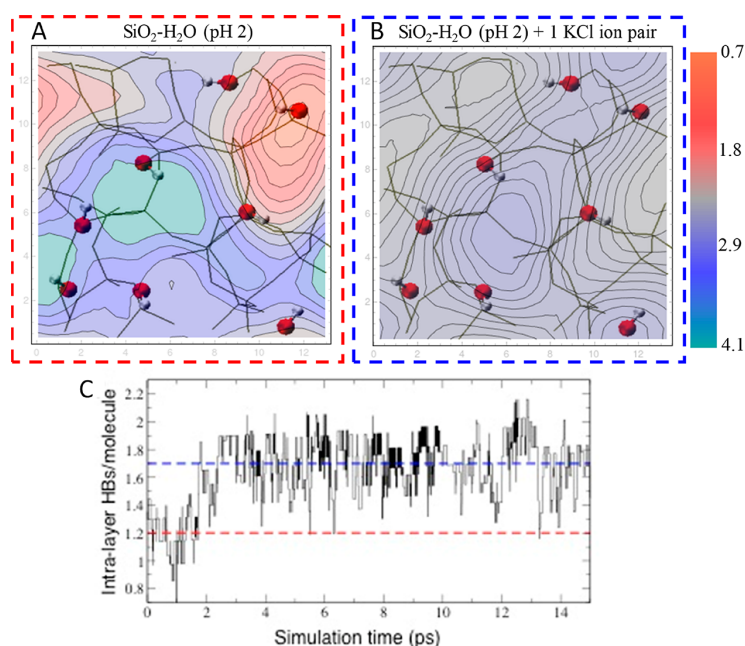


**Figure 3.** AIMD/DFT-MD simulations of the amorphous silica–water interface at pH  $\sim$  2. Time-averaged coordination number of the water molecules in the BIL spatially resolved along the lateral  $x$ – $y$  directions of the silica surface (in Å) for (A) neat aqueous silica interface and (B) aqueous silica interface with one KCl ion pair in the BIL. The water coordination is expressed in terms of the number of HBs (sum of water–water and water–silanol HBs) per water molecule (see Section S6 in the SI for details). The color coding (vertical scale in the plots) goes from light red (0.7 HBs/molecule), dark red (1.8 HBs/molecule), grayish-blue (2.9 HBs/molecule) to greenish-blue (4.1 HBs/molecule). The top view of the interface shows the solid Si–O covalent bonds in gray lines to highlight the solid surface covalent patterns. The surface silanols are marked by the O–H groups in red (O) and white (H) spheres. (C) Time-evolution of the number of intra-BIL HBs formed per water molecule located within the BIL.  $t = 0$  is the time when a KCl ion-pair is introduced in the BIL. The red and blue dashed lines indicate the average number of intra-BIL HBs per water molecule for the neat interface (red, 1.2) and for the KCl electrolyte interface (blue, 1.7), respectively.

latter polarization combination in this study. Also, hysteresis has been reported when pH is varied at constant ionic strength, which is how the above-mentioned study was conducted. In our study, we vary the ionic strength at constant pH which avoids the hysteresis issue. We see no significant increase in SS-vSFG signal at pH 2 when NaCl concentration is increased (Figure S6), which is consistent with other past studies of silica–water interfaces at pH  $\sim$  2 conditions<sup>35</sup> as well as with the estimated surface potential values (Figure SSA). On the contrary, we notice a small decrease in ppp-vSFG intensity with salt addition, which could also be in principle attributed to the screening effect of the electrolyte (by hypothesizing that a small net surface charge persists at pH 2). However, we also see an acceleration of  $T_1$  when 0.1 M salt is added. Thus, the decrease in ppp-vSFG intensity cannot be entirely due to the screening effect. As we will show later, such a decrease can be explained when the ion-induced changes in the BIL water structure are considered.

In the light of all the above-discussed evidence, the accelerations of  $T_1$  lifetimes at pH  $\sim$  2 conditions and pH 6 with [NaCl] = 0.1–0.5 M are ascribed to ion inducing order and more interconnectivity within the structure of the BIL water, i.e., a kosmotropic effect. A deep understanding of the associated microscopic mechanism, which goes beyond pure electrostatic effects and is almost entirely driven by specific ion-induced changes in water–water and water–surface interactions, is pivotal in order to improve our comprehension and modeling of electrolytic interfaces. We hence now make use of DFT-MD simulations to address this challenge.

**DFT Molecular Dynamics.** A DFT-MD simulation of the aqueous amorphous silica surface (4.5 SiOH/nm<sup>2</sup>, representative of the silica surfaces in experiments) at pH 2 was performed (see Section S5 in the SI for all computational details). In agreement with the experimental results, the simulation shows that when the surface is neutral (pH  $\sim$  2), only the water in the BIL is noncentrosymmetric and hence vSFG-active. This is summarized in Figure 2A, where water in the BIL is shown to be denser than in the bulk, forming fewer water–water HBs, and with a noncentrosymmetric orientation, while bulklike water coordination, orientation, and density are recovered right beyond the BIL, i.e., further than 3.0 Å from the SiO<sub>2</sub> surface (see also Section S6 of the SI). The absence of a DL confirms that the aqueous silica interface is at the isoelectric point at pH  $\sim$  2.

What the DFT-MD simulation also reveals is that the inhomogeneous spatial distribution of silanols at the amorphous silica surface results in a nonuniform spatial distribution of the coordination number of the water molecules in the BIL (Figure 3A, where the time averaged spatial distribution of the coordination number of water in the BIL is shown in a contour-map). Water coordination results from the sum of water–water and water–silanol HBs, where a standard HB definition is applied (O–O distance <3.2 Å and O(–H)–O angle in 140–220° interval).<sup>54</sup> If, on average, water is 3-fold coordinated in the BIL, this number is in fact due to two distinct populations: 60% of the water molecules in the BIL are tetrahedrally coordinated (HB/mol  $\geq$  3.1, blue zones in Figure 3A), while the other 40% are undercoordinated (HB/mol < 2.2,

red zones). These two water populations are located above silica areas made of high (bottom half of Figure 3A and B) and low (top half of Figure 3A and B) silanol densities, respectively, which we have recently identified as hydrophilic/hydrophobic patches on the macroscopically hydrophilic silica surface.<sup>29,56</sup>

To reveal how ions affect the BIL water structure and dynamics, eight additional DFT-MD simulations have been performed in the presence of a KCl ion-pair. In AIMD simulations, the Na<sup>+</sup> cation is known to require much larger plane wave basis sets for its accurate electronic representation than K<sup>+</sup>, hence considerably increasing the computational cost of the AIMD, and, thus, the choice of K<sup>+</sup> in the present simulations. The results obtained with KCl have been then confirmed with one supplementary MD simulation where one NaCl ion-pair is accommodated at the silica–water interface (see Section S8 in the SI). The similarity between Na<sup>+</sup>/K<sup>+</sup> behaviors found in the present work is consistent with a previous study.<sup>57</sup> As already discussed, since the silica surface is at the isoelectric point at pH ~ 2, and no static field is generated by the neutral surface, there is no surface electrostatic driving force to favor cations over anions (and vice versa) to approach closer to the silica surface. Starting from this knowledge, nine distinct initial ion configurations have been prepared for the MD simulations, where both K<sup>+</sup>/Na<sup>+</sup> and Cl<sup>-</sup> ions were randomly located within the BIL layer (see Sections S4 and S8 of the SI).

We make the choice to discuss hereafter the results from one representative DFT-MD simulation, the results of which have been validated by all the other simulations (the total of nine simulations amounts to 150 ps time-scale), revealing that our findings are independent of the average position and configuration (i.e., contact ion-pair CIP, solvent shared ion-pair SSIP) that ions have in the BIL, as well as on the K<sup>+</sup>/Na<sup>+</sup> nature of the cation (all detailed in Section S8 of the SI).

The resulting picture obtained from the DFT-MD simulations is the following. The presence of the electrolyte in the BIL leads to the BIL water becoming homogeneously 3-fold coordinated (Figure 3B); i.e., there is one single water population (91% of the water in the BIL), highly interconnected by H-bonds formed within the layer (1.7 intra-BIL HBs on average). This striking change in the water structural organization in the BIL from the neat to the electrolytic SiO<sub>2</sub>–water interface is due to two combined factors: by approaching the silica surface, the ions are able to complete their solvation shell with surface silanols on top of BIL water molecules (i.e., ions adsorbed in innerspheres, see Figure 4C), as already shown at the crystalline quartz–water<sup>58</sup> and alumina–water<sup>59</sup> interfaces, thereby breaking local water–surface H-bonds that were previously present at the neat aqueous silica interface. Innersphere ions hence locally drive the breaking of water–surface interactions which is characteristic of the hydrophobic patches at the silica surface.<sup>29,56</sup> They consequently increase the portion of the surface assigned to the hydrophobic domain. Above these ion-induced hydrophobic domains, water adapts to this change by maximizing H-bonds in between interfacial water molecules (intra-BIL HBs), hence increasing the water–water H-bond connectivity within the BIL. As a result of such an ion-catalyzed shift in the balance between water–water and water–surface interactions toward the former, a highly ordered water–water HB-network with HBs parallel to the silica surface plane is formed in the whole BIL, reminiscent of the 2D-HB-network recently revealed at

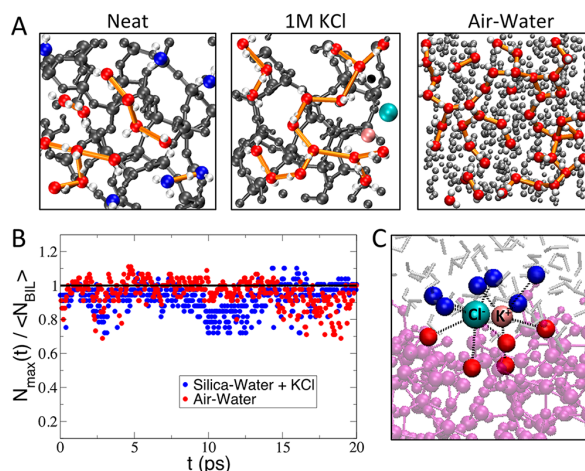


**Figure 4.** (A) Top views of the BIL water structural arrangement at the neat silica–water (left), the silica–water interface with one KCl ion pair in the BIL (middle), and the canonical hydrophobic air–water interface (right) used here as a reference for the highly interconnected H-bond network (2D-HB-network) formed by the water in the BIL.<sup>54,55</sup> The silica surface atoms are black balls (left and middle), while the gray balls in the right-hand figure are the water in the bulk liquid. The water molecules in the BIL are color-coded according to their coordination number, i.e., blue if  $\leq 2.2$  HBs/mol, red if  $> 2.2$  HBs/mol. In the absence of ions, water molecules with lower coordination number (blue) and with higher coordination number (red) are present, connected only by few H-bonds (orange). When KCl is added, blue water molecules disappear, and only red water molecules remain, resembling the canonical air–water interface. The increase in the number of orange connections between BIL water molecules from the neat to the electrolytic interface illustrates how ions increase in-plane H bonding within the BIL. (B) Evolution with time of the number of water molecules ( $N_{\max}$ ) that are interconnected by intra-BIL HBs into one single 2D-HB-network, normalized by the average number of water in the BIL ( $\langle N_{\text{BIL}} \rangle$ ). Red, reference air–water interface; blue, silica–water + KCl interface. A similar plot is not reported for the neat silica–water interface, as the 2D-HB-network does not exist at that interface. (C) Innersphere adsorption of the KCl ion-pair at the SiO<sub>2</sub>–water interface. The ions use silanols (red balls for the oxygens) and water in the BIL (blue balls for the oxygens) in order to achieve an innersphere adsorption.

the canonical hydrophobic air–water interface,<sup>54</sup> where 1.7 intra-BIL HBs are also found on average.<sup>55,60</sup> The time-evolution for the formation of the 2D-HB-network at the silica–water interface (Figure 3C) reveals that the number of intra-BIL HB/molecule increases in a few picoseconds, from 1.2 (neat interface, start of the dynamics) to 1.7, by adding one KCl ion-pair in the BIL.

The electrolyte-induced increase in water interconnectivity is further illustrated in Figure 4A where top views of the BIL water molecules (20 on average in these simulation boxes) of the neat SiO<sub>2</sub>–water (left), the SiO<sub>2</sub>–water+KCl (middle), and the air–water interface (right; taken from refs 54 and 55; be aware of the larger simulation box) are compared. One can immediately observe the 60%/40% ratio between the two water populations discussed above at the neat solution interface (Figure 4A, left), with the isolated blue-waters above the hydrophobic patches (which are too small for water to form a 2D-HB-network) on one hand and the locally interconnected, tetrahedral red-waters above the hydrophilic patches on the other hand. Once the electrolytes are present in

the BIL (pink/green balls in Figure 4A, middle), one immediately observes the disappearance of the blue-undercoordinated water molecules, and the increased HB interconnectivity in between the red-water molecules, now 3-fold coordinated and extended over the whole silica surface. This is similar to the HB interconnectivity at the air–water interface<sup>54,55</sup> (Figure 4A, right).

To understand the time-dependent behavior of the HB network of the KCl–silica–water interface with respect to the air–water, we further compare in Figure 4B the time-evolution of the 2D-HB-network size ( $N_{\max}$ ), normalized by the average number of BIL water molecules ( $\langle N_{\text{BIL}} \rangle$ ) ( $\langle N_{\text{BIL}} \rangle = 45$  and 20, respectively, at the air–water and silica–water interfaces). One can see that the two interfaces behave similarly over time, with the normalized 2D-HB-network size steadily varying between 0.8 and 1.0 during the whole simulation.

We can hence conclude that innersphere adsorbed ions alter the water organization in the BIL by shifting the balance from dominant water–surface interactions (“out-of-plane ordering”) to in-plane water–water interactions (“in-plane ordering”). Our molecular picture is consistent with previous theoretical studies<sup>61–63</sup> showing that adsorbed ions can reorder the interfacial H-bonding network at the quartz (101)–water interface by promoting the formation of intrasurface H-bonds and disrupting the surface water H-bonds. This drives an inhomogeneous interfacial water coordination landscape toward a homogeneous, highly interconnected in-plane 2D hydrogen bonding network, reminiscent of the canonical, hydrophobic air–water interface.

**Connecting TR-vSFG and AIMD.** We now make use of the structural knowledge obtained from the simulations to provide a rationalization for the  $T_1$  lifetime acceleration upon ion addition at pH 2. The MD simulations demonstrated that there is no DL contribution to the vSFG at the fully hydroxylated (pH 2) silica–water interface and hence confirmed that the acceleration of interfacial relaxation dynamics can only be due to the ion-induced changes in the BIL structure, which in turn alter the intermolecular coupling and affect the BIL dynamics. In more details, we have seen that ions change both water–water interactions and SiOH–water interactions. The question remains as to which is responsible for the experimentally measured changes in  $T_1$ . The SiOH vibrations are expected to exhibit slower relaxation dynamics than OH vibrations of water as the former do not have access to Fermi resonance coupling (which is known to be a major OH vibrational relaxation pathway<sup>51,64–68</sup>) into its SiOH bend overtone due to the large energy mismatch. The SiOH bend mode is at  $\sim 800$   $\text{cm}^{-1}$ , and thus, its overtone is at  $\sim 1600$   $\text{cm}^{-1}$ , which is far away from the SiOH stretch vibrational modes ( $>3000$   $\text{cm}^{-1}$ ).<sup>56</sup> This is consistent with time-resolved measurements done in the 1980s by Cavanagh et al.<sup>69</sup> which determined the vibrational lifetime for hydroxyls at the silica–vacuum interface as  $\sim 200$  ps, which decreased to  $\sim 56$  ps in the presence of significant amounts of physisorbed water ( $S$   $\text{H}_2\text{O}/100$   $\text{\AA}^2$ ). In our study, the silica hydroxyls are H-bonded to adjacent water and thus are expected to have a shorter vibrational lifetime than  $\sim 200$  ps, but it is highly unlikely to be anywhere close to the 100s of femtosecond time-scales we measure. Moreover, SiOH–water couplings are weakened by increasing ion concentration due to ion breaking of water–surface HBs (as discussed before). This would reasonably provoke a slowdown in the SiOH relaxation due to reduced connections to the aqueous environment. In light of all of this,

SiOH group dynamics would explain an increase in  $T_1$ , not a decrease (as observed experimentally). Based on this, we can argue that the SiOH–water coupling contribution to the overall relaxation within the BIL is much less important than the one from water–water couplings. This is consistent with the fact that water molecules in the BIL are much more abundant than surface silanols (from MD simulations, we calculate an average of 12.4 BIL waters/ $\text{nm}^2$  vs 4.5 SiOH/ $\text{nm}^2$ ), as well as with water providing the dominant contribution to the vSFG intensity of silica–water interfaces in the OH-stretching region. From integration of the theoretical vSFG spectra,<sup>29,47</sup> we find that water contributes 76% of the imaginary  $\chi^{(2)}$  vSFG spectra in the 3000–3800  $\text{cm}^{-1}$  range, while surface SiOH groups only contribute 24% at frequencies  $<3300$   $\text{cm}^{-1}$ . This 24% value is further reduced to  $\sim 6\%$  when considering that we are measuring the  $|\chi^{(2)}|^2$  signal in this study.

What remain to be evaluated are the ion-induced water–water couplings within the BIL as the reason for the acceleration of  $T_1$  at pH 2 (and 6) when ions are introduced. As mentioned above, Fermi resonance coupling is known to be a major OH vibrational relaxation pathway.<sup>51,64–68</sup> Since the  $\text{H}_2\text{O}$  bend mode is at  $\sim 1650$   $\text{cm}^{-1}$  (and so its overtone is at  $\sim 3300$   $\text{cm}^{-1}$ , without accounting for anharmonicity), there is Fermi resonance coupling between the  $\text{H}_2\text{O}$  stretch vibrations and the  $\text{H}_2\text{O}$  bend. Therefore, an ion-induced increase in water–water interactions is expected to lead to efficient coupling thereby accelerating the vibrational energy transfer and causing a decrease in  $T_1$ . Additional evidence comes from comparing the BIL water structure and  $T_1$  lifetimes at the silica–water and the air–water interfaces. As discussed previously, the BIL structure at the air–water interface is dominated by water–water couplings resulting in a 2D-HB-network, and the  $T_1$  for this hydrogen bonded water has been experimentally measured to be 200–300 fs.<sup>70–73</sup> Similarly, ion-induced water–water coupling resulting in a 2D-HB-network is detected for the silica–water interface, and consequently,  $T_1$  of 250 fs is also measured. This correlation between the BIL structure and the  $T_1$  lifetime at two different interfaces supports our claim that ion-induced water–water coupling is responsible for the reduction of  $T_1$ .

We further suggest that the acceleration of interfacial relaxation processes with increasing NaCl concentration is justified not only by the ion-induced increased HB-connectivity within the BIL (increased water–water couplings) but also by the net reduction in the number of “strongly undercoordinated” water molecules at the interface (blue water in Figure 4), which are expected to have the slowest relaxation due to the reduced connectivity with the environment.

In light of these findings, the slow  $T_1$  lifetime ( $T_1 = 577 \pm 140$  fs) measured for the neat interface at pH 2 conditions can be ascribed to the substantial density of undercoordinated water molecules (40%) and weak H-bond interconnectivity within the out-of-plane ordered BIL. The ion-induced in-plane ordering provokes the acceleration in the vibrational relaxation processes within the BIL, from  $T_1 \sim 600$  fs, typical of the water out-of-plane ordering, to  $T_1 \sim 250$  fs, typical of the water in-plane ordering, that is reminiscent of the fast vibrational relaxation measured for the air–water interface. The same microscopic mechanism revealed for pH 2 also rationalizes the acceleration of  $T_1$  at pH 6 in the presence of high salt concentration. Such an acceleration at pH 6 has been observed previously<sup>22</sup> and was hypothesized to be due to ion-induced

interfacial ordering, but in this study, we are able to provide, for the first time, a molecular mechanism that explains the  $T_1$  acceleration at the silica–electrolyte interface. Even though we are mainly probing the BIL water at pH 2 and pH 6 (with salt), it is important to note that the absolute values of  $T_1$  are not strictly identical (Figure 2B), presumably reflecting the structural variations of surface silanol groups at the two pH conditions, including the difference in the ionic species enrichment at the neutral vs charged silica surface (see the scheme in Figure 2).<sup>75</sup> Nevertheless, the ratio in the  $T_1$  values at the two ionic concentrations is identical: water systematically relaxes 1.7 times faster at the higher 0.5 M ionic concentration due to the highly interconnected 2D-HB-network formed in the BIL.

Finally, the transition from out-of-plane to in-plane ordering of BIL water due to breaking of water–surface HBs (vSFG active since oriented along the normal to the surface) and consequent formation of intra-BIL water–water H-bonds (non-vSFG active due to the orientation parallel to the surface) also explains the microscopic origin of the previously discussed decrease (albeit small) of the SS-vSFG (ppp) signal when ions adsorb at the neutral silica–water interface.<sup>35</sup>

## CONCLUSIONS

In conclusion, the interplay between experimental vibrational dynamics measurements and the interfacial structural characterization by theory provides a compelling combination to reveal the ion adsorption process at silica–water interfaces and its effect on interfacial structure and dynamics, as a function of pH/electrolytes conditions. At highly and moderately charged silica–water interfaces (pH > 6), cations are preferentially adsorbed at the surface, and their major impact on the interfacial arrangement is screening the surface charge, as expected from GC theory. However, more subtle molecular changes in the BIL are hidden below the dominant DL contribution at these high pH conditions. As revealed by both experiments and simulations performed in this work, such changes manifest at low surface charges (pH < 6) and high ionic concentrations, and they cannot be rationalized by pure electrostatic models as they are driven by local chemistry associated with the ion adsorption processes.

We here show, for the first time, that the acceleration of interfacial vibrational energy relaxation is due to the kosmotropic effect of ions that drive in-plane ordering of water within the BIL, the topmost interfacial layer. This deeper understanding of such a phenomenon, which is beyond the existing GC/SGC theories, represents a key ingredient in the development of more accurate models for describing electrolytic interfaces. Ions such as KCl and NaCl are hence shown to be able to form innersphere complexes at the silica surface, even at low pH (i.e., around PZC) conditions. This requires breaking of previously existing water–surface HBs, thereby forming local “hydrophobic” areas on the silica surface, which adds to the already present hydrophobic patches (silanol poor areas) in the BIL. In such ion-induced hydrophobic domains, water rearranges by forming the extended 2D-HB-network, similar to the canonical air–water interface. TR-vSFG experiments, directly probing interfacial vibrational dynamics, are shown to be a powerful tool to reveal such BIL structural transitions, which is modulated by the delicate balance between water–surface and water–water interactions and is marked by the ion-induced acceleration of interfacial vibrational relaxation.

The methodology employed here for aqueous silica interfaces can be broadly applied to reveal the kosmotropic/chaotropic nature of ions at other aqueous interfaces: TR-vSFG experiments provide a direct measure of BIL water ordering/disordering, while DFT-MD simulations unveil the underlying microscopic mechanisms.

## ASSOCIATED CONTENT

### Supporting Information

The Supporting Information is available free of charge at <https://pubs.acs.org/doi/10.1021/jacs.9b13273>.

Experimental and theoretical methods, additional information on the experimental vSFG setup and sample preparation, the model used to describe vibrational dynamics of O–H in water, calculations of the surface electric potential at the silica–water interface, AIMD/DFT-based molecular dynamics simulations and their interpretation in terms of BIL (binding interfacial layer) and DL (diffuse layer), and the model used to separate BIL/DL contributions to TR-vSFG (PDF)

## AUTHOR INFORMATION

### Corresponding Authors

Marie-Pierre Gageot – LAMBE UMR8587, Université d'Evry val d'Essonne, CNRS, CEA, Université Paris-Saclay, 91025 Evry, France; [orcid.org/0000-0002-3409-5824](https://orcid.org/0000-0002-3409-5824); Email: [mgageot@univ-evry.fr](mailto:mgageot@univ-evry.fr)

Eric Borguet – Department of Chemistry, Temple University, Philadelphia, Pennsylvania 19122, United States; [orcid.org/0000-0003-0593-952X](https://orcid.org/0000-0003-0593-952X); Email: [eborguet@temple.edu](mailto:eborguet@temple.edu)

### Authors

Aashish Tuladhar – Physical Sciences Division, Physical & Computational Sciences Directorate, Pacific Northwest National Laboratory, Richland, Washington 99352, United States; Department of Chemistry, Temple University, Philadelphia, Pennsylvania 19122, United States; [orcid.org/0000-0003-2449-4984](https://orcid.org/0000-0003-2449-4984)

Shalaka Dewan – Department of Chemistry, Temple University, Philadelphia, Pennsylvania 19122, United States

Simone Pezzotti – LAMBE UMR8587, Université d'Evry val d'Essonne, CNRS, CEA, Université Paris-Saclay, 91025 Evry, France

Flavio Siro Brigiano – LAMBE UMR8587, Université d'Evry val d'Essonne, CNRS, CEA, Université Paris-Saclay, 91025 Evry, France

Fabrizio Creazzo – LAMBE UMR8587, Université d'Evry val d'Essonne, CNRS, CEA, Université Paris-Saclay, 91025 Evry, France

Complete contact information is available at:

<https://pubs.acs.org/doi/10.1021/jacs.9b13273>

### Author Contributions

<sup>†</sup>A.T., S.D., and S.P. contributed equally to this work.

### Notes

The authors declare no competing financial interest.

## ACKNOWLEDGMENTS

The authors acknowledge the National Science Foundation for supporting this work (NSF Grants CHE 1337880 and MRI 1828421) and thank Dr. Ali Eftekhari-Bafrooei for helpful discussions and Dr. Mark DelloStritto for helping in making

the contour plots. A.T. acknowledges the support provided by the US Department of Energy (DOE), Office of Science, Office of Basic Energy Sciences, Materials Sciences and Engineering Division and Chemical Sciences, Geosciences, and Biosciences Division at The Pacific Northwest National Laboratory, operated by Battelle for the US Department of Energy (DOE) under Contract DE-AC05-76RL01830. HPC resources from GENCI-France Grant 072484 (CINES/IDRIS/TGCC) are acknowledged. S.P., F.S.B., F.C., and M.-P.G. acknowledge that this work was done under funding by ANR DYNAWIN Grant 14-CE35-0011-01 and LABEX CHARMA<sub>3</sub>T 11- LABEX-0039/ANR-11-IDEX-0003-02 "Excellence Laboratory" program of the University Paris-Saclay. The authors thank Dr. Daria Ruth Galimberti for discussions and advice.

## REFERENCES

- (1) Dessler, A. E.; Sherwood, S. C. A Matter of Humidity. *Science* **2009**, *323*, 1020–1021.
- (2) Jung, M.; Reichstein, M.; Schwalm, C. R.; Huntingford, C.; Sitch, S.; Ahlström, A.; Arneth, A.; Camps-Valls, G.; Ciais, P.; Friedlingstein, P.; Gans, F.; Ichii, K.; Jain, A. K.; Kato, E.; Papale, D.; Poulter, B.; Raduly, B.; Rödenbeck, C.; Tramontana, G.; Viovy, N.; Wang, Y.-P.; Weber, U.; Zaehle, S.; Zeng, N. Compensatory Water Effects Link Yearly Global Land CO<sub>2</sub> Sink Changes to Temperature. *Nature* **2017**, *541*, 516–520.
- (3) Ball, P. Water is an Active Matrix of Life for Cell and Molecular Biology. *Proc. Natl. Acad. Sci. U. S. A.* **2017**, *114*, 13327–13335.
- (4) Maddox, J. Putting Molecular Biology into Water. *Nature* **1993**, *364*, 669.
- (5) Chaplin, M. Do We Underestimate the Importance of Water in Cell Biology? *Nat. Rev. Mol. Cell Biol.* **2006**, *7*, 861–866.
- (6) Chen, S.; Itoh, Y.; Masuda, T.; Shimizu, S.; Zhao, J.; Ma, J.; Nakamura, S.; Okuro, K.; Noguchi, H.; Uosaki, K.; Aida, T. Subnanoscale Hydrophobic Modulation of Salt Bridges in Aqueous Media. *Science* **2015**, *348*, 555–559.
- (7) Ojha, L.; Wilhelm, M. B.; Murchie, S. L.; McEwen, A. S.; Wray, J. J.; Hanley, J.; Massé, M.; Chojnacki, M. Spectral Evidence for Hydrated Salts in Recurring Slope Lineae on Mars. *Nat. Geosci.* **2015**, *8*, 829–832.
- (8) McEwen, A. S.; Ojha, L.; Dundas, C. M.; Mattson, S. S.; Byrne, S.; Wray, J. J.; Cull, S. C.; Murchie, S. L.; Thomas, N.; Gulick, V. C. Seasonal Flows on Warm Martian Slopes. *Science* **2011**, *333*, 740–743.
- (9) Sposito, G.; Skipper, N. T.; Sutton, R.; Park, S.-h.; Soper, A. K.; Greathouse, J. A. Surface Geochemistry of the Clay Minerals. *Proc. Natl. Acad. Sci. U. S. A.* **1999**, *96*, 3358–3364.
- (10) Pekel, J.-F.; Cottam, A.; Gorelick, N.; Belward, A. S. High-Resolution Mapping of Global Surface Water and its Long-Term Changes. *Nature* **2016**, *540*, 418–422.
- (11) Tunuguntla, R. H.; Henley, R. Y.; Yao, Y.-C.; Pham, T. A.; Wanunu, M.; Noy, A. Enhanced Water Permeability and Tunable Ion Selectivity in Subnanometer Carbon Nanotube Porins. *Science* **2017**, *357*, 792–796.
- (12) Franzese, G.; Bianco, V. Water at Biological and Inorganic Interfaces. *Food Biophys.* **2013**, *8*, 153–169.
- (13) Shelton, D. P. Water-Water Correlations in Electrolyte Solutions Probed by Hyper-Rayleigh Scattering. *J. Chem. Phys.* **2017**, *147*, 214505.
- (14) Chen, Y.; Okur, H. I.; Dupertuis, N.; Dedic, J.; Wilkins, D. M.; Ceriotti, M.; Roke, S. Comment on "Water-Water Correlations in Electrolyte Solutions Probed by Hyper-Rayleigh Scattering" [*J. Chem. Phys.* **147**, 214505 (2017)]. *J. Chem. Phys.* **2018**, *149*, 167101.
- (15) Shelton, D. P. Response to "Comment on 'Water-Water Correlations in Electrolyte Solutions Probed by Hyper-Rayleigh Scattering'" [*J. Chem. Phys.* **149**, 167101 (2018)]. *J. Chem. Phys.* **2018**, *149*, 167102.
- (16) Chan, Y. C.; Wong, K. Y. Study of the Pair Correlations Between P-Nitroaniline Molecules in Solution by Depolarized Hyper-Rayleigh Scattering. *J. Chem. Phys.* **2012**, *136*, 174514.
- (17) O'Brien, J. T.; Williams, E. R. Effects of Ions on Hydrogen-Bonding Water Networks in Large Aqueous Nanodrops. *J. Am. Chem. Soc.* **2012**, *134*, 10228–10236.
- (18) Smith, J. D.; Saykally, R. J.; Geissler, P. L. The Effects of Dissolved Halide Anions on Hydrogen Bonding in Liquid Water. *J. Am. Chem. Soc.* **2007**, *129*, 13847–13856.
- (19) Lin, Y. S.; Auer, B. M.; Skinner, J. L. Water Structure, Dynamics, and Vibrational Spectroscopy in Sodium Bromide Solutions. *J. Chem. Phys.* **2009**, *131*, 144511.
- (20) Omta, A. W.; Kropman, M. F.; Woutersen, S.; Bakker, H. J. Negligible Effect of Ions on the Hydrogen-Bond Structure in Liquid Water. *Science* **2003**, *301*, 347–349.
- (21) Eftekhari-Bafrooei, A.; Borguet, E. Effect of Surface Charge on the Vibrational Dynamics of Interfacial Water. *J. Am. Chem. Soc.* **2009**, *131*, 12034–12035.
- (22) Eftekhari-Bafrooei, A.; Borguet, E. Effect of Electric Fields on the Ultrafast Vibrational Relaxation of Water at a Charged Solid-Liquid Interface as Probed by Vibrational Sum Frequency Generation. *J. Phys. Chem. Lett.* **2011**, *2*, 1353–1358.
- (23) Ohno, P. E.; Chang, H.; Spencer, A. P.; Liu, Y.; Boamah, M. D.; Wang, H.-f.; Geiger, F. M. Beyond the Gouy–Chapman Model with Heterodyne-Detected Second Harmonic Generation. *J. Phys. Chem. Lett.* **2019**, *10*, 2328–2334.
- (24) Darlington, A. M.; Jarisz, T. A.; Dewalt-Kerian, E. L.; Roy, S.; Kim, S.; Azam, M. S.; Hore, D. K.; Gibbs, J. M. Separating the pH-Dependent Behavior of Water in the Stern and Diffuse Layers with Varying Salt Concentration. *J. Phys. Chem. C* **2017**, *121*, 20229–20241.
- (25) DeWalt-Kerian, E. L.; Kim, S.; Azam, M. S.; Zeng, H. B.; Liu, Q. X.; Gibbs, J. M. pH-Dependent Inversion of Hofmeister Trends in the Water Structure of the Electrical Double Layer. *J. Phys. Chem. Lett.* **2017**, *8*, 2855–2861.
- (26) Macias-Romero, C.; Nahalka, I.; Okur, H. I.; Roke, S. Optical Imaging of Surface Chemistry and Dynamics in Confinement. *Science* **2017**, *357*, 784–788.
- (27) Chapman, D. L. A Contribution to the Theory of Electrocappilarity. *Philos. Mag.* **1913**, *25*, 475–481.
- (28) Grahame, D. C. The Electrical Double Layer and the Theory of Electrocappilarity. *Chem. Rev.* **1947**, *41*, 441–501.
- (29) Cyran, J. D.; Donovan, M. A.; Vollmer, D.; Siro Brigiano, F.; Pezzotti, S.; Galimberti, D. R.; Gaigeot, M.-P.; Bonn, M.; Backus, E. H. G. Molecular Hydrophobicity at a Macroscopically Hydrophilic Surface. *Proc. Natl. Acad. Sci. U. S. A.* **2019**, *116*, 1520–1525.
- (30) Covert, P. A.; Jena, K. C.; Hore, D. K. Throwing Salt into the Mix: Altering Interfacial Water Structure by Electrolyte Addition. *J. Phys. Chem. Lett.* **2014**, *5*, 143–148.
- (31) Jena, K. C.; Covert, P. A.; Hore, D. K. The Effect of Salt on the Water Structure at a Charged Solid Surface: Differentiating Second- and Third-order Nonlinear Contributions. *J. Phys. Chem. Lett.* **2011**, *2*, 1056–1061.
- (32) Hore, D. K.; Tyrode, E. Probing Charged Aqueous Interfaces Near Critical Angles: Effect of Varying Coherence Length. *J. Phys. Chem. C* **2019**, *123*, 16911–16920.
- (33) Dalstein, L.; Potapova, E.; Tyrode, E. The Elusive Silica/Water Interface: Isolated Silanols Under Water as Revealed by Vibrational Sum Frequency Spectroscopy. *Phys. Chem. Chem. Phys.* **2017**, *19*, 10343–10349.
- (34) Du, Q.; Freysz, E.; Shen, Y. R. Vibrational Spectra of Water Molecules at Quartz/Water Interfaces. *Phys. Rev. Lett.* **1994**, *72*, 238–241.
- (35) Dewan, S.; Yeganeh, M. S.; Borguet, E. Experimental Correlation Between Interfacial Water Structure and Mineral Reactivity. *J. Phys. Chem. Lett.* **2013**, *4*, 1977–1982.
- (36) Yang, Z.; Li, Q.; Chou, K. C. Structures of Water Molecules at the Interfaces of Aqueous Salt Solutions and Silica: Cation Effects. *J. Phys. Chem. C* **2009**, *113*, 8201–8205.

- (37) Myalitsin, A.; Urashima, S.-h.; Nihonyanagi, S.; Yamaguchi, S.; Tahara, T. Water Structure at the Buried Silica/Aqueous Interface Studied by Heterodyne-Detected Vibrational Sum-Frequency Generation. *J. Phys. Chem. C* **2016**, *120*, 9357–9363.
- (38) Ostroverkhov, V.; Waychunas, G. A.; Shen, Y. R. Vibrational Spectra of Water at Water/ $\alpha$ -Quartz (0001) Interface. *Chem. Phys. Lett.* **2004**, *386*, 144–148.
- (39) Lis, D.; Backus, E. H. G.; Hunger, J.; Parekh, S. H.; Bonn, M. Liquid Flow Along a Solid Surface Reversibly Alters Interfacial Chemistry. *Science* **2014**, *344*, 1138–1142.
- (40) Urashima, S.-h.; Myalitsin, A.; Nihonyanagi, S.; Tahara, T. The Topmost Water Structure at a Charged Silica/Aqueous Interface Revealed by Heterodyne-Detected Vibrational Sum Frequency Generation Spectroscopy. *J. Phys. Chem. Lett.* **2018**, *9*, 4109–4114.
- (41) McGuire, J. A.; Shen, Y. R. Ultrafast Vibrational Dynamics at Water Interfaces. *Science* **2006**, *313*, 1945–1948.
- (42) Eftekhari-Bafrooei, A.; Borguet, E. Effect of Hydrogen-Bond Strength on the Vibrational Relaxation of Interfacial Water. *J. Am. Chem. Soc.* **2010**, *132*, 3756–3761.
- (43) Wen, Y.-C.; Zha, S.; Liu, X.; Yang, S.; Guo, P.; Shi, G.; Fang, H.; Shen, Y. R.; Tian, C. Unveiling Microscopic Structures of Charged Water Interfaces by Surface-Specific Vibrational Spectroscopy. *Phys. Rev. Lett.* **2016**, *116*, 016101.
- (44) Pezzotti, S.; Galimberti, D. R.; Shen, Y. R.; Gaigeot, M.-P. Structural Definition of the BIL and DL: a New Universal Methodology to Rationalize Non-Linear  $\chi^{(2)}(\omega)$  SFG Signals at Charged Interfaces, Including  $\chi^{(3)}(\omega)$  Contributions. *Phys. Chem. Chem. Phys.* **2018**, *20*, 5190–5199.
- (45) Dove, P. M. The Dissolution Kinetics of Quartz in Sodium Chloride Solutions at 25 Degrees to 300 Degrees C. *Am. J. Sci.* **1994**, *294*, 665–712.
- (46) Pezzotti, S.; Galimberti, D.; Shen, Y.; Gaigeot, M.-P. What the Diffuse Layer (DL) Reveals in Non-Linear SFG Spectroscopy. *Minerals* **2018**, *8*, 305.
- (47) Pezzotti, S.; Galimberti, D. R.; Gaigeot, M.-P. Deconvolution of BIL-SFG and DL-SFG spectroscopic signals reveals order/disorder of water at the elusive aqueous silica interface. *Phys. Chem. Chem. Phys.* **2019**, *21*, 22188–22202.
- (48) Ohno, P. E.; Saslow, S. A.; Wang, H.-f.; Geiger, F. M.; Eiseenthal, K. B. Phase-Referenced Nonlinear Spectroscopy of the  $\alpha$ -Quartz/Water Interface. *Nat. Commun.* **2016**, *7*, 13587.
- (49) Gonella, G.; Lütgebaucks, C.; de Beer, A. G. F.; Roke, S. Second Harmonic and Sum-Frequency Generation from Aqueous Interfaces Is Modulated by Interference. *J. Phys. Chem. C* **2016**, *120*, 9165–9173.
- (50) Fecko, C. J.; Eaves, J. D.; Loparo, J. J.; Tokmakoff, A.; Geissler, P. L. Ultrafast Hydrogen-Bond Dynamics in the Infrared Spectroscopy of Water. *Science* **2003**, *301*, 1698–1702.
- (51) Lock, A. J.; Bakker, H. J. Temperature Dependence of Vibrational Relaxation in Liquid H<sub>2</sub>O. *J. Chem. Phys.* **2002**, *117*, 1708–1713.
- (52) Cowan, M. L.; Bruner, B. D.; Huse, N.; Dwyer, J. R.; Chugh, B.; Nibbering, E. T. J.; Elsaesser, T.; Miller, R. J. D. Ultrafast Memory Loss and Energy Redistribution in the Hydrogen Bond Network of Liquid H<sub>2</sub>O. *Nature* **2005**, *434*, 199–202.
- (53) Campen, R. K.; Pymmer, A. K.; Nihonyanagi, S.; Borguet, E. Linking Surface Potential and Deprotonation in Nanoporous Silica: Second Harmonic Generation and Acid/Base Titration. *J. Phys. Chem. C* **2010**, *114*, 18465–18473.
- (54) Pezzotti, S.; Galimberti, D. R.; Gaigeot, M.-P. 2D H-Bond Network as the Topmost Skin to the Air–Water Interface. *J. Phys. Chem. Lett.* **2017**, *8*, 3133–3141.
- (55) Pezzotti, S.; Serva, A.; Gaigeot, M.-P. 2D-HB-Network at the Air-Water Interface: A Structural and Dynamical Characterization by Means of Ab Initio and Classical Molecular Dynamics Simulations. *J. Chem. Phys.* **2018**, *148*, 174701.
- (56) Isaenko, O.; Borguet, E. Hydrophobicity of Hydroxylated Amorphous Fused Silica Surfaces. *Langmuir* **2013**, *29*, 7885–7895.
- (57) Pfeiffer-Laplaud, M.; Gaigeot, M.-P. Electrolytes at the Hydroxylated (0001)  $\alpha$ -Quartz/Water Interface: Location and Structural Effects on Interfacial Silanols by DFT-Based MD. *J. Phys. Chem. C* **2016**, *120*, 14034–14047.
- (58) Pfeiffer-Laplaud, M.; Gaigeot, M.-P. Adsorption of Singly Charged Ions at the Hydroxylated (0001)  $\alpha$ -Quartz/Water Interface. *J. Phys. Chem. C* **2016**, *120*, 4866–4880.
- (59) Wang, R.; DelloStritto, M.; Remsing, R. C.; Carnevale, V.; Klein, M. L.; Borguet, E. Sodium Halide Adsorption and Water Structure at the  $\alpha$ -Alumina(0001)/Water Interface. *J. Phys. Chem. C* **2019**, *123*, 15618–15628.
- (60) Serva, A.; Pezzotti, S.; Bougueroua, S.; Galimberti, D. R.; Gaigeot, M.-P. Combining Ab-Initio and Classical Molecular Dynamics Simulations to Unravel the Structure of the 2D-HB-Network at the Air-Water Interface. *J. Mol. Struct.* **2018**, *1165*, 71–78.
- (61) Kubicki, J. D.; Sofo, J. O.; Skelton, A. A.; Bandura, A. V. A New Hypothesis for the Dissolution Mechanism of Silicates. *J. Phys. Chem. C* **2012**, *116*, 17479–17491.
- (62) DelloStritto, M. J.; Kubicki, J. D.; Sofo, J. O. Effect of Ions on H-Bond Structure and Dynamics at the Quartz(101)–Water Interface. *Langmuir* **2016**, *32*, 11353–11365.
- (63) DelloStritto, M. J.; Kubicki, J.; Sofo, J. O. Density Functional Theory Simulation of Hydrogen-Bonding Structure and Vibrational Densities of States at the Quartz (1 0 1)-Water Interface and its Relation to Dissolution as a Function of Solution pH and Ionic Strength. *J. Phys.: Condens. Matter* **2014**, *26*, 244101.
- (64) Lindner, J.; Vöhringer, P.; Pshenichnikov, M. S.; Cringus, D.; Wiersma, D. A.; Mostovoy, M. Vibrational Relaxation of Pure Liquid Water. *Chem. Phys. Lett.* **2006**, *421*, 329–333.
- (65) Ashihara, S.; Huse, N.; Espagne, A.; Nibbering, E. T. J.; Elsaesser, T. Ultrafast Structural Dynamics of Water Induced by Dissipation of Vibrational Energy. *J. Phys. Chem. A* **2007**, *111*, 743–746.
- (66) Bakker, H. J.; Skinner, J. L. Vibrational Spectroscopy as a Probe of Structure and Dynamics in Liquid Water. *Chem. Rev.* **2010**, *110*, 1498–1517.
- (67) Lawrence, C. P.; Skinner, J. L. Vibrational Spectroscopy of HOD in Liquid D<sub>2</sub>O. VI. Intramolecular and Intermolecular Vibrational Energy Flow. *J. Chem. Phys.* **2003**, *119*, 1623–1633.
- (68) Rey, R.; Hynes, J. T. Vibrational Energy Relaxation of HOD in Liquid D<sub>2</sub>O. *J. Chem. Phys.* **1996**, *104*, 2356–2368.
- (69) Heilweil, E. J.; Casassa, M. P.; Cavanagh, R. R.; Stephenson, J. C. Vibrational Deactivation of Surface OH Chemisorbed on SiO<sub>2</sub>: Solvent Effects. *J. Chem. Phys.* **1985**, *82*, 5216–5231.
- (70) Inoue, K.-i.; Ishiyama, T.; Nihonyanagi, S.; Yamaguchi, S.; Morita, A.; Tahara, T. Efficient Spectral Diffusion at the Air/Water Interface Revealed by Femtosecond Time-Resolved Heterodyne-Detected Vibrational Sum Frequency Generation Spectroscopy. *J. Phys. Chem. Lett.* **2016**, *7*, 1811–1815.
- (71) Hsieh, C.-S.; Okuno, M.; Hunger, J.; Backus, E. H. G.; Nagata, Y.; Bonn, M. Aqueous Heterogeneity at the Air/Water Interface Revealed by 2D-HD-SFG Spectroscopy. *Angew. Chem., Int. Ed.* **2014**, *53*, 8146–8149.
- (72) Zhang, Z.; Piatkowski, L.; Bakker, H. J.; Bonn, M. Ultrafast Vibrational Energy Transfer at the Water/Air Interface Revealed by Two-Dimensional Surface Vibrational Spectroscopy. *Nat. Chem.* **2011**, *3*, 888–893.
- (73) Van Der Post, S. T.; Hsieh, C.-S.; Okuno, M.; Nagata, Y.; Bakker, H. J.; Bonn, M.; Hunger, J. Strong Frequency Dependence of Vibrational Relaxation in Bulk and Surface Water Reveals Sub-Picosecond Structural Heterogeneity. *Nat. Commun.* **2015**, *6*, 8384.
- (74) Wang, H.; Xu, Q.; Liu, Z.; Tang, Y.; Wei, G.; Shen, Y. R.; Liu, W.-T. Gate-Controlled Sum-Frequency Vibrational Spectroscopy for Probing Charged Oxide/Water Interfaces. *J. Phys. Chem. Lett.* **2019**, *10* (19), 5943–5948.
- (75) Dewan, S.; Carnevale, V.; Bankura, A.; Eftekhari-Bafrooei, A.; Fiorin, G.; Klein, M. L.; Borguet, E. The Structure of Water at Charged Interfaces: A Molecular Dynamics Study. *Langmuir* **2014**, *30* (27), 8056–8065.



# Bibliography

- [1] U. S. E. I. Administration, *Annual Energy Outlook 2015*, 2015.
- [2] G. Team, *ASA Goddard Institute for Space Studies*, 2009.
- [3] L. Sousa, *Energy Vision 2050-Part I*, 2008.
- [4] T. Stocker, D. Qin, G. K. Plattner, M. Tignor, S. K. Allen, J. Boschung, A. Nauels, Y. Xia, V. Bex and P. M. Midgley, *Cambridge University Press*, 2013.
- [5] C. B. Field, V. R. Barros, K. J. Mach and et al., *Cambridge University Press*, 2014, 35–94.
- [6] R. Fischer, E. M.; Knutti, *Nat. Clim. Chang.*, 2015, **5**, 560–564.
- [7] G. P. Peters, R. M. Andrew, T. Boden, J. G. Canadell, P. Ciais, C. Le Quéré, G. Marland, M. R. Raupach and C. Wilson, *Nature Climate Change*, 2012, **3**, 4.
- [8] N. R. Council et al., *Advancing the science of climate change. National Research Council*, 2010.
- [9] N. S. Lewis and D. G. Nocera, *Proceedings of the National Academy of Sciences*, 2006, **103**, 15729–15735.
- [10] D. Gust, T. A. Moore and A. L. Moore, *Accounts of Chemical Research*, 2001, **34**, 40–48.
- [11] N.-S. Choi, Z. Chen, S. A. Freunberger, X. Ji, Y.-K. Sun, K. Amine, G. Yushin, L. F. Nazar, J. Cho and P. G. Bruce, *Angewandte Chemie International Edition*, 2012, **51**, 9994–10024.
- [12] D. G. Nocera, *Accounts of chemical research*, 2012, **45**, 767–776.
- [13] K. S. Joya, Y. F. Joya, K. Ocakoglu and R. van de Krol, *Angewandte Chemie International Edition*, 2013, **52**, 10426–10437.
- [14] D. Rojas, J. Beermann, S. Klein and D. Reindl, *Solar Energy*, 2008, **82**, 746–757.
- [15] N. M. Villar, J. C. López, F. D. Muñoz, E. R. García and A. C. Andrés, *Solar energy*, 2009, **83**, 1086–1092.

- [16] R. Tang, Y. Yang and W. Gao, *Solar Energy*, 2011, **85**, 1381–1389.
- [17] K. Sankaranarayanan, H. J. Van Der Kooi and J. de Swaan Arons, *Efficiency and sustainability in the energy and chemical industries: scientific principles and case studies*, Crc Press, 2010.
- [18] L. W. Jones, 1970.
- [19] S. Barrett *et al.*, *Fuel Cells Bulletin*, 2011, **2011**, 12–15.
- [20] P. Lucchese, E. Ohira and J. Leaver, 2019.
- [21] I. Roger, M. A. Shipman and M. D. Symes, *Nature Reviews Chemistry*, 2017, **1**, 0003.
- [22] J. Wang, W. Cui, Q. Liu, Z. Xing, A. M. Asiri and X. Sun, *Advanced materials*, 2016, **28**, 215–230.
- [23] C. C. McCrory, S. Jung, J. C. Peters and T. F. Jaramillo, *Journal of the American Chemical Society*, 2013, **135**, 16977–16987.
- [24] M. G. Walter, E. L. Warren, J. R. McKone, S. W. Boettcher, Q. Mi, E. A. Santori and N. S. Lewis, *Chemical reviews*, 2010, **110**, 6446–6473.
- [25] T. R. Cook, D. K. Dogutan, S. Y. Reece, Y. Surendranath, T. S. Teets and D. G. Nocera, *Chemical reviews*, 2010, **110**, 6474–6502.
- [26] T. Reier, M. Oezaslan and P. Strasser, *Acs Catalysis*, 2012, **2**, 1765–1772.
- [27] A. Di Blasi, C. D’urso, V. Baglio, V. Antonucci, R. Ornelas, F. Matteucci, G. Orozco, D. Beltran, Y. Meas, L. Arriaga *et al.*, *Journal of Applied Electrochemistry*, 2009, **39**, 191–196.
- [28] Y. Lee, J. Suntivich, K. J. May, E. E. Perry and Y. Shao-Horn, *The journal of physical chemistry letters*, 2012, **3**, 399–404.
- [29] I. C. Man, H.-Y. Su, F. Calle-Vallejo, H. A. Hansen, J. I. Martínez, N. G. Inoglu, J. Kitchin, T. F. Jaramillo, J. K. Nørskov and J. Rossmeisl, *ChemCatChem*, 2011, **3**, 1159–1165.
- [30] J. K. Nørskov, T. Bligaard, J. Rossmeisl and C. H. Christensen, *Nature chemistry*, 2009, **1**, 37.
- [31] J. Rossmeisl, Z.-W. Qu, H. Zhu, G.-J. Kroes and J. K. Nørskov, *Journal of Electroanalytical Chemistry*, 2007, **607**, 83–89.
- [32] J. Chen and A. Selloni, *The Journal of Physical Chemistry Letters*, 2012, **3**, 2808–2814.
- [33] F. Pietrucci and A. M. Saitta, *Proceedings of the National Academy of Sciences*, 2015, **112**, 15030–15035.

- [34] F. Pietrucci, *Reviews in Physics*, 2017, **2**, 32–45.
- [35] G. Cassone, F. Pietrucci, F. Saija, F. Guyot and A. M. Saitta, *Chem. Sci.*, 2017, **8**, 2329–2336.
- [36] A. Messiah, *Quantum mechanics*, 1961.
- [37] W. Kohn, *Rev. Mod. Phys.*, 1999, **71**, 1253–1266.
- [38] M. Born and J. R. Oppenheimer, *Collection of articles for a multimedia electronic educational-methodical complex on the discipline "physics of the atom and atomic phenomena"/ed. Shundalov MB; BSU, Faculty of Physics*, 1927.
- [39] D. R. Hartree, 1928, **24**, 89–110.
- [40] L. H. Thomas, *Mathematical Proceedings of the Cambridge Philosophical Society*, 1927, pp. 542–548.
- [41] E. Fermi, *Rend. Accad. Naz. Lincei*, 1927, **6**, 32.
- [42] P. Hohenberg and W. Kohn, *Physical review*, 1964, **136**, B864.
- [43] W. Kohn and L. J. Sham, *Physical review*, 1965, **140**, A1133.
- [44] W. F. Van Gunsteren and H. J. Berendsen, *Molecular Simulation*, 1988, **1**, 173–185.
- [45] D. Marx and J. Hutter, *Ab initio molecular dynamics: basic theory and advanced methods*, Cambridge University Press, 2009.
- [46] S. Nosé, *The Journal of chemical physics*, 1984, **81**, 511–519.
- [47] W. G. Hoover, *Physical review A*, 1985, **31**, 1695.
- [48] G. J. Martyna, M. L. Klein and M. Tuckerman, *The Journal of chemical physics*, 1992, **97**, 2635–2643.
- [49] G. Bussi, D. Donadio and M. Parrinello, *The Journal of chemical physics*, 2007, **126**, 014101.
- [50] G. Makov and M. Payne, *Physical Review B*, 1995, **51**, 4014.
- [51] J. P. Perdew, K. Burke and M. Ernzerhof, *Physical review letters*, 1996, **77**, 3865.
- [52] J. P. Perdew and Y. Wang, *Physical review B*, 1992, **45**, 13244.
- [53] L. Eyring, K. A. Gschneidner and G. H. Lander, *Handbook on the physics and chemistry of rare earths*, Elsevier, 2002, vol. 32.
- [54] J. Zaanen and G. Sawatzky, *Canadian journal of physics*, 1987, **65**, 1262–1271.

- [55] A. Fujimori, F. Minami and S. Sugano, *Physical Review B*, 1984, **29**, 5225.
- [56] V. I. Anisimov, J. Zaanen and O. K. Andersen, *Physical Review B*, 1991, **44**, 943.
- [57] M. Cococcioni and S. De Gironcoli, *Physical Review B*, 2005, **71**, 035105.
- [58] J. Chen, X. Wu and A. Selloni, *Phys. Rev. B*, 2011, **83**, 245204.
- [59] A. D. Becke, *Physical review A*, 1988, **38**, 3098.
- [60] S. Grimme, *Wiley Interdisciplinary Reviews: Computational Molecular Science*, 2011, **1**, 211–228.
- [61] S. Grimme, J. Antony, S. Ehrlich and H. Krieg, *The Journal of chemical physics*, 2010, **132**, 154104.
- [62] J. VandeVondele, M. Krack, F. Mohamed, M. Parrinello, T. Chassaing and J. Hutter, *Computer Physics Communications*, 2005, **167**, 103–128.
- [63] S. Goedecker, M. Teter and J. Hutter, *Physical Review B*, 1996, **54**, 1703.
- [64] P. Hänggi, P. Talkner and M. Borkovec, *Reviews of modern physics*, 1990, **62**, 251.
- [65] G. M. Torrie and J. P. Valleau, *Journal of Computational Physics*, 1977, **23**, 187–199.
- [66] A. Barducci, G. Bussi and M. Parrinello, *Physical review letters*, 2008, **100**, 020603.
- [67] D. Branduardi, F. L. Gervasio and M. Parrinello, *The Journal of chemical physics*, 2007, **126**, 054103.
- [68] S. Pipolo, M. Salanne, G. Ferlat, S. Klotz, A. M. Saitta and F. Pietrucci, *Physical review letters*, 2017, **119**, 245701.
- [69] R. Nunes and D. Vanderbilt, *Physical review letters*, 1994, **73**, 712.
- [70] R. Nunes and X. Gonze, *Physical Review B*, 2001, **63**, 155107.
- [71] P. Umari and A. Pasquarello, *Physical Review Letters*, 2002, **89**, 157602.
- [72] R. Resta, *Physical Review Letters*, 1998, **80**, 1800.
- [73] R. Resta and D. Vanderbilt, in *Physics of Ferroelectrics*, Springer, 2007, pp. 31–68.
- [74] R. Resta, *Rev. Mod. Phys.*, 1994, **66**, 899–915.
- [75] R. D. King-Smith and D. Vanderbilt, *Phys. Rev. B*, 1993, **47**, 1651–1654.

- [76] M. V. Berry, *Proc. Royal Soc. Lond.*, 1984, **392**, 45–57.
- [77] P. Umari and A. Pasquarello, *Phys. Rev. Lett.*, 2002, **89**, 157602.
- [78] N. J. English and C. J. Waldron, *Phys. Chem. Chem. Phys.*, 2015, **17**, 12407–12440.
- [79] J. Speight, *Lange's Handbook of Chemistry, 70th Anniversary Edition*, McGraw-Hill Companies, Incorporated, 2004.
- [80] D. R. Lide, *CRC handbook of chemistry and physics*, CRC press, 2004, vol. 85.
- [81] O. V. Dorofeeva, V. S. Iorish, V. P. Novikov and D. B. Neumann, *Journal of Physical and Chemical Reference Data*, 2003, **32**, 879–901.
- [82] A. Eibner, *Chem-Ztg*, 1911, **35**, 753–755.
- [83] J. M. Coronado, F. Fresno, M. D. Hernández-Alonso and R. Portela, *Design of advanced photocatalytic materials for energy and environmental applications*, Springer, 2013.
- [84] M. Landau, *Compt Rend*, 1913, **156**, 1894–1896.
- [85] C. F. Goodeve and J. A. Kitchener, *Transactions of the Faraday Society*, 1938, **34**, 902–908.
- [86] A. Fujishima and K. Honda, *nature*, 1972, **238**, 37–38.
- [87] A. J. Nozik, *Applied Physics Letters*, 1977, **30**, 567–569.
- [88] S. Chu, W. Li, Y. Yan, T. Hamann, I. Shih, D. Wang and Z. Mi, *Nano Futures*, 2017, **1**, 022001.
- [89] W. Kreuter and H. Hofmann, *International Journal of Hydrogen Energy*, 1998, **23**, 661–666.
- [90] R. De Levie, *Journal of Electroanalytical Chemistry*, 1999, **476**, 92–93.
- [91] H. Berg, *Review of Polarography*, 2008, **54**, 99–103.
- [92] J. Zhang, L. Zhang, H. Liu, A. Sun and R.-S. Liu, *Electrochemical technologies for energy storage and conversion*, John Wiley & Sons, 2012.
- [93] M.-C. Pera, D. Hissel, H. Gualous and C. Turpin, *Electrochemical components*, Wiley Online Library, 2013.
- [94] P. Millet and S. Grigoriev, *Renewable Hydrogen Technologies: Production, Purification, Storage, Applications and Safety*, 2013, 19–41.
- [95] N. Q. Minh, *Journal of the American Ceramic Society*, 1993, **76**, 563–588.

- [96] M. Laguna-Bercero, *Journal of Power sources*, 2012, **203**, 4–16.
- [97] S. Grigoriev, V. Porembsky and V. Fateev, *International Journal of Hydrogen Energy*, 2006, **31**, 171–175.
- [98] P. Millet, F. Andolfatto and R. Durand, *International Journal of Hydrogen Energy*, 1996, **21**, 87–93.
- [99] M. Miles and M. Thomason, *Journal of the Electrochemical Society*, 1976, **123**, 1459.
- [100] M. Gong and H. Dai, *Nano Research*, 2015, **8**, 23–39.
- [101] S. Siracusano, N. Van Dijk, E. Payne-Johnson, V. Baglio and A. Aricò, *Applied Catalysis B: Environmental*, 2015, **164**, 488–495.
- [102] J. R. McKone, S. C. Marinescu, B. S. Brunschwig, J. R. Winkler and H. B. Gray, *Chemical Science*, 2014, **5**, 865–878.
- [103] E. Antolini, *Acs Catalysis*, 2014, **4**, 1426–1440.
- [104] Y. Gorlin, *Ph.D. thesis*, Stanford University, 2012.
- [105] M. Yagi, E. Tomita, S. Sakita, T. Kuwabara and K. Nagai, *The Journal of Physical Chemistry B*, 2005, **109**, 21489–21491.
- [106] E. Tsuji, A. Imanishi, K.-i. Fukui and Y. Nakato, *Electrochimica Acta*, 2011, **56**, 2009–2016.
- [107] L. Ouattara, S. Fierro, O. Frey, M. Koudelka and C. Comninellis, *Journal of applied electrochemistry*, 2009, **39**, 1361–1367.
- [108] M. Gao, W. Sheng, Z. Zhuang, Q. Fang, S. Gu, J. Jiang and Y. Yan, *Journal of the American Chemical Society*, 2014, **136**, 7077–7084.
- [109] T.-C. Wen and C.-C. Hu, *Journal of the Electrochemical Society*, 1992, **139**, 2158–2163.
- [110] R. Forgie, G. Bugosh, K. Neyerlin, Z. Liu and P. Strasser, *Electrochemical and Solid-State Letters*, 2010, **13**, B36–B39.
- [111] B. S. Yeo and A. T. Bell, *Journal of the American Chemical Society*, 2011, **133**, 5587–5593.
- [112] M. Hamdani, R. Singh and P. Chartier, *Int. J. Electrochem. Sci*, 2010, **5**, 556–577.
- [113] A. J. Esswein, M. J. McMurdo, P. N. Ross, A. T. Bell and T. D. Tilley, *The Journal of Physical Chemistry C*, 2009, **113**, 15068–15072.
- [114] F. Jiao and H. Frei, *Angewandte Chemie International Edition*, 2009, **48**, 1841–1844.

- [115] A. Y. Khodakov, J. Lynch, D. Bazin, B. Rebours, N. Zanier, B. Moisson and P. Chaumette, *Journal of Catalysis*, 1997, **168**, 16–25.
- [116] Y. Matsumoto and E. Sato, *Materials chemistry and physics*, 1986, **14**, 397–426.
- [117] S. Kim, N. Koratkar, T. Karabacak and T.-M. Lu, *Applied Physics Letters*, 2006, **88**, 263106.
- [118] P. Geijer, F. Morvaridi and S. Styring, *Biochemistry*, 2001, **40**, 10881–10891.
- [119] I. Vass and S. Styring, *Biochemistry*, 1991, **30**, 830–839.
- [120] Y. Matsumoto and E. Sato, *Electrochimica Acta*, 1979, **24**, 421–423.
- [121] M. Morita, C. Iwakura and H. Tamura, *Electrochimica Acta*, 1979, **24**, 357–362.
- [122] M. Wiechen, H.-M. Berends and P. Kurz, *Dalton Transactions*, 2012, **41**, 21–31.
- [123] Y. Gorlin and T. F. Jaramillo, *Journal of the American Chemical Society*, 2010, **132**, 13612–13614.
- [124] M. S. El-Deab, M. I. Awad, A. M. Mohammad and T. Ohsaka, *Electrochemistry communications*, 2007, **9**, 2082–2087.
- [125] A. Bergmann, I. Zaharieva, H. Dau and P. Strasser, *Energy & Environmental Science*, 2013, **6**, 2745–2755.
- [126] D. M. Robinson, Y. B. Go, M. Greenblatt and G. C. Dismukes, *Journal of the American Chemical Society*, 2010, **132**, 11467–11469.
- [127] H.-Y. Su, Y. Gorlin, I. C. Man, F. Calle-Vallejo, J. K. Nørskov, T. F. Jaramillo and J. Rossmeisl, *Physical Chemistry Chemical Physics*, 2012, **14**, 14010–14022.
- [128] T. Takashima, K. Hashimoto and R. Nakamura, *Journal of the American Chemical Society*, 2012, **134**, 1519–1527.
- [129] K. L. Pickrahn, S. W. Park, Y. Gorlin, H.-B.-R. Lee, T. F. Jaramillo and S. F. Bent, *Advanced Energy Materials*, 2012, **2**, 1269–1277.
- [130] F. Cheng, J. Shen, B. Peng, Y. Pan, Z. Tao and J. Chen, *Nature chemistry*, 2011, **3**, 79.
- [131] Y. Meng, W. Song, H. Huang, Z. Ren, S.-Y. Chen and S. L. Suib, *Journal of the American Chemical Society*, 2014, **136**, 11452–11464.
- [132] S. L. Suib, *Accounts of chemical research*, 2008, **41**, 479–487.

- [133] S. L. Suib, *Journal of Materials Chemistry*, 2008, **18**, 1623–1631.
- [134] D. M. Robinson, Y. B. Go, M. Mui, G. Gardner, Z. Zhang, D. Mastrogiovanni, E. Garfunkel, J. Li, M. Greenblatt and G. C. Dismukes, *Journal of the American chemical Society*, 2013, **135**, 3494–3501.
- [135] J. Suntivich, K. J. May, H. A. Gasteiger, J. B. Goodenough and Y. Shao-Horn, *Science*, 2011, **334**, 1383–1385.
- [136] R. Singh and B. Lal, *International journal of hydrogen energy*, 2002, **27**, 45–55.
- [137] C. Rangel, C. Soares, R. Silva, M. Carvalho, M. Jorge, A. Gomes and M. Pereira, 61st Annual Meeting of the International Society of Electrochemistry, 2010.
- [138] K. J. May, C. E. Carlton, K. A. Stoerzinger, M. Risch, J. Suntivich, Y.-L. Lee, A. Grimaud and Y. Shao-Horn, *The journal of physical chemistry letters*, 2012, **3**, 3264–3270.
- [139] L. Trotochaud and S. W. Boettcher, *Scripta Materialia*, 2014, **74**, 25–32.
- [140] M. E. Lyons and M. P. Brandon, *Int. J. Electrochem. Sci*, 2008, **3**, 1386–1424.
- [141] A. G. Marrani, V. Novelli, S. Sheehan, D. P. Dowling and D. Dini, *ACS applied materials & interfaces*, 2013, **6**, 143–152.
- [142] D. A. Corrigan, *Journal of The Electrochemical Society*, 1987, **134**, 377–384.
- [143] J. B. Gerken, S. E. Shaner, R. C. Massé, N. J. Porubsky and S. S. Stahl, *Energy & Environmental Science*, 2014, **7**, 2376–2382.
- [144] S. Trasatti and O. Petrii, *Journal of Electroanalytical Chemistry*, 1992, **327**, 353–376.
- [145] L. Trotochaud, J. K. Ranney, K. N. Williams and S. W. Boettcher, *Journal of the American Chemical Society*, 2012, **134**, 17253–17261.
- [146] M. D. Merrill and R. C. Dougherty, *The Journal of Physical Chemistry C*, 2008, **112**, 3655–3666.
- [147] R. D. Smith, M. S. Prévot, R. D. Fagan, S. Trudel and C. P. Berlinguette, *Journal of the American Chemical Society*, 2013, **135**, 11580–11586.
- [148] S. Trudel, E. D. Crozier, R. A. Gordon, P. S. Budnik and R. H. Hill, *Journal of Solid State Chemistry*, 2011, **184**, 1025–1035.
- [149] S. Sharma and B. G. Pollet, *Journal of Power Sources*, 2012, **208**, 96–119.

- [150] E. Antolini, *Applied Catalysis B: Environmental*, 2009, **88**, 1–24.
- [151] F. M. Toma, A. Sartorel, M. Iurlo, M. Carraro, P. Parisse, C. Maccato, S. Rapino, B. R. Gonzalez, H. Amenitsch, T. Da Ros *et al.*, *Nature Chemistry*, 2010, **2**, 826.
- [152] Y. Liang, Y. Li, H. Wang and H. Dai, *Journal of the American Chemical Society*, 2013, **135**, 2013–2036.
- [153] L. Roen, C. Paik and T. Jarvi, *Electrochemical and Solid-State Letters*, 2004, **7**, A19–A22.
- [154] J. Wang, G. Yin, Y. Shao, S. Zhang, Z. Wang and Y. Gao, *Journal of Power sources*, 2007, **171**, 331–339.
- [155] M. Archer, C. Corke and B. Harji, *Electrochimica Acta*, 1987, **32**, 13–26.
- [156] J. Masa, P. Weide, D. Peeters, I. Sinev, W. Xia, Z. Sun, C. Somsen, M. Muhler and W. Schuhmann, *Advanced Energy Materials*, 2016, **6**, 1502313.
- [157] J. A. Haber, Y. Cai, S. Jung, C. Xiang, S. Mitrovic, J. Jin, A. T. Bell and J. M. Gregoire, *Energy & Environmental Science*, 2014, **7**, 682–688.
- [158] Y. Yang, H. Fei, G. Ruan, C. Xiang and J. M. Tour, *ACS nano*, 2014, **8**, 9518–9523.
- [159] R. D. Smith, M. S. Prévot, R. D. Fagan, Z. Zhang, P. A. Sedach, M. K. J. Siu, S. Trudel and C. P. Berlinguette, *Science*, 2013, **340**, 60–63.
- [160] M. W. Kanan and D. G. Nocera, *Science*, 2008, **321**, 1072–1075.
- [161] D. A. Lutterman, Y. Surendranath and D. G. Nocera, *Journal of the American Chemical Society*, 2009, **131**, 3838–3839.
- [162] Y. Surendranath, D. A. Lutterman, Y. Liu and D. G. Nocera, *Journal of the American Chemical Society*, 2012, **134**, 6326–6336.
- [163] M. Dincă, Y. Surendranath and D. G. Nocera, *Proceedings of the National Academy of Sciences*, 2010, **107**, 10337–10341.
- [164] D. K. Bediako, Y. Surendranath and D. G. Nocera, *Journal of the American Chemical Society*, 2013, **135**, 3662–3674.
- [165] C. L. Farrow, D. K. Bediako, Y. Surendranath, D. G. Nocera and S. J. Billinge, *Journal of the American Chemical Society*, 2013, **135**, 6403–6406.
- [166] Y. Surendranath, M. Dinca and D. G. Nocera, *Journal of the American Chemical Society*, 2009, **131**, 2615–2620.

- [167] J. D. Blakemore, H. B. Gray, J. R. Winkler and A. M. Muller, *ACS Catalysis*, 2013, **3**, 2497–2500.
- [168] J. G. McAlpin, Y. Surendranath, M. Dinca, T. A. Stich, S. A. Stoian, W. H. Casey, D. G. Nocera and R. D. Britt, *Journal of the American Chemical Society*, 2010, **132**, 6882–6883.
- [169] D. Friebel, M. Bajdich, B. S. Yeo, M. W. Louie, D. J. Miller, H. S. Casalongue, F. Mbuga, T.-C. Weng, D. Nordlund, D. Sokaras *et al.*, *Physical Chemistry Chemical Physics*, 2013, **15**, 17460–17467.
- [170] R. Boggio, A. Carugati and S. Trasatti, *Journal of applied electrochemistry*, 1987, **17**, 828–840.
- [171] B. Y. Kim, I.-B. Shim, Z. O. Araci, S. S. Saavedra, O. L. Monti, N. R. Armstrong, R. Sahoo, D. N. Srivastava and J. Pyun, *Journal of the American Chemical Society*, 2010, **132**, 3234–3235.
- [172] J. Greeley and J. K. Nørskov, *The Journal of Physical Chemistry C*, 2009, **113**, 4932–4939.
- [173] K. S. Novoselov, A. K. Geim, S. V. Morozov, D. Jiang, Y. Zhang, S. V. Dubonos, I. V. Grigorieva and A. A. Firsov, *science*, 2004, **306**, 666–669.
- [174] Y. Liang, Y. Li, H. Wang, J. Zhou, J. Wang, T. Regier and H. Dai, *Nature materials*, 2011, **10**, 780.
- [175] Y. Liang, H. Wang, J. Zhou, Y. Li, J. Wang, T. Regier and H. Dai, *Journal of the American Chemical Society*, 2012, **134**, 3517–3523.
- [176] Q. Liu, J. Jin and J. Zhang, *ACS applied materials & interfaces*, 2013, **5**, 5002–5008.
- [177] C. Gómez-Navarro, R. T. Weitz, A. M. Bittner, M. Scolari, A. Mews, M. Burghard and K. Kern, *Nano letters*, 2007, **7**, 3499–3503.
- [178] Y. Xu, K. Sheng, C. Li and G. Shi, *Journal of Materials Chemistry*, 2011, **21**, 7376–7380.
- [179] L. Dai, D. W. Chang, J.-B. Baek and W. Lu, *small*, 2012, **8**, 1130–1166.
- [180] X. Wang, W. Li, Z. Chen, M. Waje and Y. Yan, *Journal of Power Sources*, 2006, **158**, 154–159.
- [181] X. Xie, Y. Li, Z.-Q. Liu, M. Haruta and W. Shen, *Nature*, 2009, **458**, 746.
- [182] S. Anantharaj, K. Karthick and S. Kundu, *Materials Today Energy*, 2017, **6**, 1–26.
- [183] J. Hessels, R. J. Detz, M. T. M. Koper and J. N. H. Reek, *Chem. Eur. J.*, 2017, **23**, 16413–16418.

- [184] B. S. Yeao and A. T. Bell, *J. Am. Chem. Soc.*, 2011, **133**, 5587–5593.
- [185] M. Hamdani, R. N. Singh and P. Chartier, *Int. J. Electrochem. Sci.*, 2010, **5**, 556–577.
- [186] F. Jiao and H. Frei, *Angew. Chem. Int. Ed.*, 2009, **48**, 1841–1844.
- [187] M. Zhang, M. de Respinis and H. Frei, *Nature Chemistry*, 2014, **6**, 362–367.
- [188] M. W. Kanan and D. G. Nocera, *Science*, 2008, **321**, 1072–1075.
- [189] Z. Cai, Y. Bi, E. Hu, W. Liu, N. Dwarica, Y. Tian, X. Li, Y. Kuang, Y. Li, X. Q. Yang, H. Wang and X. Sun, *Adv. Energy Mat.*, 2018, **8**, 1701694.
- [190] X. Xie, Y. Li, Z. Q. Liu, M. Haruta and W. Shen, *Nature*, 2009, **458**, 746–749.
- [191] A. Y. Khodakov, J. Lynch, D. Bazin, B. Rebours, N. Zanier, B. Moisson and P. Chaumette, *J. Catal.*, 1997, **168**, 16–25.
- [192] S. Zafeiratos, T. Dintzer, D. Teschner, R. Blume, M. Havecker, A. Knop-Gericke and R. Schlögl, *J. Catal.*, 2010, **269**, 309–317.
- [193] Y.-C. Liu, J. A. Koza and J. A. Switzer, *Electrochimica Acta*, 2014, **140**, 359–365.
- [194] S. Liu, H. Cheng, K. Xu, H. Ding, J. Zhou, B. Liu, W. Chu, C. Wu and Y. Xie, *ACS Energy Letters*, 2018, **4**, 423–429.
- [195] A. Bergmann, E. Martinez-Moreno, D. Teschner, P. Chernev, M. Glied, J. F. De Araújo, T. Reier, H. Dau and P. Strasser, *Nature communications*, 2015, **6**, 8625.
- [196] K. Klingan, F. Ringleb, I. Zaharieva, J. Heidkamp, P. Chernev, D. Gonzalez-Flores, M. Risch, A. Fischer and H. Dau, *ChemSusChem*, 2014, **7**, 1301–1310.
- [197] J. Willsau, O. Wolter and J. Heitbaum, *Journal of electroanalytical chemistry and interfacial electrochemistry*, 1985, **195**, 299–306.
- [198] M. Wohlfahrt-Mehrens and J. Heitbaum, *Journal of electroanalytical chemistry and interfacial electrochemistry*, 1987, **237**, 251–260.
- [199] F. Reikowski, F. Maroun, I. Pacheco, T. Wiegmann, P. Allongue, J. Stettner and O. M. Magnussen, *ACS Catalysis*, 2019, **9**, 3811–3821.
- [200] M. Risch, V. Khare, I. Zaharieva, L. Gerencser, P. Chernev and H. Dau, *Journal of the American Chemical Society*, 2009, **131**, 6936–6937.

- [201] M. Favaro, J. Yang, S. Nappini, E. Magnano, F. M. Toma, E. J. Crumlin, J. Yano and I. D. Sharp, *Journal of the American Chemical Society*, 2017, **139**, 8960–8970.
- [202] P. Chen, K. Xu, Z. Fang, Y. Tong, J. Wu, X. Lu, X. Peng, H. Ding, C. Wu and Y. Xie, *Angewandte Chemie International Edition*, 2015, **54**, 14710–14714.
- [203] A. Kulkarni, S. Siahrostami, A. Patel and J. Nørskov, *Chem. Rev.*, 2018, **118**, 2302–2312.
- [204] E. Skulason and H. Jonsson, *Advances Phys.:X*, 2017, **2**, 481–495.
- [205] J. Hussain, H. Jonsson and E. Skulason, *Faraday Discuss.*, 2016, **195**, 619–636.
- [206] J. Rossmeisl, Z. W. Qu, H. Zhu, G. J. Kroes and J. Nørskov, *J. Electroanal. Chem.*, 2007, **607**, 83–89.
- [207] J. Nørskov, J. Rossmeisl, A. Lagadottir, L. Lindqvist, J. R. Kitchin, T. Bligaard and H. Jonsson, *J. Phys. Chem. B.*, 2004, **108**, 17886–17892.
- [208] J. Nørskov, T. Bligaard, J. Rossmeisl and C. H. Christensen, *Nature Chemistry*, 2009, **1**, 37–46.
- [209] J. Chen, X. Wu and A. Selloni, *Physical Review B*, 2011, **83**, 245204.
- [210] V. Shinde, S. Mahadik, T. Gujar and C. Lokhande, *Applied Surface Science*, 2006, **252**, 7487–7492.
- [211] K. J. Kim and Y. R. Park, *Solid state communications*, 2003, **127**, 25–28.
- [212] J. Chen and A. Selloni, *Physical Review B*, 2012, **85**, 085306.
- [213] C. Loschen, J. Carrasco, K. M. Neyman and F. Illas, *Physical Review B*, 2007, **75**, 035115.
- [214] J. L. Da Silva, M. V. Ganduglia-Pirovano and J. Sauer, *Physical Review B*, 2007, **76**, 125117.
- [215] F. Labat, P. Baranek, C. Domain, C. Minot and C. Adamo, *The Journal of chemical physics*, 2007, **126**, 154703.
- [216] J. Paier, M. Marsman, K. Hummer, G. Kresse, I. C. Gerber and J. G. Ángyán, *The Journal of chemical physics*, 2006, **124**, 154709.
- [217] J. B. Goodenough and A. L. Loeb, *Physical Review*, 1955, **98**, 391.
- [218] C. Y. Ma, Z. Mu, J. J. Li, Y. G. Jin, J. Cheng, G. Q. Lu, Z. P. Hao and S. Z. Qiao, *Journal of the American Chemical Society*, 2010, **132**, 2608–2613.

- [219] S. Petitto and M. Langell, *Surface science*, 2005, **599**, 27–40.
- [220] C. Vaz, H.-Q. Wang, C. Ahn, V. Henrich, M. Baykara, T. Schwendemann, N. Pilet, B. Albers, U. Schwarz, L. Zhang *et al.*, *Surface Science*, 2009, **603**, 291–297.
- [221] J. Rossmeisl, A. Logadottir and J. K. Nørskov, *Chemical physics*, 2005, **319**, 178–184.
- [222] S. R. Alvarado, Y. Guo, T. P. A. Ruberu, A. Bakac and J. Vela, *The Journal of Physical Chemistry C*, 2012, **116**, 10382–10389.
- [223] R. G. Delaplane, J. A. Ibers, J. R. Ferraro and J. J. Rush, *The Journal of Chemical Physics*, 1969, **50**, 1920–1927.
- [224] J. Chen and A. Selloni, *The Journal of Physical Chemistry C*, 2013, **117**, 20002–20006.
- [225] M. Deliens and H. Goethals, *Mineralogical Magazine*, 1973, **39**, 152–157.
- [226] M. Bajdich, M. García-Mota, A. Vojvodic, J. K. Nørskov and A. T. Bell, *Journal of the American chemical Society*, 2013, **135**, 13521–13530.
- [227] M. García-Mota, M. Bajdich, V. Viswanathan, A. Vojvodic, A. T. Bell and J. K. Nørskov, *The Journal of Physical Chemistry C*, 2012, **116**, 21077–21082.
- [228] C. Changyan, D. Zhifeng, L. Hua and S. Weigu, *Chinese Journal of Catalysis*, 2012, **33**, 1334–1339.
- [229] O. Bjorneholm, M. Hansen, A. Hodgson, L. Liu, D. Limmer, A. Michaelides, P. Pedevilla, J. Rossmeisl, H. Shen, G. Tocci, E. Tyrode, M. Walz, J. Werner and H. Bluhm, *Chem. Rev.*, 2016, **116**, 7698–7726.
- [230] T. Roman and A. Gross, *Catalysis Today*, 2013, **202**, 183–190.
- [231] F. Gossenberger, T. Roman and A. Gross, *Electrochim. Acta*, 2016, **216**, 152–159.
- [232] J. Hussain, H. Jonsson and E. Skulason, *ACS Catal.*, 2018, **8**, 5240–5249.
- [233] S. Sakong, K. Forster-Tonigold and A. Gross, *J. Chem. Phys.*, 2016, **144**, 194701–194709.
- [234] S. Sakong, M. Nadarian, K. Mathew, R. G. Hennig and A. Gross, *J. Chem. Phys.*, 2015, **142**, 234107–234118.
- [235] J. Cheng and M. Sprik, *J. Phys. Condens. Matter*, 2014, **26**, 244108–244118.
- [236] A. Bouzid and A. Pasquarello, *J. Phys. Chem. Lett.*, 2018, **9**, 1880–1884.

- [237] S. Surendralal, M. Todorova, M. W. Finnis and J. Neugebauer, *Phys. Rev. Letters*, 2018, **120**, 246801–246905.
- [238] C. Zhang, *J. Chem. Phys.*, 2018, **149**, 031103–031107.
- [239] C. Zhang and M. Sprik, *Phys. Rev. B.*, 2016, **94**, 245309–245326.
- [240] M. Sulpizi, M.-P. Gaigeot and M. Sprik, *J. Chem. Theory Comput.*, 2012, **8**, 1037–1047.
- [241] S. Pezzotti, D. R. Galimberti, Y. R. Shen and M.-P. Gaigeot, *Phys. Chem. Chem. Phys.*, 2018, **20**, 5190–5199.
- [242] S. Pezzotti, D. R. Galimberti, Y. R. Shen and M.-P. Gaigeot, *Minerals*, 2018, **8**, 305–321.
- [243] M. Pfeiffer-Laplaud, M.-P. Gaigeot and M. Sulpizi, *J. Phys. Chem. Lett.*, 2016, **7**, 3229.
- [244] M. Pfeiffer-Laplaud and M.-P. Gaigeot, *J. Phys. Chem. C.*, 2016, **120**, 14034.
- [245] M. Pfeiffer-Laplaud and M.-P. Gaigeot, *J. Phys. Chem. C.*, 2016, **120**, 4866.
- [246] S. C. Petitto, E. M. Marsh, G. A. Carson and M. A. Langell, *J. Mol. Catal. A: Chem.*, 2008, **281**, 49–58.
- [247] F. Zasada, W. Pirkorz, S. Cristol, J. F. Paul, A. Kotarba and Z. Sojka, *J. Phys. Chem. C.*, 2010, **114**, 22245–22253.
- [248] X. L. Xu and J. Li, *Surf. Sci.*, 2011, **605**, 1962–1967.
- [249] J. Chen and A. Selloni, *J. Phys. Chem. Lett.*, 2012, **3**, 2808–2814.
- [250] S. Selcuk and A. Selloni, *J. Phys. Chem. C.*, 2015, **119**, 9973–9979.
- [251] J. Chen, X. Wu and A. Selloni, *Phys. Rev. B.*, 2011, **83**, 245204.
- [252] J. Chen, X. Wu and A. Selloni, *J. Phys. Chem. C.*, 2013, **117**, 20002–20006.
- [253] I. Ledezma-Yanez, W. D. Z. Wallace, P. Sebastian-Pascual, V. Climent, J. M. Feliu and M. T. M. Koper, *Nature Energy*, 2017, **2**, 17031–17036.
- [254] F. Creazzo, D. R. Galimberti, S. Pezzotti and M.-P. Gaigeot, *The Journal of chemical physics*, 2019, **150**, 041721.
- [255] J. Hutter, M. Iannuzzi, F. Schiffmann and J. VandeVondele, *WIREs Comput Mol Sci*, 2014, **4**, 15–25.
- [256] J. VandeVondele, M. Krack, F. Mohamed, M. Parrinello, T. Chassaing and J. Hutter, *Comp. Phys. Comm.*, 2005, **167**, 103–128.

- [257] K. Burke, J. Perdew and M. Ernzerhof, *Phys. Rev. Lett*, 1997, **78**, 1396.
- [258] S. Schnur and A. Groß, *New Journal of Physics*, 2009, **11**, 125003.
- [259] E. Schwegler, J. C. Grossman, F. Gygi and G. Galli, *J. Chem. Phys.*, 2004, **121**, 5400–5409.
- [260] S. Goedecker, M. Teter and J. Hutter, *Phys. Rev. B.*, 1996, **54**, 1703–1710.
- [261] J. Hubbard, *Proc. R. Soc. Lond. A*, 1963, **276**, 238–257.
- [262] V. I. Anisimov, J. Zaanen and O. K. Andersen, *Physical Review B*, 1991, **44**, 943.
- [263] S. Grimme, *J. Comput. Chem.*, 2004, **25**, 1463–1473.
- [264] S. Grimme, *J. Comput. Chem.*, 2006, **27**, 1787–1799.
- [265] W. B. D. F.R.S., *The London, Edinburgh, and Dublin Philosophical Magazine and Journal of Science*, 1915, **30**, 305–315.
- [266] S. Nishikawa, *Proceedings of the Tokyo Mathematico-Physical Society. 2nd Series*, 1915, **8**, 199–209\_1.
- [267] S. Laporte, F. Finocchi, L. Paulatto, M. Blanchard, E. Balan, F. Guyot and A. M. Saitta, *Phys. Chem. Chem. Phys.*, 2015, **17**, 20382–20390.
- [268] S. Pezzotti, D. R. Galimberti and M.-P. Gaigeot, *J. Phys. Chem. Lett.*, 2017, **8**, 3133–3141.
- [269] A. Morita and J. T. Hynes, *J. Phys. Chem. B.*, 2002, **106**, 673–685.
- [270] A. Morita and T. Ishiyama, *Phys.Chem.Chem.Phys.*, 2008, **10**, 5801–5816.
- [271] R. Khatib, E. H. G. Backus, M. Bonn, M.-J. Perez-Haro, M.-P. Gaigeot and M. Sulpizi, *Sci. Reports*, 2016, **6**, 24287.
- [272] J. D. Cyran, M. A. Donovan, D. Vollmer, F. S. Brigiano, S. Pezzotti, D. R. Galimberti, M.-P. Gaigeot, M. Bonn and E. H. Backus, *Proceedings of the National Academy of Sciences*, 2019, **116**, 1520–1525.
- [273] S. A. Corcelli and J. L. Skinner, *J. Phys. Chem. A.*, 2005, **109**, 6154–6165.
- [274] V. Shinde, S. Mahadik, T. Gujar and C. Lokhande, *Applied Surface Science*, 2006, **252**, 7487–7492.
- [275] K. J. Kim and Y. R. Park, *Solid state communications*, 2003, **127**, 25–28.
- [276] S. Pezzotti, A. Serva and M.-P. Gaigeot, *J. Chem. Phys.*, 2018.

- [277] A. Serva, S. Pezzotti, S. Bougueroua, D. R. Galimberti and M.-P. Gaigeot, *Journal of Molecular Structure*, 2018, **1165**, 71 – 78.
- [278] J. Chen and A. Selloni, *The Journal of Physical Chemistry Letters*, 2012, **3**, 2808–2814.
- [279] J. Chen and A. Selloni, *The Journal of Physical Chemistry C*, 2013, **117**, 20002–20006.
- [280] A. Cimas, F. Tielens, M. Sulpizi, M.-P. Gaigeot and D. Costa, *J. Phys: Condens. Matt.*, 2014, **26**, 244106.
- [281] Y.-C. Wen, S. Zha, X. Liu, S. Yang, P. Guo, G. Shi, H. Fang, Y. R. Shen and C. Tian, *Phys. Rev. Lett.*, 2016, **116**, 016101.
- [282] S. Pezzotti, D. R. Galimberti and M.-P. Gaigeot, *Physical Chemistry Chemical Physics*, 2019, **21**, 22188–22202.
- [283] A. Willard and D. Chandler, *J. Phys. Chem. B.*, 2010, **114**, 1954–1958.
- [284] M. T. Greiner, L. Chai, M. G. Helander, W.-M. Tang and Z.-H. Lu, *Advanced Functional Materials*, 2012, **22**, 4557–4568.
- [285] J. Filhol and M. Bocquet, *Chem. Phys. Letters*, **438**, 203.
- [286] F. Bellucci, S. S. Lee, J. D. Kubicki, A. Bandura, Z. Zhang, D. J. Wesolowski and P. Fenter, *J. Phys. Chem. C*, 2015, **119**, 4778–4788.
- [287] M. J. DelloStritto, J. Kubicki and J. O. Sofo, *J. Phys.: Condens. Matter*, 2014, **26**, 244101–244112.
- [288] A. M. Saitta, F. Saija and P. V. Giaquinta, *Physical review letters*, 2012, **108**, 207801.
- [289] G. Cassone, F. Creazzo, P. V. Giaquinta, F. Saija and A. M. Saitta, *Physical Chemistry Chemical Physics*, 2016, **18**, 23164–23173.
- [290] G. Cassone, F. Creazzo, P. V. Giaquinta, J. Sponer and F. Saija, *Physical Chemistry Chemical Physics*, 2017, **19**, 20420–20429.
- [291] G. Cassone, F. Creazzo and F. Saija, *Molecular Simulation*, 2018, 1–8.
- [292] S. Yip, *Handbook of materials modeling*, Springer Science & Business Media, 2007.
- [293] S. Surendralal, M. Todorova, M. W. Finnis and J. Neugebauer, *Physical review letters*, 2018, **120**, 246801.
- [294] E. Skulason and H. Jonsson, *Advances in Physics: X*, 2017, **2**, 481–495.
- [295] A. Kumar and C. Cucinotta, *PhD manuscript*, 2019.

- [296] J. A. Gauthier, C. F. Dickens, L. D. Chen, A. D. Doyle and J. K. Nørskov, *The Journal of Physical Chemistry C*, 2017, **121**, 11455–11463.
- [297] A. Bouzid and A. Pasquarello, *The journal of physical chemistry letters*, 2018, **9**, 1880–1884.
- [298] S. Grimme, *Journal of computational chemistry*, 2004, **25**, 1463–1473.
- [299] S. Grimme, *Journal of computational chemistry*, 2006, **27**, 1787–1799.
- [300] A. Laio and M. Parrinello, *Proceedings of the National Academy of Sciences*, 2002, **99**, 12562–12566.
- [301] P. G. Bolhuis, D. Chandler, C. Dellago and P. L. Geissler, *Annual review of physical chemistry*, 2002, **53**, 291–318.
- [302] P. L. Geissler, C. Dellago and D. Chandler, *The Journal of Physical Chemistry B*, 1999, **103**, 3706–3710.
- [303] B. Ensing, M. De Vivo, Z. Liu, P. Moore and M. L. Klein, *Accounts of chemical research*, 2006, **39**, 73–81.
- [304] N. V. Plotnikov, B. R. Prasad, S. Chakrabarty, Z. T. Chu and A. Warshel, *The Journal of Physical Chemistry B*, 2013, **117**, 12807–12819.
- [305] G. Cassone, F. Pietrucci, F. Saija, F. Guyot, J. Sponer, J. E. Sponer and A. M. Saitta, *Sci. Rep.*, 2017, **7**, year.
- [306] G. Cassone, J. Sponer, J. E. Sponer, F. Pietrucci, A. M. Saitta and F. Saija, *Chem. Commun.*, 2018, **54**, 3211–3214.
- [307] G. A. Tribello, M. Bonomi, D. Branduardi, C. Camilloni and G. Bussi, *Computer Physics Communications*, 2014, **185**, 604–613.
- [308] M. Zhang, M. De Respinis and H. Frei, *Nature chemistry*, 2014, **6**, 362.
- [309] M. T. Koper, *Nanoscale*, 2011, **3**, 2054–2073.
- [310] C. P. Plaisance and R. A. van Santen, *Journal of the American Chemical Society*, 2015, **137**, 14660–14672.
- [311] H. H. Pham, M.-J. Cheng, H. Frei and L.-W. Wang, *ACS Catalysis*, 2016, **6**, 5610–5617.
- [312] W. Rüttinger and G. C. Dismukes, *Chemical Reviews*, 1997, **97**, 1–24.
- [313] L.-P. Wang and T. Van Voorhis, *The Journal of Physical Chemistry Letters*, 2011, **2**, 2200–2204.
- [314] Y. Pushkar, J. Yano, K. Sauer, A. Boussac and V. K. Yachandra, *Proceedings of the National Academy of Sciences*, 2008, **105**, 1879–1884.

- [315] O. Diaz-Morales, D. Ferrus-Suspedra and M. T. Koper, *Chemical science*, 2016, **7**, 2639–2645.
- [316] A. Valdes, Z.-W. Qu, G.-J. Kroes, J. Rossmeisl and J. K. Nørskov, *The Journal of Physical Chemistry C*, 2008, **112**, 9872–9879.
- [317] A. Rimola, M. Fabbiani, M. Sodupe, P. Ugliengo and G. Martra, *ACS Catalysis*, 2018, **8**, 4558–4568.
- [318] N. Marzari, A. A. Mostofi, J. R. Yates, I. Souza and D. Vanderbilt, *Reviews of Modern Physics*, 2012, **84**, 1419.
- [319] F. F. Crim, *Faraday discussions*, 2012, **157**, 9–26.
- [320] A. J. Orr-Ewing, D. R. Glowacki, S. J. Greaves and R. A. Rose, *The journal of physical chemistry letters*, 2011, **2**, 1139–1144.
- [321] A. J. Orr-Ewing, *The Journal of chemical physics*, 2014, **140**, 090901.
- [322] P. Bilski, R. N. Holt and C. F. Chignell, *Journal of Photochemistry and Photobiology A: Chemistry*, 1997, **109**, 243–249.
- [323] B. Reynafarje, L. E. Costa and A. L. Lehninger, *Analytical biochemistry*, 1985, **145**, 406–418.
- [324] Y. V. Geletii, C. L. Hill, R. H. Atalla and I. A. Weinstock, *Journal of the American Chemical Society*, 2006, **128**, 17033–17042.
- [325] E. Mugnier, A. Barnabé and P. Tailhades, *Solid State Ionics*, 2006, **177**, 607–612.
- [326] S. Pezzotti, D. R. Galimberti and M.-P. Gaigeot, *J. Phys. Chem. Lett.*, 2017, **8**, 3133–3141.
- [327] L. Poitier, *University Paris-Saclay, University d'Evry val d'Essonne, 2019, NNT: 2019SACLE032*.
- [328] F. Creazzo, S. Pezzotti, S. Bougueroua, A. Serva, J. Sponer, F. Saija, G. Cassone and M.-P. Gaigeot, *Physical Chemistry Chemical Physics*, 2020, **22**, 10438–10446.
- [329] A. Hassanali, F. Giberti, J. Cuny, T. D. Kühne and M. Parrinello, *Proceedings of the National Academy of Sciences*, 2013, **110**, 13723–13728.
- [330] V. Venkateshwaran, S. Vembanur and S. Garde, *pnas*, 2014, **111**, 8729–8734.
- [331] J. A. Kattirtzi, D. T. Limmer and A. P. Willard, *pnas*, 2017.
- [332] X. Zhao, S. Subrahmanyam and K. B. Eisenthal, *Chem. Phys. Lett.*, 1990, **171**, 558 – 562.

- [333] R. Bianco, S. Wang and J. T. Hynes, *J. Phys. Chem. A*, 2008, **112**, 9467–9476.
- [334] Y. Suzuki, K. Osawa, S. Yukita, T. Kobayashi and E. Tokunaga, *Applied Physics Letters*, 2016, **108**, 191103.
- [335] R. C. Tolman, *J. Chem. Phys.*, 1949, **17**, 333–337.
- [336] A. Serva, S. Pezzotti, S. Bougueroua, D. R. Galimberti and M.-P. Gaigeot, *J. Mol. Struct.*, 2018, **1165**, 71–78.
- [337] S. Pezzotti, A. Serva and M.-P. Gaigeot, *J. Chem. Phys.*, 2018, **148**, 174701.
- [338] S. Pezzotti and M.-P. Gaigeot, *Atmosphere*, 2018, **9**, 396.
- [339] M. Nikzad, A. R. Azimian, M. Rezaei and S. Nikzad, *J. Chem. Phys.*, 2017, **147**, 204701.
- [340] A. M. Saitta, F. Saija and P. V. Giaquinta, *Phys. Rev. Lett.*, 2012, **108**, 207801.
- [341] G. Cassone, P. V. Giaquinta, F. Saija and A. M. Saitta, *The Journal of Physical Chemistry B*, 2014, **118**, 4419–4424.
- [342] E. M. Stuve, *Chem. Phys. Lett.*, 2012, **519**, 1–17.
- [343] G. Cassone, F. Creazzo, P. V. Giaquinta, J. Sponer and F. Saija, *Physical Chemistry Chemical Physics*, 2017, **19**, 20420–20429.
- [344] Z. Hammadi, M. Descoins, E. Salançon and R. Morin, *App. Phys. Lett.*, 2012, **101**, 243110.
- [345] G. Cassone, F. Creazzo, P. V. Giaquinta, F. Saija and A. M. Saitta, *Physical Chemistry Chemical Physics*, 2016, **18**, 23164–23173.
- [346] G. Cassone, J. Sponer, S. Trusso and F. Saija, *Phys. Chem. Chem. Phys.*, 2019, **21**, 21205–21212.
- [347] A. D. Becke, *Phys. Rev. A*, 1988, **38**, 3098–3100.
- [348] C. Lee, W. Yang and R. G. Parr, *Phys. Rev. B*, 1988, **37**, 785–789.
- [349] S. Goedecker, M. Teter and J. Hutter, *Phys. Rev. B*, 1996, **54**, 1703.
- [350] S. Pezzotti, D. R. Galimberti, Y. R. Shen and M.-P. Gaigeot, *Phys. Chem. Chem. Phys.*, 2018, **20**, 5190–5199.
- [351] J. A. White, E. Schwegler, G. Galli and F. Gygi, *J. Chem. Phys.*, 2000, **113**, 4668–4673.
- [352] S. Pezzotti, D. Galimberti, Y. Shen and M.-P. Gaigeot, *Minerals*, 2018, **8**, 305.

- [353] G. Cassone, F. Creazzo and F. Saija, *Molecular Simulation*, 2019, **45**, 373–380.
- [354] T. von Grotthuß, *Mémoire sur la décomposition de l'eau et des corps qu'elle tient en dissolution à l'aide de l'électricité galvanique*, 1805.
- [355] P. L. Geissler, C. Dellago, D. Chandler, J. Hutter and M. Parrinello, *Science*, 2001, **291**, 2121–2124.
- [356] R. Car and M. Parrinello, *Physical review letters*, 1985, **55**, 2471.
- [357] S. Schnur and A. Groß, *Catalysis today*, 2011, **165**, 129–137.
- [358] R. A. Persson, V. Pattni, A. Singh, S. M. Kast and M. Heyden, *Journal of chemical theory and computation*, 2017, **13**, 4467–4481.
- [359] V. Conti Nibali, S. Pezzotti, F. Sebastiani, D. R. Galimberti, G. Schwaab, M. Heyden, M. P. Gageot and M. Havenith, *Submitted to J. Phys. Chem. Lett.*, March 2020.
- [360] D. Corradini, Y. Ishii, N. Ohtori and M. Salanne, *Modelling and Simulation in Materials Science and Engineering*, 2015, **23**, 074005.

**Titre :** Réaction d'évolution de l'oxygène aux interfaces d'oxydes de cobalt/eau liquide : électrocatalyse hétérogène par simulation de DFT-MD et de metadynamique

**Mots clés :** interfaces, oxydes de cobalt, eau liquide, simulation DFT-MD, metadynamique

**Résumé :** Dans cette thèse, des simulations DFT-MD couplées à des techniques innovantes de métadynamique, sont appliquées pour acquérir une compréhension globale des interfaces aqueuses d'oxyde de cobalt  $\text{Co}_3\text{O}_4$  et  $\text{CoO}(\text{OH})$  dans la catalyse de la réaction d'évolution de l'oxygène (OER), et ainsi éventuellement aider à la conception de nouveaux catalyseurs basés sur des matériaux non précieux, un domaine clé de la recherche scientifique et technologique, particulièrement important pour l'économie de l'hydrogène, pour les technologies vertes dans une période de temps avec une demande toujours plus croissante en énergie verte. Dans cette thèse, nous révélons étape par étape les mécanismes de l'OER sur les électrocatalyseurs aqueux d'oxyde de cobalt  $\text{Co}_3\text{O}_4$  et  $\text{CoO}(\text{OH})$  via de nouvelles techniques de métadynamique. Une caractérisation détaillée

des propriétés chimiques et physiques des interfaces aqueuses est fourni (la structure, la dynamique, la spectroscopie, le champ électrique), pour les surfaces (110)- $\text{Co}_3\text{O}_4$  et (0001)- $\text{CoO}(\text{OH})$  en contact avec l'eau liquide. En conséquence, l'OER en phase gazeuse et en phase liquide sont étudiés ici aux interfaces aqueuses (110)- $\text{Co}_3\text{O}_4$  et (0001)- $\text{CoO}(\text{OH})$  en adoptant une nouvelle approche de métadynamique d'échantillonnage amélioré, capable d'identifier et caractériser les mécanismes de réaction chimique et d'intégrer pleinement le rôle des degrés de liberté du solvant, permettant ainsi de dévoiler des réactivité chimique d'une complexité remarquable. L'énergétique, la cinétique et la thermodynamique derrière l'OER sont donc trouvés à ces surfaces d'oxyde de cobalt à l'interface avec l'eau.

**Title :** Oxygen Evolution Reaction at cobalt oxides/water interfaces : heterogeneous electrocatalysis by DFT-MD simulations & metadynamics

**Keywords :** interfaces, cobalt oxides, liquid water, DFT-MD simulation, metadynamics

**Abstract :** In this thesis, DFT-MD simulations, coupled with state-of-the-art metadynamics techniques, is applied to gain a global understanding of  $\text{Co}_3\text{O}_4$  and  $\text{CoO}(\text{OH})$  cobalt oxide aqueous interfaces in catalyzing the oxygen evolution reaction (OER), and hence possibly help in the design of novel catalysts based on non-precious materials, a current key field of research in science and technology, especially of importance for the hydrogen economy, for green technology in a period of time with an ever more growing demand in green-energy. In this thesis, we step-by-step reveal the OER mechanisms on spinel  $\text{Co}_3\text{O}_4$  and  $\text{CoO}(\text{OH})$  cobalt aqueous electrocatalysts carefully and rationally via novel metadynamics techniques.

A detailed characterization of chemical and physical properties of the aqueous interfaces is provided (*i.e.* structure, dynamics, spectroscopy, electric field), for the (110)- $\text{Co}_3\text{O}_4$  and (0001)- $\text{CoO}(\text{OH})$  aqueous surfaces. Accordingly, both gas-phase and liquid-phase OER are here investigated at the (110)- $\text{Co}_3\text{O}_4$  and (0001)- $\text{CoO}(\text{OH})$  adopting a novel enhanced sampling metadynamics approach able to address a wide range of chemical reaction mechanisms and to fully include the role of the solvent degrees of freedom, allowing to unveil reaction networks of remarkable complexity. The energetics, kinetics and thermodynamics behind the OER are therefore found at these cobalt oxide surfaces.